



HAL
open science

Clay-Kinesis Occurring in Natural Cases

Gulce Dinc

► **To cite this version:**

Gulce Dinc. Clay-Kinesis Occurring in Natural Cases. Earth Sciences. Université de Pau et des Pays de l'Adour, 2020. English. NNT : 2020PAUU3027 . tel-03140327

HAL Id: tel-03140327

<https://theses.hal.science/tel-03140327>

Submitted on 12 Feb 2021

HAL is a multi-disciplinary open access archive for the deposit and dissemination of scientific research documents, whether they are published or not. The documents may come from teaching and research institutions in France or abroad, or from public or private research centers.

L'archive ouverte pluridisciplinaire **HAL**, est destinée au dépôt et à la diffusion de documents scientifiques de niveau recherche, publiés ou non, émanant des établissements d'enseignement et de recherche français ou étrangers, des laboratoires publics ou privés.

*I would like to dedicate this thesis to my lovely family,
who raised me to become who I am
and Brian,
who handed me the best stone soup I never imagined I can*

*There is a pleasure in the pathless woods,
There is a rapture on the lonely shore,
There is society where none intrudes,
By the deep Sea, and music in its roar:
I love not Man the less, but Nature more.*

Lord Byron

Acknowledgments

There are many people I would like to thank for this PhD project to take place. If I had not thanked enough personally each of these individuals, I hope they will understand my eternal gratefulness by reading this section.

I had the pleasure to work for ION Geophysical upon my graduation from Rice University, Subsurface Geoscience Master's Program in 2013 and I have been given wonderful opportunities since then. For that, first and foremost, I sincerely would like to thank from the bottom of my heart to Brian Horn, who have recruited me back at school and became the best mentor I could have ever asked for following my graduation. Brian, I will be forever in debt for everything you have done for me including this PhD opportunity. '*Stone Soups*' are not always easy to make without a stone soup chef like you. Thank you for believing in me and teaching me the true meaning of goodwill.

During my employment with ION Geophysical, I had the chance to work in a very enjoyable and pleasant work environment and I am deeply thankful to all of my colleagues (especially Kyle Reuber, Antara Goswami, Mumu De, Jim Pindell and Rod Graham) and managers (Ken Williamson, Joe Gagliardi and Adrian McGrail) for providing me this opportunity.

After I mentioned my desire to do a PhD in Structural Geology to Brian and we both started to look at options, I met with my future PhD advisors Prof. Dr. Jean-Paul Callot and Dr. Jean-Claude Ringenbach in 2017, which initiated my journey from Houston, Texas to Pau, France and led to an incredibly fortunate research experience.

Jean-Paul, it was an honor to work with you during this PhD project. Thank you for your patience, kindness and understanding through my training. I admired your over-the-top perception on every geologic topic we have discussed and I re-admired your equally impressive ability to speak fast every time I re-listened to the voice recordings I have made. Like the rest of your students, I am proud to say that I was no exception to break that reputation of yours and I got amused discovering each anecdote I have missed while taking notes and re-discovering them on these voice recordings of yours.

Jean-Claude, it was a pleasure getting to know you and working with you in this PhD journey. I learned how to make cross-sections (even though they are never as beautiful as yours and Jean-Paul's), I greatly enjoyed our conversations and the geologic missions we have taken together, which were not only limited to geology (such as waking up at 5am to taste the '*kelle çorba*', or having a barbeque extravaganza on top of a '*hook structure*' in Sivas).

I humbly would like to thank both of you for accepting me as your student and turning me into a Structural Geologist from my Geophysicist roots. I appreciate everything I learned with you and I will carry these fun memories with me till the rest of my life.

During these last three years, besides working closely with Jean-Paul and Jean-Claude, I also had the privilege to work with a very welcoming Structural Geology Department at Total E&P, CSTJF, Pau. I would like to thank all my colleagues there; Jean-Yves Froute, Charlotte Nielsen (our lovely chef), Francois Sapin (my office mate from the dark side), Remy Martin (cookie chief in order for each Thursday), Charlie Kergaravat, Edouard Le Garzic, Thomas Maurin, Michael Denis, Jean-Paul Gomez, Vincenzo Spina, Christopher Wibberley, Richard Tozer, Etienne Legeay, and Esther Izquierdo-Llavall for a warm and welcoming atmosphere they have provided for me.

I also would like to take the chance to thank Total E&P for sponsoring my PhD research and providing me excellent geologic field trip opportunities along the way as I had the chance to visit Sivas, Turkey on multiple occasions for Salt Tectonics courses (under the guidance of Jean-Claude Ringenbach and Jean-Paul Callot), Azerbaijan Baku-Alat region for Mud Volcanoes (with Patrice Imbert and Francis Odonne) and Rakhine State, Myanmar for Shale Tectonics topic (with Jean-Paul Callot, Francis Odonne and Saw Mu Tha Lay Paw).

I would sincerely like to thank my family for supporting me my whole life on every decision I have taken including this PhD project. I am beyond lucky to have my parents Gulden Dinc and Irfan Dinc standing by my side and bracing the bitterness of their 'little girl' living far far away in abroad since 2011, my twin brother Atilla for being the best friend and 'dudi' I could have ever asked for in this life (you may finally assure yourself that I am not a 'fake (geo) physicist' anymore as I am officially changing my title into a geologist), my lovely grandparents (aka my 'annannis' Makbule Ozkan and 'dedis' Hasan Ozkan) for showing me the purest form of love and caring that exist in this entire universe. I would never be where I am today without your endless love and support.

Last but not least, I would like to thank you Olivier, mon petit Viking, from the bottom of my heart, for your sweetness, understanding and enormous patience throughout my journey writing this thesis. Thank you for teaching me the true meaning of love, caring and the art of making everything easier even in the hardest times... You were there when I was the most vulnerable, in need of calmness (and sometimes craziness as a partner-in-crime) during this last year. I'm not certain of many things in this life but I know that now or in the future, all will be fine with you and with us. Zuzuuu 😊

Remerciements

Je voudrais remercier beaucoup de personnes pour ce projet de doctorat. Si par malheur je ne les avais pas déjà suffisamment remercié de vive voix, j'espère qu'ils comprendront ici ma reconnaissance éternelle.

J'ai eu le plaisir de travailler pour ION Geophysical après avoir obtenu mon diplôme de l'Université Rice, en suivant une maîtrise en géosciences souterraines en 2013, ce qui m'aura permis d'avoir depuis de merveilleuses opportunités. C'est pour cela qu'avant tout et pour tout, je voudrais sincèrement remercier, du fond du cœur, Brian Horn, qui m'a recruté dès l'école et est devenu le meilleur mentor que je n'aurais jamais pu demander après l'obtention de mon diplôme. Je serai à jamais redevable pour tout ce que tu as fait pour moi, y compris cette opportunité de doctorat. Les «soupes de cailloux» ne sont pas toujours faciles à préparer sans un « chef de soupe de cailloux » comme toi. Merci d'avoir cru et de croire en moi. Merci de m'avoir appris le vrai sens de la bienveillance.

Au cours de mon emploi chez ION Geophysical, j'ai eu la chance de travailler dans un environnement de travail très agréable et je suis profondément reconnaissante envers tous mes collègues (en particulier Kyle Reuber, Antara Goswami, Mumu De, Jim Pindell et Rod Graham) et les managers (Ken Williamson, Joe Gagliardi et Adrian McGrail) pour m'avoir offert cette opportunité.

C'est après avoir mentionné à Brian mon désir de faire un doctorat en géologie structurale et que nous commençons à en examiner les possibilités, que j'ai pu rencontrer en 2017 mes futurs directeurs de thèse, le Professeur Jean-Paul Callot et le Docteur Jean-Claude Ringenbach, ce qui m'aura permis d'initier mon voyage de Houston -Texas- vers Pau -France- et de sceller, non sans émotion, le départ de cette expérience de recherche scientifique.

Jean-Paul, ce fut un honneur de travailler avec toi pendant ce projet de doctorat. Merci pour ta patience, ta gentillesse et ta compréhension au cours de ma formation. J'ai pu admirer ta vision perçante de chaque propos géologique dont nous avons discuté et j'étais éblouie devant ta capacité -tout aussi surnaturelle- à parler si vite, m'en rendant principalement compte chaque fois que j'écoutais à nouveau nos conversations sur les enregistrements vocaux que je prenais, me permettant également de découvrir avec beaucoup d'amusement toutes les anecdotes que j'avais manqué pendant la prise de notes. Je suis ainsi fière d'avoir pu faire partie de tes élèves sans déroger à ces principes qui font ta réputation.

Jean-Claude, ce fut un plaisir de te connaître et de travailler avec toi dans ce parcours doctoral. J'y ai appris à faire des coupes transversales (même si elles ne sont pas aussi belles que les tiennes et celles de Jean-

Paul), j'ai beaucoup apprécié nos conversations et les missions géologiques que nous avons menées ensemble, qui ne se limitaient pas à la géologie (comme le réveil à 5h du matin pour goûter le «kelle çorba», ou avoir un barbecue «extravaganza» au sommet d'une hook structure à Sivas).

Je voudrais sincèrement vous remercier tous les deux de m'avoir accepté comme votre étudiante et de m'avoir transformé en géologue structurale à partir de mes racines de géophysicienne. J'apprécie tout ce que j'ai appris avec vous et je garderai pour toujours ces souvenirs si drôles en moi.

Au cours de ces trois dernières années, en plus de travailler en étroite collaboration avec Jean-Paul et Jean-Claude, j'ai également eu le privilège d'être au contact de tout un service de géologie structurale très accueillant à l'endroit de Total E&P, CSTJF à Pau. Je voudrais remercier tous mes collègues là-bas; Jean-Yves Froute, Charlotte Nielsen (notre charmante chef), François Sapin (mon partenaire de bureau, mais du côté obscur), Rémy Martin (préposé chef des biscuits chaque jeudi), Charlie Kergaravat, Edouard Le Garzic, Thomas Maurin, Michael Denis, Jean-Paul Gomez, Vincenzo Spina, Christopher Wibberley, Richard Tozer, Etienne Legeay et Esther Izquierdo-Llavall, pour tous ces moments de bonheur et de bienveillance que j'ai pu vivre à leurs côtés.

Je voudrais également profiter de l'occasion pour remercier Total E&P pour avoir parrainé mes recherches de doctorat et m'avoir fourni d'excellentes opportunités de travaux de terrains durant cette période, ce qui m'aura permis de me rendre à Sivas, en Turquie à plusieurs reprises pour des cours de tectonique salifère (sous la direction de Jean-Claude Ringenbach et Jean-Paul Callot), en Azerbaïdjan dans les régions de Baku et Alat pour l'exploration des volcans de boue (avec Patrice Imbert et Francis Odonne) et dans l'état de Rakhine en Birmanie, pour l'étude de la tectonique de l'argile (avec Jean-Paul Callot, Francis Odonne et Saw Mu Tha Lay Paw).

Je voudrais sincèrement remercier ma famille de m'avoir soutenu toute ma vie dans chaque choix que j'ai pris, y compris dans ce projet de doctorat. J'ai par-dessus tout, la chance que mes parents Gülten Dinç et Irfan Dinç se tiennent à mes côtés et bravent toujours un peu plus l'amertume de savoir leur 'petite fille' vivant très loin à l'étranger depuis 2011, mon frère jumeau Atilla pour être le meilleur ami et le 'dudi' que je n'aurai jamais pu espérer dans cette vie (et sache que je ne suis désormais plus une 'fausse (géo) physicienne' car je deviens officiellement géologue), mes adorables grands-parents (alias mon 'Annanniş' Makbule Özkan et 'Dediş' Hasan Özkan) pour m'avoir enseigné la forme la plus pure d'amour et d'attention qui soit dans tout cet univers. Je ne serais jamais là où je suis aujourd'hui sans votre amour et votre soutien sans fin.

Enfin, je tiens à toi remercier Olivier (mon petit Viking), du fond du cœur, pour ton douceur, ta compréhension et ton immense patience tout au long de mon parcours pour rédiger cette thèse. Merci de m'avoir appris le vrai sens de l'amour, de la bienveillance et de l'art de tout rendre plus facile même dans les moments les plus difficiles... Tu étais là quand j'étais la plus vulnérable, en manque de calme (et parfois de folie en tant que partenaire-du-crime) cette dernière année. Je ne suis pas certain de beaucoup de choses dans cette vie mais je sais que maintenant ou dans le futur, tout ira bien pour toi et pour nous. Zuzuuu 😊

Teşekkür

Bu doktora projesi de dahil olmak üzere aldığım her kararda tüm hayatım boyunca bana destek olan canım aileme buradan içtenlikle teşekkür etmek istiyorum. Annem Gülten Dinç ve babam İrfan Dinç'e 2011'den beri hep yurtdışında, çok uzaklarda yaşayan ve 'hiç büyümeyen küçük kızlarının' yokluğuna katlandıkları, ikiz kardeşim ve aynı zamanda bu hayatta sahip olup olabileceğim en yakın arkadaşım olan Atilla'ya yani biricik <<dudi>> me beni her zaman düşündüğü, koruyup kolladığı, en bitanecik annanişim Makbule Özkan ve dedişim Hasan Özkan'a bu evrende var olan en saf sevgi ve şefkati bana gösterdikleri için kalbimin en derininden teşekkür ederim. Siz olmadan buralara asla gelemezdim, iyi ki varsınız, iyi ki yanımdasınız 😊

Three Years of PhD in Pictures:



Abstract of the PhD Thesis:

Shale deforms under three major principles; (i) seismic scale plasticity (folding and faulting), (ii) fluidization (mud volcanism), (iii) ductile strain/plasticity (distributed slow motion) and can mimic salt deformation under stress and strain. Ductility of these two rocks are governed by processes taking place beyond the 'scale of observation' (e.g. crystalline plasticity and pressure solution for salt; shear bands, folding and faulting at small scale for shale) forming a 'distributed deformation'. Various controlling factors such as confinement pressure, temperature, water content, rate of loading, and amount of sedimentation, regulate the ductile behavior of these rocks. When these conditions are met, ductile rocks (e.g. salt and shale) display behavioral similarity to viscous materials (e.g. fluids) in nature and their specific deformation-related signature (e.g. halokinesis, argilokinesis) can be recorded within the sedimentary package surrounding these rock formations.

However, the mobilization pattern of shales and hence the topic of Shale Tectonism is not yet as-well-identified-as salt due to the usual bad quality of acquired subsurface data (seismic) and the lack of well-preserved outcrop examples we are able to access around the world. Even though certain structures depicted as 'diapirs', 'canopy features', 'minibasins' and 'welds' have been recorded by the surrounding sedimentary cover in some natural cases and reported by researchers; unlike salt, no such conclusive remarks are made on the topic of shale mobility.

In this PhD study, we worked on a well-imaged high-quality 3D seismic dataset and aimed to make a geometrical analysis of deformation in a shale-prone system (Ceduna Sub-Basin located in Great Bight Basin, Offshore Australia) in order to compare it with Salt Tectonics. The main purpose was to display the importance of mobilized shales on the structural development as well as proposing a kinematic scenario for the whole deltaic system (White Pointer Delta) driven above a thick shale detachment level (Blue Whale Formation).

The area has been previously studied by numerous researchers with 2D regional lines with an aim to understand the controlling basin dynamics (see reviews from Totterdell, et al., 2000; Totterdell and Krassay, 2003; Totterdell and Bradshaw, 2004; Totterdell et al., 2008; Espurt et al., 2009; Espurt et al., 2012). Espurt et al., (2012) defined (i) the White Pointer Delta as a structure mainly formed during the tectonic denudation of the mantle and evolved on top of the exhumed mantle and the (ii) Hammerhead Delta as a gliding delta formed during oceanic seafloor spreading and sag basin evolution of the southern Australian margin, mostly stable with only frontal gravitational sliding that is balanced by the extensional feature at the rear (Totterdell and Krassay, 2003; Espurt et al., 2009; King and Backé, 2010).

The White Pointer interval is described as a delta setting dominated by growth faults above a detachment level consisting of mobile Blue Whale shales with three main structural domains standing out as; (i) growth faulting dominated by listric faults at the proximal part, (ii) transitional zone between the zones of growth faulting and the thrust front, which is noted by a 'complex region' consisting of chaotic seismic reflections

and (iii) the compressional front featuring a northeasterly dipping imbricate thrust fan system (Totterdell & Krassay, 2003). Even though the studies made with vintage 2D seismic datasets pointed out to an inflated shale interval in this thrust front of the delta, they provided limited detailed explanations (see reviews of Totterdell & Krassay 2003, Totterdell & Bradshaw 2004; Totterdell et al., 2008; Espurt et al., 2009 and 2012; MacDonald et al., 2012; MacDonald, 2013).

We have carried out a structural analysis scheme on a 3D seismic PSDM dataset acquired by PGS in 2011 from Ceduna Sub-Basin, offshore Australia for this research, which has given us an immense advantage on (i) identifying the 'suggested shale features of the delta front' that was mainly described as a thrust complex component on previous studies due to lack of well-imaged supplementary datasets, and to (ii) re-

compare/interpret the regional 2D lines to the high resolution 3D block in order to make a cross-correlation with the current and newly-acquired knowledge on potential evidences for particular behavior of shale.

Following the seismic interpretation scheme we have developed, the study area revealed two structurally differentiating domain on time-slice view: a domain dominated by listric faulting and a minibasin domain. Characteristics of which distinctively separated from each other and certain salt-like deformation features such as wedges, welds, minibasins were identified in the minibasin domain (distal part of White Pointer Delta) of the seismic dataset.

Within the White Pointer Delta minibasin interval, we identified many salt-like features such as wedges, welds and pod-like minibasins. In addition to these salt-like deformation structures, we detected two particular domains, which are namely: (1) Minibasin Evolution & Welding and (2) Shale-Cored Growth Folds. These domains were found to be specific to the distal part of the delta, where the 'shale-cored folding' resembles 'salt diapirism' by appearance with radial faults, polygonal cracks and caldera-like collapses seen on seismic view. A key feature here is the development of a major thrust fault duplexing the minibasin domain, and evidencing a potential change in rheological behavior of the shale level; from initially mobile (enabling the development of minibasins) to lately more rigid and even fragile accommodating the delta toe shortening by thrusting.

Based on the seismic data findings, we proposed a kinematic scenario depicting the shale mobilization in the White Pointer Delta (Ceduna Sub-Basin), to be observed under four domains: (1) proximal extension, (2) mid-slope translation, (3) down-building at the base-slope and (4) shortening in the distal part. To put it into context: (1) the extension domain is where we observe extensional delta features triggered by the gravity-driven listric faults, (2) the translation domain is where we see shale-related translation features such as shale rollers, (3) the shortening domain represents the shortening/compression elements such as fish-tail features and thrusts, and (4) the down-building domain appearing primarily at the very distal part of the delta (delta toe), where we first observe the initiation of minibasins with down-building strata around the piling up gravity-driven shale deposits.

In order to complement the seismic interpretation study we have conducted on Ceduna 3D seismic dataset, we also performed a fieldwork in the Rakhine State of Myanmar to look at outcrop findings in a shale-prone environment, where we observe mud volcanoes and a shale-based deltaic setting. Fieldwork observations and samples require a detailed petrographic and quantitative inspection in order to understand the temperature and pressure conditions of shale during the time of burial as well as the environmental effects such as fluid content or thermal gradient for confirmation. However, our initial fieldwork-based first hand conclusion lies towards a scenario, in which the shale deformation did not occur at a great depth subjected to large overpressures, but rather took place at shallow depth in a

distributed slow-motion manner similar to our findings from Ceduna Sub-Basin, White Pointer Delta and Salt Tectonics as it is referred to in the literature.

At the end of our research, we have come to conclusion that:

- At large scale, shales display a plastic deformation pattern and behave like a fluid in a viscous manner mimicking salt deposits, while the deformation signature associated with shale mobilization can be recorded by the sediment strata surrounding these shale remnants (e.g. argilokinesis).
- From technical point of view, the mobile shale domain of the White Pointer Delta presents characteristics of salt tectonics such as wedges, associated unconformities, welds and minibasins. The gliding delta evolve from

a classic deep water fold and thrust belt towards a thrust duplex, which suggests a change in shale rheology and strain hardening favoring a localization of deformation.

- Locally, shales can be fluidized and form mud volcanoes in the studied Ceduna Sub-Basin area.

It is of utmost importance to further investigate these analogies in order to conclude on the fact that at large scale, shale can mimic salt deformation and that the concept of Salt Tectonics can be applied to Shale Tectonics. First hand results of our research support this idea and encourage a promising path for the way forward.

Key Words: Shale Tectonics, Ceduna Sub-Basin, White Pointer Delta, Shale Mobilization, Argilokinesis.

Résumé de la Thèse de Doctorat :

Les argiles se déforment selon trois modes principaux; (i) plasticité à l'échelle sismique (plis et failles), (ii) fluidisation (volcanisme de boue), (iii) déformation ductile / plasticité (déformation distribuée) et peut imiter la déformation du sel sous certaines conditions. La ductilité de ces deux roches est régie par des processus se déroulant au-delà de «l'échelle d'observation» (e.g. plasticité cristalline et pression-solution pour le sel, bandes de cisaillement, pliage et faille à petite échelle pour les argiles) formant une «déformation distribuée». Divers facteurs de contrôle tels que la pression de confinement, la température, la teneur en eau, le taux de chargement et la quantité de sédimentation, régulent le comportement ductile de ces roches. Lorsque ces conditions sont remplies, les roches ductiles (e.g. le sel et le schiste) présentent une similitude comportementale avec les matériaux visqueux (e.g. les fluides) dans la nature et leur signature spécifique liée à la déformation (e.g. halocinèse, argilocinèse) peut être enregistrée dans les séquences sédimentaires entourant ces formations.

Cependant, le modèle de mobilisation ductile des argiles (la tectonique argileuse) n'est pas encore aussi bien identifié que le sel, principalement en raison de la mauvaise qualité des données de subsurface acquises (sismiques) et du manque d'exemples d'affleurements bien préservés. Même si certaines structures décrites comme des «diapirs», des «canopées», des «minibasins» et des «welds» ont été mises en évidence dans la couverture sédimentaire environnant certains cas naturels et rapportées par les chercheurs, il n'y a actuellement pas de consensus, contrairement au sel, concernant la mobilité des argiles.

Dans cette étude de doctorat, nous avons travaillé sur un ensemble de données sismiques 3D de haute qualité bien imagées et avons cherché à faire une analyse géométrique de la déformation dans un système sujet à la tectonique argileuse (le bassin de Ceduna situé dans la Grande Baie, Australie) afin d'illustrer les analogies avec la tectonique salifère. L'objectif principal était de montrer l'importance de la mobilisation argileuse sur le développement structural et de proposer un scénario cinématique pour l'ensemble du système deltaïque (White Pointer Delta) gravitationnellement instables au-dessus d'un niveau de détachement (Blue Whale Formation).

La zone a été précédemment étudiée par de nombreux chercheurs avec des lignes régionales 2D dans le but de comprendre la dynamique du bassin (voir les revues de Totterdell, et al., 2000; Totterdell et Krassay, 2003; Totterdell et Bradshaw, 2004; Totterdell et al., 2008; Espurt et al., 2009; Espurt et al., 2012). Espurt et al., (2012) ont défini (i) le delta White Pointer comme une structure principalement formée lors de la dénudation tectonique du manteau et qui a évolué en glissement gravitaire global au-dessus de la marge passive du manteau exhumé et (ii) le delta Hammerhead comme un delta formé secondairement lors de l'océanisation, principalement stable avec uniquement un glissement gravitationnel frontal (Totterdell et Krassay, 2003; Espurt et al., 2009; King et Backé, 2010).

L'intervalle du White Pointer est décrit comme un delta dominé par des failles de croissance au-dessus d'un niveau de détachement constitué des argiles mobiles de la formation Blue Whale avec trois domaines structuraux principaux se distinguant comme : (i) les failles de croissance dominées par des failles listriques

en domaine proximale, (ii) la zone de transition entre les zones de failles de croissance et le front compressif, qui se caractérise par une "région complexe" constituée de réflexions sismiques chaotiques et (iii) le front compressif comportant un système d'écaillés imbriquées plongeant vers le nord-est (Totterdell et Krassay, 2003). Même si les études réalisées avec des ensembles de données sismiques 2D d'époque ont souligné un intervalle de schiste épais, elles ont fourni des explications détaillées limitées (voir les revues de Totterdell & Krassay 2003, Totterdell & Bradshaw 2004; Totterdell et al., 2008 ; Espurt et al., 2009 et 2012; MacDonald et al., 2012; MacDonald, 2013).

Nous avons réalisé une analyse structurale sur un jeu de données PSDM sismique 3D acquis par PGS en 2011, ce qui nous a donné un immense avantage sur (i) l'identification des "structures caractéristiques de la tectonique, et pour (ii) re-comparer / interpréter les lignes 2D régionales au bloc 3D haute résolution afin de faire une corrélation croisée avec les connaissances actuelles et nouvellement acquises sur les preuves potentielles d'un comportement particulier d'argile.

En suivant le schéma d'interprétation sismique que nous avons développé, la zone d'étude a révélé deux domaines structurellement différenciant cartographiquement: un domaine dominé par les failles listriques et un domaine minibasin. Des caractéristiques propres de la tectonique salifère ont été observés tels que les cicatrices, les minibasins, les séquences de type halokinetic ont été identifiées dans le domaine du minibasin (partie distale du delta du White Pointer) de l'ensemble de données sismiques.

Dans l'intervalle des minibasins du delta du White Pointer, nous avons identifié de nombreuses caractéristiques de type tectonique salifère telles que des séquences halocinétiques, des cicatrices et des minibasins. Par ailleurs, la zone comprend également des plis à coeur argileux (Shale-Cored Growth Folds), spécifiques de la partie distale du delta, et rappelant le «diapirisme salifère» avec des failles radiales, des fissures polygonales et des effondrements en forme de caldeira. Enfin ce domaine montre un chevauchement régional majeur, dupliquant le domaine de minibasin et mettant en évidence un changement potentiel du comportement rhéologique du niveau d'argile, initialement mobiles (permettant le développement de minibasins) et évoluant vers un comportement plus rigide et même fragile.

Sur la base des résultats des données sismiques, nous avons proposé un scénario cinématique illustrant la mobilisation de argiles dans le delta du White Pointer, distribué en quatre domaines: (1) extension proximale, (2) translation à mi pente, (3) minibasins gravitaires à la base de la pente et (4) raccourcissement dans la partie distale. Pour le mettre en contexte: (1) le domaine d'extension est l'endroit où nous observons les caractéristiques d'un delta en extension déclenchées par les failles listriques, (2) le domaine en translation montre le développement de radeau associés à des rouleaux d'argile, (3) le domaine de 'down-building' apparaissant principalement à la base de la pente du delta où nous observons d'abord l'initiation de minibasins avec des strates descendantes autour des dépôts d'argile gravitaires. C'est dans cette zone que le comportement des argiles semble évoluer depuis une certaine mobilité vers plus de rigidité. Enfin, le domaine de raccourcissement représente les éléments de raccourcissement / compression tels que des 'thrusts' et 'fishtails'.

Afin de compléter l'étude d'interprétation sismique que nous avons menée sur l'ensemble de données sismiques 3D Ceduna, nous avons également effectué un travail de terrain dans l'État de Rakhine au Myanmar pour examiner des affleurements d'argiles mobilisés, où nous observons des volcans de boue et cadre deltaïque à base d'argile. Les observations sur le terrain et les échantillons nécessiteraient une inspection pétrographique et diagénétique détaillée afin de comprendre les conditions de température et

de pression lors de la mobilisation ainsi que les effets environnementaux tels que la teneur en fluide ou le gradient thermique pour confirmation. Cependant, nous proposons un scénario dans lequel la mobilisation d'argile ne s'est pas produite à une grande profondeur soumise à de fortes surpressions, mais a plutôt eu lieu à faible profondeur de manière distribuée similaire à nos observations du delta du White Pointer et proche de la tectonique du sel.

À la fin de nos recherches, nous sommes arrivés à la conclusion que:

- À grande échelle, les argiles peuvent présenter un modèle de déformation plastique et se comportent comme un fluide de manière visqueuse imitant les dépôts de sel, tandis que la signature de déformation associée à la mobilisation des argiles peut être enregistrée par les strates de sédiments entourant ces restes de l'argile (argilocinèse).
- D'un point de vue technique, le domaine d'argile mobile du White Pointer Delta présente les caractéristiques géométriques propres de la tectonique du sel. Le delta instable gravitairement évolue d'un système classidue, additionné d'un domaine déformation de minibassins argileux vers un système de duplexation régional, ce qui suggère un changement de rhéologie d'argile (écrouissage) favorisant une localisation de la déformation.
- Localement, les argiles peuvent être fluidisés et former des volcans de boue dans la zone étudiée du sous-bassin de Ceduna.

Il s'agit d'approfondir ces analogies afin de conclure sur le fait qu'à grande échelle, les argiles peuvent imiter la déformation du sel et que les concepts de tectonique du sel peut être appliqué à la tectonique argileuse.

Mots Clés: Tectonique des Argiles, Sous-Bassin de Ceduna, Delta du White Pointer, Mobilisation des Argiles, Argilokinése.

Table of Contents

PART I: Introduction	1
General Introduction	1
Objectives of Research: Rationale	3
Organization of the Thesis	5
PART II: Salt and Shale Tectonics Review	7
Chapter 1: Salt Tectonics	7
I. General Concept	8
II. Deformation Mechanisms.....	9
A. General Introduction to Salt-Rock Behavior Mechanics: Plastic Strain & Ductility	9
B. Microcracking and Cataclastic Flow: Plasticity	10
C. Dislocation Creep	11
D. Solution-Precipitation Creep.....	12
III. Driving Forces for Salt Tectonism	15
A. Gravitational Forces	15
B. External Forces.....	17
C. Thermal Gradient	17
D. Restrictive Factors Against Salt Flow	18
IV. Deformation Geometries: Halokinesis.....	19
A. Review of Salt Formations: Deformed Salt Features	19
B. Review of Salt-Related Sediment Recordings	31
V. Remarks: Literature Wrap-Up of Salt Tectonics	40
Chapter 2: Shale Tectonics	41
I. General Concept	42
II. Deformation Mechanisms.....	43
A. Strain: Solid-State Distributed Deformation	43
B. Fluidization: Mud Volcanism.....	46
III. Driving Forces for Shale Tectonism and Fluidization	50
A. Overpressure: The Main Trigger	51
B. Internal Forces: Permeability-Related Constraints Induced by Overpressure	54
C. External Forces Induced with Overpressure	62
IV. Deformation Geometries: Argilokinesis	65

A. Review of Shale Formations: Deformed Shale Features	65
B. Review of Shale-Related Sediment Recordings	68
V. Remarks: Literature Wrap-Up of Shale Tectonics.....	69
Chapter 3: Review of Existing Geodynamic Settings Affected by Salt-Like Shale Tectonics	73
I. Deep Sedimentary Basins	73
A. Oceanic Basins: South Caspian Sea Example	74
B. Continental Basins: Shannon (Clare) Basin, Ireland Example	78
II. Rift Settings	82
III. Passive Margins.....	83
A. Sediment-Rich vs Sediment-Poor Margins.....	83
B. Sediment-Rich Margin Deltaic Settings: Gravity-Driven Deltas	84
IV. Accretionary Wedges/Prisms: Active Margins.....	92
V. Foreland Basins, Collisional Belts and Collapsing Orogens	110
VI. Synthesis on Shale-Driven Geodynamic Settings.....	120
Chapter 4: Transition from Salt into Shale	127
Blind Test: Salt Driven Gulf of Mexico vs Shale Driven Ceduna Sub-Basin	127
PART III: Case-Study: Ceduna Sub-Basin, Offshore Australia	131
Chapter 5: Area of Interest: Great Bight Basin – Ceduna Sub-Basin	131
I. Introduction	132
II. Geological Background.....	133
A. Geodynamic Setting	134
B. Tectonic Evolution at Crustal Scale	135
C. Basin Evolution.....	143
III. Lithostratigraphy of Ceduna Sub-Basin.....	153
A. Pre-Deltaic Lithology	154
B. Deltaic Lithology: White Pointer and Hammerhead DDFTBs.....	154
C. Post-Deltaic Lithology	155
IV. Close-Up on the Ceduna Sub-Basin Deltaic Interval	156
A. White Pointer Deltaic System (DDFTB).....	156
B. Hammerhead Deltaic System (DDFTB)	162
C. Synthesis: Review of Ceduna Sub-Basin Deltaic Interval Structural Evolution	164
Chapter 6: Study Area: Well Information, Dataset and Methodology	165
I. Ceduna Sub-Basin Exploration Wells	166

A. Potoroo-1 Well.....	167
B. Gnarlyknots-1A Well	169
II. Dataset and Methodology	171
Chapter 7: Regional Seismic View of Ceduna Sub-Basin	175
I. Classification of White Pointer Delta Compartments.....	175
II. Composite 2D Regionals Merged with 3D Seismic Lines	183
III. Compartmental Review	193
A. Proximal Delta Setting	193
B. Central Delta Setting.....	193
C. Distal Delta Setting.....	194
IV. Remarks on Ceduna Sub-Basin, White Pointer Delta Regional View	195
V. Structural Time-Slice Analysis of White Pointer Delta with 3D Seismic Cube	195
A. 5km Time Slice View:	200
B. 8km Time Slice View:	203
VI. Synthesis of White Pointer Deltaic Interval on 3D Seismic Time-Slice View	206
Chapter 8: Mobilized Shale Deformation Geometries	207
I. Salt-Like Seismic Findings.....	208
A. Wedging and Unconformities.....	208
B. Welding	210
C. Minibasins	212
II. Shale-Specific Seismic Findings	214
A. Thrusting and Duplexation	214
B. Fishtail Structures	216
C. Shale-Cored Domal Highs.....	222
III. The Kinematic Scenario Proposed for White Pointer Delta.....	229
PART IV: Discussion and Perspectives on Shale Mobility	233
Chapter 9: Fieldwork Case-Study: Rakhine State, Myanmar	233
I. Fieldwork Information:	233
II. Study Area: Rakhine State, Myanmar	234
III. Geological Setting and Geodynamic Context.....	236
IV. Coastal Region of the Rakhine State, Western Myanmar: Ramree and Cheduba Islands	241
V. Visited Sights: Minibasin Formations and Mud Volcanoes.....	246
VI. Lithologic Facies and Stratigraphic Information	251

A. Eocene	251
B. Oligocene	255
C. Miocene	257
IV. Field Observations: Mobile Shale Evidences.....	257
V. Mud Volcanoes	261
VII. Conclusion on Fieldwork Findings and Collected Samples	266
Chapter 10: Discussion and General Conclusions on Shale Mobility Based on Conducted Fieldwork and Seismic Study	267
Rakhine State, Myanmar Field Work Study	267
Ceduna Sub-Basin, White Pointer Delta Seismic Study	267
Conclusions:	269
References and Bibliography	271

Table of Figures:

Figure 1: Salt Tectonics Structures (image retrieved from Jackson and Talbot, 1986; Jackson and Hudec, 2017).....	8
Figure 2: Induced halokinetic sequences (recorded halokinesis features) observed adjacent to a steep diapir: (A) stacked composite halokinetic sequences (CHS), (B) nonspecific minibasin-scale stratal thinning and folding, and (C) a megaflop. See Giles and Rowan et al., 2016).	9
Figure 3 : Graph of Stress vs Time showing stages of Creep from yield strength through the rupture point (image retrieved from Jackson and Hudec, 2017).	10
Figure 4: Plasticity and Microcracking: First microstructure and deformation mechanism proposed for salt rocks deformed at temperatures of 20 to 200°C. Different shades of green represent crystals with different orientation (image retrieved from Urai et al., 2008).	11
Figure 5: Dislocation Creep: Second microstructure and deformation mechanism proposed for salt rocks deformed at temperatures of 20 to 200°C. Different shades of green represent crystals with different orientation (image retrieved from Urai et al., 2008).	12
Figure 6: (a) Solution-Precipitation Creep: Third microstructure and deformation mechanism diagram proposed for salt rocks deformed at temperatures of 20 to 200°C. Different shades of green represent crystals with different orientation. (b) Typical micrograph of Hengelo Rock salt, decorated to show the microstructure, with subgrains (white lines), grain boundaries (dark bands), showing clear evidence for “overgrowth” due to solution-precipitation processes such as pressure solution and grain boundary migration. Mean grainsize in Hengelo samples is between 5 and 25 mm. Width of image is 7 mm (from Schléder and Urai 2005) (images retrieved from Urai et al., 2008).....	13
Figure 7: The diagram illustration of complex changes as salt converges from the source layer, rises up a diapir’s stem, then diverges and extrudes glacially downhill. After Desbois et al., 2010. -please see the text for explanation- (image retrieved from Jackson and Hudec, 2017).	14
Figure 8: Salt Tectonism and Induced Halokinesis Features Observed in a Gravitational Setting (image retrieved from Warren, 2016).	15
Figure 9: Gravity-driven deformation of passive margins has two end members: (a) pure gravity gliding and (b) pure gravity spreading. (c) In reality, virtually all passive margins involve variable components of each end member, and hence are mixed-mode deformations. Arrows show particle paths; gray lines show successive outlines. (image retrieved from Jackson and Hudec, 2017 after Rowan et al., 2004).....	16
Figure 10: Tectonic styles of salt-bearing passive continental margins deforming first by (a) gravity gliding, then by (b) gravity spreading (image retrieved from Jackson and Hudec, 2017).	16
Figure 11: Displacement loading is imposed on salt structures by regional horizontal forces. (a) During shortening, salt is loaded horizontally by inward movement of one or both sides of the salt structure. If the horizontal displacement load exceeds the vertical gravitational load of the salt column, salt is forced to rise. (b) During extension, salt is unloaded horizontally by outward movement of one or both sides of the salt structure. The vertical gravitational load exceeds the horizontal displacement load, so salt is forced to subside (image retrieved from Jackson and Hudec, 2017 after Hudec and Jackson, 2007).	17
Figure 12: Cartoon diagram depicting a salt sheet (image retrieved from Jackson and Hudec, 2017).	20
Figure 13: a) Conceptual model of the rock salt cycle and associated rheological transitions observed at a salt glacier -see the text for explanation- (image retrieved from Urai et al., 2008). b) Characteristic of a spreading salt sheet above rigid bedrock. After Talbot et al., 2009a (image retrieved from Jackson and Hudec, 2017).	21
Figure 14: All diapirs, whether they are salt stocks, salt walls, or salt sheets have discordant contacts against their overburden (image retrieved from Jackson and Hudec, 2017).	22
Figure 15: (a) Seismic reflection, (b) reflection continuity attribute and (c) geoseismic cross-section across the Epsilon Diapir, North Sea. Dashed lines in (c) indicate where the seismic interpretation is uncertain. The locations of horizontal slices shown in (e) indicate the interpreted axis (image retrieved from Jackson & Lewis, 2012)	23
Figure 16: Main mechanisms of diapir formation: (A) passive diapirism, with the growth of the diapir due to sediment down building (based on Barton, 1933); (B) active diapirism, with the diapir piercing through sediments	

faulted by the rising salt; and (C) reactive diapirism, with the diapir rising through a fault zone formed by regional extension (modified after Vendeville and Jackson, 1992) (image retrieved from Mitra and Karam, 2016).24

Figure 17: Schematic cartoons illustrating typical features of a) active salt diapirism and, b) passive salt diapirism (image retrieved from Alsop et al., 2016).26

Figure 18: Diagram of reactive diapirism in an extensional regional setting: Diagnostic criteria of reactive walls (after Jackson et al., 1994) (image retrieved from Jackson and Hudec, 2017).27

Figure 19: Diagram of reactive diapirism in a compressional regional setting (after Coward and Stewart, 1995) (image retrieved from Lord, 2015).27

Figure 20: Radial faults form above an active diapir because, as roof strata arch and tilt outward, they extend circumferentially (hoop extension). (a) Before arching (oblique three-dimensional view); (b) after arching (vertical three-dimensional view, colors delineate individual fault blocks); after Yin and Groshong (2007) (image retrieved from Jackson and Hudec, 2017).28

Figure 21: Fault patterns above circular (upper row) and elliptical (lower row) active diapirs are controlled by different regional stress fields indicated by arrows. After Withjack and Scheiner (1982), based on their physical and analytical models (image retrieved from Jackson and Hudec, 2017).28

Figure 22: A salt canopy is composed of two or more salt sheets that have coalesced to make a large composite allochthonous structure. Boundaries between component salt sheets in a canopy are termed sutures (image retrieved from Jackson and Hudec, 2017).29

Figure 23: a) A salt weld is a surface or thin zone joining strata originally separated by salt. The weld is symbolized by pairs of dots along its length. (b) A fault weld is a salt weld along which there has been slip either before or after welding (image retrieved from Jackson and Hudec, 2017).30

Figure 24: Illustrated definitions of a complete weld, an incomplete weld, and a discontinuous weld (image retrieved from Jackson and Hudec, 2017).30

Figure 25: Halokinetic sequences in the 500 to 1000 m wide contact zone around El Papalote and El Gordo diapirs (La Popa basin, Mexico). Strata are locally overturned in hook halokinetic sequences; angular unconformities bounding the sequences are subvertical and grade into correlative conformities within about 250 m of the diapir's contact. After Rowan et al., 2003 (image retrieved from Jackson and Hudec, 2017).32

Figure 26: Halokinetic (HS), composite halokinetic (CHS) and depositional sequence stratigraphy of the Upper Cretaceous through Lower Palaeogene stratigraphy exposed on the east side of El Papalote Diapir, La Popa Basin, Mexico (image retrieved from Giles and Rowan, 2012).32

Figure 27: Two end-member types of halokinetic sequences: (a) hook halokinetic sequence; and (b) wedge halokinetic sequence (image retrieved from Giles and Rowan, 2012).33

Figure 28: Two end-member types of composite halokinetic sequences (CHS): (a) tabular CHS; and (b) tapered CHS (image retrieved from Giles and Rowan, 2012).33

Figure 29: Geometric patterns of stacked composite halokinetic sequences (CHS): (a) tabular CHS over tabular CHS; (b) tabular CHS over tapered CHS; (c) tapered CHS over tapered CHS; and (d) tapered CHS over tabular CHS (image retrieved from Giles & Rowan, 2012).34

Figure 30: Prestack depth-migrated seismic profile (reverse-time-migration sediment flood) of a secondary diapir and flanking strata from the northern Gulf of Mexico: (a) uninterpreted and (b) interpreted. Vertical exaggeration 1.5:1. Seismic data courtesy of C. Fiduk and CGGVeritas (image retrieved from Giles and Rowan, 2012).34

Figure 31: The top of this section represent the surface line at sea level. The section shows antithetic basement faults, a graben in the centre of the overburden and an erosional surface above. Note the secondary rim-syncline of the northerly adjacent diapir (not seen on this figure) in the central part (image retrieved from Mohr et al., 2005).35

Figure 32: Salt Megaflap -basal flap- Seismic Example a) uninterpreted b) interpreted. Stratigraphic interval 1 is the megaflap and 2–4 are growth packages with different thickness and onlap patterns. Vertical and horizontal black arrows show height and width of megaflap, respectively. Data courtesy of Schlumberger; no vertical exaggeration. (image retrieved from Rowan et al; 2016).36

Figure 33: Diagram of a megaflap adjacent to a salt diapir (retrieved from Rowan et al., 2016).36

Figure 34: The core of this salt anticline is pinched shut by regional shortening, during which the salt core breaks out as an injection fold, forming a small diapir at its crest. Campos basin, Brazil. Seismic data courtesy of PGS. (image retrieved from Jackson and Hudec, 2017).	37
Figure 35: Seismic example of dish-shaped minibasins on the continental slope of the northern Gulf of Mexico. Seismic data courtesy of CGG. After Hudec and Jackson (2011) (image retrieved from Jackson and Hudec, 2017). ..	38
Figure 36: Minibasins are small basins, or depressions, that fill with sediment as they sink into thick salt. These growth synclines are laterally surrounded by salt or by salt welds. (a) Two-stage evolution of secondary minibasins sinking into allochthonous salt. An older, primary minibasin underlies the canopy. The second stage shows the level of the depth slice shown in (b). (b) Minibasin planforms are typically generalized as subcircular, but they can be any shape, including elongated (image retrieved from Jackson and Hudec, 2017).	39
Figure 37: Bedding orientation in samples of Opalinus Clay subjected to triaxial compression tests (image retrieved from Parisio et al., 2015).	44
Figure 38: Typical rheology of P-Sample of Opalinus Clay in triaxial compression conditions at a confinement pressure of 3 MPa (Gräsle and Plischke, 2011) (image retrieved from Parisio et al., 2015).	45
Figure 39: Conceptual sketch of the reaction chain of the remobilization processes (image retrieved from Deville, 2009).	48
Figure 40: Azerbaijan Mud Volcano (image retrieved from personal collection of G. Dinc).	49
Figure 41: Main overpressure causal mechanisms (Grauls, 1997) (image retrieved from Grauls, 1999).	53
Figure 42: Compilation plots of published compaction trends (gray lines) of a) sandstone, b) shale, c) carbonate (Giles, 1997). The compaction trend range of each lithology is defined by three sets of exponential curves; low-end curve (dashed line), mean curve (solid line) and high-end curve (dotted line) (image retrieved from Kim et al., 2018).	55
Figure 43: Depth profile showing a not so typical gravity fold and thrust structure from the Krishna-Godavari basin; a huge amount of extension along the Oligocene–early Miocene growth fault is being accommodated by thrusting along a Paleocene detachment. The detachment is moderately overpressured and has a very steep slope, allowing the development of thrusts on the basinward side. Steepening of the detachment and location of the thrusts are also correlated to the abrupt deepening of the basin beyond the basement high at location A (image retrieved from Choudri et al., 2010).	55
Figure 44: Comparison of normal depth profile curve. Athy's original curve, shale compaction profile curve from Nagaoka basin, Gulf coast, and Beaufort Mackenzie delta. Porosity data derived from density log (Burrus 1998) (image retrieved from Das & Mukherjee, 2020).	56
Figure 45: a) Schematic diagram showing compaction process of a sedimentary layer with exponential compaction trend (porosity–depth relation) and equation (revised from Lee et al., 2019). b) Concept of the isostatic balance ($PB_1 = PB_2$) between the basal pressure (PB_1) of the new layer (PD) and pre-accumulated layer(s) (PS) and the basal pressure (PB_2) of the compacted layers (PC) and released water (PW). d , s , l and x : thicknesses of new layer, pre-accumulated layer(s), accumulated layers and compacted layers (image retrieved from Kim et al., 2018).	57
Figure 46: Acoustic velocity–vertical effective stress crossplots for the Linnan Sag. The points are on or near the loading curve, indicating normal compaction, or disequilibrium compaction (blue points), whereas the overpressured data lie on an unloading curve, suggesting that the overpressure is generated by fluid expansion or transfer processes (green and red points). DST: Drilling Stem Test (image retrieved from Li et al., 2019).	58
Figure 47: Plots of layer thickness variation with depth; a) sandstone, b) shale, c) carbonate. Total 100 layers are accumulate and compacted following the exponential curves from the compaction trend range of each lithology. The layer thickness range with depth is presented using applied curves; low-end curve (dashed line), mean curve (solid line) and high-end curve (dotted line) (image retrieved from Kim et al., 2018).	59
Figure 48: Potential structural responses to the loading of a salt layer (black) by a sediment wedge (gray). (a) Initial stage, assuming instantaneous overburden deposition; (b) differential subsidence of the proximal overburden (1) and inflation of the distal salt (2); (c) gravity spreading of the overburden causing proximal extension (1), mid-slope seaward translation (2), and distal contraction (3). Dashed lines outline the sediment wedge's geometry before deformation (image retrieved from Vendeville, 2005).	64

Figure 49: Mud Diapir Example; Squeezed Teardrop Diapir with Subvertical Weld (image retrieved from AGL Presentation: Shale Tectonics in the Alboran Sea Revisited from a Salt-Tectonics Perspective, after Soto et al., 2010).67

Figure 50: Interpreted regional seismic section along NW Borneo, showing evidence for existence of thick, extensive mobile shales in the form of extrusive shale bodies (image retrieved from J. Clark presentation, SeaPex 2017).68

Figure 51: Interpreted seismic example of two shale minibasins from NW Sabah Region, Northern Borneo, accompanied by evolutionary sketch diagram depicting minibasin evolution (a through e) illustrating how differential loading drives shale movement and in turn creates the variable sequences of minibasin fill (note the shifting locus of deposition) and intra-minibasin unconformities (image retrieved from James Clark, Sapura Energy presentation, SeaPex 2017 Convention)......69

Figure 52: Major structural features in the South Caspian Basin region. Note that alternate terms are used for some of these features in the text and in other figures, depending on the context in which they are discussed. (Map is modified from Devlin and others, 1999, and is printed with permission from Exxon/Mobil) (image retrieved from Smith-Rpuch USGS Report, 2006).75

Figure 53: Seismic Section: regional interpreted deep seismic section, showing the main subsurface structural elements with the folds above the Maykop detachment level associated in the northern part to deeply rooted thrusts. The red box shows the approximate location of the Absheron structure (modified from Stewart & Davies, 2006) (image retrieved from A. Blouin PhD Thesis, 2020).76

Figure 54: Seismic line, approximately 23 km long, across a typical South Caspian structure. Note the crestal normal faults in the shallow section and the low-angle reverse faults in the lower part of the fold. These two fault regimes are separated by an inferred neutral surface within the lower Surakhany Formation. Also note the thinning and onlap of strata above the top Surakhany Formation (pink surface), indicating the onset of structural growth. Use of seismic data courtesy of Caspian Geophysical (image retrieved from Devlin et al., 1999).77

Figure 55: Seismic section across a mud volcano system in the South Caspian Basin showing a thinning of the Maykop Formation interval interpreted as being the source layer of the mud volcano (image retrieved from A. Blouin PhD Thesis, 2020)......77

Figure 56: Much of County Clare, and the extension of the Clare Basin into counties Kerry and Limerick, was first blanketed by fine grained black shale deposits (the Clare Shale Formation) that interpreted to represent deposition during a period of sediment starvation. The area centered about the Shannon estuary then became the focus of deep water sandstone deposition (the Ross Sandstone Formation), whilst the original platform in North Clare remained starved of sediment and continued to accumulate a condensed blanket of black shale. The sandy sediment that accumulated in the Clare Basin at this time came from the southwest. Following this event, the Upper Carboniferous basin filled gradually, becoming shallower upwards and the Ross Sandstone 'turbidites' are overlain by a thick succession of unstable slope deposits (the Gull Island Formation) and eventually by shallow-water delta deposits of the Central Clare Group (after Peter Haughton, 2006) (image retrieved from the website <http://www.sepmstrata.org/page.aspx?pageid=154>).79

Figure 57: (A) and (B) View of the exposure from the northern part of the tidal platform at low tide. Strata of the Moore Bay Sandstone (MBS) thicken near the diapir, while forming a dome on the right part of the outcrop. Coloured lines mark specific stratigraphic surfaces that are important sequence stratigraphic surfaces or mark important events in diapiric evolution: (i) the green line represents the surface where beds uplifted by the horizontal mud tongue were folded and eroded; (ii) the solid red line corresponds to the stratigraphically lowest flooding surface, which is recognizable by the preservation of wave ripples overlain by a thin bed of shale (image retrieved from Blanchard et al., 2019).79

Figure 58: Photographs and interpretations of the horizontal mud tongue and syndepositional folding and erosion of the overlying strata. Faults visible in the upper part of (A) are mineralized and thus considerably post-date deposition and diapirism. The green coloured line is the surface where beds uplifted by the mud tongue were folded and eroded (image retrieved from Blanchard et al., 2019).80

Figure 59: (A) and (B) Image and paired line drawing of the large diapir exposed in the cliff at Knockroe, 400 m to the east of Diamond Rocks. Image is extracted from a 3D model constructed using drone photography. (C) - (D)

Image and paired line drawing of the diapir at a roughly orthogonal view to the upper image. These images together show the roughly triangular but elongate (ridge-like) shape of the diapir; (A) and (B) show a view perpendicular to the diapir crest and (C) and (D) are roughly parallel. (E) Map showing the location of the Knockroe diapir with the crude location of the diapir shown (black arrow), the approximate axis of the diapir crest (yellow line), the extent of the 3D model available in the supplementary material (total of green and red lines), and the approximate extent of the image in (C) and (D) (white arrow and green line) for reference. It should be noted that the static images in (A) to (D) do not show completely flat or orthogonal faces (image retrieved from Blanchard et al., 2019)......81

Figure 60: Diagram depicting the two categories of salt tectonic models: a) Dominant Gliding and b) Pure Spreading (image retrieved from Drachev S.S. (2015) Salt Diapirism in the Oceans and Continental Margins. In: Harff J., Meschede M., Petersen S., Thiede J. (eds) Encyclopedia of Marine Geosciences. Springer, Dordrecht).....85

Figure 61: A) Free-air gravity anomaly map of East African margin. N-S trending Davie Fracture Zone (>2000 km long; thicker, dotted black line) connects Somali and Mozambique Basins. At northern edge of Davie Fracture Zone, a broad gravity high represents Davy-Walu Ridge (DWR, thinner, dotted black line), a prominent basement high, uplifted since mid-Cretaceous. B) Zoom on study area, showing location of thrust front with respect to DWR and volcanoes identified on seismic profiles. DWR: southern limit of DW-FTB. Two volcanoes (V2, V3) are located in front of outermost thrusts, representing mechanical barriers to basinward propagation of DW-FTB. Gravity data from WGM2012 Earth’s gravity anomalies, bgi.omp.obs-mip.fr/data-products/Grids-and-models/wgm2012. (image retrieved from Crucaini & Barchi, 2016).86

Figure 62: Regional seismic line from the Juba-Lamu Basin showing the cross-section view and its interpretation (image retrieved from Stanca et al., 2016)......87

Figure 63: Interpretation of seismic profile P3 across southern portion of DW-FTB. Note the interpreted mud diapir (image retrieved from Crucaini & Barchi, 2016)......88

Figure 64: The innermost sector, about 65 km in length, is dominated by a set of large symmetrical detachment folds, resembling diapir-like folds (image retrieved from Crucaini & Barchi, 2016).88

Figure 65: Interpretation of a seismic reflection profile across the gravity-driven fold-thrust belt of the Niger Delta eastern lobe, Nigeria and Gulf of Guinea, after Ajakaiye and Bally (2002), Wu and McClay (2011). No vertical exaggeration. Interpreted units are stratigraphic sequences. This is the line drawing of of Ajakaiye and Bally (2002) (image retrieved from Yang et al., 2020)......89

Figure 66 : Uninterpreted and interpreted regional seismic profile across the Niger Delta showing the link between the extensional province on the shelf and the contraction in the toe thrust systems in the deep water, as well as the main structural domains. Both regional and counter regional normal faults are present in the extensional province. Slip on these faults soles onto one or a series of basal detachments and extends across a diapiric zone into the deep-water fold and thrust belts. The inner and outer fold and thrust belts are separated by a zone of little or no deformation. Along strike, this transitional zone is characterized by detachment folds. Seismic section is poststack migrated and depth converted (data courtesy of Mabon Ltd.) (image retrieved from Corredor et al., 2005)......90

Figure 67: A zoom-in caption of seismic data with a basic interpretation scheme (Yellow Markers: Diapir-Like shale intrusions originated from Akata Shale Formation, Red Markers: Deltaic sediments, Green Markers: Sequence terminations such as pinch-outs, onlaps, toplaps, Blue Markers: Normal and thrust faults of the deltaic system) (interpreted after Corredor et al., 2005)......91

Figure 68: Compartmentalization of Makran Accretionary Prism (image retrieved from Burg, 2018).94

Figure 69: Natural color Landsat satellite images of shale-related minibasin sedimentary structures in Iranian Makran. Minibasin in A is an amalgamation of four smaller single basins. Pink lines are shale walls, welds, and bedding onlaps. Pink shading shows ductile olistostrome withdrawal (partly covered by Quaternary deposits) (image retrieved from Ruh et al., 2018).95

Figure 70: Upper Panel: Satellite image showing locations of Makran, Iran (highlighted with yellow star) and Ramree-Cheduba Region of Rakhine State, Myanmar (highlighted with red question mark). Lower Left Panel: Zoomed-in geo-location of Makran region of Iran with minibasin-like features seen on satellite view. Lower Right Panel: Zoomed-in geo-location of Ramree-Cheduba region of Rakhine State, Myanmar with minibasin-like features

seen on satellite view. Note the similarity of rounded/circular patterns detected on satellite view of these two regions seen on the lower panels (image courtesy of Google Earth)97

Figure 71: Location map of northwest Borneo, modified from Morley et al., (2003) (image retrieved from Morley et al., 2008).98

Figure 72: Regional cross section illustrating the large-scale structural setting and geometry of the Baram Delta Province. Deep structure is schematic, but is based on gravity and seismic reflection data. The more detailed cross-sections focus on basin geometry and are based largely on industry seismic reflection data. NW Borneo [Morley et al., 2003; Sandal, 1996] (image retrieved from Hall & Morley, 2004).99

Figure 73: The cross-section from Sivas Salt Basin, Turkey (for detailed information see Legeay et al., 2019).100

Figure 74: Seismic sections through sites of isotopic interest. This organic group 1B site sits atop a shale-cored growth anticline with fluid plumes rising to the sea-floor surface and associated evidence of plume-related sediment collapse. The ridge is a result of ongoing gravity-driven compressional deformation, which also causes the bottom-simulating reflector (BSR) horizon to rise and break up as it approaches the sea floor. Note the disturbance and the discontinuity of the BSR caused by rising fluid plume in the vicinity of sample site 094 (image retrieved from Warren et al., 2010).101

Figure 75: Comparison of signatures of mud and salt diapirism. (A) Mud diapirism indicates a zone of fluid-charged overpressured fine-grained sediment (mostly mud). It can rise via stoping subvertical mud chimneys and periodically break out onto the sea floor. The seismic signature indicates zones of active or former fluid charge. The diapir as seen in the seismic signature is not a lithology but typically a gas effect. As such, the diapir zone can expand and encapsulate or cannibalize adjacent sediments without disturbing the bed orientation. (B) Salt diapirism indicates a zone of flowing impermeable salt (halokinesis). There is both a vertical and horizontal component to this flow and a strong response to sediment loading, and, on salt reaching the sea floor, it is tied to downslope gravity spreading. The seismic signature of a salt diapir or allochthon is a direct indicator of the salt mass, which is always impermeable. Flow sets up a mobile mass of impervious salt with edges subject to dissolution (like a block of ice). This mass and its brine halo focus fluid flow and overpressuring about its edges (see Warren, 2006, chapters 6 and 8 for a detailed discussion of relevant literature) (image retrieved from Warren et al., 2010).102

Figure 76: General sketch-map of the Orinoco siliciclastic system showing its close interaction with the compressional front of the Caribbean plate. Orange arrow: vector displacement of the Caribbean Plate with respect to the North American Plate. Red lines and arrows: turbidite systems; AABW: Antarctic BottomWater (Green arrows; location from Rhein et al., 1998); GLC: Guyana Littoral Current (white arrows); VDSC: Vidal Deep Sea Channel. A-MOR: Atlantic Mid-Oceanic Ridge. (image retrieved from Deville et al., 2015).103

Figure 77: Seismic transect across the southern part of the Barbados accretionary prism and the Atlantic abyssal plain. Light grey surfaces correspond to the main mud volcanoes and pink surfaces are transparent bodies that correspond partly to large-scale mass-flows. Dark grey lines show the main BSR. Yellow lines outline some good reflectors (with no specific interpretation). (image retrieved from Deville et al., 2015).104

Figure 78: Geological Elements and Location Map of Trinidad-Barbados (image retrieved from Battani et al., 2010).105

Figure 79: Uninterpreted (left) and interpreted (right) seismic sections, encompassing ~5 seconds travel-time depth shows mud volcano trains that have been repetitively active for well over 2 million years. This image shows the close relationship between deep, remobilized muds and compressional anticlines along the northeastern boundary of the Caribbean and South American plates. Data provided by the Ministry of Energy and Energy Industries, Trinidad and Tobago (image retrieved from Lesli J. Wood, in *Regional Geology and Tectonics: Phanerozoic Passive Margins, Cratonic Basins and Global Tectonic Maps*, 2012).106

Figure 80: An example of seismic profile across a mud volcano in the eastern offshore of Trinidad (courtesy of Shell, Agip, Petrotrin). Note the stacking of different volcanic edifices. This "Christmas tree" structure is probably the result of the cyclic development of volcanic edifices during the Pleistocene periods of high stand (low sedimentation rates, clay-rich well stratified sediments) and of the draping of the sedimentary volcanoes during the periods of low

stand (high deposition rates, notably mass-flows, Bрами et al., 2000), but the mean expulsion rate of mud is not necessary directly related with sedimentation rate (image retrieved from Deville, 2009).....106

Figure 81: Geological setting of the Cascadia active tectonic continental margin associated with the Cascadia subduction zone, which is made up of the Juan de Fuca and Gorda plates (image retrieved from Williams et al., 2002).....108

Figure 82: Seismic line from the Wash Basin, Cascadia. Yellow Markers: Diapir-Like shale intrusion. Red Markers: Deltaic sediments. Green Markers: Sequence terminations such as unconformities, onlaps and toplaps. Blue Markers: Normal faults observed at the sedimentary package above the shale formation (image retrieved and modified after Steve Holbrook, <https://earthscience.stackexchange.com/questions/4945/what-is-a-mud-diapir-and-how-does-it-form>) – Please note that the interpretation on this seismic section is made to point out the shale mobilization features without any intention attributed to the stratigraphic information of the area as it is not the purpose of this PhD research –109

Figure 83: Geological Location of EVB and its Structural Elements (image retrieved from Duerto & McClay, 2011).112

Figure 84: Detail of a regional seismic line from seismic survey. Note the distribution of mobilized shale in the south of the faults in the core of the anticlines (figure retrieved from Duerto and McClay, 2011).....113

Figure 85: Regional seismic line from the study. Note the two levels of detachments inside the shale unit. The La Pica high is interpreted as the inversion of two normal faults (image retrieved from Duerto & McClay, 2011).114

Figure 86: Tectonic map of the Gibraltar arc formed by the Betics, Rif, and the Alboran Sea Basin and the continuation of this orogenic system into the Gulf of Cadiz. (map updated from Soto et al., 2010) Mud volcanoes, shale diapirs, and salt culminations in the Gulf of Cadiz and in the Alboran Sea are compiled from numerous sources (e.g., Comas et al., 2003; Pinheiro et al., 2003; Somoza et al., 2003; Medialdea et al., 2009; Blinova et al., 2011; Somoza et al., 2012; Soto et al., 2012; Gennari et al., 2013; Hensen et al., 2015). The studied Andaluca G-1 well is indicated by G1. A rectangle marks the region in the vicinities of the studied well, where a detailed study of the mobile shale structures has been conducted. AI = Alboran Island; EAB = East Alboran Basin; SAB = South Alboran Basin; WAB = West Alboran Basin (image retrieved from Fernandez-Ibanez & Soto, 2017).....116

Figure 87 : (A) Uninterpreted seismic profile and (B) interpretation of a dip line in the northern margin of the West Alboran Sea. Reflection truncations are marked with dark red arrows. Seismic data are courtesy of ConocoPhillips. H:V = horizontal to vertical scale ratio; M= Messinian reflector; P2 = intra-Pliocene reflector; R2 = base of unit II reflector; R3 = base of unit III; R3n = intra-unit III reflector; R4 = base of unit IV seismic reflector (image retrieved from Fernandez-Ibanez & Soto, 2017).118

Figure 88: Schematic evolution of the shale structures in the northern margin of the West Alboran Basin along a conceptual dip section. The evolutionary stages correspond approximately to (A) the lower to lower middle Miocene (seismic units VI and V), (B, C) the middle Miocene (seismic units V and III, below the R3n reflection), and (D) the upper Miocene (upper Tortonian; upper part of seismic unit III). The vertical discontinuous lines express approximately the extension magnitude associated with the shale detachment formed along the basement cover surface. The encircled arrows show shale withdrawal and upbuilding associated with the downslope gravity spreading of the mobile shales (image retrieved from Fernandez-Ibanez & Soto, 2017).....119

Figure 89: Summary plot on causes for shale detachment weakness and their interrelations depending on depth, temperature, strain rate and mineralogy. Increasing burial and temperature, decreasing strain rate, as well as variations in mineralogy will favour creep, where the dominant controls on creep are mineralogy of the shale, and free water content (image retrieved from Morley et al., 2018)124

Figure 90: World Map showing the documented Shale Tectonism areas marked with red dots (image revised after Morley, 2003; Location map of the main mobile shale provinces associated with deltas world-wide with additional geodynamic settings showing shale-prone environments) (Blank map retrieved from: http://www.johomaps.com/world/worldblank_bw.html)125

Figure 91: Two sections with labeled interpretation showing mobilized features of a ductile medium (e.g. salt or shale) with associated structures such as; (i) mother/autochthonous ductile medium, (ii) canopy formation, and (iii) primary and secondary minibasins. Upper figure shows a collected seismic line from salt-driven Gulf of Mexico

<i>(image retrieved from Callot et al., 2014). Lower figure shows a collected seismic line from shale-driven Ceduna Sub-Basin, offshore Australia (image courtesy of PGS, 2011)</i>	<i>128</i>
<i>Figure 92: Location of the Bight Basin along the southern Australian margin, with component sub-basins (image retrieved from Totterdell et al., 2008).</i>	<i>131</i>
<i>Figure 93: Structural elements map of the eastern Bight Basin (after Bradshaw et al. 2003) (image retrieved from Totterdell et al., 2008).</i>	<i>133</i>
<i>Figure 94: Plate tectonic reconstructions for the southern Australia–Antarctica conjugate margin (after Norvick & Smith, 2001) (image retrieved from Totterdell & Mitchell, 2007).</i>	<i>135</i>
<i>Figure 95: Different rifting models proposed for the Australian–Antarctic conjugate system. (a) Direen et al. (2011) propose a symmetric extensional model. (b) Etheridge et al. (1989) and (c) Espurt et al. (2009) suggest an asymmetric extension above a south-dipping low-angle detachment. In this model, the Antarctica is the upper plate, and Australia, the lower plate (Red rectangle on Fig. c depicts the White Pointer Delta) (image retrieved from Espurt et al., 2012).....</i>	<i>137</i>
<i>Figure 96: Present-Day view of Australian–Antarctica conjugate margins after the sequential restoration and kinematic evolution. No vertical exaggeration (image retrieved from Espurt et al., 2012).</i>	<i>138</i>
<i>Figure 97: Structural interpretation of the two synthetic seismic transects: (a) Australian margin and (b) Antarctic margin. Sb, Sub-basin; COTZ, Continent–Ocean Transition Zone; SAAP, South Australian abyssal plain. Observed and calculated Free Air gravity anomaly and residual IGRF corrected magnetic anomaly are shown (from Colwell et al., 2006; Direen et al., 2007 and courtesy of Geoscience Australia). Inferred detachment/decollement zones are shown by thick dashed red lines (D1, D1c, D2 and D3) (image retrieved from Espurt et al., 2012).</i>	<i>139</i>
<i>Figure 98: Kinematic evolution of the Ceduna Sub-Basin, based on a sequential restoration from the Late Albian to present-day. (image retrieved from Espurt et al., 2009)</i>	<i>142</i>
<i>Figure 99: Bight Basin stratigraphic correlation chart showing basin phases and predicted source rock intervals (modified from Blevin et al. 2000 and Totterdell et al. 2000). The sea-level curve (Haq et al. 1988) is modified to the time scale of Gradstein et al (2004) (image retrieved from Totterdell et al., 2008).</i>	<i>145</i>
<i>Figure 100: Upper Seismic Section: Cross-Section across the Madura Shelf and inner Ceduna sub-basin. Horizons were calibrated using projected (pjt.) data from the Potoroo-1 and Gnarlyknots-1A wells. Mulgara faults are indicated by medium black lines. These faults branch downward onto the decollement D1 (thick black line) at the base of the shales of the Blue Whale Supersequence. Inferred half graben of the Potoroo fault system (dashed black lines) underlies the delta system. Lower Seismic Section: Cross-Section through the Ceduna and Recherche subbasins. Mulgara faults are indicated by medium black lines. These faults branch downward onto the de´collement D1 (thick black line) at the base of the shales of the Blue Whale Supersequence. Note the scarcity of compressional features at the delta toe. Vertical exaggeration is x2. Please see the article for regional line locations (image retrieved from Espurt et al., 2009).</i>	<i>147</i>
<i>Figure 101: Upper Seismic Section: Detail of northern part of seismic line 4 (transect B-B0) across the Madura Shelf and Ceduna subbasin. Horizons were calibrated using projected data from the Potoroo-1 and Gnarlyknots-1A wells. Mulgara faults are indicated by medium black lines. These faults branch downward onto the shallow de´collement D1 (thick black line) at the base of the Blue Whale Supersequence. Seismic data show typical fault-related rollover anticlines within the White Pointer delta system, sealed by strata of the Hammerhead sequence set 1. Half grabens of the Potoroo fault system underlie the delta system. Lower Seismic Section: Detail of the southern part of seismic line 4 and the northern part of seismic line 5 (transect B-B0) across the Ceduna and Recherche subbasin. Faults are indicated by medium black lines. Sediments of the White Pointer delta system overlie subcontinental mantle rocks. The Hammerhead delta system is associated with gravitational sliding of the Kowari fault system which connects downward with the shallower de´collement D2. Note the growth strata pattern within the Hammerhead sequence set 2. Vertical exaggeration is x2. Please see the article for regional line locations (image retrieved from Espurt et al., 2009).</i>	<i>148</i>
<i>Figure 102: Modelled present-day maturity zones (% Ro) for the a) northern and b) central transects (image retrieved from Totterdell et al., 2008).</i>	<i>150</i>

Figure 103: Modelled present-day transformation ratios (%) of three potential source rock units within the Blue Whale, upper White Pointer and Tiger supersequences for the a) northern and b) central transects (well locations as noted on diagrams, see the article for further details) (image retrieved from Totterdell et al., 2008).	151
Figure 104: Portion of the central Ceduna transect showing predicted accumulations for the modelled scenario and the percentage of liquids contribution from three potential source units (image retrieved from Totterdell et al., 2008).....	152
Figure 105: Stratigraphy of the Bight Basin (modified from Espurt et al., 2009). Early–Middle Jurassic and Palaeocene/Eocene intrusions are also shown (volcano) (image retrieved from Espurt et al., 2012).....	153
Figure 106: Structural Interpretation of Ceduna Sub-Basin (red rectangle), showing White Pointer and Hammerhead Delta Intervals (image retrieved from Espurt et al., 2012).	158
Figure 107: Seismic line from the transitional zone between updip growth faults and downdip contractional structures, White Pointer Delta, northern Ceduna Sub-basin. Note the presence of possible diapiric features at 6.0-7.0 s (TWT), adjacent synformal strata, and the chaotic seismic character of much of the section, particularly beneath the crests of the anticlines (image retrieved from Totterdell and Krassay, 2003).....	158
Figure 108: Comparison of White Pointer Delta and the idealised progradational delta of Morley & Guerin (1996). Note the similar distribution of extensional, diapiric/transitional and contractional structural zones (image retrieved from Totterdell and Krassay, 2003).....	160
Figure 109: Regional seismic data example of Ceduna Sub-Basin Deltaic intervals (White Pointer and Hammerhead DDFTBs) (image retrieved from Espurt, et al., 2009).	161
Figure 110: Structural interpretation of distal White Pointer and Hammerhead Deltas. Faults are indicated by medium black lines. Sediments of the White Pointer delta system overlie subcontinental mantle rocks. The Hammerhead delta system is associated with gravitational sliding of the Kowari fault system which connects downward with the shallower decollement (Tiger Formation) (image retrieved Espurt et al., 2009).....	163
Figure 111: Map showing location of seismic lines and wells in the eastern Bight Basin (image modified after Hughes et. al., 2009) (red geometrical closure shows the location of the 3D dataset studied for this PhD research).	165
Figure 112: Location of Ceduna Sub-Basin Exploration Wells (black geometrical closure shows the location of the 3D seismic cube).....	166
Figure 113: Composite NE-SW seismic line through study area showing the rotated fault blocks of the Lower White Pointer overlain by sub-parallel to gently dipping Upper White Pointer and Tiger SS. *Springboard MC3D courtesy of PGS (image retrieved from Tredrea & Horton, 2019).	167
Figure 114: Composite NW-SE seismic tie line from Potoroo-1 to Gnarlyknots-1A. Note the thickening of the White Pointer and Tiger SS away from the Potoroo-1 well. *Springboard MC3D courtesy of PGS (image retrieved from Tredrea & Horton, 2019).....	169
Figure 115: Deltaic Stratigraphy of the Ceduna Sub-Basin, Bight Basin (modified after Espurt et al., 2012) showing the White Pointer and Hammerhead delta intervals with the updated seismic interpretation and detail conducted for this PhD research via 3D seismic data.....	172
Figure 116: Map of utilized 2D regional lines and 3D seismic dataset of Ceduna Sub-Basin. Yellow marked area depicts the limits of PSDM 3D seismic dataset, while the red lines show the locations of 2D regional lines used to construct regional cross sections.	174
Figure 117: 2D regional composite lines (N1, N2, S1 and S2) interpreted to grasp the regional geological context in addition to the 3D seismic data cube (yellow geometrical shape). Black squares denote the location of two exploration wells drilled in Ceduna Sub-Basin (Potoroo 1 and GnarlyKnots 1A).	176
Figure 118: Regionally interpreted cross-sections showing four 2D seismic lines with White Pointer Delta Interval (see the color-based deltaic stage legend to the right of the figure) above Blue Whale Detachment Level (blue patches). Pin Points depict the extent of the deltaic wedge and the limit of balanced cross-section calculations performed on these lines. Red markers denote thrust faults while the black ones show listric faults and small scale normal faulting. Purple Marker: Top Tiger Formation. Green Marker: Top Hammerhead Formation. See the Location Map on Figure 117.....	177

Figure 119: Schematic diagram derived from the horizon extension-compression compensation for given regional seismic lines. Cross-Sections can be compartmentalized under four main sections, which are namely; proximal listric faulting domain, translation domain, duplexation domain and frontal thrust domain.178

Figure 120: Zoom-in at the regional seismic line S2 showing the coherent duplexation pattern above the Blue Whale detachment level (Blue Marker). See the color legend on the sketchy diagram (first panel). Mid White Pointer sequential interval differentiates into two depositional package. Yellow package represent the isopachous Lower Mid White Pointer interval, while the Orange package shows the truncational sequence pointing out to duplex mobilization.179

Figure 121: Regionally interpreted cross-sections showing the identified White Pointer Delta compartments on four 2D seismic lines (see the color-based deltaic stage legend to the right and see Figure 117) above Blue Whale Detachment Level (blue patches). Red markers denote thrust faults while the black ones show listric faults and small scale normal faulting. Purple Marker: Top Tiger Formation. Green Marker: Top Hammerhead Formation. Pin Points depict the proximal end point of the deltaic wedge as well as the measurement reference for cross-section balancing.182

Figure 122: Regional Map of Ceduna Sub-Basin showing the locations of 2D-3D composite seismic lines. Black geometrical closure shows the 3D seismic cube location.183

Figure 123: Regional seismic line interpretation depicting the big-scale White Pointer Delta setting and its structural components (V.E. 2:1).184

Figure 124: Proximal part of White Pointer Delta shown on 2D line w00fdw0022.mig08ts-rot180 (Purple Marker: Top Tiger Formation, Orange Marker: Top White Pointer Formation, Yellow Markers: White Pointer Deltaic Deposits, Blue Patches: Blue Whale Shale Deposits, Black Markers: Listric faults soling into Blue Whale detachment surface) Seismic V.E. 2:1185

Figure 125: Central part of White Pointer Delta shown on 3D xline 13300 (Purple Marker: Top Tiger Formation, Orange Marker: Top White Pointer Formation, Yellow Markers: White Pointer Deltaic Deposits, Blue Patches: Blue Whale Shale Deposits, Black Markers: Listric faults soling into branched Blue Whale detachment surface) Seismic V.E. 2:1185

Figure 126: Central-to-Distal part of White Pointer Delta shown on 3D xline 13300 (Purple Marker: Top Tiger Formation, Orange Marker: Top White Pointer Formation, Yellow Markers: White Pointer Deltaic Deposits, Blue Patches: Blue Whale Shale Deposits, Black Markers: Listric faults soling into branched Blue Whale detachment surface, red squares show the enlarging offset difference being translated further towards the distal part - migration of gravitational cell activity getting younger- indicating mobilization of deeper strata further down in the delta-toe. Some fault reactivation is also observed at top-deltaic level) Seismic V.E. 2:1186

Figure 127: Distal part of White Pointer Delta shown on 3D xline 13300 (Purple Marker: Top Tiger Formation, Orange Marker: Top White Pointer Formation, Yellow Markers: White Pointer Deltaic Deposits, Blue Patches: Blue Whale Shale Deposits, Black Markers: Thrust complex above the Blue Whale detachment surface with minor listric faulting. Detached/mobilized shale patches are carried upwards via these thrusts in between minibasin formations) Seismic V.E. 2:1186

Figure 128: Proximal part of White Pointer Delta shown on 2D line w00fdw0015.mig08ts-rot180 (Purple Marker: Top Tiger Formation, Orange Marker: Top White Pointer Formation, Yellow Markers: White Pointer Deltaic Deposits, Blue Patches: Blue Whale Shale Deposits, Black Markers: Listric faults soling into Blue Whale detachment surface) Seismic V.E. 2:1.187

Figure 129: Central part of White Pointer Delta shown on 3D xline 11000 (Purple Marker: Top Tiger Formation, Orange Marker: Top White Pointer Formation, Yellow Markers: White Pointer Deltaic Deposits, Blue Patches: Blue Whale Shale Deposits, Black Markers: Large-scale listric faults soling into Blue Whale detachment surface and small-scale faulting within the deltaic wedge related to ductile medium movement. Red rectangles show the enlarging offset difference being translated further towards the distal part indicating mobilization of deeper strata further down in the delta-toe. Some fault reactivation is also observed at top-deltaic level) Seismic V.E. 2:1187

Figure 130: Distal part of White Pointer Delta shown on 3D xline 11000 (Purple Marker: Top Tiger Formation, Orange Marker: Top White Pointer Formation, Yellow Markers: White Pointer Deltaic Deposits, Blue Patches: Blue

Whale Shale Deposits, Black Markers: Thrust complex above the Blue Whale detachment surface with minor listric faulting. Detached/mobilized shale patches are carried upwards via these thrusts in between minibasin formations. Red rectangle shows the enlarging offset difference -migration of gravitational cell activity getting younger- at the distal delta-toe above the branched thrust complex) Seismic V.E. 2:1.188

Figure 131: Central part of White Pointer Delta shown on 3D inline 5050 (Purple Marker: Top Tiger Formation, Orange Marker: Top White Pointer Formation, Yellow Markers: White Pointer Deltaic Deposits, Blue Patches: Blue Whale Shale Deposits, Black Markers: Large-scale listric faults soling into Blue Whale detachment surface and/or scooping above the ductile medium. Localized shale deposits and wedging around these structures shown in red rectangles point out to early shale mobilization patterns and ridge-like deposition) Seismic V.E. 2:1.189

Figure 132: Central part of White Pointer Delta shown on 3D inline 5050 (Purple Marker: Top Tiger Formation, Orange Marker: Top White Pointer Formation, Yellow Markers: White Pointer Deltaic Deposits, Blue Patches: Blue Whale Shale Deposits, Black Markers: Listric faults soling into Blue Whale detachment surface and scooping within the deltaic wedge above the ductile medium) Seismic V.E. 2:1.....190

Figure 133: Central part of White Pointer Delta shown on 3D inline 5050 (Purple Marker: Top Tiger Formation, Orange Marker: Top White Pointer Formation, Yellow Markers: White Pointer Deltaic Deposits, Blue Patches: Blue Whale Shale Deposits, Red Rectangle: Fingering sediment-shale interaction observed at detachment level indicating transgressional activity, Black Markers: Listric faults soling into Blue Whale detachment surface and scooping within the deltaic wedge above the ductile medium) Seismic V.E. 2:1.190

Figure 134: Distal part of White Pointer Delta shown on 3D inline 2050 (Purple Marker: Top Tiger Formation, Orange Marker: Top White Pointer Formation, Yellow Markers: White Pointer Deltaic Deposits, Blue Patches: Blue Whale Shale Deposits, Black Markers: small-scale radial faulting above shale-cored domal highs and the large-scale thrust complex dissected in perpendicular view, Pink markers with black dots: weld features separating minibasin depocenters in between the mobilized shale structures) Seismic V.E. 2:1.....191

Figure 135: Distal part of White Pointer Delta shown on 3D inline 2050 (Purple Marker: Top Tiger Formation, Orange Marker: Top White Pointer Formation, Yellow Markers: White Pointer Deltaic Deposits, Blue Patches: Blue Whale Shale Deposits, Black Markers: small-scale radial faulting above shale-cored domal highs and the large-scale thrust complex dissected in perpendicular view, Pink markers with black dots: weld features separating minibasin depocenters in between the mobilized shale structures) 1: Primary-Level Minibasin Formations, 2: Secondary-Level Minibasin Formations. Seismic V.E. 2:1.192

Figure 136: Distal part of White Pointer Delta shown on 3D inline 2050 (Purple Marker: Top Tiger Formation, Orange Marker: Top White Pointer Formation, Yellow Markers: White Pointer Deltaic Deposits, Blue Patches: Blue Whale Shale Deposits, Black Markers: small-scale radial faulting above shale-cored domal highs and the large-scale thrust complex dissected in perpendicular view, Pink markers with black dots: weld features separating minibasin depocenters in between the mobilized shale structures) Note the wedging and welding observed around the interpreted shale deposits. Seismic V.E. 2:1.192

Figure 137: Structural Time Slice Analysis for 5 and 8 km depth intervals on time-slice view.....196

Figure 138: Segmented recognizable features from 5 km depth time slice (please note the diagram on Figure 137 for additionally interpreted structures). Designated rectangles specify the clustered structures in particular portions of the dataset. Blue Rectangle: Radial faults and cracks, Green Rectangle: Circular minibasin patterns, Red Rectangle: Listric Faults, Yellow Rectabgle: Strike slip faults.198

Figure 139: Segmented recognizable features from 8 km depth time slice (please note the diagram on Figure 137 for additionally interpreted structures). Designated rectangles specify the clustered structures in particular portions of the dataset. Blue Rectangle: Welded shale deposits, Green Rectangle: Elongated minibasin patterns, Red Rectangle: Flattened Listric Fault roots, Yellow Rectabgle: Flattened strike slip faults roots.199

Figure 140: Interpreted close-up from 5 km depth seismic time-slice listric fault domain. Green Lines: Listric Faults, Dashed Orange Lines: Strike-Slip Faults.....200

Figure 141: Interpreted close-up from 5 km depth seismic time-slice. Green Lines: Listric Faults, Dashed Orange Lines: Strike-Slip Faults, Dashed Red Closures: Rounded Depocenters/Minibasins.202

Figure 142: Uninterpreted vs Interpreted close-up from 5 km depth seismic time-slice. Green Lines: Listric Faults, Pink Closures: Polygonal Cracks, Light Blue Lines: Radial Faults Surrounding shale-cored domal highs, Yellow Lines: Traces of collapsed caldera features around the shale-cored domal highs.....202

Figure 143: Interpreted close-up from 8 km depth seismic time-slice listric fault domain. Green Lines: Listric Faults, Dashed Orange Lines: Strike-Slip Faults, Fine Magenta Lines: Listric Fault Lineations at the base.....203

Figure 144: Comparison of rounded (5 km depth) vs elongated (8 km depth) depocenters from the minibasin domain of Ceduna Sub-Basin, White Pointer Delta interval.....204

Figure 145: Interpreted close-up from 8 km depth seismic time-slice. Green Lines: Listric Faults, Dashed Red Closures: Elongated Depocenters/Minibasins.....205

Figure 146: Wedging and unconformity demonstration from Ceduna Sub-Basin White Pointer Delta. Blue Packs: Blue Whale Formation, Yellow Markers: Delta Sediments, Red Arrows: Onlap/Toplap Truncations, Green Marker: Surface Unconformity (image courtesy of PGS).....208

Figure 147: Ceduna Sub-Basin, White Pointer Delta wedging examples collected from various parts of the delta (image courtesy of PGS).....209

Figure 148: Welding Examples from Ceduna Sub-Basin, White Pointer Delta. Purple Markers: Top Tiger Fm. Orange Markers: Top White Pointer Fm. Yellow Markers: White Pointer Delta Sediments. Blue Patches: Blue Whale Fm. Dashed Pink Lines with Black Dots: Welds. Green Undulations: Unconformity Surfaces. Bold Black Lines: Large-Scale Listric Faults. Thin Black Lines: Small-Scale Normal Faults. Detachment Level is marked with bold black line underneath the Blue Whale Fm. Red Lines: Thrust Faults. Dark Blue lines depict the inline-xline crossings. All seismic lines are in PSDM (image courtesy of PGS).....211

Figure 149: Ceduna Sub-Basin, White Pointer Delta Minibasin Examples. Purple Markers: Top Tiger Fm. Orange Markers: Top White Pointer Fm. Yellow Markers: White Pointer Delta Sediments. Blue Patches: Blue Whale Fm. Dashed Pink Lines with Black Dots: Welds. Green Undulations: Unconformity Surfaces. Bold Black Lines: Large-Scale Listric Faults. Thin Black Lines: Small-Scale Normal Faults. Detachment Level is marked with bold black line underneath the Blue Whale Fm. Red Lines: Thrust Faults. Dark Blue lines depict the inline-xline crossings. All seismic lines are in PSDM (image courtesy of PGS).....213

Figure 150: Thrusting and duplexation seen on 3D seismic inline and xline view. See the map on the top right corner of the figure for location. Line A-A' shows the inline seismic view, while the lines B-B', C-C', D-D' depict the xline views crossing through the A-A' inline. Purple Markers: Top Tiger Fm. Orange Markers: Top White Pointer Fm. Yellow Markers: White Pointer Delta Sediments. Blue Patches: Blue Whale Fm. Dashed Pink Lines with Black Dots: Welds. Bold Black Lines: Large-Scale Listric Faults. Thin Black Lines: Small-Scale Normal Faults. Detachment Level is marked with bold black line underneath the Blue Whale Fm. Red Lines: Thrust Faults. All seismic lines are in PSDM (image courtesy of PGS).....215

Figure 151: 3D Seismic data cube representation with inline and xline view of a fish-tail structure from Ceduna Sub-Basin. See the legend on the figure for stratigraphic information. Bold Black Lines with Triangles: Out-of-Plane Thrust Fault View. All seismic lines are in PSDM (image courtesy of PGS).....217

Figure 152: Schematic diagram of fish-tail structure evolution observed on inline and xline view of Ceduna Sub-Basin 3D seismic cube. Post fish-tail building will be detailed in the following sections. See the legend of Figure 151 for stratigraphic level information.....218

Figure 153: (A) Geological map of NW Borneo margin (compiled from Hinz et al., 1989; Hutchison, 1996; Sandal, 1996; Morley et al., 2003, 2008). Deep-water fold belt anticlines were interpreted from time structure maps in Grant (2004) and Gee et al. (2007). (B) Digital elevation model (DEM) location map. (C) Reprocessed BGR8620 two-dimensional seismic line C-C' showing the regional structural setting. The 3-D seismic area includes three folds within the inboard fold belt that we call fold 1 to fold 3. The deep-water fold belt basal detachment was projected into the 3-D study area near the lower limit of the 3-D seismic volume at a depth of ~7 s TWT (~13 km depth) from previous studies (Cullen, 2010; Cullen and de Vera, 2012). The South China Sea unconformity (SCSU) bright reflectors, shown by white arrows, mark the base of the South China Sea postrift sediments and are below the 7 s TWT limit of the 3-D seismic volume. TWT—two-way travelttime (image retrieved from Wu et al., 2019).219

Figure 154: Regional seismic dip line T24600 across the central offshore Sabah study area, where growth strata have been scaled to show ~1:1 scale: (A) uninterpreted seismic line, (B) line drawing interpretation of A, (C) structural-filtered display of fold 3 in A, showing lack of vertical continuity between shallow and deep thrust fault cutoffs, and (D) coherency-filtered display of fold 1 in A, showing an array of shallow, seaward-dipping extensional faults. The structures in the study area are characterized by blind, forward-vergent thrusts, footwall synclines, shorter forelimbs, and long backlimbs. The footwall synclines cannot be fully explained by seismic velocity pull-up artifacts, which are approximately on the order of 100 ms two-way time (~100 m) under the thrust-related folds (see Fig. S1 [text footnote 1]). Faults are dashed where inferred. Ages of syngrowth units (SG) are labeled in Ma. BSR—bottom simulating reflector (image retrieved from Wu et al., 2019).220

Figure 155: (A–D) Proposed kinematic model for the triangle zones in fold 3. A shear fault-bend fold (redrawn from Suppe et al., 2004) in A and B is deformed by a late-stage footwall backthrust in C. Tightening of the triangle zone fold-thrust in D oversteepens the forelimb and back-rotates the backlimb. The final fold geometry shows similarities to the offshore Sabah folds in this study (image retrieved from Wu et al., 2019).221

Figure 156: Shale-cored domal high surface expression at 5 km time-slice (image courtesy of PGS)223

Figure 157: Ceduna Sub-Basin, White Pointer Delta Minibasin Examples. Purple Markers: Top Tiger Fm. Orange Markers: Top White Pointer Fm. Yellow Markers: White Pointer Delta Sediments. Blue Patches: Blue Whale Fm. Dashed Pink Lines with Black Dots: Welds. Green Undulations: Unconformity Surfaces. Bold Black Lines: Large-Scale Listric Faults. Thin Black Lines: Small-Scale Normal Faults. Detachment Level is marked with bold black line underneath the Blue Whale Fm. Red Lines: Thrust Faults. Dark Blue lines depict the inline-xline crossings. All seismic lines are in PSDM (image courtesy of PGS). Examples for salt diapir surface expressions in the upper panel; left image retrieved from Davison et al., 2000; right image retrieved from Harding & Huuse, 2015.225

Figure 158: Geo-Chronological Evolution Diagram of White Pointer Delta Shale-Cored Domal Highs above Fishtail Structures.....228

Figure 159: Ceduna Sub-Basin, White Pointer Delta Kinematic Scenario explained in evolutionary geologic stages (see the text for explanation).232

Figure 160: Google Map view of Rakhine State, Myanmar and the surrounding region. Study area is indicated with red geometrical closure (Image Courtesy of Google Earth, 2020).235

Figure 161: Regional tectonic map (modified from Wang et al., 2014) Blue arrow shows the direction of Indian plate motion relative to Sunda Plate (e.g. Socquet et al., 2006). The black arrows show the opening direction of the Central Andaman spreading center. Velocities are in mm/yr. Burma Plate (Curry et al., 1979) is bounded by the Sunda Mega Thrust; NGT = Naga Thrust; CMB: Central Myanmar Basin; MP: Mt. Pona (red star). Box shows location of the central coastal region (image retrieved from Moore et al., 2019).237

Figure 162: Mud dome diapir in the seismic profile across the northern segment of the accretionary wedge of the Andaman Sea Basin (see He & Zhu, 2018 for line location to the south of Ramree and Cheduba Islands) (image retrieved from He & Zhou, 2018).238

Figure 163: Structural sketch map of Western Myanmar showing the two seismic line locations (Section A and Section B) (modified from Morley et al., 2011) (image retrieved from Racey & Ridd, 2015).239

Figure 164: Representative cross-sections through offshore Rakhine blocks A4 (top) and A5 (bottom) (modified from Morley et al., 2011) (image retrieved from Racey & Ridd, 2015).240

Figure 165: Rakhine Basin seismic examples (Courtesy of MOGI, U Lynn Myint) (image retrieved from Cliff & Carter, 2016) Note the very nice turtle-back-like depo center inverted and located on the right hand side of seismic line A, which is similarly imaged on seismic line B.....240

Figure 166: Outcrop photos of sheared serpentinite. (A) Large randomly-oriented blocks cut by veins, exposed on SW coast of Cheduba Island. (B) Large block with shear zone at base exposed at Mazin Point. (C and D) Closeup of the base of the large block pictured in (B) showing smaller serpentinite phacoids surrounded by sheared serpentinite matrix; the phacoids are similar in appearance to the adjacent parts of the large block (image retrieved from Moore et al., 2019).242

Figure 167: Outcrop photos of steeply- to vertically-dipping turbidite units with interbedded MTDs 2 and 3 (yellow circle = 1.7 m geologist for scale). (A) MTD-2 with thick undeformed sandstone beds above. (B) MTD-3 with

<i>undeformed sandy turbidite beds above and below. (C) Detail of MTD-3 showing internal deformation and relationships with overlying and underlying sandstone beds. Yellow arrows show local erosive contacts. (D) Chaotic internal structure of MTD-3; yellow arrows point to folded strata (image retrieved from Moore et al., 2019).....</i>	<i>243</i>
<i>Figure 168: Outcrop photos of mud volcanoes. (A) Side view of young MV that formed on top of an older mud volcano surface. Gryphon is an active mud vent. (B) Photo of surface of active mud volcano showing variation in size of fragments exposed on the surface. Note angular chert fragment. (C) Exposure of deeper part of MV along stream cut. Note random orientation of clasts and lack of fabric. (D) Clasts on surface of the MV. Note that clasts are subrounded (image retrieved from Moore et al., 2019).....</i>	<i>244</i>
<i>Figure 169: Location map of visited sites during the fieldwork (Image Courtesy of Google Earth).....</i>	<i>246</i>
<i>Figure 170: Visited sites of Ngapali along the shoreline (image courtesy of Google Earth).....</i>	<i>247</i>
<i>Figure 171: Visited sites of Ngapali - Toungup Road (image courtesy of Google Earth).....</i>	<i>247</i>
<i>Figure 172: Central Ramree minibasin formation with visit site/sampling locations (image courtesy of Google Earth).....</i>	<i>248</i>
<i>Figure 173: Approximate stratigraphic column of central Ramree area and pictures illustrating these various stratigraphic units (image retrieved from Maurin & Rangin, 2009).....</i>	<i>249</i>
<i>Figure 174: Northern Ramree Island Mud Volcano Site, Rakhine State, Myanmar.....</i>	<i>250</i>
<i>Figure 175: Northern Ramree island visit site/sampling locations (image courtesy of Google Earth).....</i>	<i>250</i>
<i>Figure 176: Debris flow observed at Southern Ngapali shoreline (~ 15m thick) (Stop 1).....</i>	<i>251</i>
<i>Figure 177: Eocene Age black shale mélangé sighted at Central Ramree (Stop 14).....</i>	<i>252</i>
<i>Figure 178: Strongly folded flysch formation in backthrust position (NE to the right of the right side of the picture (Stop 16).....</i>	<i>252</i>
<i>Figure 179: Left hand-side figure: Foliated shales with incipient S/C bands. Right hand-side figure: Recumbent folding of sandy levels (Stop 4).....</i>	<i>253</i>
<i>Figure 180: Left hand-side figure: Alternating sand and clay sequences within the Eocene Flysch Belt of Northern Ramree. Right hand-side figure: 35cm sand body displaying the internal structure of a sand sequence with a complex dynamic emplacement.....</i>	<i>253</i>
<i>Figure 181: Example of an interpretative model and its representative log showing the seismo-turbidites from Calabrian Sea (image retrieved from Polonia et al., 2017).....</i>	<i>254</i>
<i>Figure 182: Left hand-side figure: Along-strike view of a littoral sand bar. Right hand-side figure: Large-scale channel-like structures.....</i>	<i>255</i>
<i>Figure 183: Left hand-side figure: Delta-like alternanc of sand and clay with 3D ripples and through cross-beds (Stop 19). Right hand-side figure: Oligocene Age potential paleo-soil in the upper part of an alternating sand-clay level (Stop 18).....</i>	<i>256</i>
<i>Figure 184: N directed view of the second main sequence of the minibasin showing the major sandy levels capping the deltaic sequence.....</i>	<i>256</i>
<i>Figure 185: Flattening fabric within the clay debris flow. Two directions of sheer are observed (Top South and Top North) with respect to the vertical bedding. This formation is observed on a 5m thick upper contact of flow with a clear alteration of clay mélangé (Stop 5).....</i>	<i>257</i>
<i>Figure 186: Steep foliation within the major debris flow turning parallel to bedding below the upper limit of the debris flow (Stop 4).....</i>	<i>258</i>
<i>Figure 187: Example of mobilized block in the mélangé. Left hand-side figure: An ophiolite block in a flattening fabric. Right hand-side figure: Pebbles and cuttings floating within the clay matrix (cm scale).....</i>	<i>259</i>
<i>Figure 188: Syn-sedimentary gravitational spreading/gliding on top of the debris flow (Stop 4).....</i>	<i>259</i>
<i>Figure 189: Satellite view of Minibasin 2 from East direction showing the sequential organization and geometry (Image Courtesy of Google Earth). Note the strong decrease of the basin thickness from left (NW) to right (SE) related to the deltaic geometry, which is much thinner from the delta foreset packages to the bottom set.....</i>	<i>260</i>
<i>Figure 190: Possible paleo-geographic path related to a northerly directed source of clastics super-imposed on Bengal / Bramahputre clastics forming minibasin-like depo-centers onto the mobile Eocene clays.....</i>	<i>261</i>

Figure 191: Ramree Island mud volcano satellite image, Rakhine State, Myanmar (Image Courtesy of Google Earth).262

Figure 192: Ramree Island mud volcano, Rakhine State, Myanmar.263

Figure 193: Upper sketch: A seismic line interpretation from offshore Cheduba Island showing the thrust slices and remobilized clays (Maurin and Rangin, 2009). Lower sketch: Synthetic EW oriented cross-section showing the possible location of hydrocarbon levels sourcing mud volcanoes from the lower tectonic slices below the Ramree Thrust (Yellow: Miocene, Red: Oligocene, Brown and marked folded lines: Eocene).264

Figure 194: Left hand-side figure: Geological Map of Ramree and Cheduba Islands with the location of two main thrust faults and the seismic line. Right hand-side figure: A possible scenario for clay mobilization for minibasins and mud volcanoes (Maurin and Rangin, 2009) Both mechanisms are still to be tested and understood.265

List of Tables:

Table 1: Potoroo-1 Well Information Sheet obtained from Geoscience Australia dbforms.ga.gov.au.....168
Table 2: Gnarlyknots 1A Well Information Sheet obtained from Geoscience Australia dbforms.ga.gov.au170
Table 3: Ceduna Sub-Basin 3D PSDM Seismic Data Acquisition Parameters.....173

PART I: Introduction

General Introduction

Salt and Shale are two types of rock that deforms under stress and strain. Ductility of these rocks is governed by processes taking place beyond ‘the *scale of observation*’ (e.g. principle of crystalline plasticity for salt; shear bands, folding and faulting for shale) and ‘*distributed deformation*’. Some controlling factors such as the *confinement pressure, temperature, water content, rate of loading, and amount of sedimentation*, control the ductile behavior of these rocks. When these aforementioned controlling factors are met, ductile rocks (e.g. salt and shale) display behavioral similarity to viscous materials (e.g. fluids) in nature and their specific deformation-related signature (e.g. halokinesis, argilokinesis) can be recorded within the sedimentary package surrounding these rock formations.

Salt Tectonics is a relatively well-known topic displaying such properties while being observed in various onshore (e.g. Zagros, Iran; Sivas, Turkey; La Popa, Mexico in review papers by Jahani et al. (2017), Callot et al. (2014), Rowan et al. (2012), respectively) and offshore (e.g. Gulf of Mexico, US/Mexico; Campos/Santos Basins, Brazil; Kwanza Basin, Angola) parts of the world due to abundance of high-quality seismic datasets and various outcrop examples we now have access to.

One of the best examples that have contributed immensely to the topic and broadened our understanding of Salt Tectonics at outcrop level is the ‘rediscovery’ of Sivas Salt Basin, Turkey. The role of salt was evidenced with numerous world-class outcrop examples by Yavuz Çubuk in his PhD thesis that was published in 1994, at the same time when the topic was being popularized by pioneer names of its time such as Martin P. A. Jackson and Mike R. Hudec. However, (1) the lack of academic support and (2) publications/dissertation made only in Turkish shaded his big discovery (which would likely to be recognized internationally had it been published in English) led to the hypothesis he proposed for the region to be forgotten for more than two decades. The simultaneous publications of its time depicted the Sivas Basin as a geological setting that was controlled purely by Thrust Tectonics without mentioning the salt formations that were proposed by Çubuk. The region was rediscovered by Google Satellite Imagery in 2011 and later studied by four PhD students (C. Ribes, C. Kergaravat, A. Pichat and E. Legeay) under supervision of J.P. Callot and J.C. Ringenbach only to be recognized as one of the best preserved and most informative Salt Basins around the world. The example of Sivas Basin shows once again the importance of technology and innovations that can improve our understanding massively on a highly important geological topic such as Salt Tectonics.

Shale is another type of rock formation that deforms under three major principles; (i) seismic scale plasticity (folding and faulting), (ii) fluidization (mud volcanism), and (iii) ductile strain/plasticity (distributed slow motion). Small scale plastic deformation pattern, which could display ductile behavior similar to salt deformation under certain conditions (e.g. Morley, 2003). However, its mobilization pattern and hence the topic of Shale Tectonism is not yet as-well-identified-as salt due to its variable brittle vs ductile behavior on different scales of observation (e.g. microscopic vs macroscopic) and lack of well-preserved outcrop examples we are able to access/detect around the world.

Shale is an important topic of research both for industry and academia applications as it plays a crucial role on determining subsurface storage alternatives for pollutants such as: nuclear, industrial, chemical, and biologic wastes, as their release to the atmosphere would catastrophically contribute to global warming and ocean acidification issues. CO₂ (carbon dioxide) storage and injection methods into shale-related subsurface formations have been adapted both for enhanced oil recovery/sealing and reduced gas mitigation/release applications respectively with an aim to reduce the heavy consequences of intensified global industry outlets.

We initiated this PhD Research Project in April 2017 with the aim of making a detailed structural and geometrical analysis of a shale-prone environment in order to shed light on the topic of *Shale Tectonism* and to understand its resemblance/connection with *Salt Tectonism*. This PhD Thesis aims to further detail the research-related findings on the phenomena of *Shale Mobility* with an effort to suggest an advanced/updated perspective and understanding of the topic with detailed seismic data analysis, analogous salt-shale comparison and fieldwork observations.

Objectives of Research: Rationale

This PhD project aims to better understand the dynamics of shale-dominated environments and their interaction/mobilization pattern with the surrounding sedimentary package in a delta setting. Salt and shale rocks both deform under stress, while the scale of deformation for salt is much smaller than that of shale. Nevertheless, they both work with same principle at macro scale; by summing up the plastic displacement within the particles. Hence, they may mobilize with a similar pattern under macroscopic scale.

At a general sense; *Shale Tectonism* can be described as the study of shale-related deformation observed in nature. The ductile behavior of shales recorded in the syn-tectonic sedimentary packages are observed at large-scale while the brittle deformation is observed at small-scale in terms of fracturing (e.g. under microscopic investigation). Moreover, clays can be fluidized under pressure and existence of gases/hydrocarbons. Therefore, the mobility of shales can be determined by three mechanisms; *Classical Tectonism* (e.g. large scale folding/faulting) [1], *Fluidization/Liquefaction* (e.g. mud volcanism) [2], and *Strain/Plasticity* (e.g. distributed slow motion) [3]. Although the mobilization of shales is classified under these three styles; only the latter leads to what-seems-to-be similar with Salt Tectonics in terms of ‘diapirism’, sequential pattern recorded by surrounding sediment packages, and/or ‘minibasin formations’ compared to the geometrical analogy of salt.

When not fluidized, the brittle failure of shale/clay occurs at such a small scale that the whole system appears to behave in a ‘ductile manner’ at large-scale over geological timelines leading to salt-like deformation structures such as ‘*diapirs*’, canopy features, minibasins and welds recorded by the surrounding sedimentary cover (e.g. Alboran Sea, Baram Delta/Northern Borneo, Eastern Venezuela Basin in Soto et al., 2010; Morley, 2003; Duerto, 2007 respectively). However, the real challenge for this statement is to find demonstrative analogues backed by coherent seismic datasets and convincing fieldwork observations. Therefore, the most important questions to answer are;

[1] What are the most diagnostic features of salt-controlled deformation settings in nature?

[2] Do we have examples of such features in shale-controlled deformation settings observed in nature?

[3] Can we apply salt-like deformation concepts (e.g. Salt Tectonics) to shales?

For this purpose; our goal and objectives in this study are to work on a well-imaged high-quality seismic dataset to rebuild the long-term clay motion/mobilization scenario by unfolding the overlying sedimentary package in order to demonstrate that clay can act as a long-term viscous material resembling salt and later to combine the seismic findings with fieldwork observations to strengthen its credibility.

In terms of Salt Tectonism; the rate and thickness of sedimentation introduced into a salt-prone environment play a key role defining the deformation geometries also known as ‘*halokinesis*’. Halokinesis

features define the patterns of salt mobilization interacting with the surrounding sedimentary cover. Similarly, by applying the same methodical approach, we aim to show that '*argilokinesis*' (also known as '*claykinesis*') features formed as a result of shale deformation recorded by the thick sedimentary cover can be compared to salt deformation.

Given the brief reasoning about the emerging point of this research; this PhD Thesis aims to take a look at a high quality seismic dataset collected from offshore Australia, Great Bight Basin, Ceduna Sub-Basin consisting of two shale-prone deltaic systems (namely; White Pointer and Hammerhead Delta Deepwater Fold & Thrust Belt Systems -DDFTB-). The area of study is already a quite well described and understood geological setting in terms of geodynamic evolution and structural framework (see reviews from Totterdell and Krassay, 2003; Totterdell et al., 2008; Espurt et al., 2009; Espurt et al., 2012; MacDonald et al., 2012; MacDonald, 2013; MacDonald et al., 2013). However, the ambiguity of previously studied seismic datasets did not give a chance to further distinguish the shale-related features observed at the distal deltaic setting.

Thus with the light of a well-imaged 3D Seismic dataset we utilized for this study, we aim to:

1. Contribute to the existing knowledge of Ceduna Sub-Basin deltaic systems with a focus on the White Pointer Delta, where we observe mobilized shale features.
2. Further detail the shale-driven mobilization pattern of distal White Pointer Delta toe as well as comparing the findings to the geological fieldwork observations we have conducted in Rakhine State, Myanmar, where we studied a shale-driven minibasin domain.
3. Suggesting a mechanism of salt-like shale mobilization for global shale-driven delta examples and demonstrate that clay can act as a long-term viscous material resembling salt.

Organization of the Thesis

PART I

This part is designed to familiarize the reader with the research topic and purpose of study. It aims to deliver the topic under three main categories; *General Introduction*, *Objectives of Research*, and *Organization of the Thesis*. It is aimed to give a general conduct of research to the audience introducing the topic and problematic proposed to be addressed throughout the study.

PART II

This section is focused to review the literature on Salt and Shale Tectonics. The purpose of this section is to engage the reader with what have been studied so far on the topic and where we are standing in terms of conducted research on salt and shale mobility.

Chapter 1

This chapter will be reviewing the topic of Salt Tectonism under five sub-sections; (1) General Concept, (2) Deformation Mechanisms, (3) Driving Forces, (4) Deformation Geometries and (5) Remarks. The purpose of this chapter is to present/summarize the current knowledge about Salt Tectonics.

Chapter 2

Similar to the Salt Tectonics chapter, this chapter will be reviewing the topic of Shale Tectonism under five sub-sections; (1) General Concept, (2) Deformation Mechanisms, (3) Driving Forces, (4) Deformation Geometries and (5) Remarks in order to give a better chance to the reader for comparing Salt with Shale.

Chapter 3

This chapter is set to summarize what we know so far about the shale-prone geodynamic settings, where we observe Salt-Like Shale Tectonism and to review its resemblance to salt as well as understanding the controlling factors of shale mobility.

Chapter 4

This chapter aims to make a blind comparison of a salt vs shale-prone environment in order to emphasize the importance and quality of seismic data imaging as well as its convenience for identifying realistic salt/shale tectonism.

PART III

This part is constructed to deliver a comprehensive geological review of Offshore Southern Australia, Great Bight Basin, Ceduna Sub-Basin, with an aim to engage the reader with the study area and its geologic components in order to set the ground for further structural analysis. In this section, we detail the findings and observation made on 2D – 3D seismic data focusing on the structural analysis of the Ceduna Sub-Basin with an emphasis on White Pointer Delta interval, where we observe indications salt-like shale tectonism at the distal part.

Chapter 5

This chapter consists of three main sub-sections; Introduction (i), Geological Background (ii), Lithostratigraphy (iii), and Ceduna Sub-Basin Deltaic Systems (iv), in order to give a comprehensive geological review about the area of interest, the Ceduna Sub-Basin, and its deltaic components. It is aimed

to set the ground for detailed distal delta interval analysis of White Pointer Delta, where we observe Shale Tectonism.

Chapter 6

This chapter will be summarizing all of the accessible seismic data material we have utilized in this research as well as the only two exploration well information (Potoroo and Gnarlyknots) within close vicinity of 3D seismic dataset.

Chapter 7

The seismic interpretation scheme we have conducted on a 3D seismic dataset and complimentary regional 2D seismic lines display various and distinctive examples of shale mobilization observed within the distal part of a shale-driven deltaic system (White Pointer Delta) of Ceduna Sub-Basin.

This chapter summarizes the physiological properties of gravitationally gliding *White Pointer Delta* and how these features dominate different compartments of the deltaic system; proximal (1), central (2) and distal (3) delta setting. Each sub-section aims to showcase the characteristic properties of aforementioned delta compartments and its interaction with shale-driven detachment level.

Chapter 8

This chapter aims to detail the Salt-Like Shale Tectonics features (a.k.a. Shale Deformation Geometries: Argilokinesis) interpreted within the *distal part of White Pointer Delta: Minibasin Domain* resembling salt deformation. Following the conducted seismic study, we propose a regional kinematic scenario for shale mobilization in the area with seismic data examples associated with the concept of Salt Tectonics, which showcases the delta development under a shale-driven kinematic evolution.

PART IV

This part is devoted to wrap up the thesis research and present a discussion about the findings and perspectives on Shale Mobility based on the conducted seismic study of Ceduna Sub-Basin and preliminary work on the Rakhine State of Myanmar. It consists of two sub-chapters complimenting the subject.

Chapter 9

This chapter aims to present the findings of an 8-day fieldwork study conducted in Ramree-Cheduba region of Rakhine State, Myanmar in November 2018 with an effort to supplement the seismic findings from Ceduna Sub-Basin, White Pointer Delta interval. This region is exposed to a shale-related deformation pattern and mud volcanism. The area was previously thought to be a tectonically controlled system with highly pressurized fluids and mobile shales at depth without a major control on the sedimentation pattern and strata. Hence, it is excluded from our literature review of Shale Tectonism.

Chapter 10

This chapter proposes a conclusion on the research in the light of a well-imaged seismic dataset (Ceduna Sub-Basin, White Pointer Delta interval) and fieldwork observations made at a shale-prone outcrop setting; Ramree-Cheduba region of Rakhine State, Myanmar.

PART II: Salt and Shale Tectonics Review

This part will be summarizing the main characteristics of salt and shale and what we know about the tectonism induced by these rocks. The purpose of the first two chapters are to familiarize the reader to the concepts of Salt and Shale Tectonics based on the literature knowledge we have so far. The third chapter will be reviewing the existing geodynamic settings, where we observe salt-like shale tectonism in order to make a comparison of shale-prone settings with salt-prone areas. Lastly, Chapter 4 will be delivering the starting point of this research in order to transition the reader from the literature information into the basics of the PhD study.

Chapter 1: Salt Tectonics

The topic of Salt Tectonics encompasses all interactions between tectonic and sedimentary deposits related to salt flow (i.e. evaporates). The topic refers to the deformation processes of salt bodies that consist of evaporitic minerals (but mostly halite) (Jackson and Hudec, 2017). Mobile evaporates are hereafter denoted as 'salt'. Salt is a mechanically weak solid that deforms under stress and loading. The deformation pattern induced by salt gets recorded within the sedimentary package, which gives us an idea about how it formed, behaved, interacted and was modified during the sedimentary deposition (Jackson and Hudec, 2017). This chapter will be summarizing the concept, deformation mechanism and deformation geometries responsible of and resulting in Salt Tectonism observed in nature.

From 1930s to 1980s, Salt Tectonism was thought to be controlled by buoyancy, enabling blobs of salt rise through a yielding overburden similar to lava lamps (Jackson, 1995; 1997). As we made more research on the topic and gained further knowledge, it is now known that differential loading is the main driving force for salt flow, while the buoyancy is only a small contributor to the phenomena (Jackson and Hudec, 2017) [*Buoyancy* is still a driver for salt flow like *differential loading*, however, it generalizes the viscous flow for all types of rocks, which is not the case for limestones or sandstones]. Hubbert, 1937 and Ramberg, 1981a defined the main forces of Salt Tectonism as gravity (i), pressure (ii), viscosity (iii), and friction (iv); all of which can be triggered via several driving forces (i.e. gravitational loading, tectonic displacement and thermal subsidence) among others (Jackson and Hudec, 2017). Burial depth, basin geometry, tectonic setting and thermal subsidence are the controlling factors effecting the salt mass and its mobilization pattern.

I. General Concept

Salt acts ductile/viscous under compression due to its specific rheology, driven mostly by its crystalline properties. Upon exceeding the flow resistance by these driving forces, salt rocks flow like a viscous material under and/or at surface with geologically rapid strain rates. Salt Tectonism is described as the distributed slow motion of salt primarily controlled by the gravitational and external forces (e.g. basin geometry, sedimentation rate/load, and tectonism) (Figure 1) and recorded within the sedimentary pile surrounding itself.

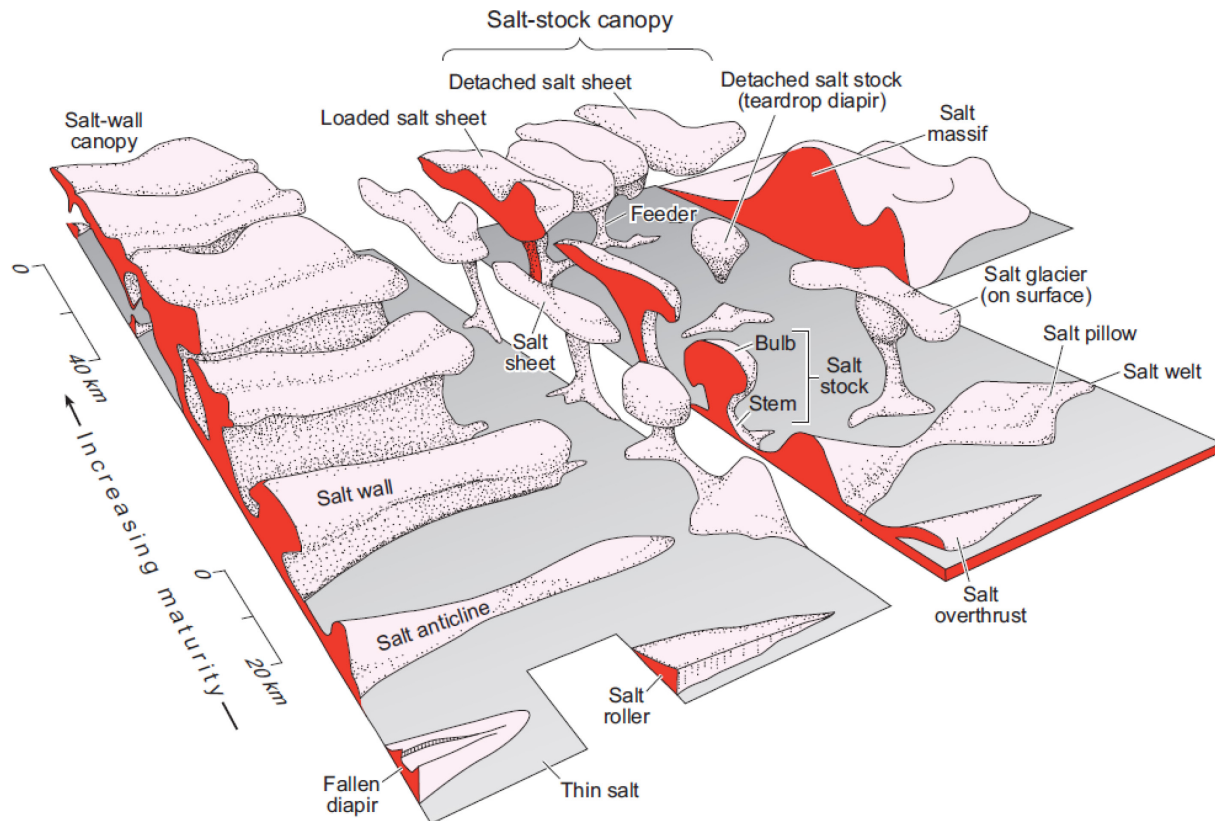


Figure 1: Salt Tectonics Structures (image retrieved from Jackson and Talbot, 1986; Jackson and Hudec, 2017).

Terminologically, these recordings are classified as halo-kinesis features. Halo-kinesis defines the deformation geometries/patterns of salt deposits recorded/interacting with the sedimentary package surrounding the salt mass (Jackson and Hudec, 2017). Halo-kinesis features (also known as salt-related deformation geometries recorded by the sedimentary load) display the growth history of a salt structure much clearer than the salt body itself due to its recorded interaction within the sedimentary strata (Figure 2). Hence, they help us to better understand the structural evolution and mobilization of salt features. The following sections will be reviewing the aspects of Salt Tectonism under three categories; Deformation Mechanisms (i), Driving Forces (ii) and Deformation Geometries (iii), and the main points will be summarized from the book of Salt Tectonics: Principles and Practice by Jackson and Hudec, 2017.

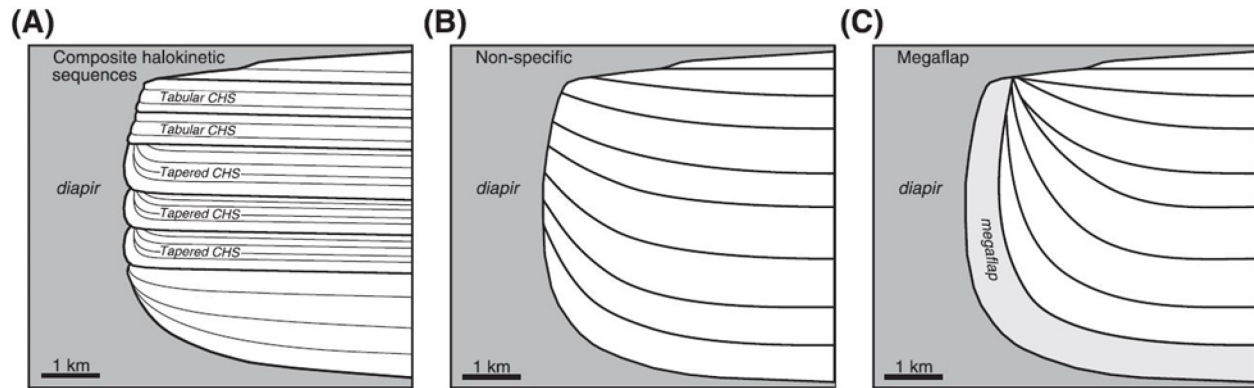


Figure 2: Induced halokinetic sequences (recorded halokinesis features) observed adjacent to a steep diapir: (A) stacked composite halokinetic sequences (CHS), (B) nonspecific minibasin-scale stratal thinning and folding, and (C) a megaflap. See Giles and Rowan et al., 2016).

II. Deformation Mechanisms

A. General Introduction to Salt-Rock Behavior Mechanics: Plastic Strain & Ductility

Salt rock deformation mechanisms are triggered by intra-crystalline and inter-crystalline processes when the rock itself undergo sufficient differential stress (Jackson and Hudec, 2017). Mineralogy, grain size, porosity, permeability, fluid content, grain size, impurity and fabric are the internal controlling factors defining the micro-structural dynamics of rocks, while the external controlling factors are listed as; temperature, differential stress, strain rate, lithostatic and fluid pressure (Passchier and Trouw, 1998). This chapter will be summarizing these mechanisms enabling salt to deform with sediment interaction in nature.

Rocks can display microscopic fracturing, which can appear as ductile strain on macroscopic scale depending on scale of observation. Therefore, *ductility* is a generic term as it refers to the scale-dependent behavior of rocks (Jackson and Hudec, 2017). In natural cases, the rock salt flows/acts ductile under low strain rates and long-term time scales (e.g. geological time-lines) but the small changes in shear stress makes a significant effect on time to yield in ductile behavior. As it is stated by Senseny et al. (1992), “*the compressive strength (the maximum principal stress) increases when the confining pressure and temperature are increased, while it slightly increases with decreasing deformation rate or loading rate*”. Hence rheology, *the study for flow of materials to determine their stiffness*, is a fundamental tool to understand the deformation mechanisms of salt tectonics over long-term in nature (i.e. salt outcrops exposed to geologic time-scales) and over short-term in-situ experiments (i.e. sandbox models) (Jackson and Hudec, 2017).

Increasing temperature arriving with burial depth, enhances ductile behavior over brittleness. For salt rocks, the brittle-ductile transition takes place at or near the surface due to its unique rheology and nature. Gradual flow of a crystalline material (i.e. salt) under a differential load is called *creep*. While most rocks require high temperatures for initial *creep movement* leading to permanent material distortion, salt rocks can creep at room temperatures when it’s assisted with traces of water (i.e. fluid content) (Jackson and Hudec, 2017).

Material distortion occurs when the yield stress limit is exceeded. Upon reaching the yield stress threshold, plastic behaving materials begin to deform at a constant stress ratio, which is also known as the *Plastic Strain*. *Viscous Strain* is a highly variable quantity in terms of steady-state, as it requires constant and stable temperature for the material to preserve its viscous (Newtonian) state. However, under geologic time-scales, salt rocks display *Effective Viscosity* as they adapt to a linear pattern/relationship between stress and strain rate (Jackson and Hudec, 2017).

When the rocks are exposed to variable strain rates, therefore a change in viscosity, the viscous flow behavior becomes unsteady and non-linear. In such situations, the differential stress needed for deformation increases with strain and leads to *Strain Hardening*. Conversely, the differential stress can decline upon increase of strain, which leads to *Strain Softening* behavior. *Transient Creep* (also known as the primary creep) defines the stage, where the rock hardens and declines the strain rate while making the strain-time curve less steep (Figure 3). If the loading stabilizes and remains constant, the strain-time curve becomes linear as the material transitions into the *Steady-State Creep* (also referred as the secondary creep), which indicates that hardening is now balanced with recovery. Steady-State Creep is quite applicable for salt tectonics as it operates over geologic time-scales while the Transient Creep becomes relatively insignificant (Jackson and Hudec, 2017).

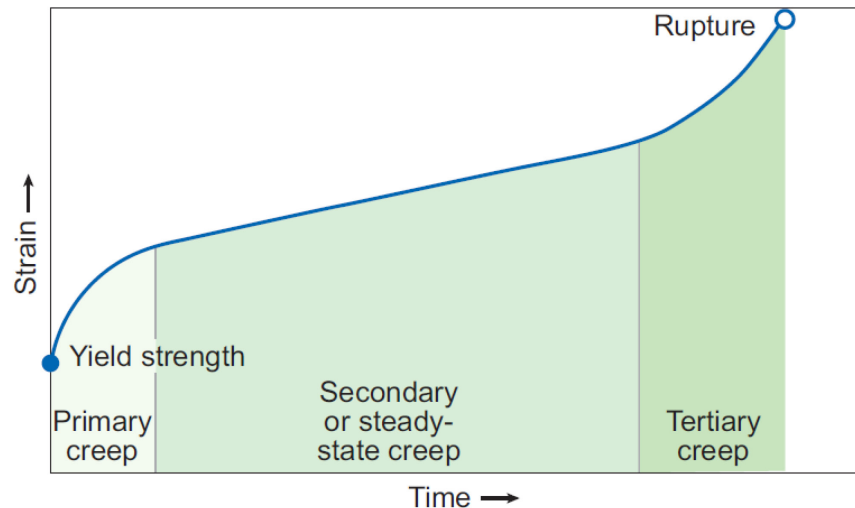


Figure 3 : Graph of Stress vs Time showing stages of Creep from yield strength through the rupture point (image retrieved from Jackson and Hudec, 2017).

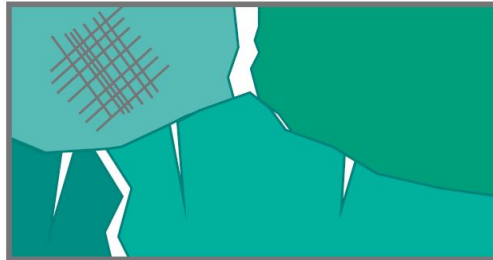
There are three main microstructural processes that take place in rock salt for most geologic conditions, which are namely; (1) *microcracking and cataclastic flow -plasticity-*, (2) *dislocation creep*, and (3) *solution-precipitation creep* (Jackson and Hudec, 2017). The following sections will be detailing these three processes with an effort to better understand salt rock rheology and its properties under microscopic scale.

B. *Microcracking and Cataclastic Flow: Plasticity*

Microcracking and Cataclastic Flow are two mechanisms accounted for the plasticity of salt rocks. *Microcracking* is quoted as *the granulation of rocks under low confining pressure, high strain rates and low-to-moderate homologous temperatures* while *Cataclasis Flow* states *the brittle process in which*

fragments in an aggregate fracture, slide, and rotate to produce gouge, cataclasite, breccia and voids filled by veins (Jackson and Hudec, 2017). During this state, rock volume is increased by cataclasis as fractures dilate. Halite with low temperature, low effective confining pressure and high differential stress is dominated by cataclasis process (Figure 4).

Plasticity, microcracking



Crystal plasticity, microcracking dilatancy, permeability increase

Figure 4: Plasticity and Microcracking: First microstructure and deformation mechanism proposed for salt rocks deformed at temperatures of 20 to 200°C. Different shades of green represent crystals with different orientation (image retrieved from Urai et al., 2008).

Urai and Spiers, 2007; describe this process under three stages;

- (1) Formation of micro-fractures within the grains and cutting across several grains
- (2) Rotation of grains and their fragments while sliding each other
- (3) Dilation of the rock salt and increment on its permeability

As more sediments are introduced into the system; the confining pressure increases with burial, greater deviatoric stress is required to break the rock, which suppresses micro-cracking and dilation while dominating the crystal plasticity (Cristescu and Hunsche 1988; Peach and Spiers, 1996; Cristescu, 1998; Peach et al., 2001; Jackson and Hudec, 2017).

Micro-cracks/fractures play an important role on fluid transport, and understanding fracture healing processes is crucial to figure out fluid circulation dynamics (Moore et al., 1994) as small amount of free water trapped inside crystals can completely modify the rheology of rocks. Moreover, damaged porous solids that have been invaded by a liquid cannot usually recover their initial mechanical properties (Renard, et al., 2002). In terms of salt rocks; processes such as diffusion or hydration of grains can lead to micro-fracture healing, while inclusion of oil and hence the oil staining of micro-fractures disable/disrupt such healing mechanisms for salt.

C. Dislocation Creep

Dislocation Creep defines a form of crystal plasticity that is combined of *dislocation glide* and *dislocation recovery* (Jackson and Hudec, 2017). A crystal is distorted by slipping along one or more crystallographic directions or slip planes during dislocation glide, where a weakly bonded grid is present. When the slip exploits the defects of this grid, it changes the relative positions of atoms/molecules, which eventually leads to slip of these dislocations through a crystal while changing the crystal shape but not distorting its grid structure. The dislocation intensifies as the crystal deforms, which increases the strain energy and

leads to strain hardening (Figure 5). Differential stresses, high strain rates, and temperatures above 100° C are the elements that dominates Dislocation Creep. Such crystal-plastic processes lead to crystals changing its shape and reaching large ductile strains even at lower confining pressures (10 MPa) (Jackson and Hudec, 2017).

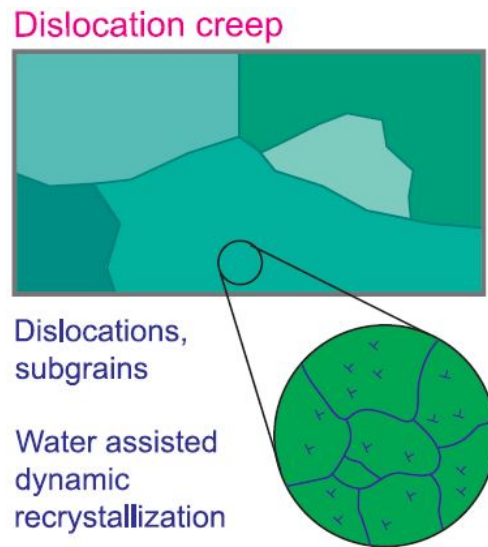


Figure 5: Dislocation Creep: Second microstructure and deformation mechanism proposed for salt rocks deformed at temperatures of 20 to 200°C. Different shades of green represent crystals with different orientation (image retrieved from Urai et al., 2008).

D. Solution-Precipitation Creep

Urai et al., 2008; states solution-precipitation creep as an important deformation mechanism in most *wet rock systems* in the Earth's crust (Renard and Dysthe, 2003), but especially *rapid in rock salt*. The grain boundaries dissolve by impinging at high normal stress areas during pressure solution, which increases solubility. Dissolved ions are diffused via solution transfer at the grain boundaries and precipitated at lower differential stress areas. This water-assisted process is called as the Solution-Precipitation Creep, where the grains change shape without internal strain (Jackson and Hudec, 2017). This type of creep functions when there is a pore fluid, and moderate homologous temperatures along with relatively low strain rates in the environment (Figure 6).

Unlike *dislocation creep* occurring in the crystal lattice of the halite grains, solution precipitation creep (also known as *pressure solution*) takes place at grain boundaries. In an environment with small amount of saturated grain boundary brine, grains tend to *dissolve at highly stressed boundaries* and the material *crystallize at interfaces under low normal stress* following the diffusion through grain boundary fluid (Schutjens & Spiers, 1999, Spiers et al., 2004). As it is stated by Spiers et al. (1999) this process is accompanied by intergranular sliding and rotation (grain rearrangement), and can lead to compaction of porous salt or to deviatoric strain of non-porous aggregates (Urai & Spiers, 2007).

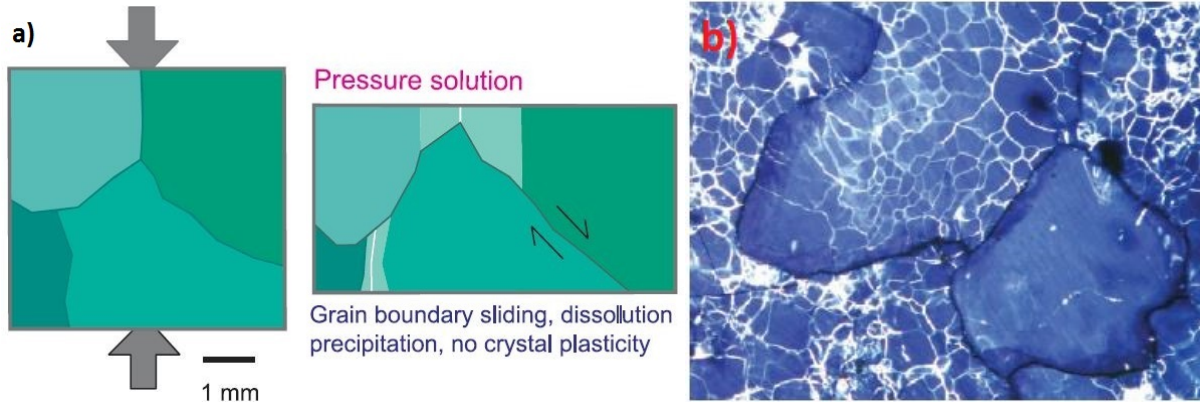


Figure 6: (a) Solution-Precipitation Creep: Third microstructure and deformation mechanism diagram proposed for salt rocks deformed at temperatures of 20 to 200°C. Different shades of green represent crystals with different orientation. (b) Typical micrograph of Hengelo Rock salt, decorated to show the microstructure, with subgrains (white lines), grain boundaries (dark bands), showing clear evidence for “overgrowth” due to solution-precipitation processes such as pressure solution and grain boundary migration. Mean grain size in Hengelo samples is between 5 and 25 mm. Width of image is 7 mm (from Schléder and Urai 2005) (images retrieved from Urai et al., 2008).

Deformation of salt is maintained by these two mechanisms in combination; *Solution-Precipitation Creep* dominates the deformation of extrusive salt sheets since it is driven by low differential stress, while *Solution-Precipitation Creep and Dislocation Creep* contribute together and roughly equally to the strain rate of salt masses (Jackson and Hudec, 2017).

As a result of these collaborative processes, as it is pointed out by Urai et al., 2008; the corresponding deformation mechanisms are inferred to be a combination of dislocation creep, dynamic re-crystallization and solution-precipitation processes. Grain boundaries with small amount of brine activates solution-precipitation processes, while the subgrain size-derived differential stress values higher than the distinguished laws of flow for dislocation creep and for pressure solution (Carter et al. 1993) yields transitional strain rates.

Overall, salt bodies differ greatly due to the deformation mechanisms controlling the microstructuration at various salt segments. Figure 7 aims to summarize these various deformation mechanisms taking place in different parts of salt structures as well as describing those microstructure processes. As it is explained by Jackson and Hudec, 2017;

- During rise inside a salt stock, the increasing differential stress forms subgrains by dislocation within the porphyroclasts (Figure 7a) (Urai and Spiers 2007; Desbois et al. 2010).
- With the rise of diapiric salt to the summit, as meteoric water seeps in, the exposed salt begins to recover and dynamically recrystallize as grain boundaries migrate and create abundant growth bands in the growing grains (Figure 7b) (Desbois et al. 2010).
- Dominant dislocation creep in the upstream and middle parts of a salt glacier transitions to dominant water assisted grain-boundary sliding in the downstream part (Figure 7c).
- At the surface, porphyroclasts become smaller and fewer downslope as they disperse within increasing volumes of fine grains in the groundmass (Figure 7d) (Talbot 1981).

Salt Rocks become weaker than siliciclastics (i.e. sedimentary rocks) over geologic time-scales and flow/act ductile (like a viscous matter) under stress and strain. However, it can also deform in brittle manner under these four settings or combination of these four settings (Jackson and Hudec, 2017);

- (1) Low confining pressure and high differential stress
- (2) Low effective stress
- (3) Very high strain rates and shear stresses
- (4) When the salt is dry without interference of any fluid

The following section will be defining the Driving Forces for Salt Tectonism under four sections; (A) Gravitational Forces, (B) External Forces, (C) Thermal Gradient and (D) Restrictive Factors Against Salt Flow.

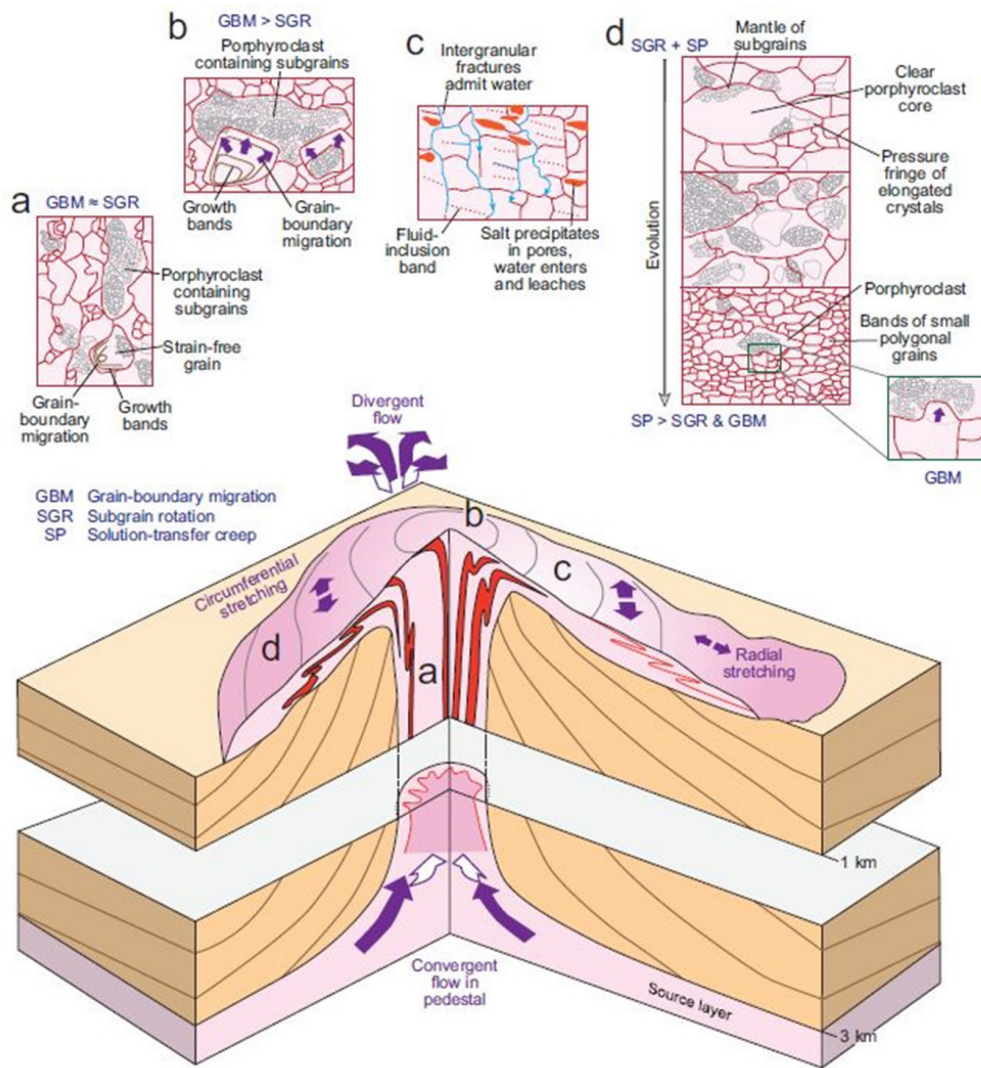


Figure 7: The diagram illustration of complex changes as salt converges from the source layer, rises up a diapir's stem, then diverges and extrudes glacially downhill. After Desbois et al., 2010. -please see the text for explanation- (image retrieved from Jackson and Hudec, 2017).

III. Driving Forces for Salt Tectonism

Differential Loading is the main driving force for Salt Tectonism. Differential loading can be induced into the system by three mechanisms namely: gravity, tectonism and thermal gradient. This section will be describing these three differential forces and how they affect/contribute to salt mobility in their own context.

A. Gravitational Forces

Gravitational Loading (induced/triggered by the sedimentary input) displaces salt in lateral direction by applying a downward force onto the salt layer. Following this downward force, dislocated/mobilized salt can feed a nearby diapir and/or inflate a salt layer it is connected to. Salt Withdrawal or Salt Expulsion are the terms depicting a flow of salt away from a gravitational load (Jackson and Hudec, 2017) (Figure 8).

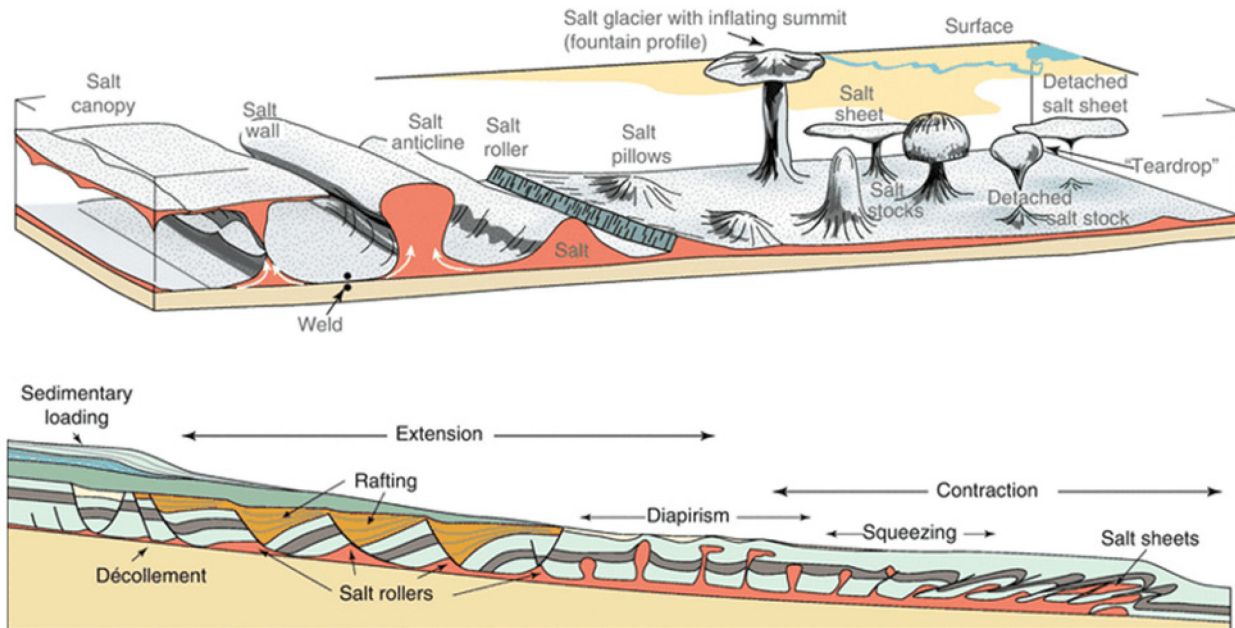


Figure 8: Salt Tectonism and Induced Halokinesis Features Observed in a Gravitational Setting (image retrieved from Warren, 2016).

Gravity spreading and gravity gliding are the two main instabilities driven by gravitational loading at passive margins (De Jong and Scholten 1973; Ramberg 1981a, b). Gravity spreading is represented by a collapsing mass of rock (e.g. salt glaciers controlled by gravity) under its own weight via vertical shortening and horizontal extension translated above a detachment layer that dips toward seaward. The concept has also been used/defined as the downslope sliding of a rigid block (Ramberg 1981a, b; originally termed gravity sliding by Schardt, 1893), downslope translation of a rigid block detaching on a viscous substrate (Kehle, 1970), and to a viscous fluid spreading down an inclined plane (Brun and Merle, 1985) (Figure 9).

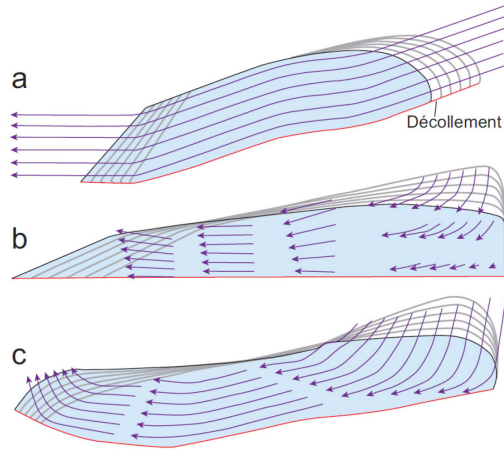


Figure 9: Gravity-driven deformation of passive margins has two end members: (a) pure gravity gliding and (b) pure gravity spreading. (c) In reality, virtually all passive margins involve variable components of each end member, and hence are mixed-mode deformations. Arrows show particle paths; gray lines show successive outlines. (image retrieved from Jackson and Hudec, 2017 after Rowan et al., 2004).

As the sedimentary input is introduced into the system; the gravitational potential energy in a *gliding system* down a uniform slope is released via constant rate/unit. On the contrary; when it's a *spreading system*, released energy of displacement diminishes with increasing displacement (Jackson and Hudec, 2017). Even though the gravity spreading and gliding are generally found as a mix in nature; in salt-prone environments, the hierarchical dominance of gravity gliding vs gravity spreading depends on (1) the position within a linked system, (2) the stage of evolution, and (3) the geologic setting. For example, during the early stages of continental margin evolutions, we observe rapid cooling of thinned continental crust and emergence of juvenile oceanic crust. Through time, they become denser and sink while generating a seaward tilt of the entire margin, favoring a dominance of gravity gliding (i). On the other hand; when excessive load of the growing sedimentary prism arrives and depresses a continental crust setting isostatically while thickening the crust, arriving sedimentary prism favors gravity spreading (ii) (Jackson and Hudec, 2017). (Figure 10).

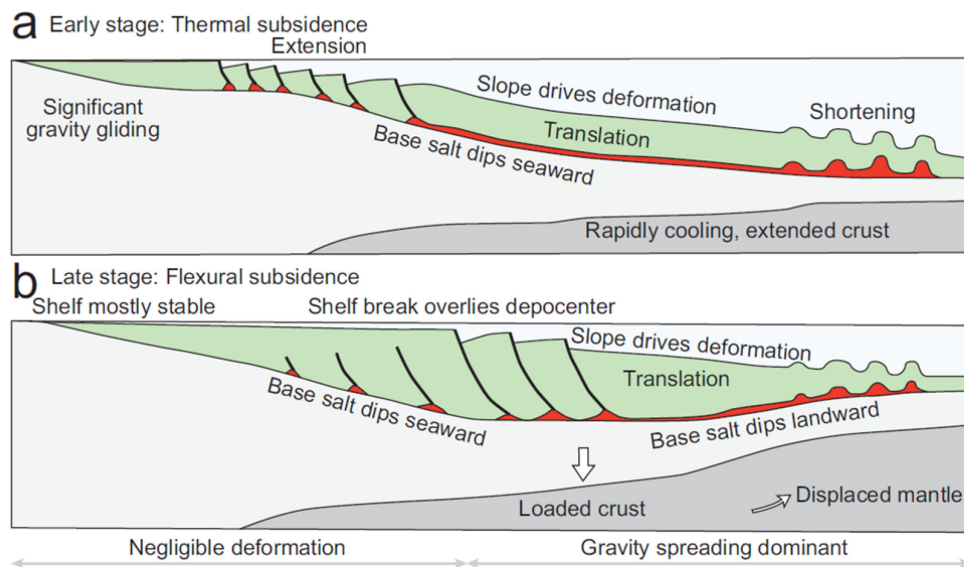


Figure 10: Tectonic styles of salt-bearing passive continental margins deforming first by (a) gravity gliding, then by (b) gravity spreading (image retrieved from Jackson and Hudec, 2017).

B. External Forces

Displacement loading results from the forced displacement of one boundary of a rock body relative to another boundary of a rock (Suppe, 1985; Jackson and Hudec, 2017). As the flanks of a salt body move towards or away from its core, the system showcases a displacement (tectonic) loading due to the lateral forces applied during regional shortening or extension (Figure 11). It is abundantly observed on basin settings, where pre-existing and deformed salt structures are present, because weak salt structures generally display a localizing effect on regional strain (Jackson and Hudec, 2017).

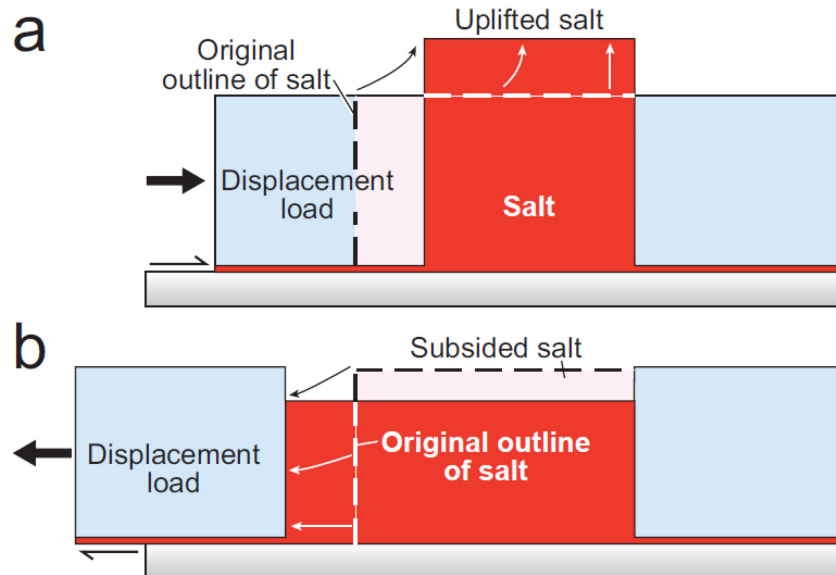


Figure 11: Displacement loading is imposed on salt structures by regional horizontal forces. (a) During shortening, salt is loaded horizontally by inward movement of one or both sides of the salt structure. If the horizontal displacement load exceeds the vertical gravitational load of the salt column, salt is forced to rise. (b) During extension, salt is unloaded horizontally by outward movement of one or both sides of the salt structure. The vertical gravitational load exceeds the horizontal displacement load, so salt is forced to subside (image retrieved from Jackson and Hudec, 2017 after Hudec and Jackson, 2007).

C. Thermal Gradient

The heat transfer within Earth is enabled by conduction, convection flow and radiation. The thermal behavior is an important aspect to understand the internal mechanism of Earth as its one of the controlling factors on rock rheology as a function of depth (Allen & Allen, 2013). Thermal type of loading results from change of volume due to changing temperatures. It is stated by Jackson and Hudec (2017) that the thermal expansivity of hot salt is seventy times higher than that of quartz. When a salt body is contained and not expansible, thermal loading introduces stress into the system. As a case example, when a surge in heat flow occurs by magmatism at depth, it leads to expansion of deep salt faster than the shallow cooler salt or sediments, which results in vertical stress increment. Expanded salt increase in buoyancy while decrease in density. Thermal convection enhancement is achieved either by (1) increase of temperature gradient, thermal expansivity or layer thickness, or (2) decrease in thermal diffusivity or kinematic viscosity (Jackson and Hudec, 2017).

D. Restrictive Factors Against Salt Flow

Even though the differential loading is common in nature, which subjects salt bodies to lateral driving forces, frictional and viscous forces maintain a resistance against the flow of salt. The *strength of overburden* defines the frictional force while the boundary drag accounts for viscous force within a salt layer (Jackson and Hudec, 2017). When the salt is bounded above and below by stronger rocks and a thick overburden, even though it tends to be highly mobile and buoyant in nature, it remains stable unless an external force such as regional extension or shortening is introduced into the system to apply displacement loading. Iterated by this loading, the salt can then be squeezed and/or stretched via this process by faults being introduced into the overburden, which defies the strength of overburden and enables salt to flow (Jackson and Hudec, 2017).

Another resisting force against salt flow is the *boundary drag*, which can be initiated within the system by viscous forces and observed along the top and bottom surfaces of a relatively thin salt layer. A zone of restricted flow observed along the margins of many salt bodies defines an area, where salt shears past static country rocks in case of the overburden not moving parallel to the upper salt contact and introducing traction. Aforementioned boundary shear zone for a certain salt layer thickness gets wider when the salt flow is described as Newtonian viscous, having a constant isothermal viscosity irrelevant of its strain rate (Jackson and Hudec, 2017).

The resistance proposed by this viscous shear force is less effective in thick salt layers compared to thin salt layers since only a small portion of thick salt layers is affected by this shear force along its boundary. When the salt layer is thin, mentioned boundary drag force can be capable of immobilizing the salt (Jackson and Hudec, 2017). As it is stated by Waltham (1997) *drag dominates when the salt layer is thinner than a few hundred meters*. Wagner and Jackson, 2011; also points out to the fact that *when a salt expulsion thins a layer below a threshold thickness, which may refer to few tens of meters, the salt becomes unable to move much even under a large differential load*. In such extreme cases; the growth of a salt diapir ceases due to exhaustion of nearby salt reserve sourced from the main layer resulting of creep flow or dissolution, which leads to depletion of salt to emerge and formation of salt welds in the area (Jackson and Hudec, 2017).

IV. Deformation Geometries: Halokinesis

Halo-Kinesis is the study of salt flow underneath a sediment burial. It depicts the structural deformation geometries of salt and adjacent sediments within a sedimentary/tectonic environment recorded by the sedimentary packages surrounding the salt mass. Halo-kinetic salt deformation geometries gives important clues about salt-sediment interaction and helps us to understand salt mobilization. This chapter will aim to describe the geometries and sequences formed by mobilized/triggered salt and recorded within the sedimentary input in various geological settings and forms.

A. Review of Salt Formations: Deformed Salt Features

When the restrictive factors against salt to flow is overcome by driving forces (e.g. gravitational, tectonic, thermal), salt flows as a viscous material under geologically rapid strain rates. Through this process, depending on the geological setting, we observe various salt deformation patterns with specific features. This section will be reviewing these salt deformation features under three categories; (1) Salt Sheets and Glaciers, (2) Salt Diapirs, Walls and Canopies, and (3) Salt Welds with an aim to better understand their rheology and interaction with the surrounding sediments.

i. Salt Sheets and Glaciers

Following the deposition/precipitation phase, the still pile of deposited salt starts to deform under the thickening sedimentary burden or its own weight within a geological time-scale and strain rate. The differential loading is triggered by incoming sediments being introduced into the system and deposited above the thick salt layer. Upon reaching sufficient amount of sediments introduced into the system, salt begins to deform and hence detach/weld from its originally placed pile, which is called the 'mother salt' (originally deposited salt layer in its primal, undisturbed setting). There are two terminological terms that are used to define the attached and detached/welded form of salt, which are namely; (1) autochthonous and (2) allochthonous salt. Jackson and Hudec, 2017; define these two forms as;

- (1) *Allochthonous Salt: Subhorizontal or moderately dipping, sheetlike salt diapir emplaced at stratigraphic levels above the autochthonous source layer. Allochthonous salt overlies stratigraphically younger strata. The term can be applied even if the salt sheet remains attached to its source layer.*
- (2) *Autochthonous Salt: Salt layer that rests on its original, stratigraphically older subsalt strata or basement; informally known as "mother salt."*

Salt Sheets

Salt sheet is a form of allochthonous salt originated from a single salt feeder (Figure 12). The first salt sheets described by Mrazec, 1907, were *slivers in the hanging walls of thrust sheets*. There are numerous basins around the world that have been marked with salt sheet formations; Agadir, Atlas, Aquitaine, Benguela–Namibe, Campos, Carpathian, Cantabrian–West Pyrenees, Dnieper Donets, Eritrean, Essaouira, Espirito Santo, Flinders, Guinea-Bissau, Great Kavir–Garmsar–Qom, Gabon, Guadalquivir, Isthmian, Katanga, Kwanza, Lower Congo, Louann, Majunga, Mauritania, Oriente-Ucayali, Precaspian, Rio Muni, Sable, Safi, Somali–Kenya, Santos, Salt Range, Scotian Slope; Suriname, Sverdrup, Yemeni, Zagros, Zipaquirá, Zechstein, after Hudec and Jackson, 2006; information retrieved from Jackson and Hudec, 2017 p. 120).

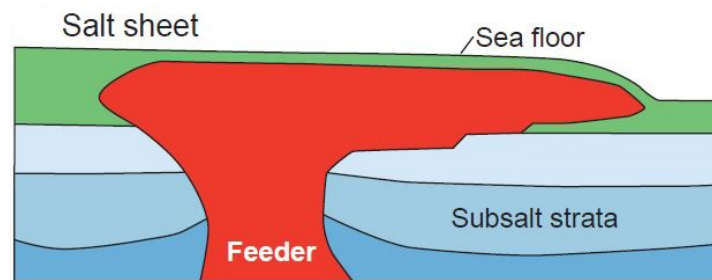


Figure 12: Cartoon diagram depicting a salt sheet (image retrieved from Jackson and Hudec, 2017).

Salt glaciers (also known as *namakiers*) are the second type of salt sheet that are observed in salt-prone areas (e.g. Zagros, Iran; Talbot and Jackson, 1987a-b). They originate from a rising diapir or salt flow breaching to the surface. The phenomena was first described by researchers Lees 1927, Busk 1929 and De Böckh et al. 1929 in Iran (Jackson and Hudec, 2017). Allochthonous salt bodies can be emerged from: (i) subaerial salt glacier flows, (ii) salt sheet exhumations, and (iii) salt sheet formations originated on passive margins.

Salt Glaciers

Salt glaciers are unique features due to their formation pattern (Littke et al., 2008). They are sourced from deeper salt deposits, as sediments cover the primary salt deposit over time, due to its crystalline structure, salt stays stable at same density while the building sediments get denser and compressed. The density contrast grows over time between salt and the deposited sediments and eventually leads to salt rising in terms of diapirism. As the diapiric salt continues to rise; it pierces through the roof of the diapir, reaches to the surface and starts to flow under the influence of gravitational forces similar to ice glaciers. Increasing precipitation rates makes salt glaciers move faster, however, too much precipitation may lead to salt dissolution (Jackson & Vendeville, 1994).

Based on microstructures observed in gamma-irradiated sections (after Schlöder and Urai 2007), Urai et al. (2008), suggested that the principal deformation mechanism for salt glaciers is solution-precipitation creep accompanied by grain boundary migration and grain boundary sliding. The shape and internal structure of *namakiers* can be explained under six zonal observation (Urai et al., 2008) (Figure 13);

- *Undisturbed Rock Salt / Zone (1)*: Primary microstructures reflect the deposition conditions with common microstructure of fluid-inclusion-outlined grains.
- *Slightly Deformed Rock Salt / Zone (2)*: Sub-grains develop, together with incipient grain boundary migration. As the grain boundary sweeps through a fluid-inclusion-rich part of a grain, the primary inclusions get collected at the grain boundary. Alternatively, in fine grained salt, solution-

precipitation creep becomes dominant. Large contrasts in rheology are common in layered salt, from the onset of tectonic deformation.

- *Salt Rise and Deformation* / Zone (3): Steady-state microstructure is produced after complete recrystallisation, although primary fluid-inclusions are still preserved.
- Zone (4): High stress and small sub-grains develop.
- Zone (5): Weak mylonitic shear zones form at the surface.
- Zone (6): Salt glacier starts to flow downhill at unusually high strain rates, dissolution of the salt glaciers in rainwater and re-deposition produces secondary evaporites.

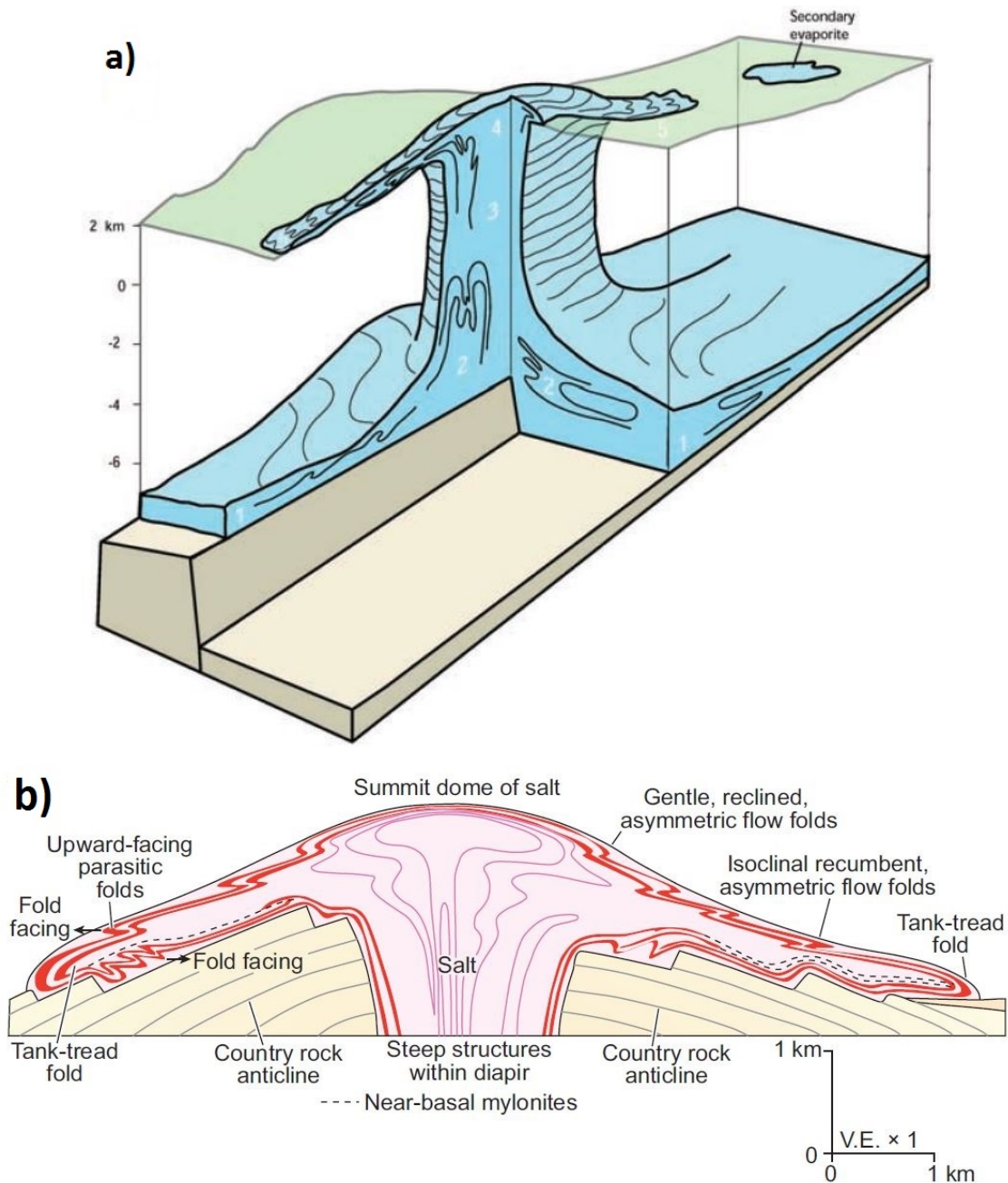


Figure 13: a) Conceptual model of the rock salt cycle and associated rheological transitions observed at a salt glacier -see the text for explanation- (image retrieved from Urai et al., 2008). b) Characteristic of a spreading salt sheet above rigid bedrock. After Talbot et al., 2009a (image retrieved from Jackson and Hudec, 2017).

ii. Salt Walls, Pillows and Diapirs

Salt-cored folds define the general and abundantly found type of salt structures observed in salt-prone regions. Salt walls and salt stocks are diapiric salt structures piercing through their overburden. By definition; salt pillows (similar to salt anticlines) are upwellings of salt overlain by strata parallel to the upper salt contact. Such features can form by; (i) halokinesis (e.g. their growth is driven by differential loading), (ii) contractional folding (e.g. via local/regional contraction, being deformed by buckling), and (iii) within the cores of normal fault rollovers (e.g. extensional roll overs) (Jackson and Hudec, 2017).

Compared to salt pillows (a.k.a. upwellings of salt parallel to the overlying strata), salt diapirs display a more complex structure as diapirical emplacement requires the overburden to be removed or displaced. In terms of *active diapirism*, the active rise takes place through arching, uplifting and shouldering against the overburden of a salt structure, which can be driven by halokinetic processes (e.g. overburden load from differential loading) and/or shortening (e.g. tectonic influences). The viscosity of salt, weight and strength of overburden can all restrict the active rise of a diapir. In cases of unrestricted active rise, *arched roofs* (where the salt is not pierced to the surface), and *upturned collars* (when the formerly active diapir show evidences of a previous breakthrough to the surface) can be formed within the diapir vicinity (Jackson and Hudec, 2017).

One of major salt diapir properties is the discordancy against the overburden sediment load cutting through the bedding. Diapiric formations stay in discordant contact with the overlying strata. Salt stocks define plug-like salt extrusions while the salt walls depict elongated version of these plug-like salt features (Jackson and Hudec, 2017) (Figure 14). ‘Diapirism’, adapted from the Greek rooted word ‘diaperein’ (to pierce), was first applied to Miocene salt in the Romanian Carpathians by Mrazec, 1907 (cited by Jackson and Hudec, 2017) and defined as the forceful movement of a plastic body from an area of greater pressure to an area of lower pressure by Mrazec in 1915 (cited by Kopf, 2002) (Blanchard et al., 2019).

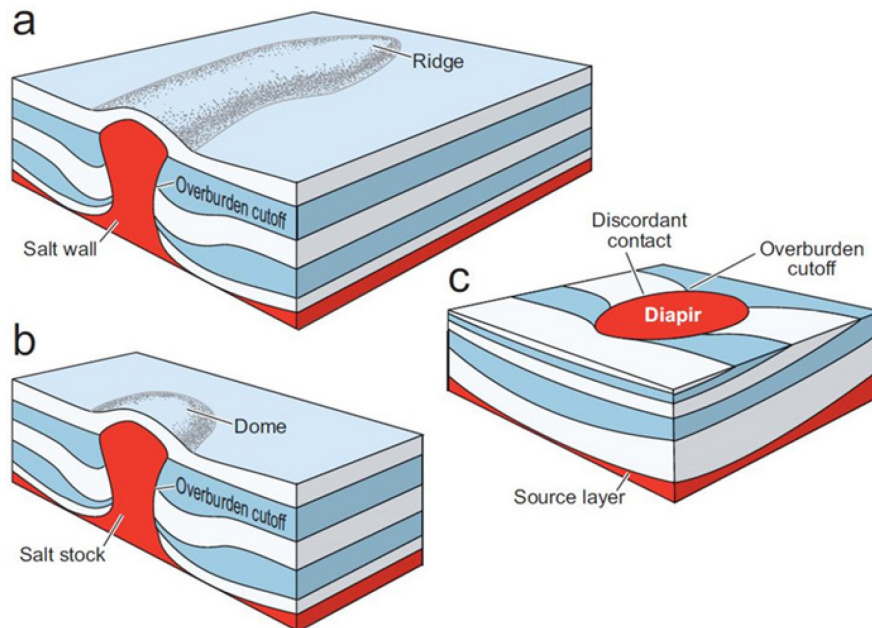


Figure 14: All diapirs, whether they are salt stocks, salt walls, or salt sheets have discordant contacts against their overburden (image retrieved from Jackson and Hudec, 2017).

Salt Diapirs are forms of salt extrusion that emerge and pierce from an ‘overpressured zone of sedimentary pile’ and nest toward a ‘lower pressure zone of weakness’ (Jackson and Hudec, 2017). The concept of ‘diapirism’, which was initially used to define salt diapirs, later extended to describe intrusive/piercing features emerged from igneous/metamorphic complexes (i.e. serpentinite, gneiss, migmatite), soft rocks (i.e. shale, limestone, gypsum, coal), and soft sediments (i.e. peat, sand, mud) (Jackson and Hudec, 2017). High pressured diapiric tops tend to detach and/or weld from the mother salt (i.e. main depo-center of salt accumulation) and confine through an upper sedimentary layer while deforming the surrounding sediment strata and reflecting the deformation pattern recorded within the adjacent sediment load (Figure 15). Today, with the help of high-quality seismic examples (e.g. offshore Gulf of Mexico, North Sea, Brazil) and number of well-preserved outcrops (e.g. Zagros, Iran; Sivas, Turkey; La Popa, Mexico), we are able to better understand their evolutionary scheme and detail their physiology.

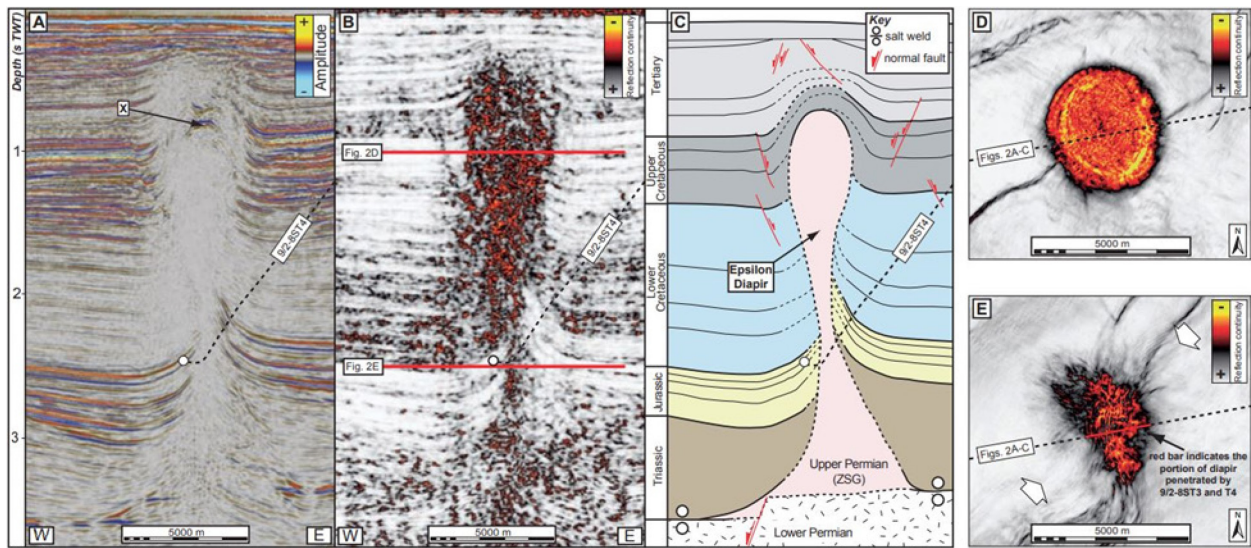


Figure 15: (a) Seismic reflection, (b) reflection continuity attribute and (c) geoseismic cross-section across the Epsilon Diapir, North Sea. Dashed lines in (c) indicate where the seismic interpretation is uncertain. The locations of horizontal slices shown in (e) indicate the interpreted axis (image retrieved from Jackson & Lewis, 2012)

There are various ways that lead to salt piercing through the sediment overburden, which are namely; (1) active salt diapirism rising and pushing the burden upwards/sideways due to high density contrast (Figure 16a), (2) passive salt diapirism occurring near surface and enabling sediments to be deposited around the salt body (Figure 16b), (3) reactive diapirism caused by rifting and regional extension leading to overburden relaxation and salt movement upwards (Figure 16c) (Vendeville & Jackson, 1992; Jackson & Vendeville, 1994).

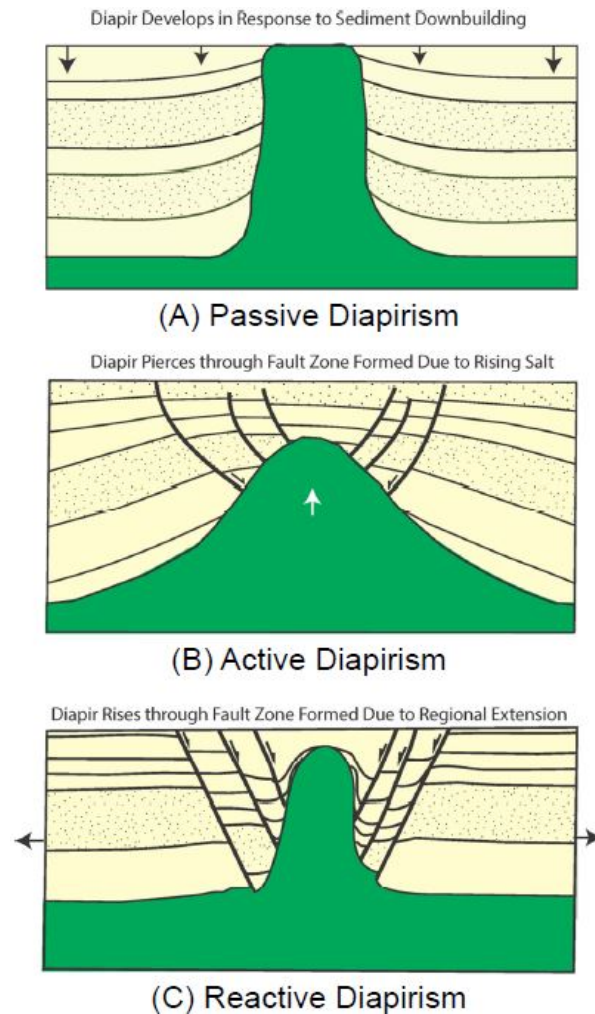


Figure 16: Main mechanisms of diapir formation: (A) passive diapirism, with the growth of the diapir due to sediment down building (based on Barton, 1933); (B) active diapirism, with the diapir piercing through sediments faulted by the rising salt; and (C) reactive diapirism, with the diapir rising through a fault zone formed by regional extension (modified after Vendeville and Jackson, 1992) (image retrieved from Mitra and Karam, 2016).

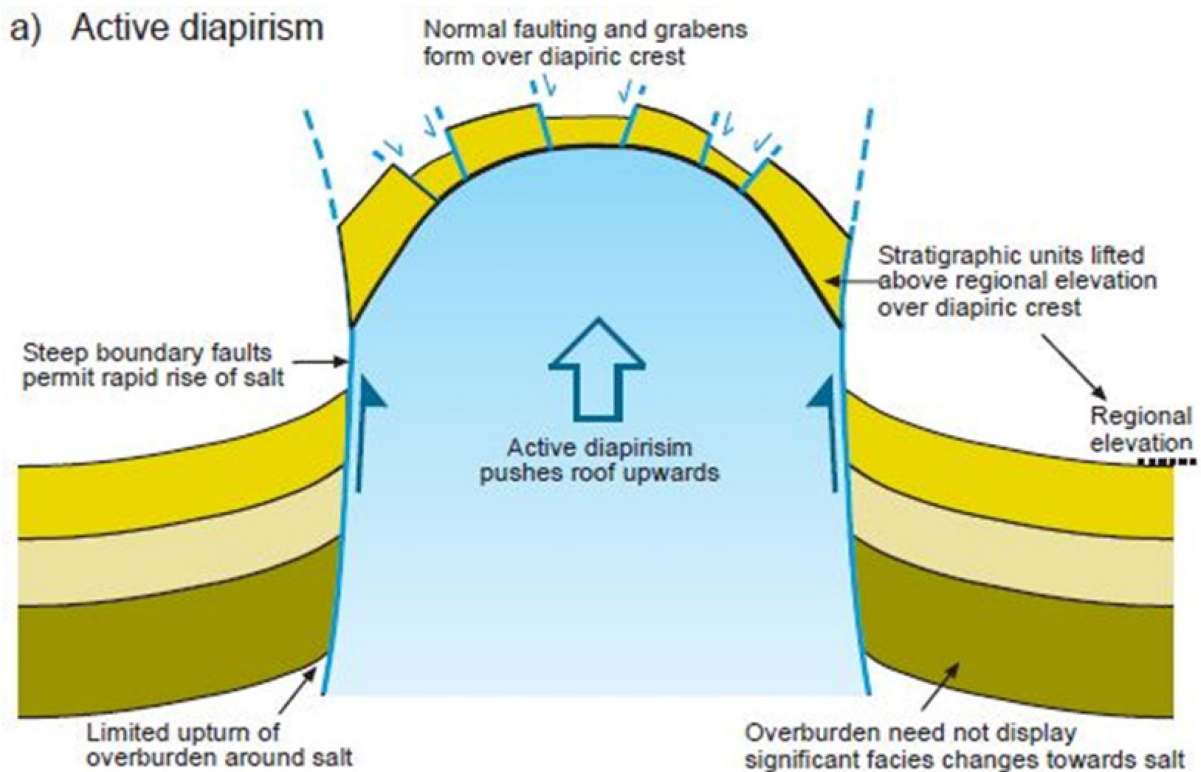
The conducted study of Alsop et al. (2016), depicts the cycles of passive versus active diapirism recorded along an exposed salt wall with an outcrop analysis on Sedom salt wall, on the western side of the Dead Sea Basin, which proposes an opportunity for detailed outcrop analysis of diapiric salt and the associated depositional and deformational record of its movement during both passive and active phases of diapirism. As it is explained in their paper;

Active salt diapirism can be defined as a ‘*diapir rise by arching, uplifting, or shouldering aside it’s roof*’ (Hudec and Jackson, 2011, p269), which are designated by (Figure 17a):

- i) Stratigraphic units being lifted above their regional elevations on the diapiric crest
- ii) Normal faulting and grabens forming in sediments over the diapiric crest
- iii) Large boundary faults permitting the relative rise of salt along the diapiric flanks
- iv) A lack of significant facies change in surrounding sediments (e.g. Nelson, 1991; Schultz-Ela et al., 1993; Rowan, 1995, p.204)

Passive salt diapirism is described as 'syndepositional growth of a diapir whose exposed crest rises as sediments accumulate around it' (Hudec and Jackson, 2011, p.275). In passive diapirism, the crest of diapir can sometimes be buried, however, the diapir repeatedly breaks through the thin and temporary roof strata. Throughout halokinetic evolution, the base of the salt continues to subside with the basin as it fills with sediments, while the crest of the diapir keeps pace with sedimentation in a 'downbuilding' process (e.g. Vendeville and Jackson, 1991; Hudec and Jackson, 2011 p.275) . As a result, the passive diapirs are generally associated with the following measures and a distinct stratigraphic and sedimentological record of salt movement (Figure 17b):

- i) Pronounced areas of bedding upturn
- ii) Sedimentary facies changes
- iii) Unconformities and breccia horizons within overburden around the flanks of the diapir



b) Passive diapirism

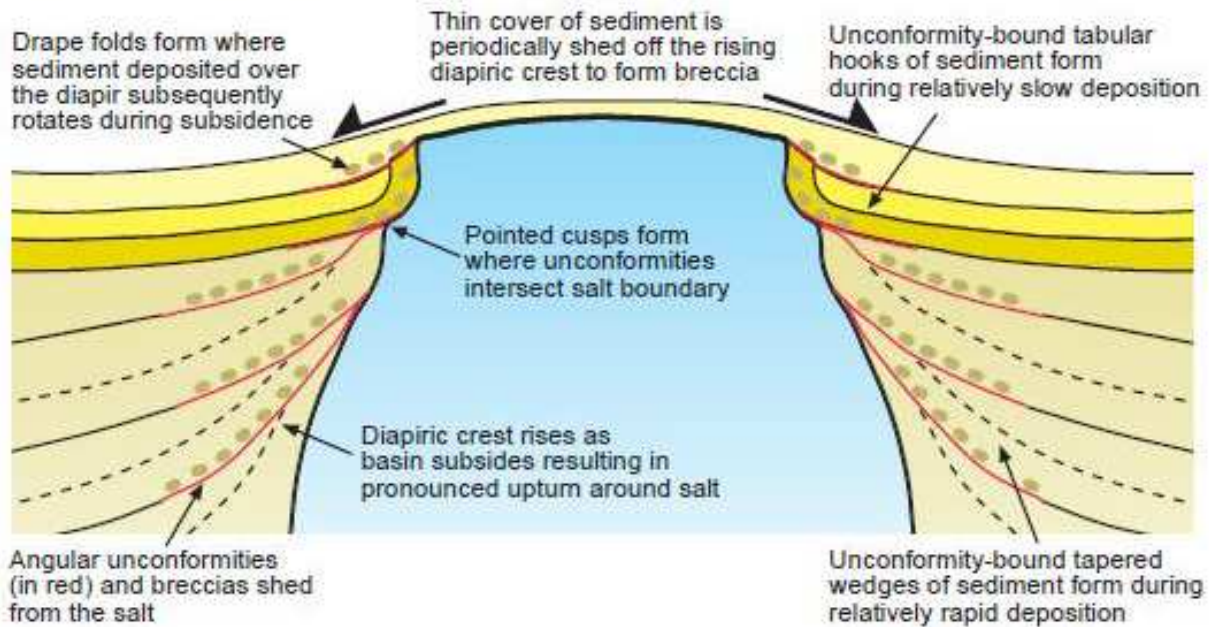


Figure 17: Schematic cartoons illustrating typical features of a) active salt diapirism and, b) passive salt diapirism (image retrieved from Alsop et al., 2016).

In case of *reactive salt diapirs*, as it is summarized by Lord, 2015; a salt layer, which is buried by a constant thickness/greater density overlying strata, does not form a *diapir* until external forces are applied. Upon receiving an external force (e.g. regional extension or compression), the salt diapir forms (Figure 16c).

- (i) When it is *regional extension*, the overburden is lengthened and thinned allowing the salt to fill the space and grow in a diapiric form (Figure 18)
 - a. The salt diapir widens and grows if the salt source is still available/active
 - b. The salt diapir widens and collapses if the salt source is being depleted
- (ii) When it is *regional contraction*, the overburden shortens via folding, uplifting, faulting and eroding with differential sediment load allowing the salt to break through and grow in a diapiric form (Figure 19)
 - a. The salt diapir shortens and salt flow rates increase with differential loading if the salt source is still available/active
 - b. The buried salt body responds passively to tectonic forces by being displaced and 'appearing' to actively push up the overburden if the salt source is being depleted, which is also called '*Diapir Rejuvenation*'

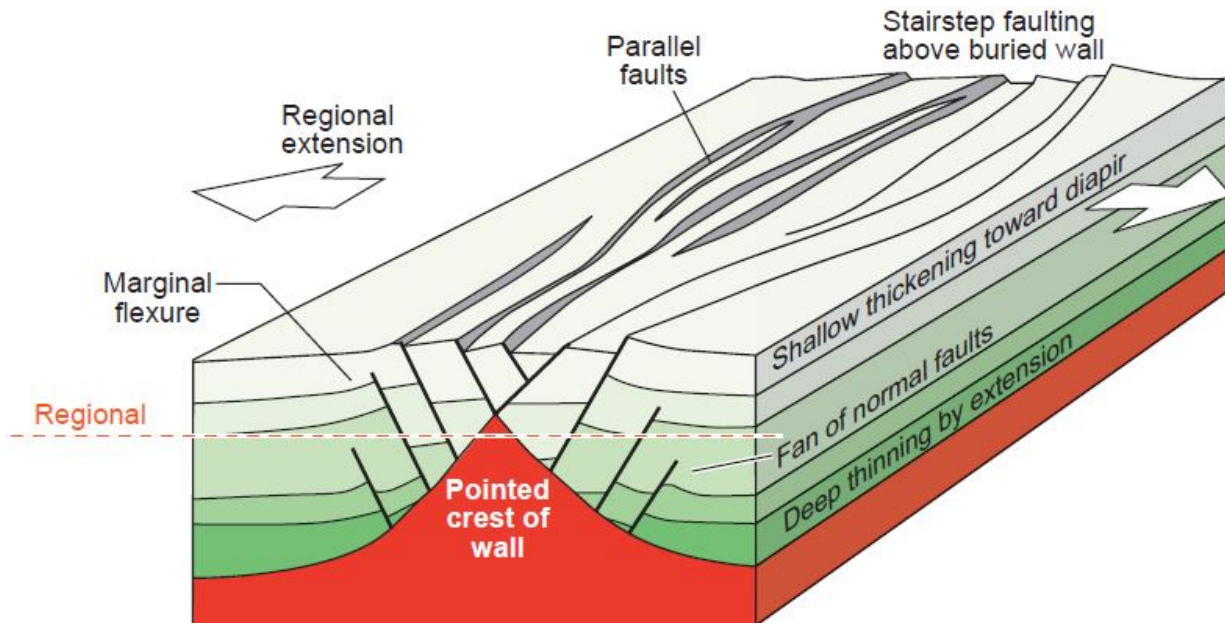


Figure 18: Diagram of reactive diapirism in an extensional regional setting: Diagnostic criteria of reactive walls (after Jackson et al., 1994) (image retrieved from Jackson and Hudec, 2017).

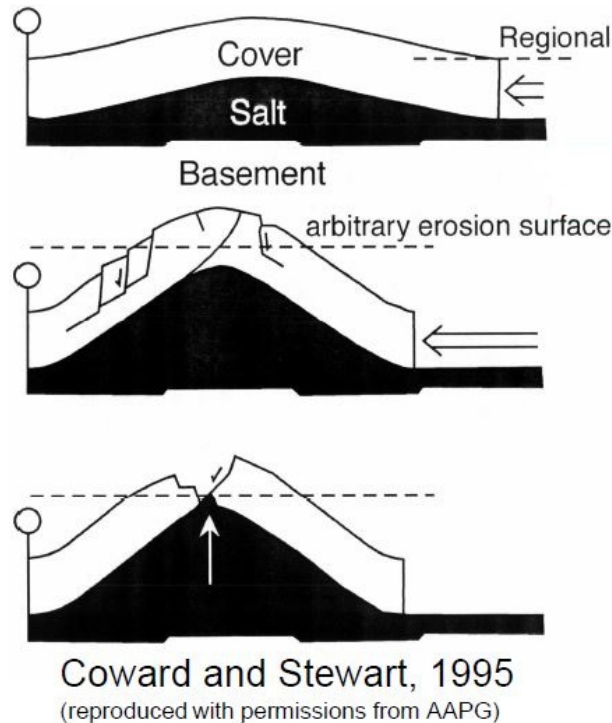


Figure 19: Diagram of reactive diapirism in a compressional regional setting (after Coward and Stewart, 1995) (image retrieved from Lord, 2015).

Arched roofs can lead to radial faulting/fracturing above the diapiric top due to upward and radially-outward strata rotation (Figure 20). Yin and Groshong, 2007, explain this phenomena as; *strata tilting outward by flexural slip radial to the dome along the center line of each block*. As a result, roof particles move and adapt a radially-outward divergence pattern (e.g. circumferential extension), which only

happens if the overlying sediment strata is not too soft to break. Radial faulting increase with intensified doming, in other words, the smaller diapir's curvature radius gets, the higher number of radial faults takes place above a diapiric high (Jackson and Hudec, 2017). As a consequence of this, radial faults cluster towards the ends of elliptical diapirs (Withjack and Scheiner 1982; Davison et al. 2000a; Stewart 2006; Sims et al. 2013).

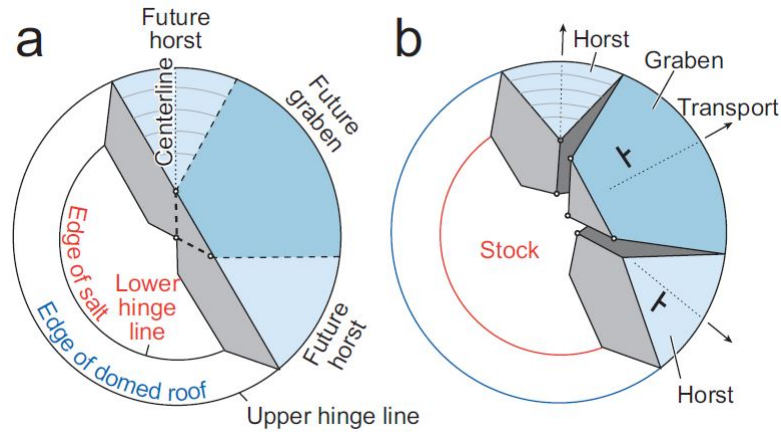


Figure 20: Radial faults form above an active diapir because, as roof strata arch and tilt outward, they extend circumferentially (hoop extension). (a) Before arching (oblique three-dimensional view); (b) after arching (vertical three-dimensional view, colors delineate individual fault blocks); after Yin and Groshong (2007) (image retrieved from Jackson and Hudec, 2017).

The model of regional extension or regional shortening affected the pattern of faults above gentle active domes is seen on the model of Withjack & Scheiner, 1982 (Figure 21). As a consequence of regional extension or shortening, the radial pattern of normal faults is suppressed where far-field stresses dominate local doming stresses (Jackson and Hudec, 2017). Hence, the normal faults strike perpendicular to the regional extension direction regardless of the shape of the underlying diapir instead of radiating (Sims et al. 2013).

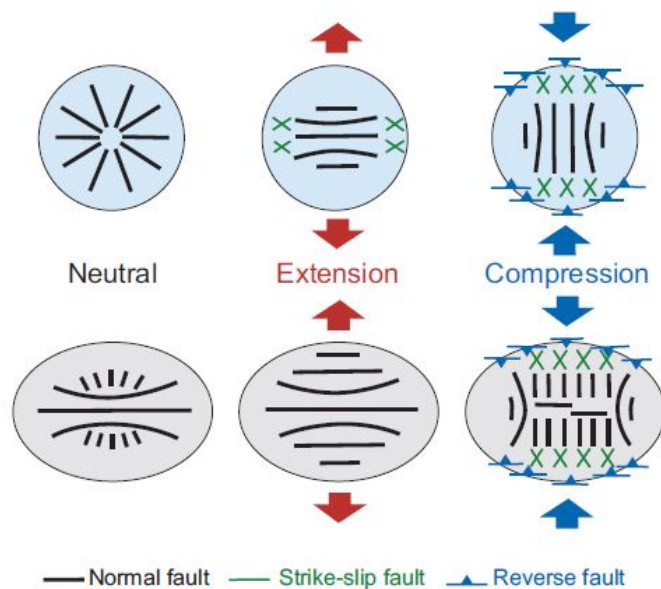


Figure 21: Fault patterns above circular (upper row) and elliptical (lower row) active diapirs are controlled by different regional stress fields indicated by arrows. After Withjack and Scheiner (1982), based on their physical and analytical models (image retrieved from Jackson and Hudec, 2017).

iii. Salt Canopies

Similar to salt sheets explained in the previous section, salt canopies are the types of allochthonous salt composed of multiple salt sheets connecting together from several salt feeders. Canopy formations may stay attached (via their feeder) and/or detached from their primal source (e.g. autochthonous salt, mother salt). In areas, where we see combination of two or more *salt sheets* creating a *canopy* feature, suture sections (i.e. junction points of contact) can be observed (Figure 22) (Jackson and Hudec, 2017).

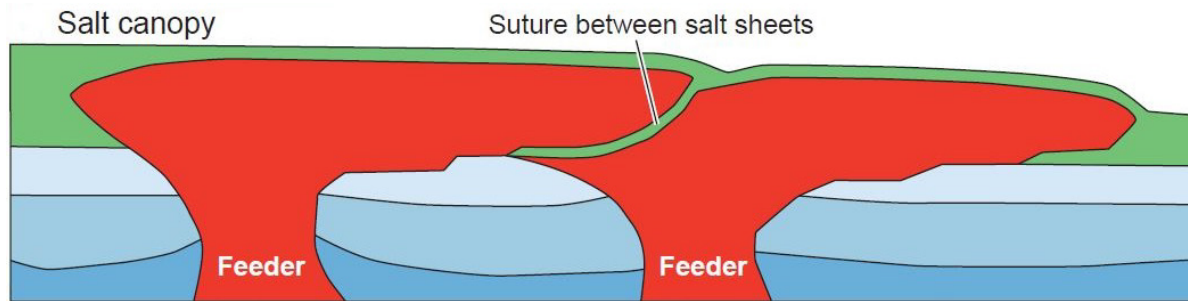


Figure 22: A salt canopy is composed of two or more salt sheets that have coalesced to make a large composite allochthonous structure. Boundaries between component salt sheets in a canopy are termed sutures (image retrieved from Jackson and Hudec, 2017).

iv. Salt Welds

Jackson and Hudec, 2017, state a salt weld “as a surface or thin zone marking a vanished salt body”, resulting from an absence/loss of salt by creep or dissolution and recognized by the discordant strata entailed at weld surface. The term *salt weld* and its annotation; two dots separated by a linear line denoting the salt escape path, was used by Jackson & Cramez for the first time in 1989, after an extensive review of previously studied salt structures. Even though the *vanished salt* term used by Stille in 1924, a comprehensive understanding and nomenclature have not been developed for many afterwards until Burollet, 1975, defined a salt feature as a ‘*cicatrice salifère*’, “*subvertical residual smear of salt left by a subsiding diapir*” in Angola (Jackson and Hudec, 2017). Following this recognition, the term gained popularity and similar ‘*salt evacuation surfaces*’ were observed in Gulf of Mexico by Worrall and Snelson, 1989 (Figure 23).

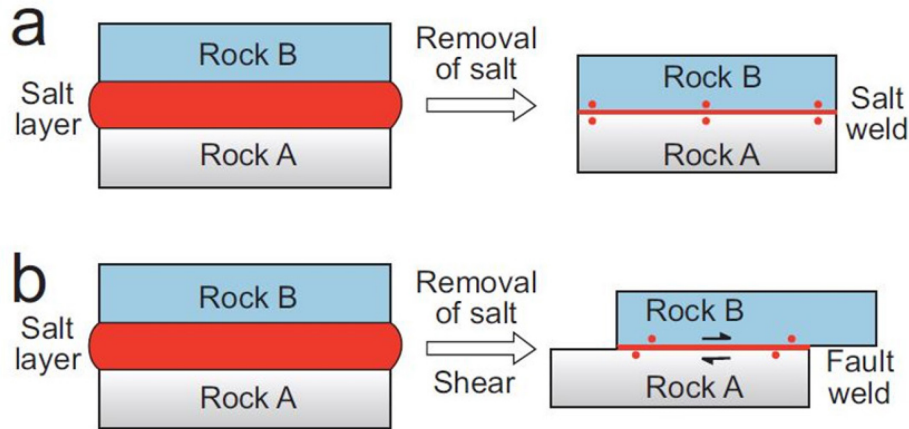


Figure 23: a) A salt weld is a surface or thin zone joining strata originally separated by salt. The weld is symbolized by pairs of dots along its length. (b) A fault weld is a salt weld along which there has been slip either before or after welding (image retrieved from Jackson and Hudec, 2017).

Salt welds depict evidence for escaped/vanished salt bodies, and can be used to trace back deformed salt structures to their original form if the original salt body was preserved within an encased sediment overburden. Complete welds represent a discordant contact that separate two sedimentary packages (e.g. autochthonous or allochthonous bodies), while incomplete welds are defined as narrow zones of evaporitic strata representing former and thicker autochthonous or allochthonous salt. Discontinuous welds stand as intermittently continuous structures separating evaporates and interbedded sediments. Apparent welds are thin zones of welding at certain scale of observation, which can indeed contain more than 50m thickness worth of evaporate and interbedded material (Figure 24). Geometry of pre-welding salt structures can be used as an important tool to determine well classification/hierarchy; primary welds are formed after autochthonous salt removal generally in subhorizontal location, while the secondary welds are generated after removal of salt from the side of a steep-sided diapir (Jackson and Hudec, 2017).

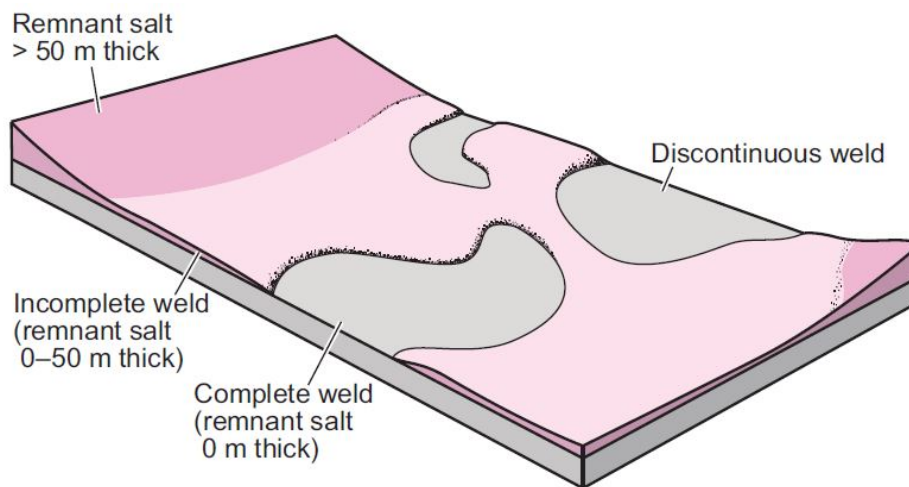


Figure 24: Illustrated definitions of a complete weld, an incomplete weld, and a discontinuous weld (image retrieved from Jackson and Hudec, 2017).

B. Review of Salt-Related Sediment Recordings

Salt related sediment recordings (also known as *halokinetic features*) help to analyze the salt deformation pattern at a given geological setting. Thanks to advanced seismic imaging, satellite and drone technology we have today, identifying halokinetic sequence successions in various salt deformation zones around the world became more accessible and hence better understood. With the help of these recordings, we can verify the stratal history of mobilized salt bodies via the surrounding sediment pile in a salt-related deformation zone. Adjacent sediment deposits act as a shaping material (e.g. modelling dough) that record and freeze the deformation pattern of mobilized salt that build up in a geological time-scale frame. In this section, our aim is to familiarize the reader with the halokinesis features we observe at salt-prone settings, which are namely; (i) halokinetic sequences, (ii) hooks and wedges, (iii) rim synclines, (iv) megaflaps, and (v) minibasins.

i. Halokinetic Sequences

By definition, as it is stated by Giles and Rowan, 2012; *halokinetic sequences are unconformity-bound packages of thinned and folded strata adjacent to passive diapirs*. These stacked and stratal package sequences are recorded within the sedimentary pile adjacent to a salt body to evidence the interplay of salt body growth rate vs the sediment input rate along the characteristically mature, vertical-to-flaring parts of passive diapirs and involve minibasin strata with a broad age distribution that are locally thinned adjacent to diapiric formations (Rowan et al., 2016).

Complexity of most passive diapirs points out to repeated phases of; (i) relative uplifts of the salt body related to sedimentation, (ii) partial-to-complete coverage of salt during high sediment input periods, and (iii) breakouts during low sediment input periods producing *tilted beds*. Stacking of these tilted beds lead to halokinetic sequences we observe adjacent to salt diapirs with stratigraphic coherency. Each of these halokinetic sequences preserve a record of burial, breakout, downbuilding episode (Giles & Rowan, 2012; Jacskon and Hudec, 2017). Stacking halokinetic sequences can be classified under two end-member units; tabular and tapered (Giles and Rowan, 2012), which will be mentioned in detail in the next section; *Hooks and Wedges*. Rowan et al., 2003, also noted that the deformational circle roofing the diapiric top is expected to correlate loosely with lithology and aggradation rate, while the aggradation rate directly impacts the thickness of the halokinetic wedge (Figure 25-Figure 26).

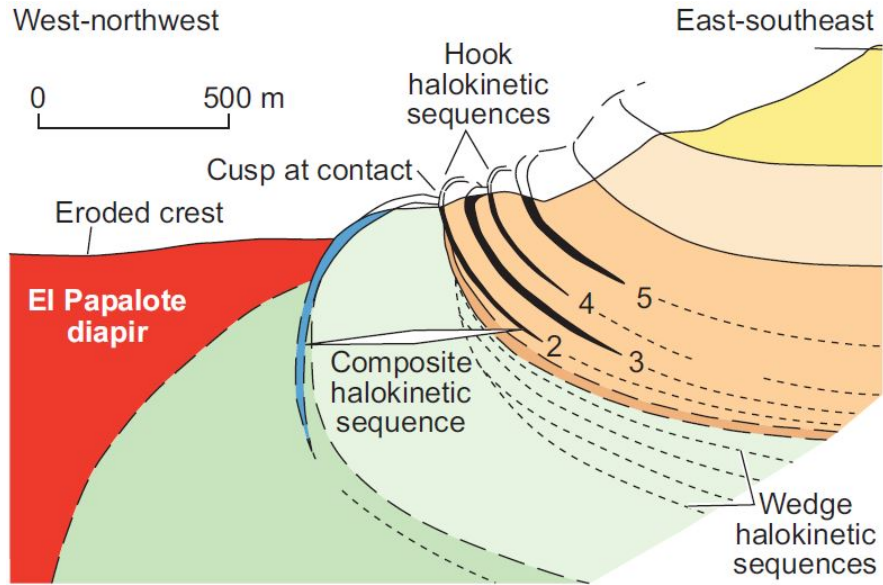


Figure 25: Halokinetic sequences in the 500 to 1000 m wide contact zone around El Papalote and El Gordo diapirs (La Popa basin, Mexico). Strata are locally overturned in hook halokinetic sequences; angular unconformities bounding the sequences are subvertical and grade into correlative conformities within about 250 m of the diapir's contact. After Rowan et al., 2003 (image retrieved from Jackson and Hudec, 2017).

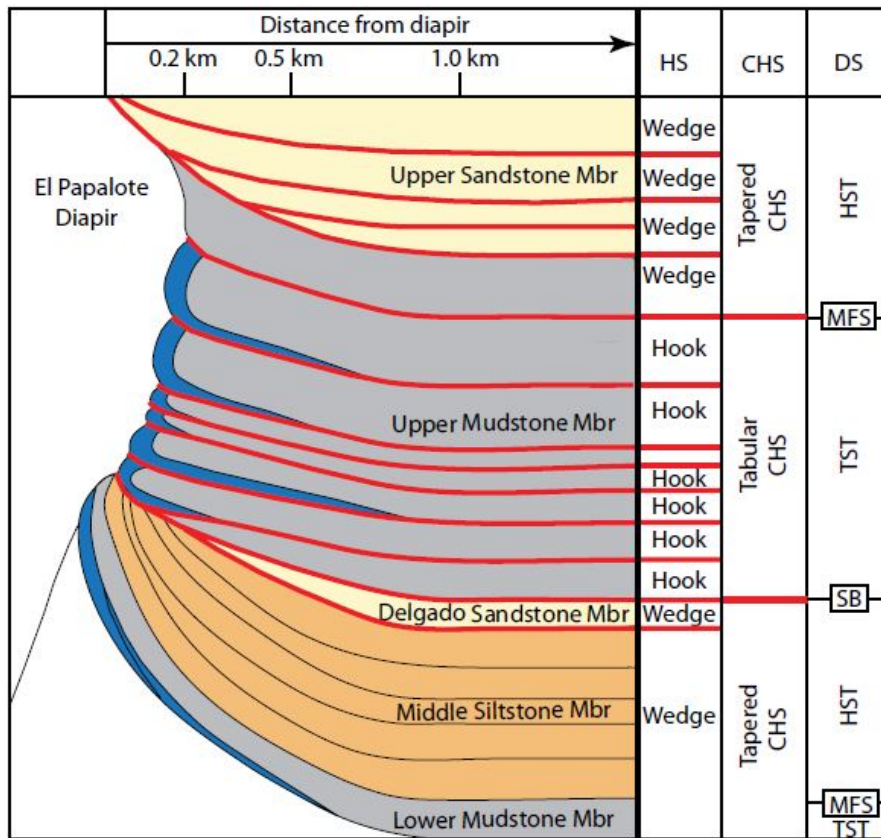


Figure 26: Halokinetic (HS), composite halokinetic (CHS) and depositional sequence stratigraphy of the Upper Cretaceous through Lower Palaeogene stratigraphy exposed on the east side of El Papalote Diapir, La Popa Basin, Mexico (image retrieved from Giles and Rowan, 2012).

ii. Hooks and Wedges

The two end-member type of halokinetic sequences are called; hooks and wedges, while the stacked packages of these halokinetic sequence types are defined as tabular and tapered. These two types of halokinetic sequences are differentiated due to their drape-fold geometry, degree of angular discordance and bounding unconformities (Giles and Rowan, 2012). Hook halokinetic sequences display narrow and steep drape-fold geometries and stack to form *tabular* composite sequences during slow aggradation, while the wedge halokinetic sequences show broad and gentle drape-fold geometries and stack to form *tapered* composite sequences during fast aggradation (Giles and Rowan, 2012) (Figure 27).

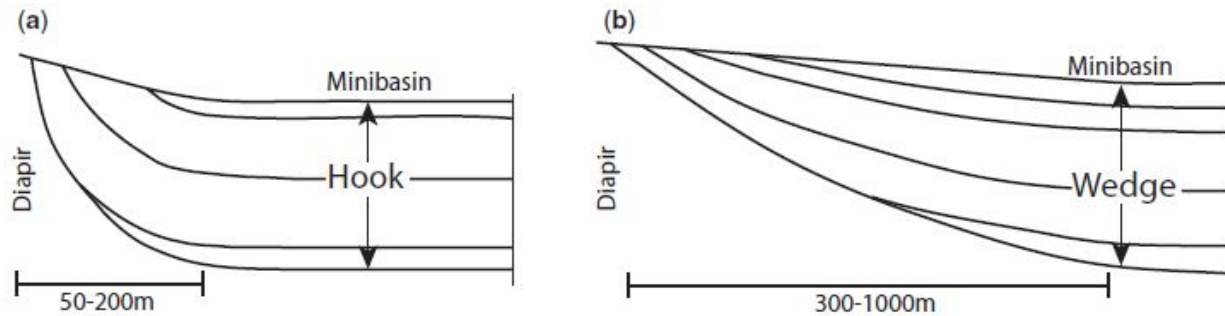


Figure 27: Two end-member types of halokinetic sequences: (a) hook halokinetic sequence; and (b) wedge halokinetic sequence (image retrieved from Giles and Rowan, 2012).

As explained exclusively by Giles and Rowan, 2012 (Figure 28-Figure 29);

- Tabular composite halokinetic sequences (tabular CHS) form by vertically stacking hook sequences, creating a large-scale package with tabular form (upper and lower bounding surfaces are parallel to sub-parallel). In other words, the stack of tabular CHS suggests faster diapir rise rates than the surrounding sediment-accumulation rates (Jackson et al. 1994).
- Tapered composite halokinetic sequences (tapered CHS) form by stacking wedge sequences, creating a large-scale package with a broadly folded tapered form (upper and lower bounding surfaces gradually converge towards the diapir). Therefore, tabular CHS occurs when overall sediment accumulation rate adjacent to the diapir is less than the diapir-rise rate.

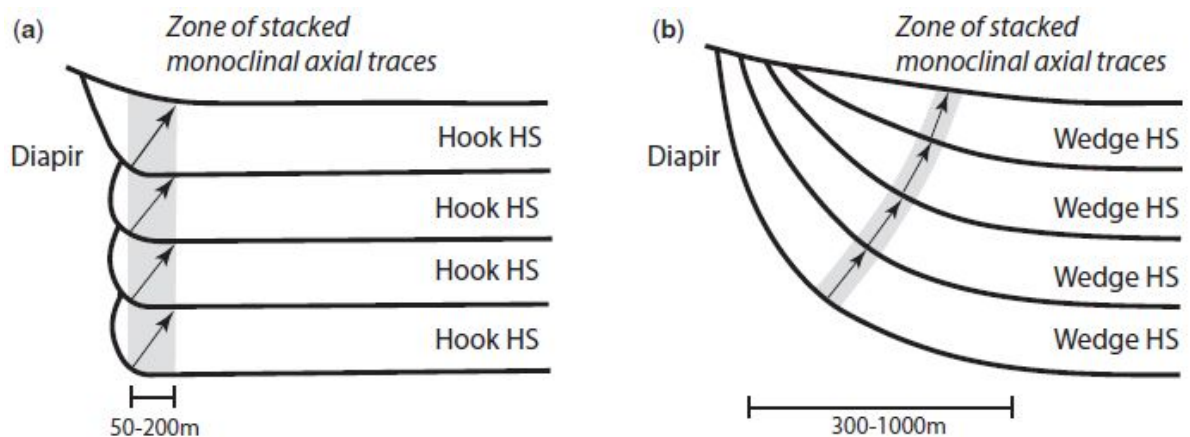


Figure 28: Two end-member types of composite halokinetic sequences (CHS): (a) tabular CHS; and (b) tapered CHS (image retrieved from Giles and Rowan, 2012).

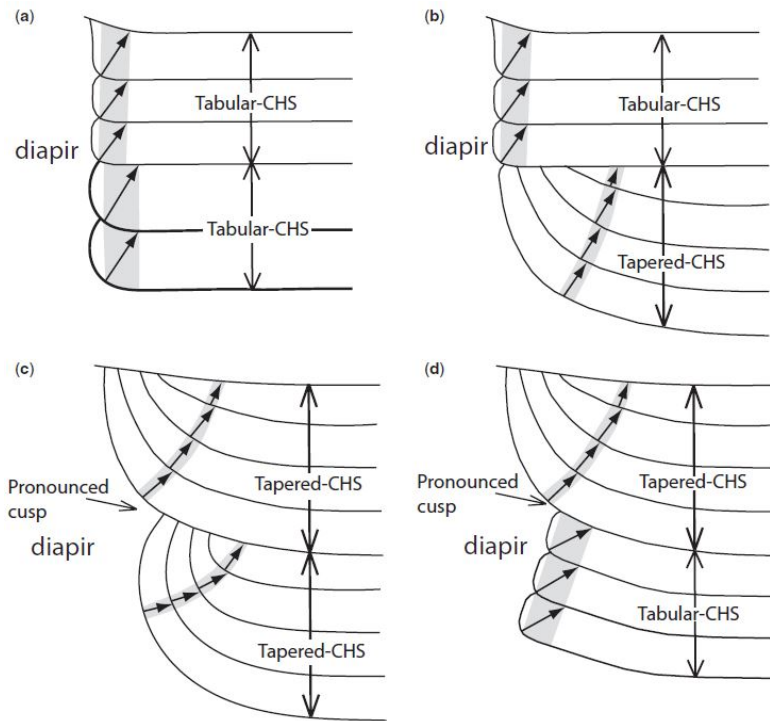


Figure 29: Geometric patterns of stacked composite halokinetic sequences (CHS): (a) tabular CHS over tabular CHS; (b) tabular CHS over tapered CHS; (c) tapered CHS over tapered CHS; and (d) tapered CHS over tabular CHS (image retrieved from Giles & Rowan, 2012).

Figure 30 depicts an outstanding seismic example for composite halokinetic sequences observed at adjacent salt diapir in Gulf of Mexico. The edge of the diapir display cusps and stacked unconformities defining the tabular or tapered halokinetic sequences (Giles and Rowan, 2012).

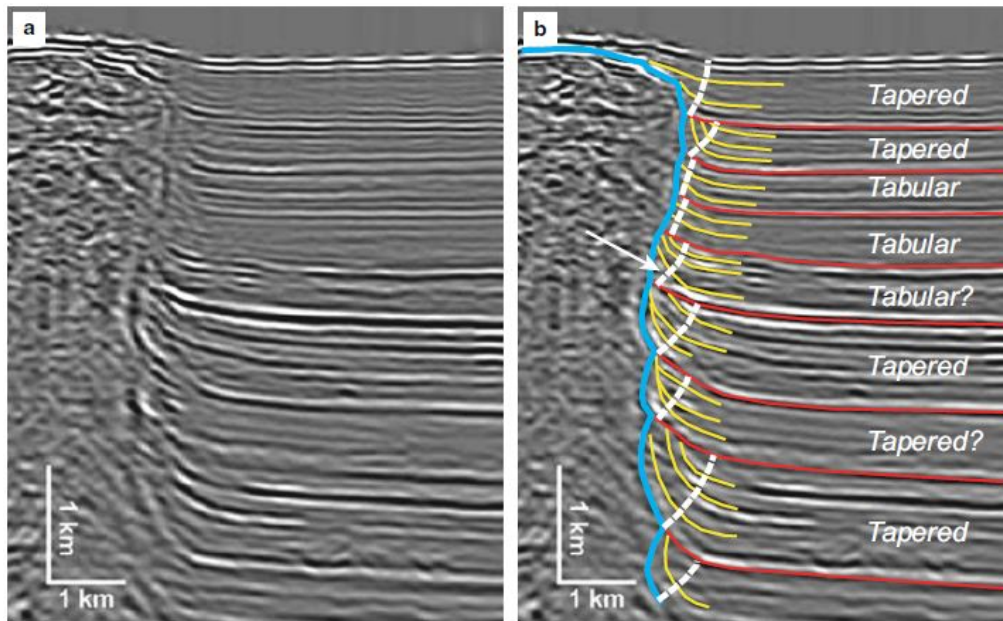


Figure 30: Prestack depth-migrated seismic profile (reverse-time-migration sediment flood) of a secondary diapir and flanking strata from the northern Gulf of Mexico: (a) uninterpreted and (b) interpreted. Vertical exaggeration 1.5:1. Seismic data courtesy of C. Fiduk and CGGVeritas (image retrieved from Giles and Rowan, 2012).

Overall, it is important to keep in mind that (Giles and Rowan, 2012);

- The sediment accumulation rate vs the diapir rise rate play a crucial role in defining the type of halokinetic sequence.
- Stack of halokinetic hooks and wedges lead to composite halokinetic sequences with convergent lower and upper boundaries.
 - o Tabular composite halokinetic sequences form when sediment-accumulation rate is relatively slow.
 - o Tapered composite halokinetic sequences form when sediment-accumulation rate is rapid relative to diapir-rise rate
- Such halokinetic sequences can be observed in various depositional environments but their timing of origin and functionality differ.
 - o In deepwater settings, composite halokinetic sequence boundaries typically develop due to slow deposition during the transgressive and highstand systems tracts.
 - o In shelf setting, the slowest deposition takes place during the lowstand to transgressive systems tracts.
 - o In subaerial depositional settings, even with relatively rapid sedimentation rates, erosional unroofing of the diapir may lead to gradual thinning of the roof.

iii. Rim Synclines

Harding and Huuse (2015) report the rim-synclines as *the indicative of an adjacent low amplitude non piercing salt structure, which in turn indicate the pillow stage of salt diapirism* (Trusheim, 1960; Sanneman, 1968; Stewart and Coward, 1995). However, these geometries adjacent to the salt diapirs are non-unique and can be associated with number of other structures as well (Stewart, 2007) (e.g. adjacent to salt pillows, which are initiated by extensional processes [Vendeville and Jackson, 1993] or buckle folds created by compression, with the underlying salt responding to the space created by movement in the sediment overburden [Stewart and Coward, 1995]) (Figure 31). The thickening of sediments into rim-synclines suggests an increase in subsidence within adjacent mini basins and salt withdrawal during active stage of diapirism (Hardin and Huuse, 2015).

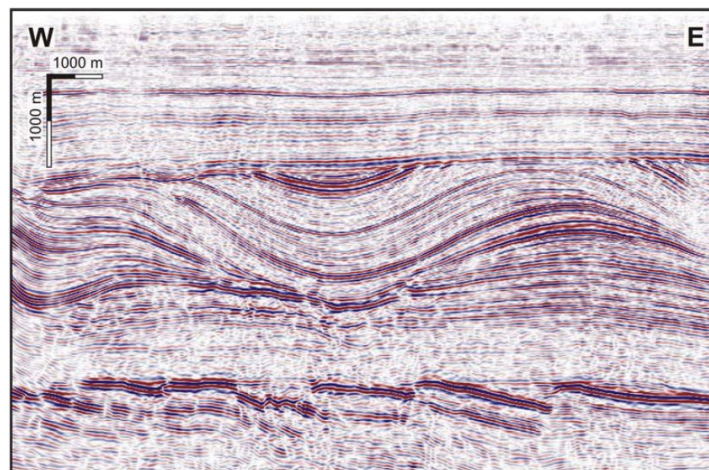


Figure 31: The top of this section represent the surface line at sea level. The section shows antithetic basement faults, a graben in the centre of the overburden and an erosional surface above. Note the secondary rim-syncline of the northerly adjacent diapir (not seen on this figure) in the central part (image retrieved from Mohr et al., 2005).

iv. MegaFlaps

Megaflaps are salt-related deformation structures forming at the flank and carapace of active salt diapirs, the rise of which can rotate the minibasin edge from near-vertical to completely-overturned. They can be listed as steep stratal panels that extend far up the sides of diapirs or their equivalent welds (Rowan et al., 2016) (see also the definitions by Graham et al., 2012; Giles and Rowan, 2012; Callot et al., 2016). Typically, a megaflap depicts the oldest minibasin stratal package deposited above an inflated salt high (e.g. active salt pillow or initiating diapir) as a structurally concordant roof layering during differential subsidence of minibasins, which differs from small-scale young halokinetic sequence formations lying above mature passive diapirs (see Rowan et al., 2016 and Callot et al., 2016 for detailed review) (Figure 32).

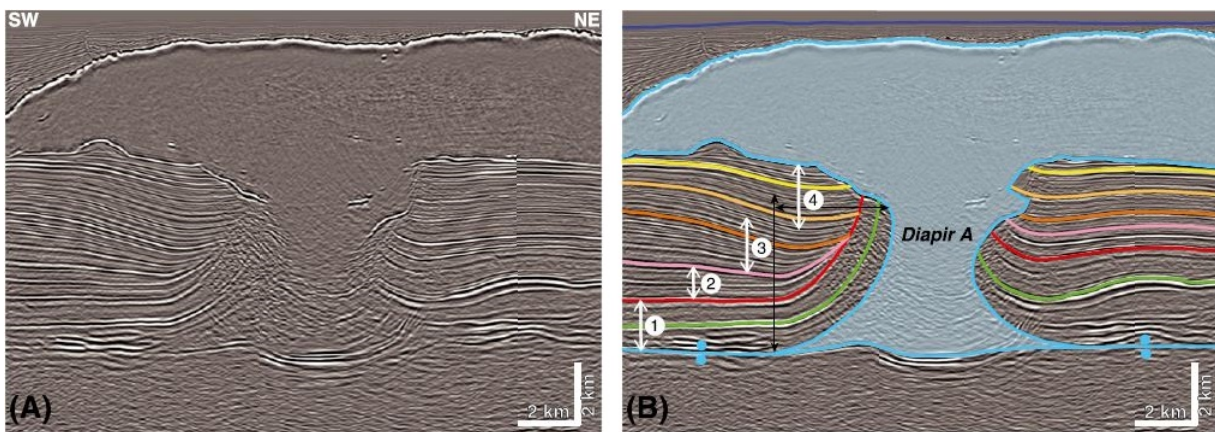


Figure 32: Salt Megaflap -basal flap- Seismic Example a) uninterpreted b) interpreted. Stratigraphic interval 1 is the megaflap and 2–4 are growth packages with different thickness and onlap patterns. Vertical and horizontal black arrows show height and width of megaflap, respectively. Data courtesy of Schlumberger; no vertical exaggeration. (image retrieved from Rowan et al; 2016).

Common styles include simple broad synclines, turtle structures, and expulsion-rollover structures, where megaflaps define the extreme cases near vertical or even overturned strata, with a zone of folding having both vertical and lateral components (Rowan et al., 2016). They differentiate from smaller scale composite halokinetic sequences as their fold width and structural relief can reach up to multiple kilometers. Rowan et al., 2016, depicts the structure *with the oldest strata typically concordant to the top salt or slightly onlapping* as it is seen in Figure 33.

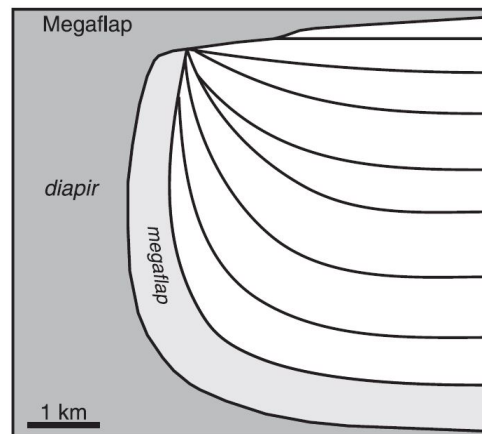


Figure 33: Diagram of a megaflap adjacent to a salt diapir (retrieved from Rowan et al., 2016).

Rowan et al., 2016, define megaflaps as structures commonly occurring in contractional deformation zones with a distinctive boundary between the megaflap and the overlying growth strata marked by stratal thinning. As the diapir rises upwards, adjacently placed flank megaflap rotates up to 90° in order to accommodate the movement, which results in diapir widening. Three types of flaps can be formed in salt-prone settings, which are namely; basal flaps (1), perched flaps (2), and injection fold flaps (3) (Jackson and Hudec, 2017);

- (1) Basal flaps (Giles and Rowan 2012, Graham et al. 2012) occur at the base of salt diapirs, starting as a thick sequence, thinning upwards along the flank, and eventually pinching out and/or eroding towards the crest, while folding upwards by the rise of the salt (Schultz-Ela, 2003).
- (2) Perched flaps take place partway up the flank of salt diapirs and occur during piercing of a diapiric roof by rise of the active diapir, hence they mark the active diapirism phase following the reactive growth. They are comparably smaller and thinner than the basal flaps.
- (3) Injection fold limbs can lead to flap formation during active diapirism occurred at the crest of contractional anticlines (Belousov, 1959). During the growth of diapir anticline, the salt core becomes pressurized due to displacement loading urged by tightened fold limbs, and eventually arrives at surface when the overburden is thin enough. Such diapirs happen to be smaller than the forming injection folds (Figure 34).

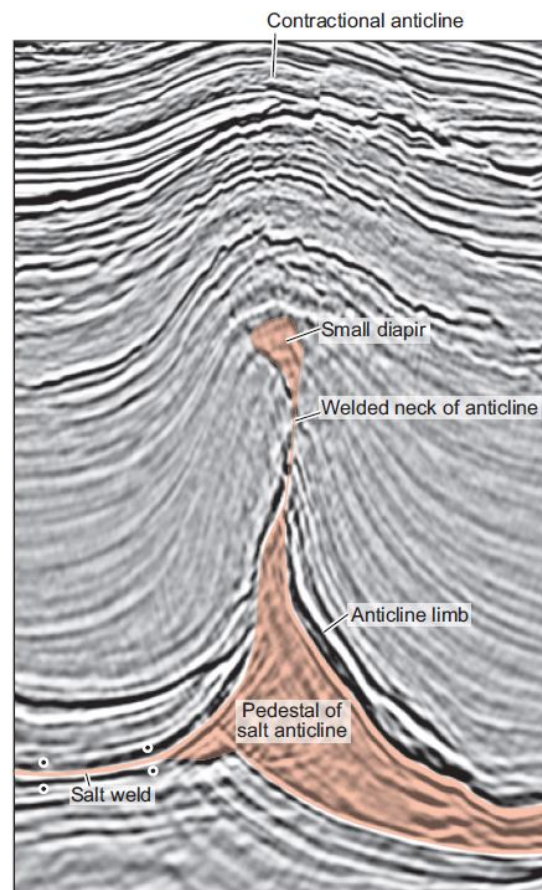


Figure 34: The core of this salt anticline is pinched shut by regional shortening, during which the salt core breaks out as an injection fold, forming a small diapir at its crest. Campos basin, Brazil. Seismic data courtesy of PGS. (image retrieved from Jackson and Hudec. 2017).

v. Minibasins

Minibasins can be described as small basins or depressions, sinking into relatively thick salt deposits (Jackson and Hudec, 2017). As it is explained by Peel (2014), the energy that drives the subsidence, and the movement of salt which accommodates it, derives from net lowering of the centre of mass, as denser sediments move downwards, and less dense salt moves upwards (Kehle, 1988; Ramberg, 1967, 1981; Trusheim, 1960). They are primal forms of sedimentary pods that are mobilized above a thick salt deposition due to differential loading and buoyancy. Initially, Gealy, 1955, reported the irregular and hummocky continental slope bathymetry during bathymetric profiling of northern Gulf of Mexico. Later in 1966, it was stated by Ewing and Antoine that the minibasins with synclinal fills and the bathymetric highs between them were the crests of diapirs. Forrest published an article with ‘minibasin’ term the first time in 1986. Following that, many adaptations of minibasins were identified in various part of the world and started to be used abundantly (see Jackson and Hudec, 2017 for a review).

Minibasins are dish-shaped synclines of sediments sinking into a medium of thick salt and extending few tens of kilometers in diameter. With high sedimentation rates and excessive differential loading, salt escapes underneath the minibasin and rises around its perimeter. The escape of minibasin flooring material gradually decrease the amount of sinking up until all of the underlying salt welds out. Salt expulsion creates space for the minibasin to deepen and eventually sinking stops underneath the minibasin (Callot et al., 2014; Callot et al., 2016) (Figure 35).

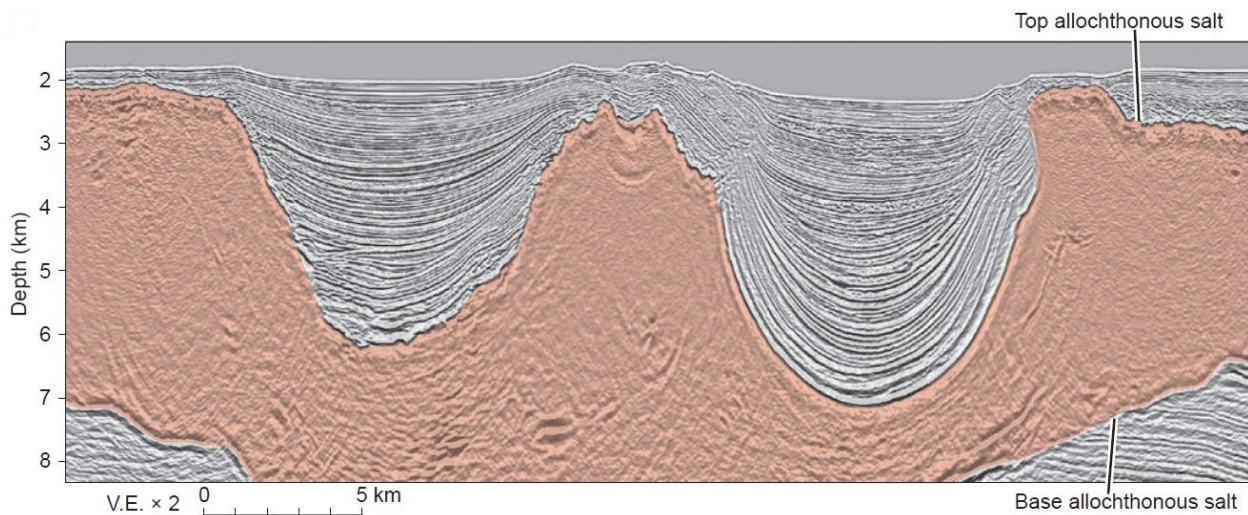


Figure 35: Seismic example of dish-shaped minibasins on the continental slope of the northern Gulf of Mexico. Seismic data courtesy of CCG. After Hudec and Jackson (2011) (image retrieved from Jackson and Hudec, 2017).

Primary and secondary minibasins are two types of minibasins defined for salt-prone areas. A *primary minibasin* rests on *autochthonous salt* or on an *equivalent salt weld* (Jackson and Hudec, 2017), while a *secondary minibasin* rests on *allochthonous salt* or an *equivalent salt weld* and lacks the oldest *postsalt stratigraphy* (Pilcher et al. 2011). Secondary minibasins are derivatives of primary minibasins, which have been emerged from autochthonous salt deposits. They originate from allochthonous salt that have mobilized from an autochthonous body (see Callot et al., 2016) (Figure 36).

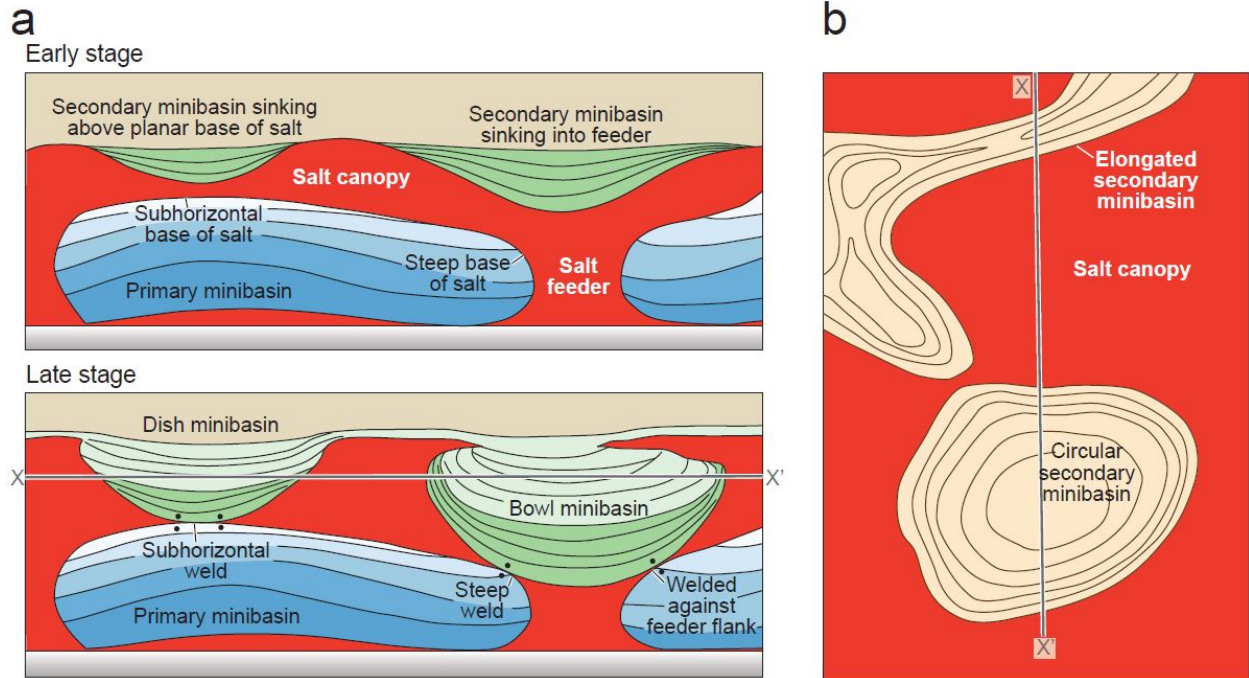


Figure 36: Minibasins are small basins, or depressions, that fill with sediment as they sink into thick salt. These growth synclines are laterally surrounded by salt or by salt welds. (a) Two-stage evolution of secondary minibasins sinking into allochthonous salt. An older, primary minibasin underlies the canopy. The second stage shows the level of the depth slice shown in (b). (b) Minibasin planforms are typically generalized as subcircular, but they can be any shape, including elongated (image retrieved from Jackson and Hudec, 2017).

V. Remarks: Literature Wrap-Up of Salt Tectonics

Salt Tectonics is a very broad topic that have been investigated quite intensively especially for the last three-to-four decades. Initial ideas have been proposed in early 20th century and later developed/enhanced with the help of advancements in the seismic imaging technology. Improvements on seismic processing techniques gave the researchers a chance to better interpret the salt-related structures they observe on collected seismic data. Moreover, the advanced satellite imagery and drone technology opened a new era for various branches of geology including the Salt Tectonics. Today, in addition to the high quality seismic datasets, we also have access to high-quality airborne imagery tools.

The previous sections of this chapter aimed to summarize the topic of Salt Tectonism in its own frame by making a literature synthesis.

- Salt is a ductile rock that deforms under geologic time-scales and strain rates by summing up the plastic deformation at particle scale (e.g. microcracking and cataclastic flow, dislocation creep, and solution-precipitation creep).
- The main driving force for salt mobility is the differential loading, which can be induced into the system by three differential forces; gravity, tectonism and thermal gradient. Restrictive forces against salt flow are listed as strength of overburden (i.e. friction) and boundary drag.
- Halokinesis, also known as the deformation geometries of salt, can be investigated under two sub-category; (1) deformed salt features, and (2) salt-related sediment recordings.
 - o Deformed salt features are listed as; salt sheets and glaciers (i), salt diapirs walls and pillows (ii), salt canopies (iii), and salt welds (iv).
 - o Salt-related sediment recordings are listed as; halokinetic sequences (i, minibasins (ii), hooks and wedges (iii), rim synclines (iv), and megaflaps (iv). Unconformity-bounded sediment packages observed near salt deposits/remnants are also the diagnostic features defining salt tectonism.
- Each specific salt deformation geometry 'halokinesis feature' depicts a deformed/mobilized salt form and its signature recorded within the sediment pile adjacent to the salt body. Such recordings (observable both on seismic and outcrop scale) are preserved within the geological setting and give vital clues about salt mobilization.

Chapter 2: Shale Tectonics

Shale is a fine-grained/stratified sedimentary rock, which is composed of mud that is a mix of flakes of clay minerals and tiny fragments (silt-sized particles) of other minerals, especially quartz and calcite (Blatt and Tracy, 1996), forming a laminated and fissile type of mudstone. Shale is one of the most abundant sedimentary rocks found in nature; which can be loosely consolidated (undercompacted) and/or overpressured, when it is subjected to a sedimentary overburden in a geologic setting. As it is stated by Morley et al. (2017), *“argillaceous sedimentary units are the most common lithology followed by thrusts in sedimentary basins due to their generally great volume in sedimentary basins, their inherent weakness, and their ability to retain or channel high pore fluid pressures”*.

The concept of Shale Tectonics has been first developed back in late 1960s-80s as an analogy to Salt Tectonics in order to describe and sometimes interpret the structures from poorly imaged geometries depicted on seismic data (e.g. Morgan et al., 1968; Evamy et al., 1978; Bol and Hoorn, 1980; Khalivov and Kerimov, 1983; Westbrook and Smith, 1983; James, 1984; Barber et al., 1986; Bredehoeft et al., 1988; Shaw and Primmer, 1989). ‘Shale Masses’ have been first described by Musgrave and Hicks in 1968, followed by the term ‘Shale Diapirism’ suggested by Morgan et al., 1968; Hedberg, 1974; and Chapman, 1974. Musgrave and Hicks, 1968, directly quoted these features as;

“Large bodies of shale at least several hundred feet thick. They may be either diapiric masses or depositional masses. The shale masses act like salt masses, and the two may combine to form domal masses; either or both may form the updip seal for a stratigraphic accumulation of oil. The shale masses have four properties, which seem to be caused by the high porosity and low permeability of these structures:

1. *Low-velocity sound transmission, in the range of 6,500-8,500 ft/sec with very little increase in velocity with depth*
2. *Low density, estimated to be in the range of 2.1-2.3 g/cm³*
3. *Low resistivity, approximately 0.5 ohm-m*
4. *High fluid pressure, about 0.9 of the overburden pressure*

The reflection-seismic method can be used to map shale masses. The mapping generally is based on the loss of reflections. If a homogeneous mass is present, there will be no reflecting interfaces, and therefore no reflections will occur. Ambiguity is possible because the mass can be another type of homogeneous mass, such as salt, or a combination of shale and salt, which is referred to as a domal mass (Atwater and Forman, 1959)”.

Even though the term and concept of shale diapirism was well adopted in the 1980s (Bol and Hoorn, 1980; Khalivov and Kerimov, 1983; Westbrook and Smith, 1983; James, 1984; Barber et al., 1986; Bredehoeft et al., 1988; Shaw and Primmer, 1989), it was later discarded due to incoherent seismic datasets and lack of well-preserved outcrop examples. However, the concept has been brought back to attention in early 2000s as a result of advanced seismic imaging technology and the research studies conducted by Morley and Guerin, 1996; Morley et al., 1998; Morley, 2003; Day Stirrat et al., 2010; Maurin and Rangin, 2009; Morley et al, 2017; Morley et al., 2018; helped us better understand the processes defining the stratal geometries associated with shale tectonics.

Shale Tectonics is defined as; *the structuring within a basin associated with shale or mudstone plasticity or mobility, either as the cause of such mobility or as a result of such mobility, while mobile shales are depicted as any manifestation of clay constituents (indurated or not) that show evidence of microscopic-*

scale fluid or plastic movement' (Wood, 2010; AAPG Memoir 93 Ch1, 2010). In this PhD thesis, we will be using the same terminology/nomenclature in order to detail the research, however, it is important to note that within this thesis research, we refer to *mud volcanism* as fluidization of shales, and *shale mobility* as strain/plasticity of shales mimicking salt-like behavior observed in salt tectonism.

I. General Concept

Shale Tectonics is the study of a shale-controlled deformation interval observed at nature within sedimentary basins/units aiming to focus on shale mobility triggered by internal (e.g. load-driven) and external forces (e.g. tectonically-driven). As a terminology, it depicts a deformational behavior that involves/functions with over-pressured, under-compacted, fine-grained sediments (e.g. clays, mudstones) (Soto et al., 2010).

As it is stated by Wood, 2010 (Shale Tectonics, AAPG Memoir 93); in order to develop a working classification of shale tectonics, we need to focus on these two critical primary classes of features: (1) those associated with extrusion of fluids and material that does not involve grain-to-grain contact (Battani et al., 2010; Delisle et al., 2010), and (2) those associated with larger scale deformation of apparent highly overpressured mud or shale substrates involving grain-to-grain plastic flow (Elsley and Tieman, 2010; Wiener et al., 2010). In other words, these two types of deformation defined for shale can be simplified as; [1] *fluidization* and [2] solid-state distributed deformation (*strain*), which will be further detailed under the Deformation Mechanisms section of this chapter.

In nature, overpressured shale intervals act as detachments or as décollements facilitating the gravity-driven gliding or sliding of overlying strata (Warren et al., 2010). Shale-prone environments can lead to hundreds of km long laterally extended detachment levels while their mechanical properties are determined at microscopic level. A multi-scale approach is necessary in order to have a comprehensive understanding of clay mechanics and shale detachments (Morley et al., 2018) due to its scale-dependent deformation character (e.g. brittle on microscopic level, ductile on macroscopic level). Clay minerals and clay-rich rocks interacting on macroscopic and microscopic heterogeneity level, result in strain localizations for pre-detachment shale horizons, which points out to important insights understanding their mechanical characteristics (Morley et al., 2018).

The conducted studies about mechanic behavior of various types of clays by Abdullah et al., 1997; Deng et al., 2012; Mesri and Vardhanabhuti, 2009; Walker and Raymond, 1968; showed that the secondary deformation in fine-grained rocks is linearly related to compression characteristics (e.g. Raymond, 1966; Gregoy et al., 2006) (Morley et al., 2018). Formation of heterogeneities and later structure localizations are strongly controlled by increase and decrease of porosity (e.g. by studying compressibility and pore morphology (Desbois et al., 2009)) observed in clays during the early stages of deformation (Morley et al., 2018).

Formation of a shale detachment horizon display both brittle fracturing and ductile shear band properties depending on its scale of observation. As it is suggested in the study of Dehandschutter et al., 2005; based on the micro-structural analysis, ductile deformation is observed within the zones of low strain areas while the brittle deformation and structures govern the high strain zones depicted by higher strain rates (Morley et al., 2018). Moreover, compaction and consolidation forces interacted with combined tectonic forcing play a key-role during the earliest stages of deformation over the development of brittle and ductile structures in clay shear zones (Labaume et al., 1997; Dehandschutter et al., 2005). During progressive

deformation of clays; interconnecting slickensides, also known as the *polished shear fractures*, form as a result of grain size reduction, particle alignment, pore collapse and crystal plasticity (Morley et al., 2018; see Laurich, 2015 and Laurich et al., 2017 for recent reviews).

II. Deformation Mechanisms

In a counter-intuitive manner, sediments may lose their strength through burial as a result of a complex interplay between *stress*, *permeability* and *deformation*, which enables the mobilization of these sediments via variety of processes (Maltman & Bolton, 2003; Morley et al., 2017; Blouin et al., 2020). Such processes differentiate with depth and pressure conditions as well as the internal, external, and hydraulic loads these sediments are exposed to (Maltman & Bolton, 2003; Blouin et al., 2020). As a result of changing conditions, sediments can either (i) retain some residual strength and achieve large displacements through shearing under certain states (detachment levels and mobile shales; Maltman & Bolton, 2003; Morley et al., 2017; Blouin et al., 2020), (ii) start acting like a viscous material through *liquefaction* (when the load is entirely sustained by fluids) or (iii) adapt to *fluidization* (when the grains become buoyant through rapid input and circulation of external fluids) (Maltman & Bolton, 2003; Morley et al., 2017; Blouin et al., 2020).

There are two types of deformation defined for shale; strain (a) and fluidization (b). Strain defines the plastic deformation pattern triggered by distributed slow motion for shale while fluidization represents the mud volcanoes. The major 'apparent' difference between salt and shale emerges from this phenomena as salt rocks do not fluidize and form mud-volcano like structures when pressured with fluids similar to shale. The following two sections will be reviewing these two deformation mechanisms defined for shale rocks in order to better understand their mobilization/fluidization pattern.

A. Strain: Solid-State Distributed Deformation

Strain is the deformation of a solid caused by the application of stress (Allen and Allen, 2013). It defines the distributed slow motion plastic deformation pattern for shale rocks. Elasticity defines the 'reversible' strain and plasticity denotes the 'irreversible' strain that impose a permanent deformation on the rock. Plasticity can be summarized under two parts; fracturation and ductility. Fracturation represents brittle deformation, while the ductility point out to slow-motion, distributed deformation. As previously mentioned, ductile rocks deform under stress and strain. When the controlling factors are met, shale rocks flow in a viscous manner (e.g. like a fluid) and deform plastically similar to salt rocks.

Parisio et al., 2015; summarize shale acts as a quasi-brittle material (i.e. when '*dissipation prior to cracking exists with no or negligible permanent strains*' (Lemaître and Desmorat, 2005)) showing linear elasticity before the arrival of peak stress, which marks the accumulation of irreversible strains due to decohesion mechanisms and growth of micro-cracks. Deterioration of elastic moduli and hence the accumulation of such inelastic (also known as irreversible) strains lead to debonding mechanisms within shale rock structure. However, under a constant deviatoric stress regime, softened clays become residually stable and display pure plastic flow. The main (but not all) factors controlling the geomechanical behavior of shales can be listed as microstructural features, inter and intra-granular porosity, static deformability and

failure properties, anisotropy degree, petrophysical characteristics, mineralogy (clay content and mineral type), thermal history and organic matter content.

Due to its unique behavior and internal structure, the deformation pattern of shale cannot be determined by one single model (e.g. Continuum Damage Mechanics -CDM- representing micro-crack/micro-void formation and growth) and rather be explained by a multiple model that unifies elastic, plastic and damage theories; such as coupled plastic-damage models. As stated by Parisio et al., 2015; in these models, *the plastic dissipation mechanism controls the accumulation of irreversible strains and the damage dissipation mechanism is responsible for the degradation of elastic parameters and the softening of the material*. Microfabric signatures developed during sedimentation and burial can be triggered by; (i) physicochemical processes (e.g. electrostatic interaction between particles, thermally driven movement of particles); (ii) bioorganic processes (e.g. bioturbation, biochemical mechanisms); and (iii) burial diagenetic processes (e.g.) compaction and cementation (Faas and O'Brien, 1991) (Morley, et al., 2018).

As a well-studied example, Bossart et al, 2002; classified Opalinus Clay (OPA) as a *stiff, over-consolidated clay* that can clearly showcase intrinsic structural anisotropy, quasi-brittle behavior, strength dependency on mean pressure and degradation of stiffness. Moreover, micro-crack formation and growth of which lead to softening behavior and irreversible plastic strain (Parisio et al., 2015). Triaxial compression tests conducted by Gräsle & Plischke, 2011 and Salager et al., 2013 in order to better understand the mechanical behavior of OPA reveals that three bedding plane orientation with respect to the vertical stress direction can be obtained from this clay group; P-Samples, Z-Samples and S-Samples (Figure 37) (Parisio et al., 2015).

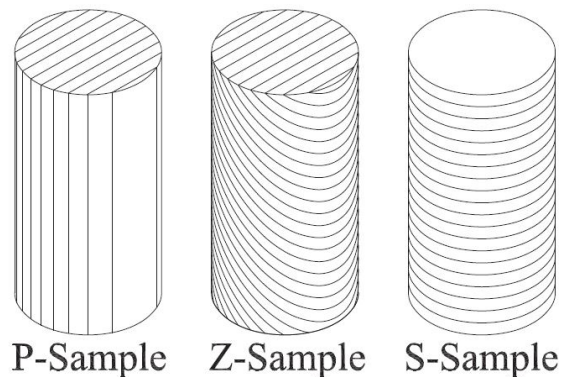


Figure 37: Bedding orientation in samples of Opalinus Clay subjected to triaxial compression tests (image retrieved from Parisio et al., 2015).

Based on the study of Gräsle and Plischke, 2011, and their test report; it is concluded that the rheology of Opalinus Clay can be observed as representative of the behavior of quasi-brittle shale (Parisio et al., 2015). The results of stress–strain response of a triaxial compression test conducted by Gräsle and Plischke (2011) reveal that the P-Samples under 3 MPa confinement can be defined by three phases (I, II, III) (Figure 38) (Parisio et al., 2015);

- **Phase I:** *Material behaves almost linear-elastically while the irreversible strains are small but comparable to the elastic ones.*
- **Phase II:** *Micro-cracks start to grow rapidly and carbonate bonds are broken, damage accumulates and after the peak is reached the material shows a softening response.*
- **Phase III:** *Micro-cracks are believed to be stable and the material plastically flows, exhibiting the accumulation of permanent strains at constant values of deviatoric stress.*

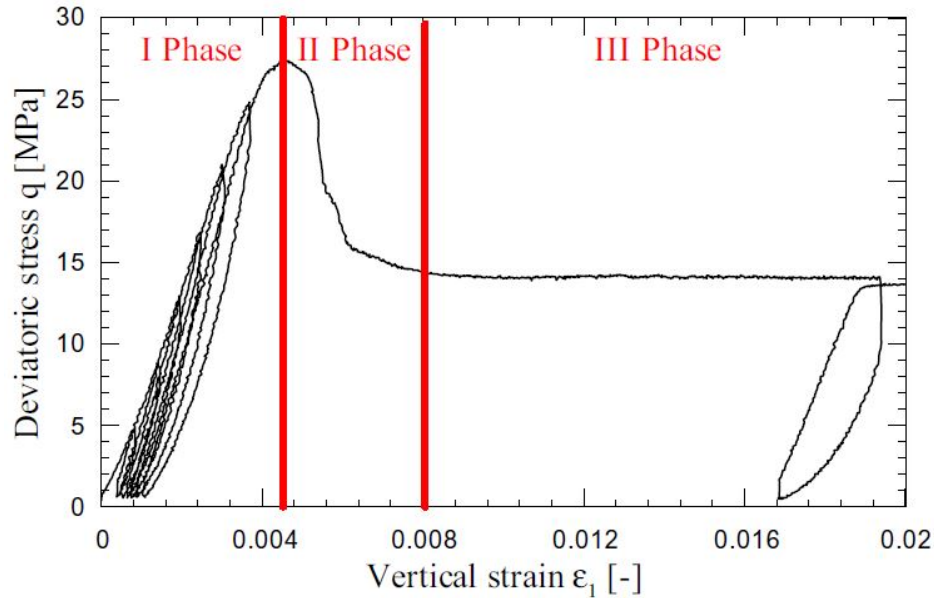


Figure 38: Typical rheology of P-Sample of Opalinus Clay in triaxial compression conditions at a confinement pressure of 3 MPa (Gräsle and Plischke, 2011) (image retrieved from Parisio et al., 2015).

Gräsle and Plischke, 2011, reports that the main observations out of the test results of OPA are *the brittleness of shale, in terms of its post peak softening response, and the residual conditions of constant deviatoric stress, in which the material is plastically flowing and exhibits a plateau*. Important points to note from this compression (loading-unloading) experiment are (Parisio et al., 2015);

- Permanent strains stay comparable to elastic strains before the peak of stress (Phase I).
- Following the softening phase, the elastic moduli degrades while the permanent stress values increase, which can be related to the quasi-brittle nature of clays and the accelerated breakage of bonds prior to reaching the peak of stress within Phase I.
- Degrading elastic moduli results from deformation, which points out to the fact that the material might behave *elastically brittle with negligible accumulated plastic strains* during Phase I.
- Phase II marks the plastic flow behavior under deviatoric stress conditions and accumulation of permanent inelastic strains.
- When the peak of stress is reached, within Phase II, advanced micro-cracking leads to permanent deformation. Accumulation of deformation transitions the stress response towards a brittle softening phase (Phase III).
- During Phase III, the material does not develop any more damage/deformation as it displays plastic flow at constant stress.

Skempton, 1964, relates the mechanical characteristics shale to amount of strain accommodated, and as it is stated by Morley et al., 2018; *the strength of shale detachments and their decrease of shear resistance at large strains is partly related to structure*. Morgenstern & Tchalenko, 1967, described this finding by evaluating various shear zones under microscopic scale and showing consistent correlation of displacement on observed structures. The mechanical behavior of shales can be affected by grain boundaries, the contrast between different types and orientations of grains, as well as pores and microcracks (Paterson and Wong, 2005).

B. Fluidization: Mud Volcanism

i. Generalities

Different than salt, shale can be *fluidized* and flow with overpressure and the fluidization of shales is represented by *mud volcanism* in nature. Mud volcanoes are found in various onshore/offshore geologic settings such as compressional belts, deltaic settings, hydrothermal regions and depict the *surface and/or seafloor expression of a subsurface transfer of fluidized clayey sediments* (Dimitrov, 2002; Kopf, 2002; Deville, 2009; Blouin et al., 2020). Fluidization of shales is enabled by fluids migrating upwards (under pressure) in the subsurface via a fracture network (Morley, 2003).

Mud volcanoes are expressed as a topographic structure, varying in size and shape, resulting from the natural seepage of a mix of liquids, gas and fine-grained sediments (Dimitrov, 2002; Kopf, 2002; Judd & Hovland, 2007; Blouin et al., 2020). They occur with thick sedimentation and circumstance of fluid overpressure at depth, overpressure of which comes from fluids contained in quickly-buried relatively impermeable clay-rich sediments. The overpressured fluid flow pierces through the sedimentary column resembling salt diapirs, domes, chimneys, or pipes (Dimitrov, 2002; Kopf, 2002; Kirkham, 2015; Mazzini & Etiope, 2017). Upon piercing the impermeable sediment layer via migration pathways due to accumulated overpressure, fluids from deeper sections are transferred through the surface, where mud volcanoes represent the surface vents for these fluids (Deville, 2009).

As it is stated by Deville, 2009; *the key part of the process of mud volcanism, absent from salt diapirism, involves fluid being transported upward through a conduit system initiating a reaction chain of subsurface sediment remobilization processes associated to the development of several distinctive structural elements and to sediment remobilization at several levels* (Deville et al., 2003a; Davies and Stewart, 2005; Stewart and Davies, 2006), which feeds the extrusive mud edifices developed through the surface.

ii. Mechanisms

Edberg, 1974, and Higgins & Saunders, 1974, primarily suggested that *mud volcanism is associated to overpressure generation at depth*, which became a scientifically accepted/proven statement that is globally accepted today. However, the inner mechanism of mud volcanoes is still a matter of debate today (Deville, 2009) due to their unique and uncertain nature. Historically; Milkov (2000) and Kopf (2002), described mud volcanoes as *derived from the rise of a unique shale rich-source horizon by a process of balloon-like mud diapirism mirroring salt diapir emplacement* (which by the way is ironic as clay fluidization is fundamentally different from salt flow). However; studies of Cooper (2001a, b); Deville et al., (2003a, b); Deville & Prinzhofer (2003); Stewart & Davies (2006) concluded that such process models do not fully account for mud volcano system geometry (Deville, 2009). Ductile deformation of shales resembling salt occurring at deeper segments of Earth triggered by overpressure (and co-existing components) is still a valid point of discussion that will be addressed throughout the course of this thesis. However, piercing of a 'shale diapir' in an 'extrusive' mobile shale manner mimicking salt diapirs have never been noted in any part of the world with the studied cases so far (Van Rensbergen et al., 2003; Deville et al., 2006; Deville, 2009).

Mud volcanoes act as a fluid outlets, allowing degassing and dewatering of deep stratigraphic units (Osborne & Swarbrick, 1997; Milkov, 2000; Deville, 2009; Kirkham, 2015; Blouin et al., 2020). The materials ejected by mud volcanoes consist of fine solid particles suspended in overpressured fluids, such as clasts and breccias, which do not necessarily come from a single stratigraphic layer and suggest a systematic mixing of species (Deville et al., 2003a; Blouin et al., 2020). *Presence of gas in these ejected materials* is another common property shared by all mud volcanoes around the world (Blouin et al., 2019; Etiope et al., 2009; Hedberg, 1974). The PhD study of A. Blouin detailed this phenomena and it is stated on Blouin et al. (2019) that, even though the initial trigger of a mud volcano (e.g. Absheron Mud Volcano) is not related to gas, as hydrofracturing due to overpressure builds up and weakness of the fold-crest initiates the succession of events, methane would have three essential effects:

- a. *Gas needs to saturate the porous network in its dissolved state before hydrofracturing in order to provoke remobilization of sediments. Exsolution of methane helps to weaken and disaggregate host sediments (Sultan et al., 2012; M. R. P. Tingay et al., 2015).*
- b. *Since free gas has very low density (typically about 1/1000 of that of water in normal conditions), it flows towards the surface (Brown, 1990), carrying the mud away (solid particles and formation water).*
- c. *As gas goes up into the pipe, it expands (Brown, 1990), accelerating the mud ascent, sustaining mud pressure and eroding fracture walls, creating clasts, to end-up with mud breccia extrusion at the surface.*

As a consequence, *methane exsolution* stands as the key element to mud formation and also the main driver for mud remobilization towards the surface due to its *low density* and *expansion capacity* (Blouin et al., 2019; Blouin et al., 2020; Blouin et al., 2020). Overall, *the mud consists of a mixture of microscopic elements of various origins issued from all the sedimentary formations pierced by the mud conduits* (Deville, 2009) as well as free gas (Blouin et al., 2019), and the mobilized sediments consist of various clay minerals and thin quartz particles (Deville et al., 2003a; Deville et al., 2006).

In terms of shale fluidization, there are several fundamental aspects: (a) overpressure generation, (b) hydraulic fracturing and (c) fluid migration (Deville, 2009) (Figure 39);

a. Sediment loading triggered by fast sedimentation rates accelerates overpressure generation as the fluids get trapped/physically handicapped in escaping the reduced pore space and hence the phenomena results in building up on pore pressure. The temperature increment with depth adds on overpressure generation as well as the gas content reducing the sediment density and increasing the overpressure conversely.

b. As stated by Brown & Westbrook (1988); Brown (1990); Deville et al. (2003a-b); *progressive deformation within the sedimentary pile is susceptible to generate high pore pressure in the center of geological depressions which is susceptible to be transmitted laterally by permeable horizons towards highs where sedimentary thickness and load are smaller.* As the pore pressure builds up on vertical load, hydraulic fracturing initiates, which enables fluidized material to propagate upwards.

c. Following the overpressure generation and hydraulic fracturing, relatively impermeable shale layers ease up the fluid migration and remobilized fluids guide their way from deeper parts through the surface via these pathways. The outlets letting fluids migrate upwards via overpressure/hydraulic fracturing help the *pressure gradient* carried to normal pressurized upper compartments and enable the fluid flow to diverge from main conduits. The fluid expulsion regime/intensity differs based on cyclic phases of each mud volcano.

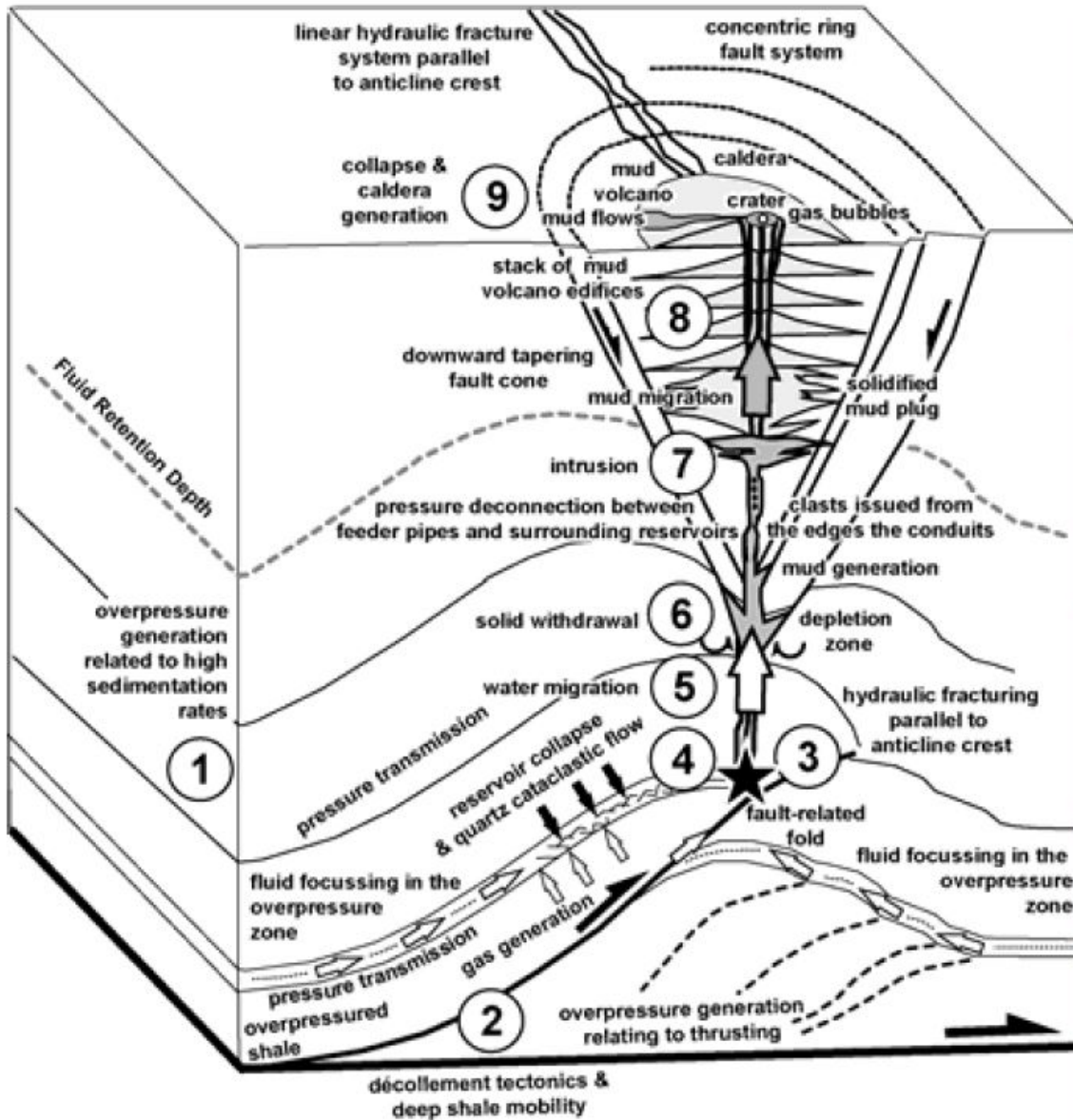


Figure 39: Conceptual sketch of the reaction chain of the remobilization processes (image retrieved from Deville, 2009).

iii. Morphology

Size-wise, mud volcanoes can have a diameter of several kilometers and up to several hundred meters of height. They typically display a cone-like shape resembling magmatic strata-volcanoes, while others exhibit smoother domes/mud shields, when the mud eruption spreads out and flow far away from a vent. Steep-sided cones shorter than 10-meter height are called '*gryphons*'. A circular depression surrounds the mud volcano mouth comparable to the magmatic calderas (in small-scale). Such circular depressions occasionally develop inside a cone. When the circular depression of a mud volcano is filled with extruded mud/clay material, they generate a flat topography bounded by steep flanks at the surface, which are called '*mud-pies*' (Deville, 2009) (Figure 40). Apart from the review given in this thesis, global examples of shale fluidization (e.g. mud volcanoes) can also be reviewed in large set of papers (Milkov, 2000; Kopf, 2002; Ivanov et al., 1996; Robertson & Kopf, 1998; Chamot-Rooke et al., 2005; Martinelli & Judd, 2004; Planke et al., 2003; Stewart & Davies, 2006; Grando & McClay, 2007; Duerto, 2007; Duerto & McClay, 2011 and Blouin et al., 2019).



Figure 40: Azerbaijan Mud Volcano (image retrieved from personal collection of G. Dinc).

III. Driving Forces for Shale Tectonism and Fluidization

Shale displays plastic deformation at macro-scale while being brittlely deformed at micro-scale. The driving mechanisms both for salt and shale tectonics include differential loading, basin geometry and external tectonic forces. Similar to salt, the major driving force for Shale Tectonism is the differential loading, which can be introduced into the system by;

1. *Internal Forces: Permeability-Related Constraints Induced by Overpressure;*
 - a. Sedimentation Rate
 - b. Disequilibrium of Compaction
 - c. Diagenesis
 - d. Maturation

2. *External Forces Affecting Fluid Pressure:*
 - a. Basin Geometry
 - b. Tectonism
 - c. Differential Subsidence

However, differing from salt, the driving forces affecting on shale work co-dependently and the main trigger for shale in this regard is the *overpressure*. Even if the following sections will aim to describe these forces under their given title context, in a shale-prone geological setting, most of the driving forces we distinguish derive directly and/or indirectly as a result of pore pressure by various means of co-dependency (e.g. internal or external). Hence, the given scheme of driving forces for Shale Tectonism cannot be thought or handled individually as in the case of Salt Tectonism (e.g. gravitational, external, thermal) [even though the *differential loading* is the *main engine* for salt mobility, which can arise from these listed various mechanisms, similar to '*shale tectonism and overpressure*', '*salt tectonism and differential loading*' partly has the same intervening problem] without independently describing the overpressure phenomena in its own context.

For this reason, the following section will be describing the Overpressure as the main trigger mechanism in Shale Tectonics Driving Forces and then detailing the internal and external forces and their influence on Shale Tectonism as clear as possible, while interchangeably cross-referencing to overpressure.

A. *Overpressure: The Main Trigger*

The mechanisms producing overpressure, which is a function of both porosity and permeability, at various depths within sedimentary basin settings can be listed as (Morley et al., 2018): 1) compaction disequilibrium in response to burial, 2) compaction disequilibrium in response to horizontal compression-induced shortening, 3) thermo-chemical reactions (e.g. smectite to illite, kaolinite to illite, kerogen to oil and gas, and oil to gas transformations, see reviews in Osborne and Swarbrick, 1997, and Morley et al., 2014), and 4) permeability decrease due to increased shear strain (Ikari et al., 2009a, 2009b).

Overall, the aspects to consider for shale overpressurization can be summarized as (Grauls, 1999), (i) mechanical assumptions (e.g. vertical stress and lateral boundary conditions), (ii) irreversible sediment compaction processes, (iii) complex basin history (e.g. major deformation, uplift/erosion, stress regime changes), (iv) existence of additional/supplementary causal mechanisms (e.g. lateral stresses, thermal effect, fault-related dynamic transfers), and (v) combined existence of internal and external causes difficult to differentiate in the same geological setting effecting the global present-day abnormal pressure regime.

i. *Historical Point of View*

When the sufficient permeability level is reached/met upon sediment loading within a shale-prone environment, the fluids are expelled out of the shale rock matrix during compaction. During this phase, with occurrence of high compaction disequilibrium in between the sand bodies and the hosting shale rock, certain features with particular characteristics such as; clastic dykes and injected cells cutting through clays, emerge as a result of overpressure and compaction, which in general are originated from sand bodies that are trapped within shale bodies/masses. These sedimentary features, unrelated to any sort of volcanism, breach out and form dyke extrusions.

Low permeability is a shale-related aspect and does not come from the sand bodies trapped within the shale deposits as sand bodies display high permeability component. However, since these sand bodies are trapped within a shale-prone setting, they result in a differential compaction between shale and the sand bodies. With excessive compaction stress being introduced into the system with incoming sediments, and hence the unavailability of reorganizational space; the sand cannot expel its fluid content into the shale mass medium. Therefore, it is preserved at high pressure while breaching the shale rock during this phase.

In shale-prone intervals with low permeability, overpressure builds with the weight of overburden or vertical stress (S_v) (Grauls, 1999). The main cause of overpressure in sedimentary basins (as first claimed by Dickinsen, 1963), is considered to be the compaction disequilibrium (Fertl, 1976; Magara, 1978), magnitude of which was derived from the soil mechanics principles of Terzaghi (1968) (see Grauls, 1999). Following these innovations, as it is stated by Grauls, 1999; empirical approaches or porosity versus vertical effective stress relationships have been developed (Mann and Mackenzie, 1990), which showed that mechanical and thermal stress along with dynamic transfers are the main drivers for overpressure generation in sedimentary settings (Grauls, 1999).

ii. *Measurements and Characterization*

The mechanisms of overpressure are determined by loading-unloading curve data collected from the *acoustic velocity vs vertical effective stress* graphs (Tingay et al., 2009; Ruth et al., 2004). Li et al., 2019; states that the origin of overpressure can be defined as (i) compaction disequilibrium *if the overpressured points lie on the loading curve*, and as (ii) fluid expansion or transfer processes *if the overpressured points lie off the loading curve* (Ruth et al., 2004; Hermanrud et al., 1998).

Low permeability ratios makes it difficult for direct measurement of pressure in mud stones (Li et al., 2019) and hence mud pressure and prediction studies are carried out by indirect methods such as sonic velocity, bulk density, resistivity and log data measurements via geophysical applications (Bowers, 1995; 2002). Since the various overpressure mechanisms can be identified based on their response to loading-unloading processes (Ruth et al., 2004; Hermanrud et al., 1998; Bowers & Katsube, 2002; Zhang, 2013; Lahann, 2017; Swarbrick, 2012) (i.e. pressure generation mechanisms) (Magara, 1978; Dasgupta et al., 2016; Fan et al., 2016; Tingay et al., 2007), it is important to analyze these petrophysical properties in order to define the pattern of overpressured effective stress sequence (Li et al., 2019). Mudstone overpressures generated by compaction disequilibrium are estimated via porosity-based pore pressure prediction methods (e.g. equivalent depth method) (Bowers, 1995; Swarbrick, 2001; Sayers et al., 2002).

iii. Major Triggers for Overpressure

Compaction disequilibrium and fluid expansion (also known as vertical transfer of overpressure) are the two types of overpressure mechanisms (Tingay et al., 2009; Law et al., 1998; Ruth et al., 2004). Compaction disequilibrium can be described as a *loading overpressure generation mechanism* (Tingay et al, 2013; Ruth et al., 2004; Osborne & Swarbrick, 1997) triggered by (i) fast sedimentation rate of the basin or (ii) lateral tectonic compression associated to low permeability preventing fluid escapes, which in normally compacting sediments re-equilibrate the stresses. Rapid sedimentation rates lead to vertical stress increase while the tectonic compression impose an increase on horizontal stress (Li et al., 2019). Conversely, *unloading overpressure generation mechanisms* are described as processes eliminating effective stress on sediments such as gas generation, clay diagenesis and pressure transfer caused by lateral or vertical fluid flow (Tingay et al, 2013; Tingay et al., 2009; Osborne & Swarbrick, 1997).

Redistribution of pressure is determined by the transfer of pressure (Yardley & Swarbrick, 2000; Swarbrick & Osborne, 1998). As it is stated by Muggerridge et al., 2005; Luo et al., 2003; Grauls & Baleix, 1994; and Luo, 2004; *the transfer overpressure is one of the most common mechanisms that produce high pressure in a permeable formation* (Li et al., 2019).

Overall, there are many factors affecting mudstone compaction such as lithology, mineral composition, faults and conformities. These factors can also be grouped as main trigger mechanisms; (1) *lithology of shales* determine the maximum compaction ratio the formation can bare, (2) *mineral composition* stands out effecting the porosity and water content, while (3) *faults and unconformities* represent the structural components of a geologic setting influencing the overpressure regime. Equilibrium compaction causes overpressure and the overpressure of mudstones gradually increase with depth and approach at hydrostatic pressure in the uplift (Li et al., 2019) (Figure 41).

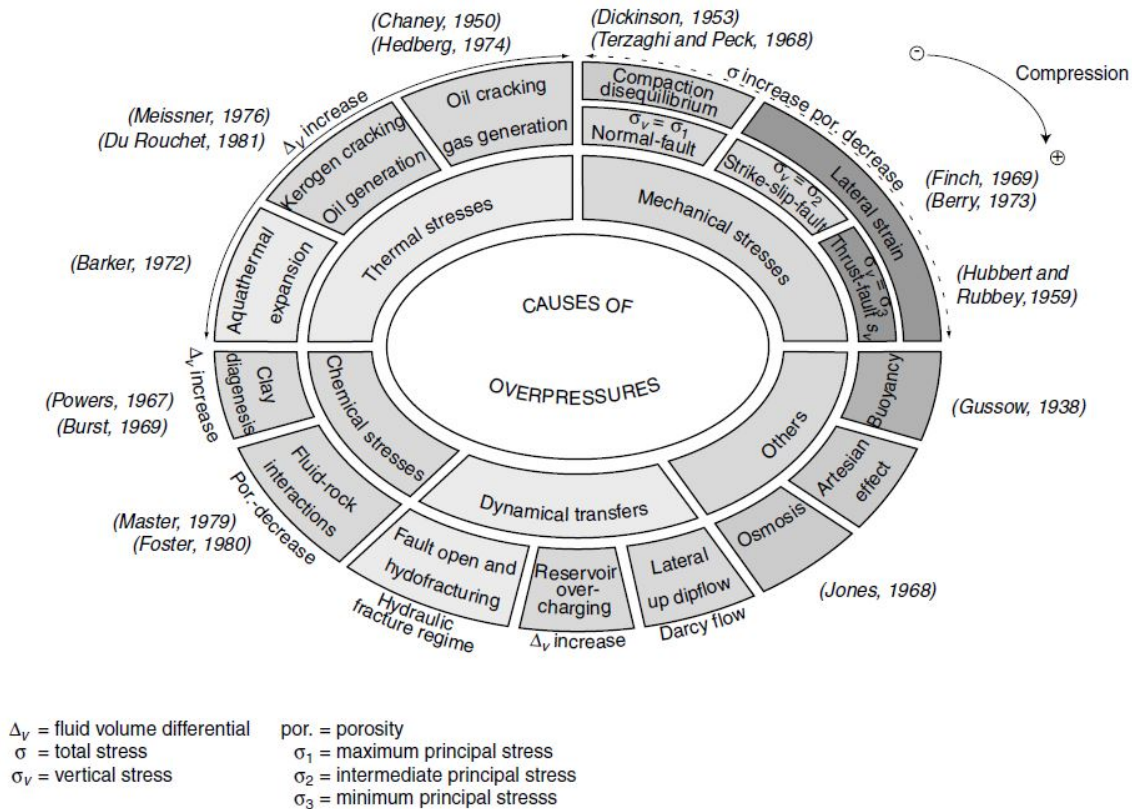


Figure 41: Main overpressure causal mechanisms (Grauls, 1997) (image retrieved from Grauls, 1999).

iv. Effect of Overpressure on Seismic Imaging

From a seismic imaging point of view, overpressured shales with bedded strata are observed with chaotic seismic facies (Al-Ghamdi & Watkins, 1996). Moreover, the studies of Morley and Guerin, 1996, suggested that the seismic facies of overpressured shales in Niger Delta converts into a chaotic/mobile shale signature below the peak oil generation depth, which corresponds to 4-6 km in the region. Increased pore fluid overpressure with gas generation (Barker, 1990) leads to overpressured, undercompacted low-density, low-viscosity shale that becomes isostatically unstable and mobile through distributed strain (Rensbergen & Morley, 2000). The study of Rensbergen and Morley, 2000 and Van Rensbergen et al., 1999, suggest that the transition from stratified seismic signature into chaotic facies might occur *by increase of overpressure due to fracturing and dimming effects* even though overpressure does not directly trigger a deformable shale mass motion. However, the laboratory experiments conducted by Bolton & Maltman (1998), showed that the ductile deformation of shale occurs only with overpressure below lithostatic stress levels, while the processes such as brittle deformation, fracturing and fluid expulsion increase the overpressure above lithostatic stress levels (e.g. in Morley et al., 1998; Van Rensbergen et al., 1999; for onshore/offshore Brunei; shale diapirism associated with hydrocarbon-generated overpressuring occurs through upward flow of low-viscosity shale along shale dykes and results in mud volcanism at the sea floor) and mobilization of shales take place at some considerable depth - several kilometers- when overburden loading of undercompacted shale leads to overpressured conditions of the pore fluids (Rensbergen & Morley, 2000).

B. *Internal Forces: Permeability-Related Constraints Induced by Overpressure*

As explained in the previous section, the deformation mechanisms for shale can be grouped under four distinctive aspects (sometimes cross-influencing); internal forces, external forces, diagenesis and maturation. The *Internal Forces* triggering shale deformation can also be defined as *Permeability-Related Constraints*. Permeability is the ability of a porous rock and/or unconsolidated material to permit fluid content pass through it. Porosity, internal rock structure (e.g. shape and geometry of the pore medium) and the connectivity of porous media are the properties that effect permeability of a rock formation.

Since the compaction rate of highly permeable sand is negligible compared to the low permeability ratio of shale; overpressure (i), sedimentation rate (ii), and compaction disequilibrium (iii) become mostly a matter of shale-permeability. Diagenesis and maturation are not directly related to permeability (unless the size and geometrical properties of pore space are changed) due to the fact that permeability is not affected by the generation of fluids. However, the change in mineralogical content, and transformation of kerogen into bitumens and oil (or gas) affect permeability. In confined environments, where fluids are expelled into a system that is already highly pressurized, the porosity decrease noticeably during diagenesis and maturation while the overpressure increases.

For this reason, it is important to differentiate the permeability-related constraints of an existing medium from the diagenesis and maturation of a modified medium, which can be introduced into the system via fluid content or pore size distribution. Permeability, diagenesis and maturation can all be related to the increment of fluid pressure (i.e. overpressure) but in case of permeability, the system stays open/not confined, while diagenesis and maturation take place within a closed or open system. The following sections will aim to further explain these subjects with respect to their roles in shale-prone environment.

i. Sedimentation Rate

Overpressure is built by sedimentation in nature and certain overpressure patterns (e.g. unruptured surface via stress transmittance) are observed in classic sedimentary basins at times without any major apparent gliding, but with building of clastics and dykes (e.g. forceful fluid expulsion mechanisms) in the system instead as a way of overpressure release. As a consequence of this forceful fluid expulsion mechanism, growth faults can be emerged/initiated. The study of Kim et al., 2018 quantifies lithology-based compaction trends as an attainable range concept, based on compilation plots of field-based compaction trends of sandstone, shale and carbonate arranged by Giles (1997) (Figure 42).

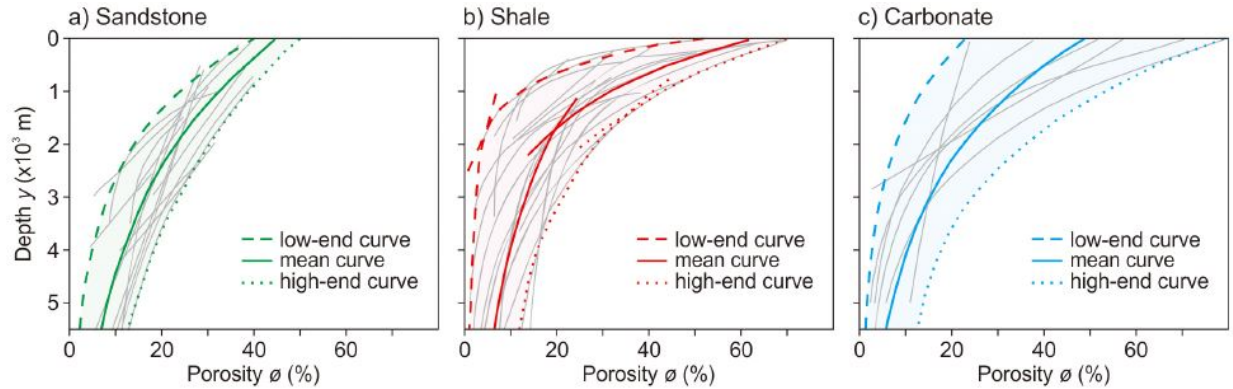


Figure 42: Compilation plots of published compaction trends (gray lines) of a) sandstone, b) shale, c) carbonate (Giles, 1997). The compaction trend range of each lithology is defined by three sets of exponential curves; low-end curve (dashed line), mean curve (solid line) and high-end curve (dotted line) (image retrieved from Kim et al., 2018).

As the sedimentation accelerates, pore fluids get trapped within sediments and inability to escape the medium in a timely manner leads to pressure building, hence the overpressure accumulation. Increment of pressure triggers forceful fluid expulsion via growth fault initiation in the system leading to later gravity-driven linked structures. In places, where sufficient pore pressure is not present, the surface stays unruptured and the detachment of upper layer contact relays the overpressure upwards as a way of stress transmittance (Choudri et al., 2010).

As it is further pointed out by Choudri et al., 2010; (i) the shale-prone settings with overpressure promote gravity-driven growth faulting, (ii) diapiric shale bulges and (iii) cohesionless interfaces in order to transmit the tectonic stress (iii) (Figure 43). Ongoing sediment input steepens the shelf slope up to a point where the angle of friction exceeds, after which the gravity gliding takes place and continues as long as the overpressure sustain the frictionless interface along the detachment.

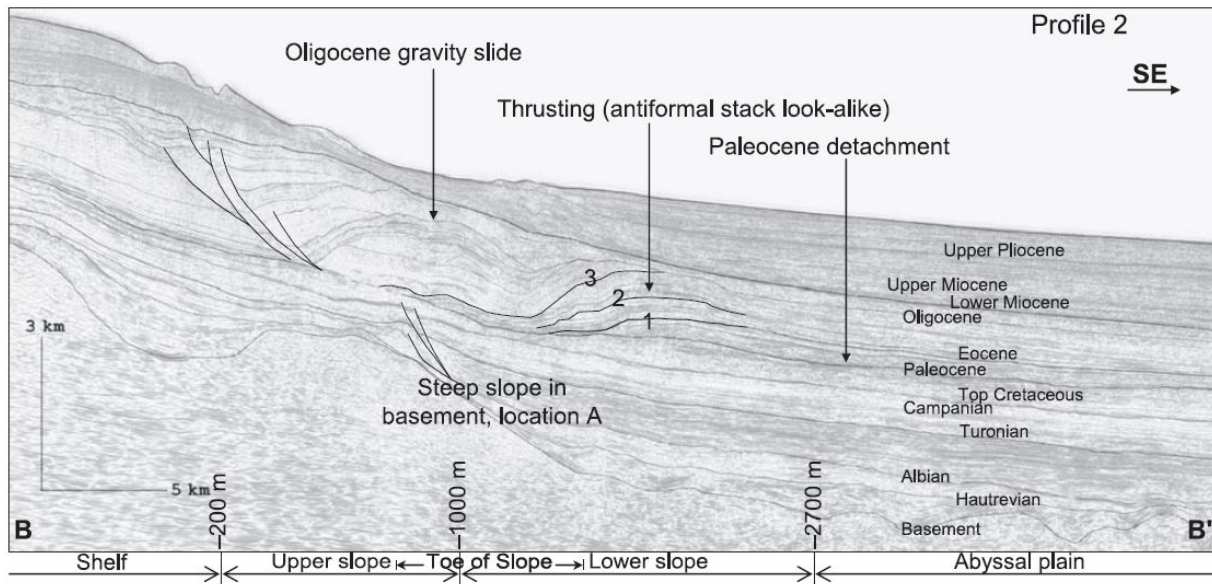


Figure 43: Depth profile showing a not so typical gravity fold and thrust structure from the Krishna-Godavari basin; a huge amount of extension along the Oligocene–early Miocene growth fault is being accommodated by thrusting along a Paleocene detachment. The detachment is moderately overpressured and has a very steep slope, allowing the development of thrusts on the basinward side. Steepening of the detachment and location of the thrusts are also correlated to the abrupt deepening of the basin beyond the basement high at location A (image retrieved from Choudri et al., 2010).

ii. Disequilibrium of Compaction

Moderate sediment rates allow pore fluids being expelled from sedimentary deposits under normal circumstances with a normal compaction trend and compaction of sediments reduces porosity and increases density (Bjørlykke et al. 2009) (see Figure 44 for shale compaction curve comparisons for selected geologic settings [Athy's Curve: Athy's (1930a) widely used exponential relation showed decrease of porosity from 0.5 to 0.05 pu (*porosity unit*: pu), from surface up to 2.3 km depth. The normally compacted shales show concave downward patterns (e.g., Weller 1959; Perrier and Quiblier 1974; Rieke and Chilingarian 1974; Magara 1980). Other curves of shales with surface porosity ranging 0.70–0.80 pu indicates different compaction histories]) (Das & Mukherjee, 2020).

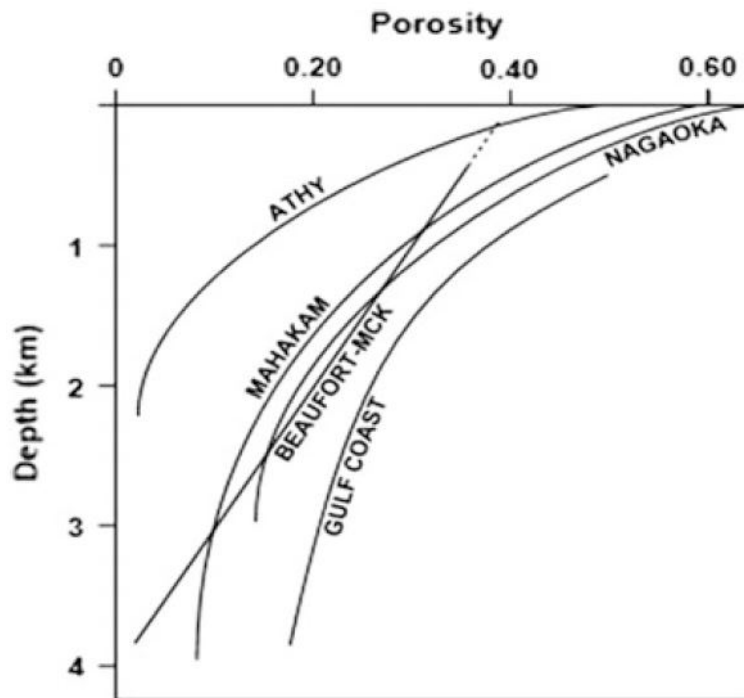


Figure 44: Comparison of normal depth profile curve. Athy's original curve, shale compaction profile curve from Nagaoka basin, Gulf coast, and Beaufort Mackenzie delta. Porosity data derived from density log (Burrus 1998) (image retrieved from Das & Mukherjee, 2020).

Sediments get compacted with burial, which decrease porosity and increase effective stress within the system. Overpressure and undercompaction are typical properties observed in shale-prone settings with thick deposition. When clay-rich sediments are dumped into the system quickly (in terms of rapid burial), pore fluids do not have enough time expelling out of this low-permeability overburden to stay in hydrostatic equilibrium, which causes overpressure in the system (Li et al., 2019). Had the pore pressure ratio stay at hydrostatic level, the sediments maintain greater porosity than its original capacity, which is known as the disequilibrium compaction creating abnormal pressure regimes in sedimentary basins (Luo & Vasseur, 1992; Osborne & Swarbrick, 1997).

The compaction processes of various sediment layers are shown on the schematic diagram of Kim et al., 2018 (Figure 45). As it is reported on the same study; *porosity loss during burial is affected mainly by three sets of interrelated processes; mechanical compaction, physicochemical compaction and cementation* (Giles, 1997; Bogg, 2012; Allen and Allen, 2013).

1. *Mechanical compaction* driven by loading of overlying sediments is mainly by grain sliding, mechanical rearrangement and grain crushing, which is dependent on burial depth and vertical effective stress.
2. *Physicochemical compaction* is controlled by processes such as pressure solution, which is particularly important in carbonates due to their high chemical susceptibility.
3. *Cementation*, which involves the filling of pore space by chemical precipitation, is related to temperature and fluid flow rather than to loading (Giles, 1997; Croizé et al., 2010; Bjørlykke, 2014).

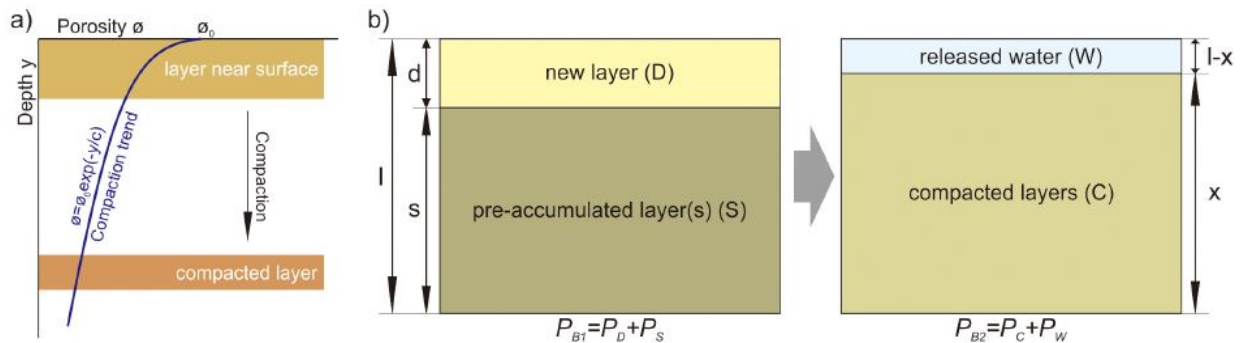


Figure 45: a) Schematic diagram showing compaction process of a sedimentary layer with exponential compaction trend (porosity-depth relation) and equation (revised from Lee et al., 2019). b) Concept of the isostatic balance ($P_{B1}=P_{B2}$) between the basal pressure (P_{B1}) of the new layer (P_D) and pre-accumulated layer(s) (P_S) and the basal pressure (P_{B2}) of the compacted layers (P_C) and released water (P_W). d , s , l and x : thicknesses of new layer, pre-accumulated layer(s), accumulated layers and compacted layers (image retrieved from Kim et al., 2018).

In these environments, overpressure is primarily maintained by compaction disequilibrium when the pore fluids cannot escape the system fast enough for the sediments to compact normally, hence as a consequence, they get compacted in an unbalanced way (Rensbergen & Morley, 2000). Such overpressure mechanisms are favored by; (i) relatively impermeable fast sedimentation rates, (ii) compressive stress regimes by layer-parallel shortening, and (iii) tectonic overloading (Deville, 2009). However, compaction disequilibrium is not a permanently-imposed aspect as it dissipates over time and may rejuvenate from secondary causes such as pore space reduction with tectonic compression or fluid volume increase with diagenesis or maturation (see review by Osborne & Swarbrick, 1997) (Rensbergen & Morley, 2000).

During compaction, vertical effective stress decreases from increasing pore pressure. However, as it is stated by Li et al., 2019; since the overpressures generated by unloading process follow a porosity-vertical effective stress path away from the loading curve (Ruth et al., 2004; Bowers, 2002; Bowers, 1995) (Figure 44), compaction remains mostly as an irreversible process, and unloading mechanism is only associated with a small change in porosity because of the slight elastic contraction of sediment grains. When the equilibrium between the overburden and decreasing pore fluid volume is preserved with hydrostatic pore pressure, normal sediment compaction takes place under slow burial-rate. Controlling factors for disequilibrium compaction can be listed as; rapid and continuous burial rate (i), thick clay content (ii), and low permeability (iii) (Audet & McConnell, 1992; Luo & Vasseur, 1995).

However, in cases, where the overpressure is generated by 'disequilibrium' in compaction, sediment deposits end up with drastically high porosity rates as the compaction gets delayed. As a result; sediment pore pressure increases, while the effective stress stays constant with burial and the compaction disequilibrium gets identified with the lithostatic stress (Li et al., 2019). Regarding this aspect; on a porosity vs vertical effective stress graph, sediments gone through disequilibrium compaction stay on the loading curve (i) (Ruth et al., 2004; Bowers, 2002; Bowers, 1995), while the sediments primarily compacted

under normal hydrostatic pressure and then became overpressured from fluid expansion or vertical transfer go along with an unloading curve (ii) (Li et al., 2019) (Figure 46).

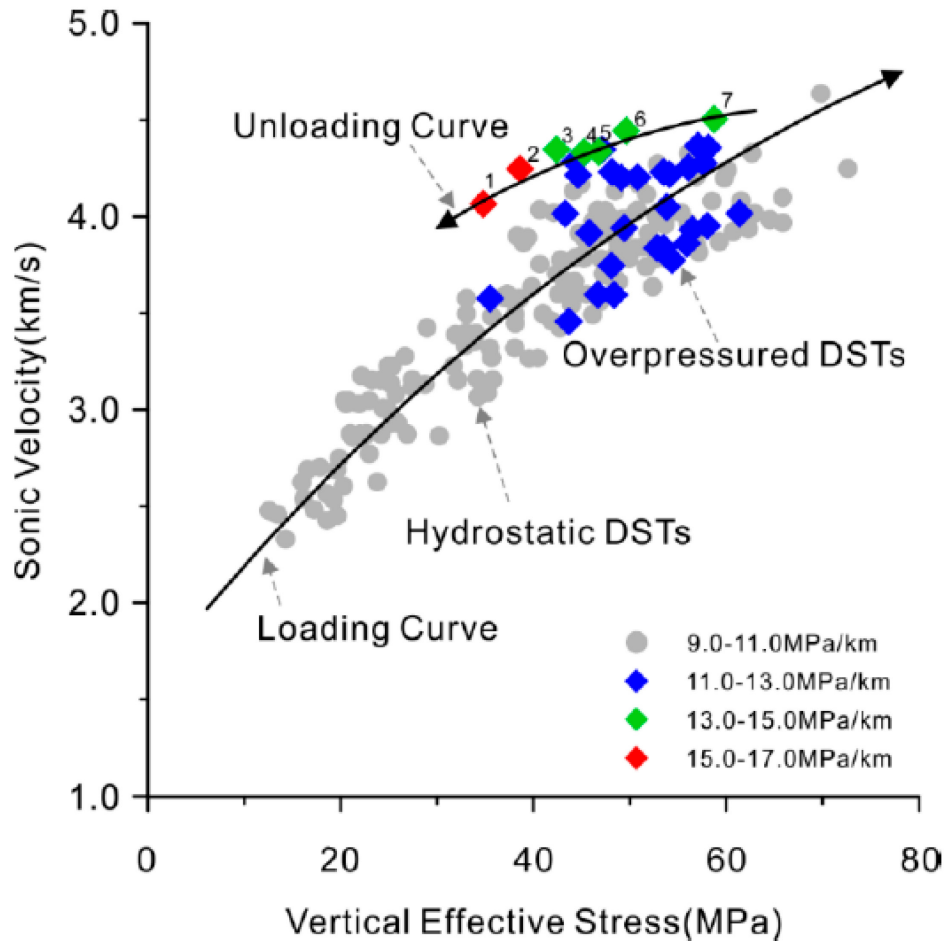


Figure 46: Acoustic velocity–vertical effective stress crossplots for the Linnan Sag. The points are on or near the loading curve, indicating normal compaction, or disequilibrium compaction (blue points), whereas the overpressured data lie on an unloading curve, suggesting that the overpressure is generated by fluid expansion or transfer processes (green and red points). DST: Drilling Stem Test (image retrieved from Li et al., 2019).

As it is stated by Grauls, (1999) and Choudry et al., (2010); compaction disequilibrium is favored as the mechanism to explain overpressure in a number of basins, including the Gulf Coast (Dickinson, 1953), Caspian Sea (Bredehoeft et al., 1988) and the North Sea (Mann and Mackenzie, 1990; Audet and McConnell, 1992) (Osborne and Swarbrick, 1997, p. 1025), Niger, Mississippi, Nile and Mahakam Deltas, or in offshore passive margins (West African, North and South American margins) with fast sedimentation, overpressure takes place within low permeable shale units leading to disequilibrium compaction within the system.

Overall, each lithology (e.g. sand, shale and carbonate) has unique characteristics in compaction trend that are represented by different variation types and reduction rates of porosity and layer thickness with increasing depth. Such characteristics are driven by lithological features such as *mineral composition*, *chemical reaction*, *sorting* and *grain shape*, which influence on sediment thickness reduction, subsidence and thermal effect during basin evolution (Kim et al., 2018) (Figure 47).

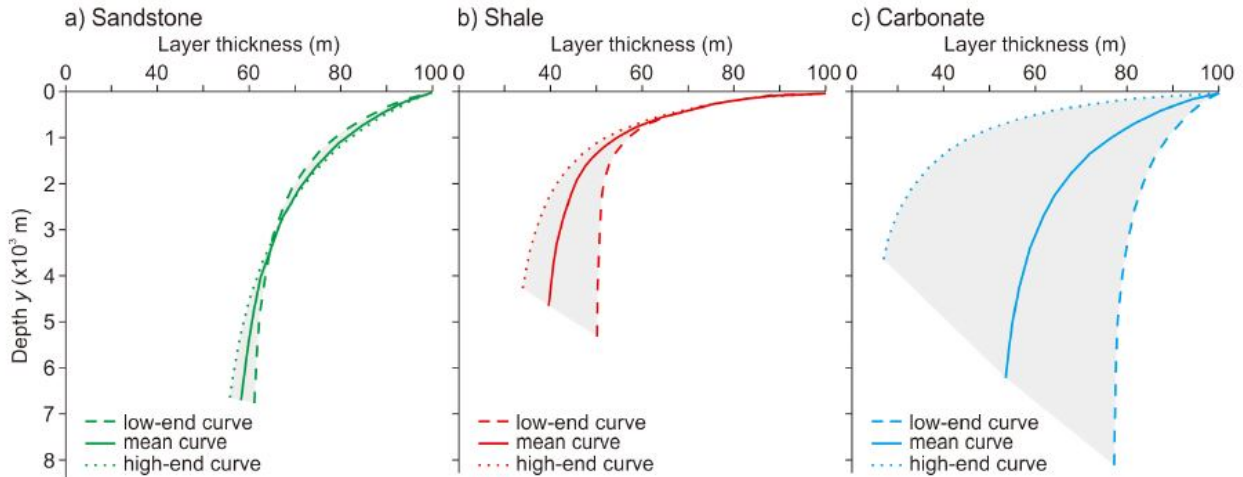


Figure 47: Plots of layer thickness variation with depth; a) sandstone, b) shale, c) carbonate. Total 100 layers are accumulate and compacted following the exponential curves from the compaction trend range of each lithology. The layer thickness range with depth is presented using applied curves; low-end curve (dashed line), mean curve (solid line) and high-end curve (dotted line) (image retrieved from Kim et al., 2018).

iii. Diagenesis

Clay diagenesis is controlled by temperature (T), pressure (P), and water content (H₂O). As it is summarized by Vidal (2014), clay diagenesis increases with decreasing pressure and decreases with increasing water content (as the pressure builds up with increased water content during burial) due to water activity in the chemical equilibrium reaction of clays (Total E&P Lectures 2016, Gravity Gliding/Spreading: Mechanics and Structures). When the mechanism is pertained with decreasing pressure, catastrophic clay mobilization in terms of distributed plastic strain is likely to take place, because the increased fluid pressure in shale formations promotes failure as the effective stresses decrease with pore pressure (Terzaghi's Law, see Deville, 2011). The (i) change in mineral content, (ii) porosity, and (iii) generation of fluids play a significant role in diagenesis of shales and the diagenesis itself is controlled by:

- i. Pressure – Temperature Conditions
- ii. Initial Clay Content
- iii. Initial Pore Fluid Composition (amount of water and minerals)

Peltonen et al., 2009; conducted some experiments on *clay mineral diagenesis and quartz cementation* in mudstones in order to understand the effects of smectite to illite (S-I) reaction on rock properties. Their observations suggested that compaction of mudstones can be categorized based on their depth and temperature; in shallow depths and temperatures (<2.0 km/70 °C) only mechanical compaction takes place without a change in the physical properties of mudstones (similar to what has been measured by experimental compaction of mudstones), while the log derived velocities and densities get higher (compared to what has been measured by experimental compaction of mudstones) at greater depths due to chemical compaction. Progressive alteration of S-I takes place below 2 km depth / above 70 °C temperature values and leads to significant amount of silica released into solution, which consequently

limits the area of (i) *free surface* and (ii) *pore space* for quartz overgrowth as a result of clay matrix *grain isolation*. Within this specific depth range; chemical analyses (XRF) point out to silica conservation and local precipitation of S-I alteration, accompanied by velocity and density increase suggesting that the S-I reaction leads to a significant change in stiffness of the rock (Peltonen et al., 2009).

The rock framework can be weakened by diagenetic and catagenic changes induced into the system in terms of compaction (e.g. Meissner, 1981; Osborne and Swarbrick, 1997; Swarbrick et al., 2002). The main changes under compaction can be summarized as; (i) solid kerogen hydrocarbon conversion to liquids, (ii) gases and residuals; and (iii) grain-size changes associated with the smectite-to-illite (S-I) and kaolinite-to-illite (K-I) transformations (Morley et al., 2018). Transformation of smectite-to-illite is stated as *one of the key diagenetic effects in smectite-rich mudrocks*, causing release of fine grained quartz that stiffens mudstones to form a pervasive network at burial depths of around 2500 m or 80°–85 °C (Thyberg et al., 2010). When the fluid cannot escape, and the rock cannot compact anymore, then the load partially transfers into the fluids (also called as ‘load transfer’ type of disequilibrium compaction, Swarbrick et al., 2002). This load-transfer process of S-I transition occurs at temperatures starting between 60°–80 °C based on the carbonate phases, and finishes around 110 °C (see reviews of Hower et al., 1976; Buller et al., 2005; Morley et al., 2018).

Dissolution of smectite and re-precipitation as fibrous authigenic illite can be listed as the main permeability-reducing processes subdividing the existing pore space (Nadeau et al., 2002), and leading to the precipitation of micro-quartz (Thyberg and Jahren, 2011). Briefly, Kaolinite transforms into illite via dissolution and precipitation when an extra source of potassium (such as feldspar) is present in the system (Bjørlykke, 1998) at temperatures around 130–140 °C. As a consequence, the *load transfer* can result in fluid pressures that are 1500–3000 psi higher than pressures interpreted from shallow compaction trends (e.g. Lahann and Swarbrick, 2011; Goultly et al., 2013) (Morley et al., 2018).

Following reactions (smectite/illite to illite, kaolinite to illite) taking place at deeper burial depths around ~90° - 150°C result in precipitation of quartz flakes, and ultimately development of sheet-like quartz cement (Thyberg et al., 2010). In other words, as stated by Morley et al., 2018; *the effects of diagenesis, particularly stiffening of the mudrocks by silica precipitation during the transformation of smectite to illite* (Thyberg et al., 2010; Thyberg and Jahren, 2011), *indicates that shallow plastic behavior in unlithified clays (i.e. the conditions for shale diapirs to develop) is likely to cease when buried more than about 4 km, even under low geothermal gradients (2° C, sea floor temperature of 0° C)*. As a result of this transformation, mechanically soft, plastic ‘mobile’ shale are not be expected below depths of around 2000–3000 m (depending upon geothermal gradient) (Morley et al., 2017). Shale detachment weakness is associated with high overpressured fluids (e.g. Hubbert and Ruby, 1959; see review in King & Morley, 2017).

Disequilibrium compaction through mechanical compaction of sediments is thought to be the key reason for overpressure in deltaic settings (e.g. Osborne and Swarbrick, 1997; Tingay et al., 2009). This mechanism ceases porosity loss as impermeability slows down the escape of pore fluids during diagenesis. As a result, the pore fluid pressure increases within the zone of trapped fluids (Morley et al., 2017). However, the study of Bjørlykke and Hoeg (1997) suggests the compaction of mudstones occurring at depths less than 2–3 km to be predominantly chemical, as a consequence, it is thought that in places with chemical compaction domination, *mudrocks should not be expected to display porosities greater than normally pressured rocks* (Bjørlykke, 1998). Following these arguments;

- Day-Stirrat et al. (2010) urges the interpretation of mobile shales below depths of about 2 km to be treated with considerable skepticism (Morley et al., 2017).
- Goultly et al. (2016) challenges some of these ideas by determining the Cretaceous mudstones at Haltenbanken wireline-log and pressure data to be consistent with mechanical compaction continuing along with chemical compaction at least up to temperatures of 130 °C (Morley et al., 2017).

iv. Maturation (Organic Content)

Morley et al. (2018) states that “porosity is enhanced in areas around irregular surfaces of non-clay minerals within the clay matrix (e.g. Keller et al., 2013), and thus the spatial density of these non-clay minerals affects clay mechanics”. During this process, unbound water/fluids such as oil and gas occupy pore spaces and exert a control on rock strength through means of overpressure. The conversion of kerogen to oil and/or gas, and particularly cracking of oil to gas is regarded as the most significant volume expansion mechanism of overpressure occurring in the subsurface besides clay diagenesis (see in the previous section) (e.g. Osborne and Swarbrick, 1997; Tingay et al., 2013).

Capability of source rocks generating oil or gas when exposed to appropriate pressures (P) and temperatures (T) can be explained in its own maturation process (Al Areeq et al., 2018). When a source rock begins to mature by producing organic content, it generates hydrocarbons (HCs). The maturity of a source rocks reflect the ambient pressure and temperature as well as the duration of conditions favorable for any kind of hydrocarbon generation, which depends on steps dictated by (i) temperature increase, (ii) lateral transfer of fluids, (iii) oil-to-gas secondary cracking, and (iv) P/T conditions.

As it is stated by Pinna et al., 2011; *Kerogen–oil conversion starts at a given depth in a volume whose permeability is sufficiently low so that the increase in pressure due to oil generation greatly exceeds the dissipation of pressure by flow.*

Source rock evaluation of hydrocarbon studies depends on the determination of organic matter content, which is usually expressed as total organic carbon (TOC) and the hydrocarbon potentiality depends on the type and quantity of organic matter (kerogen) preserved in the petroleum source rock, thermal maturity and finally the generation potential of kerogen (Al Areeq et al., 2018). Kerogen to oil conversion generates porosity in the kerogen and newly formed pore fluids (oils).

Oil to gas conversion is known to be the main diagenesis mechanism for maintaining overpressure conditions (Osborne & Swarbrick, 1998), through an increase of the volume of pore fluid up to 50-80 times (Barker, 1990). The depth of maximum oil generation or the start of the gas window (e.g. Khalivov & Kerimov 1983; Sandal 1996; Morley & Guerin 1996; Paterson 1997) at 4-5 km of burial coincides with the top of the main overpressured shale mass (Morley, 2003). As it is stated by Li et al., 2019; *hydrocarbon generation may induce fluid expansion in mudstones and result in increased pressure. The magnitude of overpressure produced by kerogen maturation depends upon the kerogen type, abundance of organic matter, and thermal maturity* (Osborne & Swarbrick, 1997; Swarbrick et al., 2002).

Generally, overpressures generated below 3 km of burial depth play a key role in secondary hydrocarbon migration and transfer of fluid dynamics, which can be associated with the conventional Darcy’s Law noted at large-scale tilted reservoir units of Gullfaks Field in offshore Norway (Grauls, 1999). Additionally, as it

is proposed by Morley, 1992; Morley and Guerin, 1996; Cobbold et al., 2013; Zanella et al., 2014; hydrocarbon maturation contributes greatly to overpressure generation in shale detachments and thrusts at depths around 3-6 km (Morley et al., 2018) encompassing the oil and gas peak. Cobbold et al., 2009, pointed out to elevated pore pressure ratios observed at Niger Delta thrust belt and suggested the thrust front tracking the onset of hydrocarbon maturation window as a way of maturation dynamics mandating the location and advance of the detachment (Morley et al., 2018).

The *lateral transfer of pressure gradient* related to overpressure was explained by Traugott (1996) and Yardley (1999). Grauls (1999) emphasized the fact that this gradient reaches at its maximum at the highest structural closure point of a hydrocarbon column and decreases downward with depth while the overpressure regime stays homogeneous within the same pressure cell. Migration of hydrocarbons and dynamic transfers can be related to the vertical hydraulic flow of the system, which can be enhanced by hydrofracturing and/or open fault zones/discontinuities (Grauls and Cassagnol, 1992; Grauls and Baleix, 1993). During this phase, pressure regimes show a tendency to rise in response to 'overcharging' (Grauls and Baleix, 1993). Following this period, any extra addition on pressure depends on volume of the fluid (i), rate of charge (ii), extension of the reservoir (iii), drainage efficiency (iv), and compressibility of pores and fluids (Grauls, 1999).

C. External Forces Induced with Overpressure

External forces depict the exterior factors that have an effect on shale tectonism driving forces. These factors can be listed under three categories; basin geometry, tectonism and differential subsidence. The following sections will be detailing these aspects in terms of their effect and influence on shale mobility.

i. Basin Geometry

Basin geometry defines the architectural setting of a basin environment from geological point of view. It depicts the elements of basin in terms of structure, basement physiology and morphology. In shale-prone basin settings, where a thick pile of shale deposition settles within a basinal form, understanding the sediment dispersal regime and its time-variable accumulation becomes important to figure out the geometrical effects. As it is pointed out by Choudri et al., 2010; sediment dispersal and accumulation through time appear to be the indicators of linkage between the thin-skinned tectonic style and its localization in space and time.

Geometry of a basin (e.g. slope angle) has a great influence on gravitational instability triggered by a change of dynamics in a geologic setting. Gravity-driven linked systems emerge from differential sediment loading that takes place at different time and parts of the basin influencing the tectonic episodes of the region. Their occurrence is triggered by the basement architecture (i) and its control on the basin morphology (ii). The sequential events leading to gravity-driven linked systems under the influence of basin geometry can be summarized as;

- Rift margin development (extensional domain)
- Basin evolution within a marginal setting

- Gravitational cell formation (*Gravity-Driven Linked Systems* reviewed in Choudri et al., 2010):
 - Detachment slope initiates the *gravity slides* as it steepens the shelf break
 - Continuous sediment input contributes to the increment of the shelf slope
 - Upon exceeding the angle of friction, *gravity gliding* commences and continues as long as the frictionless state of detachment is preserved by overpressure
- Over-steepening of the shelf slope can also be contributed by; uplifts at basin-margin or local scale (e.g. subsidence)
- Eventually, localization of shale-bulges and/or toe thrusts seem to correlate with *a break in gradient at the upper lower slope junction or a sudden change caused by change in basement architecture*
- As a consequence of possible *combined result of overpressure and basement structures*, mobilized shale features/structures develop at locations of least gradient

ii. Tectonism

Tectonism, meaning 'pertaining to building' is defined as the study of 'rock deformation' and 'forces leading to deformation' of Earth. Various tectonic activities, such as extension, compression and gravitational gliding, trigger certain conditions within a shale-prone system and lead to a change in shale stability and hence it is categorized as an externally induced driving force for Shale Tectonics.

As mentioned previously, overpressure acts as the main mechanism that trigger internal and external driving forces for shale. In terms of tectonism, several tectonic environments can stimulate overpressure generation leading to shale-related deformation mechanisms. When over-pressured, shale-prone deltas display lateral tectonically-induced stress, dynamic transfer (hydro-fracturing and polygonal fault systems), kerogen cracking, fluid-rock interaction (diagenesis) and clay diagenesis. Since mechanical stress, diagenesis, fluid dynamics and temperature are the components generating over-pressure (Deville, 2011), over-pressured shales in a delta setting may lead to gravity gliding, slumping, growth faulting above the shale detachment, dyke formations (liquefaction), and shale-related features such as mud volcanoes, ridges and mud diapirs. As a result, tectonism observed at such geo-settings amplify shale mobility.

Overpressure can also be increased by changing tectonics as well as loading stress conditions. For example, in a geological setting, where extensional faulting regime gradually changes into a thrust faulting regime, the minimum principal stress value shifts from sub-lithostatic to near-lithostatic. Such a change leads to hydrofracturing, and hence a consequent loss of overpressure, due to higher pore fluid pressure brought by pore fluids prior to hydrofracturation (e.g. Osborne & Swarbrick, 1998), which can be observed on tectonically active margin deltaic settings, but not on passive margins (Morley, 2003).

iii. Differential Subsidence/Loading

Differential subsidence is imposed into a shale-prone system with (i) the arrival of sediments overlying the shale medium/detachment level and rarely via (ii) convectional inner Earth movements (e.g. thermal convections) if the deltaic system is at the scale of a basin. It poses a time and dumped-material

dependent effect on shale deformation as the subsidence takes place when the sediment equilibrium is changed and/or a thermally-relevant event occurs at a given geological setting and time interval.

Vendeville, 2005, proposes a sketchy diagram to describe the two end-member processes that occur spontaneously in response to the deposition of a sediment wedge above a mobile layer made of salt or overpressured shale (Figure 48):

- The image illustrates the steps of salt/overpressured shale mobilization starting from an instantaneous overburden deposition (Figure 48a).
- Following the overburden deposition; overburden subsidence starts to kick in as a result of differentially loaded sediment pile on a seaward-thinning wedge, which makes the thicker and proximal portion of the wedge subside more than the thinner distal portion (Figure 48b).
- As salt/shale withdraws towards distal portion of the wedge beneath the sediment pile, inflation ratio of ductile material depends on the length and thickness of salt/shale being accumulated at the distal front. On the next stage, gravity spreading described by Vendeville, 2005 as; '*a gravity instability that forces the overburden to spread spontaneously seaward above the weak salt layer*' takes place (Figure 48c).

This phenomena can occur along passive margin settings, where the critical taper wedge angle is low (e.g. 1° or less, see Davis & Engelder, 1985) (i) and the critical slope is assisted entirely by sediment deposition without a tectonic trigger/pulse (ii) (Vendeville, 2005). Even though the example of Vendeville, 2005, was mainly applied/relevant to salt-floored deltas, and only suggested to give a generalized not-so-detailed idea about shales with a thick sedimentary cover, it holds an important point suggesting over-pressured shale behavior in deltaic settings.

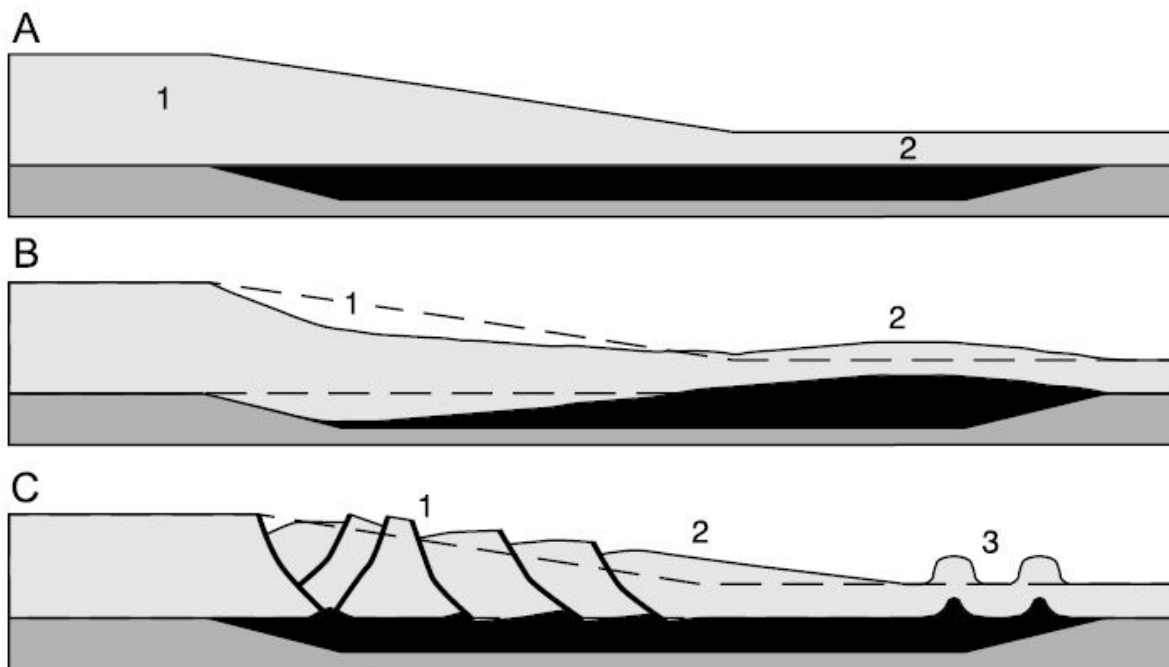


Figure 48: Potential structural responses to the loading of a salt layer (black) by a sediment wedge (gray). (a) Initial stage, assuming instantaneous overburden deposition; (b) differential subsidence of the proximal overburden (1) and inflation of the distal salt (2); (c) gravity spreading of the overburden causing proximal extension (1), mid-slope seaward translation (2), and distal contraction (3). Dashed lines outline the sediment wedge's geometry before deformation (image retrieved from Vendeville, 2005).

IV. Deformation Geometries: Argilokinesis

Argilokinesis (also known as *claykinesis*) is a broadly applied, all-encompassing term used to describe the dynamics of uncompacted mobile clays. (Wood, 2010). Argilokinesis is a relatively less well-established phenomena compared to halo-kinesis of salt tectonism but similar to salt, it aims to depict the deformation geometries resulting from distributed slow-motion behavior of shale that is recorded within the sedimentary cover surrounding the mobilized shale.

A. Review of Shale Formations: Deformed Shale Features

i. Mud Diapirism

As previously mentioned; several dynamic subsurface processes generate overpressure generation at depth, which consequently leads to mobilization of the mud/clay deposits towards the surface via breaching, flowing and/or fracturing. Moreover, as overpressure reduces the strength of associated subsurface layer, sediment remobilization is enabled/observed in shale-prone geological settings such as thick shale-rich sedimentary basins. In these subsurface environments, fluid-migration and remobilization of sediments result in forming various types of geological structures associated with mud deformation geometries (Deville, 2009).

One of those deformation geometries is defined with '*mud diapirism*', which can also be known as '*shale diapirism*'. Salt diapirism is a fairly well-known and fundamentally-established phenomena we know today (see the review on Chapter 1, Section IV). Even if some comparisons have been made previously, due to lack of well-imaged and coherent seismic datasets collected from shale-prone environments, mud/shale diapirism have not been as well-understood and/or clearly explained as salt diapirism. However, recent advancements on seismic imaging technology and reprocessed/reinterpreted datasets have brought this topic back onto the scientific stage and researchers reevaluated the topic under this newly acquired perspective. Soto et al. (2010) focused on the evolution of mobile shale in the northern margin of the western Alboran Basin during the Miocene and concluded that the deformation styles depict a consistent tectonic history driven by lateral migration and rise of the overpressured shale is controlled by basement slope and a laterally varying thickness of the overburden and the source layer. In an interpreted and uninterpreted seismic data example (Figure 49), they pointed out to the following facts;

i. *Sedimentary sequences appear congruently folded in synforms between shale-cored anticlines and walls, with local unconformities along the flanks of the shale diapir, similar to the structures known as halokinetic sequences in salt basins (e.g., Giles and Lawton, 2002; Rowan et al., 2003).*

ii. *The relationships between the Miocene overburden and diapirs have two extreme geometries:*

(a) sedimentary sequences are slightly deformed and uplifted toward diapir flanks, which show discordant piercing shapes.

(b) they are progressively and congruently deformed and folded above shale-cored anticlines.

- iii. *These geometries reflect a complex history of diapirism, with a simultaneous active and passive rise in nearby shale diapirs (Vendeville and Jackson, 1992a, b).*
- iv. *They also reflect contrasting rates between diapir rise and sediment aggradation, which vary significantly between adjacent and nearby minibasins (e.g., Jackson et al., 1994; Talbot, 1995; Giles and Lawton, 2002).*
- v. *Sedimentary sequences in discordant diapir flanks show examples of thickening wedges. This geometry is consistent with growth faulting, which is linked to diapir rise (reactive diapirism; Vendeville and Jackson, 1992a; Jackson and Vendeville, 1994).*

In the same research study, Soto et al., 2010, detailed the most important contrasts between salt and shale-cored diapirs as;

1. *In seismic reflection imaging, shale diapirs show poorly reflective fabrics with chaotic reflections, and the surrounding beds generally lose reflectivity toward diapir borders, defining a diffuse zone with dimmed reflections*
2. *Shale diapirs show complex geometries, with abundant pipe and finger-like diapirs, and whether allochthonous sheets can develop as in salt basins is a point of debate*
3. *Differences in geometry, structural style, and diapir evolution result from the different mechanisms causing flow in the two materials.*
4. *The physical properties of shale and salt are considerably different in many attributes (e.g. Weijermars et al., 1993; Jackson and Vendeville, 1994).*
5. *Salt shows moderately constant physical properties, whereas shale density, viscosity, and reflectivity depend mostly on clay mineralogy, fluid content, and temperature-depth conditions (e.g., Chapman, 1974; Bird, 1984; Kopf and Behrmann, 2000; Kopf et al., 2005; Mondol et al., 2007, 2008).*
6. *Another important difference between both materials is that fluid content in shale (and consequently shale properties) can change during basin evolution and over the duration of active diapirism (e.g., Tingay et al., 2007; Morley et al., 2008).*
7. *Overpressured shale may induce liquefaction and fluid migration and injection in the overburden during diapirism (e.g., Van Rensbergen et al., 1999; Maltman and Brown, 2003; Morley, 2003).*

Given this description and additional examples from various shale-prone parts of the world (Alboran Sea (e.g. Soto et al., 2010), Niger Delta (e.g., Cohen and McClay, 1996; Morley and Guerin, 1996; Graue, 2000; Hopper et al., 2002), the Gulf of Mexico (e.g., Bruce, 1973; Ewing, 1986), the Baram Delta in northwestern Borneo (e.g., Van Rensbergen et al., 1999; Morley et al., 2008), eastern Indonesia (e.g., Barber et al., 1986; McClay et al., 2000), southern Australia (Totterdell and Krassay, 2003), the Panama thrust belt (Breen et al., 1988), and the offshore Trinidad and Barbados accretionary wedge (e.g., Brown and Westbrook, 1988; Wood, 2000), mud/shale diapirism, as they are referred to in the literature is still a matter of debate under seismic data and outcrop examples with their lack of coherence but understanding up to a certain degree compared to salt diapirs.

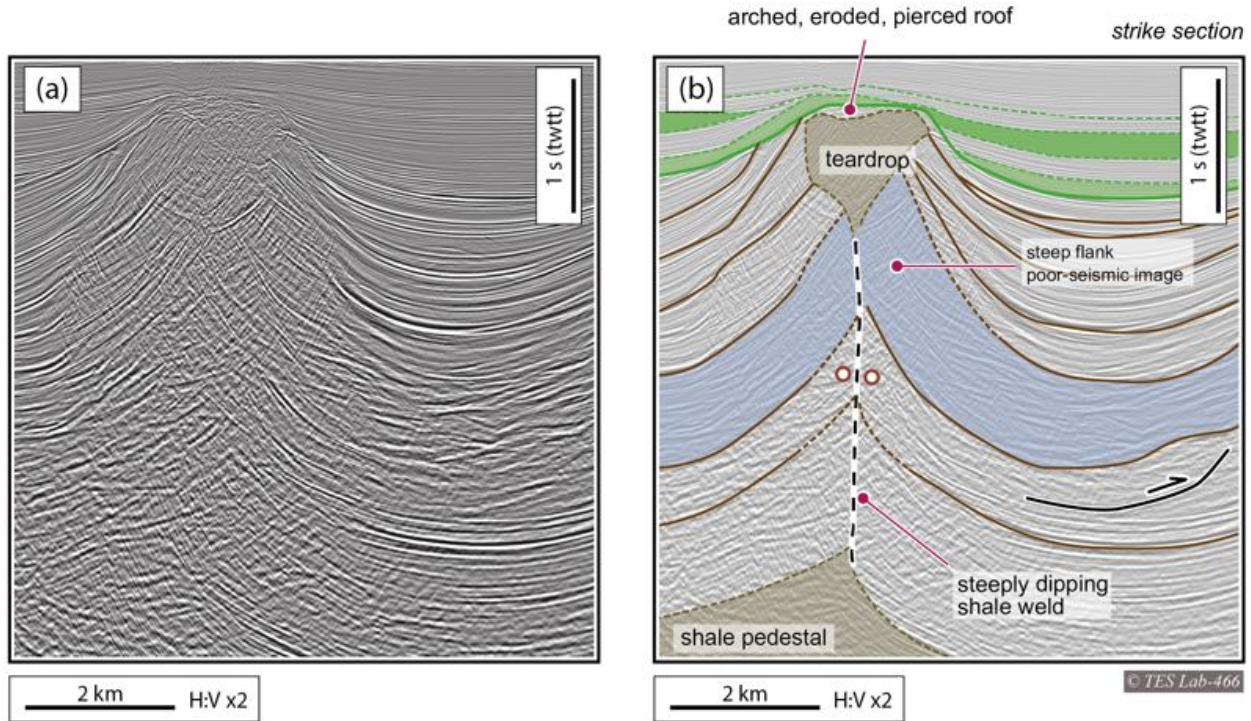


Figure 49: Mud Diapir Example; Squeezed Teardrop Diapir with Subvertical Weld (image retrieved from AGL Presentation: Shale Tectonics in the Alboran Sea Revisited from a Salt-Tectonics Perspective, after Soto et al., 2010).

ii. Allochthonous Shale Bodies

Shale-related mobilization features adapts the same terminology with salt in literature. As previously explained; even though the deformation mechanisms for shale differs from salt in terms of fluidization (e.g. mud volcanoes). Therefore, although they are not defined in seismic examples and nature as precise as the salt structures, certain shapes of shale deformation depicts well-established salt geometries such as canopies.

By definition, a (salt) canopy is composed of multiple (salt) sheets and/or diapiric bulbs. Such features are triggered by the thick sediment load overlying the (salt) ductile medium. When this ductile medium is defined by shale in shale-prone environments, similar features originate from autochthonous (mother) ductile medium in certain cases, where fluidization of shales (mud volcanoes) does not take place and the system is driven under a strain-related deformation pattern (e.g. plasticity). Following this recipe, a 'shale canopy' can be described as a form of shale mass/allochthonous body fed by feeders (combined of multiple shale sheets in Figure 50) emplaced at stratigraphic levels above its source layer (i.e. mother shale), which can be detached or attached via a feeder to its origin; the initially deposited thick shale interval (i.e. stratigraphically older shale strata).

Due to shale deposits' incoherent signature on seismic data, current seismic examples for shale canopies are not as well-defined as salt canopies. However, some examples stand out such as Northern Borneo, NW Sabah region, where we see clearer seismic images depicting canopy-like shale features. In this part of Borneo; the primarily interpreted thrust sheet domain by Hinz et al. (1989) is a common feature found in Sabah Region literature. However, as it is reported by Clark (SeaPex 2017 Convention, Sapura Energy presentation), new seismic datasets led to reinterpretation of the distal thrust zone and revealed this section as *a thickened, inflated mobile shales similar to that documented in the distal Niger Delta and similar to the distal part of the Angola salt province, where the thin sedimentary cover overlying the mobile layer is compressed and responds by forming short wavelength folds* (Figure 50).

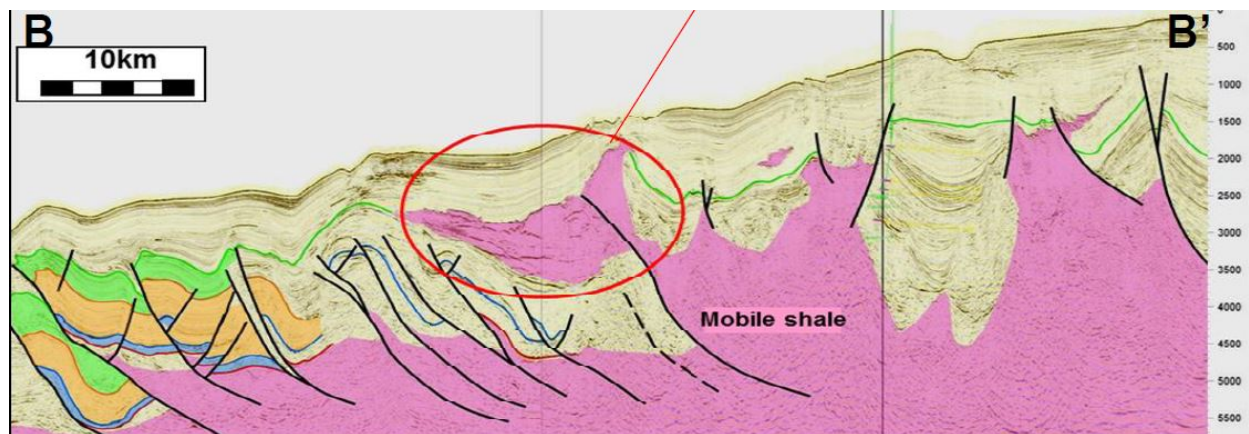


Figure 50: Interpreted regional seismic section along NW Borneo, showing evidence for existence of thick, extensive mobile shales in the form of extrusive shale bodies (image retrieved from J. Clark presentation, SeaPex 2017).

B. Review of Shale-Related Sediment Recordings

i. Shale-Driven Minibasins

Similar to salt canopy structures explained in the Salt Tectonics Section, in terms of shale-driven geologic settings (James Clark, SeaPex 2017 Convention, Sapura Energy presentation);

- Minibasins are observed in regions with thick mobile shale detachments, where differential loading occurs before a thick pre-kinematic cover is developed (e.g. NW Sabah Region, Northern Borneo; Makran Region, Iran; Alboran Sea)
- These features are generally initiated by extension but once a differential load is established on the mobile shale layer, they may evolve without further tectonic enhancement.

Following the conducted seismic study and structural evaluation, the minibasin phenomena of NW Sabah region in Northern Borneo was summarized with illustrative examples under four iterative stages (Figure 51); During minibasin formation;

- Overpressure starts to build up as early progradation and rapid burial of distal shales take place in deepwater setting
- Continuous arrival of deltaic sediments lead to gravity-driven shelf collapse into deepwater
- As the collapse of shelf progresses, mobile shale triggered by differential load drive minibasin subsidence and diapiric activity around its edges
- Once the minibasin has 'hit bottom', if there is continued extension, the minibasin no longer subsides whilst the surrounding shale accommodates the extension by thinning and collapse

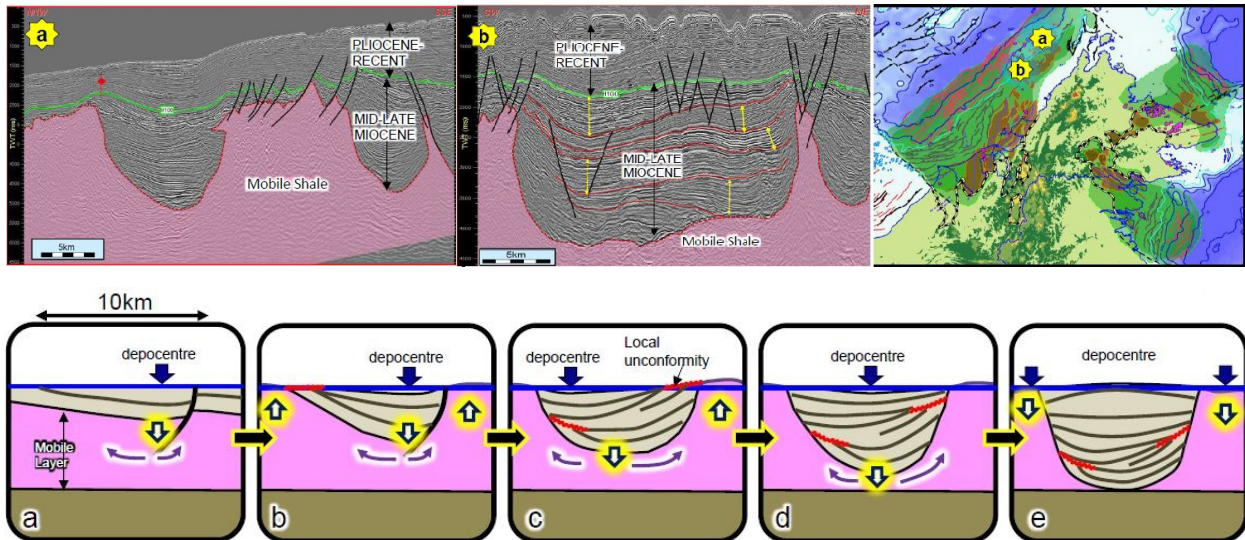


Figure 51: Interpreted seismic example of two shale minibasins from NW Sabah Region, Northern Borneo, accompanied by evolutionary sketch diagram depicting minibasin evolution (a through e) illustrating how differential loading drives shale movement and in turn creates the variable sequences of minibasin fill (note the shifting locus of deposition) and intra-minibasin unconformities (image retrieved from James Clark, Sapura Energy presentation, SeaPex 2017 Convention).

V. Remarks: Literature Wrap-Up of Shale Tectonics

Previous chapter aimed to give a literature review on Shale Tectonics with an emphasis on the important aspects such as; i. Historical Review, ii. Deformation Mechanisms, iii. Driving Forces and iv. Deformation Geometries. Following the studies of numerous researchers and advancements on seismic imaging technology, we have a better idea on Shale Tectonism and its functionality today. As an overall summary;

The ductility of shale rocks are determined by: Confinement Pressure, Temperature, Water Content, Rate of Loading and Amount of Sedimentation.

There are two defined deformation mechanisms for shale, which are namely; strain (e.g. plasticity) and fluidization (e.g. mud volcanism).

- **Strain (solid-state distributed deformation)** defines the distributed slow motion (plastic) behavior of shales resembling the flow of a viscous material.

- **Fluidization** depicts the fluidized state of shales represented with mud volcanoes in nature under an overpressured setting.

The driving forces for shale tectonism can be explained under three main aspects; (i) overpressure, (ii) internal forces induced by overpressure, and (iii) external forces induced by over pressure.

- **Geologic overpressure** in stratigraphic layers is caused by the inability of connate pore fluids to escape as the surrounding mineral matrix compacts under the lithostatic pressure caused by overlying layers. Shale-prone intervals with low permeability becomes overpressured with the weight of overburden or vertical stress.
 - Pore fluid pressure influences crustal strength and may exceed hydrostatic conditions at depth (e.g. Terzaghi, 1943, Hubbert and Rubey, 1959; see review in Osborne and Swarbrick, 1997) (Morley et al., 2018).
- **Inherent Controlling Factors Influencing Overpressure:** These factors have an effect on shale tectonism driving forces. Such components can be listed under four categories; sedimentation rate, disequilibrium compaction, diagenesis and maturation. Pressure is the most important factor at the start of burial leading to early stage mechanical compaction and porosity loss. Mechanical compaction can delay fluid escape from the deeper section, and the consequent onset of disequilibrium compaction-type overpressures (Osborne and Swarbrick, 1997) in rapidly buried, fine-grained sediment environments (Morley et al., 2018).
 - **Sedimentation Rate:** With high sediment rates pore fluids get trapped within sediments and inability to escape the medium in a timely manner leads to pressure building, hence the overpressure accumulation.
 - **Compaction Disequilibrium** can be described as a loading overpressure generation mechanism triggered by (i) fast sedimentation rate of the basin and enhanced by (ii) lateral tectonic compression.
 - Disequilibrium compaction overpressure is thought to be the most widespread cause of overpressure in sedimentary basins, but is certainly not the only cause, and as burial increases other causes of overpressure become increasingly important (Osborne and Swarbrick, 1997; Nadeau, 2011; Morley et al., 2018).
 - **Diagenesis** is controlled by temperature (T), pressure (P), and water content (H₂O). Clay diagenesis results in an increase of fluid content in the pore space favoring overpressures.
 - Post-deformational cementation may decrease fault zone permeability (Clennell et al., 1998). Below a certain *fluid-retention depth*, overburden loading becomes partially supported by pore fluids rather than rock compaction (Suppe, 2014). This process modifies the classic linearly increasing brittle strength-depth relationship (Brace and Kohlstedt,

1980), where increased pore fluid pressures lead to constant and low brittle strength below this depth (Suppe, 2014).

- **Maturation:** Organic matter maturation (thermal or biologically controlled) generates oil and gas by increasing the fluid content in source rocks leading to overpressure.
- **External Forces Influencing Overpressure** depict the external factors that have an effect on shale tectonism driving forces. These factors can be listed under three categories; basin geometry, tectonism and differential subsidence.
 - **Basin Geometry:** Some basin types are prone to localized high sedimentation rates (e.g. rifts, foreland basins) and to build lateral pressure gradient related to gravity (e.g. slopes/margins).
 - **Tectonism** is a potential way to increase stress either by (i) *local strain/distributed deformation* or (ii) topography (e.g. via slopes and flexural basins increasing the sediment deposition/collection with gravitational loads).
 - **Differential Subsidence** is imposed into a shale-prone system via (i) sediment arrival and/or (ii) inner Earth movements (e.g. thermal convections). This leads to a sediment equilibrium change causing subsidence and hence the shale deformation.
- **Deformation Geometries** are the shale deformation geometries observed in nature. Argilokinesis (also known as claykinesis) is a broadly applied, all-encompassing term used to describe the dynamics of uncompacted mobile clays. Even though the scale of observation for salt is much smaller than shale, they both work with the same principle in terms of mobilization pattern; by summing up the plastic displacement within the particles. Therefore argilokinesis resembles the deformation geometries observed within salt as halo-kinesis under stress, strain and particular scale of observation.
 - **Mud/Shale Diapirs:** certain dynamic subsurface processes cause overpressure generation at depth, leading to transmittance of the mud/clay deposits towards the surface via breaching, flowing and/or fracturing. Mud/Shale diapirs depict geological forms associated with mud deformation geometries resembling salt diapirs and are observed in thick shale-rich sedimentary basins.
 - **Shale Canopies:** A 'shale canopy' can be described as a form of shale mass (combined of multiple shale sheets) emplaced at stratigraphic levels above its source layer (i.e. mother shale), which can be detached or attached via a feeder to its origin; the initially deposited thick shale interval (i.e. stratigraphically older shale strata).
 - **Shale Minibasins:** Similar to salt minibasins, they are described as dish-shaped synclines of sediments sinking into a medium of thick shale. The main driving mechanism for minibasin formation for both salt and shale is the differential loading leading to synclinal fill and welded ductile medium features (e.g. diapirs, walls, canopies).

Chapter 3: Review of Existing Geodynamic Settings Affected by Salt-Like Shale Tectonics

As reviewed by Morley et al., 2011; shale detachments are the key slip horizons in many structural settings such as; fold and thrust belts, accretionary prisms, gravity driven systems ranging from major deltas to mass transport complexes and hybrid gravity-lithospheric-stress driven systems (Morley et al., 2018). Following the literature-related information we currently have for mobile shales, we have decided to investigate shale-related geodynamic settings under five sub-categories; (1) *Deep Sedimentary Basins*, (2) *Rift Settings*, (3) *Passive Margins*, (4) *Accretionary Wedges/Prisms: Active Margins* and, (5) *Foreland Basins, Collisional Belts and Collapsing Orogens* followed by a *Synthesis on Shale-Driven Geodynamic Settings* section. Each sub-category will aim to address the associated shale-prone geologic setting with a literature example and context relevant to the research.

I. Deep Sedimentary Basins

Sedimentary basins are formed over hundreds of millions of years by the combined action of deposition of eroded material and precipitation of chemicals and organic debris within water environment (Onajite, 2014). Continental sags (cratonic basins), rifts, failed rifts, continental rim basins, proto-oceanic troughs and passive margins are listed as evolutionary sequences unified by lithospheric extension processes (Dietz 1963; Dewey & Bird 1970; Falvey 1974; Kinsman 1975; Veevers 1981).

Lithosphere is made up of tectonic plates interacting with each other due to plate motion (i.e. Plate Tectonics) and mantle flow, which give the fundamental background for sedimentary basin formation (Allen & Allen, 2013). As result of various tectonic regime exposure, sedimentary basins differ in their preservation potential (Allen & Allen, 2005; Busby & Ingersoll, 1995; Dickinson 1974), which can affect the degree of shale-interaction in a given environment since the amount of sedimentation is one of the controlling factors for Shale Tectonism.

Sedimentary basins are formed in response to subsidence and sediment production, related to (i) extensional processes (rift and passive margins), (ii) flexure linked to plate convergence and lithosphere buckling, (iii) plate flexure due to loading (sedimentary/volcanic loading, or flexural subsidence related to convergence, and (iv) dynamic topography related to mass motion in deep mantle (Allen and Allen, 2013; Busby & Ingersoll, 1995; Burov and Diament, 1995; Cloetingh and Burov, 1996; Burov, 2007; Braun 2006; Cloetingh et al., 2005; 2006).

Two types of basins can be identified at Earth's surface; *Oceanic Basins* are developed above *oceanic lithosphere and passive margins* while the *Continental Basins* result from the flexure/rifting of *continental lithosphere* (Allen & Allen, 2013). Following their origin associated to plate tectonic activity, the long-term subsidence patterns differ and lead to various type of infilling of the accommodation space by sediments (Allen & Allen, 2005). The observations in such basin/rift/margin settings are explained by two linked mechanisms; (i) brittle extension of the crust, causing extensional fault arrays and fault-controlled

subsidence, and (ii) cooling following ductile extension of the lithosphere or negative dynamic topography sustained by downwelling mantle flow, leading to regional sag-type subsidence (Allen & Allen, 2013). As previously mentioned, the basins above oceanic crust are likely to be subducted while the basins above marginal continental crust may be partially preserved (Choudri, et al., 2010). The following two sections will be focusing on Oceanic and Continental Basins respectively with examples of Shale Tectonism observed within those geodynamic settings.

A. Oceanic Basins: South Caspian Sea Example

Oceanic basins are floored by *oceanic lithosphere* that originates from seafloor spreading at tectonic plate boundaries triggered by internal mantle convection movements of Earth. Such basins are likely to be subducted with sediment burial due to increasing pressure and lithification process (Busby & Ingersoll, 1995; Choudri et al., 2010). The following section will be present an example of a deep oceanic basin, namely the South Caspian Sea affected by Shale Tectonism.

The Caspian and Black Sea represents the part of a Mesozoic chain of back-arc basins stretching over a distance of 3,000 km (Dercourt et al., 1986). According to Zonenshain and Le Pichon (1986), the back-arc basins were formed during three separate tectonic episodes, which are namely Middle Jurassic, Late Jurassic, and Late Cretaceous times. The continental part is interpreted to be Proterozoic age, while the oceanic basement is associated to Middle-Late Jurassic period (Smith-Rouch USGS Report, 2006; Egan et al., 2009). The whole region stands as a tectonically active ground evidenced by earthquakes and mud volcano eruptions (Etiope et al., 2004).

By location, the South Caspian Sea covers the southern portion of Caspian Sea reaching to Eastern Azerbaijan, western Turkmenistan, and Northern Iran, while the South Caspian Basin extends onshore in West Turkmenistan in the east and the Lower Jura in the west forming one of the deepest basins of the world with an estimated basement depth of 20–25 km (e.g. Shikalibeily & Grigoriantz 1980; Zonenshain & Le Pichon 1986; Brunet et al. 2003; Egan et al., 2009). As it is stated by Egan et al. (2009), “*the northern boundary of the South Caspian Basin lies along the Apsheron Sill, a structural high that links to the Apsheron peninsula and the eastern Greater Caucasus*”.

From geodynamic point of view, the basin is formed as a result of the interaction between Eurasia, India and Arabia plates as well as several micro-plates during Triassic times. During Late Triassic – Early Jurassic era, Paleotethys Ocean was closed by several microplates suturing to the Eurasian margin, while giving rise to a Jurassic – Cretaceous north-dipping subduction along this new continental margin located to the south of Pontides, Trans-Caucasus, *which was formed as an orogenic belt by compressional deformation resulting from the closure of a Jurassic–Eocene back-arc basin* (e.g. Zonenshain & Le Pichon 1986; Ershov et al. 1999) (Egan et al., 2009), and Iranian micro-plates (Smith-Rouch USGS Report, 2006). As it is stated by Golonka, 2007; this subduction zone trench-pulling effect caused rifting, creating the back-arc basin of the Greater Caucasus–proto-South Caspian Sea (Figure 52).

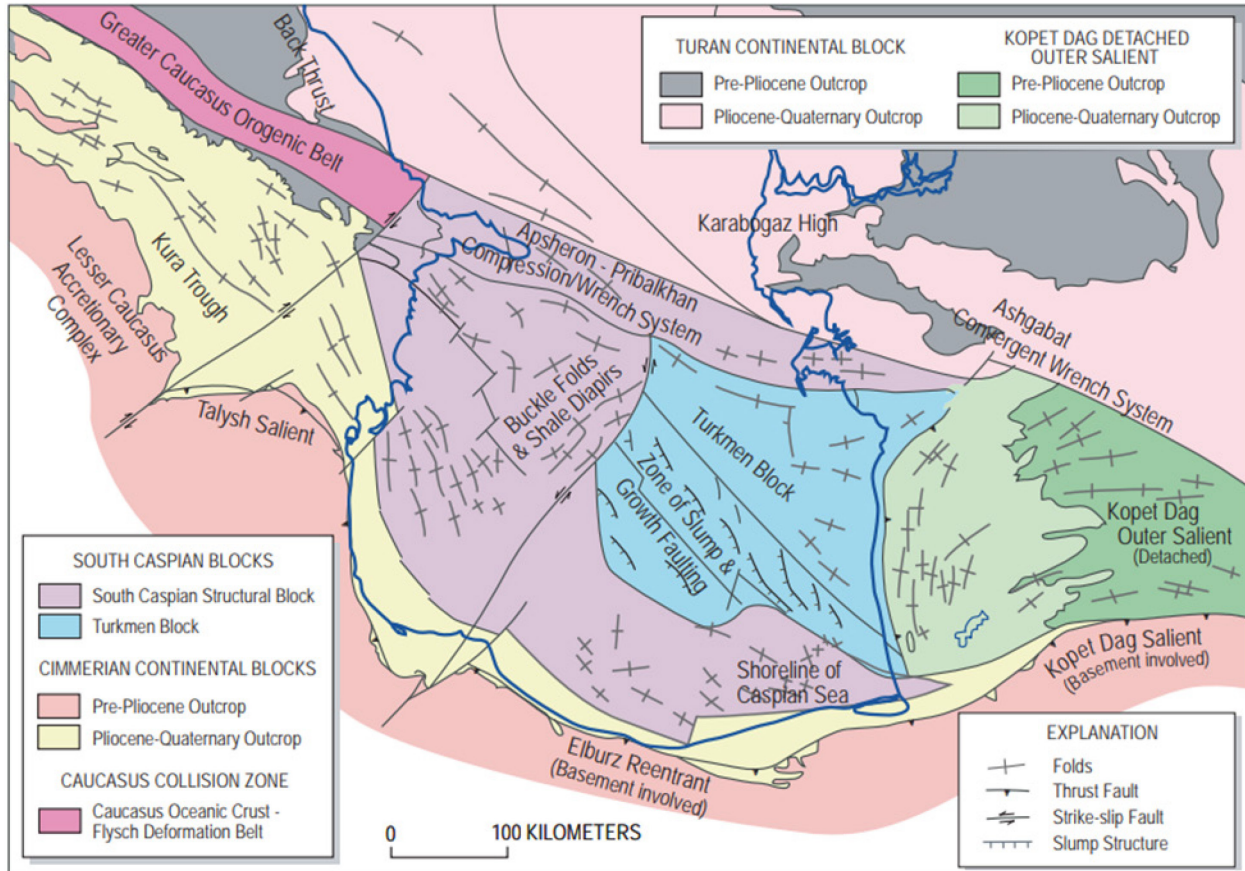


Figure 52: Major structural features in the South Caspian Basin region. Note that alternate terms are used for some of these features in the text and in other figures, depending on the context in which they are discussed. (Map is modified from Devlin and others, 1999, and is printed with permission from Exxon/Mobil) (image retrieved from Smith-Rpuch USGS Report, 2006).

From geodynamic point of view; the basement origin of South Caspian Basin is debated under two possible scenarios. The first scenario suggests the basement to be a 'modified' oceanic or sub-oceanic crust (Berberian, 1983; Knapp et al., 2004; Brunet et al., 2007) due to its abnormal thickness (8-10 km) and yet responsive P-wave values (6,6 – 7 km/s) (Knapp, Knapp & Connor, 2004; Brunet et al., 2007; Egan et al., 2009). The second scenario proposes the basement to be inconsistent with the normal subsidence behavior of an oceanic crust due to the increasing subsidence of the SCB through its history (Artyushkov, 2007), hence points out to the possibility of a deep phase change of gabbro to denser eclogite, process used by Brunet et al. (2007) to model the subsidence history of the North Caspian Basin. Overall, South Caspian Sea is a particular oceanic basin in the form of a back-arc basin (in other words, a deep extensional basin) with an oceanic crust ground at a place, where it suffers a double lithospheric backing associated to shortening. For these combined reasons, it is a very deep sedimentary basin merging multiple external components and standing as a unique example.

However, all of these studies unite upon the conclusion that South Caspian Basin can be defined as a remnant of a marginal sea (Berberian, 1983; Zonenshain & Pichon, 1986; Brunet et al., 2007; Golonka, 2007). As it is not the purpose of this research, we will be adapting the first scenario and refer to South Caspian Basin as a deep and thick basin formed by oceanic crust, central part of which reaches to the depths as great as 20 km below sea level, making it one of the deepest sedimentary basins of the world. As it is pointed out by Abrams (1996) and Tagiyev et al. (1997), the basin stands out due to; (i) sediment accumulation at exceptionally high rates (as high as 4.5 km/m.y.), (ii) low sediment compaction, (iii)

relatively low geothermal gradient ($1.5^{\circ}\text{C}/100\text{ m}$), and (iv) abnormally high pressures (Smith-Rouch USGS Report, 2006).

The South Caspian Basin can be evaluated by structures oriented (i) NW-SE in the western part (e.g. Lower Kura Depression), and (ii) N-S to NE-SW in the eastern part (e.g. The Turkmen Block). The western part is governed by oblique thrusting along thrust faults, high sediment loading, and extremely high pore pressures produced gravity-driven diapirism (Lebedev et al., 1987; Smale et al., 1997; Abdullayev, 1999), while the eastern part is defined with a zone of slumps and growth faulting. Given this aspect; with the help of excessive sediment amount (e.g. up to 25km Tertiary sediment) that is introduced into Caspian Sea Basins, Smith-Rouch USGS Report, 2006 stated that mobile shales may be widespread throughout the basin, but can be concentrated on active tectonic trends, particularly along strike-slip faults.

In terms of shale tectonism; the region has been studied and divided into two main zones by researchers; (i) *fold and shale-diapir zones* (Lebedev et al., 1987), and (ii) *structured zones* (Devlin et al., 1999). Abdullayev, 1999 and Devlin et al., 1999 reported that the tectonic movement along the Absheron Pribalkhan Ridge area has created shale diapirs and mud volcanoes in the central and western parts of the basin via forcing overpressured shales into zones of weakness (i.e. faults), and thereby piercing sedimentary layers as single-diapir stocks or forming shale-diapir ridges and walls (Smith-Rouch USGS Report, 2006). This specific area is referred to as '*the zone of buckle folds and shale diapirs*' (Philip et al., 1989; Devlin et al., 1999) (Figure 53-Figure 55). Based on the structural analysis conducted on regional 2D seismic data by Devlin et al. (1999); *the majority of the structures are interpreted to be large buckle folds overlying a regional ductile detachment zone at depth*. Their interpretation suggested that upper Miocene to Holocene sediments behaved in a relatively rigid fashion and deformed as folds with a bedding parallel flexural slip in a relatively symmetrical sense. Buckle fold interpretation is backed by low-angle reverse faults in the lower parts of the folds, and normal faults in the upper part (Figure 54). As it is seen on Figure 54 interpretation and reported by Devlin et al. (1999), there is a *relatively constant sedimentary thickness to the top of the Surakhany Formation (blue marker) above which, the sedimentary section displays marked thinning over the crest and onlap onto the flanks of the growing structures* as the stratal thinning begins with deposition of the Akchagyl Formation (pink marker).

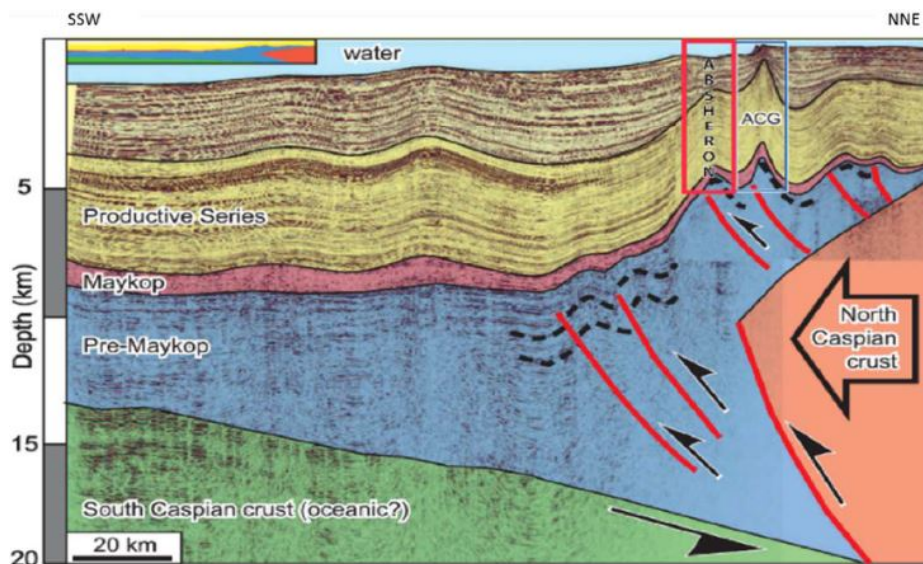


Figure 53: Seismic Section: regional interpreted deep seismic section, showing the main subsurface structural elements with the folds above the Maykop detachment level associated in the northern part to deeply rooted thrusts. The red box shows the approximate location of the Absheron structure (modified from Stewart & Davies, 2006) (image retrieved from A. Blouin PhD Thesis, 2020).

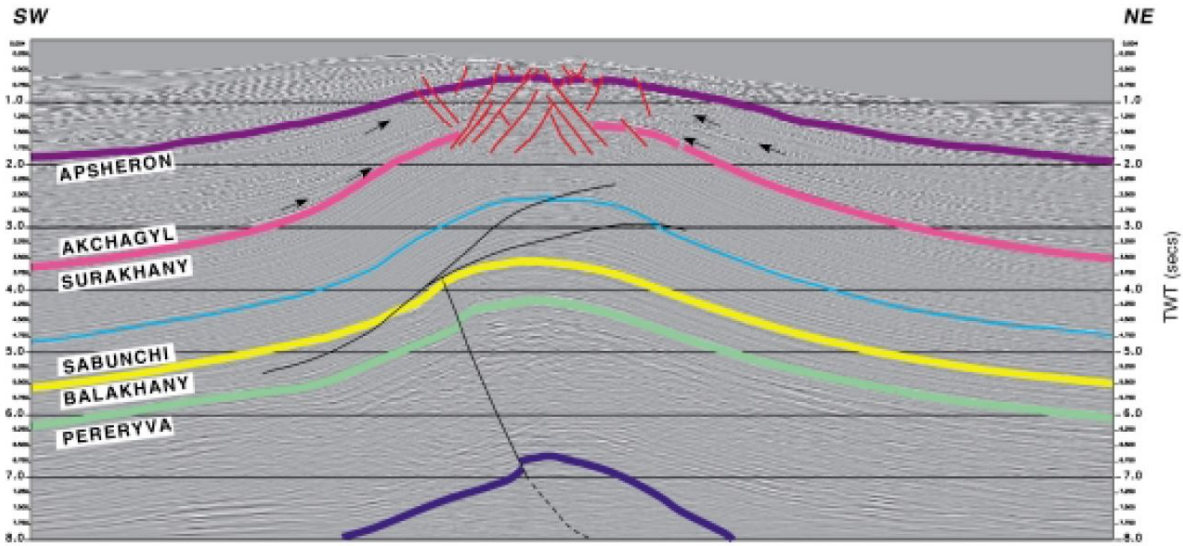


Figure 54: Seismic line, approximately 23 km long, across a typical South Caspian structure. Note the crestal normal faults in the shallow section and the low-angle reverse faults in the lower part of the fold. These two fault regimes are separated by an inferred neutral surface within the lower Surakhany Formation. Also note the thinning and onlap of strata above the top Surakhany Formation (pink surface), indicating the onset of structural growth. Use of seismic data courtesy of Caspian Geophysical (image retrieved from Devlin et al., 1999).

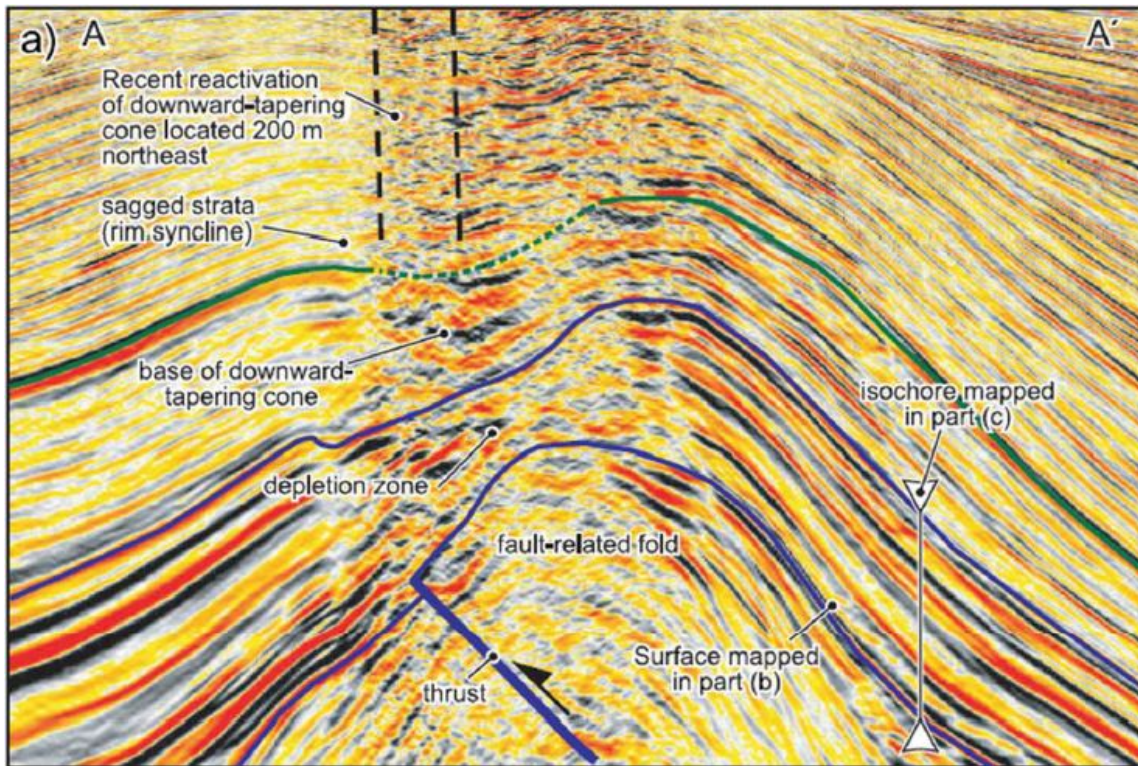


Figure 55: Seismic section across a mud volcano system in the South Caspian Basin showing a thinning of the Maykop Formation interval interpreted as being the source layer of the mud volcano (image retrieved from A. Blouin PhD Thesis, 2020).

B. Continental Basins: Shannon (Clare) Basin, Ireland Example

The Shannon Basin (*sensu* Sevastopulo, 2001; also known as the *Clare Basin* or Western Irish Namurian Basin; Croker, 1995; Wignall & Best, 2000) results from the assembly of Pangaea during the Carboniferous as a consequence of the reactivation of the Iapetus suture (Phillips et al., 1976; Klemperer, 1989; McKerrow & Soper, 1989). As a consequence, the Shannon Basin stands as a part of a network of Carboniferous basins founded on stretched continental crust throughout NW Europe and including the British Isles (Blanchard et al., 2019), which has an elongated WSW–ENE orientation stretching from the Atlantic Ocean towards the Central Ireland (Collinson et al., 1991; Martinsen et al., 2003).

From geochronological point of view, the regional crustal stretching observed during Lower Carboniferous is thought to bring the initial accumulation of limestones as a thick succession within the region, the character of which coincides with the Early Carboniferous subsidence phase argument of Western Clare that is being suggested as a platform-to-basin transition (Collinson et al., 1991). The basin then filled by a thick succession of siliciclastic sediments displaying the overall depositional system progradation from deep-marine turbidites to delta slope and fluvio-deltaic environment (Rider, 1974; Pulham, 1989; Wignall & Best, 2000, 2016; Martinsen et al., 2003; 2017).

The deltaic succession of the basin showcase noticeable examples for soft-sediment deformation (Gill, 1979; Pulham, 1989; Best et al., 2016). As a result, observed soft sediment deformation features within this deltaic succession are attributed to the (i) gravitational instability at the delta-front slope, (ii) rapid rates of deltaic sediment supply, and (iii) rapid burial with consequent overpressuring of muddy intervals, which are mobilized (Gill, 1979; Martinsen, 1989; Pulham, 1989; Blanchard et al., 2019). These observed mud masses are depicted as mud diapirs by Blanchard et al., 2019 (Figure 56-Figure 59).

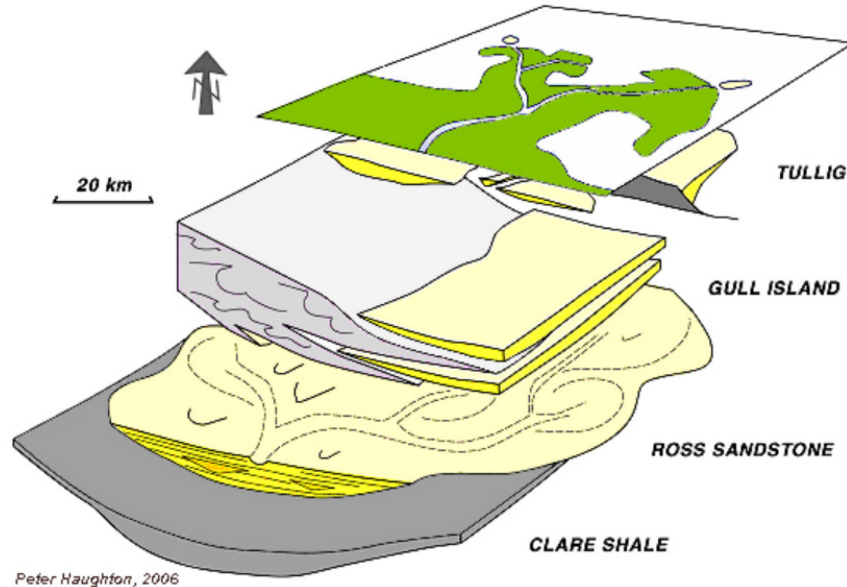


Figure 56: Much of County Clare, and the extension of the Clare Basin into counties Kerry and Limerick, was first blanketed by fine grained black shale deposits (the Clare Shale Formation) that interpreted to represent deposition during a period of sediment starvation. The area centered about the Shannon estuary then became the focus of deep water sandstone deposition (the Ross Sandstone Formation), whilst the original platform in North Clare remained starved of sediment and continued to accumulate a condensed blanket of black shale. The sandy sediment that accumulated in the Clare Basin at this time came from the southwest. Following this event, the Upper Carboniferous basin filled gradually, becoming shallower upwards and the Ross Sandstone 'turbidites' are overlain by a thick succession of unstable slope deposits (the Gull Island Formation) and eventually by shallow-water delta deposits of the Central Clare Group (after Peter Haughton, 2006) (image retrieved from the website <http://www.sepmstrata.org/page.aspx?pageid=154>).

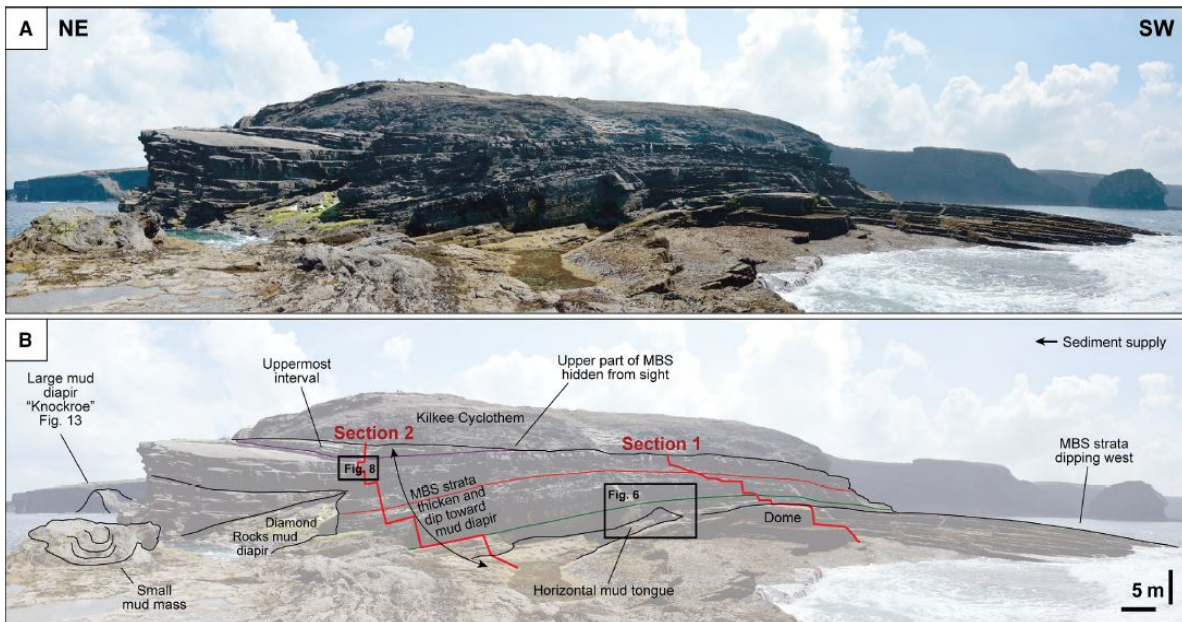


Figure 57: (A) and (B) View of the exposure from the northern part of the tidal platform at low tide. Strata of the Moore Bay Sandstone (MBS) thicken near the diapir, while forming a dome on the right part of the outcrop. Coloured lines mark specific stratigraphic surfaces that are important sequence stratigraphic surfaces or mark important events in diapiric evolution: (i) the green line represents the surface where beds uplifted by the horizontal mud tongue were folded and eroded; (ii) the solid red line corresponds to the stratigraphically lowest flooding surface, which is recognizable by the preservation of wave ripples overlain by a thin bed of shale (image retrieved from Blanchard et al., 2019).

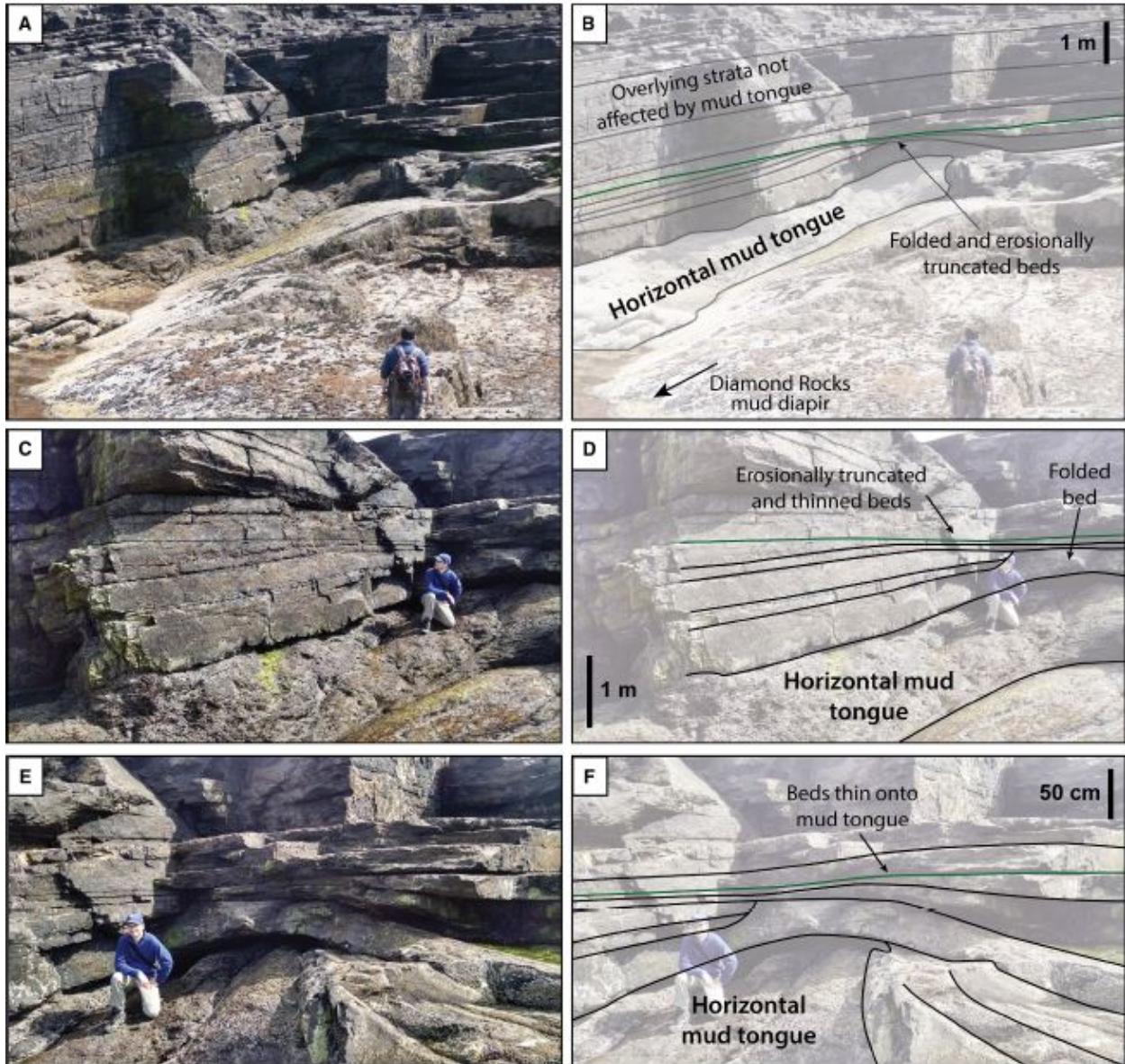


Figure 58: Photographs and interpretations of the horizontal mud tongue and syndepositional folding and erosion of the overlying strata. Faults visible in the upper part of (A) are mineralized and thus considerably post-date deposition and diapirism. The green coloured line is the surface where beds uplifted by the mud tongue were folded and eroded (image retrieved from Blanchard et al., 2019).

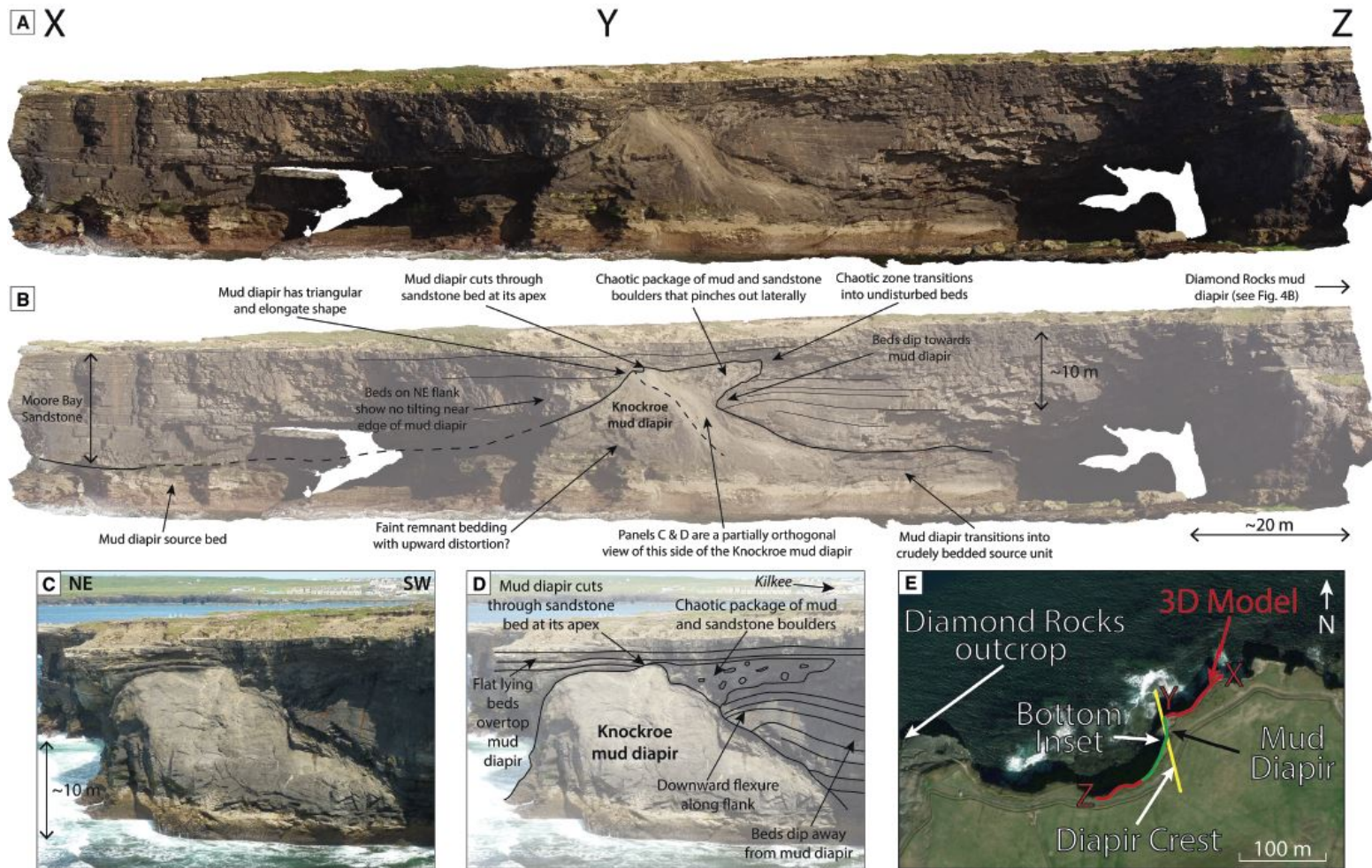


Figure 59: (A) and (B) Image and paired line drawing of the large diapir exposed in the cliff at Knockroe, 400 m to the east of Diamond Rocks. Image is extracted from a 3D model constructed using drone photography. (C) - (D) Image and paired line drawing of the diapir at a roughly orthogonal view to the upper image. These images together show the roughly triangular but elongate (ridge-like) shape of the diapir; (A) and (B) show a view perpendicular to the diapir crest and (C) and (D) are roughly parallel. (E) Map showing the location of the Knockroe diapir with the crude location of the diapir shown (black arrow), the approximate axis of the diapir crest (yellow line), the extent of the 3D model available in the supplementary material (total of green and red lines), and the approximate extent of the image in (C) and (D) (white arrow and green line) for reference. It should be noted that the static images in (A) to (D) do not show completely flat or orthogonal faces (image retrieved from Blanchard et al., 2019).

II. Rift Settings

Rift settings define the areas of crustal extension overlying the thinned crust and they evolve as linked fault arrays that control sediment dispersal during the syn-rift phase. Therefore, they are also defined by high seismic activity (Allen & Allen, 2013). Rifting are characterized by well-developed extensional faulting and can be defined under two categories; (i) *active rifting* (i.e. stretching of the continental lithosphere in response to an active thermal process in the asthenosphere), and (ii) *passive rifting* (i.e. mechanical stretching of the continental lithosphere from unspecified distant extensional forces, with passive upwelling of asthenosphere) (Allen & Allen, 2013). Current or recently active rift zones display an elevated rift flank topography bordering a depositional basin setting (Allen & Allen, 2013).

Continental Rift Basins take place at a rift setting floored by continental crust shaping via tectonic subsidence and sediment discharge they receive during their evolution. Based on the research we have conducted, to our best knowledge, there is no continental rift example showing shale tectonism. Therefore, we will be continuing with shale tectonism examples observed in Passive Margin settings in the next section.

III. Passive Margins

Passive margins define the transition portion of a tectonically-inactive rift setting between oceanic and continental crust. Extensional faulting, large-scale gravity tectonics such as slumps, slides, glide-sheets are basic characteristics of fully developed passive margins. During the cooling process, continental passive margins are exposed to regional subsidence following the complete attenuation of the continental lithosphere overlaid by sediment-poor or sediment-rich prism (e.g. continental crust stretching over a region of 50-150 km, and exceptionally as much as 400-500 km (Keen et al., 1987; Allen & Allen, 2013). Allen & Allen, 2013, categorizes passive margins under three aspects: (i) *abundance of volcanic products* (e.g. magma-rich vs magma-poor), (ii) *thickness of sediments* (e.g. sediment-rich vs sediment-poor), and (iii) *presence or absence of gravity-driven tectonics and salt tectonics* in the post-rift phase. In compliance with the topic of this research, we will be defining the sediment-rich and Sediment-Poor Passive Margins in the following section and later focus on the Sediment-Rich Passive Margin Deltaic Settings: Gravity-Driven Deltas under shale control.

A. Sediment-Rich vs Sediment-Poor Margins

Passive margins can be categorized under two groups based on the sediment input they receive; *Sediment-Poor (Starved) Margins* (1) and *Sediment-Rich (Deltaic) Margins* (2). The main difference between starved margins and the deltaic systems are the type of subsidence they are exposed to. Starved margins are defined by *slow thermal subsidence* as a consequence of limited sediment input they receive, while the deltaic margins are dominated by mixed thermal and *load-driven subsidence* bringing rapid accumulation of sediments into the pre-delta environment.

Starved margins can turn/transform into sediment-rich deltaic margins when the course of sedimentation rate accelerates through time. In terms of salt-prone margins, there are existing examples for both sediment-rich and sediment-poor. However, shale-prone margins only function with high sedimentation rate, which correspond to the sediment-rich deltaic settings. Therefore, this section will be detailing the sediment-rich margin examples driven by shale as the detachment level deltaic medium.

Deltaic margins are triggered by a load-driven subsidence arriving into the system with high input rate. Such environments can be driven by two deltaic mediums at the detachment level; salt or shale. Salt-controlled deltas display both gravity gliding and spreading. As it is earlier reviewed by Morley et al., 2003a; various seismic datasets and some outcrop examples point out to the fact that shale-dominated thrust zones thicken, thin, display down-building geometries, weld structures and diapir-like features, which can resemble salt tectonism. However, when the mud rocks are buried at depths < 2-3 km in large delta settings, they are hardened due to diagenesis and tend to have decreased pore fluid pressure with increased viscosity (Morley et al., 2017; e.g. Day-Stirrat et al., 2010; Morley et al., 2011). However, as the material properties of clay change with time/environment, they may evolve into narrow detachment zones and display resistance against gravity spreading, which contrasts with salt behavior (Morley et al., 2017).

B. Sediment-Rich Margin Deltaic Settings: Gravity-Driven Deltas

Gravity-driven gliding and spreading deltas can be described as linked systems characterized by an up-dip extensional domain accommodated by listric faulting, connected to a down-dip compressional domain at the toe of the delta accommodated by thrusting due to salt/shale expulsion, which display a translational interface in between these extensional and compressional domains. With incoming sediments and hence progressive evolution, they detach from their stable shelf/margin slope and start to prograde as a '*gravitational cell*' supported via the extensional-translational-compressional domains above a ductile medium (e.g. salt or shale) (Morley, 2003; Rowan et al., 2004; Peel, 2014; Jackson et al., 2015).

More specifically, *gravity gliding* (observed both in salt and shale-driven deltas) defines the *downslope movement of a delta*, while the *gravity spreading* (only observed in salt-driven deltas) defines the *movement of an internally-deforming mass material* along a sloping detachment level via *vertical flattening* (Figure 60). Rowan et al. (2004), Morley et al. (2011), and MacDonald (2013) list the components effecting the structural style of the deltas as, (i) basal pore fluid pressure, (ii) detachment medium, (iii) detachment thickness, (iv) thickness of deltaic wedge and (v) geometry of deltaic wedge.

Gravity spreading is inclined to lessen the gravitational potential by reducing the regional slope of the detachment surface in two possible ways; (i) *horizontally extending and vertically thinning the thicker-and-proximal part of the wedge*, and (ii) *horizontally shortening and vertically thickening the thinner-and-distal part of the wedge*. This mechanism can be investigated under three compartmental deformation domains, which are namely; proximal (upper slope and parts of the shelf), central (seaward translation of overburden), and distal (on and in front of the lower slope, where overburden deforms by thrusts and folds) (Vendeville, 2005). The amount of sediment spreading is mainly controlled by geometrical and mechanical properties of the distal sediment cover above the ductile medium (e.g. salt/shale). As it is stated by Vendeville, 2005; unlike differential subsidence, spreading can lead to large-scale horizontal movements of the sedimentary overburden above a lubricating layer.

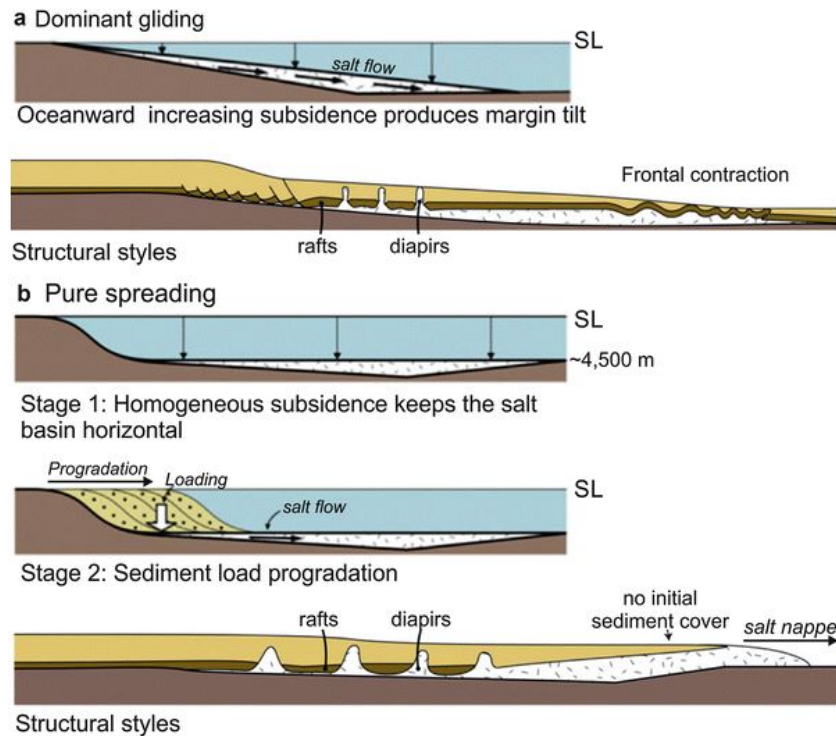


Figure 60: Diagram depicting the two categories of salt tectonic models: a) Dominant Gliding and b) Pure Spreading (image retrieved from Drachev S.S. (2015) Salt Diapirism in the Oceans and Continental Margins. In: Harff J., Meschede M., Petersen S., Thiede J. (eds) Encyclopedia of Marine Geosciences. Springer, Dordrecht)

As a result of thick shale succession, flexural loading of the crust by the delta pile in major deltas results in the base of the delta wedge dipping gently back towards the continent hence differential loading of the mobile shales by uneven deltaic sedimentation seem to govern shale mobilization driving mechanism rather than gravity sliding (e.g. Edwards 1976; Morley & Guerin 1996; Ge et al., 1997; McClay et al., 2003) (Morley, 2003).

In shale-prone deltaic settings, mobility do not stay confined to a specific stratigraphic unit as the mobility can change with time depending upon (i) burial rate, (ii) amount of overburden, (iii) lateral changes in shale thickness, (iv) regional and local stresses, (v) local drainage conditions (faults, carrier beds, fluidized pipes) and (vi) internal overpressuring conditions (e.g. Osborne & Swarbrick 1998) (Morley, 2003).

The East African Margin originated from Karoo rifting, which had taken place intermittently over 150 Myr ago (Coffin & Rabinowitz, 1988), during Late Paleozoic together with the development of several rift segments (Catuneau et al., 2005). As it is summarized by Cruciani & Barchi, 2016; *Karoo Phase* refers to the intra-continental rifting events that have taken place during Pangea supercontinent break-up (Martin et al., 2018), associated sediments of which found on the margin display variance of age from Late Carboniferous through the Permo-Triassic and into Early Jurassic until Pangea's maximum extent was reached (Catuneau et al., 2005).

We will be showcasing three examples in the following sections, which are namely: (i) Lamu Basin, (ii) Kutai Basin/Mahakam Delta, (iii) Krishna-Godavari Basin, and (iv) Niger Delta. Lamu Basin example from Kenya represents a sediment rich setting without a deltaic evolution, while the others document shale-related mobilization pattern emerged from interactions with the overlying sediment table in a deltaic setting.

i. Lamu Basin, Kenya

Extension of Karoo rifting continued until the seafloor spreading between Madagascar and Africa during Early-Mid Jurassic times. Although the timing is debated, the breakup is suggested to occur about 183 Ma, together with the outbreak of the Karoo large igneous province (Svensen et al., 2012).

During this period, *Lamu Basin* was believed to be part of a major tri-radial rift system (Cannon et al., 1981; Reeves et al., 1987; Bosellini, 1992). As it is stated by Cruciani & Barchi, 2016; following the N-S drift of Madagascar along a major transform fault, the Davie Fracture Zone (DFZ), the continental margin was divided into a rifted segment (SE Somalia) and a transform segment (eastern Tanzania); the Lamu Basin lies at their junction [Coffin and Rabinowitz, 1988] and is floored by both thinned transitional crust to the west and Jurassic oceanic crust to the east.

Following the cessation of seafloor spreading during Early Cretaceous about 120 Ma (Rabinowitz et al., 1983; Reeves, 2014) or 130 Ma (Kent & Gradstein, 1985), and hence the cessation of relative motion between Madagascar and Africa; the whole East African Margin was exposed to tectonic deformation and associated volcanism (Coffin & Rabinowitz, 1988). As a result (Cruciani & Barchi, 2016); *the Lamu Basin got affected by episodes of renewed basement uplift from the Late Cretaceous to the end of the Early Paleocene (Nyagah, 1995), forming a complex pattern of NW-SE and N-S trending structural highs (Nyaberi and Rop, 2014) (Figure 61-Figure 62).*

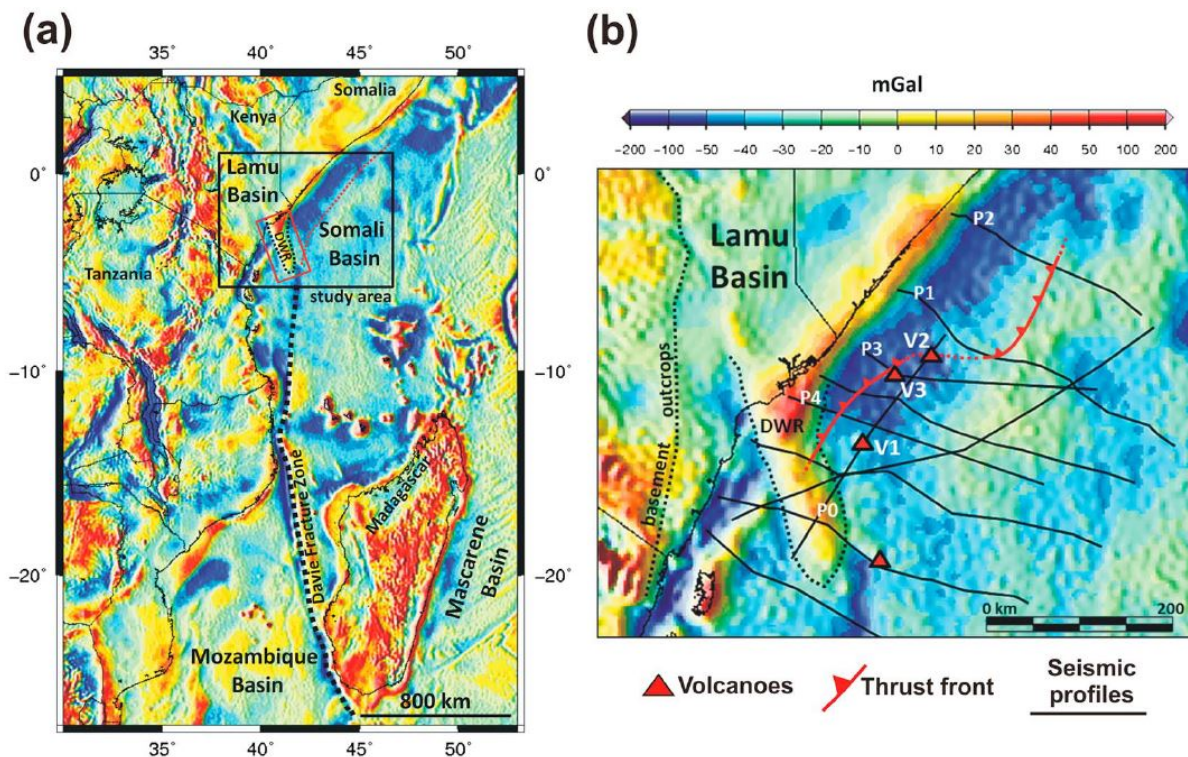


Figure 61: A) Free-air gravity anomaly map of East African margin. N-S trending Davie Fracture Zone (>2000 km long; thicker, dotted black line) connects Somali and Mozambique Basins. At northern edge of Davie Fracture Zone, a broad gravity high represents Davy-Walu Ridge (DWR, thinner, dotted black line), a prominent basement high, uplifted since mid-Cretaceous. B) Zoom on study area, showing location of thrust front with respect to DWR and volcanoes identified on seismic profiles. DWR: southern limit of DW-FTB. Two volcanoes (V2, V3) are located in front of outermost thrusts, representing mechanical barriers to

basinward propagation of DW-FTB. Gravity data from WGM2012 Earth's gravity anomalies, bgi.omp.obs-mip.fr/data-products/Grids-and-models/wgm2012. (image retrieved from Cruaini & Barchi, 2016).

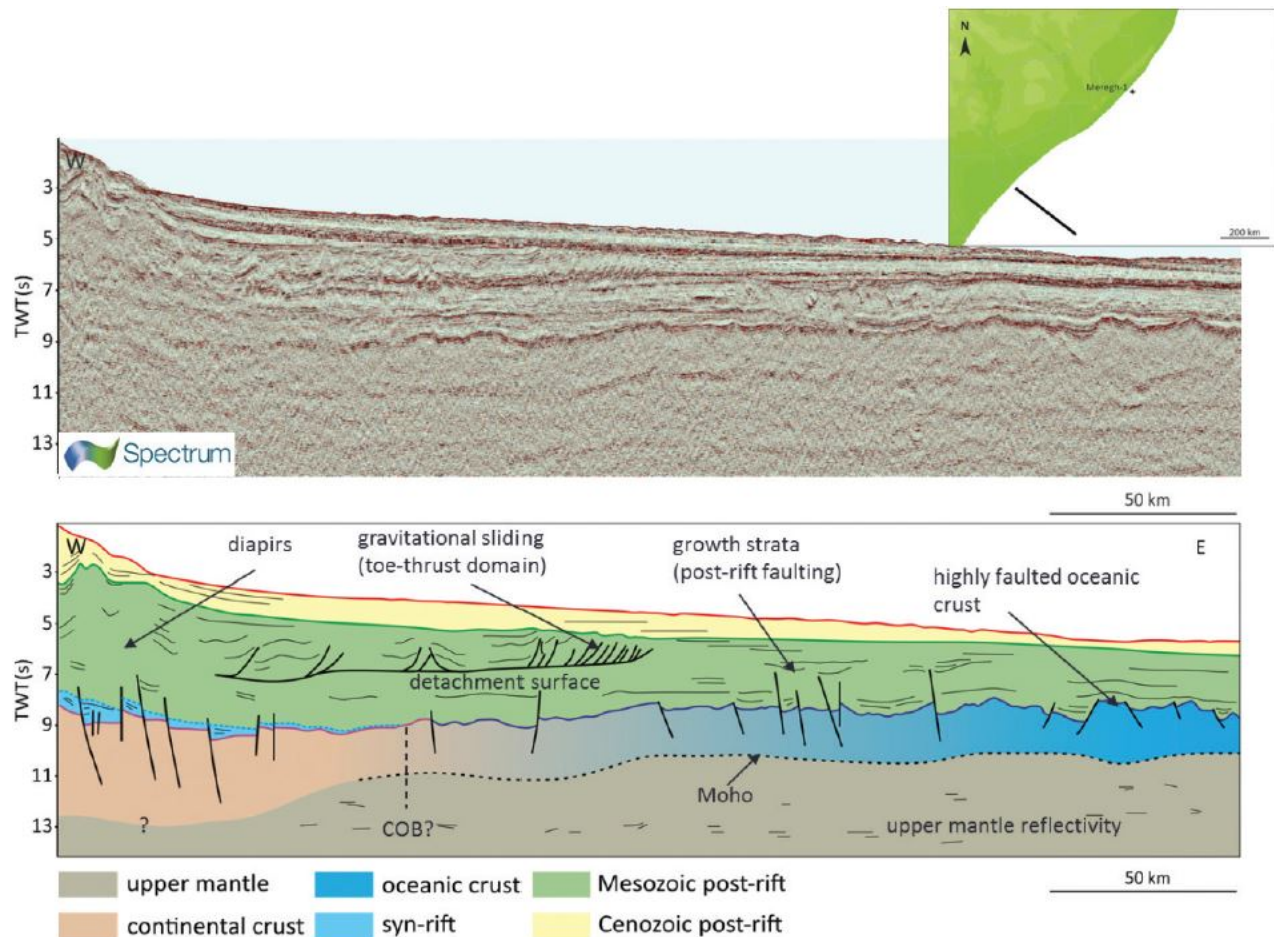


Figure 62: Regional seismic line from the Juba-Lamu Basin showing the cross-section view and its interpretation (image retrieved from Stanca et al., 2016).

In terms of Shale Tectonism; the existence of a deepwater fold & thrust belt (DDFTB) system was known since 1980s (Coffin & Rabinowitz 1982; 1988; 1992). However, lack of high quality seismic dataset examples avoided further investigation of the region. Cruaini & Barchi, 2016; stated that the system originated over an Early to mid-Cretaceous shale detachment due to a mainly gravity-spreading mechanism. The DWFTB extends over 450 km along East Africa (Zhang et al., 2019), and its offshore sedimentary section reaches up to 13 km thickness (Nyagah, 1995; Yuan et al., 2012). After the conducted seismic interpretation scheme on selected lines (Figure 63), Cruaini & Barchi, 2016, concluded that:

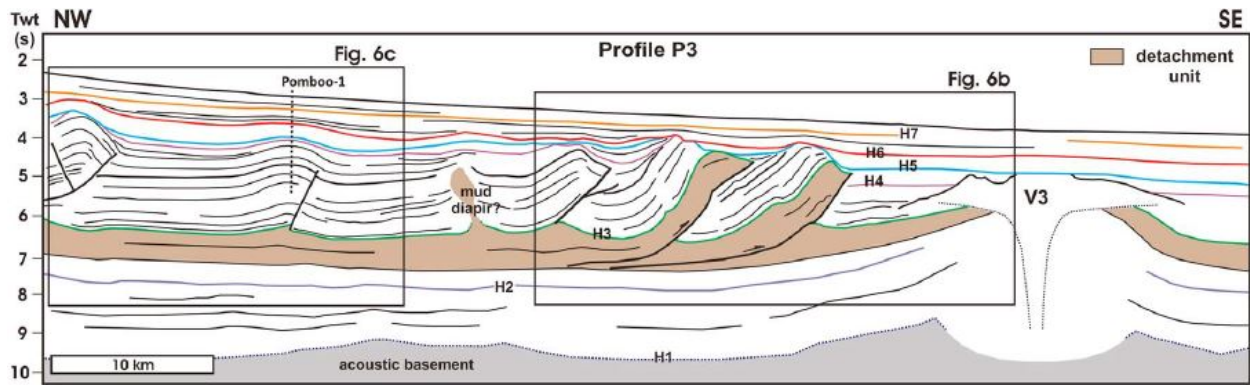


Figure 63: Interpretation of seismic profile P3 across southern portion of DW-FTB. Note the interpreted mud diapir (image retrieved from Cruaini & Barchi, 2016).

- The basal detachment unit, hitherto assumed as salt, is interpreted here as a thick sequence (up to 1.5 km) of Early to mid-Cretaceous, overpressured, deep marine shales (Walu Shales).
- The basal detachment surface progressively descends toward the base of the detachment unit, causing landward thickening of the shales involved in deformations; the dominant structural style thus changes from a basinward verging, closely stacked thrust system to widely spaced thrusts and pseudo-symmetric (i.e. shale-cored) detachment folds (Figure 64).
- The main deformation phase was triggered by rapid sediment inputs (the deltaic Kofia Sands), during the Turonian-Early Paleocene; the increased amount of clastics may have caused overpressure within the basal shales, inducing gravity-spreading collapse.

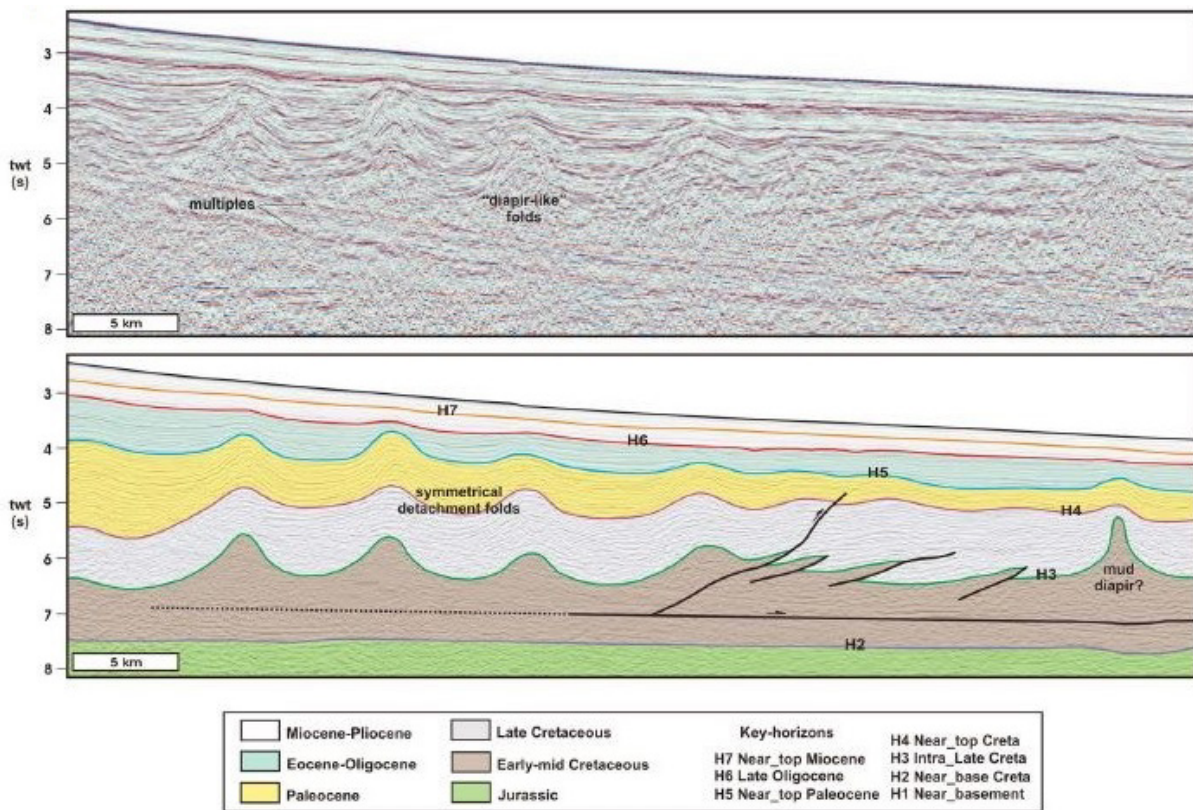


Figure 64: The innermost sector, about 65 km in length, is dominated by a set of large symmetrical detachment folds, resembling diapir-like folds (image retrieved from Cruaini & Barchi, 2016).

ii. Niger Delta

The Niger Delta is defined as a well-developed deltaic province located on the West African continental margin, displaying (i) an onshore-to-shelf zone of growth fault dominated depo-centers, (ii) a belt of shale diapirs around the outer-shelf-to-slope zone, and (iii) a fold & thrust belt in the slope area (e.g. Evamy et al., 1978; Doust and Omatsola, 1989; Morley and Guerin, 1996; Haack et al., 2000; Ajakaiye and Bally, 2002) (Yang et al., 2020). The basalt detachment/ductile medium, which dips gently seaward beneath the extensional domain and landward beneath the contractional domain, is interpreted to be within or at the top of overpressured, compacted Akata shale interval (Bilotti and Shaw, 2005; Higgins et al., 2009; Morley et al., 2011; King and Morley, 2017; Yang et al., 2020) (Figure 65).

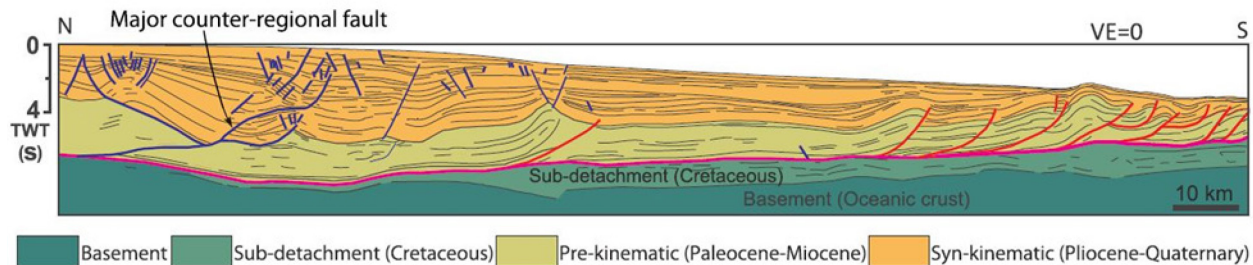


Figure 65: Interpretation of a seismic reflection profile across the gravity-driven fold-thrust belt of the Niger Delta eastern lobe, Nigeria and Gulf of Guinea, after Ajakaiye and Bally (2002), Wu and McClay (2011). No vertical exaggeration. Interpreted units are stratigraphic sequences. This is the line drawing of of Ajakaiye and Bally (2002) (image retrieved from Yang et al., 2020).

Number of studies depict seismic examples of *shale weld features under the concept that 'shale can flow considerable distances like salt with -welded regions- along shale detachment zones'* (Morley et al., 2017; e.g. Morley and Guerin, 1996; Wu and Bally, 2000; Maloney et al., 2010; Morley, 2003). Even though the accessibility to well-imaged seismic data reshaped some of its aspects, Niger Delta stands as one of the most important deltaic settings showing shale tectonism with many aspects still-to-be-confirmed (Morley et al., 2017; e.g. areas of broad shale diapirs have been re-interpreted as narrower regions with a central fluid pipe (Morley, 2003a, 2003b), rather than a mass of plastic, fluid-rich mud-rock. Multiple discrete detachment levels have been identified in some parts of the external Niger Delta fold and thrust belt (Briggs et al., 2006, Maloney et al., 2010). Complex thrust and fold geometries within a shale unit can explain thickness variations in place of plastic flow (Duerto and McClay, 2011). A number of published seismic examples demonstrate that stratified shales are present in areas once thought to be regions of chaotic, diapiric shales (Van Rensbergen and Morley, 2003; Elsley and Tieman, 2010; Duerto and McClay, 2011). Morley et al., 2017 summarizes the shale-related findings of Niger Delta as;

- *The thickness of the pre-kinematic and syn-kinematic section (34–5.7 Ma) in the mobile shale belt ranges between about 1.5 and 4 km thickness (Wiener et al., 2010).*
- *Mobile shale thickness ranges from < 1 to 3 km.*
- *The mobile shale deformation is broadly distributed under the inner fold and thrust belt, becoming focused on more discrete detachment horizons around the outer fold and thrust belt (Kruger & Grant, 2012).*
- *The maximum thickness in any one area from the top of the syn-kinematic section to the base of the mobile shales is about 5 km (based on the data in Wiener et al., 2010).*
- *The upper thickness range of the main syn-kinematic section (17.3–5.7 Ma) is 2.5 km, which suggests that most of the mobile shale zone was at depths shallower than 2.5 km at the start of deposition (around 17.3 Ma) and was able to form a thick (~2 km) detachment zone.*

As it is pointed out by Corredor, et al. (2005), deep water Niger Delta contains two complex, imbricated FTBs as the inner and outer systems accommodating the contraction caused by gravitational gliding/extension on the shelf. The seismic cross-section illustrated in the same study exhibits a good example for showing shale-related features of the delta setting (Figure 66). The interpretation shown on Figure 66 depicts the region with normal faults belonging to the extensional domain both in basinward-dipping and counter regional directions beneath the continental shelf to the north, while the lower slope area is dominated with a major detachment zone in the Akata Formation linking the extensional province across *the mud-diapir zone* to the contractional fold & thrust belt (FTB). Highly imbricated fold and thrust zone towards the south form the inner and outer FTBs, which are separated by a zone of little deformation and characterized by large detachment folds. Majority of these thrust faults except the ones in the northern and central parts of the delta, verge towards the deep-ocean and sole into the shale detachment surface within the Akata Formation. (Corredor et al., 2005). The counter regional faults seen on Figure 65 actually define ‘expulsion rollovers’ as they are similarly observed in salt-prone deltaic intervals, which evidence a salt like behavior in this shale-prone environment.

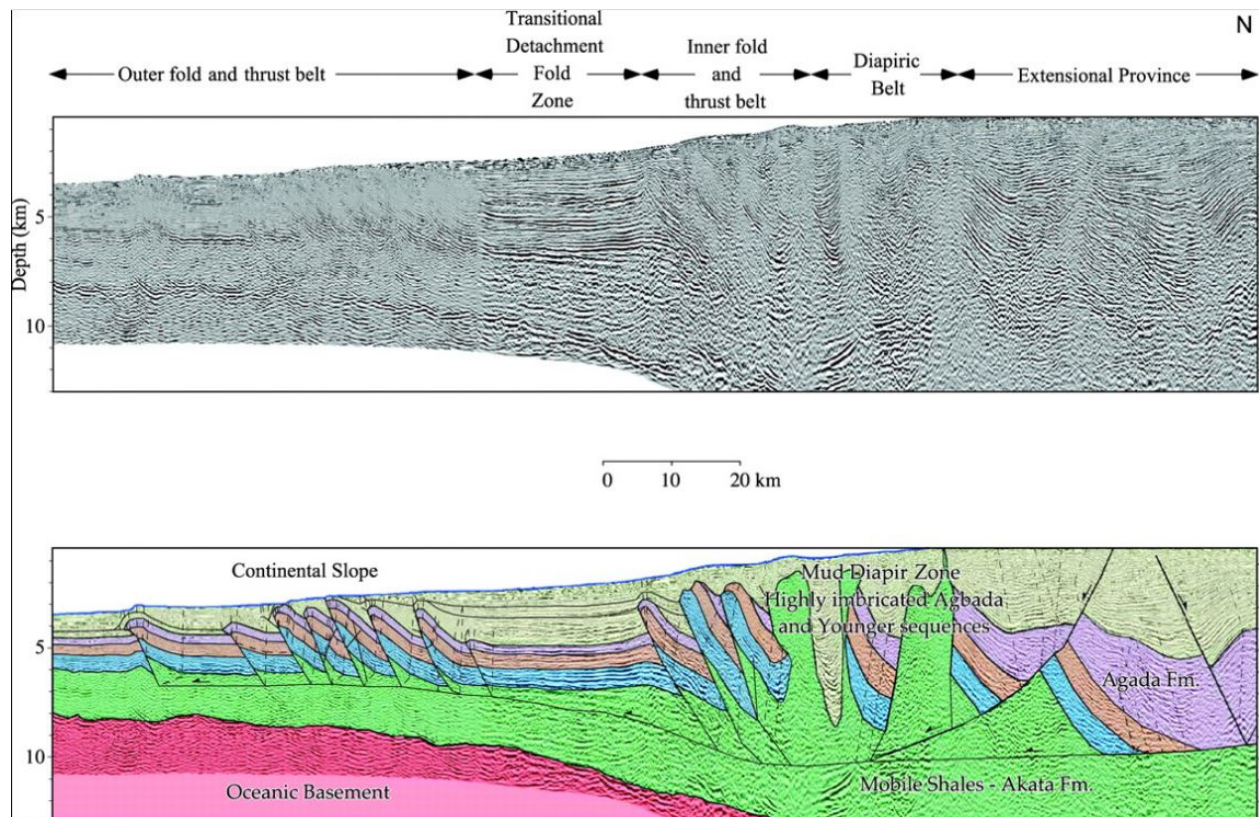


Figure 66 : Uninterpreted and interpreted regional seismic profile across the Niger Delta showing the link between the extensional province on the shelf and the contraction in the toe thrust systems in the deep water, as well as the main structural domains. Both regional and counter regional normal faults are present in the extensional province. Slip on these faults soles onto one or a series of basal detachments and extends across a diapiric zone into the deep-water fold and thrust belts. The inner and outer fold and thrust belts are separated by a zone of little or no deformation. Along strike, this transitional zone is characterized by detachment folds. Seismic section is poststack migrated and depth converted (data courtesy of Mabon Ltd.) (image retrieved from Corredor et al., 2005).

A zoom-in caption of the shale tectonics related (*‘Diapiric Belt’* or *-Mud Diapir Zone-* as it is called in Figure 66) portion of Niger delta seismic section from Corredor et al. (2005) is shown on Figure 67. The basic

interpretation made on the figure depicts the details of ‘diapir-like’ features detected in the area. Deltaic sediments are carried towards the deeper portion of the ocean above a ductile medium/shale unit (a.k.a. Akata Formation). The *Diapiric Belt* section takes place between the Extensional Province and FTB domains. The delta deposits display terminations in terms of *pinch-outs*, *onlaps* and *toplaps* against the *diapiric* bodies rising from the shaly detachment unit. The pod-like shapes observed in between the diapiric formations resemble minibasins attributed to Salt Tectonism and mobilization.

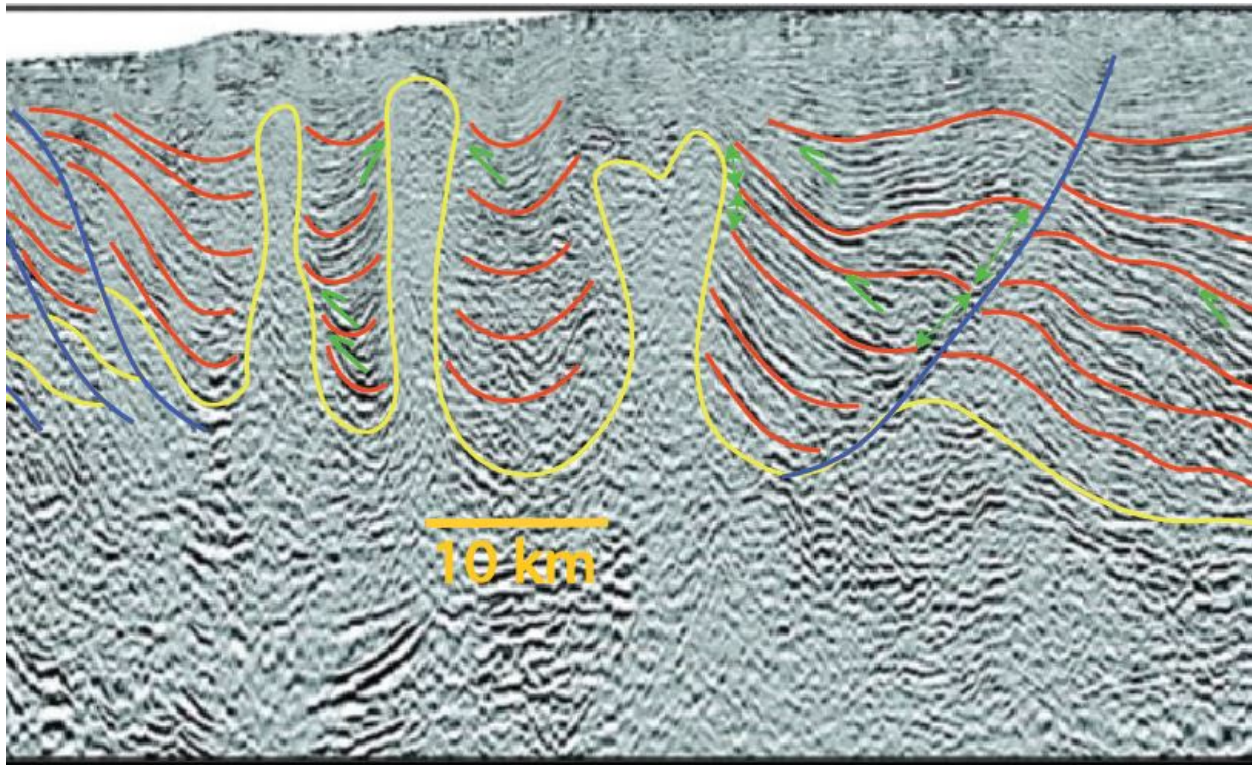


Figure 67: A zoom-in caption of seismic data with a basic interpretation scheme (Yellow Markers: Diapir-Like shale intrusions originated from Akata Shale Formation, Red Markers: Deltaic sediments, Green Markers: Sequence terminations such as pinch-outs, onlaps, toplaps, Blue Markers: Normal and thrust faults of the deltaic system) (interpreted after Corredor et al., 2005).

IV. Accretionary Wedges/Prisms: Active Margins

As it is stated by Meschede, 2015; *accretion defines a process at a convergent plate margin above a subduction zone where material of the subducting lower plate is scraped off and transferred to the overriding upper plate*. Following the subduction process, the *offscraped material* gets accumulated in a wedge-shaped stack of sedimentary layers, which may also contain some offscraped material from the oceanic crust of the subducting plate. Such geologic formations take place directly at the boundary between two converging plates, and called the *forearc region of the convergent plate boundary*. The accretionary wedges can evolve as compressional fold-and-thrust belts composed of (i) oceanic-plate deposits, and (ii) continentally derived trench-floor sediment from a nearby continental plate.

Fold and thrust belts associated to mass transport complex and gravity-driven systems display shallow detachment development. In deepwater settings, these detachment settings lie within poorly lithified, high porosity, water-rich, fine grained sediments and they consecutively can be completely chaotic, and exhibit ductile behavior (Morley et al., 2017).

We see in examples like Zagros Mountains (Colman-Sadd, 1978; McQuarrie, 2004), Jura Mountains (Laubscher, 1977), Appalachians (Wiltschko and Chapple, 1977), Brooks Ranges, Alaska (Homza and Wallace, 1997) and Svalbard (Morley et al., 2017) that the detachment folds are generally more concentrated through the external zones of fold and thrust belts, where more competent units are detached above a weak salt/shale unit.

Even though the improvements of seismic imaging technologies reduced the mis-interpreted/over-interpreted shale features (e.g. chaotic facies in diapirs, and overthickened regions) to a certain degree, as it is stated by Morley et al., 2017; there are evidence that shale rich units have been squeezed out of some areas (typically synclines) and moved by creep, pressure solution cleavage, pressure dissolution, folding, large and small-scale faulting into other areas (e.g. the inner fold and thrust belt and diapir belt of the Niger Delta, see reviews of Morley & Guerin, 1996; Connors et al., 2009; Wiener et al., 2010; Kruger and Grant, 2012). The following section will be summarizing three geologic examples of this phenomena, namely; (i) Makran, (ii) Baram Delta, (iii) Barbados and Trinidad Accretionary Prism, and (iv) Cascadia, in relation with shale tectonism and high sedimentation rates in a clay and fluid-rich environment enhanced by the tectonic setting (i.e. delta or prism).

i. Makran Accretionary Prism/Wedge

Makran accretionary wedge is formed by the subduction of the Arabian Plate beneath the Eurasian plate at ~4 cm/yr offshore Pakistan and Iran throughout the Cenozoic (Harms et al., 1984b; Burg, 2018; Yang et al., 2020). The prism owns the largest documented sediment input (Gutscher & Westbrook, 2009) of the world with about 350 km length (e.g. Smith et al., 2012) and sediment thicknesses up to 7.5 km (Davis et al., 1983; Kopp et al., 2000). Today, the Makran Accretionary Prism is associated with the ongoing subduction of the oceanic lithosphere flooring the Gulf of Oman at about 2 cm/yr in a roughly N–S direction, beneath the Iran and Afghan Blocks (McQuarrie et al. 2003; Bayer et al. 2006; Vigny et al. 2006; Masson et al. 2007 in Burg, 2018). Yang et al., 2020, states that; although the Makran accretionary prism started to grow since the Cretaceous, it was still completely submarine until ~12 Ma ago, which is known from a submarine olistostrome, that allowed the growth of minibasins and represent the entire Coastal Makran today (Ruh et al., 2018). Since the offshore part of the prism is defined mainly by the last ~10 Ma of wedge growth, the onshore and offshore sections of Makran subduction zone are studied separately.

Burg (2018) described four major onshore compartments of Makran: (1) North Makran, (2) Inner Makran, (3) Outer Makran and (4) Coastal Makran (Burg et al., 2013; Dolati, 2010) (Figure 68).

1. North Makran contains Cretaceous to at least Paleocene deep-marine sediments and volcanic rocks, in tectonic '*mélanges*'. The tectonically assembled rocks of North Makran show weak folding.
2. Inner Makran is dominated by Upper Eocene to Lower Miocene terrigenous sandstone–shale sequences of 'flysch'-type sediments, which are thought to be part of a proto-Indus fan recording the Himalayan collision (e.g. Kopp et al., 2000; Ellouz-Zimmermann et al. 2007a; Carter et al. 2010).
3. Outer Makran exposes mostly Lower–Middle Miocene sediments including deeper-water sandstones and marls, grading up-section into slope and coastal deposits and locally shallow-water limestones.
4. Coastal Makran comprises Upper Miocene and younger sediments and displays weak deformation and normal faulting not seen in other units.

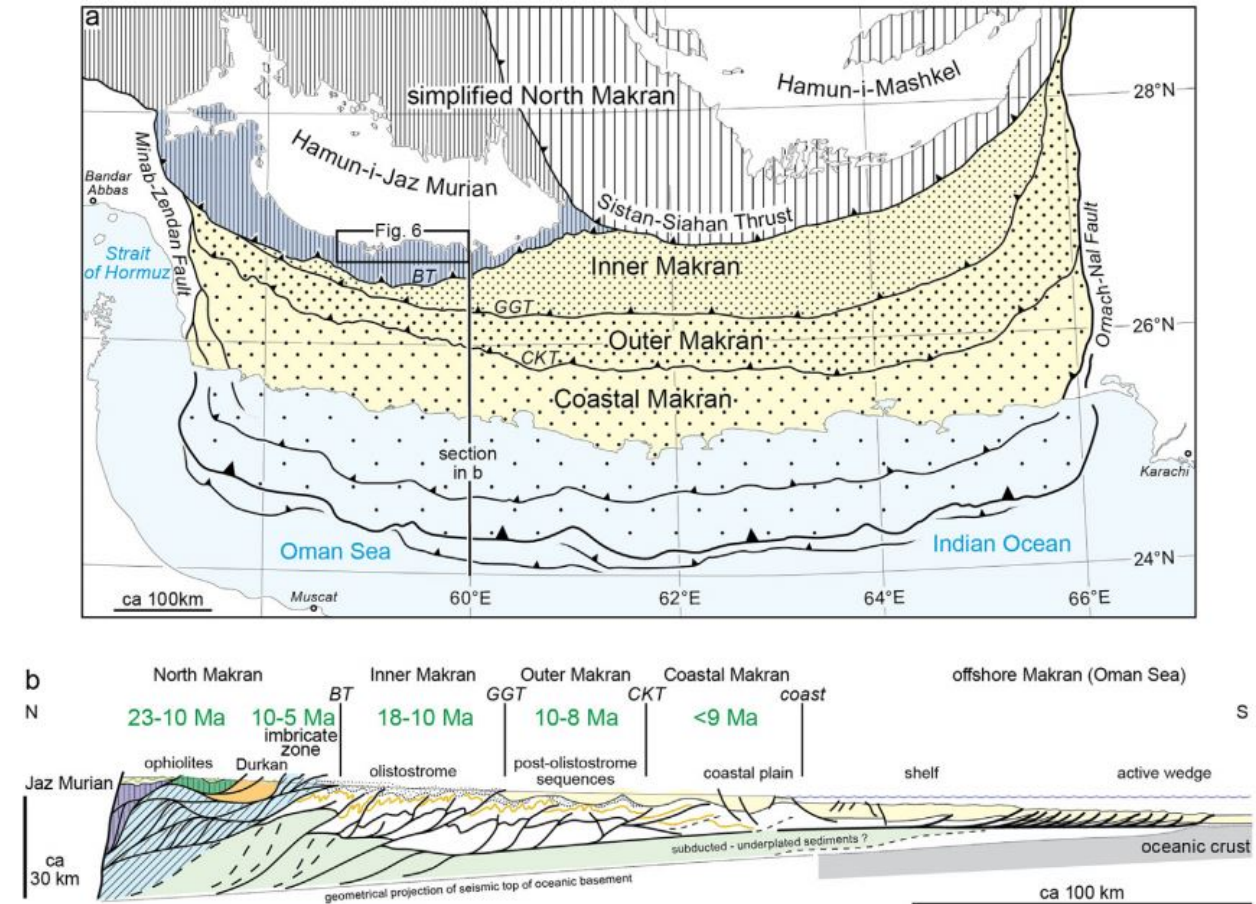


Figure 68: Compartmentalization of Makran Accretionary Prism (image retrieved from Burg, 2018).

Burg et al., 2008 described the Makran Olistostrome as a ‘matrix-supported chaotic formation with a shaly, muddy matrix and ‘mm-to-km-sized blocks of various compositions’, which exhibits a weak scaly fabric and floating folded, disrupted sandstone beds, ball-and-pillow structures, and contorted laminae, typical for soft-sediment deformation structures (Mills, 1983) (e.g. water-saturated, undrained, unconsolidated argillaceous sediments (Dehandschutter et al., 2005).

In terms of shale tectonism, the Makran area is quite noticeable due to its impressive minibasin-like domain developed on the regional-scale olistostrome underlined a shaly-matrix (Ruh et al., 2018). The numerical experiments carried out by Ruh et al. (2018) in order to (i) investigate whether the growth of such minibasins above a shale-dominated unit is feasible and (ii) how the presence of a regional, shale-dominated olistostrome may affect the structural evolution of active accretionary wedges.

The strata overlying the Tortonian olistostrome in the Iranian part of the Makran accretionary complex consist of shallow-water, sandstone- and marl-dominated turbiditic sequences (Dolati, 2010) and they occur in a number of concentric, synformal basin locations in the region (Ruh et al., 2018). Figure 69 displays two of these asymmetric basins associated with typical halokinetic structures to describe their sedimentary pattern.

Figure 69a depicts the southern basin covering an area of 35 km (N-S) by 42 km (W-E) and consisting of an amalgamation of four smaller basins. According to the interpretation of Ruh et al. (2018), these four basins are now either separated by narrow bands of shales comparable to the matrix of the underlying olistostrome or totally welded (similar to salt). The largest of the amalgamated minibasins in this area has a stratigraphic thickness of ~ 4.5 km and it shows an upward-increasing width indicating basin expansion over the surrounding olistostrome shale until it joined the adjacent minibasins. Halokinetic-type sedimentary structures such as large lateral hooks can also be observed in this satellite image figure with a large flap in the southwestern basin indicating a change in tilt direction during basin growth (Figure 69a).

Figure 69b showcases the 22-km-long (N-S) and 16-km-wide (W-E) northern basin with an approximate ~ 4.25 km thickness. Sedimentary beds observed in this minibasinal closure dip toward the N-NE with an open syncline at the top of the stratigraphic succession (Ruh et al., 2018). This isolated minibasin becomes narrower upwards (like a bowl-shape minibasin) and display a relatively homogeneous width in its lower to middle part. Within this setting, several unconformities separate the sedimentary sequences and one of the most prominent feature is a large flap located in the lower western part of the minibasin (similar to flap structures) observed in salt tectonics). Additionally, most of these sedimentary beds show drag folding close to the minibasin boundaries, while a large hook is observed below the large sedimentary unconformity located near the middle part of the minibasin (Ruh et al., 2018) (Figure 69b).

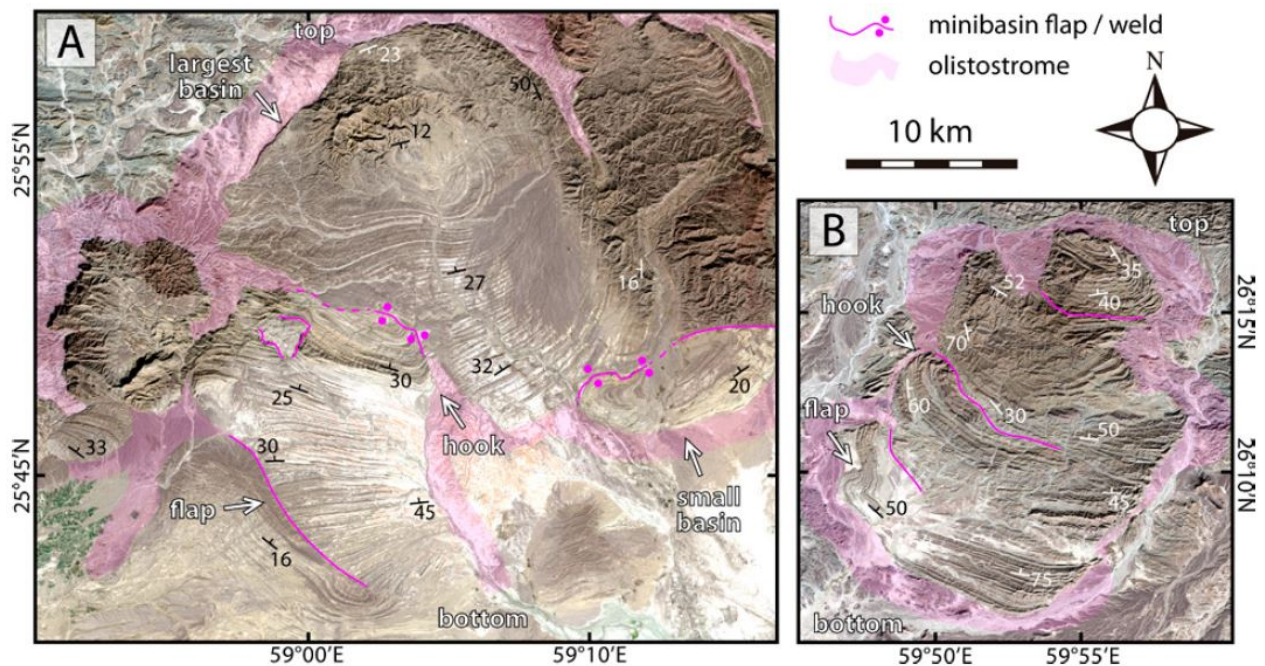


Figure 69: Natural color Landsat satellite images of shale-related minibasin sedimentary structures in Iranian Makran. Minibasin in A is an amalgamation of four smaller single basins. Pink lines are shale walls, welds, and bedding onlaps. Pink shading shows ductile olistostrome withdrawal (partly covered by Quaternary deposits) (image retrieved from Ruh et al., 2018).

Diminishing size of olistoliths from North to South point out to a source coming from NE Iranian Makran. Based on their results, Ruh et al. (2018) concluded that; *rapid mass-flow emplacement triggers thickening of the rear of the wedge while minibasins grow in a more frontal, tectonically quiet region and further wedge growth leads to a jump forward of frontal accretion explaining the structural characteristics of the Coastal Makran.*

Onshore coastal Makran is characterized by scattered synclinal basins with short axes and thick sedimentary sequences. Different than the rest of onshore Makran compartments, this region was exposed to further convergence and shortening and hence led to horizontal squeezing of these synclinal province. Satellite images and numerical modeling suggest that these synclines can be interpreted as shale-related minibasins (Ruh et al., 2018).

In an overall sense, as it is stated by Ruh et al. (2018), even though the sedimentary structures of the western Makran did not evolve on rock salt affected by salt tectonism; the *size, distribution, and general tilt* of these minibasins with respect to tectonic vergence are comparable to minibasins described above salt horizons as in the Sivas Basin, Turkey (Kergaravat et al., 2017) or in the Gulf of Mexico (e.g. Hudec et al., 2009), which suggest a very plausible analogy of shale mobilization with salt.

Despite the remarkable Shale Tectonism examples proposed in the selected literature references given above, in terms of accessibility, Makran still stands as a difficult geo-location for the international research community. For this reason, we will be proposing Cheduba-Ramree region of Rakhine State, Myanmar as an alternative and perspective research ground for Shale Tectonism (). Coastal portion of Rakhine state has been previously reported as a tectonically controlled system with highly pressurized fluids and mobile shales at depth without a major control on the sedimentation pattern and strata (Maurin & Rangin, 2009), hence it is not included in this portion of the thesis under *Review of Existing Geodynamic Settings Affected by Salt-Like Shale Tectonics* reflecting Shale Tectonism Bibliography. However, we will be looking at fieldwork observations conducted around the same region for our PhD research with a perspective scope of shale mobilization taken place at a shallower depth similar to Makran following the Ceduna Sub-Basin seismic case study (Chapter 5 and forward).



Figure 70: Upper Panel: Satellite image showing locations of Makran, Iran (highlighted with yellow star) and Ramree-Cheduba Region of Rakhine State, Myanmar (highlighted with red question mark). Lower Left Panel: Zoomed-in geo-location of Makran region of Iran with minibasin-like features seen on satellite view. Lower Right Panel: Zoomed-in geo-location of Ramree-Cheduba region of Rakhine State, Myanmar with minibasin-like features seen on satellite view. Note the similarity of rounded/circular patterns detected on satellite view of these two regions seen on the lower panels (image courtesy of Google Earth)

ii. Baram Delta

The offshore portion of Borneo is a deltaic province with numerous delta systems composed of Mid Miocene-to-present day marine deltaic deposits (up to 10 km thick), displaying shale-related gravity structures such as growth faults, shale diapirs, toe thrusts and (more unusually) inversion folds and thrusts related to episodic phases of compression (e.g. James 1984; Sandal 1996). Baram Delta stands as a Plio-Pleistocene deltaic system located at the western part of the Brunei shelf (Rensbergen & Morley, 2000) *on an active post-collisional margin*, which makes it unique among other passive margin deltas due to its setting; being developed on a tectonically active margin has led the inner shelf and onshore part of the delta to undergo episodes of (i) shortening, (ii) inversion of older extensional growth faults, and (iii) thrusting & folding of the continental slope region (e.g., James, 1984; Sandal, 1996; Morley et al., 2003; Morley, 2007). As a result of this aspect, Baram Delta displays a mixture of typical delta-associated gravity tectonics (e.g. growth faults, mobile shale tectonics, toe thrusts) and episodic compressional tectonics (Sandal, 1996; Morley et al., 2003; Morley et al., 2008) (Figure 71).

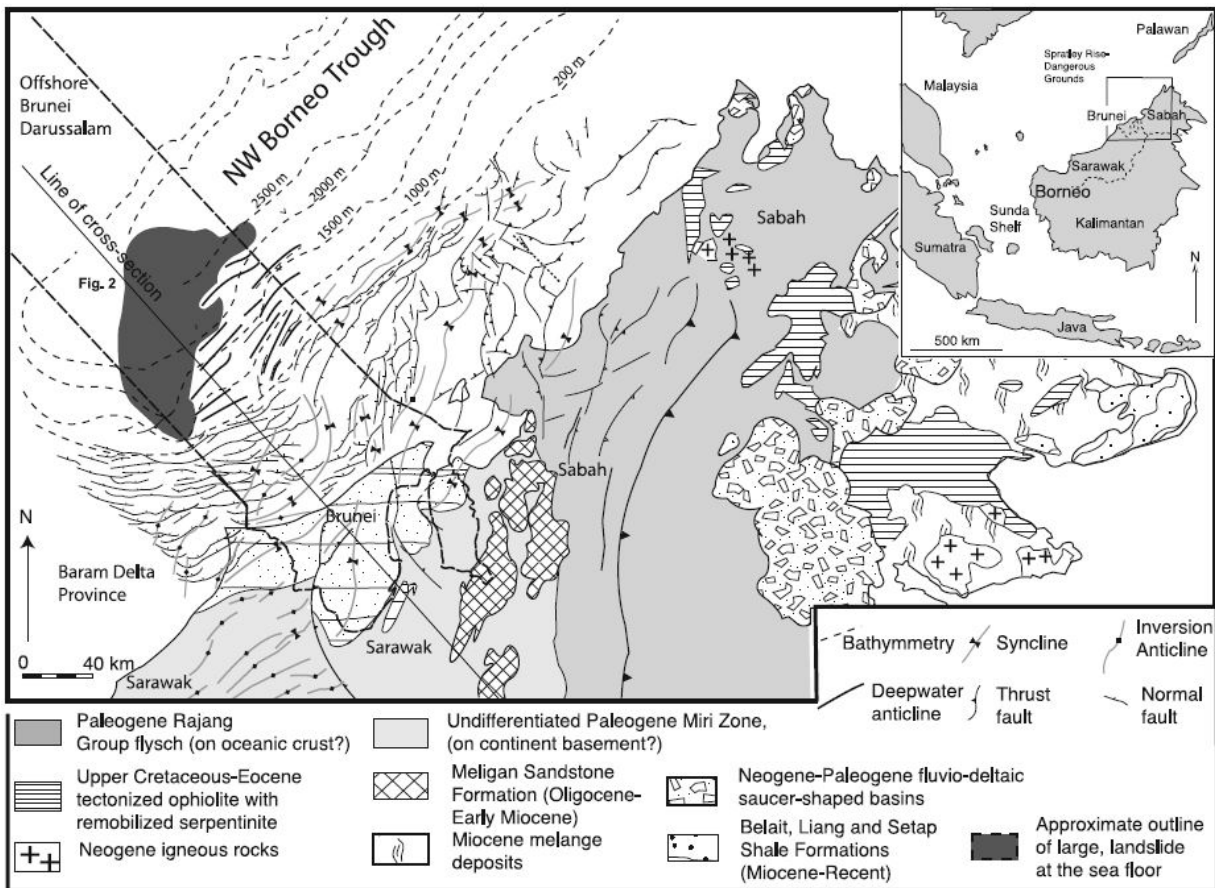


Figure 71: Location map of northwest Borneo, modified from Morley et al., (2003) (image retrieved from Morley et al., 2008).

The basal detachment zone of the deltaic system is defined by the Setap Formation. As it is stated by Rensbergen & Morley, 2000; the structure of the Baram delta is characterized by a Gulf of Mexico structural style (e.g. Bradshaw & Watkins, 1996) of parallel, down-to-basin growth faults perpendicular to the direction of sediment supply from the Baram river, which root the overpressured fine-grained detachment unit (Setap Formation) at the base of a thick, rapidly prograding sequence of shelfal, shallow marine to continental sediments (Morley et al., 2008). As a consequence, shale patterns mimicking viscous flow are emerged creating growth faults, overpressured shale intrusions into the overburden, and toe folds and thrusts (e.g., James, 1984; Sandal, 1996; Morley, 2003a). The mobile shale unit is reported to be several km thick as indicated by the relief of the gravity-driven structures, in particular growth faults with depocenters up to 7 km thick (Morley et al., 2008) (Figure 72).

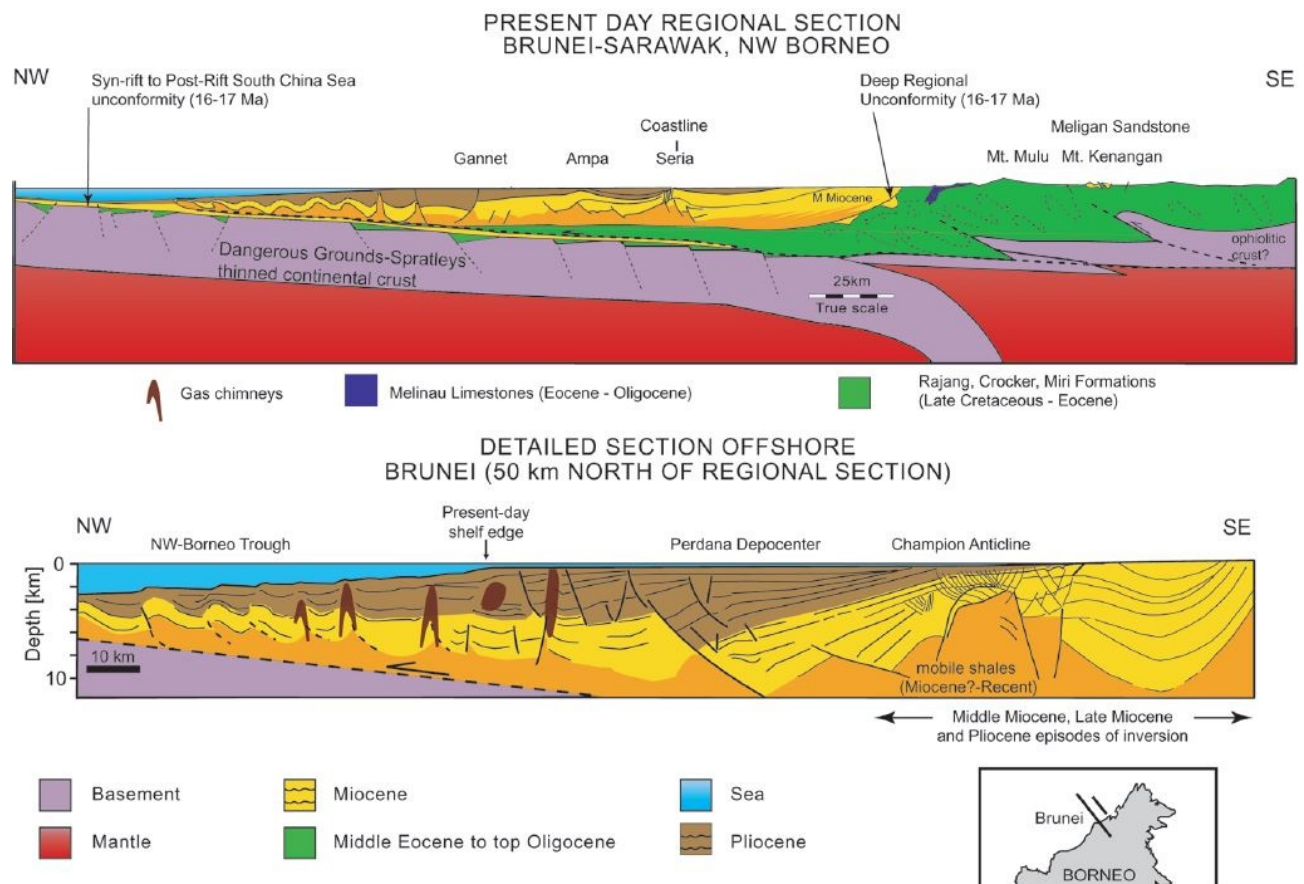


Figure 72: Regional cross section illustrating the large-scale structural setting and geometry of the Baram Delta Province. Deep structure is schematic, but is based on gravity and seismic reflection data. The more detailed cross-sections focus on basin geometry and are based largely on industry seismic reflection data. NW Borneo [Morley et al., 2003; Sandal, 1996] (image retrieved from Hall & Morley, 2004).

From analogical point of view with salt, the regional view seen on the upper section of Figure 72 with the mobile shale above the folded units strikingly resembles the cross-section that has been depicted by Legeay et al. (2019) from Sivas Basin, Turkey (Figure 73).

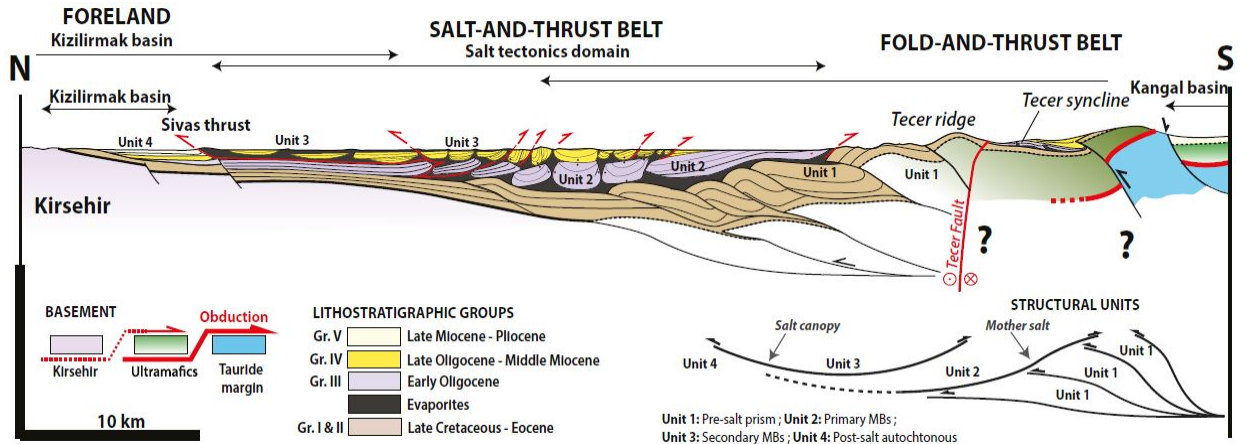


Figure 73: The cross-section from Sivas Salt Basin, Turkey (for detailed information see Legeay et al., 2019).

The study of Warren et al. (2010) utilized a 3D seismic dataset covering fluid escape features across several sediment-damming growth anticlines and a large landslide below the mouth of the Baram Delta with an aim to detect organic geochemical, isotopic, and seismic indicators of fluid flow in pressurized growth anticlines and mud volcanoes. Following the investigation of fluid escape features across several sediment-damming growth anticlines and a large landslide below the mouth of the Baram Delta, they concluded that;

- Mud volcanoes show a sequence of events indicating (i) *inflation*, (ii) *breach or fluid release*, and then (iii) *deflation of the structure*, which corresponds to the transition from sea-floor mound to pockmark and to a transition from convex reflectors and loss of the BSR in the mound to concave reflectors and the re-establishment of the BSR beneath the pockmark. Even though the purpose of their study focuses on *hydrocarbon exploration implications* for mud and salt diapir provinces, the seismic data display remarkable examples of shale mobilization patterns resembling salt. Figure 74 shows seismic representations of coring sites piercing through shale-cored growth anticlines in the region (note the truncations such as *onlaps*, *toplaps* and *pinch-outs* around the shale-cored growth anticlines). Figure 74a Figure 74b and Figure 74c show onlap truncations to the sides of Site 094, Site 013 and Site 161 respectively adjacent to shale-cored folds (drilling points).

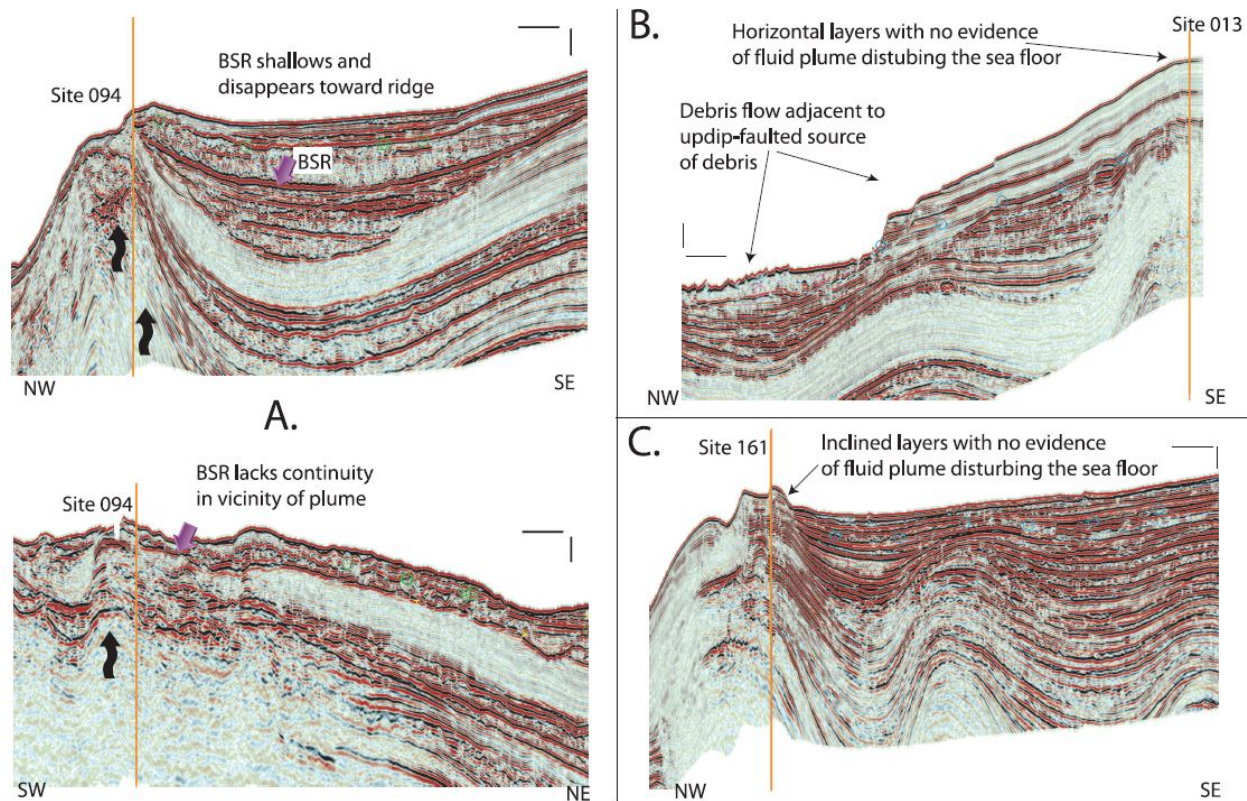


Figure 74: Seismic sections through sites of isotopic interest. This organic group 1B site sits atop a shale-cored growth anticline with fluid plumes rising to the sea-floor surface and associated evidence of plume-related sediment collapse. The ridge is a result of ongoing gravity-driven compressional deformation, which also causes the bottom-simulating reflector (BSR) horizon to rise and break up as it approaches the sea floor. Note the disturbance and the discontinuity of the BSR caused by rising fluid plume in the vicinity of sample site 094 (image retrieved from Warren et al., 2010).

- The gravity-driven and active growth anticlines observed at offshore Brunei overlie a zone of ramping thrusts while the Miocene–Pliocene anticlines and the mud volcanoes of Brunei accretes in a tectonic setting where subduction ceased in the early Miocene (Hall and Morley, 2004). As a result of this *subduction ceasing* beneath the wedge setting, Brunei stands apart from many other mud-rich growth anticline systems with active accretionary wedges atop or adjacent to zones of active subduction (e.g. Mediterranean and Tethyan collision belts).
- As it is proposed by Morley (2007a), Brunei has one of the most acute angles recorded for any submarine critical-taper wedge due to its very low surface slopes (1–2.5°) and basal detachment dips (2° to 5°), which would require the basal pore-fluid pressures to be *near lithostatic* for the wedge to propagate at such angles. Therefore, regionally quiescent tectonic setting for mud diapirism in the Brunei slope and rise is perhaps more reminiscent of argilokinesis along passive margins similar to Niger and Rhone deltas.
- Moreover, if these angles are compared to those of typical orogenic belts, Brunei plots very near fields occupied by compressional belts with a salt decollement. Study of Ford (2004) points out to very low surface angles (<18°) in the slope and rise prisms of salt-prone compressional terrains on some of the world's orogenic belts. Warren (2006) describes this property of salt-prone settings as; *any sediment pod sitting atop a thick salt mass will tend to sink or slide and rotate atop the salt mass as it seeks gravitational equilibrium atop the fluid-like salt body.*

Figure 75 summarizes the statements of Warren et al., 2010 in a comparative manner of *salt vs shale diapirism* following their conclusions points (please see the paper of Warren et al., 2010 for details and additional figures/tables);

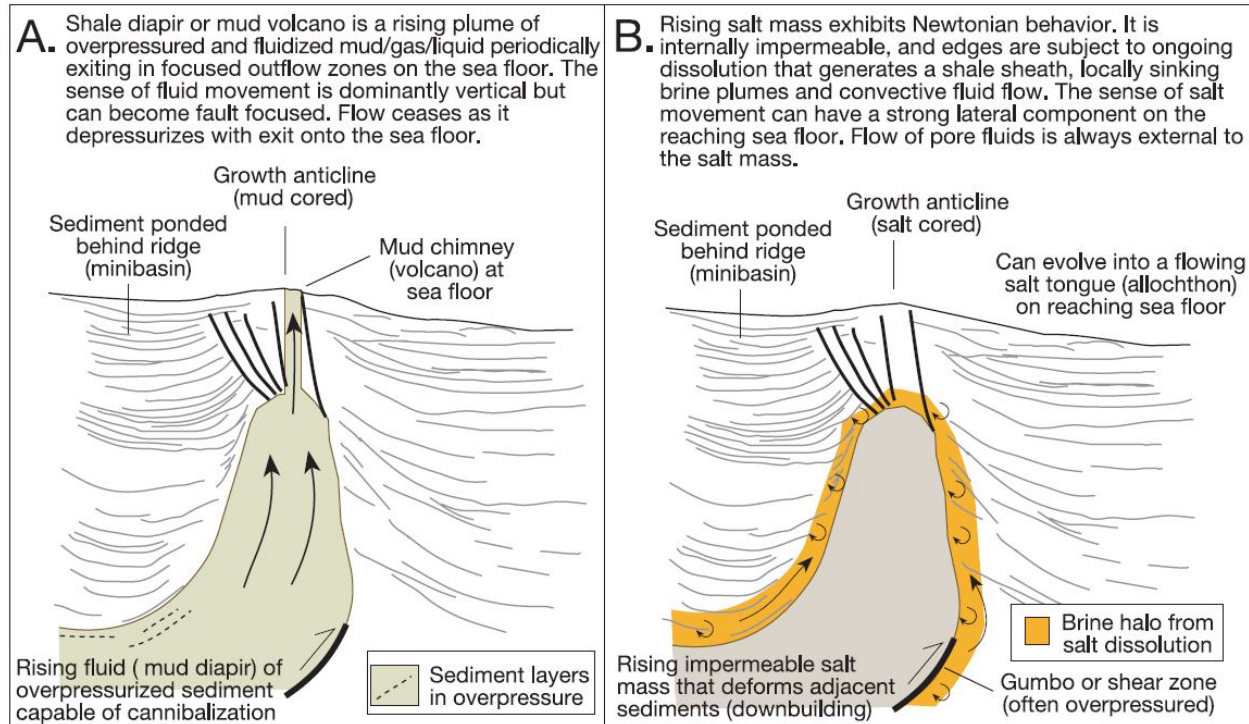


Figure 75: Comparison of signatures of mud and salt diapirism. (A) Mud diapirism indicates a zone of fluid-charged overpressured fine-grained sediment (mostly mud). It can rise via stopping subvertical mud chimneys and periodically break out onto the sea floor. The seismic signature indicates zones of active or former fluid charge. The diapir as seen in the seismic signature is not a lithology but typically a gas effect. As such, the diapir zone can expand and encapsulate or cannibalize adjacent sediments without disturbing the bed orientation. (B) Salt diapirism indicates a zone of flowing impermeable salt (halokinesis). There is both a vertical and horizontal component to this flow and a strong response to sediment loading, and, on salt reaching the sea floor, it is tied to downslope gravity spreading. The seismic signature of a salt diapir or allochthon is a direct indicator of the salt mass, which is always impermeable. Flow sets up a mobile mass of impervious salt with edges subject to dissolution (like a block of ice). This mass and its brine halo focus fluid flow and overpressuring about its edges (see Warren, 2006, chapters 6 and 8 for a detailed discussion of relevant literature) (image retrieved from Warren et al., 2010).

iii. Barbados and Trinidad Accretionary Prism

The Caribbean active margin, which is geodynamically located at the triple junction area between (1) the North American plate, (2) the South American plate and (3) the Caribbean plate is characterized by complex and multidirectional recent deformations. Within this complex, North and South American plates subduct westward underneath the active margin of East Caribbean, which highlights the geometry of the subduction of the Atlantic oceanic lithosphere beneath the Caribbean plate (Deville et al., 2015). To the north of the active margin, the subduction slab continues and extends far to the west below Puerto Rico, while it sinks below the island of Trinidad and the Paria Peninsula in north-eastern Venezuela to the south of the active margin (Deville and Mascle, 2012).

As it is stated by Deville et al., 2015; the latest GPS studies shows that the Caribbean plate is moving E-NE in the direction $N70^\circ$ at a speed of 20 ± 3 mm/yr with respect to the North American plate and the convergence associated with the subduction below the Lesser Antilles volcanic arc causes the deformation of the sedimentary pile and the formation of the Barbados accretionary prism which is one of the largest accretionary wedges in the world (Westbrook, 1975, 1982; Stride et al., 1982; Westbrook et al., 1982, 1983, 1984, 1988; BijuDuval et al., 1982, 1984; Westbrook and Smith, 1983; Mascle et al., 1988; Mascle and Moore, 1990; Henry et al., 1990; Deville and Mascle, 2012) (Figure 76). The recent study of Morley et al., 2018, points out to the significant studies of Barbados accretionary prism (e.g. Maltman et al., 1997; Labaume et al., 1997) as a starting point for understanding many of the common characteristics of major shale prone thrust zones.

The foreland portion of the Barbados Accretionary Prism showcases deformation processes associated with the relative displacement between the South and North American plates, moreover, the Orinoco turbidite deposits partly cover the accretionary prism in its southern portion; close vicinity of Trinidad-Venezuelan continental platform seafloor displays a regular and punctually disturbed patchy pattern with isolated mud volcanoes (Brami et al., 2000; Rutledge and Leonard, 2001; Deville et al., 2003; Deville et al., 2004; Moscardelli et al., 2006; Deville et al., 2006; Deville and Mascle, 2012), while the downslope geometry of the seafloor of the southern Barbados area is controlled by tectonics and mud volcanism processes generating local highs and syntectonic piggyback basins (Biju-Duval et al., 1982; Mascle et al., 1990; Gonthier et al., 1994; Huyghe et al., 1996, 1999, 2004; Callec et al., 2010; Faugères et al., 1993; Griboulard et al., 1991, 1996) (Deville et al., 2015) (Figure 77)

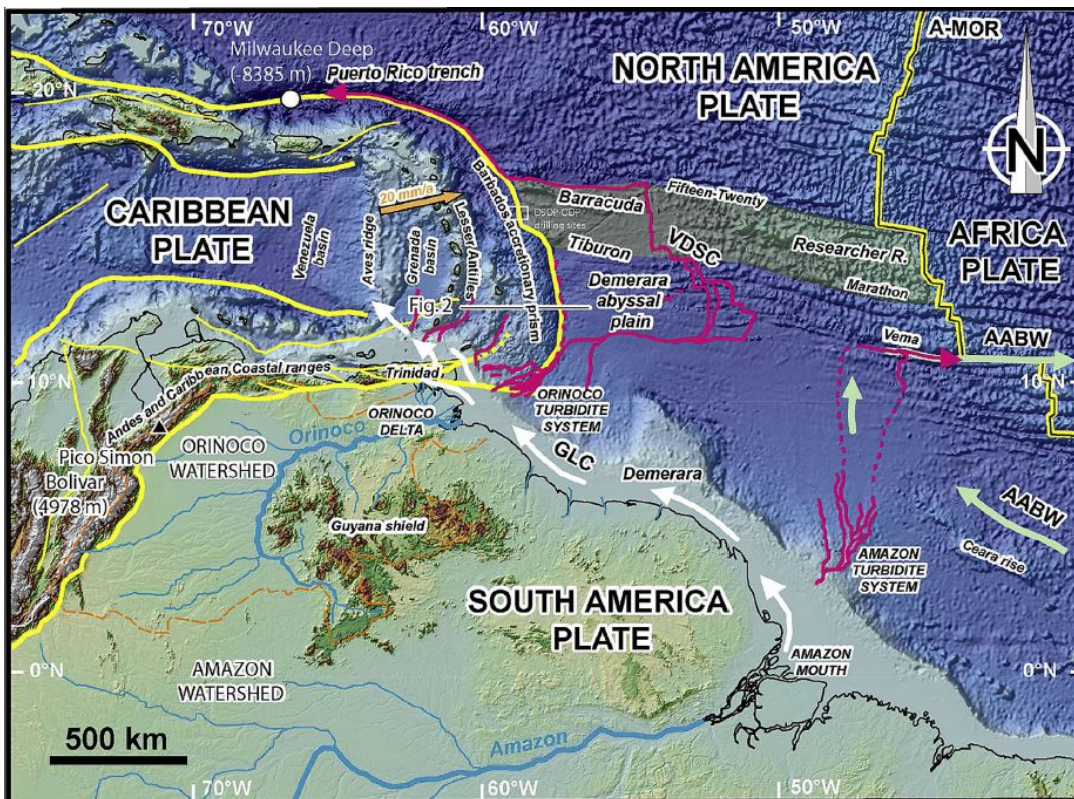


Figure 76: General sketch-map of the Orinoco siliciclastic system showing its close interaction with the compressional front of the Caribbean plate. Orange arrow: vector displacement of the Caribbean Plate with respect to the North American Plate. Red lines and arrows: turbidite systems; AABW: Antarctic BottomWater (Green arrows; location from Rhein et al., 1998); GLC: Guyana Littoral Current (white arrows); VDSC: Vidal Deep Sea Channel. A-MOR: Atlantic Mid-Oceanic Ridge. (image retrieved from Deville et al., 2015).

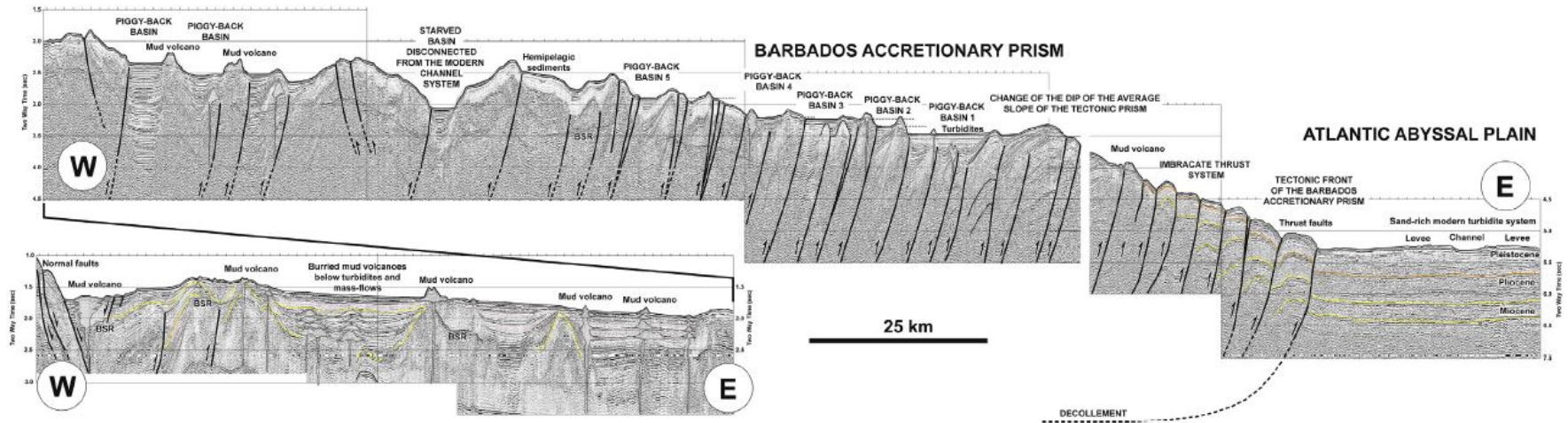


Figure 77: Seismic transect across the southern part of the Barbados accretionary prism and the Atlantic abyssal plain. Light grey surfaces correspond to the main mud volcanoes and pink surfaces are transparent bodies that correspond partly to large-scale mass-flows. Dark grey lines show the main BSR. Yellow lines outline some good reflectors (with no specific interpretation). (image retrieved from Deville et al., 2015).

Mud volcanism observed in Trinidad (located at the southeastern foreland portion of Barbados Accretionary Prism) takes place in the plate boundary area between the Caribbean plate and the South American plate at the junction between the prism and the transform system of northern Venezuela (Speed, 1985; Stein et al., 1988; Robertson and Burke, 1989; De Mets et al., 1990) and develops as an active mud volcano belt from the Barbados tectonic wedge to the fold-thrust belt of northern Venezuela. (Biju-Duval et al., 1982; Brown and Westbrook, 1987; Deville et al., 2003a, b, 2006) (Battani et al., 2010). The area is bounded by the Southern Range anticline to the south, the Los Bajos fault to the north and east, and the Erin syncline to the north (Battani et al., 2010; Henry et al., 2010) (Figure 78-Figure 79).

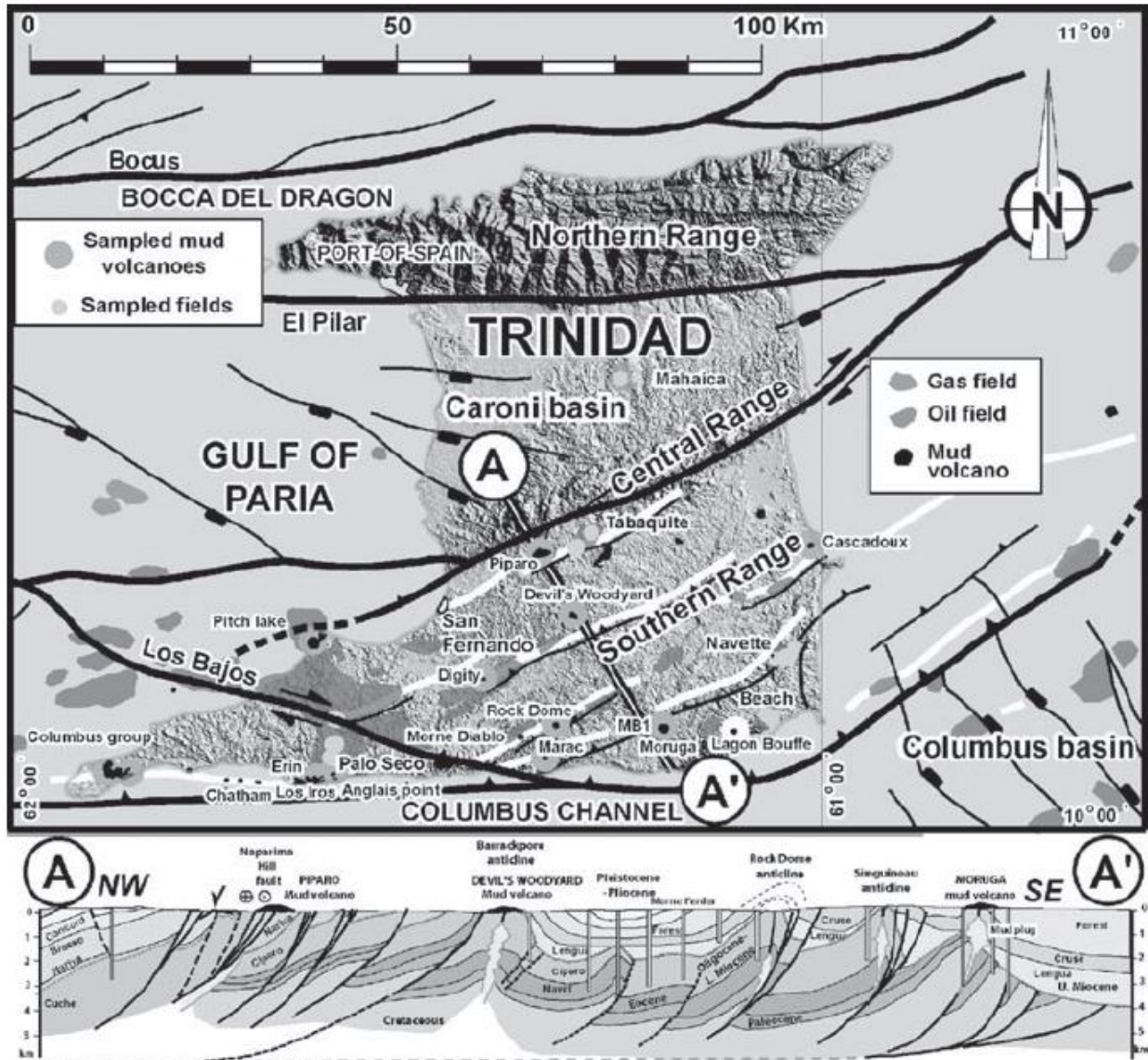


Figure 78: Geological Elements and Location Map of Trinidad-Barbados (image retrieved from Battani et al., 2010).

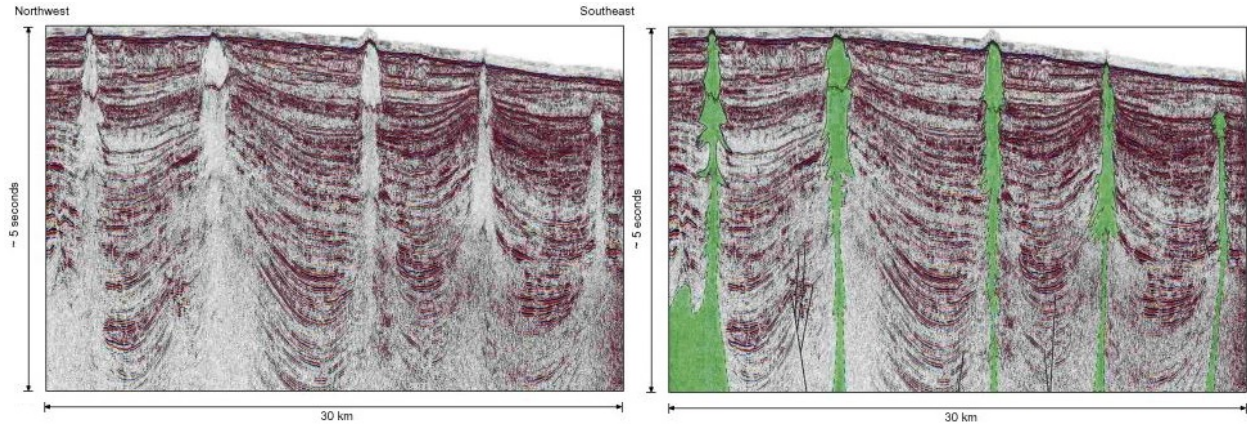


Figure 79: Uninterpreted (left) and interpreted (right) seismic sections, encompassing ~5 seconds travel-time depth shows mud volcano trains that have been repetitively active for well over 2 million years. This image shows the close relationship between deep, remobilized muds and compressional anticlines along the northeastern boundary of the Caribbean and South American plates. Data provided by the Ministry of Energy and Energy Industries, Trinidad and Tobago (image retrieved from Lesli J. Wood, in *Regional Geology and Tectonics: Phanerozoic Passive Margins, Cratonic Basins and Global Tectonic Maps*, 2012).

Mud volcanoes of the region are mapped along the extent of the Southern Range anticline, seismic data of which showed these features associated with the core of anticlines. Previously, similar subsurface structures have been depicted as deep diapiric features with the frontal edge of a buried fold and thrust belt interpreted at depth (Duerto and McClay, 2002). As it is stated by Henry et al. (2010), “mentioned transpressional fold and thrust belt is extrapolated to incline SW-to-NE, from Venezuela through Trinidad, parallel with the indicated mud volcano trend”. In 2009 publication of Deville, when the mud volcano material collected from the core data found to be corresponding to a stacking of mud flows or to gravity destabilization on the slopes of the mud volcanoes, some of which are classified rich in carbonated diagenetic crusts (Aloisi et al., 2000; Deville et al., 2006). Moreover, mud volcanism activity interacted with high recent sedimentation rate (e.g. eastern offshore Trinidad), are noted to display a Christmas tree geometry related to the stacking of successive edifices of subsurface mud volcanoes (Deville, 2009) (Figure 80).

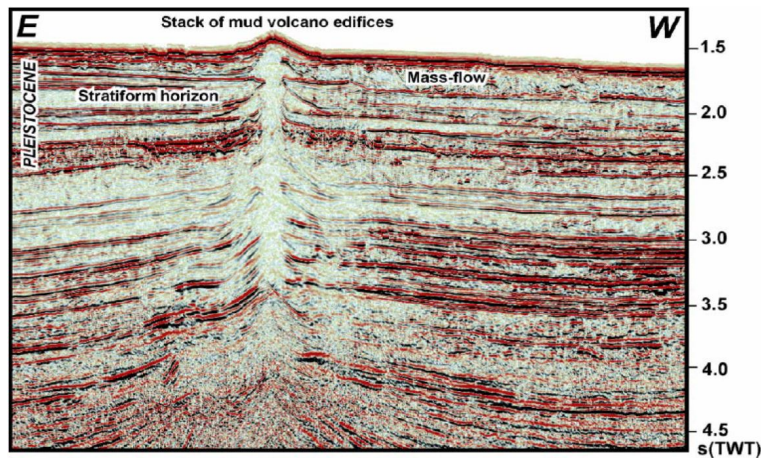


Figure 80: An example of seismic profile across a mud volcano in the eastern offshore of Trinidad (courtesy of Shell, Agip, Petrotrin). Note the stacking of different volcanic edifices. This “Christmas tree” structure is probably the result of the cyclic development of volcanic edifices during the Pleistocene periods of high stand (low sedimentation rates, clay-rich well stratified sediments) and of the draping of the sedimentary volcanoes during the periods of low stand (high deposition rates, notably mass-flows, Brama et al., 2000), but the mean expulsion rate of mud is not necessary directly related with sedimentation rate (image retrieved from Deville, 2009).

Based on these studies and the data collected from unlithified cores, the fractal-like nature of the scaly fabric is observed on clays and the scaly fabrics of Barbados décollement were interpreted by Labaume et al. (1997) to result from porosity collapse as clay particles rotated and aligned (Morley et al., 2018). It is also known that Barbados accretionary prism and small mass transport complexes (MTCs) (Alsop et al., 2007; Alsop and Marco, 2014) display examples of strain localization in a narrow zone at the base of the sliding mass occurring even in unlithified sediments at depths less than 1 km. Even the initial flattening fabric observed at such shallow depths may be related to mechanical porosity loss and development of overpressure, as soon as the clay mineral diagenesis starts between 60° and 80° C (particularly smectite-illite transition; Hower et al., 1976, Buller et al., 2005) the effect of mechanical compaction becomes less important and authigenic mineral growth dominates the changes in (i) pore size, (ii) volume and shape, (iii) overpressure development, and (iv) shale fabrics (Morley et al., 2018).

iv. Cascadia

The Cascadia continental shelf is underlain by a thick sedimentary sequence extending from the Eel River basin in the south to offshore Vancouver Island in the north (McNeill et al., 2000). The present-day Cascadia Accretionary Prism and volcanic arc is established (~40 Ma) with disappearance of the Farallon plate and development of the Juan de Fuca plate (Humphreys, 2008). As it is stated by Wannamaker et al., 2012; in middle Cenozoic time, the arc extended farther south to present day southwestern Nevada but has shortened northward with migration of the Mendocino triple junction, formation of a growing slab window, and growth of the San Andreas-Walker Lane strike-slip fault systems (Wilson et al., 2005; Faulds and Henrys, 2008; Colgan et al., 2011; Busby, 2013). Cascadia back-arc and fore-arc regions are underlied by the Mesozoic and Paleozoic metamorphic, volcanic, and plutonic basement blocks (Wright and Wyld, 2006; Dorsey and LaMaskin, 2007; Dickinson, 2008; Blakely et al., 2011). The Siletz volcanic terranes of the region are accreted in the early Cenozoic and lie beneath the forearc and arc from north-central Oregon through Washington to southernmost Vancouver Island (Wells et al., 2014; Wannamaker et al., 2014) (Figure 81).

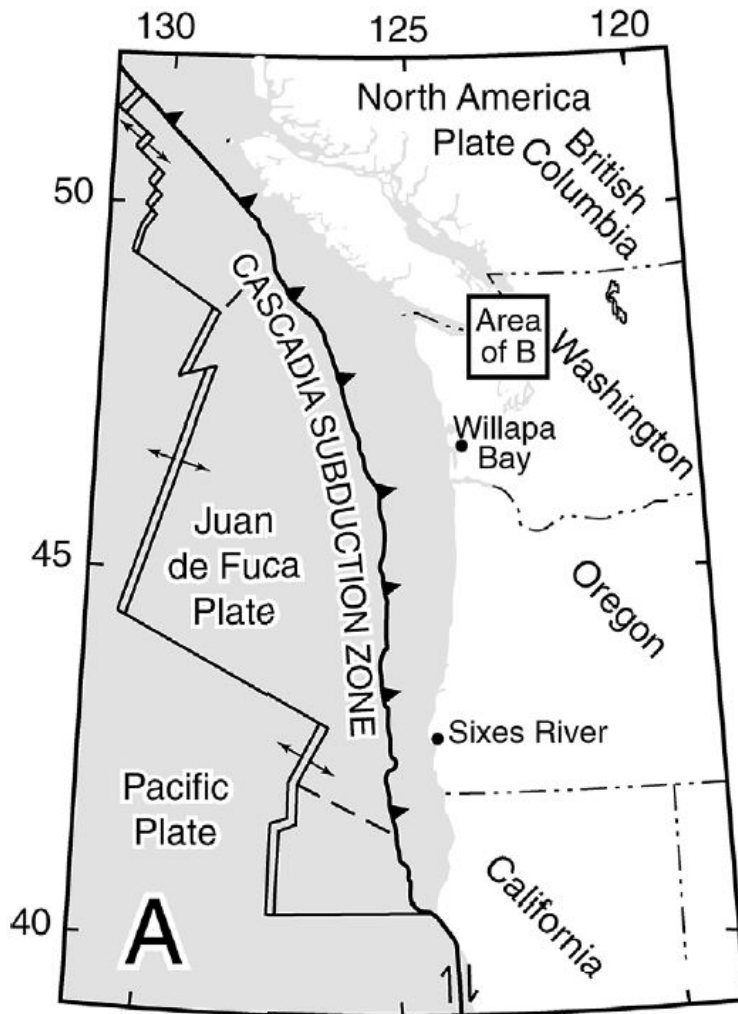


Figure 81: Geological setting of the Cascadia active tectonic continental margin associated with the Cascadia subduction zone, which is made up of the Juan de Fuca and Gorda plates (image retrieved from Williams et al., 2002).

As it is stated by Morley et al., 2018; *local negative-polarity seismic reflections of Oregon accretionary prism indicate well-defined zones of high fluid pressure within proto-thrusts and frontal thrusts, which are bounded by discrete permeability barriers* (Moore et al., 1995). The seismic example of Figure 82 from the Wash Basin depicts a very nice example of Cascadia shale mobilization. In this seismic image interpretation annotated with shale mobilization indicators, we see the shale-based decollement layer deformed under the burden of Wash Basin sediments. Sedimentary package surrounding the diapir-like shale cored intrusion seen on Figure 82 display shale mobilization features such as onlaps, toplaps and unconformities resembling salt tectonism-related rim syncline development. Moreover, the sedimentary pod formed in between the mobilized shale deposits (seen on TWT 1 – 1.6 s interval to the right of Figure 82) very much resembles a *minibasin* formation that is also associated with salt and its ductile behavior.

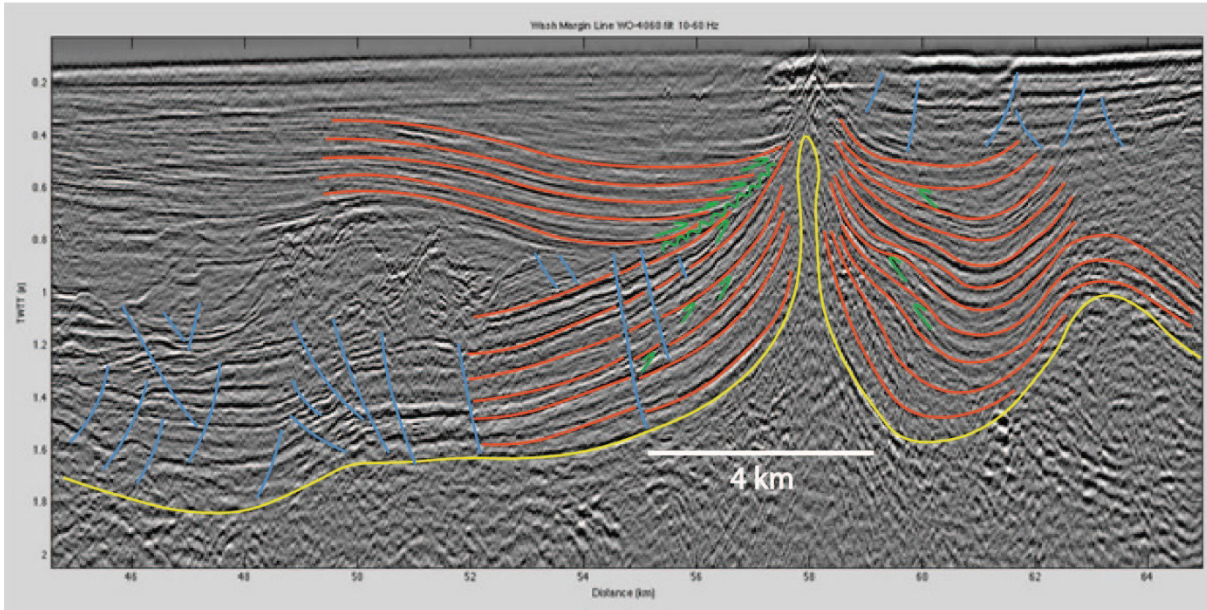


Figure 82: Seismic line from the Wash Basin, Cascadia. Yellow Markers: Diapir-Like shale intrusion. Red Markers: Deltaic sediments. Green Markers: Sequence terminations such as unconformities, onlaps and toplaps. Blue Markers: Normal faults observed at the sedimentary package above the shale formation (image retrieved and modified after Steve Holbrook, <https://earthscience.stackexchange.com/questions/4945/what-is-a-mud-diapir-and-how-does-it-form>) – Please note that the interpretation on this seismic section is made to point out the shale mobilization features without any intention attributed to the stratigraphic information of the area as it is not the purpose of this PhD research –

Comparison between Active Margin Accretionary Prism Settings

This section of Shale Tectonism related Geodynamic Settings chapter aimed to compile examples of shale-prone active margin settings, where we observe a shale deformation patterns similar to Salt Tectonism. The seismic examples from all of these locations (Makran Accretionary Prism, Baram Delta, Mahakam Delta, Barbados Accretionary Prism and Cascadia) have common features that can be attributed with mobilized shale examples;

- Each geodynamic setting evolve on an active margin with abundant sediment cover underlined by a thick shale layer.
- Data examples (some in poorly-quality, others in well-imaged seismic examples and/or satellite images) show minibasin-like structures surrounding diapiric mud intrusion forms. Some of them show signs of fluidization and expressed as mud volcanoes on the surface, while being recorded in terms of Christmas-tree structures on seismic (e.g. Barbados).
- Interpreted seismic lines from Cascadia and Baram Delta display truncations such as onlaps, toplaps and pinch outs against diapiric folds/anticlines resembling salt tectonism.

- Makran Accretionary Prism demonstrate spectacular onshore satellite image examples featuring similar sediment recordings (e.g. onlaps, truncations, minibasinal forms) against mobilized shale features supporting the seismic interpretation made on other accretionary prism examples (e.g. Cascadia)

Overall, all of these comparisons relate and point to a mobilization pattern driven by shale above an active margin setting. The shale deposition seem to be driven either by (i) fluidization (e.g. mud volcanoes), (ii) distributed deformation (e.g. strain), and/or (iii) combination of both. Due to the typical environment of accretionary prisms, each of these examples showcase high sedimentation rate and/or thickened sediment accumulation overlying the shale layer, which coincides with shale mobilization rules of thumb similar to salt.

V. Foreland Basins, Collisional Belts and Collapsing Orogens

Foreland Basins: The basins formed by *flexure* are associated with plate convergence and two subjects aroused from that based on the type of lithosphere they form upon. The flexure of oceanic lithosphere leads to *deep oceanic trench* formation as it approaches the subduction zones, while the flexure of continental lithosphere give rise to *foreland basins* in continental collision zones. Foreland basin pairs may also take place at intra-continental mountain processes without subduction (Allen & Allen, 2013). Within foreland basin classification; flexure of lower or subducting plate defines *pro-foreland basins*, and flexure of upper or overriding plate defines *retro-foreland basins* (Naylor & Sinclair, 2008).

Collisional Belts: As it is summarized by DiPietro, in *Geology and Landscape Evolution* (2nd Edition, 2018), the word 'orogeny' refers to the deformation process of mountain building, which is associated with *the convergence and accretion of two or more tectonic plates developing along an entire continental margin* by geologists. Such compressional (mountain) systems define orogenic belts/systems (also known as deformational belts). Collision of orogens/continents takes place at subduction zones with progressive compression of buoyant terranes, which can vary in scale (e.g. seamounts, island arcs, continents) and dictate the style, duration, intensity, and sequence of strain systems (Dewey et al., 1986; von Raumer et al., 2003). In case of irregular continental collisions; prior to terminal collision, one or both continental margins may have had a long complex history of terrane assembly, which makes collision regions structurally and geologically complicated (Condie, in *Earth as an Evolving Planetary System* (3rd Edition), 2016).

Orogens and Orogenic Collapse: Collapse of orogens results from the aftermath of orogeny collision processes. Orogenic collapse can be explained as the collapse of mountain ranges under their own weight. When mountain ranges are produced by the collision between continents, the crust is thickened as a result of that collision. During that process, and following the thickening in response to mass balance (isostasy), the bottom of the crust (Lower Crust) is heated up and becomes gooey, which leads to the mountains sinking under their own weight (Damian Nance, in press 2014, co-author of *Physical Geology Today*). As it is stated by Dewey, (1988) such a collapse occurs especially where rapid advective thinning of the shortened thermal boundary conduction layer takes place beneath an orogen and causes rapid uplift.

As it is stated by Roeder, in *Regional Geology and Tectonics: Principles of Geologic Analysis*, 2012; in terms of collision orogens, the tectonic history partly reverses the geographic order of depocenters, (e.g. the former oceanic externides can be beached on a new cratonic foreland), while the collision belts may involve internide elements (such as arcs) of the pre-collisional system. The following sub-sections of this section will detail Eastern Venezuelan Basin (EVB) as *Foreland Basin* example, and Alboran Sea as *Collapsing Orogen* example, within the conjunction of Shale Tectonism.

i. Eastern Venezuelan Basin: Foreland Basin

Eastern Venezuelan Basin (EVB) is a foreland basin that emerges from the diachronous and oblique subduction of Caribbean plate beneath the South American Plate (e.g. Ave Lallemand, 1997; Pindell, 1993-1998) and develops to the south of the Caribbean accretionary complexes (e.g. Ave Lallemand, 1997) (Duerto, 2007). Chronologically, as it is summarized by Duerto, (2007): (i) the northern margin of Venezuela deformed as a result of E-SE Caribbean Plate motion in relation to the South American Plate, (ii) western section of Venezuela started to deform during Eocene, and got younger towards the East with the Pleistocene age deformation taking place in Trinidad (e.g. Lugo, 1991; Audemard, 1991, Pindell, 1993), (iii) as a result, the accretionary complex of the Cordillera de la Costa was obducted diachronously onto the Cretaceous-Tertiary age passive margin of northern Venezuela due to plate convergence (Ostos, 1990; Ave Lallemand, 1997), and (iv) finally aforementioned collision of the Cordillera de la Costa accretionary complex and passive margin of northern Venezuela led to the formation of the Caribbean Mountain system and the Serrania Del Interior fold and thrust belt of the EVB.

Following the formation, the successively formed foreland basins of the accretionary complex together with Eastern Venezuelan Basin were infilled with deep-water black shales and turbidites of mixed provenance (e.g. syn-orogenic terrigenous deposits) both from Serrania Del Interior uplift and Palaeo-Orinoco delta systems (Rodriguez, 1999). As it is stated by Duerto (2007); the main shale sequences, located in the foredeep areas were folded and thrust into shale core anticlines, which later established the shallow structures of the fold-and thrust belt of the EVB within these deformed foredeep areas (Giraldo et al., 2000; Coward and Ries, 2001) (Figure 83).

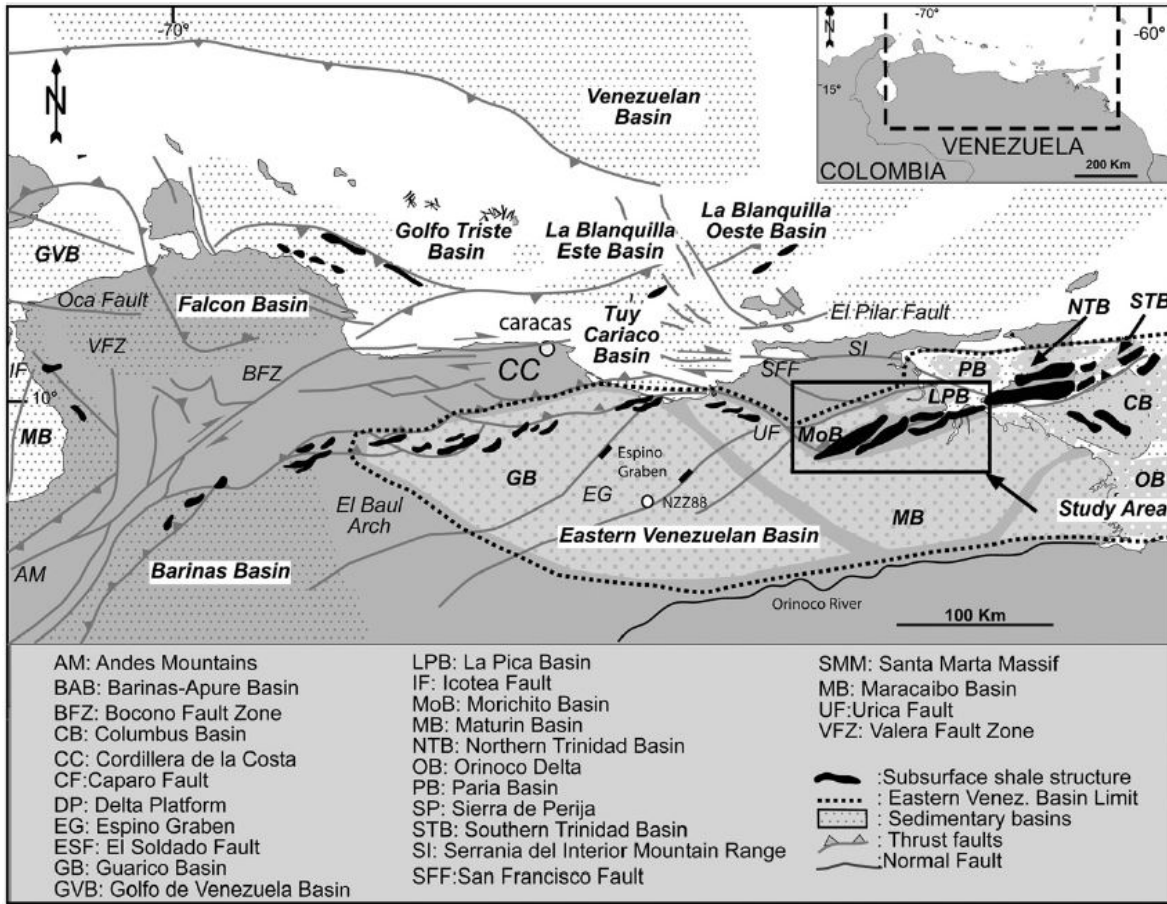


Figure 83: Geological Location of EVB and its Structural Elements (image retrieved from Duerto & McClay, 2011).

Duerto and McClay, (2011) stated that the internal shale deformation is considered to be driven mainly by development of shale thrust sheets accompanied by fluid expulsion. However, their findings of shale mobility differ from the classical definition of ‘shale diapirism’: it refers to ‘shale diapirs’ as localized overpressured shale units, where fluids are accumulated (Duerto and McClay, 2011).

In case of Venezuelan Foreland, excessive sediment rates and translation of overpressured strata to the foreland are two main reasons triggering shale mobility via anticlinal-shaped stacked shale units with normal fracturing above. The normal faults surrounding/roofing these stacked, tight anticlinal shaped shale units suggest an attractive location for hydrocarbon exploration (Duerto and McClay, 2011). They point out to the fact that conventional definition of ‘shale diapirs’, which refers to the areas of low signal-to-noise seismic imaging surrounding/resembling salt-diapir-like shale features, may have been indirectly (misleadingly) associated to overpressured shales since the main deformation mechanism is not driven by diapirism in shale-prone basins. Diapirism is conceived within a pressured/compressed, shale-dominated foreland system as a ductile material intrusion stressing into the overlying strata (Duerto & McClay, 2011) (Figure 84).

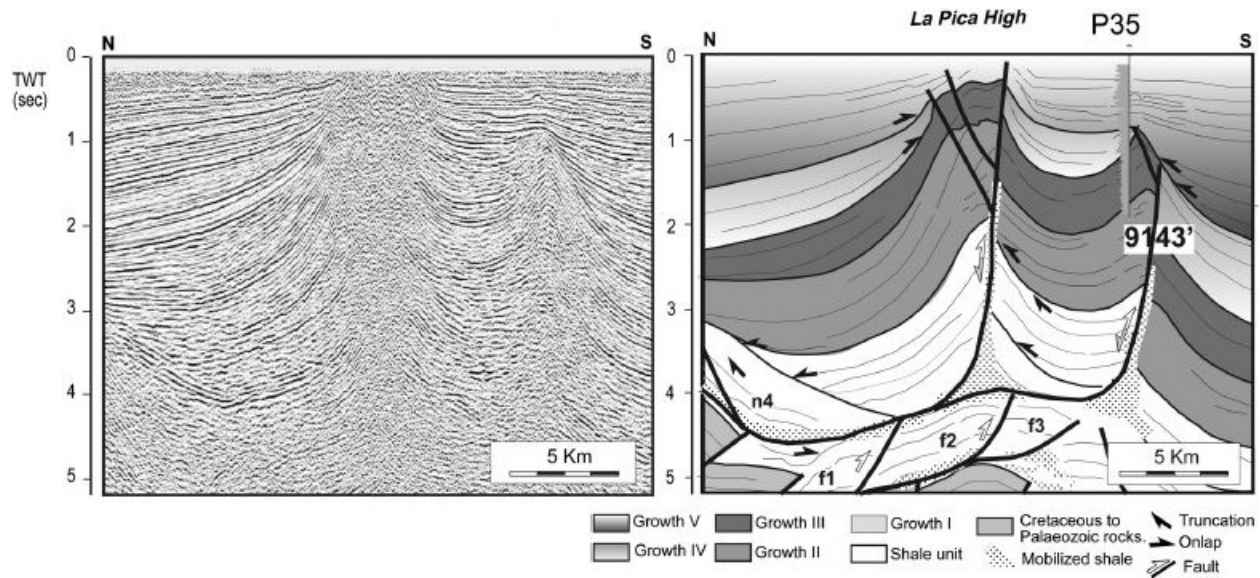


Figure 84: Detail of a regional seismic line from seismic survey. Note the distribution of mobilized shale in the south of the faults in the core of the anticlines (figure retrieved from Duerto and McClay, 2011).

Based on the study of Duerto and McClay (2011), most internal structures of individual anticlines present in the EVFB consist of imbricated structures overlaid by thick growth strata (Figure 84-Figure 85), and the only indication of real chaotic shale mobilization that could be related to the classical concept of diapir is located in specific areas of the fold-belt, especially at the base and top and between adjacent thrust sheets. Therefore, they propose that shale deforms in two main evolutionary stages:

- Stage I, folding and restricted basin formation: This stage corresponds to the effect of a sedimentary load deposited at the foothills of the mountain front and under a continuous sedimentary influence, the resulting morphology above the shale becomes the wedging of the growth strata towards the foreland in each side of the foreland fold.
- Stage II, 'break-through normal faults': If we consider that internal deformation in the shale may be the product mainly of thrusting (although overpressured fluids mobilization also takes place), we can apply the principle proposed in Duerto and McClay, 2009 to the deformation of the Carapita shales. If this model is applied to the foreland-fold-and-thrust belt, the pre-tectonic unit may be associated to the shale (Carapita Fm.). The anticline areas represent the footwall of normal faults, where they grow vertically, as a product of the stacking, and additionally they are displaced southward product of contraction (late middle Miocene to Lower Pliocene). The overall effect is the progressive clockwise rotation of the foreland side of the structures contemporaneous with divergent and down-bended growth strata towards the faults. Therefore, the morphology of the system is very different from listric normal faults where sedimentation encompasses extension, and growth strata is bended upwards. We suggest that the depo-center, as it is progressively filled, migrates towards the basin.

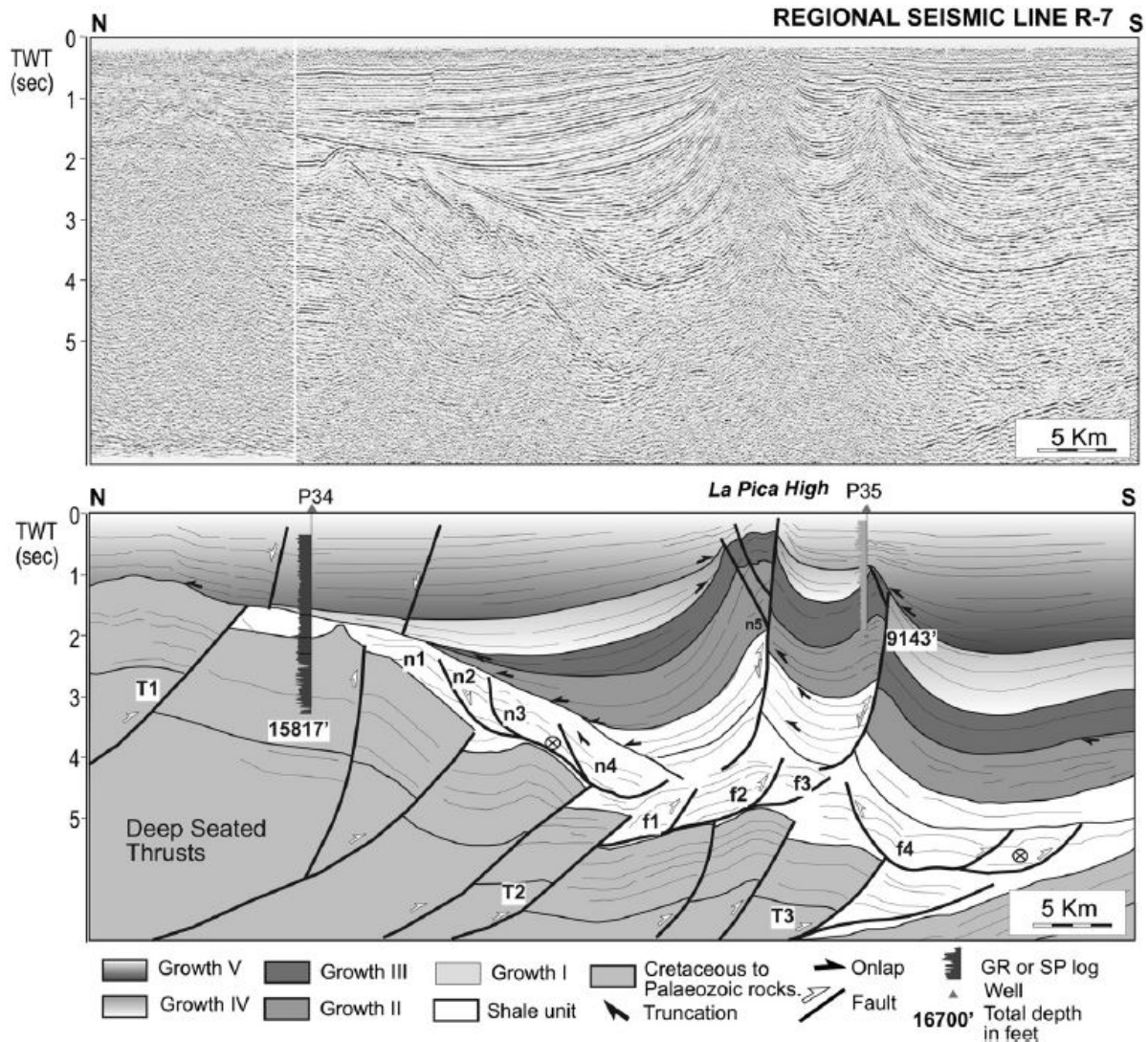


Figure 85: Regional seismic line from the study. Note the two levels of detachments inside the shale unit. The La Pica high is interpreted as the inversion of two normal faults (image retrieved from Duerto & McClay, 2011).

The internal deformation mechanism of shales is explained by Duerto & McClay (2011), as *not diapirism* (e.g. structures conceived as a lateral or vertical passive motion of ductile material into the overlying strata) but *with a deformation pattern considered to be driven mainly by development of shale thrust sheets accompanied by fluid expulsion*. The shale structures of the studied region showed fluids to be accumulated in certain areas inside the shale unit (mainly anticlines) creating localized overpressuring, fluidization of which only occurred when contraction took place as fluids were injected in to the overlying strata through faults producing mud volcanoes. Hence, they suggested a reviewed tectonic model in contrast to the conventional model proposed with 'shale diapirs'. In this model, it is proposed that the studied shale structures, which are developed above a shale unit, form a *break through normal fold bounded end-member* that results from combination of (i) *high sedimentation rate in the foreland*, and (ii) *migration of overpressure conditions to the foreland* factors (Duerto & McClay, 2011). Shale intrusions depicted in this study are not classically defined 'shale diapirs' or localized fluid pipes like 'mud volcanoes' because there are signs of diffused slow deformation pattern evidenced by progressive onlaps interpreted on the dataset, which point out to an analogy with salt deformation and strain-related mobilization scheme.

ii. Alboran Sea: Collapsing Orogen

Soto et al. (2010) defines the *Alboran Sea* as a *back-arc basin* in the Mediterranean developed during the Miocene by the extensional collapse of the thick continental orogen known as the Betic (Southern Iberia) - Rif (Maghrebian, Northern Africa) arc chain of the Gibraltar arc, whose collision and basin formation took place in Neogene as a result of oblique convergence of the Eurasian and African plates (e.g., Platt and Vissers, 1989; Garcia-Duenas et al. (1992); Jolivet and Faccenna, 2000). Geodetic models suggest a moderate, NW–SE contemporary convergence rate (~ 5.1 mm/yr [~ 0.2 in/yr]; e.g., Serpelloni et al., 2007) between these two plates (Eurasian and African). Even though Garcia-Duenas et al. (1992), Martinez-Martinez et al. (2002), and Platt et al. (2003; 2006) explained the late orogenic extension as a superimposed structure on an earlier collisional orogeny, the causes of extension is still under debate (e.g., Platt et al., 1998) (Soto et al., 2010).

Within this Gibraltar arc complex consists of three pre-Neogene crustal domain, which are namely; (1) the southern Iberian (external zone of Betic) and Maghrebian (external zone of Rif) continental passive margins, (2) the flysch trough units, and (3) the Alboran domain (thrust stack of three nappe complexes constituting the Betic-Rif internal zones and the floor of the Alboran Sea basin) (Soto et al., 2010). The Alboran Sea bares three main sub-basins; (i) Western Alboran Sea -WAB-, (ii) Eastern Alboran Sea -EAB-, and (iii) Southern Alboran Sea -SAB- (Soto et al., 2010). These sub-basins are separated from each other via ridges, seamounts and troughs revealing a complex seafloor morphology. Among these topographic features, the NE-SW striking Alboran Ridge stands as one of the most important features bounded by strike-slip and reverse faults (e.g., Bourgeois et al., 1992; Comas et al., 1992, 1999; Fernandez-Ibanez et al., 2007). The Alboran Basins differ from each other in terms of sediment input. The majority of the sedimentary input (12km) is located in the western Alboran Basin with a N-S oriented curved depo-centric formation mimicking Gibraltar Arc (Soto et al., 1996; Weinzapfel et al., 2003), which rotates to an E-W direction along the northern margin of the Alboran Sea (Alonso and Maldonado, 1992; Campillo et al., 1992; Ercilla et al., 1992; Soto et al., 1996), while the eastern Alboran Basin have a sediment accumulation of about 3 km and the eastern Alboran Basin sediment thickness reaches up to 2-3 km (1.2-1.3 mi) (Comas et al., 1997; Booth-Rea et al., 2007; Mauffret et al., 2007). As a consequence of thick sediment accumulation, the depo-center of western Alboran Basin is also recognized as a major shale diapir province covering of about approximately 1800 km² (~ 695 mi²) (Mountfield et al., 2002; Talukder, 2003) (Soto et al., 2010). As it is stated by Soto et al. (2010) and references therein; *diapirs are formed by undercompacted shales of the lowermost sedimentary units within this shale-prone area* (Figure 86).

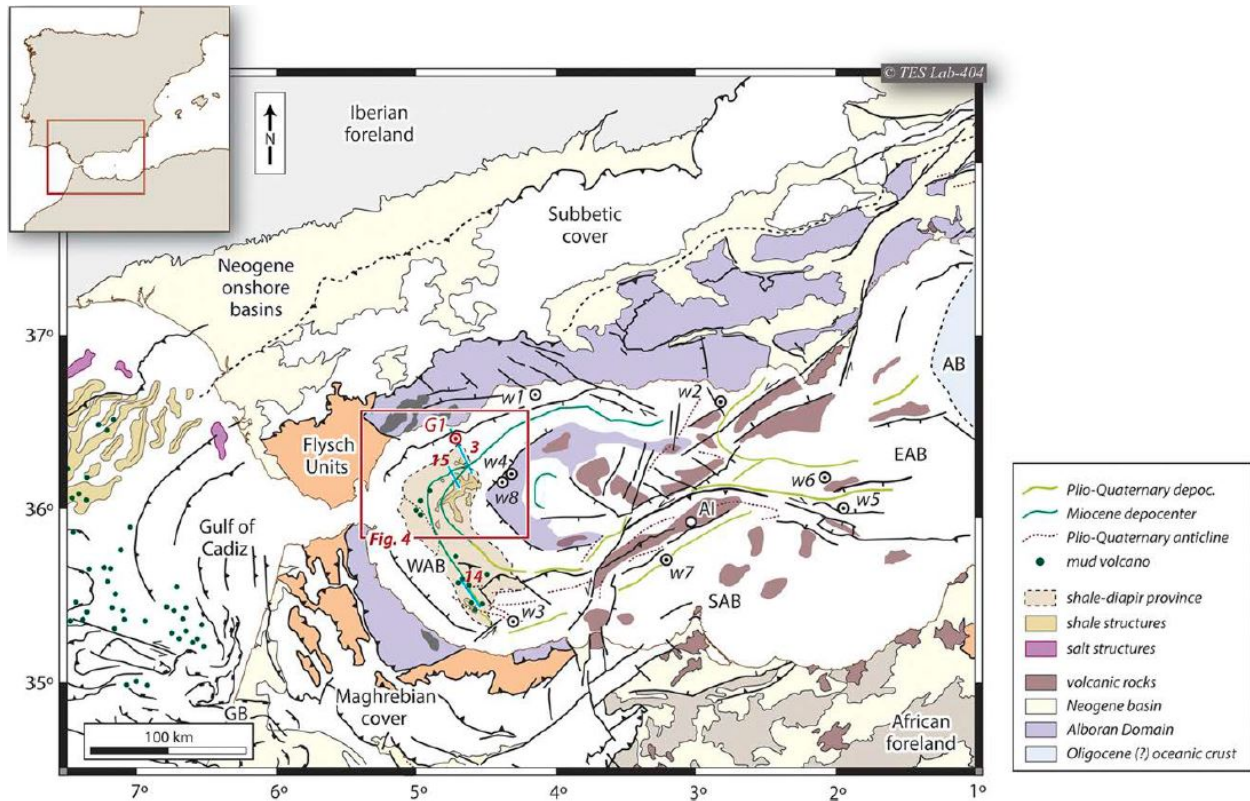


Figure 86: Tectonic map of the Gibraltar arc formed by the Betics, Rif, and the Alboran Sea Basin and the continuation of this orogenic system into the Gulf of Cadiz. (map updated from Soto et al., 2010) Mud volcanoes, shale diapirs, and salt culminations in the Gulf of Cadiz and in the Alboran Sea are compiled from numerous sources (e.g., Comas et al., 2003; Pinheiro et al., 2003; Somoza et al., 2003; Medialdea et al., 2009; Blinova et al., 2011; Somoza et al., 2012; Soto et al., 2012; Gennari et al., 2013; Hensen et al., 2015). The studied Andalusia G-1 well is indicated by G1. A rectangle marks the region in the vicinities of the studied well, where a detailed study of the mobile shale structures has been conducted. AI = Alboran Island; EAB = East Alboran Basin; SAB = South Alboran Basin; WAB = West Alboran Basin (image retrieved from Fernandez-Ibanez & Soto, 2017).

Shale tectonism in the region takes place during Mid-to-Late Miocene consisting of several faulting events accompanying simultaneous marginal extension and seaward shale thrusting. Soto et al. (2010) defined the shale-driven events as stated below:

- Shale sheet translation was driven by marginal faulting and ceased during the latest Tortonian.
- Shale emplacement was accompanied by asymmetric sheet collapse occurring up to the Early Pliocene.
- The extension direction in listric growth faults, in conjunction with the parallel and simultaneous advance of shale driven by toe thrusts, is consistent with the gravitational gliding of shale, driven by marginal extension and progressive basement tilting during the Mid-to-Late Miocene.
- Shale diapir culminations show contrasting structures and geometries in the shale roof, varying from a progressive thinning and folding of the overburden to discrete normal faults dipping landward. Crestal structures (following Rowan et al., 1999) in shale roofs differ also between shale-cored anticlines and shale walls; i.e., they vary following the basement down-dip direction.

Study of Fernandez-Ibanez & Soto (2017) focused on the *pore pressure and stress regime* of the same shale-prone region in order to better understand the controls on these shale structures as they were not fully-understood due to (i) lack of stress information and (ii) reconstruction of the pore pressures. Within this study, they modeled the stress magnitudes via *wellbore failure observations, well logging data, and drilling information* to constrain the present-day stress tensor in the northern margin of the West Alboran Basin (WAB) to discuss the possible triggering mechanisms behind the mud injection structures and their subsequent evolution and concluded that (Figure 87-Figure 88 shows their seismic interpretation and proposed evolution diagram of shale structures respectively);

- *Wellbore failure modeling suggests a current normal faulting stress regime with an E-W orientation of the S_{Hmax} [maximum horizontal stress] behind the orogenic front of the Gibraltar arc, which complements previous reconstructions of the current stress field within this orogeny.*
- *The low-velocity and low-density zone observed within unit Vb (middle Miocene) corresponds to overpressured shales. Temperature data suggest that thermally induced overpressures may also occur within the deepest sedimentary sequences (>5 km) of the basin, (unit VI, Lower Miocene).*
- *Disequilibrium compaction is the main source of overpressure down to approximately 5000 m. At this depth, effective stresses are low, and additional sources of overpressure are likely to develop within unit VI (Early Miocene in age).*
- *Hydraulic fracturing of the overburden layer is the most likely mechanism triggering mud injection at the deepest levels of the basin. Shear failure along pre-existing faults becomes the most likely mechanism to promote vertical mud transfer to the shallower levels of the basin, feeding the edifices of active mud volcanoes throughout the WAB.*

Figure 88 summarizes schematic view of the processes operating in shale-prone West Alboran Basin (WAB) proposed by Fernandez-Ibanez & Soto, 2017;

- *Unit VI (Early Miocene in age) is assumed as the source of overpressure that triggers shale diapirism in the WAB.*
- *The downslope migration of the shale is promoted by the syn-growth faulting of basinward faults, which accompanied the progressive subsidence and basinward tilting of the basin floor.*
- *Marginal extension accompanied sedimentation during the middle to late Miocene and promoted the downslope migration of the shale.*
- *Faulting pulses slightly preceded the episodes of shale upbuilding in these anticlines (Soto et al., 2010), which have also been reconstructed as a process in other 'linked systems of marginal extension and distal shortening' in shale basins (e.g., Morley et al., 2008; Oliveira et al., 2012).*

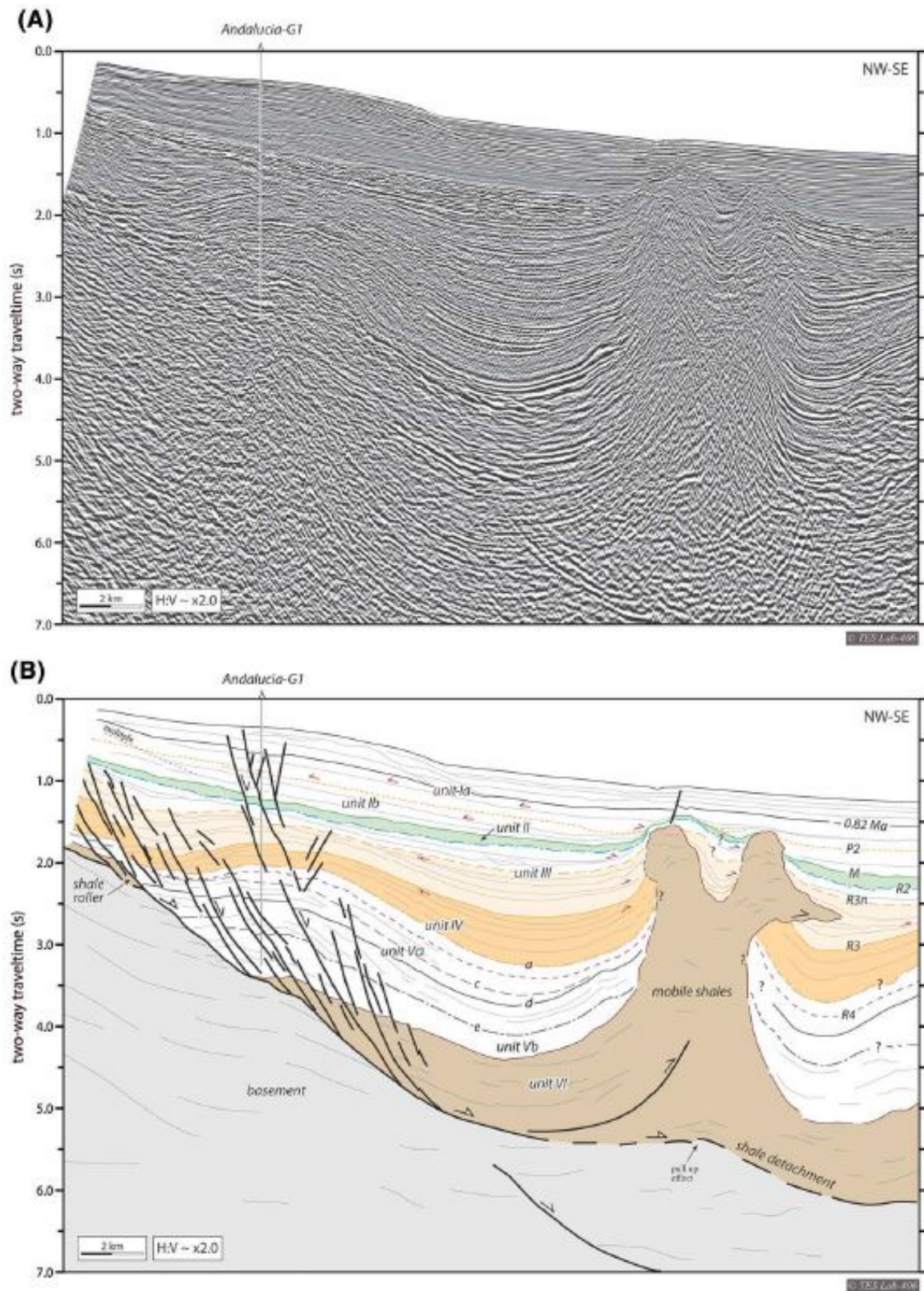


Figure 87 : (A) Uninterpreted seismic profile and (B) interpretation of a dip line in the northern margin of the West Alboran Sea. Reflection truncations are marked with dark red arrows. Seismic data are courtesy of ConocoPhillips. H:V = horizontal to vertical scale ratio; M= Messinian reflector; P2 = intra-Pliocene reflector; R2 = base of unit II reflector; R3 = base of unit III; R3n = intra-unit III reflector; R4 = base of unit IV seismic reflector (image retrieved from Fernandez-Ibanez & Soto, 2017).

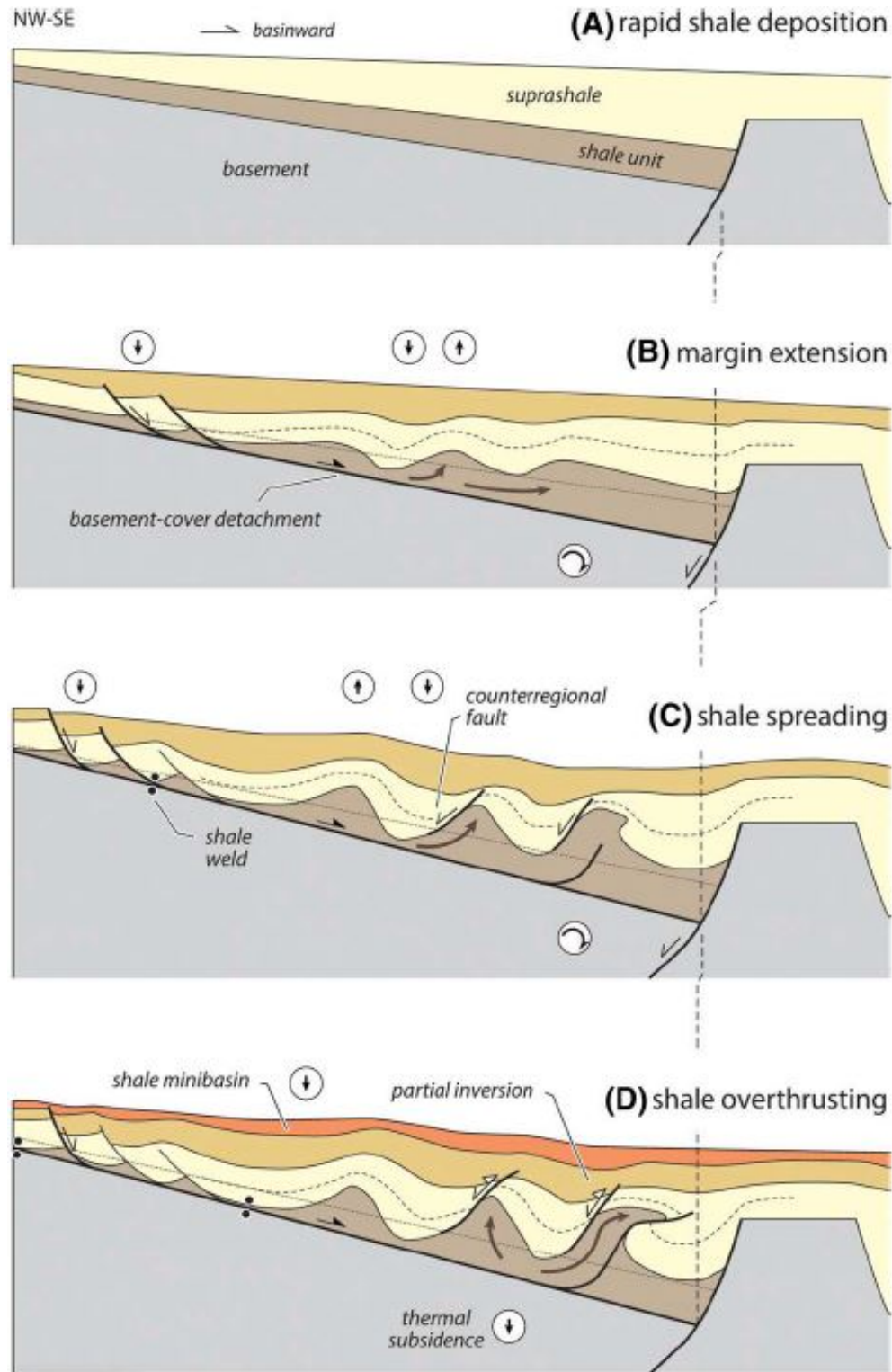


Figure 88: Schematic evolution of the shale structures in the northern margin of the West Alboran Basin along a conceptual dip section. The evolutionary stages correspond approximately to (A) the lower to lower middle Miocene (seismic units VI and V), (B, C) the middle Miocene (seismic units V and III, below the R3n reflection), and (D) the upper Miocene (upper Tortonian; upper part of seismic unit III). The vertical discontinuous lines express approximately the extension magnitude associated with the shale detachment formed along the basement cover surface. The encircled arrows show shale withdrawal and upbuilding associated with the downslope gravity spreading of the mobile shales (image retrieved from Fernandez-Ibanez & Soto, 2017).

VI. Synthesis on Shale-Driven Geodynamic Settings

The previous sections of this chapter aimed to summarize the major literature examples of shale-prone geologic settings. Based on our conducted literature review, we have synthesized the following take-away points;

Shale Tectonism can mimic Salt Tectonism under certain conditions, which can be listed as but not limited to *tectonism, over pressurization, water content high sedimentation rate* and *thick clay content*. Each of these components together and/or separately can lead the shale table to deform in a viscous manner within a specified geologic setting (e.g. deep sedimentary basins, deltas, accretionary prisms).

Deep Sedimentary Basins:

- Shale-based sedimentary basins can be triggered with excessive amount of sedimentation and display shale deformation patterns.

Active vs Passive Margins:

- Passive margins (e.g. Nile, Niger, Mississippi, Mekong deltas) host more deltas than active margins (e.g. Ganges-Brahmaputra rivers-Bengal Basin) (Coleman & Prior 1980; Davis 1980; Morley, 2003).
- Passive margins with comparatively thin sediment layer (in comparison to active margins), the post-rift thermal subsidence section tends to have a gentle regional offshore dip favoring structures formed by gravity sliding (Morley, 2003).

Deltaic Provinces:

Based on the scientific observations that have been conducted (Morley, 2003);

- The most important factor for delta tectonics is the rapid progradation of delta sediments across thick, water-rich pro-delta shales (Bruce 1973; Evamy et al. 1979; Knox & Omatsola 1989), which leads to (i) preserving porosity and pore fluids within the shales, and (ii) undercompaction of shales and overpressurization of pore fluids. Following this stage, excessive sediment load accumulated above the shale unit triggers viscous-like ductile flow of shales and leads to gravity-driven development of growth faults, shale-cored folds (sometimes interpreted as '*mud diapirs*'), mud volcanoes, toe thrusts and folds (e.g. Morgan et al. 1968; Evamy et al. 1979; Knox & Omatsola 1989).
- The main driving forces of gravity tectonics are buoyancy forces, gravity sliding and differential loading (e.g. see reviews by Jackson & Talbot 1986; Kehle 1989; Vendeville & Jackson 1992a) (Morley, 2003).
- Morley, 2003, states that maintaining and regenerating overpressured conditions when fluids are lost during deformation requires mechanisms other than burial-undercompaction. As reviewed by Osborne & Swarbrick (1998), most diagenetic mechanisms (such as the smectite/montmorillonite → illite transition) for the production of water can only produce volume increases of several percent (see Dubacq et al., 2018).
- As a result, the main diagenetic mechanism for 'topping up' established overpressure conditions is the conversion of oil to gas (Osborne & Swarbrick 1998), which can cause a large volume increase of (Barker 1990). The top of the main overpressured shale mass commonly lies at depths of 4-5 km, which is coincident with the depth of maximum oil generation, or the start of the gas window (e.g. Khalivov & Kerimov 1983; Sandal 1996; Morley & Guerin 1996; Paterson 1997; Cobbold et al., 2009).

There are some locations observed around the world (e.g. Appenines, Northern Italy), in which we are only limited to mud volcanism (e.g. fluidization of shales) and no such shale mobility (e.g. strain of shales). The main reason for differentiation of sole mud volcanism and/or mobilization of shales in a salt-like manner is not known/fully understood yet. However, we now have a better chance to investigate its reasons with improved subsurface imaging technologies.

Accretionary Prisms:

As it is stated by the review of Morley et al., 2018;

1. Based on geochemical analysis and temperature anomalies, it has been shown that in accretionary prisms, faults are the main locus of fluid flow (Moore et al., 1987; Gieskes et al., 1990; Fisher and Hounslow, 1990a, 1990b), as fault-parallel permeability may be 10–10,000 time greater than the permeability of adjacent rocks (Moore et al., 1995).
2. While the detachment weakness can be entirely due to material properties, overpressure is commonly invoked as a means of attaining the narrow taper of critical taper wedges observed in many natural fold and thrust belt examples (e.g. Dahlen, 1990; Davis et al., 1983; Bilotti and Shaw, 2005; Suppe, 2007). In saturated systems, fluids support some of the applied load, lowering the total stress on the grain framework.

Shale Detachments:

Morley et al., 2017 and Morley et al., 2018, reviewed the shale detachment zones with a macroscopic and microscopic approach respectively focusing on how our understanding of these diagenetic changes in mudrocks has been used in the debate over the extent of salt-like behavior of ‘mobile’ shales in deltas. These two reviews point out to the following findings on shale detachments;

- Flow of salt and possibly mudrocks can be seen as (1) Poiseuille vs (2) Couette Flow.
- While the Couette type of flow governs the characteristic flow of some detachment zones or parts of detachment zones, in complex geologic settings with mobile salt/shale occurrence (e.g. thickening/thinning detachment zones), where we notice changes in material properties, feeding of sediments/fluids into pipes and diapirs; superimposition of these two flow types (Poiseuille and Couette) are observed.
- Thickness and strength are two important aspects for shale detachments, mechanical properties are affected by strength, while the structural style is impacted by the thickness. Therefore, the mechanical behavior of shale detachment zones can vary from a hard, well lithified shale (e.g. Cobbold et al., 2004), to a zone of ‘plastic’ clay (Maltman et al., 1997).
- Shale Detachments display two different states of burial and consolidation;
 - o *State 1:* In well lithified units typically deposited tens of millions of years before deformation in basins that are unrelated to the tectonic setting that caused the contractional deformation to develop (e.g. Andean/Himalayan type fold and thrust belts).
 - o *State 2:* In well-to-poorly lithified units where deposition and contractional deformation occur in the same basinal setting (e.g. deepwater fold and thrust belts formed either by gravitational processes or in the upper regions of accretionary prisms).

- The zone of mobile shale evolves with time (e.g. Morley & Guerin, 1996; Morley et al., 2011) as (i) the base of the mobile shale moves upwards, (ii) disequilibrium compaction overpressures diminish in the lower parts of the mobile shales due to pore fluid loss, and may be replacement by overpressures related to diagenesis, and (iii) hydrocarbon generation and cracking take place during burial (Morley et al., 2017).
- Overthickened shale masses can take place at; (i) cores of detachment faults, (ii) footwalls of thrusts, and (iii) between more complex fault arrangements spanning from outcrop scale to 100-to-1000s of km³. Morley et al., 2017 explains their formation as *thickening of shale units by folding and thrusting* rather than *movement of thick, water-rich plastic zones of overpressured shale*, which can apply to 'mobile' shale interpretation in some cases. In this context, cleavage duplexes, S-C fabrics, duplexes, imbricates, pseudo-duplexes and vein formations are all mixed brittle and solution/diffusion structures causing the affected shale unit to display flow-like viscous characteristics.
- Cores of detachment anticlines take place at thickened shale-prone locations, where shale is collected in the core of detachment folds. Morley et al. (2017), and literature examples (e.g. Eppard & Groshong, 1995; Homza & Wallace, 1997; Mitra, 2002; Gonzalez-Mieres & Suppe, 2006; Mourgues et al., 2009; Maloney et al., 2010; Maloney, 2011) summarize the moving ways of material through these cores as flow of shale, to ductile folds, to a wide variety of fault structures. The great variety of these structures result from the interplay of many variables that can affect deformation style such as: mechanical stratigraphy, pore fluid pressure, shale mineralogy, deformation rate, and pressure-temperature conditions (Morley et al., 2017).
- Deformation of shale primarily occurs by fracturing, folding, cleavage formation, pressure solution and diffusion. Once deformed shales tend retain their shape, which can be a result of (i) *diagenetic stiffening of the rock*, and/or (ii) *loss of overpressure*. As it is noted by Richards et al., 2015; Warren, 2016; different than salt, they tend not to continue to flow simply under their own weight, or readily recrystallize and lose their syn-kinematic textures (Morley et al., 2017).
- Both ductile shear bands and brittle fracturing occur during formation of detachment horizons, for example in Boom Clay (e.g. Dehandschutter et al., 2005), zones of low strain display ductile deformation under microstructural analysis, while the zones of higher strain showcase domination of brittle structuration (Morley et al., 2018). There are many influences and heterogeneities effecting the fracture propagation in a geologic medium, which make it extremely challenging to define it in a given mathematical formulation (Morley et al., 2018). Limited studies from Patrício and Mattheij, 2010; Virgo et al., 2014; and Ougier-Simonin et al., 2016, attempt to address this phenomena.
- In terms of geologic setting and shale detachment relationships (Morley et al., 2018);
 - o Shale detachment associated overpressure conditions can be provided by mud volcanoes and fluid escape features present in most deepwater fold and thrust belts (see review in Morley et al., 2011).
 - o The deep-seated nature of numerous fluid escape and mud volcano features imaged on seismic data reveal fluid pipes rising from large thrust faults (e.g. Oregon margin, MacKay et al., 1992; Niger Delta, Cobbold et al., 2009; Baram Delta Province, Morley, 2009; Hikurang subduction zone, Barnes et al., 2010) and sea floor sampling of mud volcanoes, point to high heat flows and thermogenic hydrocarbons contained fluids (e.g. Deville et al., 2003, 2006; Dolan et al., 2004; Zielinski et al., 2007; Warren et al., 2011).
 - o Based on the review of King & Morley, 2017; detachments beneath Deepwater Fold & Thrust Belts (DWFTBs) in different tectonic settings are not analogously weak and deepwater fold thrust belts at passive margins generally have smaller wedge-taper angles

- and weaker detachments, than those at continent convergent zones or active margins. Same study of whom differentiates the driving stresses of DWFTBs into three groups;
- Near-field (gravitational) stress-driven systems confined to the sedimentary section
 - Far-field stress-driven systems (predominantly accretionary prisms)
 - Systems driven by mixed near- and far-field stresses (e.g. NW Borneo)
- In gravity driven systems, fore-arc basins and some external fold and belts, syn-kinematic sedimentation drives the basal detachment deeper with the fold and thrust belt development, which leads to significant diagenetic changes with temperature-driven burial. As a result, detachment weakness and structural style conditions change with time by various deformation and overpressure mechanisms.
- The strength of shale thrust zones is impacted by (i) changing mineralogy, (ii) water content, (iii) degree of lithification, (iv) porosity, (v) overpressure magnitude, and (vi) type of overpressure mechanisms, while the basal detachment strength, is controlled by frictional strength and pore fluid pressure. Critical taper wedges and wedge taper angle are important means to test the strength of basal detachment (Suppe, 2007; von Hagke et al., 2014; Tesei et al., 2015). Therefore, the differences in critical taper and implied basal detachment strength between gravity driven systems and accretionary prisms suggests a significantly different behaviour that is not simply explained as differences in clay mineralogy (King & Morley, 2017). Morley et al., 2018; suggests that the possible differences in how pore fluid pressure is retained are critical since aseismic basal detachments of gravity driven systems are able to retain high pore fluid pressures along the basal detachment than the seismogenic basal detachments (see review in King & Morley, 2017).

Overall, there are considerable variability of driving mechanisms for shale thrust weakness zones that enable shales (i) to be weak despite considerable lateral changes in composition, and (ii) to remain weak as they evolve during burial. As a consequence, numerous similarities and differences between various fold and thrust belt types related to the characteristics of the basal detachment can arise from these aforementioned processes as well as the associated tectonic environment. The diagram shown in Figure 89 summarizes a wide variety of factors influencing the shale detachment weakness phenomena with highlighted preferential occurrence of certain mechanisms in particular tectonic provinces such as; gravity driven, Andean or Himalayan type, and accretion prism fold and thrust belts (Morley et al., 2018).

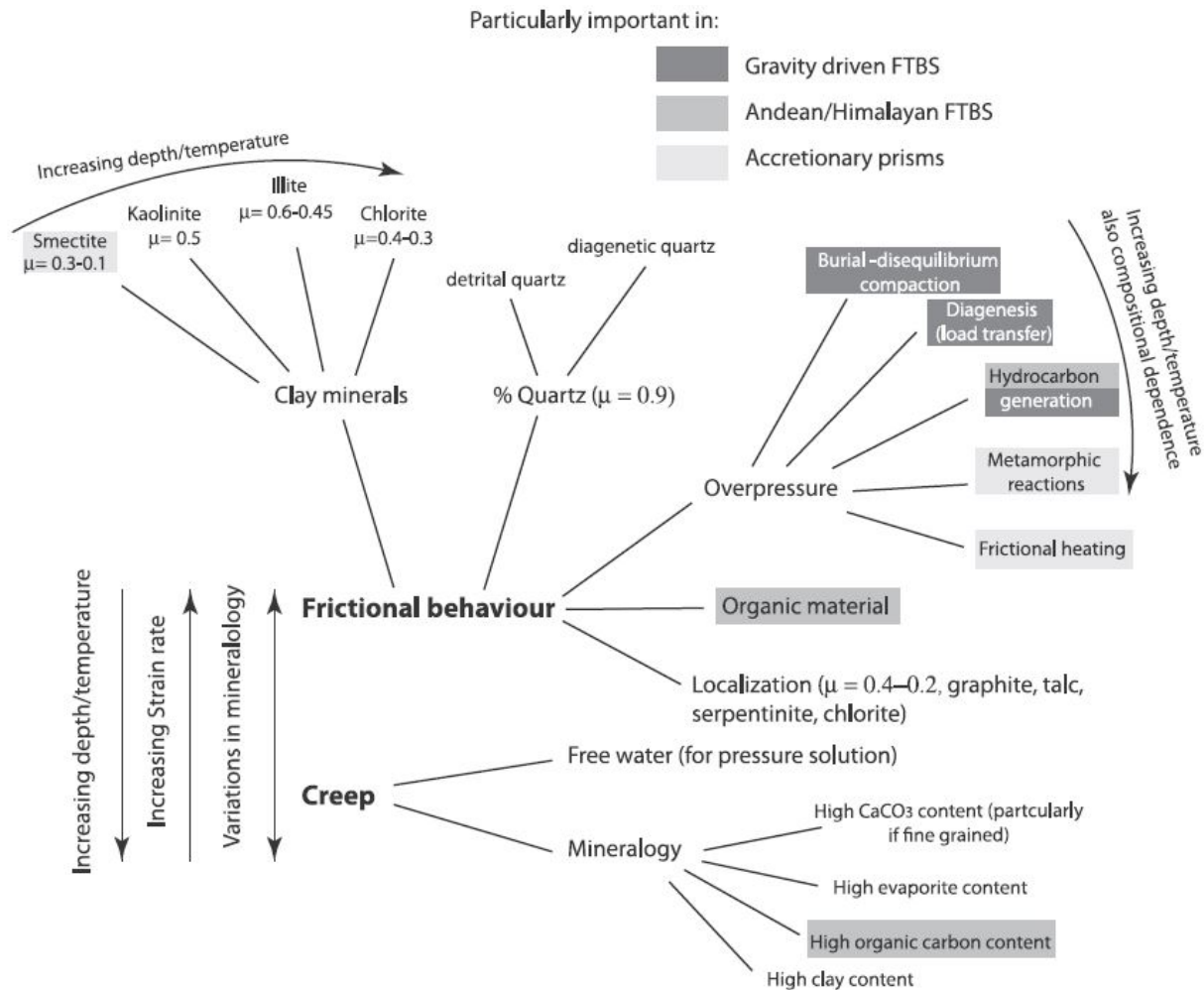


Figure 89: Summary plot on causes for shale detachment weakness and their interrelations depending on depth, temperature, strain rate and mineralogy. Increasing burial and temperature, decreasing strain rate, as well as variations in mineralogy will favour creep, where the dominant controls on creep are mineralogy of the shale, and free water content (image retrieved from Morley et al., 2018)

Figure 90 aims to display all and/or so far detected/documentated cases of Shale Tectonism published with examples around the world. It is fair to say that, unlike salt, there are still ambiguities in defining an established mobilization mechanism for shale. However, as a short synthesis, (i) high sedimentation rate, and (ii) high fluid content and generation at depth, in a (iii) tectonically favorable setting such as *deepwater deltas on unstarved margins*, and highly-fed / sediment-rich accretionary prisms can be counted as the main factors to take place in shale tectonism and mobilization.

For all these estimations/suggestions/reviews/studies performed by previous researchers and in order to better assist the Shale Tectonism topic; we will be focusing on an example of gravitationally gliding delta driven by shale, where we observe shale tectonics features reflected on a high quality seismic dataset on the next part of this thesis, and try to understand the mobilization mechanism observed at large scale in nature with an aim to better define the mobilization (e.g. salt-like flow) criteria for shale.

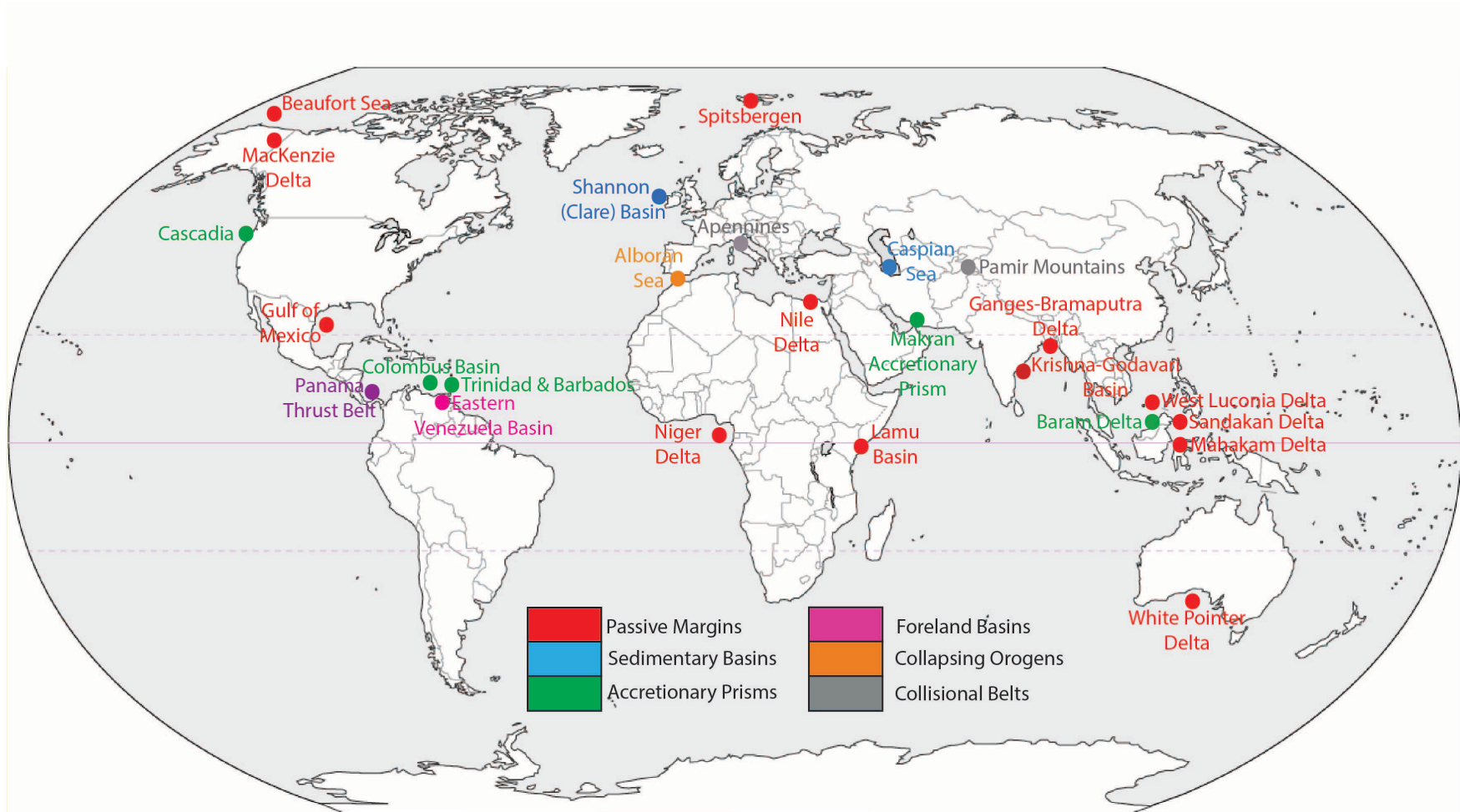


Figure 90: World Map showing the documented Shale Tectonism areas marked with red dots (image revised after Morley, 2003; Location map of the main mobile shale provinces associated with deltas world-wide with additional geodynamic settings showing shale-prone environments) (Blank map retrieved from: http://www.johomaps.com/world/worldblank_bw.html)

Chapter 4: Transition from Salt into Shale

Blind Test: Salt Driven Gulf of Mexico vs Shale Driven Ceduna Sub-Basin

Unlike salt, the obscurity of shale interpretation on seismic datasets is still a matter of debate especially with older datasets due to poor imaging and low resolution, which can be an individual or combined result of; fault shadow effects in the footwall area, shale intrusion complexes, fluid/gas effects, complex structural geometries, very steep structural dips and/or low impedance contrasts within a shale-dominated region (Morley et al., 2017). Therefore; researchers tend to be more cautious with their 'mobile shale' interpretation with newer seismic datasets, especially with 'shale diapirs', where some diapiric regions have been re-interpreted as narrower sections with a central fluid pipe (e.g. Morley 2003a, 2003b) rather than plastically behaving fluid-rich mud rock masses. Following the advancements of seismic imaging technology; such formations of 'plastic flow' are suggested to be complex thrust and fold geometries within a shale unit explaining the thickness variations (e.g. Duerto and McClay, 2011) as well as number of publications demonstrating the formation of stratified shales in areas where once thought to be composed of chaotic shale diapirs (e.g. Van Rensenberg and Morley, 2003; Elsley and Tieman, 2010; Duerto and McClay, 2011; Morley et al., 2017).

However, there are some recent seismic datasets collected with the latest seismic acquisition techniques and standards. In various parts of the world, we are now able to access such good quality datasets providing coherent details that enable us to better examine subsurface structures interacted both with salt and shale. Figure 91 depict two seismic lines collected from two different domains; one from a salt-prone environment (Gulf of Mexico), the other from a shale-prone environment (Ceduna Sub-Basin, Offshore Great Bight / Australia). As it is geologically proven, Gulf of Mexico is a salt-driven setting with abundant salt features while the Ceduna Sub-Basin is a less-well-known shale-driven setting showing almost identical features with those from Gulf of Mexico.

What is interesting is that they resemble strikingly similar features; such as primary minibasins, canopy-like features, secondary minibasins and welds. At first glance, had we not known the titles and geologic locations of these two seismic lines, they both point out to a ductile medium mobilized by a substance triggered by differential loading (e.g. salt or shale) and it is practically impossible to differentiate one from another in terms of determining ductile medium type since they both almost identically depict Salt Tectonism.

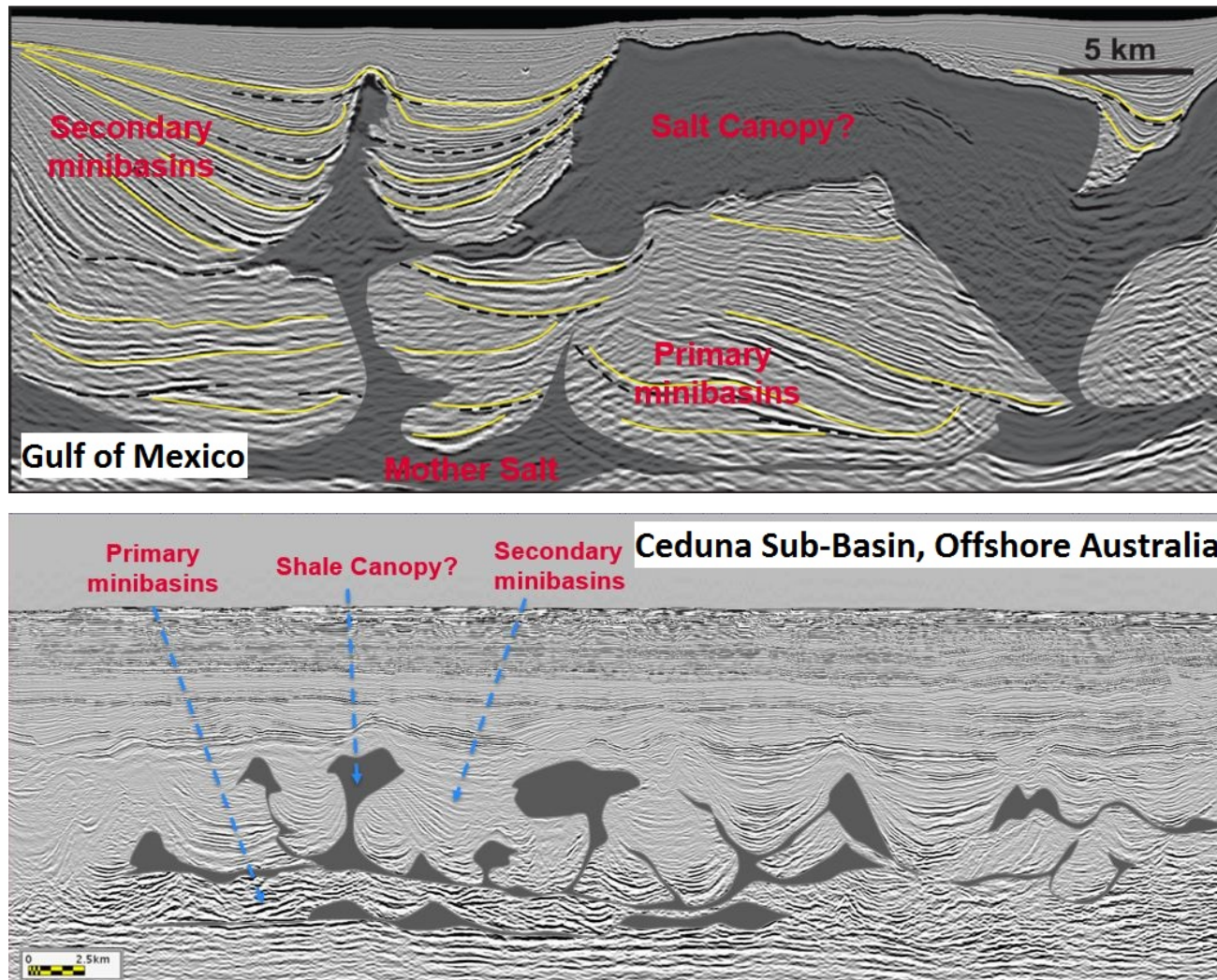


Figure 91: Two sections with labeled interpretation showing mobilized features of a ductile medium (e.g. salt or shale) with associated structures such as; (i) mother/autochthonous ductile medium, (ii) canopy formation, and (iii) primary and secondary minibasins. Upper figure shows a collected seismic line from salt-driven Gulf of Mexico (image retrieved from Callot et al., 2014). Lower figure shows a collected seismic line from shale-driven Ceduna Sub-Basin, offshore Australia (image courtesy of PGS, 2011)

i. Importance of Research

During the course of this PhD study, we aimed to have a deep understanding of the seismic datasets we have utilized as well as the dynamics of shale-prone gravitationally gliding delta systems. The ambiguity of shale mobilization still limits our understanding of clay characteristics at large scale, its effect on basin geometry and impact on the structural geology. Our main goal is to understand the basin structure. Clay can play an active role of deformation within the basin formation cycle but also as a transported, reactivated component inherited from the basin evolution process itself. If the 'mobile' clays are present and actively participating in the deformation process and dynamics of the delta by emplacing thrusts, rafting structures, minibasin formations and/or various styles of deformation geometry characteristics resembling salt, then we can better understand the phenomena of shale tectonics by classifying the clay behavior based on scale of observation.

Shale related geometries are more difficult to interpret in comparison to salt features due to its chaotic seismic signature. Shale cored-folds are frequently defined as areas with a low signal-to-noise reflection that represents overpressured shales that pierce the overburden (Duerto, 2007). However, thanks to well-imaged, high quality 3D seismic datasets collected from various parts of the world, we have a better chance of understanding today. For this purpose; we try to understand the role of 'inherited' mobile clays by looking at well-imaged seismic datasets and preserved outcrops displaying shale-interacted formations with an aim to be more predictive in terms of geometric subsurface interpretation when it comes to the topic of Shale Tectonics. We still do not have enough renewable energy resources and/or technology to sustain the whole world population, therefore, we are dependent on further research in the field of subsurface geoscience and its applications for geo-resources. Understanding the characteristics of various delta settings/basin environments will help us better tackle the ongoing uncertainties in exploration and focus on a solution-driven path.

ii. Ultimate Goal of Research

Given the review of what we know so far for shale and salt, our aim in this thesis is to make a geometrical analysis of deformation in a shale-prone system and compare the findings to salt tectonics. The main idea is to illustrate the analogies of shale with salt in terms of geometry and kinematics in order to display the importance of it on the structural development. Shale-prone deltas are among the most classical examples displaying shale tectonism resembling salt-like shale features. In order to better understand the mechanism of shale mobility, we will take a look at a high quality seismic dataset collected from one of the largest under-explored offshore basins with a shale-prone delta setting; Ceduna Sub-Basin, offshore Southern Australia, which is already quite well described and understood geologic setting in terms of geodynamic evolution and structural framework (see reviews from Totterdell and Krassay, 2003; Totterdell et al., 2008; Espurt et al., 2009; Espurt et al., 2012; MacDonald et al., 2012; MacDonald, 2013; MacDonald et al., 2013).

Rapid progradation of delta sediments in a salt/shale-prone environment defines the most important delta dynamic. The ultimate takeaway of this study is to understand the role of clay deformation on various scales, observe the deformation geometries of shale in delta settings and basin environments, see its resemblance to salt tectonics if any, revisit the concept of shale tectonics based on the current findings and aim to conceptualize a well-constrained shale mobilization model.

PART III: Case-Study: Ceduna Sub-Basin, Offshore Australia

The main scope of this PhD work is performed with a seismic interpretation scheme applied on a 3D PSDM dataset collected from Offshore Southern Australia, Great Bight Basin (GBB), Ceduna Sub-Basin. Chapter 5 focuses on the geological setting and literature review of Ceduna Sub-Basin, while Chapter 6 aims to deliver the seismic framework and well information, and Chapter 7 details the dataset and methodology by displaying the seismic findings/interpretations obtained during this research.

Chapter 5: Area of Interest: Great Bight Basin – Ceduna Sub-Basin

The offshore Southern Australia (Figure 92) is defined by Cape Howe to the East, Cape Leeuwin to the west, and offshore Tasmania / South Tasman Rise / Australian Maritime Jurisdiction (AMJ) of the Kerguelen Plateau to the South. The Great Bight Basin (GBB) is a Jurassic-Cretaceous Age basin that covers the area from the southern tip of Western Australia along the Great Australian Bight to the western tip of Kangaroo Island. It overlies Australian continental shelf and slope including the two bathymetric terraces; Eyre and Ceduna, depths of which vary from less than 200 to over 4000 meters (Totterdell et al., 2000; Totterdell & Krassay, 2003; Totterdell & Bradshaw, 2004; Hughes et al., 2009).



Figure 92: Location of the Bight Basin along the southern Australian margin, with component sub-basins (image retrieved from Totterdell et al., 2008).

The main depo-centers of GBB are located in the eastern part. A thin succession of GBB overlies the Gawler Craton basement and Early Palaeozoic rocks of Kanmantoo Trough to the east of these depo-centers. Northern side basement consists of various Proterozoic and older terranes.

I. Introduction

Bight Basin (BB) represents the deep offshore portion of Great Bight Basin located at the magma-poor southern margin of Australia, separated ~3500 km from the eastern Antarctic margin by the Southern Ocean today. These two extensional conjugate margins are correlated by the old basement rocks from the Terre Adélie–George V Land coastline with the southern Australian Gawler Craton (Oliver & Fanning, 1997). Bight Basin consists of series of Mesozoic-to-Cainozoic depo-centers that formed along Australia's southern margin during a period of extension and passive margin evolution started in Mid-to-Late Jurassic time (Fraser & Tilbury 1979; Bein & Taylor, 1981; Wilcox & Stagg, 1990; Stagg et al., 1990; Hill, 1995; Totterdell et al., 2000; Norwick & Smith, 2001; Totterdell & Bradshaw, 2004).

The Basin is unconformably overlain by Cenozoic Age Eucla Basin cool-water carbonates while the shallowest sequences of Bight onlap onto highly extended continental crust and continent-ocean transition of Australia and Antarctica within the abyssal plain to the south (Sayers et al., 2001; Hughes et al., 2009). Basement trends have had a profound influence on the structural development of the GBB, controlling the location and orientation of early basin-forming structures (Stagg et al., 1990; Totterdell et al., 2000; Teasdale et al., 2001; Totterdell & Bradshaw, 2004; Hughes et al., 2009; MacDonald et al., 2012).

BB formed during Late Jurassic / Early Cretaceous rifting and continued to develop during the breakup of Gondwana, separating Australia and Antarctica (Norwick & Smith, 2001; Totterdell & Bradshaw, 2004). Following the Santonian-Campanian break-up, rifting and crustal thinning of the Australian plate formed three structurally-controlled sub-basins within BB, Ceduna, Eyre and Recherche, all of which are separated by NW striking accommodation zones (Stagg et al., 1990; Wilcox and Stagg, 1990; Totterdell et al., 2000; MacDonald et al, 2012). The Ceduna, Recherche and Eyre Sub-Basins, together with the Bremer and Denmark sub-basins (located further to the west), form the offshore portion of the Jurassic–Cretaceous Great Bight Basin, which overlies the continental shelf and slope as well as extending over 300 km onshore from the coast (Figure 93) (Hughes et al., 2009; MacDonald et al., 2012). The basement trends depict an intense signature on the Bight Basin controlling the location and orientation of early basin-forming structures (Stagg et al., 1990; Totterdell et al., 2000) as a strong E-W oriented basement lineament seems to control the location of Jurassic-age extensional structures elongating towards the northern boundary of Eyre and Ceduna Sub-Basins (Totterdell & Bradshaw, 2004). Ceduna Sub-Basin is the deepest depo-center with maximum sediment thickness of 15 km (Totterdell et al., 2000; Krassay and Totterdell, 2003; Totterdell and Bradshaw, 2004; Souliki & Callot, 2010) showing numerous seismic indications/structures appealing to the subject of this research. Therefore, the course of this PhD work will be focusing on Ceduna Sub-Basin and its structural components from here forward in the following sections.

II. Geological Background

The deepest depo-center of GBB/BB; Ceduna Sub-Basin, is defined by the Ceduna bathymetric terrace forming the Southern Australian continental shelf and slope (Totterdell et al., 2000; MacDonald et al., 2012). It covers an area of 90000 km² of seafloor (MacDonald et al., 2012) and lying in water depths from 200 m to more than 4000 m (Espurt et al. 2012). It is bounded by the Madura Shelf to the north, Eyre sub-basin to the west, Recherche sub-basin to the south (as it translates into the abyssal plain of underlying South Australian Oceanic Crust) and Duntroon Basin to the south east. The areal coverage of the sub-basin extends across the upper and lower continental slope; the upper continental slope is occupied by the *Ceduna Terrace*: a seaward sloping surface that is 700 km in length and has a maximum width of approximately 170 km (Hughes et al., 2009), while the lower continental slope continues beyond the outer skirts of Ceduna Sub-Basin forming the Recherche Sub-Basin adjoining to the abyssal plain (Harris et al., 2005) (Figure 93). There are two deltaic succession stacked on top of each other within the Ceduna Sub-Basin: the White Pointer and Hammerhead DDFTBS (Delta Deepwater Fold & Thrust Belts), which will be detailed in the following sections.

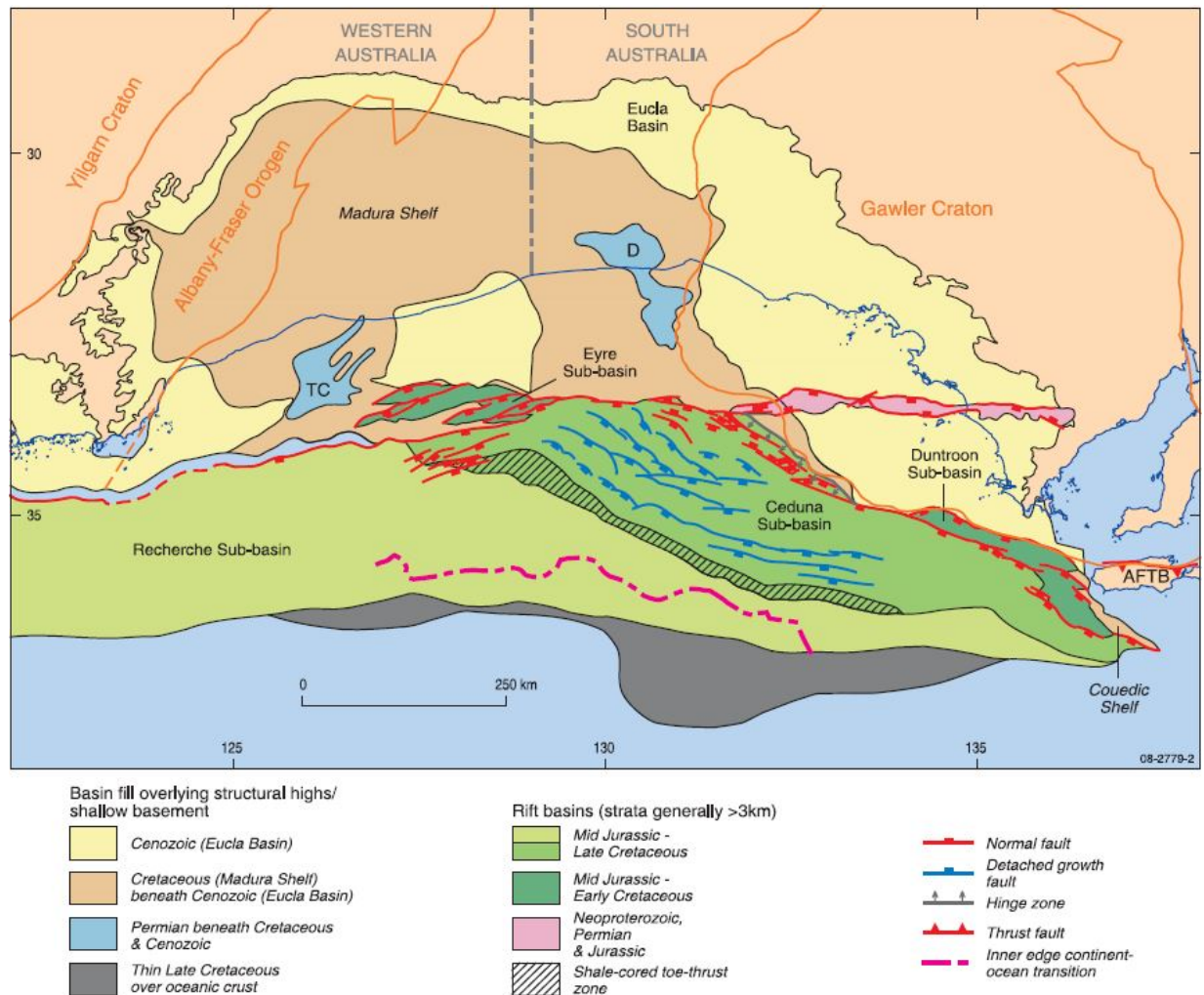


Figure 93: Structural elements map of the eastern Bight Basin (after Bradshaw et al. 2003) (image retrieved from Totterdell et al., 2008).

A. Geodynamic Setting

The Great Bight Basin (GBB) emerged from rifting during Late-Jurassic to Early-Cretaceous and continued to develop during the breakup of Gondwana; separating Australia and Antarctica (Norvick & Smith, 2001; Totterdell & Bradshaw, 2004). During this time, a convergent margin existed on the eastern margin of the Gondwana continent and incipient rifts were developing between Australia and Antarctica, India and Antarctica, and India and Western Australia, while the extensional systems were forming a triple junction (Norvick & Smith 2001; Totterdell & Mitchell, 2007). As stated by Espurt et al. (2012), the transition from rifting to seafloor spreading is marked by the exhumation of mantle rocks as the serpentinized upper mantle peridotite ridges and remnants of continental crust form a band that ranges in width from ~30 to >100 km in the outer parts of both margins, included in the ocean–continent transition zone (Chattin et al., 1998; Sayers et al., 2001; Beslier et al., 2004; Close et al., 2009; Direen et al., 2011).

Repeated episodes of extension and thermal subsidence later led to the commencement of sea floor spreading between Australia and Antarctica (Totterdell & Bradshaw 2004). Sea-floor spreading in the Bight Basin (offshore portion of GBB) occurred in Late Santonian–Campanian (83 Ma) (Sayers et al., 2001) and were followed by the thermal subsidence of the passive margin (Espurt et al., 2012) (Figure 94).

Sediment deposition of the basin occurred during a global, 1st-order, transgressive-regressive cycle (a period of Middle–Late Jurassic to Early Cretaceous upper crustal extension) (Totterdell & Mitchell, 2007; Totterdell et al., 2008). BB later formed three structurally-controlled sub-basins within the BB, namely the Ceduna, Eyre and Recherche. All of these sub-basins result from rifting and crustal thinning of the Australian plate and are separated by NW striking accommodation zones (Stagg et al., 1990; Wilcox and Stagg, 1990; Totterdell et al., 2000; Totterdell & Bradshaw 2004; MacDonald et al, 2012). Totterdell and Mitchell (2007) states that in the Bight Basin *a NW–SE to NNW–SSE extension direction, superimposed on E–W and NW–SE oriented basement structures, resulted in oblique to strongly oblique extension and the formation of en-echelon half graben in the Eyre, inner Recherche, northern and eastern Ceduna, and Duntroon sub-basins* (Totterdell et al., 2000; Williams et al., 2011; Espurt et al., 2012) (Figure 93). For this reason, the areal extent of the early extensional structures beneath the thick Ceduna Sub-basin cannot be determined due to the thick nature of the sedimentary section. However, the anomalously thick nature of the sub-basin may indicate the presence of Jurassic–Early Cretaceous rifts at depth.

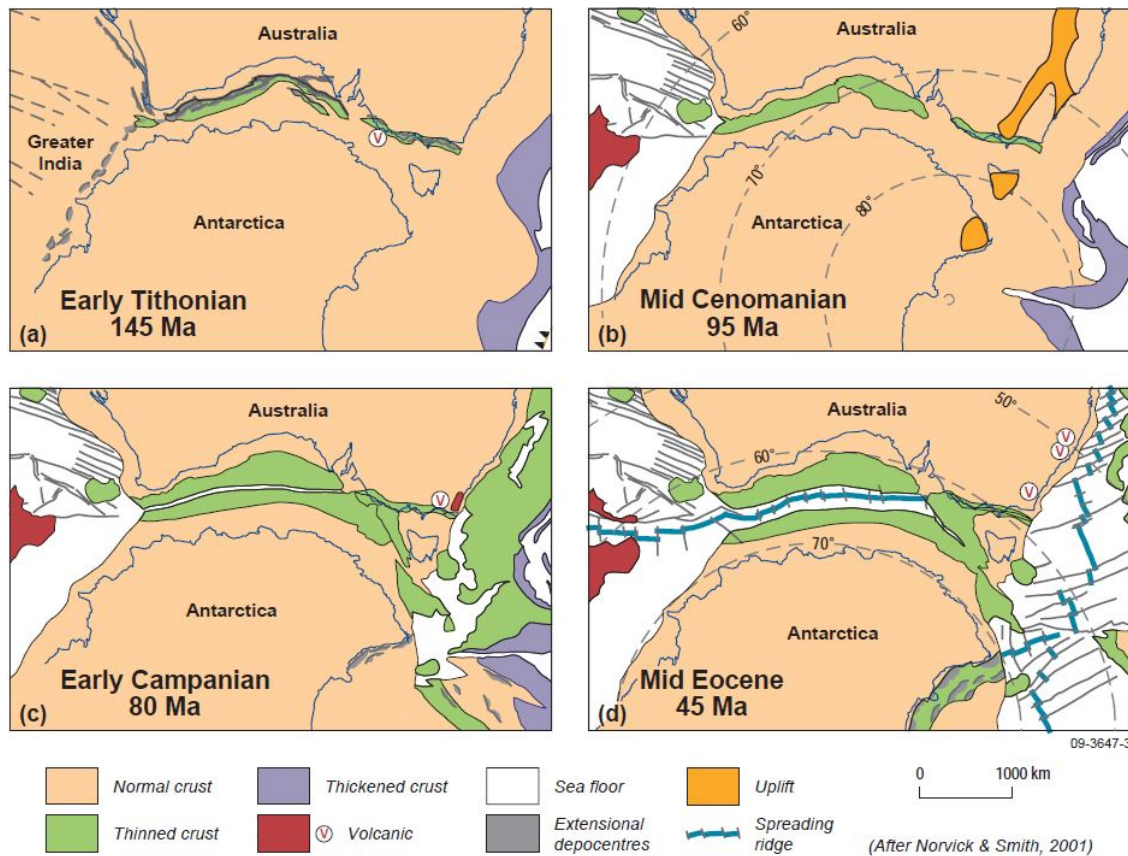


Figure 94: Plate tectonic reconstructions for the southern Australia–Antarctica conjugate margin (after Norvick & Smith, 2001) (image retrieved from Totterdell & Mitchell, 2007).

B. Tectonic Evolution at Crustal Scale

i. Lithospheric Domains

The study of Espurt et al., 2009, points out to crustal structure findings regarding the basement setting of the area. Based on the 2D-seismic research; the geometry of the underlying continental crust is not well defined landwards due to poorly imaged seismic data caused by the thick overlying sedimentary section of the Ceduna delta system. However, their study showed the substratum consisting of Middle Jurassic–Early Cretaceous half-grabens related to a thick-skinned fault system, the basement faults of which sole onto a south-dipping detachment level within the upper crust, while Late Cretaceous sedimentary series of the Recherche Sub-Basin and the outer part of the Ceduna Sub-Basin overlie a zone of broad (~110 km wide) highly attenuated and stretched continental crust (continent–ocean transition zone) oceanward characterized via exhumed mantle (Espurt et al., 2009; 2012) topped by an isolated distal klippe of continental crust (Direen et al., 2007). The basement ridge analyses conducted by Sayers et al. (2001) and Direen et al. (2007) suggested the basement to be composed of serpentized peridotites and mafic rocks at the oceanward end (South Australian Abyssal Plain) of the seismic profile shows a zone of relatively low relief sea floor interpreted as oceanic crust (Sayers et al., 2001) draped by thin Cretaceous and Cenozoic sediments (Espurt et al., 2009).

ii. Rifting Geometry

The Eastern Australian and Antarctic margin tectonism is related to the dynamic topographical effects of the cessation of Pacific Plate subduction at c. 95 Ma (Matthews et al., 2011). The timing of rifting/drifted processes involved during extension and breakup between Australia and Antarctica (as summarized in the previous section) define a well constrained geodynamic setting on the Australian margin (Totterdell et al., 2000; Norvick and Smith, 2001; Espurt et al., 2012).

The rifting models proposed on Figure 95 depict two possible opening scenarios (symmetric vs asymmetric) for the Australian-Antarctic conjugate system, which occurred in Late Cretaceous time during Australian–Antarctic continental breakup and the opening of the East Antarctica Ocean. As it is noted by Totterdell et al. (2000) and Norvick & Smith (2001), both of these margins, which have evolved through rifting, continental breakup and passive margin formation, are characterized by successive depocenters today (Espurt et al., 2012).

As it is stated by Espurt et al., 2012; the variations in extension direction during Early Cretaceous rifting preserved in southeastern Australia and the location of rift zones have been controlled by substantial rheological differences in the lithosphere and the presence of a Proterozoic/Paleozoic basement grain (Miller et al., 2002). Miller et al. (2002) further proposes that the failure along this lithospheric boundary is linked to a region of diverging extension between these two fold belts that developed during the younger stage of early Late Cretaceous rifting, therefore, hindering of extension due to the presence of a Proterozoic/Paleozoic basement trend appears to have been a factor in the development of a sinistral transtensional graben/transfer fault in the early Late Cretaceous.

As a consequence, despite the lack of control on the rheological and thermal properties of the lithosphere in the balanced cross-section, the study of Espurt et al. (2012) suggests that the early geometry of the margins was controlled by pre-existing structure of the lithosphere such as weaknesses relative to the rift paleo-stress field and inherited Proterozoic/Paleozoic basement grain (Van Wees and Beekman, 2000; Miller et al., 2002) or rheological heterogeneities and mechanical anisotropy (Audet and Burgmann, 2011) (Figure 95).

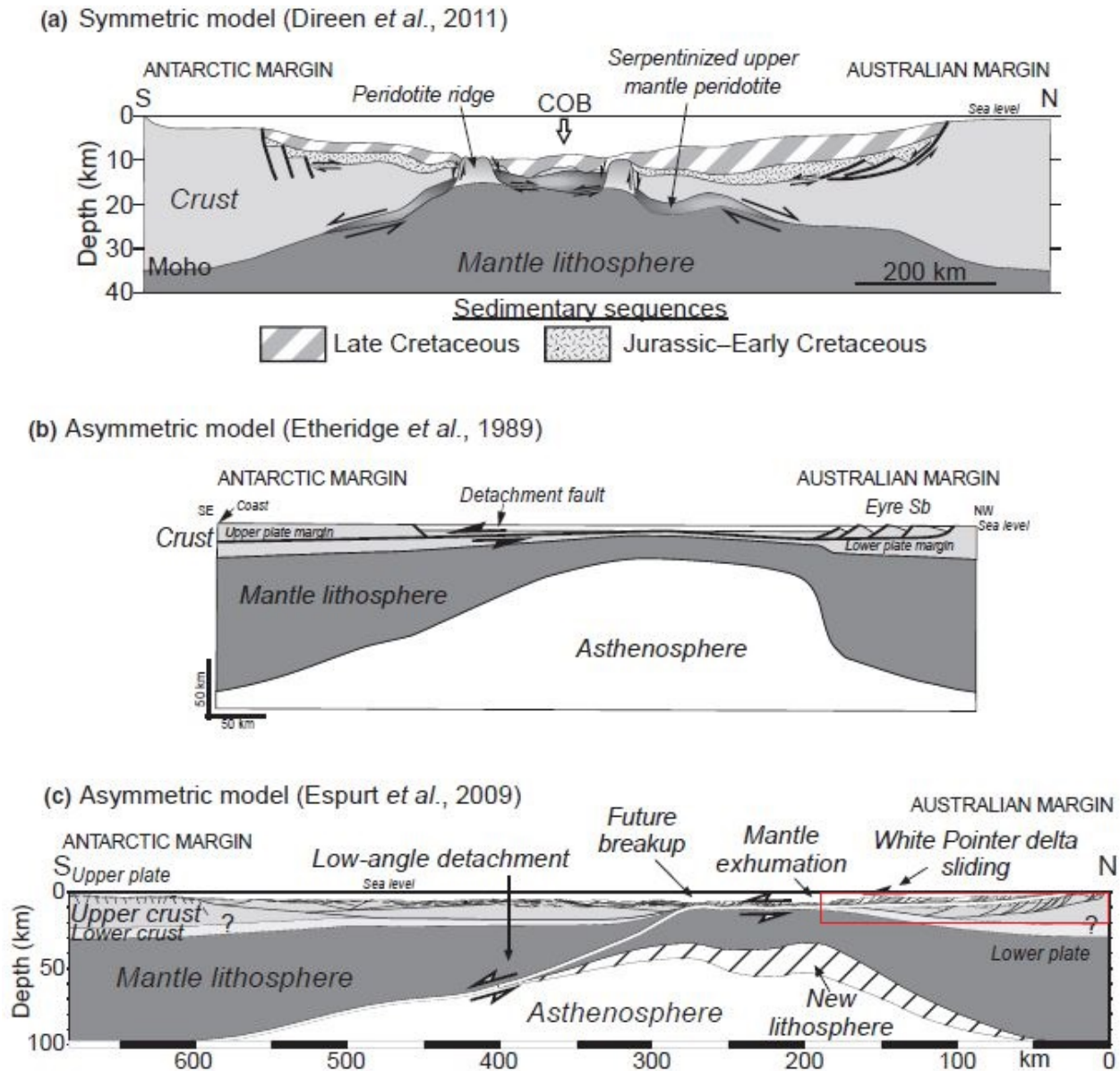


Figure 95: Different rifting models proposed for the Australian–Antarctic conjugate system. (a) Direen *et al.* (2011) propose a symmetric extensional model. (b) Etheridge *et al.* (1989) and (c) Espurt *et al.* (2009) suggest an asymmetric extension above a south-dipping low-angle detachment. In this model, the Antarctica is the upper plate, and Australia, the lower plate (Red rectangle on Fig. c depicts the White Pointer Delta) (image retrieved from Espurt *et al.*, 2012).

iii. Lithosphere and Crust Structure

The lithospheric-scale cross-section proposed by Espurt *et al.* (2012) on Figure 96 shows the overall end result of Australian-Antarctica conjugate margin sequential restoration and kinematic evolution present-day view. These two conjugate margins are ~3000 km apart and the adopted model assumed an unstretched crust thickness of 42.5 and 37.5 km for Australia and Antarctica margins respectively (after Kuszniir, 2009) with a highly asymmetric geometry supported by;

- (i) Half *graben systems*, *crustal klippe* and *serpentinized peridotite ridges* below thick Cretaceous deltaic successions on the Australian side
- (ii) Localized *inner-shelf grabens*, a *crustal high* and seaward *serpentinized mantle* rocks below a thin Cretaceous succession on the wider Antarctic side.

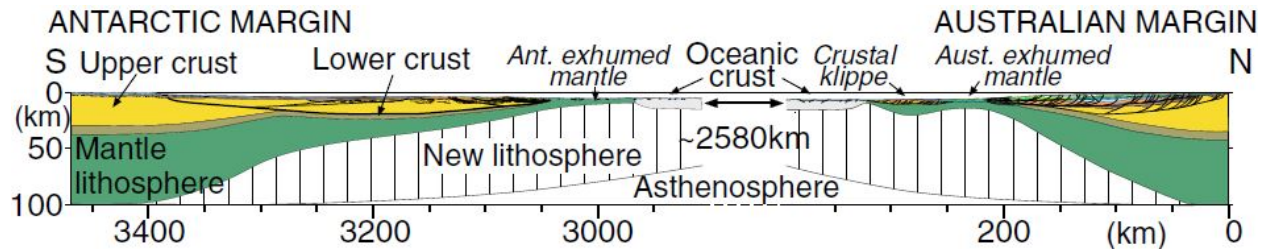


Figure 96: Present-Day view of Australian–Antarctica conjugate margins after the sequential restoration and kinematic evolution. No vertical exaggeration (image retrieved from Espurt et al., 2012).

Figure 97 depicts two regional seismic lines (interpreted vs uninterpreted) from the conjugate margins of Australia–Antarctica. In these lines, we see that the geometry of the underlying continental crust is not well defined due to poor seismic quality on both margins. However, based on the 2D seismic interpretation of Espurt et al. (2012) Australian side crustal structure is seen to be dominated by Middle Jurassic–Early Cretaceous half-grabens related to a thick-skinned fault system beneath the deltaic interval (White Pointer Delta) landwards, while *consisting of a zone of broad (110 km wide) highly attenuated and stretched continental crystalline crust (continent–ocean transition zone), which is characterized by basement ridges topped by an isolated distal klippe of continental crust* (Direen et al., 2007) oceanwards from Ceduna through Recherche Sub-Basin. The oceanward end (South Australian Abyssal Plain) of the same seismic profile displays a zone of relatively low relief sea floor interpreted as the *oceanic crust* (Sayers et al., 2001) that is draped by thin Cretaceous and Cenozoic sediments (Figure 97 Australian Coast).

The same study defined the crustal structure of the Antarctic side based on their seismic interpretation as a *margin that shows considerably more extended continental crust compared with the passive margin further to the west* (Colwell et al., 2006; Close et al., 2009; Direen et al., 2011). Within this section, the Terre Adélie sector of the Antarctic margin that is labelled as the ‘Adélie Rift Block’ (by Colwell et al., 2006), is characterized by atypical gravity anomalies for a continental margin and a complete absence of seafloor spreading magnetic anomalies (Close et al., 2009). The structure of the Adélie Rift Block refers to a *broad zone of continental crust* that was extended before breakup and the formation of oceanic crust (Colwell et al., 2006). The structure covers the north-eastwards area of the margin from shelf to the oceanic domain, with (i) the landward part consisting of a *broad crustal high bounded by half-graben systems with listric normal faults* (Colwell et al., 2006; Close et al., 2007), and (ii) the oceanward part crustal structure composed of *seismically and structurally complex highly attenuated continental zone, interpreted as the continent–ocean transition zone* (e.g. Close et al., 2009). The oceanward part of Antarctica points out to the presence of serpentinized peridotite ridges (Tanahashi et al., 1997; Yuasa et al., 1997; Colwell et al., 2006; Close et al., 2009), similar to those of the Australian margin (Sayers et al., 2001) (Figure 97 Antarctic Coast).

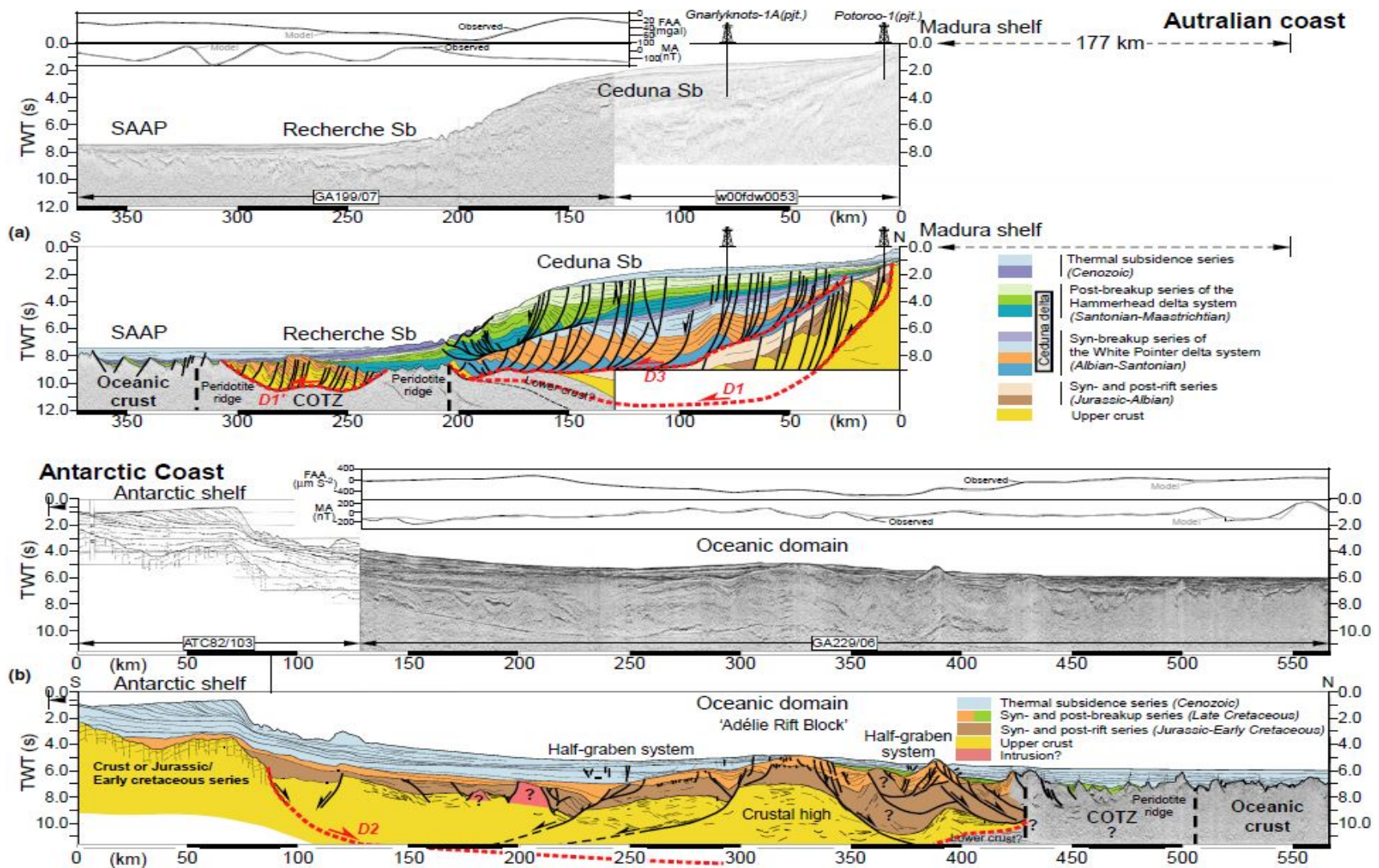


Figure 97: Structural interpretation of the two synthetic seismic transects: (a) Australian margin and (b) Antarctic margin. Sb, Sub-basin; COTZ, Continent–Ocean Transition Zone; SAAP, South Australian abyssal plain. Observed and calculated Free Air gravity anomaly and residual IGRF corrected magnetic anomaly are shown (from Colwell et al., 2006; Direen et al., 2007 and courtesy of Geoscience Australia). Inferred detachment/decollement zones are shown by thick dashed red lines (D1, D1', D2 and D3) (image retrieved from Espurt et al., 2012).

iv. Kinematic Scenario at Crustal Scale

Figure 98 shows the kinematic evolution of the Ceduna Sub-Basin based on the sequential restoration study (from Late Albian to Present Day) performed by Espurt et al., 2009. Through the restoration stages as it is seen on the figure from a-h (summarized from Espurt et al., 2009, note that this summary will be focusing primarily on their findings about (i) the D1 -Blue Whale- detachment level underneath the White Pointer Delta and briefly on (ii) the Hammerhead Delta interval and above on Figure 98 as the deeper, crust-related detachment level they suggest is beyond the scope of this research);

- States a-d illustrate the Late Albian-Santonian basin evolution during the post-rift and thermal subsidence periods before the Australia-Antarctica breakup, as well as the progradation of the White Pointer delta system.
 - **State 1 (a):** Deposition of Late Albian shales of the Blue Whale Supersequence along the seaward dipping margin, which had been previously deformed and structurally thinned during the Middle Jurassic-Early Cretaceous.
 - **State 2 (b):** Sedimentation and seaward sliding of the Cenomanian White Pointer progradational clastic series above the ductile shales of the Blue Whale Supersequence associated with the formation of White Pointer Delta detachment surface in a weak substrate (shales of the Blue Whale Supersequence) due to gravity tectonics
 - **State 3 (c):** Sedimentation of Tiger Supersequence with the active thin-skinned faults remaining similar to those initiated during the deposition of the White Pointer series. The 'concave' geometry of this section is thought to be caused by progressive flexure and subsidence in the delta system, or partly related to the compaction processes.
 - **State 4 (d):** Abrupt decrease of extension within the deltaic system and only about 3 km of displacement along the detachment during deposition of Tiger Supersequence set 2.
- States e-g show the Late Santonian-Maastrichtian basin evolution after breakup, and also reflect the progradation of the Hammerhead delta system.
 - **State 5 (e):** Illustration of the coarse clastic progradation of Hammerhead Supersequence set 1 as it seals both the structures of the White Pointer delta system, and the exhumed mantle core complex and crustal klippe in the Recherche Sub-Basin. It also shows that the Mulgara fault system was slightly reactivated (cumulative displacement < 1 km), probably due to compaction processes.
 - **State 6 (f):** Progradation of the Hammerhead Supersequence set 2 across the shelf without any syndepositional faulting. The thickening of the Hammerhead Supersequence set 2 is associated with the formation of gravitational instability. The newly formed Kowari fault system connects downward to the shallower decollement (detachment level for

Hammerhead Delta Interval) which probably developed within fine-grained facies, or prodelta shales, localized at the base of Hammerhead Supersequence set 1 (Totterdell and Krassay, 2003). The total displacement accommodated during state 6 by the Kowari fault system is about 10 km.

- State g shows the Cenozoic evolution of the Ceduna delta system during continuous seafloor spreading until present-day.
 - o **State 7 (g):** The amount of slip related to Kowari fault system decreases greatly (~2 km) during deposition of the Hammerhead Supersequence set 3. States 6-7 show that the total amount of displacement (i.e. 12 km) related to the Kowari fault system of the upper Hammerhead delta system is entirely accommodated within the frontal imbricate fan of the delta toe similar to other examples of compressional features at a delta toe (accommodating landward extensional deformation is well known from other comparable delta systems).
- State h depicts the relatively stable Cenozoic tectonic environment, where the Ceduna Sub-Basin was not fed by a large drainage system and sediment influx decreased at the end of the Maastrichtian.
 - o **State 8 (h) -Present Day-:** Hiatus in the inboard parts of the basin and the establishment of a shallow marine shelf across most of the Ceduna Sub-Basin. The Ceduna deltaic system is sealed by platform rocks of the Wobbegong and Dugong Supersequences and the weak apparent extension occurring during this time (<1 km), consisted essentially of compaction processes. Seaward, newly formed oceanic crust is draped by upper Cenozoic sediments.

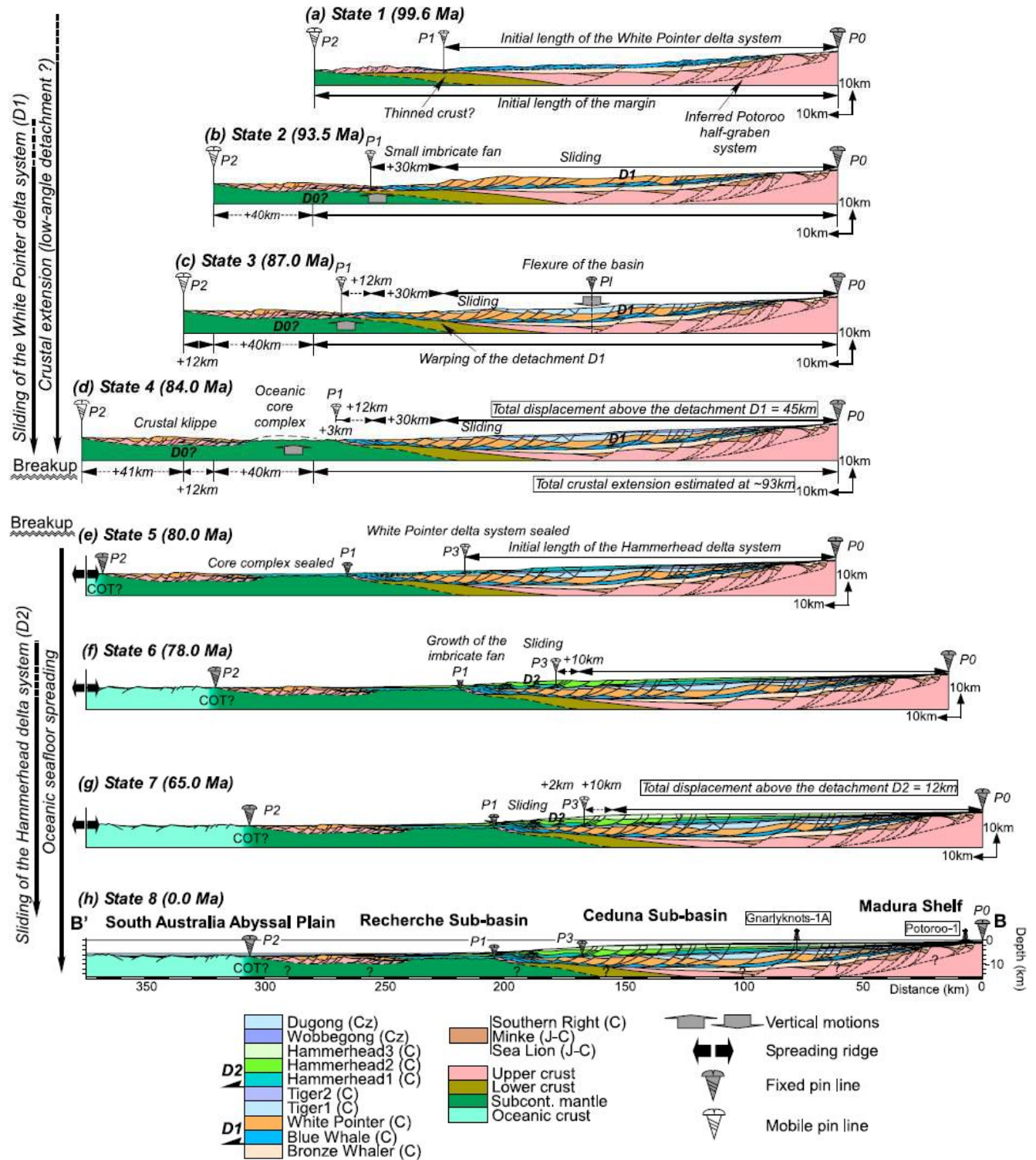


Figure 98: Kinematic evolution of the Ceduna Sub-Basin, based on a sequential restoration from the Late Albian to present-day. (image retrieved from Espurt et al., 2009)

C. Basin Evolution

i. Ceduna Wedge

Today, Bight Basin stands as a E-W to NW-SE trending offshore basin extending ~2100 km along the southern Australian margin (Bradshaw et al., 2003) and consisting of a number of Mesozoic-to-Cenozoic depo-centers that developed during the rifting, continental breakup and thermal subsidence of the passive margin (Fraser and Tilbury, 1979; Bein and Taylor, 1981; Stagg et al., 1990; Willcox and Stagg, 1990; Hill, 1995; Totterdell et al., 2000; Norvick and Smith, 2001; Totterdell and Bradshaw, 2004; Direen et al., 2007; Espurt et al., 2012). The southern transect of Australia covers the southwestward portion from (i) Madura Shelf, passing through (ii) Ceduna Sub-Basin, extending over (iii) Recherche Sub-Basin and reaching to the (iv) Australian Abyssal Plain. These four geologically-constrained elements define the passive margin setting of *Southern Australia*. Ceduna Sub-Basin vicinity, standing as the deepest depo-center/sedimentary wedge of the region containing a Late Jurassic-to-Cenozoic succession of 15 km thickness (Espurt et al., 2012), defines the study area of this thesis.

ii. Sedimentation History

Geochronologically, the Bight Basin was controlled by post-rift thermal subsidence during Early Cretaceous. In Mid Cretaceous, open ocean and a seaway extended along margin to the eastern part of Bight Basin. Accelerated thermal subsidence took place following the post-rift thermal subsidence during Mid-Albian and continued until the continental break-up in the Late Santonian - Early Campanian, which also marked the era of deltaic progradation supplemented by a system of gravity-driven, detached extensional and contractional structures in Cenomanian (Totterdell & Mitchell, 2007). At around 90-100 Ma, subduction ceased along the eastern Australian margin, resulting in dynamic rebound of the cratonic platform (Waschbusch et al., 1999). According to Totterdel & Mitchell, 2007; this rebound likely resulted in a regional drainage gradient developed to the west and hence much of the sediment eroded from this area was transported west and southwestwards towards the Bight Basin depo-center (Totterdell et al, 2000; Totterdell & Bradshaw, 2004). Following the tectonic uplift of Eastern Australia/Antarctic Margin, a km-scale denudation in the eastern part of the Australian continent is triggered and covered the southern rift system, which is also accounted for a major source of the siliciclastic sediments of the Ceduna delta system of the Bight Basin (Totterdell et al., 2000). However, progressive subsidence of the southern Australian margin was only partially compensated by scarce sediment supplies during the Cenozoic (Espurt et al., 2012). As it is stated by Totterdell & Mitchell (2007) several authors (Veevers et al., 1991; Raza et al., 1995; Totterdell et al., 2000; Krassay & Totterdell, 2003), have speculated that the deltas of the Ceduna Sub-basin were fed by sediments derived from the eastern Australian highlands about 1500 km to the E-NE.

The tectonostratigraphic development of the basin can be described under four Basin Phases defined for Ceduna Sub-Basin by Totterdell et al., 2000; Totterdell & Krassay 2003, and Totterdell & Bradshaw, 2004. The Sub-Basin evolution started with two successive episodes of extension and thermal subsidence during Mid-Late Jurassic (Figure 99).

Basin Phase-1:

The basin was initiated during a period of Middle–Late Jurassic to Early Cretaceous upper crustal extension, this phase is defined by the sedimentation onset started during Mid-Late Jurassic rifting extension/half graben formation (Totterdell et al., 2008) (pre State 1 on Figure 98, Figure 99).

Basin Phase-2:

This phase is marked by an episode of slow thermal subsidence during Early Cretaceous, which ceased abruptly upon the arrival of Basin Phase-3, consisted of a rapid subsidence. The deposited rocks were largely non-marine, with some marine influence becoming evident late in this phase during the Late Aptian, in wells located on the inboard margins of the basin (Totterdell et al., 2008) (pre State 1 on Figure 98 pre State 1, Figure 99).

Basin Phase-3:

The phase started by an abrupt increase in subsidence rate in the mid-Albian (Totterdell et al. 2000; Totterdell & Bradshaw 2004). This period of accelerated subsidence, which continued until the beginning of sea-floor spreading between Australia and Antarctica in the Late Santonian, coincided with a period of global sea level rise. The combination of these factors resulted in a high rate of creation of accommodation, the first major marine flooding event in the basin and the widespread deposition of marine silts and shales of the Albian–Cenomanian Blue Whale Supersequence (Totterdell et al., 2008) (State 1-4 on Figure 98, Figure 99).

Basin Phase-4:

This phase arrived during Late Santonian as the latest thermal subsidence episode initiating/establishing the South Australian passive margin era (Totterdell et al., 2000; Totterdell & Krassay 2003, and Totterdell & Bradshaw, 2004) and it is represented by the latest Santonian–Maastrichtian Hammerhead Supersequence, a sand-rich deltaic system characterized by strongly prograding stratal geometries. The commencement of ultra-slow to very slow sea floor spreading in the latest Santonian was followed by a period of thermal subsidence. Due to slow sea floor spreading rates, the seaways for delta progradation got narrower into which the deltas prograded. Moreover, a dramatic reduction in sediment supply at the end of the Cretaceous led to the abandonment of deltaic deposition. In the Middle Eocene (around 45 Ma), the increase of seafloor spreading rate (Tikku & Cande 1999) resulted in widespread subsidence of the margin (Totterdell et al., 2008) (State 5-7 on Figure 98, Figure 99).

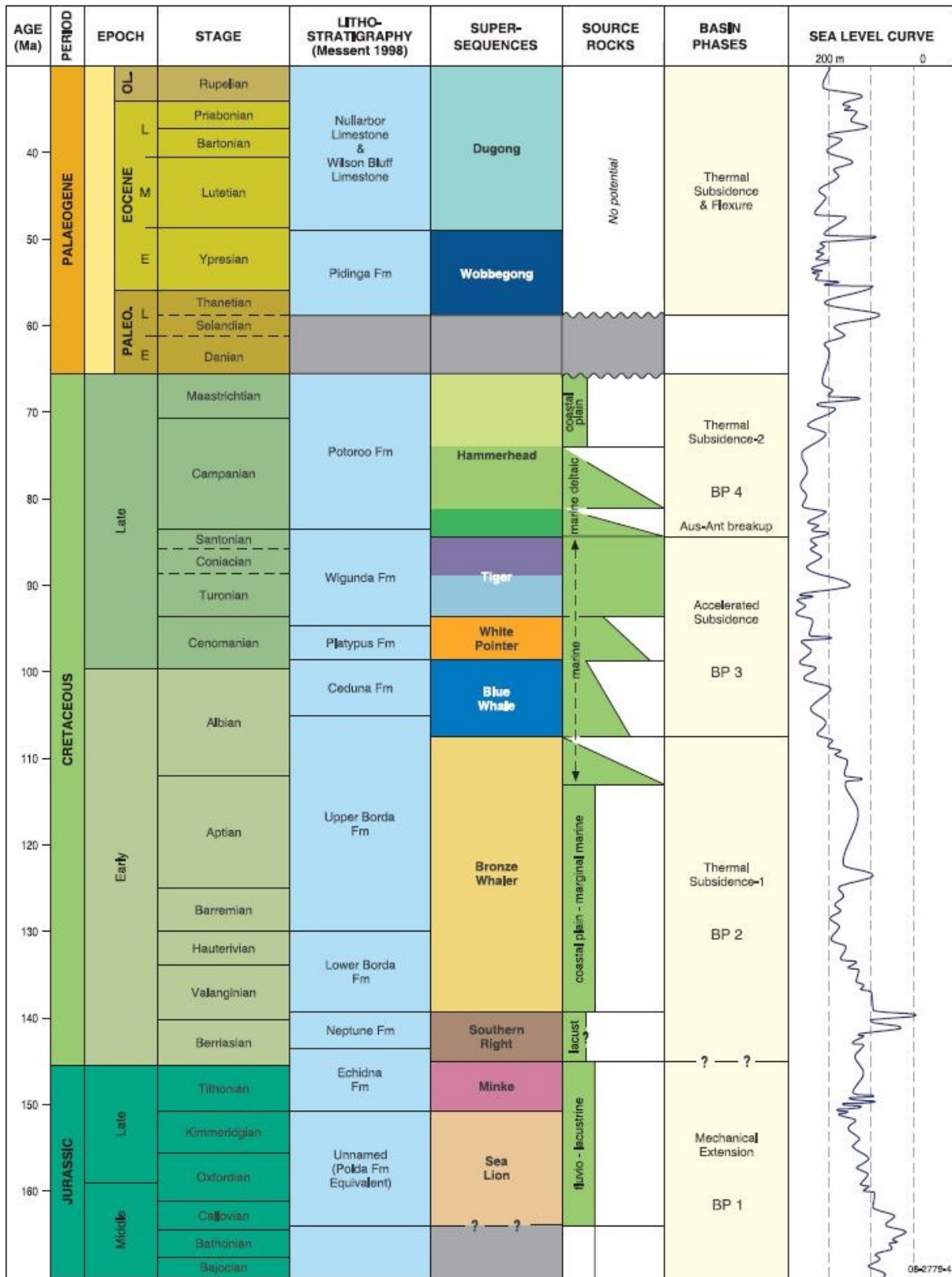


Figure 99: Bight Basin stratigraphic correlation chart showing basin phases and predicted source rock intervals (modified from Blevin et al. 2000 and Totterdell et al. 2000). The sea-level curve (Haq et al. 1988) is modified to the time scale of Gradstein et al (2004) (image retrieved from Totterdell et al., 2008).

Based on previously studied seismic datasets, Ceduna Sub-Basin is defined as a ~170-km long, oceanward-thickening sedimentary wedge of up to ~10 km thickness that has developed above the rifted Australian margin. It regionally detaches from the underlying crustal section and the deltaic complex of the sub-basin composes of two stacked and structurally independent delta systems (Delta Deepwater Fold & Thrust Belt -DDFTB-) (Totterdell and Krassay, 2003; Espurt et al., 2009; Espurt et al., 2012). Late Albian–Santonian age White Pointer Delta is formed during the tectonic denudation of the mantle, while the Late Santonian–Maastrichtian age Hammerhead Delta is formed during oceanic seafloor spreading and sag basin evolution of the southern Australian margin (Espurt et al., 2009). Further details of these deltaic systems will be given in the following sections, however, as it is seen on Figure 100-Figure 101, the initial sets of work depicted these two deltaic systems as ‘*coupled*’ without a separation in between indicating a structural independence from one another.

Figure 100 and Figure 101 display the observed sedimentary wedge of the area thickening seaward. The sedimentary wedge, which detaches (decollement D1) from the underlying substratum above ductile Late Albian shales of the Blue Whale Supersequence, thins onto the Madura Shelf landward, while pinching out onto highly extended continental crust and rocks of the continent-ocean transition zone seaward. Due to poorly-image seismic data, the underlying substratum of the Ceduna sedimentary wedge and its geometry is not well defined (Espurt et al., 2009).

Within the deltaic system, the Ceduna sedimentary wedge is subdivided into two stacked delta systems as described by Totterdell and Krassay (2003). As it is summarized by Espurt et al. (2009), *the lower, Late Albian-Santonian White Pointer delta system is formed by the Blue Whale Supersequence, the strongly progradational White Pointer Supersequence and the progradational-to-aggradational Tiger Supersequence*. Structurally, the dominant style of deformation of the White Pointer delta system comprises thin-skinned listric growth faults of the Mulgara fault system (Totterdell & Bradshaw, 2004), which branches downward onto the regional decollement level called D1 developed in the shales of the Blue Whale Supersequence and associates with some delta toe thrusts (Totterdell and Krassay, 2003; Totterdell and Bradshaw, 2004).

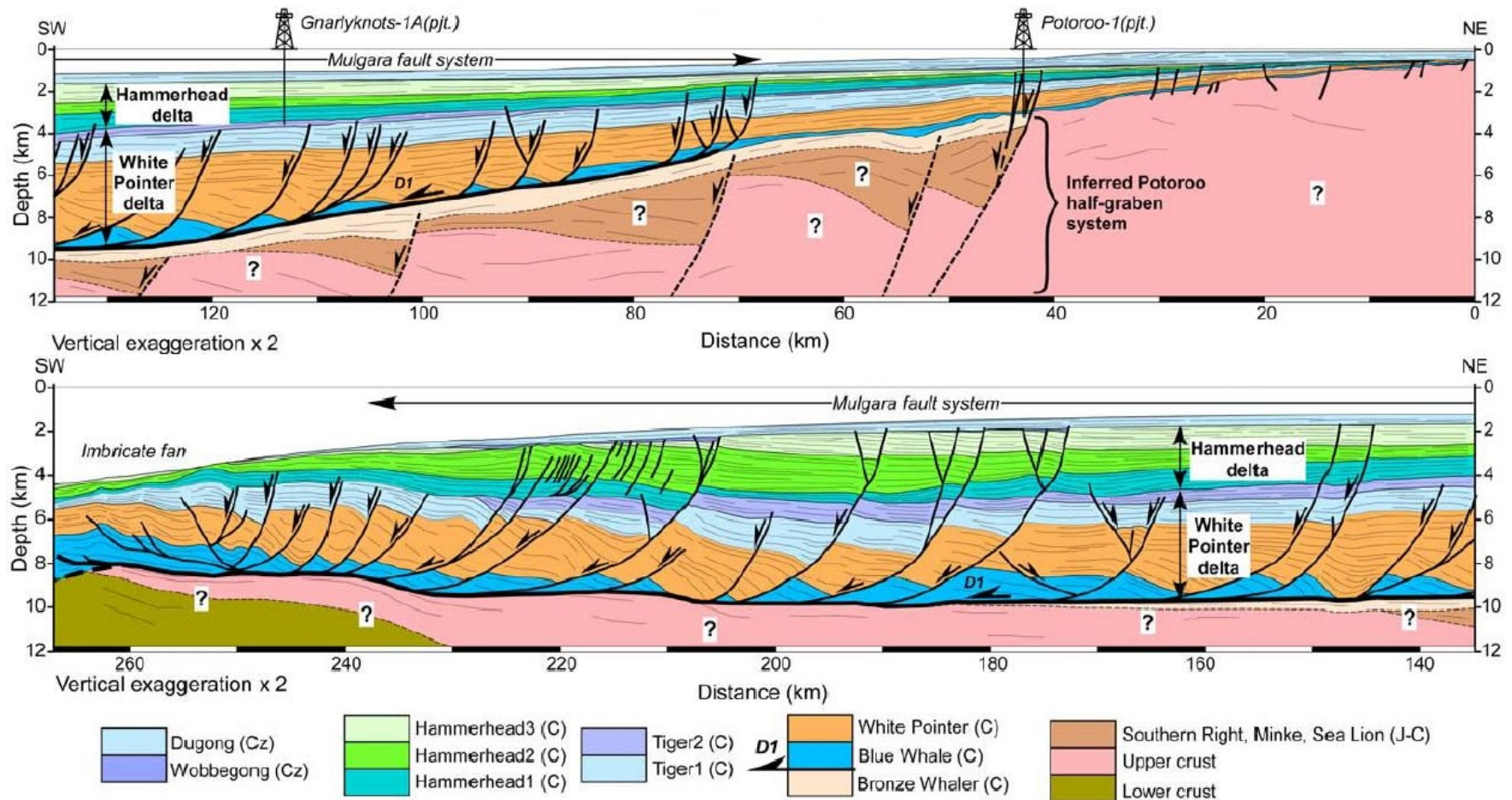


Figure 100: Upper Seismic Section: Cross-Section across the Madura Shelf and inner Ceduna sub-basin. Horizons were calibrated using projected (pjt.) data from the Potoroo-1 and Gnarlyknots-1A wells. Mulgara faults are indicated by medium black lines. These faults branch downward onto the decollement D1 (thick black line) at the base of the shales of the Blue Whale Supersequence. Inferred half graben of the Potoroo fault system (dashed black lines) underlies the delta system. Lower Seismic Section: Cross-Section through the Ceduna and Recherche subbasins. Mulgara faults are indicated by medium black lines. These faults branch downward onto the de'collement D1 (thick black line) at the base of the shales of the Blue Whale Supersequence. Note the scarcity of compressional features at the delta toe. Vertical exaggeration is x2. Please see the article for regional line locations (image retrieved from Espurt et al., 2009).

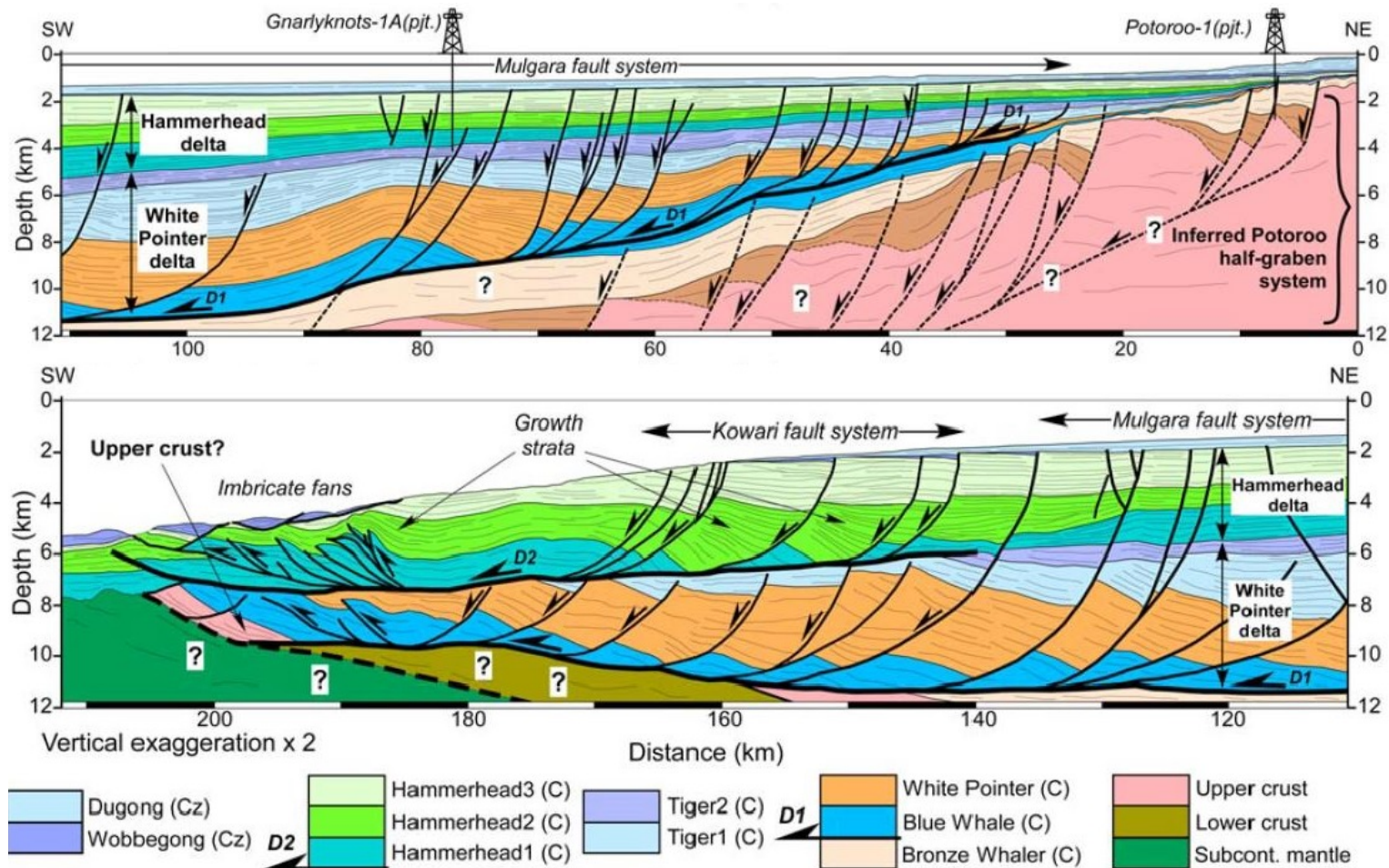


Figure 101: Upper Seismic Section: Detail of northern part of seismic line 4 (transect B-B0) across the Madura Shelf and Ceduna subbasin. Horizons were calibrated using projected data from the Potoroo-1 and Gnarlyknots-1A wells. Mulgara faults are indicated by medium black lines. These faults branch downward onto the shallow de'collement D1 (thick black line) at the base of the Blue Whale Supersequence. Seismic data show typical fault-related rollover anticlines within the White Pointer delta system, sealed by strata of the Hammerhead sequence set 1. Half grabens of the Potoroo fault system underlie the delta system. Lower Seismic Section: Detail of the southern part of seismic line 4 and the northern part of seismic line 5 (transect B-B0) across the Ceduna and Recherche subbasin. Faults are indicated by medium black lines. Sediments of the White Pointer delta system overlie subcontinental mantle rocks. The Hammerhead delta system is associated with gravitational sliding of the Kowari fault system which connects downward with the shallower de'collement D2. Note the growth strata pattern within the Hammerhead sequence set 2. Vertical exaggeration is x2. Please see the article for regional line locations (image retrieved from Espurt et al., 2009).

iii. Hydrocarbon Potential

In terms of hydrocarbon exploration activities, the study of Totterdell et al., 2008, showed that even though there is only two exploration wells drilled on the site, both of which have been abandoned before reaching down to their targeted depth, there is potential prospectivity in the area (Figure 102) (summarized from Totterdell et al., 2008);

- *Based on geochemical and palynological data; the source rocks were deposited in open marine conditions, and are consistent with Cenomanian-Turonian boundary oceanic anoxic event (OAE2).*
- *The coaly Cenomanian White Pointer Supersequence and the marine Cenomanian-Albian Blue Whale Supersequence (Boreham et al. 2001; Struckmeyer et al. 2001) could sustain viable petroleum systems.*
- *Santonian-Maastrichtian Hammerhead Supersequence was the critical factor driving maturation and generation in the basin (Struckmeyer et al. 2001).*
- *Potential accumulations are predicted to have a large component of black oil contributed from the Cenomanian–Turonian boundary source rock.*
- *The variations in maturation and expulsion patterns suggest a likelihood of considerable changes in hydrocarbon compositions across the basin.*

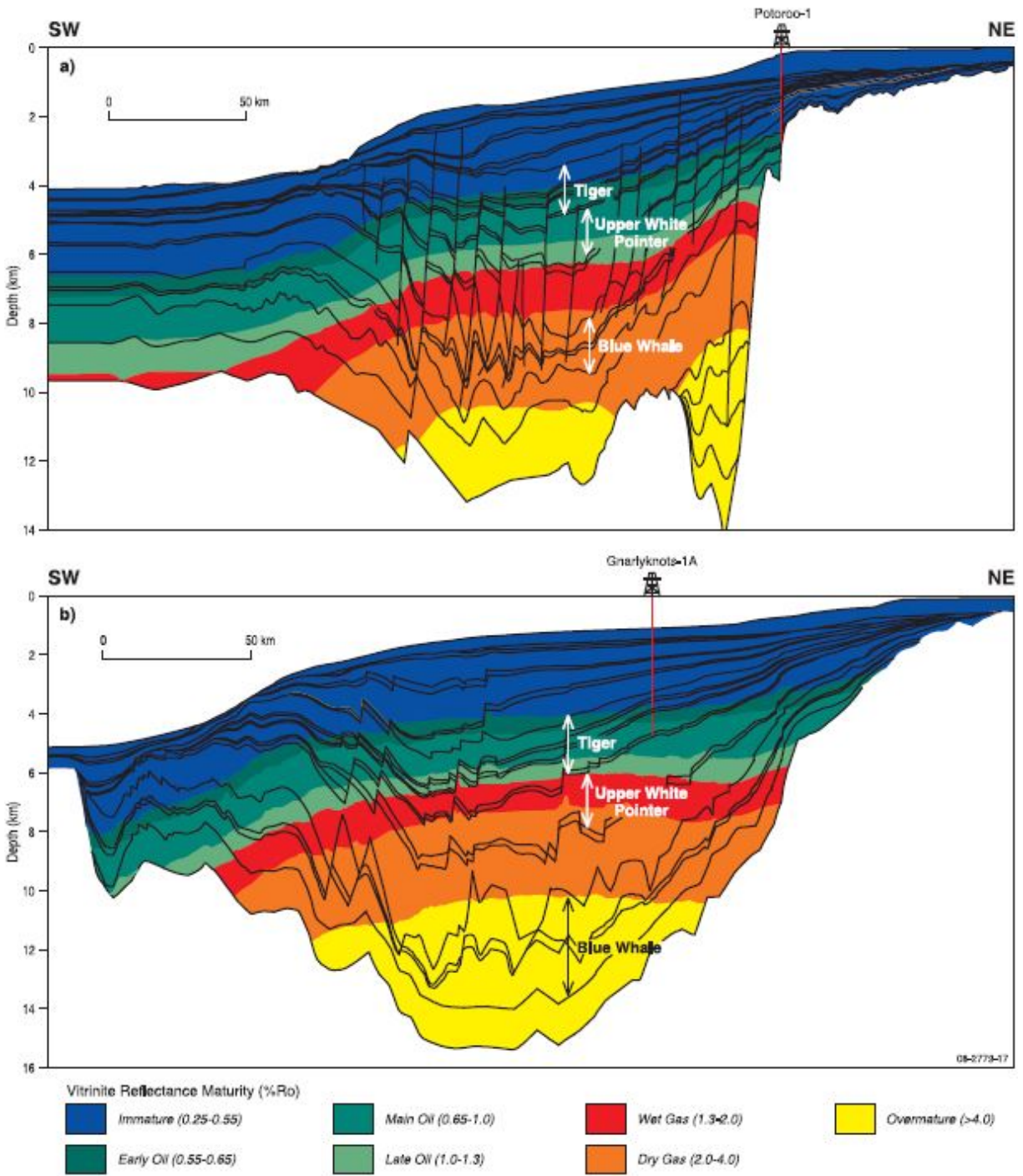


Figure 102: Modelled present-day maturity zones (% Ro) for the a) northern and b) central transects (image retrieved from Totterdell et al., 2008).

Figure 103 depicts two cross sections with drilled well locations used by Totterdell et al., 2008 basin modeling and prospectivity study, while Figure 104 shows the predicted hydrocarbon accumulation scenario within the vicinity of Gnarlyknots 1A well location.

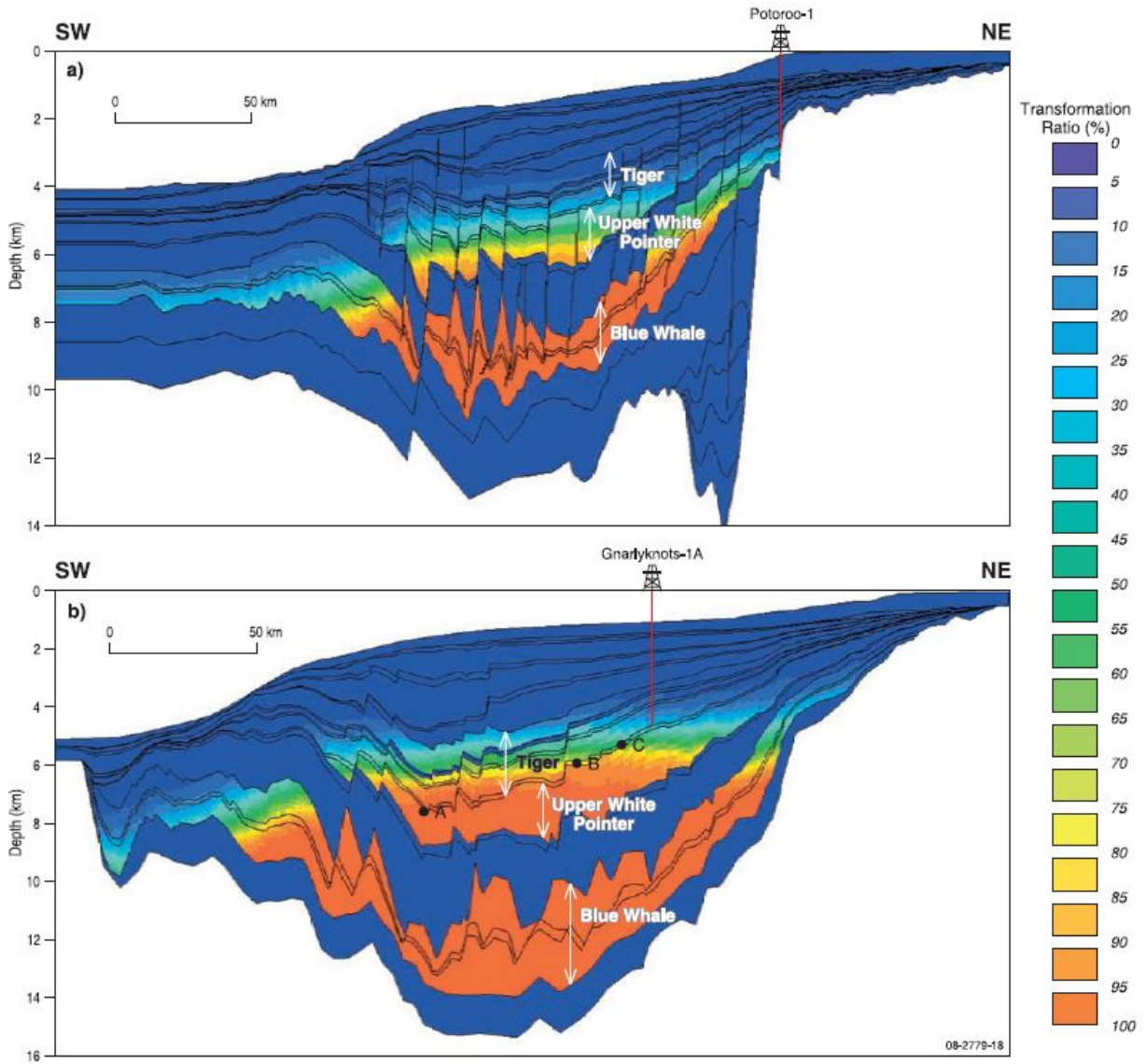


Figure 103: Modelled present-day transformation ratios (%) of three potential source rock units within the Blue Whale, upper White Pointer and Tiger supersequences for the a) northern and b) central transects (well locations as noted on diagrams, see the article for further details) (image retrieved from Totterdell et al., 2008).

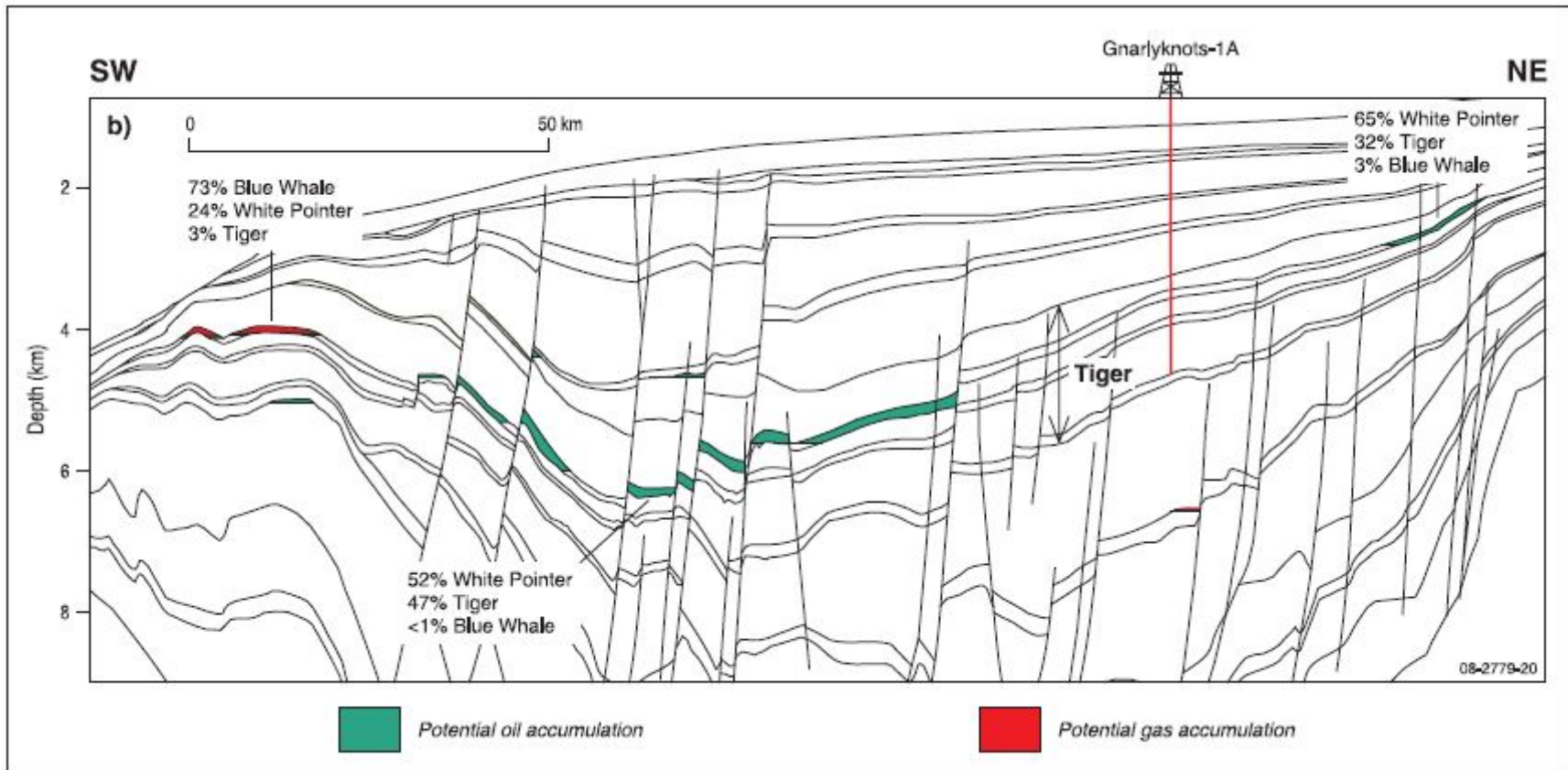


Figure 104: Portion of the central Ceduna transect showing predicted accumulations for the modelled scenario and the percentage of liquids contribution from three potential source units (image retrieved from Totterdell et al., 2008).

III. Lithostratigraphy of Ceduna Sub-Basin

The lithology of Ceduna Sub-Basin can be categorized under three sections; (A) Pre-Deltaic, (B) Deltaic and (C) Post-Deltaic. The *Pre-Deltaic* section is composed of four sequences: (i) Sea Lion, (ii) Minke, (iii) Southern Right, and (iv) Bronze Whaler, which are controlled by basement rooted tilted rift blocks and geometries. Within the *Deltaic* Interval, we observe four megasequences namely Blue Whale, White Pointer, Tiger and Hammerhead successions. They form the *White Pointer* and *Hammerhead* deltaic wedges, underlined by the Blue Whale and Tiger maximum flooding surfaces respectively. This interval is governed by gravitationally gliding systems above shale-prone substrates. The *Post-Deltaic* section consists of the Wobbegong and Dugong formations respectively, which seal off the deltaic interval of Ceduna Sub-Basin and show no deformation related to the underlying strata. The schematic stratigraphy diagram of Espurt et al., 2012 (modified after Espurt et al., 2009) depicts the whole system (e.g. pre-deltaic, deltaic and post-deltaic) of Ceduna Sub-Basin nicely in an informative manner, including the tectonostratigraphic evolution the basin has gone through (Figure 105).

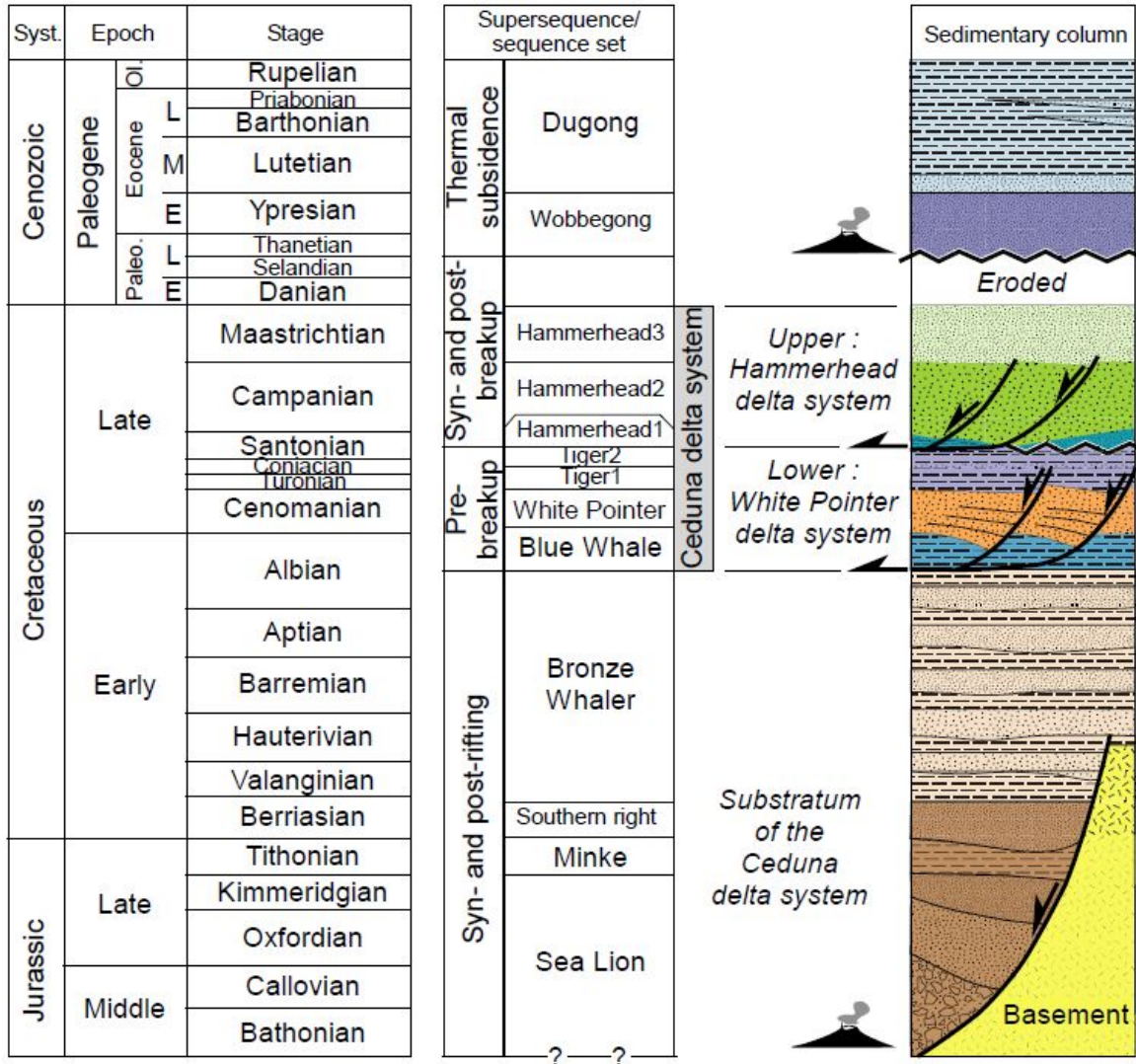


Figure 105: Stratigraphy of the Bight Basin (modified from Espurt et al., 2009). Early–Middle Jurassic and Palaeocene/Eocene intrusions are also shown (volcano) (image retrieved from Espurt et al., 2012).

A. Pre-Deltaic Lithology

The Pre-Deltaic lithology of Ceduna Sub-Basin is composed of four super sequence formations, which are namely and respectively: the Sea Lion, Minke, Southern Right, and Bronze Whaler Formations. The Sea Lion and Minke formations consist of ~3000m syn-rift related fluvio-lacustrine sand stone, claystone, siltstone and mudstone sediments, which have accumulated in the hanging walls of a set of predominantly seaward dipping extensional faults involving the Proterozoic basement. The Southern Right formation (Berriasian age) lies above these formations, followed by the Valanginian-to-Early Albian Bronze Whaler Supersequence, both of which consist of an aggradational succession deposited during the postrift thermal subsidence period. They present fluvial channel and floodplain deposits with some marine influence in the upper part of the section with thicknesses reaching ~1700m.

B. Deltaic Lithology: White Pointer and Hammerhead DDFTBs

The Ceduna Sub-Basin consists of two successively stacked and independent deltaic systems: the *White Pointer* and *Hammerhead* Delta Deepwater Fold & Thrust Belt (DDFTB) of Albian-Santonian and Santonian-Maastrichtian ages respectively (MacDonald, 2013; MacDonald et al., 2012; Totterdell and Krassay, 2003). The following sub-parts will be detailing these stacked delta interval (from Blue Whale up to the Hammerhead Formation) in terms of lithology and their sequential order.

i. Blue Whale Formation

The Middle Albian – Cenomanian Age Blue Whale Formation uncomfortably overlies the rift and post-rift strata of the first late Jurassic to lower Cretaceous rifting phase. It marks the first major maximum flooding surface within the Ceduna Sub-Basin, where the near shore / restricted marine sandstones and a thick package of marine mudstones were introduced into the basin and created the detachment level for the overlying White Pointer deltaic system. Thickened shale interval accommodates the gravitationally gliding White Pointer Delta and its listric fault network. Progradation of deltaic sediments into a narrow seaway took place during Cenomanian (arrival of White Pointer supersequence), rapid deposition of which resulted in a short-lived period of shale mobilization and growth faulting throughout the northern half of the Ceduna Sub-basin (Totterdell and Krassay, 2003)

ii. White Pointer Formation

The Late Albian – Santonian Age White Pointer Supersequence defines the older DDWFTB system underlined by Blue Whale shales within the Ceduna Sub-Basin geological setting. It is a gravitationally gliding delta interval dominated by major listric faults soling into the Blue Whale detachment level on proximal-to-central part of the delta, associated with a compressional domain at the distal toe (Totterdell and Krassay 2003; Espurt et al., 2009). The Cenomanian deltaic facies include a broad band of coaly sediments in the inner part of Ceduna Sub-basin. The formation is primarily composed of fluvial to

lagoonal siltstones and mudstones intercalated with minor sandstones and coal units that arrived with a southwesterly progradation of deltaic sediments into a narrow seaway (Totterdell et al., 2008)

iii. Tiger Formation

The Turonian to Santonian age Tiger Formation is an aggradational sediment package consisting of marine and marginal marine mudstones that were deposited in a predominantly marine environment. The supersequence is dominated by mudstones and a few thick sandstone units in well data (Totterdell and Mitchell, 2007), while it has a largely flat-lying aggradational character on seismic data. It defines the shaly detachment base for the overlying Hammerhead Delta sequence. The formation is heavily faulted due to reactivation of older faults (Mulgara Fault Family) that is controlled by the underlying ductile shale units of Blue Whale Supersequence (MacDonald et al., 2012).

iv. Hammerhead Formation

The Late Santonian – Maastrichtian Age Hammerhead Supersequence defines the younger deltaic system that is independently placed above the White Pointer Delta system arriving after the continental break-up (~ 83 Ma) and a major regression event. It is marked by a basal erosion surface (break-up unconformity) and consists of amalgamated/interbedded sandstones, mudstones displaying a progradational-to-aggradational character. The formation lies comfortably above the Tiger Formation detachment surface, which accommodates the gliding of the Hammerhead delta interval. Based on well data information, in proximal parts of the basin, the Hammerhead supersequence consists mainly of amalgamated fluvial channel sandstones, while in distal parts of the basin, it exhibits basinward-thinning wedges of marine shale at the toe of slope (Totterdell and Krassay, 2003).

C. Post-Deltaic Lithology

The Post-Deltaic interval of Ceduna sub-basin is defined by two geological formations, which are called respectively; Wobbegong and Dugong supersequences. As it is stated by Sharples (2014) the Wobbegong supersequence represents a siliciclastic deltaic episode from the Paleocene–Early Eocene (Totterdell et al., 2003), which unconformably overlies the Cretaceous clastics of the Hammerhead Supersequence (Li et al., 2004). The Wobbegong supersequence consists of marginal marine-to-fluvial sandstone and minor siltstone succession of about ~100 and 280 m thick (Espurt et al., 2009). Cande & Mutter (1982) and Veevers et al., 1991, noted that *following a period of very slow spreading until the Middle Eocene, spreading rates increased noticeably from about 43 Ma* and hence as a result, the uppermost Middle Eocene-to-Pleistocene Dugong Supersequence unconformably overlies the Wobbegong Supersequence (Espurt et al., 2009). This formation consists of basal coarse sandstone overlain by a monotonous carbonate succession, representing deposition of predominantly cool water carbonate shelf with an aggradational-progradational stratal geometry that reaches a maximum thickness of approximately 300 m in the Ceduna Sub-Basin (Espurt et al., 2009).

IV. Close-Up on the Ceduna Sub-Basin Deltaic Interval

Ceduna Sub-Basin consists of two structurally independent deltaic systems (delta–deepwater fold–thrust belt -DDWFTB-) that stack on top of each other; the Late Santonian–Maastrichtian Hammerhead DDWFTB and the Late Albian–Santonian White Pointer DDWFTB. White Pointer Delta detach above the shale-rich Blue Whale maximum flooding surface while the Hammerhead Delta detach above the Tiger Supersequence (MacDonald et al., 2012).

A. *White Pointer Deltaic System (DDFTB)*

Ceduna Sub-Basin's White Pointer interval is described as a delta setting dominated by growth faults above a detachment level consisting of mobile Blue Whale shales with a narrow band of compressional structures (Totterdell and Krassay, 2003; Espurt et al., 2009). The area has been previously studied with 2D regional lines with an aim to understand the controlling basin dynamics by numerous researchers (see reviews from Totterdell, et al., 2000; Totterdell and Krassay, 2003; Totterdell and Bradshaw, 2004; Totterdell et al., 2008; Espurt et al., 2009; Espurt et al., 2012).

In Ceduna Sub-Basin, three main structural domains stand out within the White Pointer Delta interval; the thrust front, transitional zone and growth faulting. Totterdell and Krassay (2003) define these domains with their interpretation as (i) the 150km long central-to-northern section, which is found to be subjected to contractional deformation featuring northeasterly dipping imbricate thrust fan system, (ii) a transitional zone that is marked between the zones of growth faulting and thrust front, which is noted by a 'complex region' consisting of chaotic seismic reflections and upright, and (iii) the classically formed gravitationally gliding zone dominated with listric faults at the proximal part.

Based on the analysis made by Totterdell and Krassay (2003) it is proposed that the Blue Whale detachment level underneath the White Pointer Delta interval has a very gentle seaward dip, which may dip landward in some areas, and the growth faulting developed above this decollement is accompanied by reactive shale diapirism (mobilized shales), whose seismic character is found to be chaotic, suggesting overpressured shale facies. These aforementioned properties of the delta interval will be covered in the following sections under three specific/focused titles respectively; Facies, Structure and Shale Tectonism.

i. Facies of White Pointer Delta

White Pointer Delta succession consists of deltaic sediments of the White Pointer Supersequence and the underlying marine silts and shales of the Blue Whale Supersequence. Deposition of this deltaic wedge took place rapidly over a period of about 5 million years above the undercompacted marine shales of the Blue Whale Supersequence leading to the development of overpressure within the shales.

In terms of geological facies, the well data suggests the Blue Whale formation being comprised of nearshore-or-restricted marine siltstones while the overlying White Pointer formation to be dominantly fluvial-to-lagoonal siltstone and mudstone (Totterdell & Krassay, 2003). In this geologic setting, deltaic wedge of White Pointer Delta is dominated by growth faults developed above a regionally extensive décollement level within the ductile the Blue Whale Supersequence and the seismic character of these underlying mobile shales are reported to be typically chaotic, with little seismic penetration beneath it (e.g. characteristics of overpressured facies).

Growth fault controlled depo-centers observed on delta with limited seismic imaging quality suggests (i) *interbedded sandstone and mudstone accumulations*, possible (ii) *folds consisting of shale-cored anticlines with lack of coherent seismic reflections beneath the crests of the anticlines*, and (iii) *thickening of strata between those folds suggesting a diapiric movement of overpressured shales* (Totterdell & Krassay, 2003). Towards the northern part of sub-basin, the growth section is topped by Upper White Pointer Supersequence, a uniformly-thick aggradational unit that lacks syn-sedimentary growth, which points out to ceasing of faulting during the late Cenomanian (Totterdell & Krassay, 2003).

ii. Structure of White Pointer Delta

The growth fault pattern of the delta has a generally arcuate trace and a NW-SE strike with the regional faults dipping to the W-SW or SW direction. The study of Totterdell and Krassay, (2003) associated the faulting pattern of White Pointer Delta to Lewis, 1997's findings to say that *when the mobile substrate is relatively thinner than other large delta settings* (e.g. Setap Shales of the Baram Delta are more than 3000 m thick [Van Rensbergen et al. 1999], and the Akata Shales of the Niger Delta over 6000 m thick [Cohen & McClay 1996]), *counter-regional faults might not be developing in places like Ceduna Sub-Basin* as the maximum pre-deformation thickness of the Blue Whale is noted to be probably around 1500-2000 m with the available seismic data observations. Consequently, the change of sedimentary architecture from *growth strata-to-simple aggradation* was connected to the *cessation of growth faulting* and *suggested to be controlled by the vertical limit of mobile shale rather than dewatering of shales* (Totterdell and Krassay, 2003) (Figure 106).

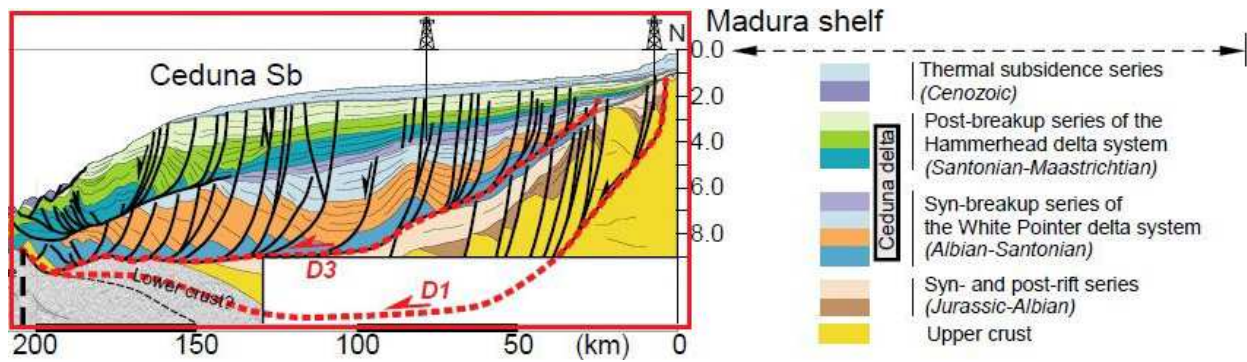


Figure 106: Structural Interpretation of Ceduna Sub-Basin (red rectangle), showing White Pointer and Hammerhead Delta Intervals (image retrieved from Espurt et al., 2012).

iii. Shale Tectonism in White Pointer Delta: Evidence of Mobile Shales

In terms of Shale Tectonism; Totterdell and Krassay (2003) explained that across the continental slope, there is a *zone of contractional deformation* that features northeasterly-dipping imbricate thrust fans, which sole out within the overpressured Blue Whale Supersequence. They further pointed out to the fact that the *structurally complex region* (transitional zone), which has been termed as the ‘*Outer Basin High*’ by previous workers (Stagg et al. 1990), containing zones of chaotic seismic reflection character and upright folds *could be simply shale-cored anticlines, but the absence of coherent seismic reflections beneath the crests of the anticlines, and thickening of strata between them suggests diapiric movement of the overpressured shales* (Figure 107).

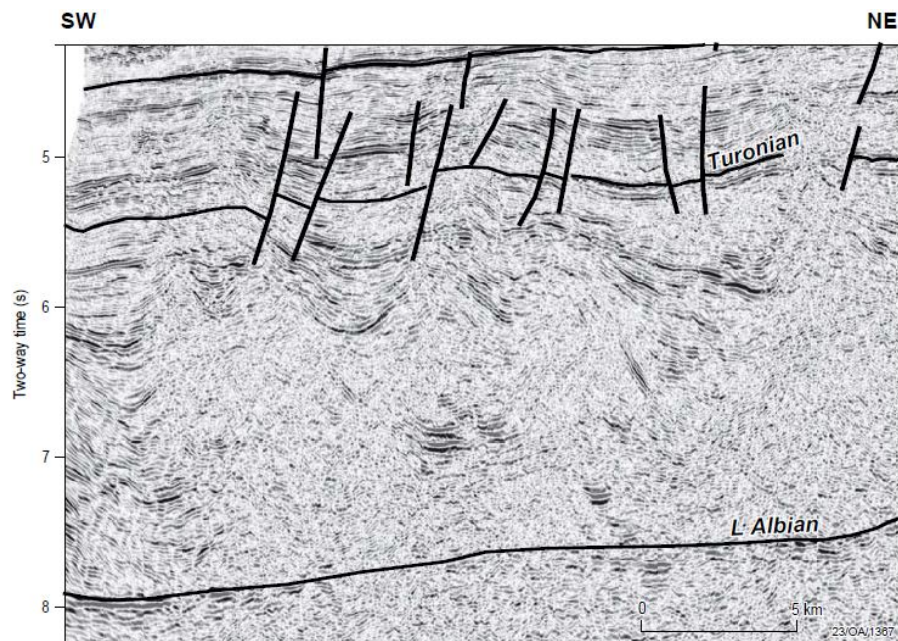


Figure 107: Seismic line from the transitional zone between updip growth faults and downdip contractional structures, White Pointer Delta, northern Ceduna Sub-basin. Note the presence of possible diapiric features at 6.0-7.0 s (TWT), adjacent synformal strata, and the chaotic seismic character of much of the section, particularly beneath the crests of the anticlines (image retrieved from Totterdell and Krassay, 2003).

In the same study, Totterdell and Krassay (2003) wrapped up their argument by saying the structural style of the White Pointer Delta is comparable to that of many other large progradational deltas around the world such as the Niger and Baram (e.g. Doust & Omatsola 1990; Damuth 1994; Cohen & McClay 1996; Morley & Guerin 1996; McClay et al. 1998; Van Rensbergen et al. 1999), as well as the Gulf of Mexico (Buffler et al. 1978; Winker & Edwards 1983) with similar zones of growth faulting, accompanied farther basinward by zones of diapirism and contractional deformation, developed above a mobile substrate have been described from deltas. However, they also draw attention to the fact that these structural similarities, the extent of active diapirism in the White Pointer Delta is *significantly less* than in the Niger and Baram deltas and provided a comparison sketch with the structural architecture of the White Pointer Delta in the northern Ceduna Sub-basin with Morley & Guerin's (1996) idealized profile of a progradational delta (Figure 108), and ended their argument saying it is likely that *differential loading* and *gravity sliding* might have contributed to the development of the White Pointer Delta as *the differential load provided by the prograding wedges of sediment triggered the reactive rise of shale diapirs and the commencement of growth faulting*.

Another observation made by Totterdell & Krassay, 2003 was that the shale deformation and growth faulting within the White Pointer Delta appeared to be restricted to the *northern half of the Ceduna Sub-Basin*. While the thicker successions of the Blue Whale and White Pointer Supersequences occur in the southern half of the basin, there is *no such found evidence of the shale tectonism that are evident to the north*. The most likely explanation proposed in their study for this phenomena is to not have overpressure developed within the Blue Whale Supersequence in this part of the basin, which can be related to either (i) changes in lithofacies, or to the (ii) rate of sediment burial. They also noted the aggradational stratal geometry of White Pointer supersequence in certain parts of the study area pointing out to non-direct delta influence and being away from the locus of rapid sediment progradation, which consecutively lead to underdevelopment of (i) overpressure, (ii) differential loading and (iii) shale mobility/diapir triggering (Totterdell & Krassay, 2003).

However, these observations were made with under-quality vintage seismic datasets, which limited researchers' interpretation ability on structural features compared to well-imaged and coherent seismic data examples. A generic representation of White Pointer Delta based on 2D seismic dataset interpretation is seen on Figure 109. We will be elaborating on all of these aforementioned observations made on 2D regional lines from the previous studies in the following sections with the help of additional 3D seismic dataset we have utilized for the research in an effort to better understand/explain these structures and dynamics of White Pointer Delta system.

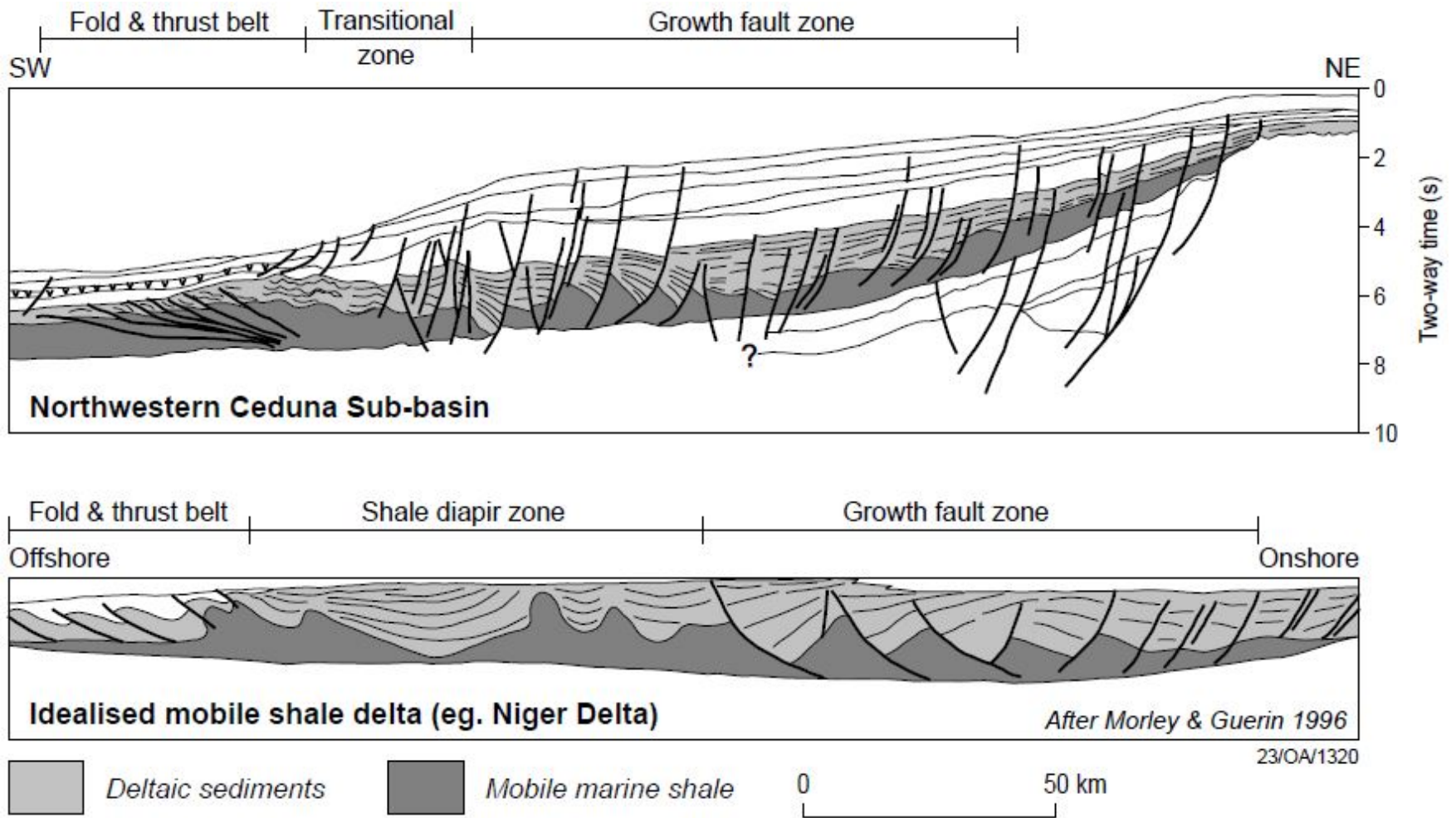


Figure 108: Comparison of White Pointer Delta and the idealised progradational delta of Morley & Guerin (1996). Note the similar distribution of extensional, diapiric/transitional and contractural structural zones (image retrieved from Totterdell and Krassay, 2003)

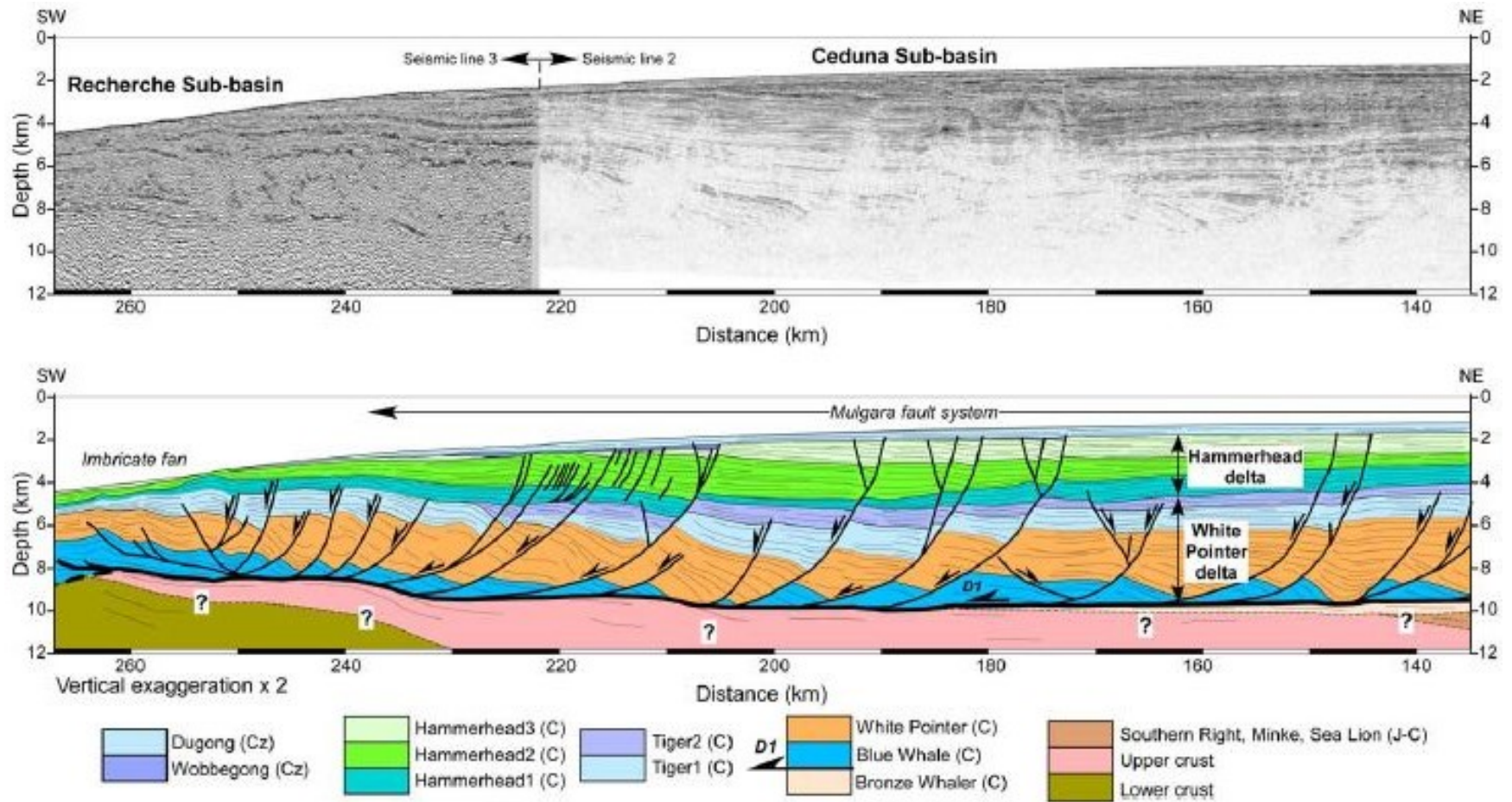


Figure 109: Regional seismic data example of Ceduna Sub-Basin Deltaic intervals (White Pointer and Hammerhead DDFTBs) (image retrieved from Espurt, et al., 2009).

B. Hammerhead Deltaic System (DDFTB)

The Late Santonian – Maastrichtian Age Hammerhead Supersequence defines the younger deltaic system that is independently placed above the White Pointer Delta system arriving after the continental break-up (~ 83 Ma) and a major regression event. Deposition took place in a rapidly subsiding and dominantly restricted marine environment between Turonian to the Late Santonian, which has led to accumulation of marine and marginal marine sediments of the aggradational Tiger Supersequence defining the detachment surface for the deltaic succession. The Hammerhead delta is marked by a basal erosion surface (break-up unconformity) and consists of amalgamated/interbedded sandstones, mudstones displaying a progradational-to-aggradational character. This major unconformity separating the deltaic Hammerhead Supersequence from the underlying Tiger Supersequence, displays an angular unconformity in places where the gently-dipping tilted blocks of the Tiger Supersequence have been eroded, which suggests at least local uplift, possibly related to the commencement of seafloor spreading, occurred prior to deposition of the Hammerhead Supersequence (Totterdell & Krassay, 2003). Following this erosional surface, the formation lies comfortably above the Tiger Formation detachment surface, which accommodates the gliding of the Hammerhead delta interval (Figure 110). Totterdell & Krassay, 2003, defines the delta sequences as *a 19 million year period of sustained deltaic sedimentation in the Bight Basin, representing a sand-rich, shelf-margin delta complex that is subdivided into three internal sequence sets*;

- The lower two sequence sets (Late Santonian to Campanian) exhibiting strongly progradational geometries.
- The upper sequence set (Maastrichtian) governing a dominantly aggradational geometry indicating a major change in basin dynamics due to a gradually decreasing rate of sediment supply.

Structurally, the fault density within the Hammerhead Supersequence shows an increment to the south and west. Series of high-offset, listric growth faults (reaching up to 3500m thicknesses in places) occurring near the SW margin of the Ceduna Sub-Basin across a narrow belt subparallel to the palaeo shelf-margin. These extensional faults are accompanied downdip by contractional deformation in the form of imbricate thrust fans, whose deformation appears to happen in the Campanian, while the strongly progradational phase of deltaic development took place. It is important to note that Hammerhead Delta structural and stratigraphic architecture is (Totterdell & Krassay, 2003);

1. Remarkably different than that of the deltas involving deformation of a mobile ductile medium such as White Pointer Delta, and Niger Delta and Baram Delta; the underlying sediments across the shelf, show no evidence of overpressure and deformation. Observed erosional surface at the sequence boundary point out to the underlying sediments being buried in a slow manner (not rapidly).
2. Quite similar to the relatively coarse clastic progradational delta of the Orange Basin and others on the West African passive margin (Muntingh & Brown 1993; Duval et al. 1992; Turner 1995) as such deltas exhibit strongly progradational-to-aggradational stratal geometries, and load-induced gravitational failure at the shelf margin and a general lack of syn-depositional shale deformation or faulting.

- However, as the supersequence gets thicker at the palaeo-shelf margin, consequential gravitational instability results in localised deformation, with large growth faults compensated down-dip by folds and imbricate thrust systems. It is Totterdell & Krassay (2003)'s suggestion that in this portion of the deltaic succession (both basinward and towards the south); Hammerhead Supersequence was probably detaching above overpressured pro-delta shale or fine-grained slope facies with deformation accompanied by limited shale mobilization beneath large growth faults while detachment folding took place at the transitional zone between growth faults and toe-thrusts.

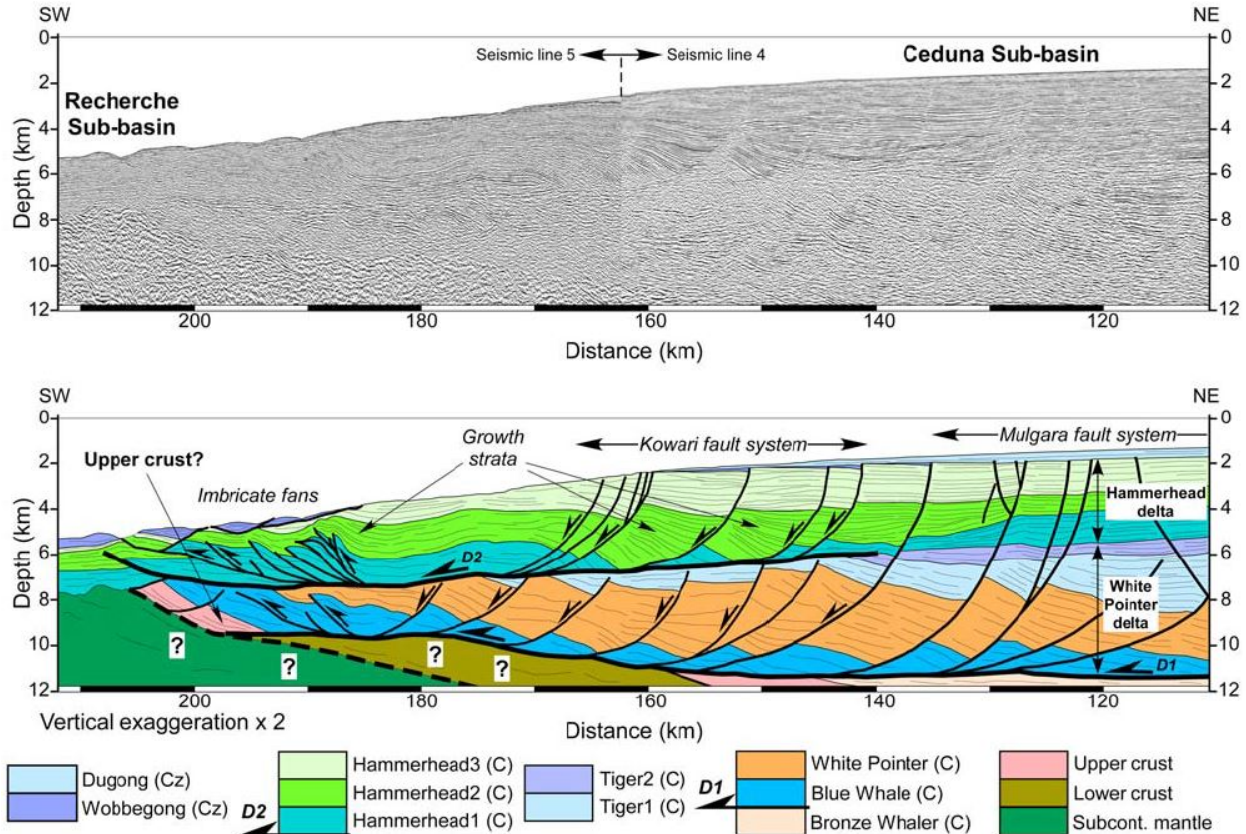


Figure 110: Structural interpretation of distal White Pointer and Hammerhead Deltas. Faults are indicated by medium black lines. Sediments of the White Pointer delta system overlie subcontinental mantle rocks. The Hammerhead delta system is associated with gravitational sliding of the Kowari fault system which connects downward with the shallower decollement (Tiger Formation) (image retrieved Espurt et al., 2009).

C. *Synthesis: Review of Ceduna Sub-Basin Deltaic Interval Structural Evolution*

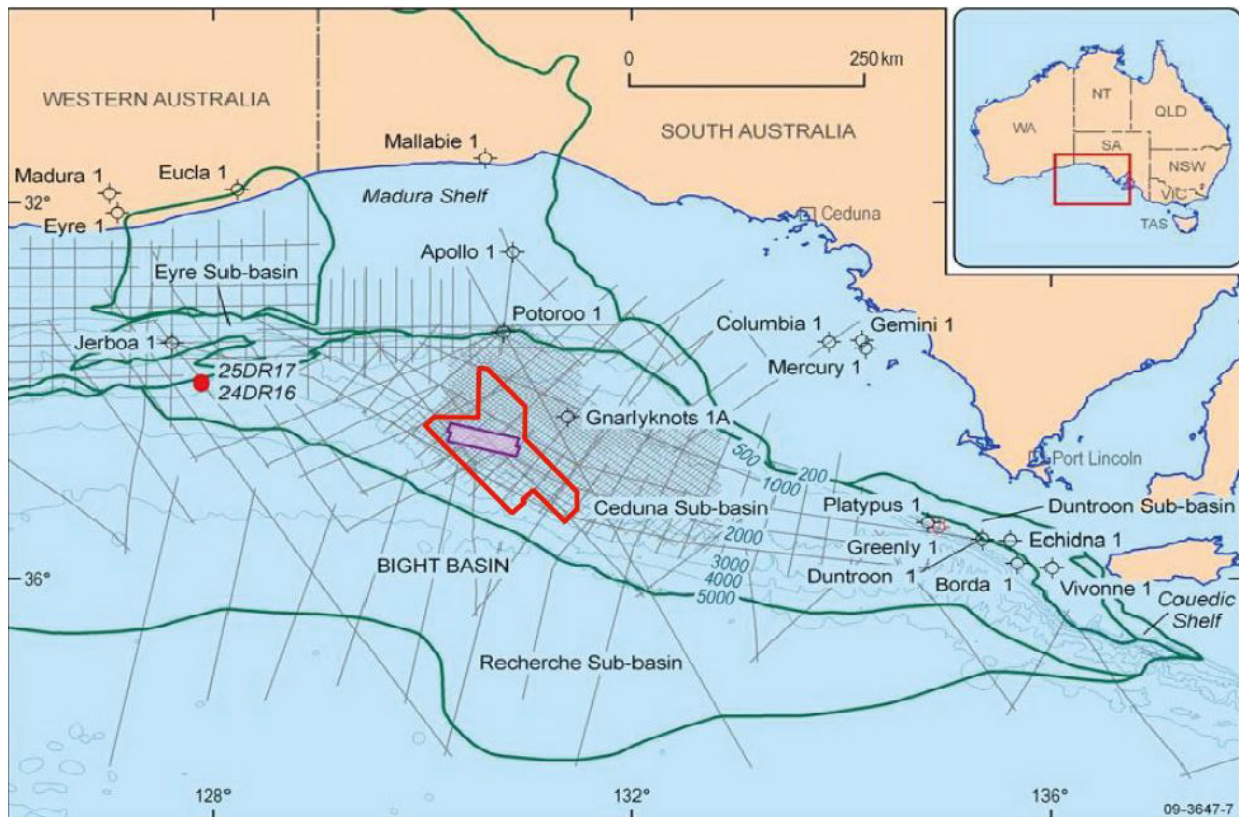
Ceduna Sub-Basin is seen as a deep sedimentary basin, which holds two stacked but structurally independent deltaic systems (namely White Pointer and Hammerhead) detaching above shale-prone maximum flooding surfaces (Blue Whale and Tiger formations respectively). The Albian-Cenomanian age White Pointer and Santonian-Maastrichtian age Hammerhead deltaic systems of Ceduna provide an example of two very different types of progradational delta systems (DDFTBs) (Totterdell & Krassay, 2003).

With the limited quality of available seismic data, the White Pointer deltaic system was attempted to be explained as a gravitationally-gliding delta with a listric fault pattern. Studies made with vintage 2D seismic datasets pointed out to an inflated shale interval in the thrust front of the delta with limited detailed explanations (see reviews of Totterdell & Krassay 2003, Totterdell & Bradshaw 2004; Totterdell et al., 2008; Espurt et al., 2009 and 2012; MacDonald et al., 2012; MacDonald, 2013). Espurt et al., (2012) defined (1) the White Pointer Delta as a structure *mainly formed during the tectonic denudation of the mantle and evolved on top of the exhumed mantle*, and (2) the Hammerhead Delta as a gliding delta *formed during oceanic seafloor spreading and sag basin evolution of the southern Australian margin*, mostly stable with only frontal gravitational sliding that is balanced by the extensional feature at the rear (Totterdell and Krassay, 2003; Espurt et al., 2009; King and Backé, 2010).

Chapter 6: Study Area: Well Information, Dataset and Methodology

This chapter will be summarizing all of the accessible seismic data material we have utilized in this research as well as the only two exploration well information (Potoroo and Gnarlyknots) within close vicinity of the 3D seismic dataset.

Our area of interest, Ceduna Sub-Basin, located in the Great Bight Basin, occupies 90000 km² of seafloor in offshore Southern Australia. Based on the Ceduna Sub-Basin: Environmental Summary Report, there are >33,000 line km of deep seismic data and core data from 10 wells in the Ceduna and Eyre Sub-basin region, Geoscience Australia is the custodian for >9,000 line km of multi-beam data and >8,000 line km of shallow sub-bottom profiler data (Figure 111). Metadata for these geophysical data sets and controlled access is available through the Petroleum Information Management System (PIMS) at <http://www.ga.gov.au/oracle/npd/> (Hughes et al., 2009).



Where well symbol information is sourced from publicly available "open file" data, it has been provided by Geoscience Australia from Well Completion Reports. These symbols were generated from open file data as at 31 March 2009. Where well symbol information is not publicly available from titleholders' data, the information has been extracted from other public sources.






- | | |
|--|---|
|  3D Trim seismic survey |  Petroleum exploration well - Dry hole |
|  Basin outline |  Petroleum exploration well - Gas show |
|  2D seismic survey line |  Potential source rocks |
|  Bathymetry contour (depth in metres) |  dredge sample location |

Figure 111: Map showing location of seismic lines and wells in the eastern Bight Basin (image modified after Hughes et al., 2009) (red geometrical closure shows the location of the 3D dataset studied for this PhD research).

I. Ceduna Sub-Basin Exploration Wells

Ceduna is an underexplored basin with only two exploration wells, namely Potoroo 1 and Gnarlyknots 1A, drilled to date locating on the inboard margins of the delta with limited calibration of lithologies (Tredreu & Horton, 2019). The stratigraphic information of the region is obtained from these two exploration wells called Potoroo-1 and Gnarlyknots-1A, (Figure 112).

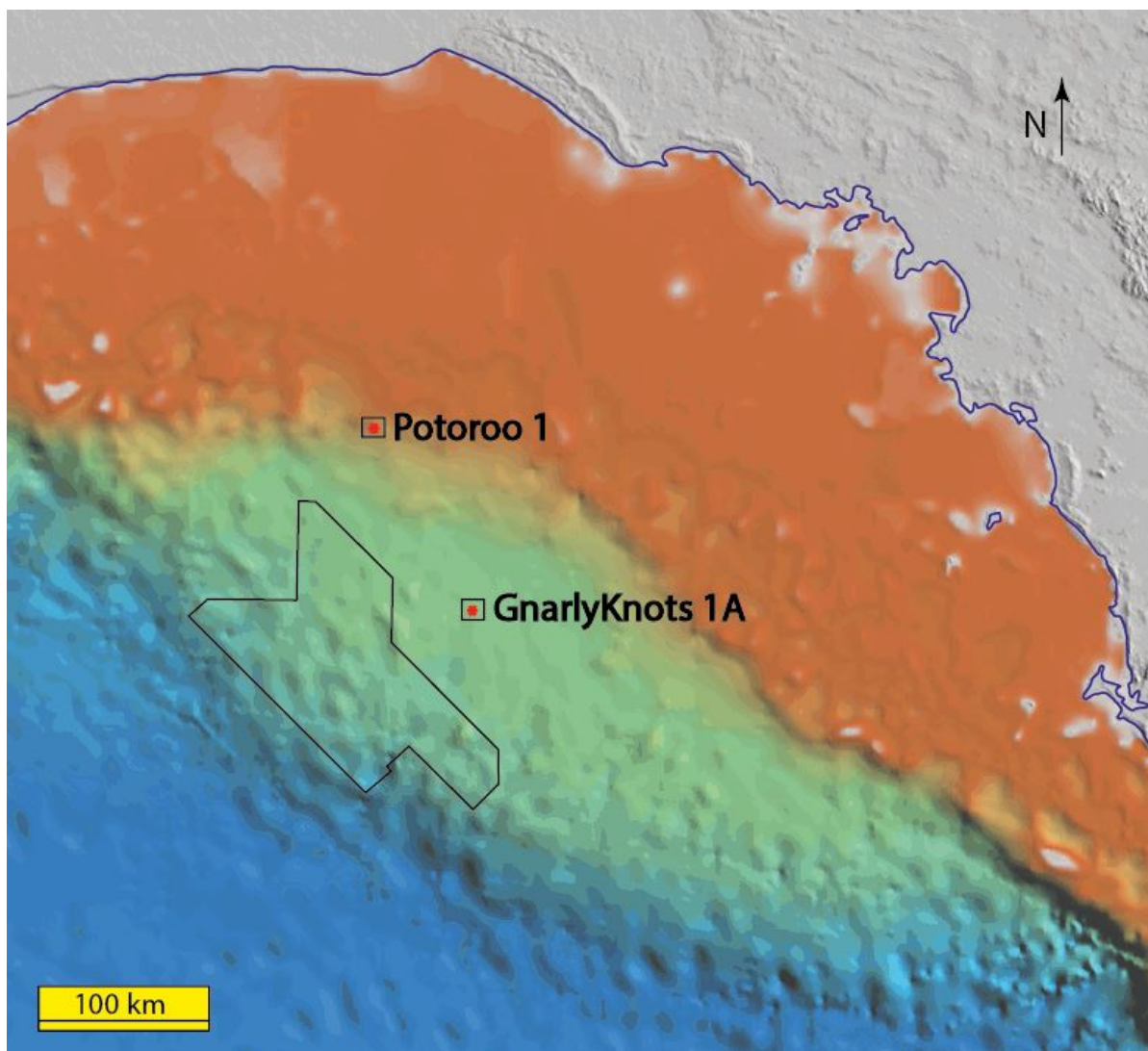


Figure 112: Location of Ceduna Sub-Basin Exploration Wells (black geometrical closure shows the location of the 3D seismic cube).

A. Potoroo-1 Well

Potoroo-1 is located on the southern edge of the Madura Shelf reaching down to the granitic basement rocks of the Gawler Craton. The exploration well has an abundance of claystone and interbedded siltstones to provide seal for any underlying Tiger and White Pointer reservoirs (Messent, 1998) and intersects a thin mid-Late Cretaceous succession at the edge of the sub-basin and provides a stratigraphic control in the *northern Ceduna Sub-Basin* as no other well is drilled farther basinward (Figure 113). To the east of the main depocentres, a thin Bight Basin succession overlies Proterozoic basement of the Gawler Craton and deformed Early Palaeozoic rocks of the Kanmantoo Trough, while to the north, basement includes a variety of Proterozoic and older terranes (Totterdell & Krassay, 2003; Totterdell & Mitchell, 2007). Tredrea and Horton, 2019, states that according to the recent palynological interpretation performed by the Murphy-Santos Joint Venture. The Tiger supersequence ranges from brackish through marginal-shallow marine and the White Pointer is deposited in a restricted marine to brackish environment while the Lower to Middle Hammerhead is dominantly fluvio-deltaic. Due to the restricted marine environment of the well location away from the main delta fairways throughout the Tiger and White Pointer time, Potoroo 1 reservoir development is generally poor (Tredrea and Horton, 2019), which explains the non-deposition, erosion and bypass of coarser clastics in the area (King & Mee, 2004). Table 1 displays the summary report of this well data (information retrieved from Australian Government, Geoscience Australia, Potoroo 1 - Geoscience Australia Well Report dbforms.ga.gov.au).

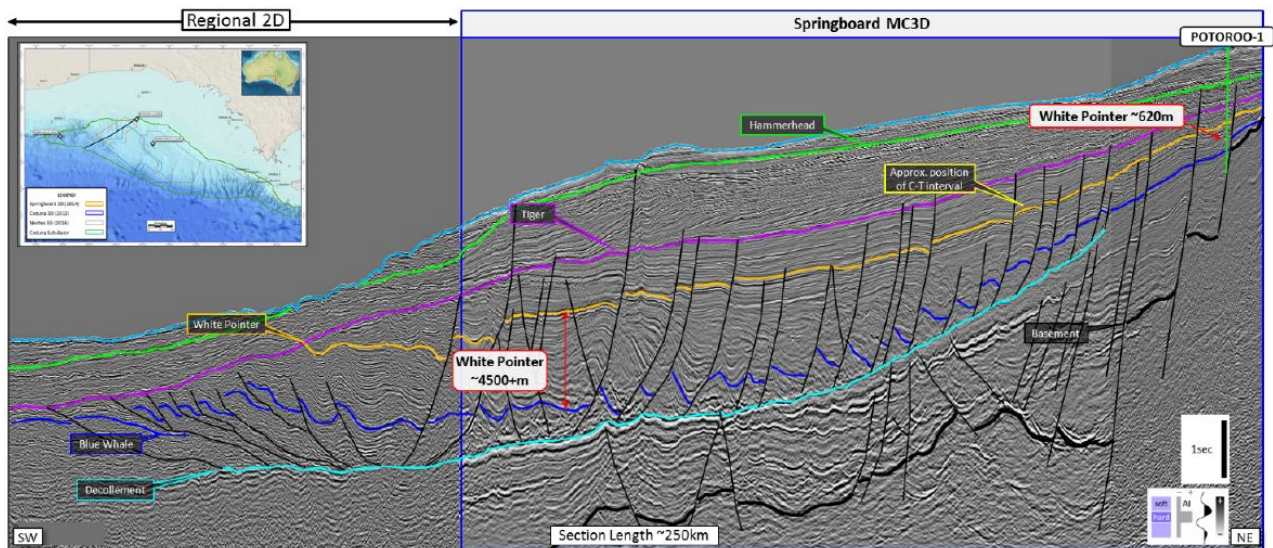


Figure 113: Composite NE-SW seismic line through study area showing the rotated fault blocks of the Lower White Pointer overlain by sub-parallel to gently dipping Upper White Pointer and Tiger SS. *Springboard MC3D courtesy of PGS (image retrieved from Tredrea & Horton, 2019).

WELL DATA

UNO	W5750001	ENO	14937
Region	SA	Purpose	exploration
Latitude	-33.385733	Longitude	130.770003
Well Status	abandoned	HC Shows	dry
TD Date	17-APR-1975	Total Depth	2924m
Platform		Field	none
Position	Offshore	Seafloor	-252m MSL
Title	SA 5	Legislation	PSLA
Operator	Shell Development (Australia) Proprietary Limited	Contractor	Atwood Oceanics
Rig Make/Model		Kelly Bushing/Rotary Table	rotary table 9m
Spud Date	17-MAR-1975	Rig Release Date	26-APR-1975
Remark	The well was drilled to test a dip closure against a basement controlled fault in the Cretaceous section. Potoroo 1 penetrated a sedimentary section ranging in age from Holocene to Neocomian and bottomed in granitic basement of presumed Precambian age. The primary objective proved to be composed of Upper Cretaceous glauconitic siltstones and mudstones, with no significant sandstone development. The basal Cretaceous sandstone had porosities ranging from 15-25% but was water-bearing. The only hydrocarbon indications were numerous methane shows associated with coal and carbonaceous material. Potoroo 1 is located offshore in the Great Australian Bight, South Australia. Well completion report coordinates Lat -33 23' 13.571" S, Long 130 46' 6.899" E. Coordinates displayed are WGS84 calculated using block shifts Lat -5.0876" S, Long 5.0208" E.		
Basins	Great Australian Bight Basin (WCR) Bight Basin Eucla Basin (GA)		
Sub-Basins	Ceduna Sub-basin (GA)		
Location (WCR)	Potoroo 1 is located offshore in the Great Australian Bight, South Australia. Well completion report coordinates Lat -33 23' 13.571" S, Long 130 46' 6.899" E. Coordinates displayed are WGS84 calculated using block shifts Lat -5.0876" S, Long 5.0208" E.		
Objective (WCR)	Petroleum		
Summary (WCR)			
Scanned and other files	N/A		

Table 1: Potoroo-1 Well Information Sheet obtained from Geoscience Australia dbforms.ga.gov.au

B. Gnarlyknots-1A Well

Gnarlyknots-1A is located in the center of the Ceduna Sub-Basin (more proximal part of the delta system) and reaches to the upper part of the Tiger Supersequence. This well is drilled by Woodside Petroleum and its partners in 1316 m of water aiming to test the petroleum systems within more distal Late Cretaceous depositional systems of the Ceduna Sub-Basin in 2003 (Figure 114) (Tapley et al. 2005; Totterdell et al., 2008). The well intersected dominantly sand rich intervals with minor interbedding of silts and clays and thinner shale units than prognosed pre-drill (Tredrea and Horton, 2019), however, due to extreme weather conditions it later got abandoned in Santonian age sandy coastal plain deposits, some 1500 m above the planned completion depth, with several key targets untested and no hydrocarbons encountered (Tapley et al. 2005; Walker 2007; Totterdell et al., 2008). It has excellent sand development interbedded with minor interbedding of silts and clays and only two shales of appreciable thickness punctuating the top of the Tiger SS and at the Upper-Middle Tiger boundary (Tredrea and Horton, 2019). Table 2 displays the summary report of this well data (information retrieved from Australian Government, Geoscience Australia, Gnarlyknots 1A - Geoscience Australia Well Report dbforms.ga.gov.au).

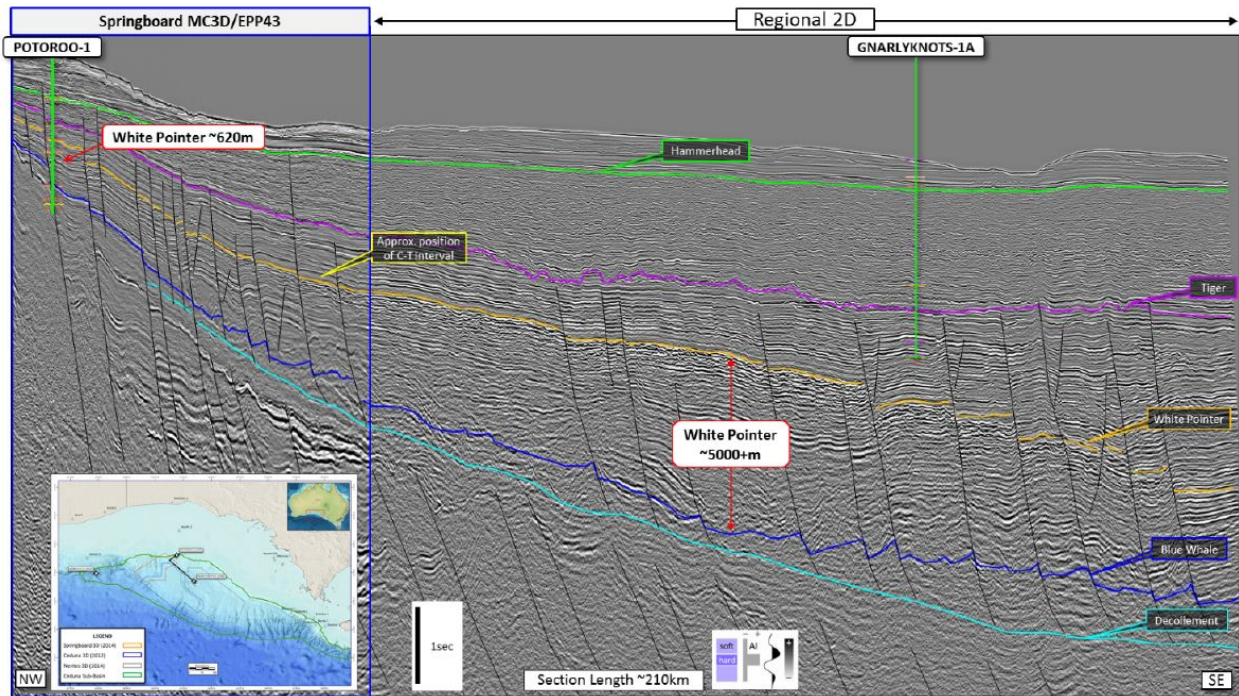


Figure 114: Composite NW-SE seismic tie line from Potoroo-1 to Gnarlyknots-1A. Note the thickening of the White Pointer and Tiger SS away from the Potoroo-1 well. *Springboard MC3D courtesy of PGS (image retrieved from Tredrea & Horton, 2019).

WELL DATA

UNO	W5200332	ENO	33577
Region	SA	Purpose	exploration
Latitude	-34.294184	Longitude	131.384168
Well Status	suspended	HC Shows	dry
TD Date	10-MAY-2003	Total Depth	4736m
Platform		Field	none
Position	Offshore	Seafloor	-1316m MSL
Title	EPP 29	Legislation	PSLA
Operator	Woodside Energy Ltd.	Contractor	Global Sante Fe
Rig Make/Model		Kelly Bushing/Rotary Table	rotary table 25.1m
Spud Date	20-APR-2003	Rig Release Date	29-MAY-2003
Remark	Plugged and abandoned due to deteriorating weather.Gnarlyknots 1A was spudded 20/4/03. Gnarlyknots-1A was spudded some 50 metres southwest of Gnarlyknots-1 on 20 April 2003. A largely sandstone sequence of Late Cretaceous age was penetrated beneath a carbonate dominated Tertiary interval. No significant hydrocarbons were encountered. Significant downtime due to bad weather occurred during the drilling of Gnarlyknots-1A and with the likelihood of further bad weather to come, the decision was taken to suspend the well, after penetrating only two of the original five objective levels (Figure 7). The well confirmed the presence of good quality reservoir sands within the Campanian (K58) and Santonian (K56) succession and two potentially sealing claystone packages, the "K58 Shale" and the "315 Shale".Gnarlyknots-1A was suspended as a dry hole at a total depth of 4736 mRT in sandstones and claystones of Coniacian age, on 26/5/03.		
Basins	Great Australian Bight Basin (WCR) Bight Basin Eucla Basin (GA)		
Sub-Basins	Ceduna Sub-basin (GA)		
Location (WCR)			
Objective (WCR)	Petroleum		
Summary (WCR)			
Scanned and other files	N/A		

Table 2: Gnarlyknots 1A Well Information Sheet obtained from Geoscience Australia dbforms.ga.gov.au

II. Dataset and Methodology

This study focuses on Ceduna Sub-Basin with a seismic scheme. The seismic framework of the study area consists of vintage regional 2D lines and a 3D cube. We have utilized the 2D regional lines and well locations outside of the 3D seismic cube in order to construct a regional geologic concept. Well top information from the Potoroo-1 and Gnarlyknots-1A exploration wells was carried into the 3D seismic cube via the 2D regional lines collected from the closest vicinity of these wells. Upon bringing the stratigraphic markers of interest (Blue Whale Formation, White Pointer Formation and Tiger Formation) into the 3D seismic data cube, we adopted a seismic interpretation scheme in order to conduct the study. Additional 2D regional lines (TWT) were used to constrain the regional view of the basin. The following sections will be detailing the seismic dataset and methodological interpretation scheme adopted for Ceduna Sub-Basin shale tectonics study.

i. Dataset: Translation of 2D Seismic-Based Literature Knowledge into 3D Seismic Data

Based on all of the geological findings we have referenced from the so-far published literature in the previous parts of this chapter, it is fair to say that the sedimentary succession of Ceduna Sub-Basin, White Pointer deltaic wedge is quite well known/studied in terms of geodynamics, tecto-evolution and lithostratigraphy. However, the shale-driven history of distal delta toe has limited information due to lack of well-imaged 3D seismic datasets.

Even though they pointed out to possible Shale Tectonism in the region, the seismic examples were not satisfyingly good/sufficient in terms of imaging quality, which called attention to the dire necessity for well-imaged/high quality 3D seismic datasets of the region in order to fully grasp the geologic setting and deltaic evolution pattern associated with mobilized shale features. We have carried out a structural analysis scheme on a 3D seismic PSDM dataset acquired by PGS in 2011 from Ceduna Sub-Basin, offshore Australia for the extensive chunk of this PhD research, which has given us an immense advantage on (i) identifying the '*suggested shale features of the delta front*' that was mainly described as a thrust complex component on previous studies due to lack of well-imaged supplementary datasets, and to (ii) re-compare/interpret the regional 2D lines to the high resolution 3D block in order to make a cross-correlation with the *current* and newly-acquired knowledge on potential evidences for particular behavior of shale.

Figure 115 shows a compilation of 2D seismic data-based stratigraphic chart and cross-section depicted by Espurt et al., (2009, 2012), for the delta interval of Ceduna Sub-Basin. The figure is supplemented with 3D seismic data examples we utilized in this study, which make a striking difference compared to the old seismic datasets with the amount of detail added to the geologic structure of White Pointer Delta distal thrust front. The following chapters will be further detailing the 3D seismic dataset interpretation we have adopted in order to investigate shale tectonism of the region.

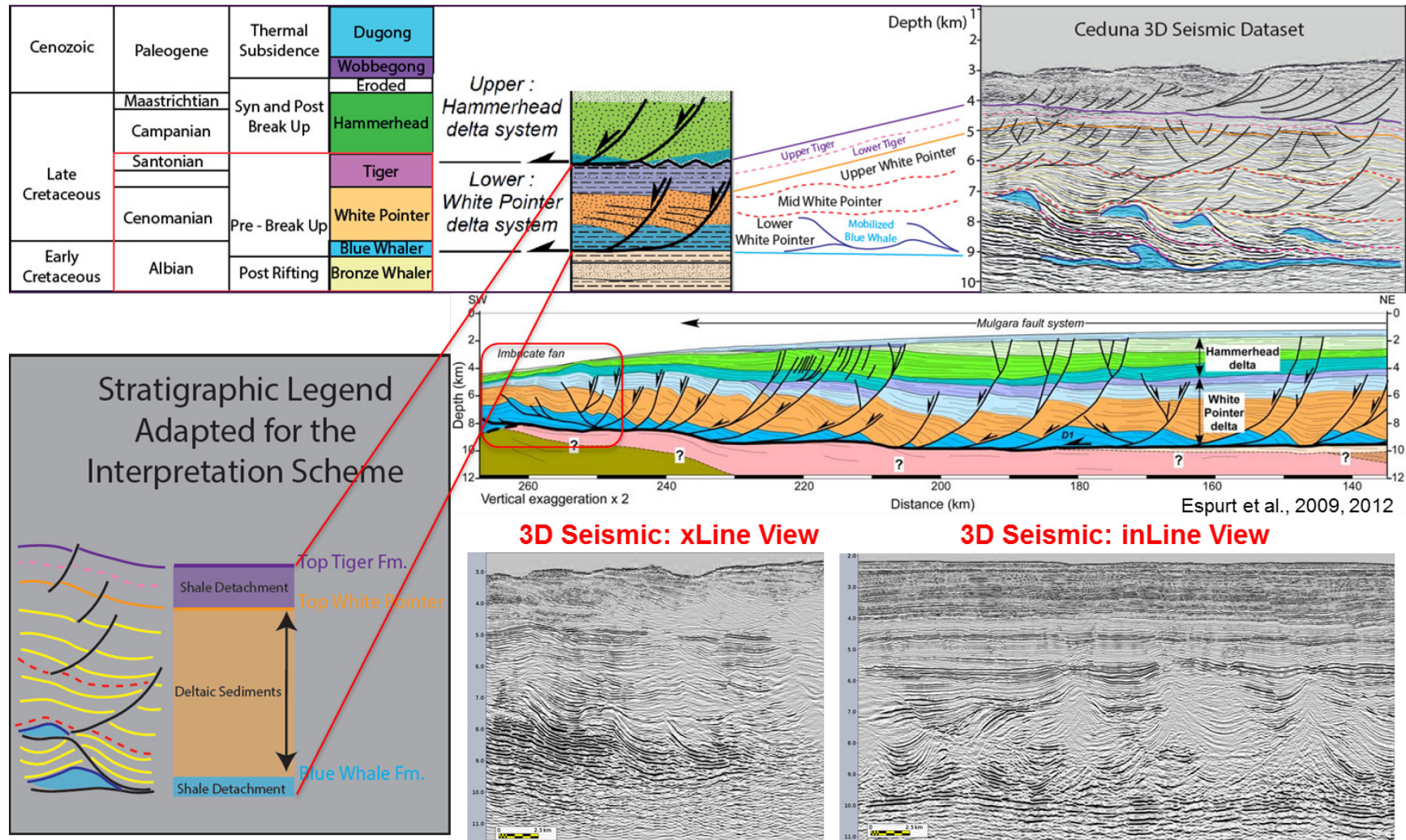


Figure 115: Deltaic Stratigraphy of the Ceduna Sub-Basin, Bight Basin (modified after Espurt et al., 2012) showing the White Pointer and Hammerhead delta intervals with the updated seismic interpretation and detail conducted for this PhD research via 3D seismic data.

ii. Methodology: Interpretation Scheme Based on 2D-3D Seismic Coverage

The bulk of this study is based on a 3D seismic PSDM (pre-stack depth migration) dataset acquired by PGS in 2011 from Ceduna Sub-Basin, offshore Australia (Table 3). The 3D seismic data cube covers an area of 12,413 km². In addition to the 3D dataset studied for the research, well top information acquired from the Potoroo 1 and Gnarlyknots 1A wells were brought into the 3D cube area for seismic well top correlation via the regional 2D TWT (two-way time) seismic lines previously acquired in the region. Even though we do not have additional well-top/stratigraphic marker information within the 3D dataset area, we did our best to comply with the two closest wells and bibliographic information available for the litho-stratigraphy of Ceduna Sub-Basin.

Survey Summary	Acquisition Parameters
Type: 3D	Number of Streamers: 12
Geometry: Standard	Streamer Length: 8,100 m
Size: 12,413 km ²	Streamer Separation: 120 m
Acquisition Year: 2011	Shot Interval: 25 m
Completion of Processing: 2016	Record Length: 9216 ms
Reprocessed: Yes	Source Depth: 7 km
Vessel: Ramform Sterling	Sample Rate: 2 ms

Table 3: Ceduna Sub-Basin 3D PSDM Seismic Data Acquisition Parameters

The seismic interpretation scheme was carried out by using the Total in-house software Sismage (Guillon & Keskes, 2004). Following the literature review of the study area, we conducted the research on 3D seismic dataset by the following order;

1. Structural analysis on PSDM data time slice views with a focus on White Pointer Delta interval (e.g. delta-top vs delta-base)
2. Classification of fault patterns throughout the dataset (e.g. listric, strike-slip, radial, polygonal)
3. Identification of delta segments (e.g. proximal, central, distal)
4. Structural domain evaluation (e.g. listric vs minibasin)
5. Investigation of minibasin domain features (e.g. shale-driven deformation)
6. Classification of specific shale-driven delta toe structures (e.g. thrusts, minibasins, duplexes, welds, shale-cored highs etc.)
7. Synthesizing the main characteristics of the deltaic system
8. Combining the characteristics in a kinematic-scenario view representing the 3D seismic cube findings

Upon finalizing the 3D seismic interpretation, we decided to reinforce the kinematic scenario into the regional context via 2D seismic line re-evaluation in order to better calibrate the findings proposed by the 3D dataset and to enlarge the scenario in a combined 2D-3D view. Figure 116 shows the locations of four main regional arbitrary/composite 2D seismic lines chosen to be represented via cross-sections depicting the structural aspects of White Pointer Delta along with the location of 3D seismic dataset. Further details regarding the seismic interpretation of these 2D-3D seismic datasets will be given in the following part; Ceduna Sub-Basin, White Pointer Delta Analysis.

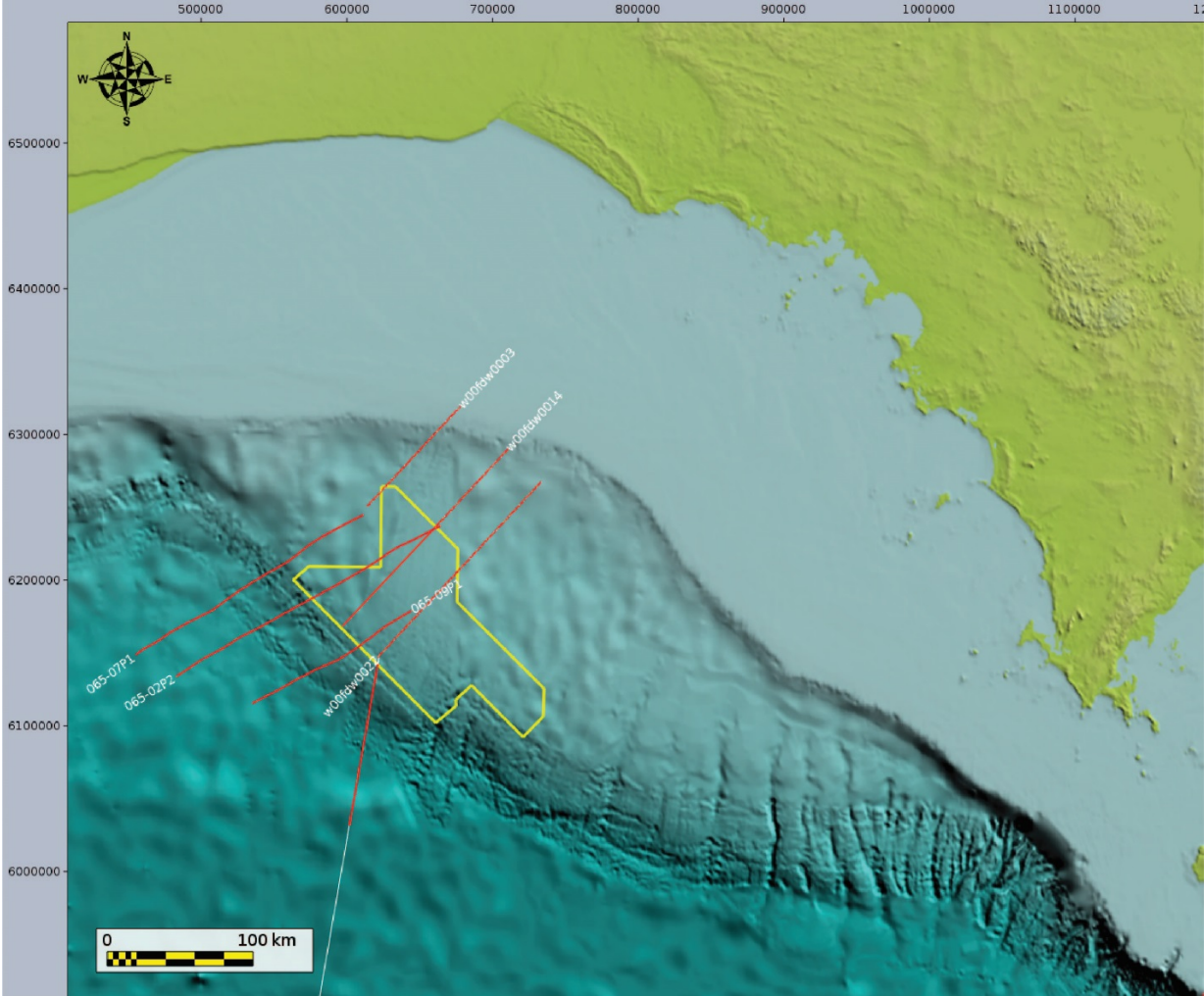


Figure 116: Map of utilized 2D regional lines and 3D seismic dataset of Ceduna Sub-Basin. Yellow marked area depicts the limits of PSDM 3D seismic dataset, while the red lines show the locations of 2D regional lines used to construct regional cross sections.

Chapter 7: Regional Seismic View of Ceduna Sub-Basin

This chapter will be detailing the regional characteristics of the Ceduna Sub-Basin, White Pointer Delta interval from its proximal end to the distal delta-toe portion. Both 2D and 3D seismic lines are utilized to construct a composite view showing the true structure of the basin with added 3D seismic imaging quality. The purpose of this chapter is to familiarize the reader with structural aspects of the delta discovered on 3D seismic view, which were not coherently displayed on previously studied vintage 2D seismic sections.

I. Classification of White Pointer Delta Compartments

The White Pointer Delta wedge, which initially evolved as a gravity-driven system fed by extensional listric faults accommodating the gliding at proximal-to-distal part, is underlined by Blue Whale maximum flooding surface setting the shale-driven detachment surface for the delta sediments. Previous literature studies reviewed the delta system as an unstable tectonic wedge regionally detaching above the Late Albian Blue Whale shale deposits that consists of extensional growth faults in the upper part of the delta coupled with a narrow band of preserved deep-water compressional structures (Espurt et al., 2009). This conclusion was made based on available subsurface datasets (regional 2D seismic lines) used for the geologic re-construction studies at the time. MacDonald et al. (2012), also noted that the White Pointer Delta can be divided into two tectonic provinces: extensional part associated with the delta top and the compressional part associated with the delta toe. Extensional province is dominated by listric growth faults while numerous imbricate thrust sheets define the compressional province.

However, when observed on 3D seismic scale, the deltaic setting displays three structurally-different compartments showing various characteristics that have not been clearly identified previously with 2D seismic lines through proximal, central and distal portion of the delta. Therefore, before detailing the small-scale findings, we will be using all 2D and 2D-3D combined regional seismic lines we have evaluated in this chapter in order to showcase the regional context and display the findings of interest in a generic sense before focusing on zoomed-in/detailed shale tectonism indicators on well-imaged 3D seismic PSDM data. For this purpose, the next two sections will be describing the regionally constructed seismic lines under two sub-sections called *Composite 2D Regionals* and *Composite 2D Regionals Merged with 3D Seismic Lines* for clarity. *Composite 2D Regionals* are based on four regionally constructed 2D TWT (two-way-travel time) seismic lines aiming to present the structurally important features of White Pointer Delta interval in a regional perspective, while the *2D Regionals Merged with 3D Seismic Lines* aim to point out to the significance of 3D seismic imaging merged with 2D regional lines to detect the kinematically evolved/mobilized features of the shale-driven delta and harder-to-see structural elements on vintage 2D seismic lines.

Composite 2D Regionals

Ceduna Sub-Basin, White Pointer Delta interval is represented by a deltaic system wedged above a shale-prone ductile medium (Blue Whale Formation). Figure 117 shows the four cross-sections chosen to depict the regional setting of White Pointer Delta from proximal front till the distal end. Following the convention shown on this map, these four cross-sections will be referred to as N1, N2, S1 and S2 lines from now on regarding their directional location (N1 and N2 northerly seismic lines, S1 and S2 southerly seismic lines).

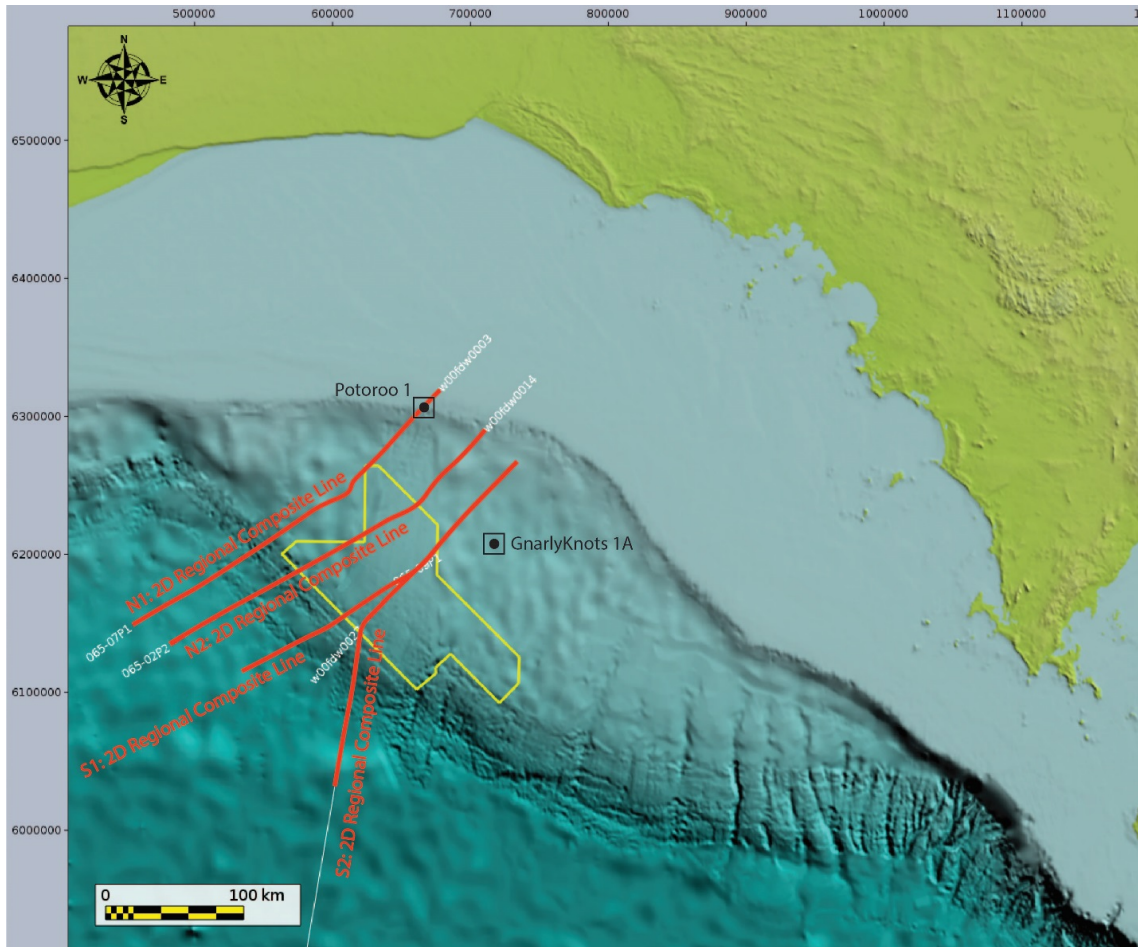


Figure 117: 2D regional composite lines (N1, N2, S1 and S2) interpreted to grasp the regional geological context in addition to the 3D seismic data cube (yellow geometrical shape). Black squares denote the location of two exploration wells drilled in Ceduna Sub-Basin (Potoroo 1 and GnarlyKnots 1A).

The diagrams seen on Figure 118-Figure 121 show the interpreted White Pointer deltaic interval on these regional lines. On all of the seismic lines the deltaic wedge display three compartments, which are classified as proximal, central and distal deltaic provinces. The proximal deltaic province is dominated by listric faults that sole into the shale-prone detachment level. Central province displays elongated listric faults and some translation features such as thrusting/shortening, which indicate some early shale mobilization patterns. The distal province significantly differentiates from each of the previous domains as it branches outward with multiplied trusting and duplexation as well as shift of spoon-like listric faulting into small-scale normal faulting. Following the duplexed domain, the further distal region is governed by an imbricated fan of trust complex that spreads throughout the outer skirts of Ceduna Sub-Basin before the abyssal plain setting.

Each of these lines display the large-scale deltaic setting within the Ceduna Sub-Basin. The proximal setting ranges between 50-75 km in length; the central province covers an area of 35-50 km; while the distal domain spreads to an area of 50-110 km in length, which points out to a regionally established geodynamic setting riding above a shale-prone ductile medium.

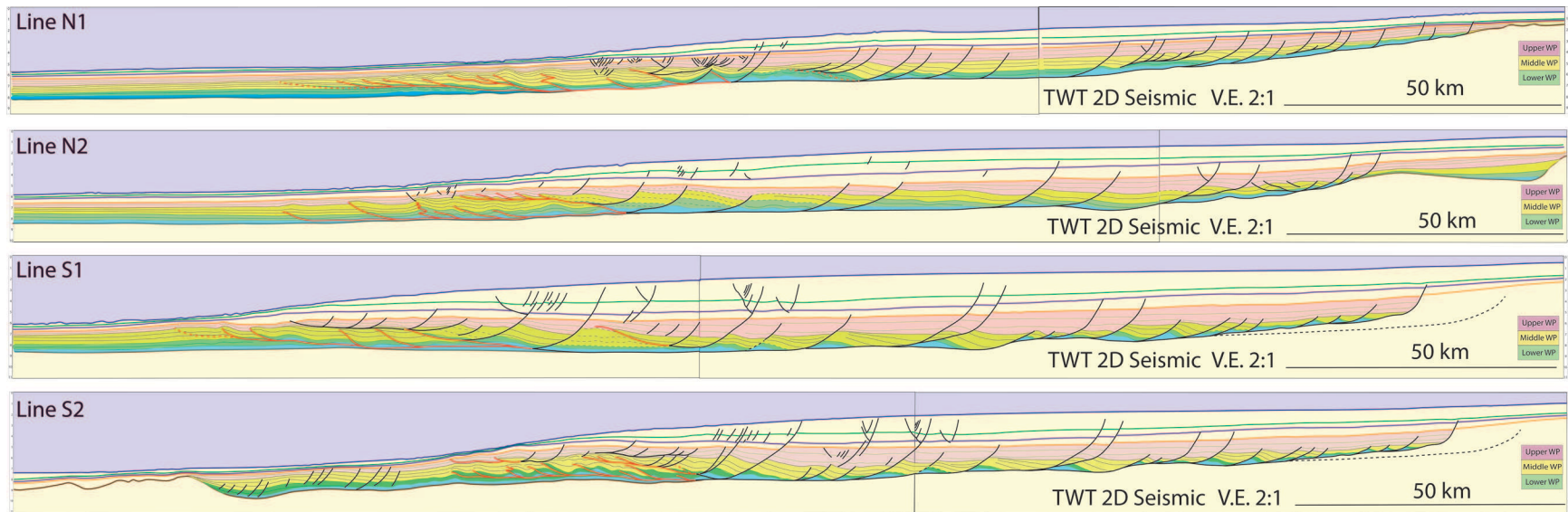


Figure 118: Regionally interpreted cross-sections showing four 2D seismic lines with White Pointer Delta Interval (see the color-based deltaic stage legend to the right of the figure) above Blue Whale Detachment Level (blue patches). Pin Points depict the extent of the deltaic wedge and the limit of balanced cross-section calculations performed on these lines. Red markers denote thrust faults while the black ones show listric faults and small scale normal faulting. Purple Marker: Top Tiger Formation. Green Marker: Top Hammerhead Formation. See the Location Map on Figure 117.

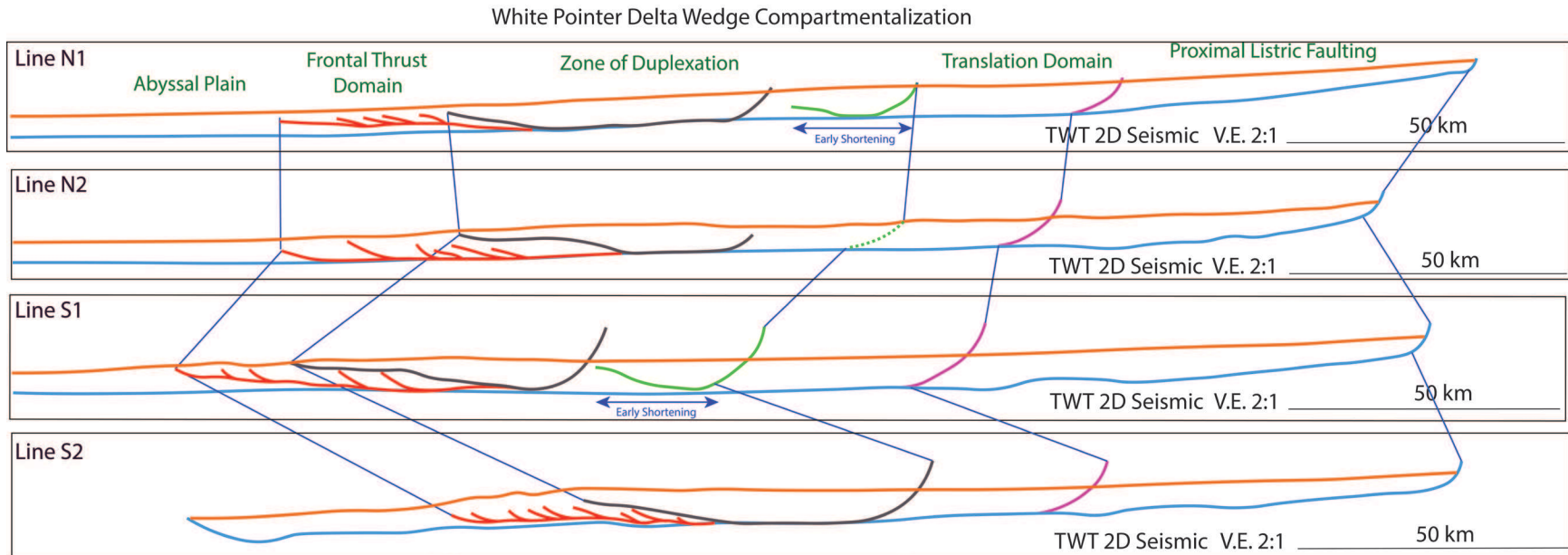


Figure 119: Schematic diagram derived from the horizon extension-compression compensation for given regional seismic lines. Cross-Sections can be compartmentalized under four main sections, which are namely; proximal listric faulting domain, translation domain, duplexation domain and frontal thrust domain.

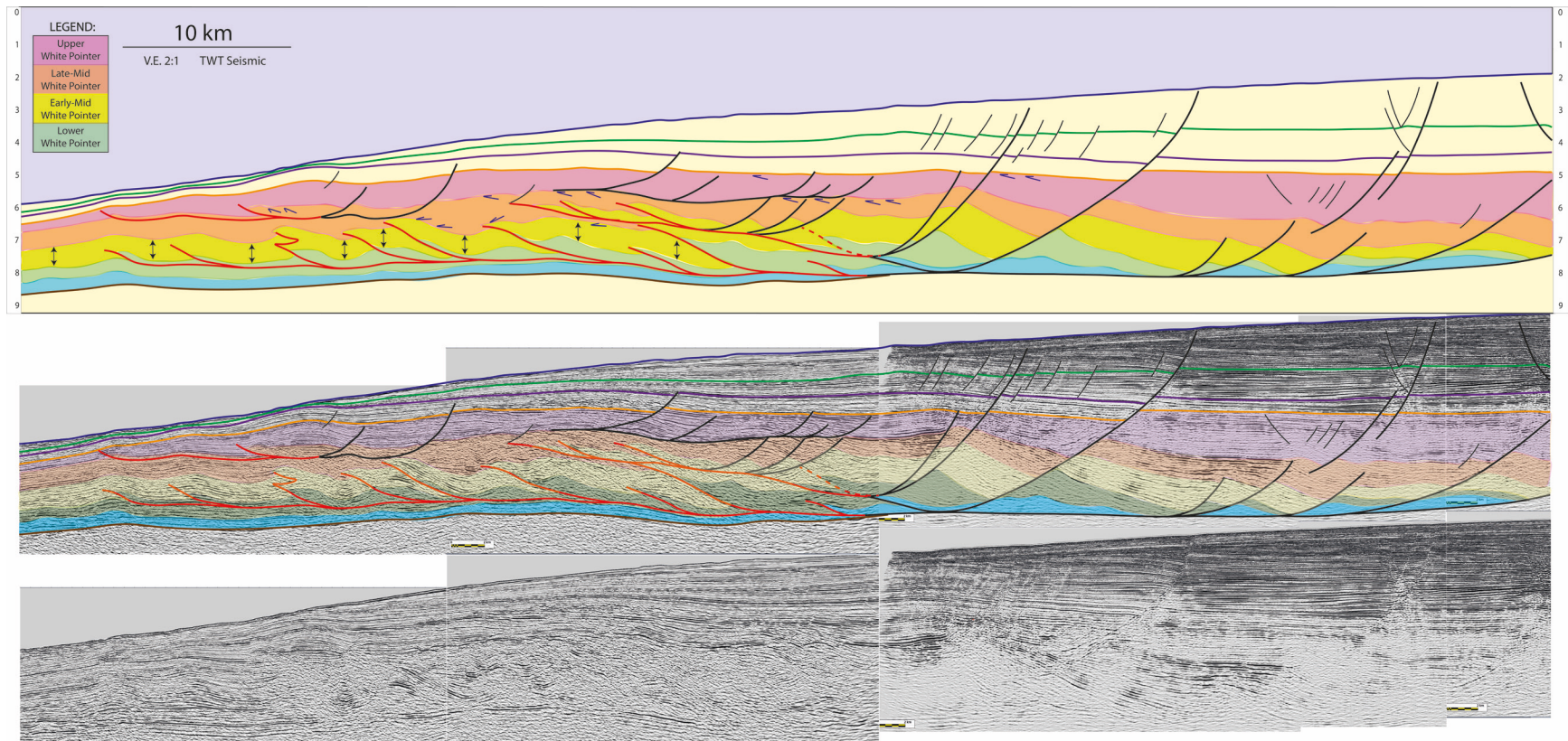


Figure 120: Zoom-in at the regional seismic line S2 showing the coherent duplexation pattern above the Blue Whale detachment level (Blue Marker). See the color legend on the sketchy diagram (first panel). Mid White Pointer sequential interval differentiates into two depositional packages. Yellow package represents the isopachous Lower Mid White Pointer interval, while the Orange package shows the truncational sequence pointing out to duplex mobilization.

For each of these composite seismic lines (N1, N2, S1, S2), we have measured/calculated the following items;

- L0: Original seismic line and deltaic wedge length (km)
- L1: Horizon lengths (km) for Water Bottom, Hammerhead, Tiger and Upper-Middle-Lower White Pointer Formations as it is interpreted on the seismic line.
- Horizon extensions (km) caused by listric fault offsets (length to subtract, L1_extension)
- Horizon compressions (km) caused by thrusting and duplexation, where applicable (length to add, L1_compression)

Based on the performed interpretation and horizon-based calculations, we sketched a compartmental diagram showing structurally various domains of the White Pointer deltaic interval (Figure 119). The most coherently represented duplexation example among these four regional lines is seen on seismic line S2 (see Figure 117 for location). Figure 120 depicts the zoomed-in distal portion of that regional seismic line, where we observe duplexed thrust branching outward above the Blue Whale detachment level. Interpreted section on this seismic line reveals the following items:

Pink Package: Upper White Pointer

Orange Package: Late-Mid White Pointer package with downlapping and toplapping terminations

Yellow Package: Isopachous Early-Mid White Pointer sequence

Green Package: Lower White Pointer

Yellow isopachous interval suggests a balanced depositional rhythm arriving to the delta toe up until the Late-Mid White Pointer sequence (orange package), upon that threshold, the truncations we observe (downlaps above the Early-Mid White Pointer) points out to the duplexed thrust activity within the distal section with the mobilization of Blue Whale shales underlining the deltaic wedge. Towards the end of Mid White Pointer sequence, we observe toplaps truncating against the younger depositional package (pink color). These terminations emerge from mobilization taking place simultaneously in a depositing environment.

Based on our observations, what we think has happened in this geologic setting is that the duplexed thrust fault (i.e. the duplexation plane) got mobilized during a time at which the upper portion of the normally offsetted Lower White Pointer strata. As a result, it was ridden and got translated further ahead in the deltaic setting via advancement of the duplexed thrust fault. Following this mobilization pattern, Lower White Pointer strata got reversed offset above the duplexed plane compensating the original normal offset that we are not seeing on the interpreted section compared to Early-Mid and Late-Mid White Pointer deposition (yellow and orange packages respectively). It tell us that the maximum offset is seen on the isopachous Early-Mid White Pointer section instead of the Lower White Pointer, which means that Early-Mid White Pointer sequence was flat and undeformed at the time the thrust duplex system was developed.

Below Early-Mid White Pointer strata, there is a ~ 10 km offset along the duplexed thrust plane, we see the Lower White Pointer with minimal offset compared to upper depositions, this can only be the case if originally deposited Lower White Pointer (older strata) was offset in a normal motion and the thrust mobilization occurred during the deposition of Late-Mid White Pointer (younger strata). The large offset of Lower White Pointer is compensated upon duplex placement via reverse offsetting. Lower White Pointer moved along the thrust plane during that time and originally placed large offset of which sutured along the duplexation by means of reverse offsetting (Figure 120).

The \pm minor errors from interpreted horizon markers can be caused by several reasons such as; *basin geometry, topographic changes, delta slope, parallel layer shortening issues, compaction processes taking place at the distal toe, and/or misinterpretation due to vintage seismic data coherency problems especially in deeper horizons associated with thrusting and shale mobilization*. However, these findings also comply with 2D-3D merged composite lines to be showcased in the following section and thrusting and shale mobilization characteristics will be addressed in detail within the next chapter on well-imaged 3D seismic data examples in order to supplement the first order observations made here on 2D regional vintage seismic data.

Following the schematic diagram given in Figure 119 with balanced compartmentalization, Figure 121 shows these regional composite lines in order with identified delta compartments. White Pointer Delta interval consists of three major structural domains differentiated under proximal, central and distal parts of the delta. The distal domain divides into two sections characteristics of which differ from the classic deep-water fold and thrust belt; (i) the zone of duplexation and (ii) frontal thrust complex. Zone of duplexation proposes a step-up, while the *thrust complex* display a typical imbricate fan system above the ductile shale layer consisting of Blue Whale formation, the detachment surface for White Pointer Delta. These first order observations will be detailed in the following sections.

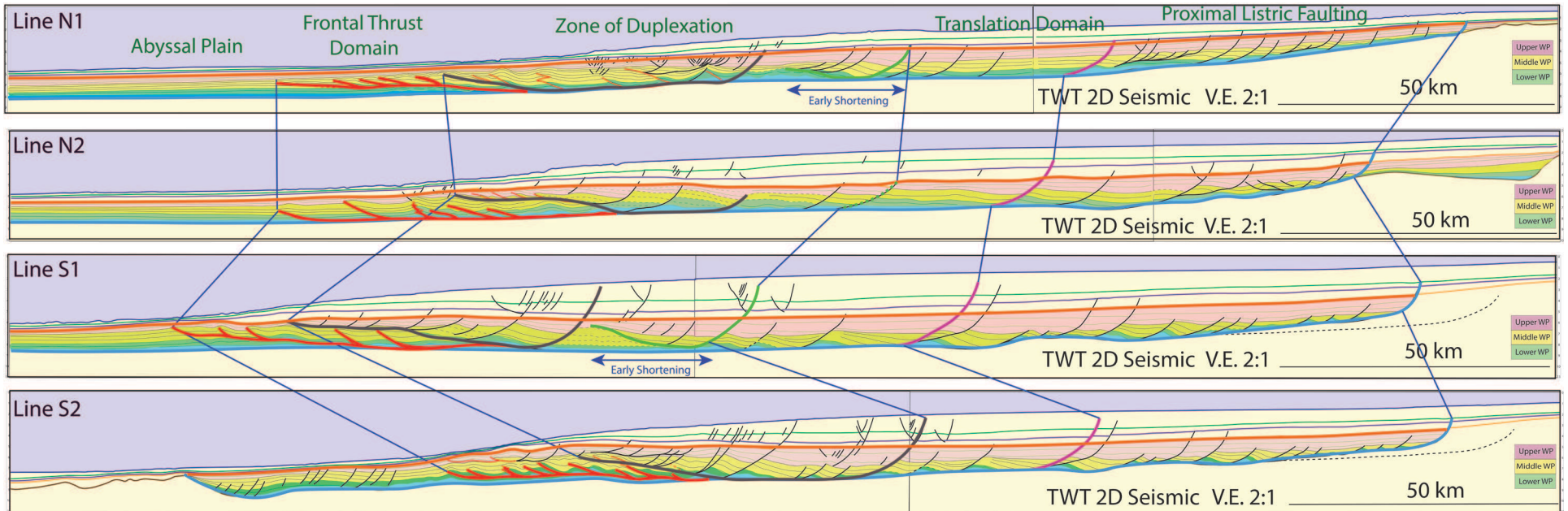


Figure 121: Regionally interpreted cross-sections showing the identified White Pointer Delta compartments on four 2D seismic lines (see the color-based deltaic stage legend to the right and see Figure 117) above Blue Whale Detachment Level (blue patches). Red markers denote thrust faults while the black ones show listric faults and small scale normal faulting. Purple Marker: Top Tiger Formation. Green Marker: Top Hammerhead Formation. Pin Points depict the proximal end point of the deltaic wedge as well as the measurement reference for cross-section balancing.

II. Composite 2D Regionals Merged with 3D Seismic Lines

The map shown in Figure 122 displays four regional lines from the area for this purpose;

- i. Two 3D xline views extended with two 2D regional lines
- ii. Two 3D inline views passing through the central and distal part of the delta

Those lines are selected in order to give a generic regional sense of the White Pointer Delta system to the reader with the important structures.

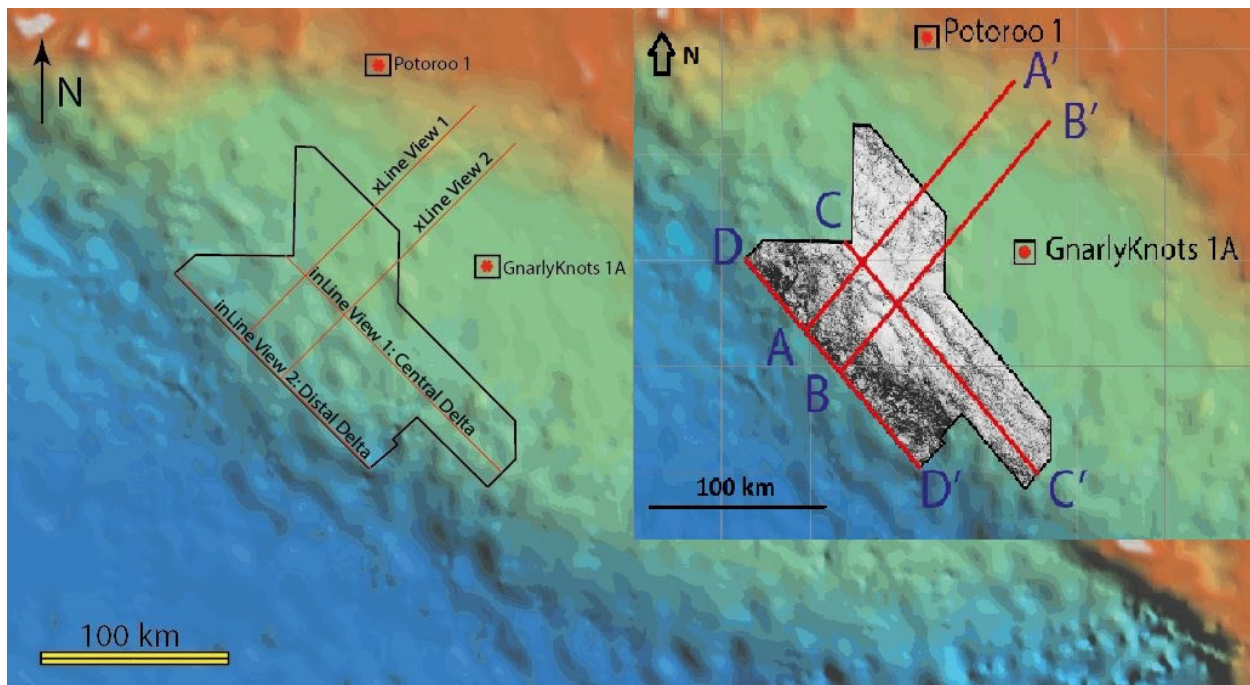


Figure 122: Regional Map of Ceduna Sub-Basin showing the locations of 2D-3D composite seismic lines. Black geometrical closure shows the 3D seismic cube location.

For the sake of simplicity, we will be adapting the representation shown on the right-hand side of Figure 122 (2D-3D merged composite seismic lines A-A', B-B', C-C', D-D') for seismic line names and locations. These four seismic lines are chosen to describe the delta dynamics observed on 2D-3D seismic scale with an aim to display structural changes from proximal-to-central-to-distal part of the White Pointer Delta underlined by Blue Whale shale formation. The White Pointer Delta package migrates in NE-SW direction following the stages of *extension*, *translation* and *shortening*, while the deltaic system displays distinct structural style for each of its proximal, central and distal domains. The following four sections aim to summarize these elements under associated cross-section with zoomed-in seismic pieces (see Figure 122 and Figure 123 for location and overall regional seismic view);

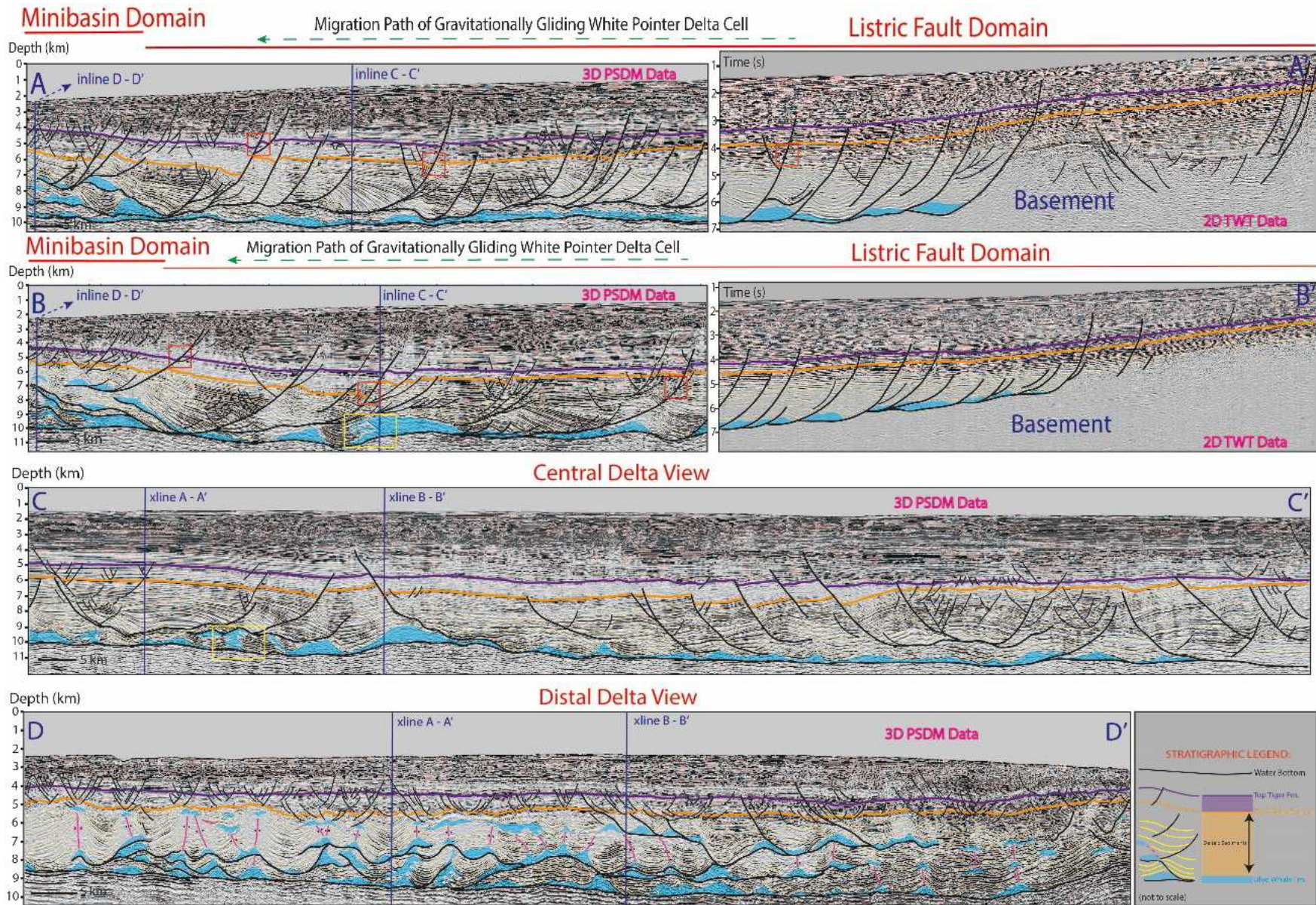


Figure 123: Regional seismic line interpretation depicting the big-scale White Pointer Delta setting and its structural components (V.E. 2:1).

i. Cross Section A-A':

Cross Section depicting the 3D *xline 13300* combined with 2D *line w00fdw0022.mig08ts-rot180*

Migration path of gravitationally-gliding deltaic cell direction: NE-SW

Proximal Section: Gravitationally gliding delta pattern with listric faults soling into the Blue Whale detachment level

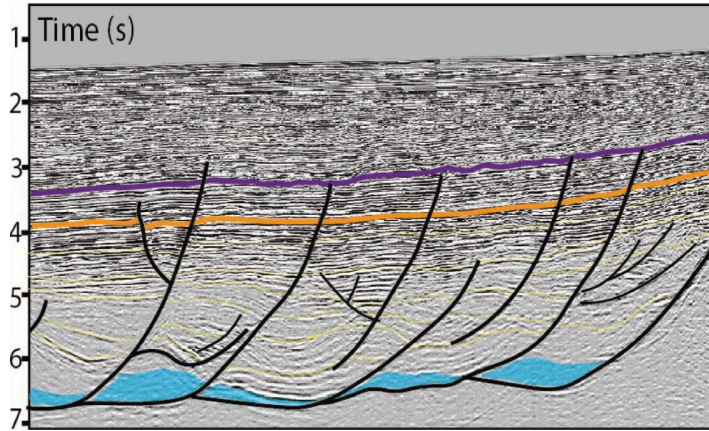


Figure 124: Proximal part of White Pointer Delta shown on 2D *line w00fdw0022.mig08ts-rot180* (Purple Marker: Top Tiger Formation, Orange Marker: Top White Pointer Formation, Yellow Markers: White Pointer Deltaic Deposits, Blue Patches: Blue Whale Shale Deposits, Black Markers: Listric faults soling into Blue Whale detachment surface) Seismic V.E. 2:1

Central Section: Elongated/translational gliding features with branched detachment level leading to local intermediate decollement surfaces (Figure 125 and Figure 126).

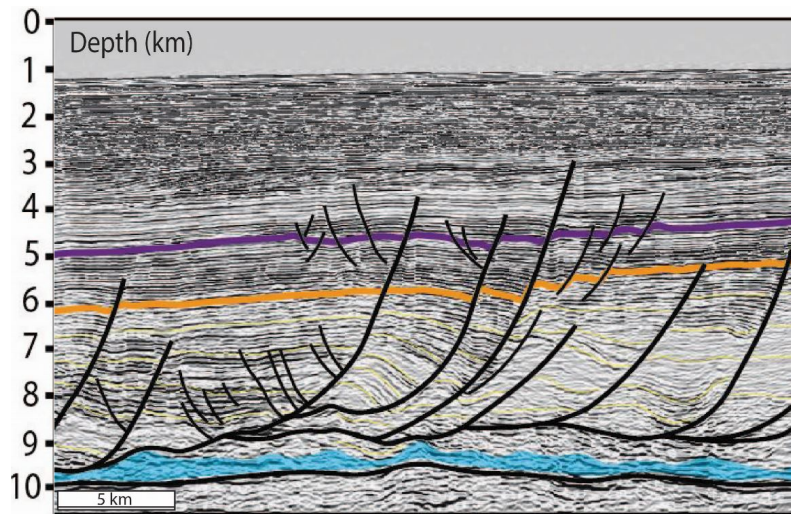


Figure 125: Central part of White Pointer Delta shown on 3D *xline 13300* (Purple Marker: Top Tiger Formation, Orange Marker: Top White Pointer Formation, Yellow Markers: White Pointer Deltaic Deposits, Blue Patches: Blue Whale Shale Deposits, Black Markers: Listric faults soling into branched Blue Whale detachment surface) Seismic V.E. 2:1

The gravitationally-gliding delta cell migrates upwards besides moving down-slope-the-delta. Age of offset activity getting younger from central-to-distal part indicating mobilization of deeper strata through distal delta-toe, showing a down-dip migration of the extensional activity (Figure 126 and Figure 127).

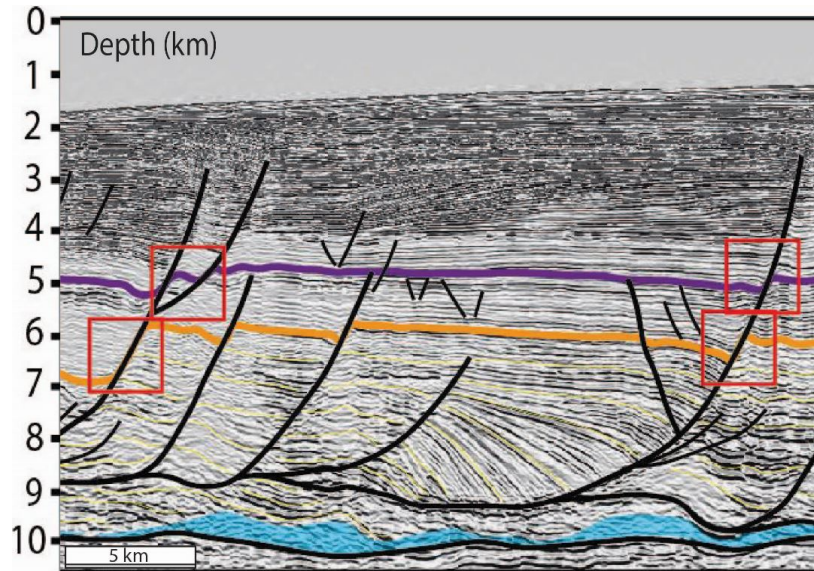


Figure 126: Central-to-Distal part of White Pointer Delta shown on 3D xline 13300 (Purple Marker: Top Tiger Formation, Orange Marker: Top White Pointer Formation, Yellow Markers: White Pointer Deltaic Deposits, Blue Patches: Blue Whale Shale Deposits, Black Markers: Listric faults sining into branched Blue Whale detachment surface, red squares show the enlarging offset difference being translated further towards the distal part -migration of gravitational cell activity getting younger- indicating mobilization of deeper strata further down in the delta-toe. Some fault reactivation is also observed at top-deltaic level) Seismic V.E. 2:1

Distal Section: Initiation of thrusting and duplexation of thrusts with mobilized shale features being translated into upper levels of the deltaic wedge. Formation of minibasins separated by the thrustured mobile shale strata. Wavelength of normal faulting decrease in possible response to the decrease in the thickness of the faulted section.

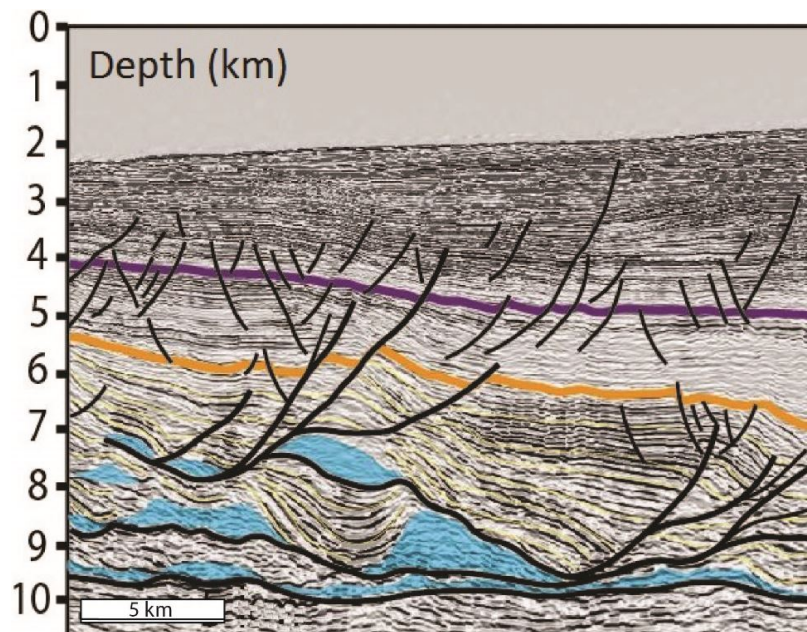


Figure 127: Distal part of White Pointer Delta shown on 3D xline 13300 (Purple Marker: Top Tiger Formation, Orange Marker: Top White Pointer Formation, Yellow Markers: White Pointer Deltaic Deposits, Blue Patches: Blue Whale Shale Deposits, Black Markers: Thrust complex above the Blue Whale detachment surface with minor listric faulting. Detached/mobilized shale patches are carried upwards via these thrusts in between minibasin formations) Seismic V.E. 2:1

ii. Cross Section B-B':

Cross Section depicting the 3D xline 11000 combined with 2D line w00fdw0015.mig08ts-rot180

Migration path of gravitationally-gliding deltaic cell direction: NE-SW

Proximal Section: Gravitationally gliding delta pattern with listric faults soling into the Blue Whale detachment level (Figure 128).

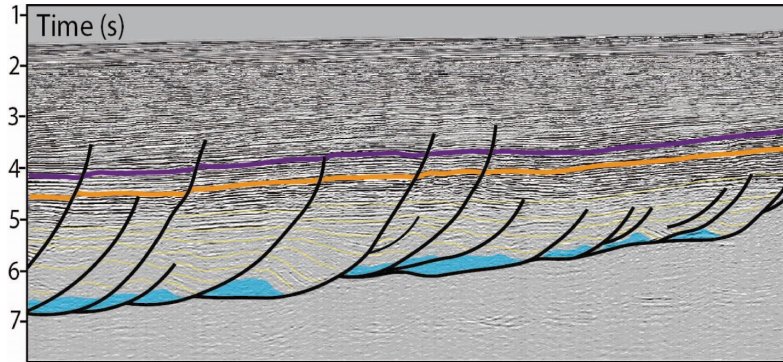


Figure 128: Proximal part of White Pointer Delta shown on 2D line w00fdw0015.mig08ts-rot180 (Purple Marker: Top Tiger Formation, Orange Marker: Top White Pointer Formation, Yellow Markers: White Pointer Deltaic Deposits, Blue Patches: Blue Whale Shale Deposits, Black Markers: Listric faults soling into Blue Whale detachment surface) Seismic V.E. 2:1.

Central Section: Elongated/translational gliding features with transgressional shale-sediment interaction (indicated with yellow rectangle on Figure 129 seismic view) at the further end. Note that the amount of extensional faulting for a given horizon (e.g. Figure 129 orange Top White Pointer Marker) increases with the downdip position and is located further downdip for the younger stratas. This clearly illustrates the downdip migration pattern of extensional activity. The Lower White Pointer section shows the early interaction between shale deposition and mobilization (see yellow rectangle on Figure 129). The early depo-center geometry is that of small minibasin-like structures.

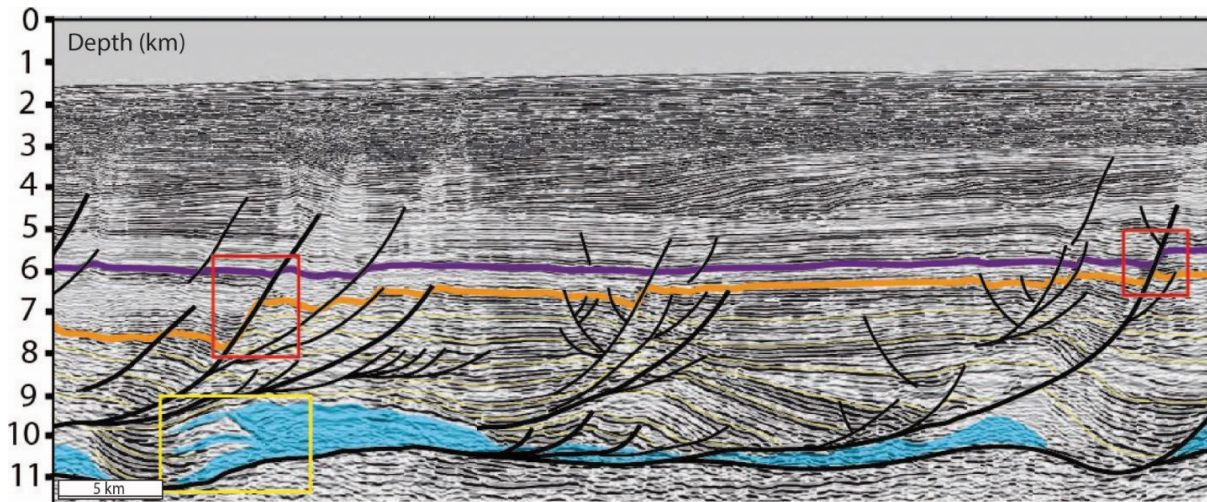


Figure 129: Central part of White Pointer Delta shown on 3D xline 11000 (Purple Marker: Top Tiger Formation, Orange Marker: Top White Pointer Formation, Yellow Markers: White Pointer Deltaic Deposits, Blue Patches: Blue Whale Shale Deposits, Black Markers: Large-scale listric faults soling into Blue Whale detachment surface and small-scale faulting within the deltaic wedge related to ductile medium movement. Red rectangles show the enlarging offset difference being translated further towards the distal part indicating mobilization of deeper strata further down in the delta-toe. Some fault reactivation is also observed at top-deltaic level) Seismic V.E. 2:1.

Distal Section: Initiation of thrusting and duplexation of thrusts with mobilized shale features being translated into upper levels of the deltaic wedge. Formation of minibasins separated by the thrust mobile shale strata. Again we can observe the decrease of the normal fault spacing in relation with the decrease in the thickness of the implicated sedimentary sequence. The duplex domain is clearly visible showing the offset of the bottom and mid White Pointer deposits, as well as the decrease in normal faulting wavelength in the transported domain (Figure 130).

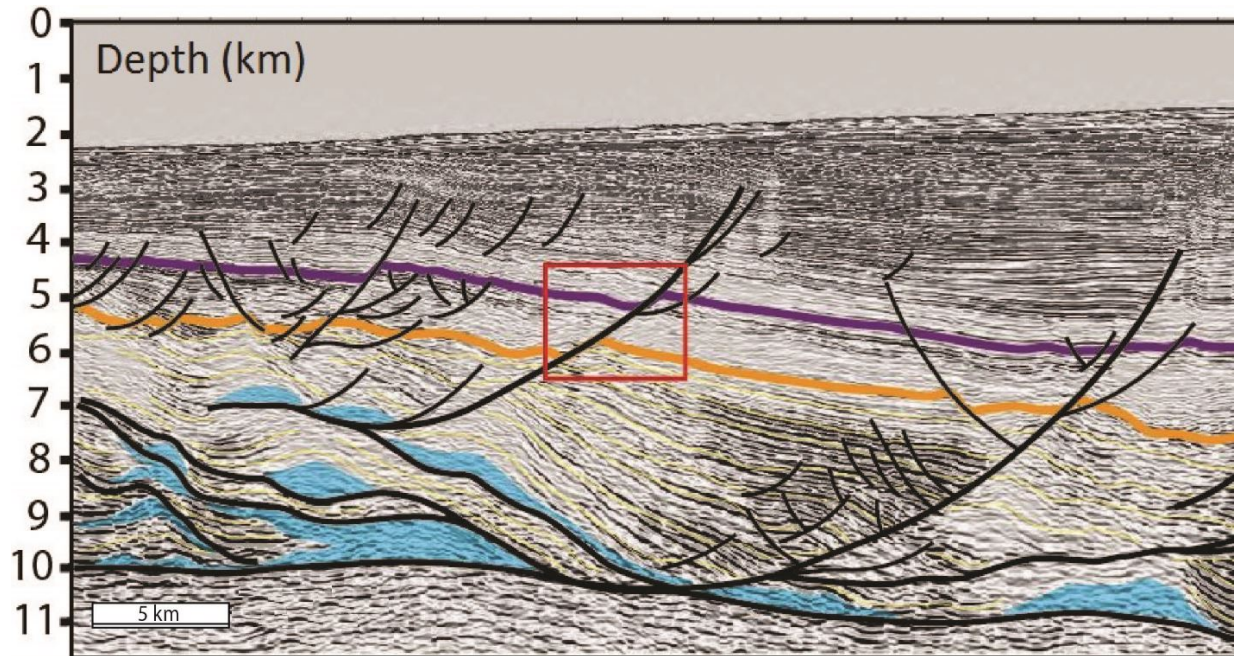


Figure 130: Distal part of White Pointer Delta shown on 3D xline 11000 (Purple Marker: Top Tiger Formation, Orange Marker: Top White Pointer Formation, Yellow Markers: White Pointer Deltaic Deposits, Blue Patches: Blue Whale Shale Deposits, Black Markers: Thrust complex above the Blue Whale detachment surface with minor listric faulting. Detached/mobilized shale patches are carried upwards via these thrusts in between minibasin formations. Red rectangle shows the enlarging offset difference - migration of gravitational cell activity getting younger- at the distal delta-toe above the branched thrust complex) Seismic V.E. 2:1.

iii. Cross Section C-C':

Cross Section of 3D inline 5050 shows the central delta view. The NW-SE oriented cross-section view, depicts the central-delta physiology perpendicular to the sediment input direction. In this cross-section, some early wedging features are noticed surrounding the ridge-like shale deposits. These small-scale depo-centric wedge forms are located at Lower White Pointer level separated by ridges of mobilized Blue Whale shale deposits (Figure 131). These depo-centers display wedging and thinning reflections on their sides suggesting a coeval growth of shale ridges and ongoing deposition of the Lower White Pointer deposits.

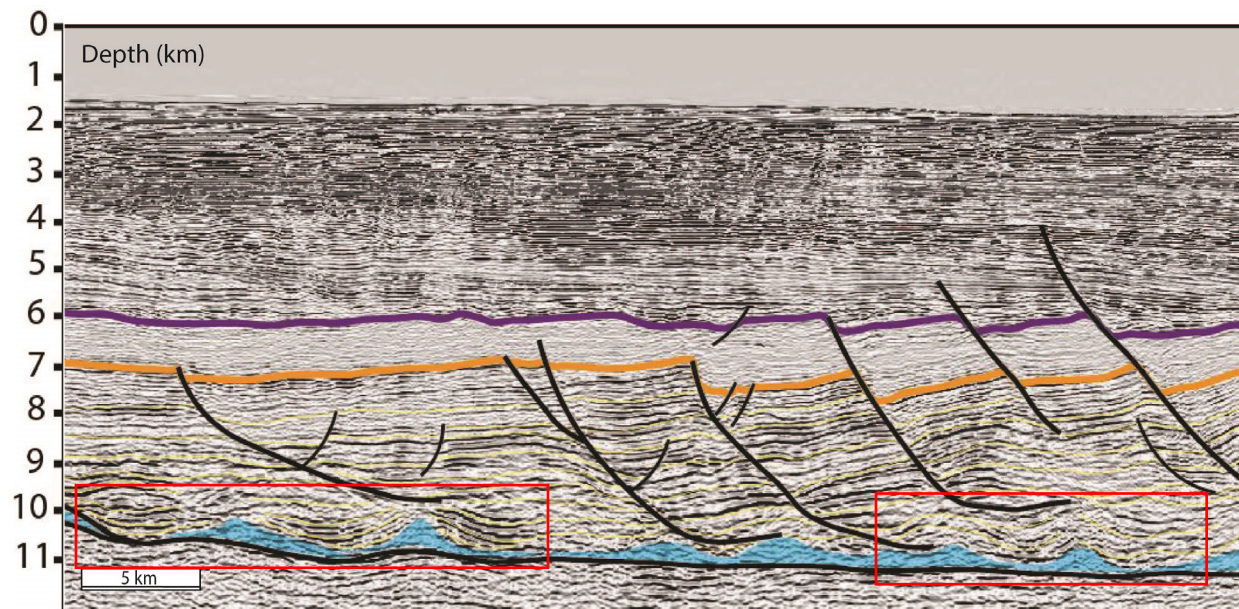


Figure 131: Central part of White Pointer Delta shown on 3D inline 5050 (Purple Marker: Top Tiger Formation, Orange Marker: Top White Pointer Formation, Yellow Markers: White Pointer Deltaic Deposits, Blue Patches: Blue Whale Shale Deposits, Black Markers: Large-scale listric faults soling into Blue Whale detachment surface and/or scooping above the ductile medium. Localized shale deposits and wedging around these structures shown in red rectangles point out to early shale mobilization patterns and ridge-like deposition) Seismic V.E. 2:1.

Scooping listric faults are shown in perpendicular view soling into the Blue Whale detachment surface (Figure 132), while some of them branch out to create intermediate detachment surfaces within the deltaic wedge as it has already been observed in the cross section from the central part of the delta. These structures coincide with the location of branching observed at xline cross sections, which indicate a transitional phase from listric faulting into a more concentrated depo-centric system. The small Lower White Pointer depo-center separated by mobilized shale mass can be noticed at the bottom part of the section, some examples of which showcase again the wedging and thinning of the reflection packages toward the shale masses.

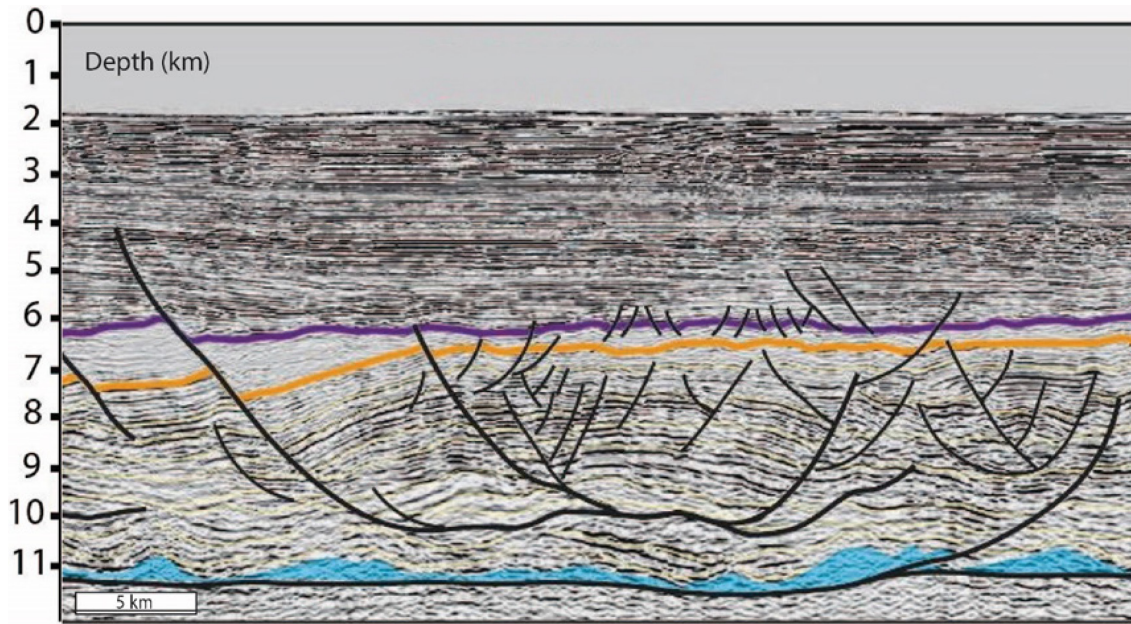


Figure 132: Central part of White Pointer Delta shown on 3D inline 5050 (Purple Marker: Top Tiger Formation, Orange Marker: Top White Pointer Formation, Yellow Markers: White Pointer Deltaic Deposits, Blue Patches: Blue Whale Shale Deposits, Black Markers: Listric faults soling into Blue Whale detachment surface and scooping within the deltaic wedge above the ductile medium) Seismic V.E. 2:1

Transgressional shale-sediment interaction features similar to the one observed at B-B' xline view cross-section (Figure 133).

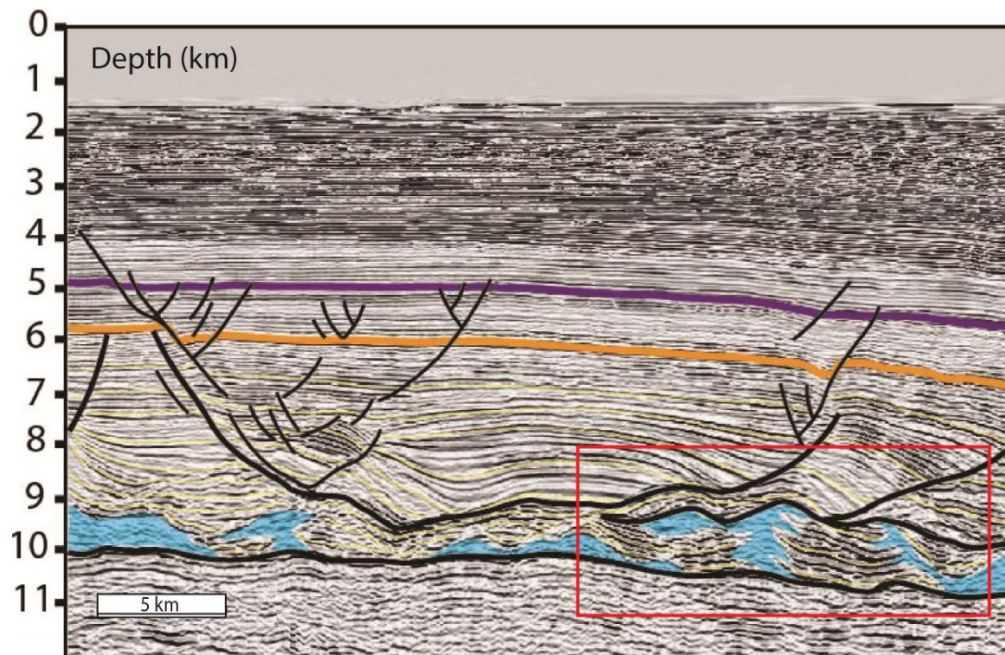


Figure 133: Central part of White Pointer Delta shown on 3D inline 5050 (Purple Marker: Top Tiger Formation, Orange Marker: Top White Pointer Formation, Yellow Markers: White Pointer Deltaic Deposits, Blue Patches: Blue Whale Shale Deposits, Red Rectangle: Fingering sediment-shale interaction observed at detachment level indicating transgressional activity, Black Markers: Listric faults soling into Blue Whale detachment surface and scooping within the deltaic wedge above the ductile medium) Seismic V.E. 2:1.

iv. Cross Section D-D':

Cross Section depicting the 3D inline 2050 showing the distal delta view

NW-SE oriented cross-section view depicting the distal-delta physiology perpendicular to the sediment input direction, where we observe mobilized shale features resembling *salt tectonism* with radial fault closures above shale-cored domal highs similar to *salt diapirs* on seismic view (Figure 134). These salt-like features can be summarized as, small rounded depotcentres, wedging on their side, thinning of reflection packages, transparent shale masses (represented with blue color on seismic), shale masses terminating against abnormal vertical contacts, which will be mentioned in detail later in the welds section and on flat abnormal contacts corresponding to the duplexed thrust domain.

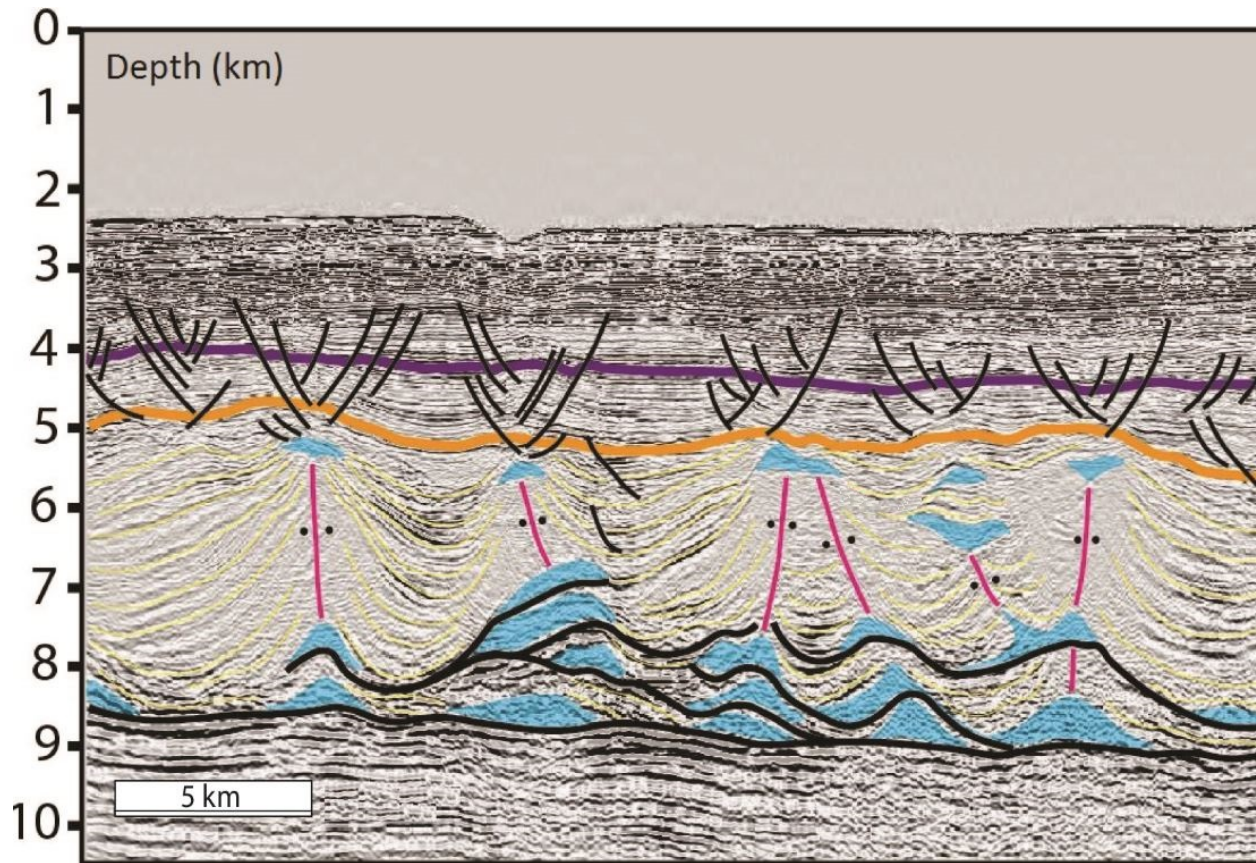


Figure 134: Distal part of White Pointer Delta shown on 3D inline 2050 (Purple Marker: Top Tiger Formation, Orange Marker: Top White Pointer Formation, Yellow Markers: White Pointer Deltaic Deposits, Blue Patches: Blue Whale Shale Deposits, Black Markers: small-scale radial faulting above shale-cored domal highs and the large-scale thrust complex dissected in perpendicular view, Pink markers with black dots: weld features separating minibasin depocenters in between the mobilized shale structures) Seismic V.E. 2:1.

Switch from listric fault domain into a pod-like *minibasin-prone setting* separated by mobilized shale features.

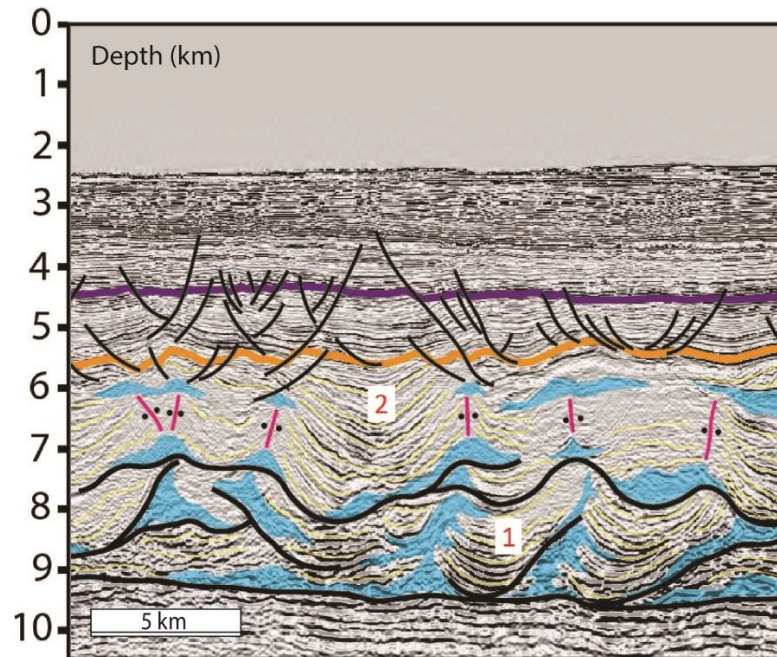


Figure 135: Distal part of White Pointer Delta shown on 3D inline 2050 (Purple Marker: Top Tiger Formation, Orange Marker: Top White Pointer Formation, Yellow Markers: White Pointer Deltaic Deposits, Blue Patches: Blue Whale Shale Deposits, Black Markers: small-scale radial faulting above shale-cored domal highs and the large-scale thrust complex dissected in perpendicular view, Pink markers with black dots: weld features separating minibasin depocenters in between the mobilized shale structures) 1: Primary-Level Minibasin Formations, 2: Secondary-Level Minibasin Formations. Seismic V.E. 2:1.

Branching and duplexation of the thrust complex carrying the detached/mobilized shale deposits upwards in the system (deltaic wedge). Wedge and weld-like formations observed in the minibasin domain separating the deltaic sediment depo-centers.

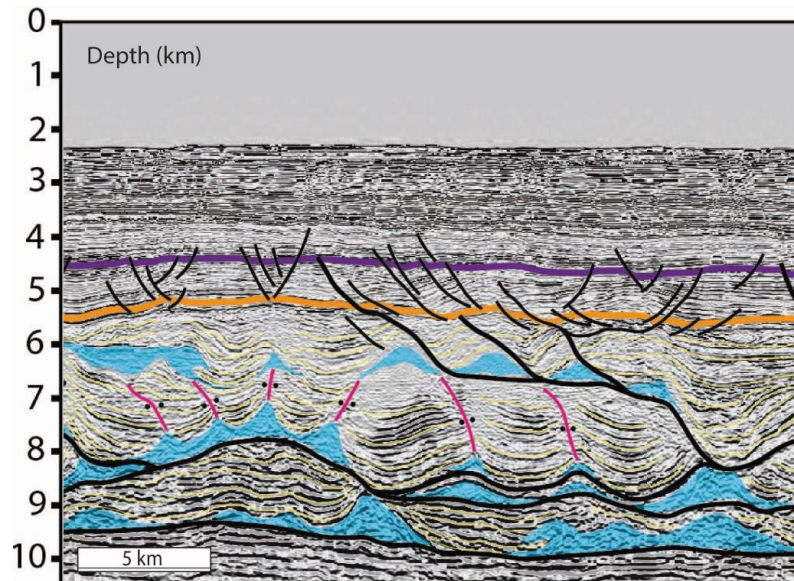


Figure 136: Distal part of White Pointer Delta shown on 3D inline 2050 (Purple Marker: Top Tiger Formation, Orange Marker: Top White Pointer Formation, Yellow Markers: White Pointer Deltaic Deposits, Blue Patches: Blue Whale Shale Deposits, Black Markers: small-scale radial faulting above shale-cored domal highs and the large-scale thrust complex dissected in perpendicular view, Pink markers with black dots: weld features separating minibasin depocenters in between the mobilized shale structures) Note the wedging and welding observed around the interpreted shale deposits. Seismic V.E. 2:1.

III. Compartmental Review

A. Proximal Delta Setting

The proximal portion of White Pointer Delta is dominated by gravity-driven thin skinned growth faults forming the *Mulgara Fault System* (Toterdell & Krassay, 2003). These large offset listric faults sole into the underlying Blue Whale detachment level while translating the White Pointer deposits into the central delta lobe. The migration path of gravitationally gliding delta cell can be traced via the sediment package offsets through the regional crossline sections.

Most of the listric faults observed in this part of the delta detaching onto the shale rollers have individual history of activity as large displacement take place at the base. The wedges noted around these displacements in the proximal part point out to an early gliding phase; as the first pulse of sediments arrive in the deltaic wedge and glide further downslope above the shale-prone ductile medium (Blue Whale Formation) leaving a trace of displacement recorded in early White Pointer delta deposits (Figure 124 and Figure 128). This section of delta development is characterized with:

- Early Setting: Listric faults starting with small displacement, few gliding and block rotations.
- Late Setting: Arrival of continuous deltaic sediments leading to amplification of the gliding and large block rotations, initiating the translation of sediments into the central delta lobe with practically no more activity in the Upper White Pointer section of proximal delta setting, only few fault propagations to the delta top due to compaction not associated with gliding.

B. Central Delta Setting

When we look at the middle part of the delta, we still observe some fault activity within the Lower White Pointer delta portion but not with large displacements as we have observed in the proximal part. Central White Pointer Delta displays a pattern of large displacement within the Mid-to-Upper White Pointer delta interval advancing into the Tiger Formation. In other words, the age of fault activity starts to migrate upward within the delta setting as a consequence of more deltaic sediment arrival. This section of delta development is characterized with:

- Relatively smaller-scale listric faults compared to the proximal portion and translation structures above the ductile Blue Whale shale layer such as: mini thrust faults/branching (towards the end of central part), rollovers and/or raft features.
- As juvenile thrust faults are introduced into the system, few shale mobilization features (e.g. wedging and shortening) are observed at the transition from central to the distal part of the delta.
- Counter regional faults are rare and limited to the center of the wedge as the motion of these faults are purely associated with gravitational gliding and late fault reactivation triggered by overlying sediments.

- The major growth faults display sustained activity during the deposition of White Pointer interval, but pace down upon the arrival of Tiger sequence. Most of these faults show a long-lasting residual activity up to the Hammerhead sequence with some fault reactivation due to compaction.
- Some listric faults sole into the Blue Whale detachment level while others display a basal flattening on top of Blue Whale layer and glide over the shale packs rather than soling into them and/or create a branching secondary detachment level in some places (Figure 129 and Figure 132).
- The White Pointer decollement surface becomes relatively flatter in the central section with respect to the proximal part.

C. Distal Delta Setting

The distal portion of White Pointer Delta distinctively differs from the proximal and central part. Gravitationally gliding activity is carried further down in the deltaic wedge towards the delta toe, while a new thrust complex is introduced into the system. Within this part of the delta, we observe shale-sediment interaction triggered by shale mobilization features during early stages of White Pointer deposition, which changes the overall delta dynamics we have observed in previous sections (central and proximal parts);

- Listric fault pattern weakens/disappears as shortening takes place via the advanced thrusts being introduced into the system at the transition from central-to-distal part of the delta.
- Evolving thrust complex emerges from the Blue Whale Detachment level as a result of compression induced by incoming delta sediments. Branching thrust faults seem to be associated with mobilized shale features at the distal delta toe.
- Through the distal part, this thrust complex lead to a duplexation of the down-building minibasins on top of the former down-building strata; eventually growing into shale-cored domes supported by what-seems-to-be weld-like features in between the duplexed/transported minibasins.
- Above these welded shale-cored tops we observe small-scale radial faulting, which is completely different than the listric fault pattern both in terms of scale and characteristics but similar to the seismic character of top salt diapiric-faulting.
- Advancement of fault offsets in Tiger Formation (pointed out with red rectangles in Figure 126, Figure 129, Figure 130) suggest that the gliding was active during Tiger Formation deposition and gravitationally gliding delta system/cell does not only migrate in space but also in time.

IV. Remarks on Ceduna Sub-Basin, White Pointer Delta Regional View

As a general overview of White Pointer Delta, the four regional lines investigated between Figure 123 - Figure 136 sum up the regional context coherently and show a distinctive structural transition from a *classical gravitationally-gliding delta view into a thrust-related shale mobilization domain* with abundant salt-like shale features while suggesting an idea of the early delta kinematics. These four regional lines depicted in Figure 123 reveal that;

- The delta at large can be compartmentalized in three sections; proximal, central and distal part, showing extension, translation, and compression features respectively, in a very classic manner, as it has already been proposed by many authors (see the previous sections).
- Proximal part of the delta display large displacements in Lower White Pointer and some fault growth in Mid White Pointer followed by cessation in Upper White Pointer.
- Central delta is dominated by Lower-to-Middle White Pointer fault activity where larger displacements are observed in the Mid White Pointer with limited displacement reaching as high as Lower Tiger sequence. Shale-related translation features (e.g. rollovers, rafts) are observed in this area.
- Distal part of the delta is associated with a thrust complex that initiates shale mobility. Wedging, welding and minibasin formations as well as shale-cored domes surrounded by radial faults resembling *salt-related deformation diapirism* are interpreted within this interval.

V. Structural Time-Slice Analysis of White Pointer Delta with 3D Seismic Cube

The whole system of White Pointer Delta resembles the classical view of a gravitationally-gliding system in a regional context. As it is explained in the previous section, the system consists of three structurally-different compartments; *proximal, central* and *distal* depicting the view of a typical delta setting underlined by a ductile medium (e.g. salt) with extension (e.g. listric faults), translation (e.g. rollovers) and compression (e.g. thrust faults) features. However, in addition to these symptomatic findings we observed on regional-scale, with the help of high-quality 3D PSDM dataset acquired from the region, we also had the chance to better focus on the shale-related mobilization features of Ceduna Sub-Basin, White Pointer Delta. This section of the thesis will be detailing the structural analysis performed on 3D cube time slices in order to better define the White Pointer Delta structural characteristics.

The White Pointer Delta section is generally observed within the 5-10 km depth interval of the 3D seismic cube (see 3D regional lines C-C' and D-D' cross sections on Figure 123). This interval is represented by two structurally different domains as seen on Figure 137;

(1) Gravitationally gliding *Listric Domain* dominated by listric faults covering the proximal-to-central part of the delta

(2) *Minibasin Domain* dominated by a thrust complex and mobilized shale features covering the distal part of the delta

The following sections will be detailing these two domains in terms of their (i) physical appearance, (ii) structural characteristics and (iii) differences through depth on the time-slice view. Figure 137 shows the interpreted and uninterpreted versions of two time-slice views from 5km and 8km depth with an explanatory legend associated to it. 5 km time slice view depicts the upper listric domain and upper minibasin domain, while the 8 km time slice view depicts the lower listric domain and lower minibasin domain respectively.

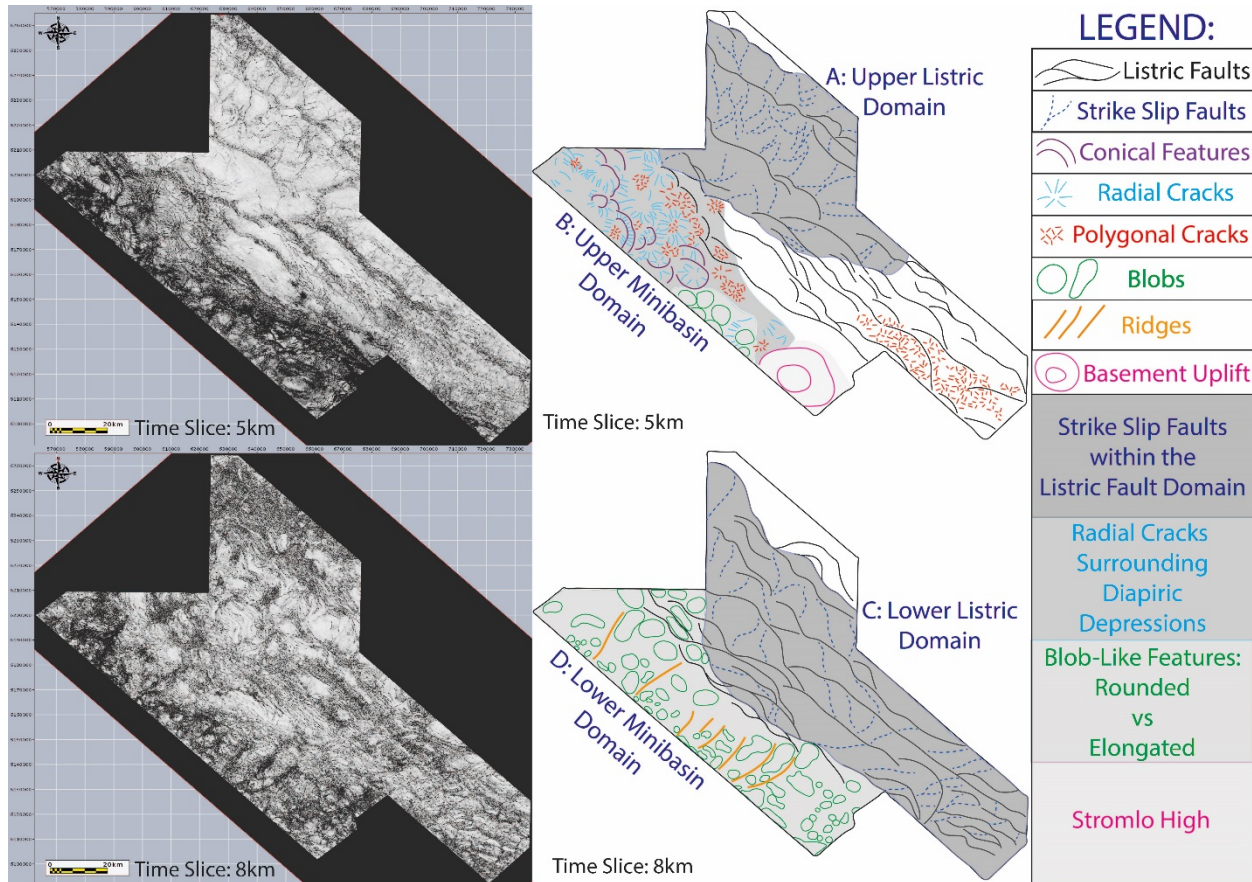


Figure 137: Structural Time Slice Analysis for 5 and 8 km depth intervals on time-slice view.

As it is clearly seen on Figure 137 the area is divided into two visually different segments on both depth intervals (5 km and 8 km respectively). There is (i) an area of listric faulting associated to gravitational gliding pattern of the delta, and (ii) an area of depo-centric closures representing the minibasin domain. On 5 km time slice we also observe a basement structure called Stromlo High, which have been identified as a basement uplift in the previous studies. The legend seen on the right hand side of the figure represents all of the identified structural features of these two depth intervals.

As a first order observation between these two time-slices, there is a change in wavelengths. From shallower to deeper section, we can observe the difference on both listric and minibasin domains;

1. The listric fault wavelengths shorten with depth due to their spoon-like scooping structure soling into the detachment level.
2. Wavelength of listric faults also shorten towards the transition from listric domain into the minibasin domain. Within this interval, where we observe initiation of thrusting, we start to see shrinkage of listric fault scaling and therefore a wavelength change with respect to the normal faults classically formed within the rear gliding domain.

Strike-slip faults are observed within the listric domain of 3D data-cube throughout the deltaic interval. These faults are formed in between the listric pattern accommodating the stress related to the relay zones (overlapping or not) in between the listric faults. Their concentration changes by location/depth (time and space) through the gravitationally-gliding delta setting while their occurrence is maintained all along the listric fault field.

The polygonal cracking seen on the southeastern end of 5 km deep time-slice interval is thought to be caused by some sort of fluidization effect. However, we are not able to comment on these features since it does not represent the scope of this study and the 3D seismic dataset do not further cover the region of the basin fronting this section.

Additionally, the *Stromlo High* is a basement feature observed at the SW corner of the seismic dataset on 5km time-slice view as a surface signature (Figure 137). It will also not be covered during the course of this study due to conflict of interest. However, more information on this structure can be found on the article by Cunneen et al., 2017; *Evolution of the outer basin high, Ceduna Sub-basin, southern Australia*. The rest of time-slice aspects seen on Figure 137-Figure 139 will be discussed in the following sections labelled; *5km Time Slice View* and *8km Time Slice View*. Figure 137 summarizes all of these structures together in a schematic illustration while Figure 138 and Figure 139 aim to give a comparison of change through depth comparing the points of interest on 5 km and 8 km time-slices respectively.

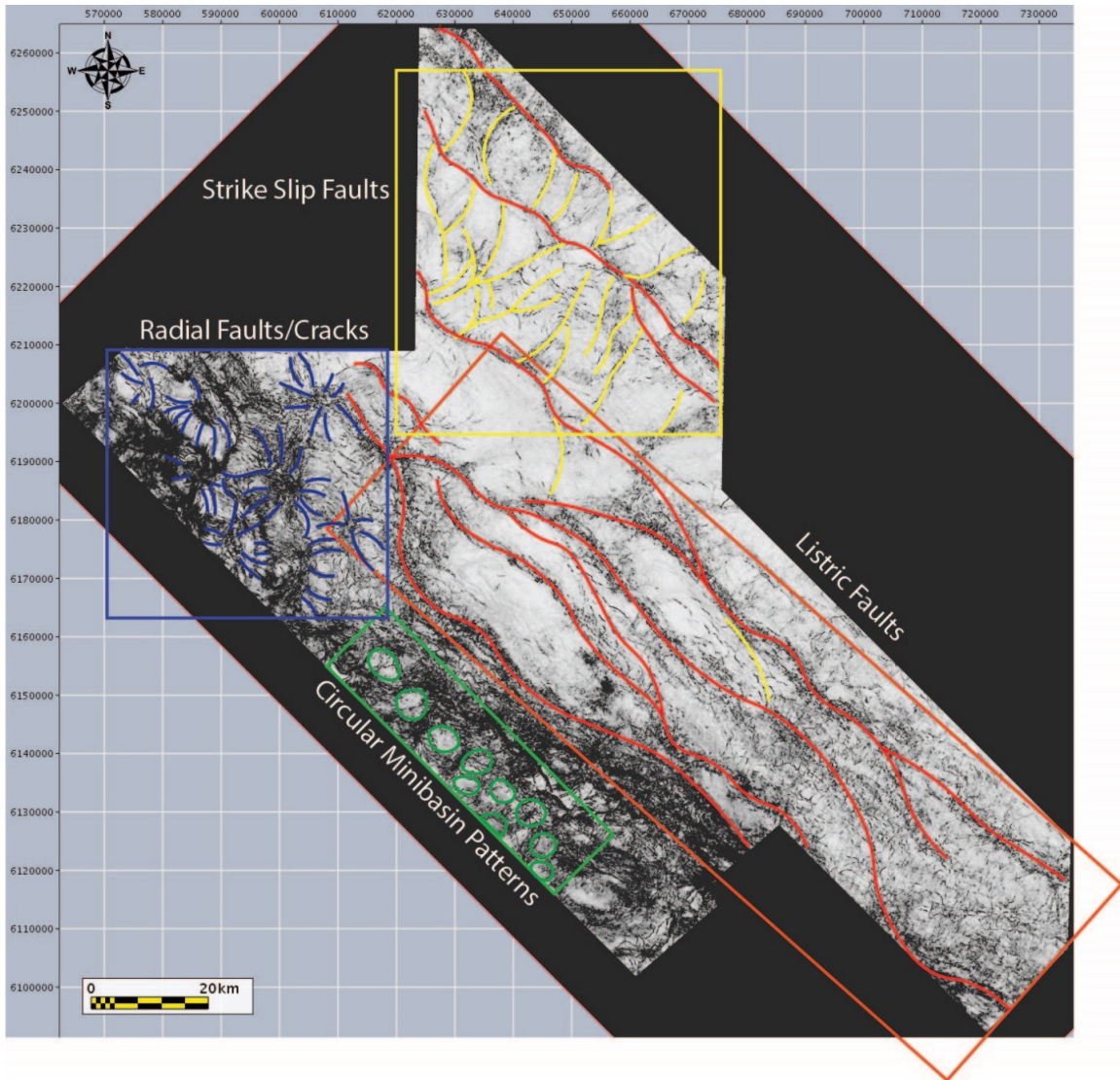


Figure 138: Segmented recognizable features from 5 km depth time slice (please note the diagram on Figure 137 for additionally interpreted structures). Designated rectangles specify the clustered structures in particular portions of the dataset. Blue Rectangle: Radial faults and cracks, Green Rectangle: Circular minibasin patterns, Red Rectangle: Listric Faults, Yellow Rectangle: Strike slip faults.

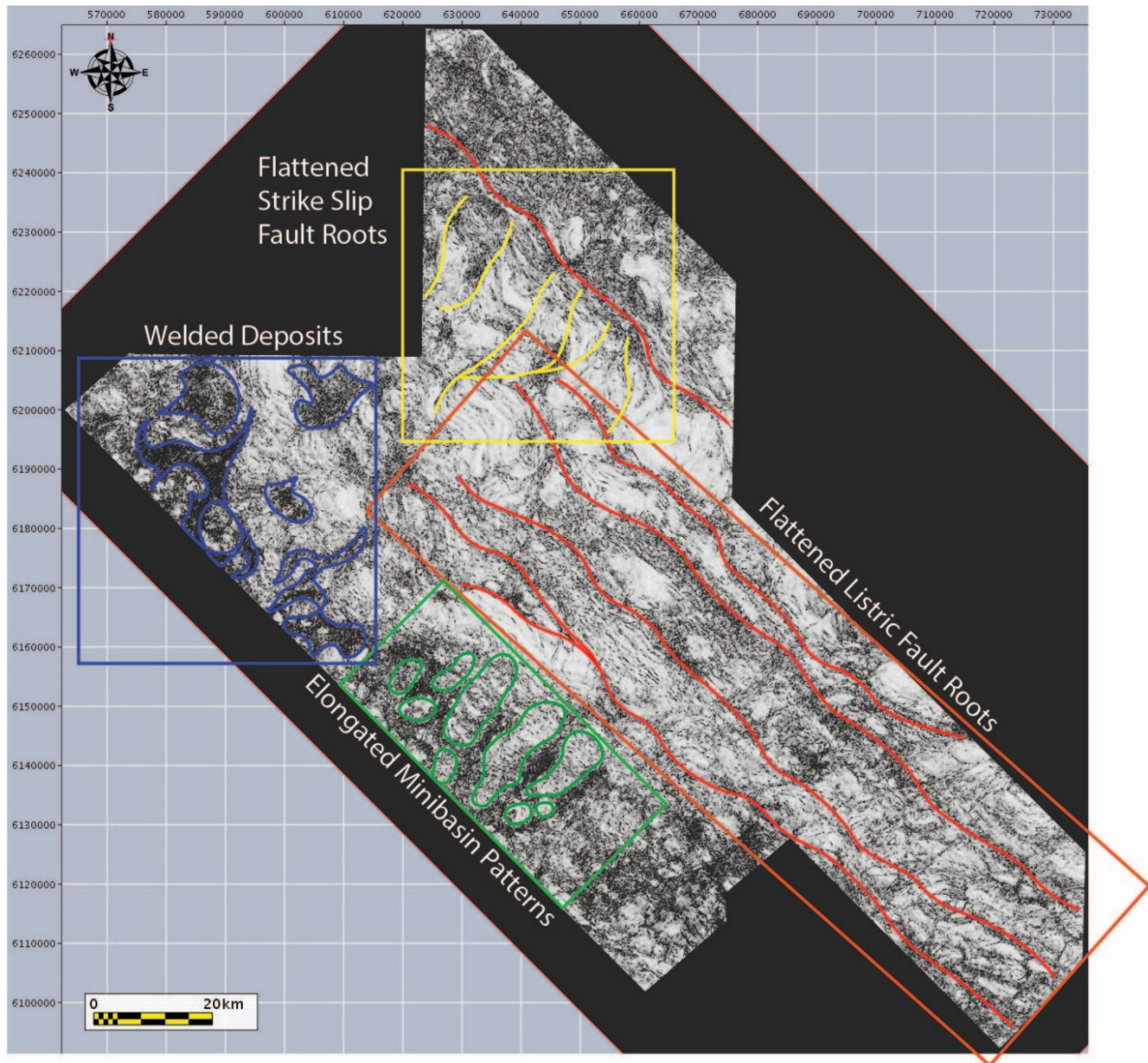


Figure 139: Segmented recognizable features from 8 km depth time slice (please note the diagram on Figure 137 for additionally interpreted structures). Designated rectangles specify the clustered structures in particular portions of the dataset. Blue Rectangle: Welded shale deposits, Green Rectangle: Elongated minibasin patterns, Red Rectangle: Flattened Listric Fault roots, Yellow Rectangle: Flattened strike slip faults roots.

A. 5km Time Slice View:

As it is explained with regional lines on the previous chapter, White Pointer is a compartmentalized delta setting with (i) *listric fault-related gliding* and a (ii) *compressional belt linked to a trust complex* above the shale-driven Blue Whale detachment level. The 5 km depth interval coincides with the top White Pointer Delta surface on 3D seismic data cube of Ceduna Sub-Basin and both of these aforementioned structural features have a unique surface signature on this time slice view.

i. Upper Listric Fault Domain

Within the proximal-to-central part of Ceduna Sub-Basin, White Pointer Delta interval is dominated by a large-scale gravitationally gliding listric fault system, where large offsets separated by listric faults soling into the Blue Whale detachment level within the delta clastics are observed. Time slice view displays a spoon-like listric fault pattern that is connected to one another at some places via the strike-slip faults in between (Figure 140).

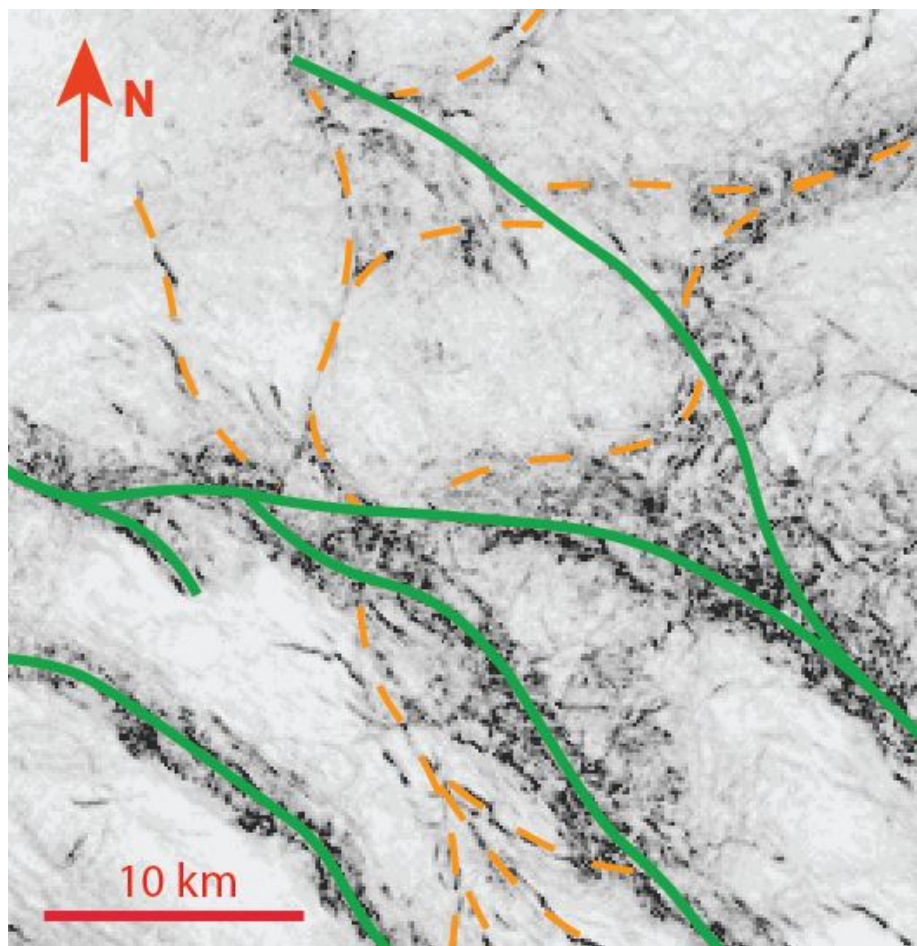


Figure 140: Interpreted close-up from 5 km depth seismic time-slice listric fault domain. Green Lines: Listric Faults, Dashed Orange Lines: Strike-Slip Faults.

ii. Minibasin Domain

The transition from central to distal part of White Pointer Delta on 5km time-slice view marks an abrupt domain change. The listric faults domain associated with the gravitationally gliding delta dynamics transitions into to a new domain characterized by four distinctive features;

- Rounded depo-centers, mimicking minibasin formations (Figure 141)
- Radial faults surrounding the domal highs resembling *salt diapir tops*
- Polygonal cracks/faults above these domal features
- Caldera-like collapse features connecting the terminations of the radial faults

Circular depocenters observed on 5 km deep time-slice view (Figure 141) depict rounded sedimentary pods/minibasin formations originated from the Lower White Pointer deltaic deposits as a result of underlying shale mobilization. Mobilized Blue Whale shale deposits emerging from the detachment level seem to be carried upwards through a *kinematic evolution pattern* while separating the rounded minibasin formations. The same region coincides with shorter wavelength fault patterns distinctively differing from the rear listric fault domain.

In addition to the rounded depocenters noted towards the SE portion of the dataset on the minibasin domain, there are strikingly similar features resembling *salt diapir* signatures concentrated to the NW corner of the seismic dataset on 5 km time-slice seismic view. Such features are described in the literature strongly as associated to Salt Tectonics and Diapirism, where the rise of an active salt diapir detached from mother salt through a salt weld deforming its overburden. The surface impression of a salt diapir is generally represented by a diapiric depression surrounded by radial cracks/faults. In extreme cases, where we have abundance of salt followed by salt withdrawal, caldera-like collapses are formed peripherally around these radial cracks/faults in order to accommodate the depression caused by salt withdrawal (Figure 142).

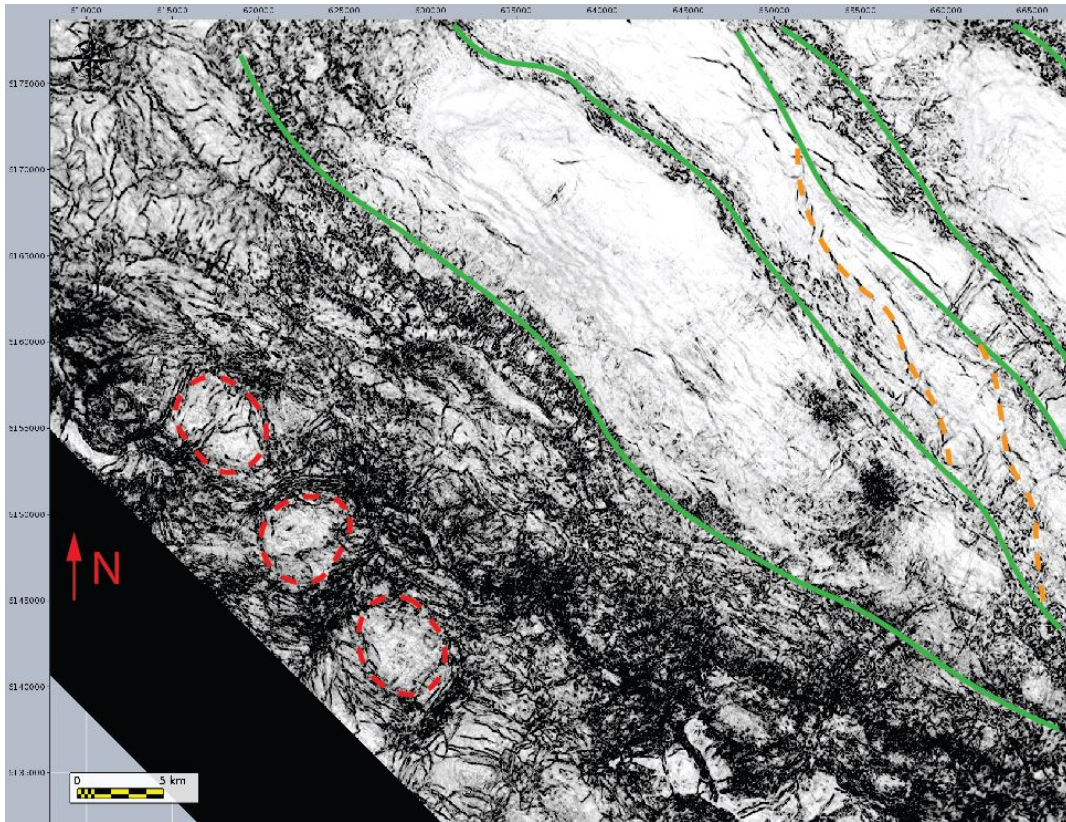


Figure 141: Interpreted close-up from 5 km depth seismic time-slice. Green Lines: Listric Faults, Dashed Orange Lines: Strike-Slip Faults, Dashed Red Closures: Rounded Depocenters/Minibasins.

Such structures point out to a sequential rise, depression and collapse caused by a diapir-like structure. These signatures also indicate a mobile layer detached from its main source and deformed upwards through time resembling a viscous material emerging from ‘weakness zones’. Looking into Salt Tectonics literature, several authors depicted polygonal faults/cracks that are formed above diapiric tops as laterally anisotropic stress fields when a near field stress is present (e.g. Harding and Huuse, 2015) similar to Ceduna Sub-Basin time-slice case study.

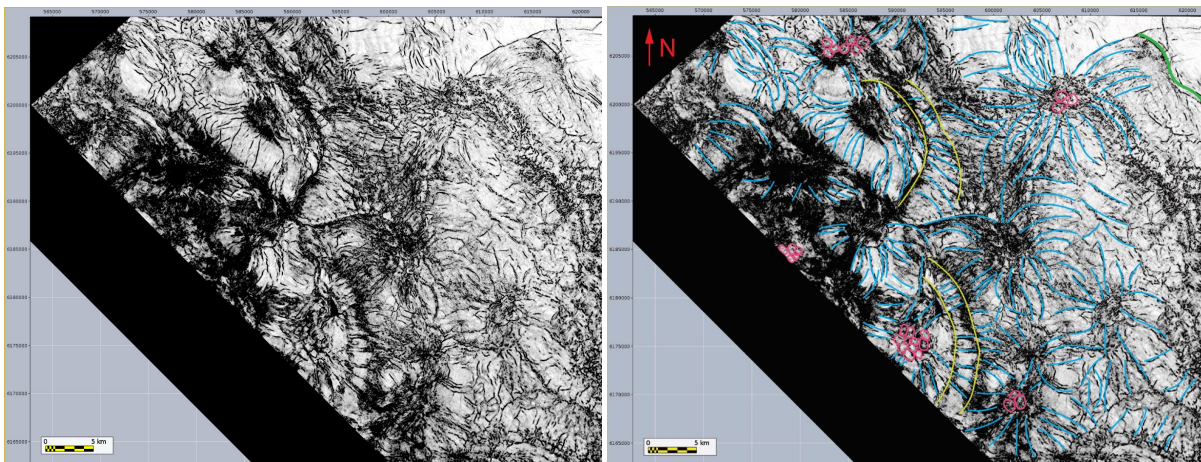


Figure 142: Uninterpreted vs Interpreted close-up from 5 km depth seismic time-slice. Green Lines: Listric Faults, Pink Closures: Polygonal Cracks, Light Blue Lines: Radial Faults Surrounding shale-cored domal highs, Yellow Lines: Traces of collapsed caldera features around the shale-cored domal highs.

B. 8km Time Slice View:

The 8 km deep time-slice of Ceduna Sub-Basin 3D seismic data coincides with the lower part of White Pointer Delta interval, where we observe the base of listric faulting and early minibasin setting.

i. Lower Listric Fault Domain

Deeper portion of White Pointer (8km time-slice view) displays a similar listric pattern to the 5km time-slice view on the proximal-to-central part of the delta, where listric faults sole into the Blue Whale shale sequence. However, they display a *gently dipping but flatter* geometry on xline-view, their dipping angle gets flatter on deeper portion of the seismic dataset. Therefore, flatter, ramp-like fault signatures are observed on deeper time-slice views, some of which turn into scoop-like listric fault bases riding on top of the ductile Blue Whale deposits, while others still sole into the detachment level. Numerous strike-slip faults are still formed at some places in between the gravitationally gliding listric faults (Figure 143).

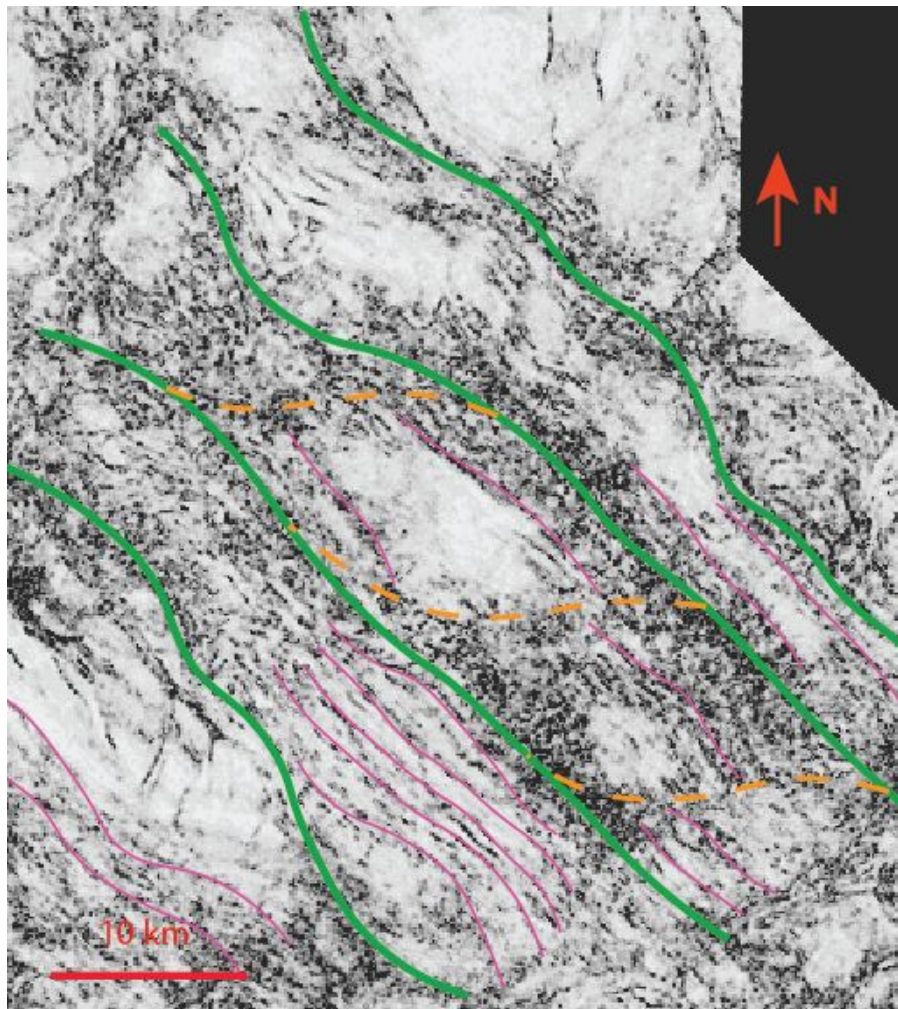


Figure 143: Interpreted close-up from 8 km depth seismic time-slice listric fault domain. Green Lines: Listric Faults, Dashed Orange Lines: Strike-Slip Faults, Fine Magenta Lines: Listric Fault Lineations at the base.

ii. Minibasin Domain

As the time-slice view gets deeper, some structural changes are observed with respect to the 5 km one, which marks the top of White Pointer Delta sequence. The 8 km depth on seismic dataset defines approximately the Mid-to-Lower portion of the delta, where more localized clay features are present. The most significant difference of this time-slice when compared to the shallower example, is the prominently well-preserved shale ridges and the elongated deposition features.

The NE-SW oriented elongated clay ridges are associated with the early formation of gravitationally gliding White Pointer Delta. Direction of these deep, elongated clay ridges results from gliding pattern of the delta. As it is pointed out in Figure 144-Figure 145, 5 km vs 8 km time-slice views display structural change evolving through time such elongated ridge features are later transformed into more rounded structures (depo-centers), suggesting a mobilization and focus within the minibasin domain through time. The following sections will be describing some of the salt-like features observed within the minibasin domain of distal White Pointer Delta interval with an effort to illustrate the analogies of shale with salt in terms of geometry and kinematics.

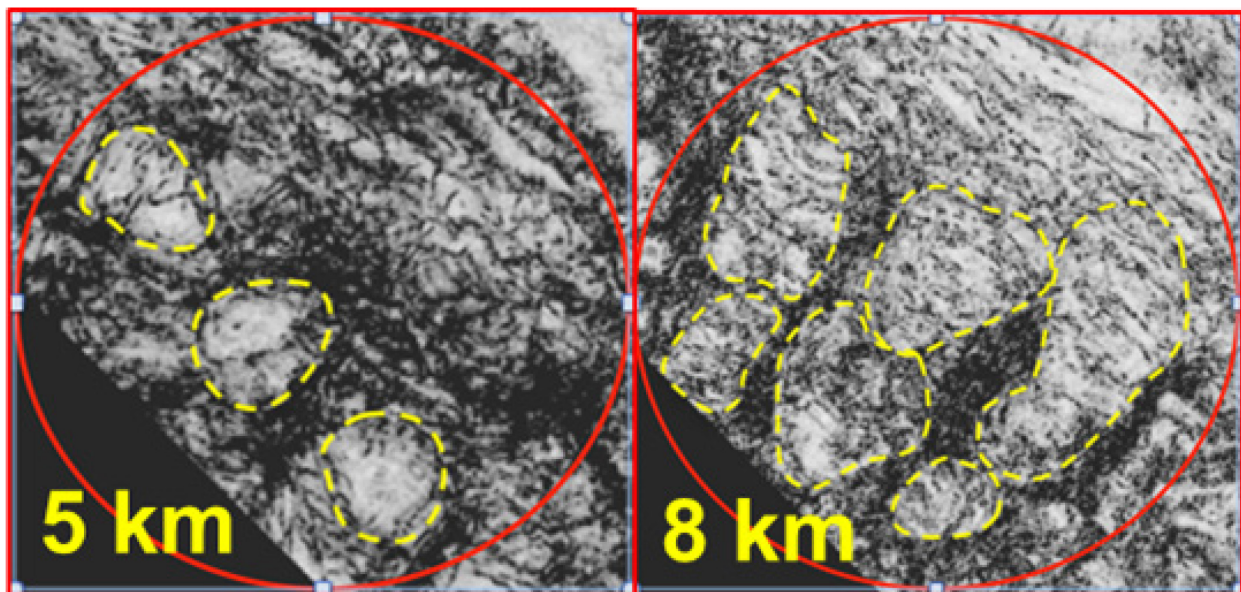


Figure 144: Comparison of rounded (5 km depth) vs elongated (8 km depth) depocenters from the minibasin domain of Ceduna Sub-Basin, White Pointer Delta interval.

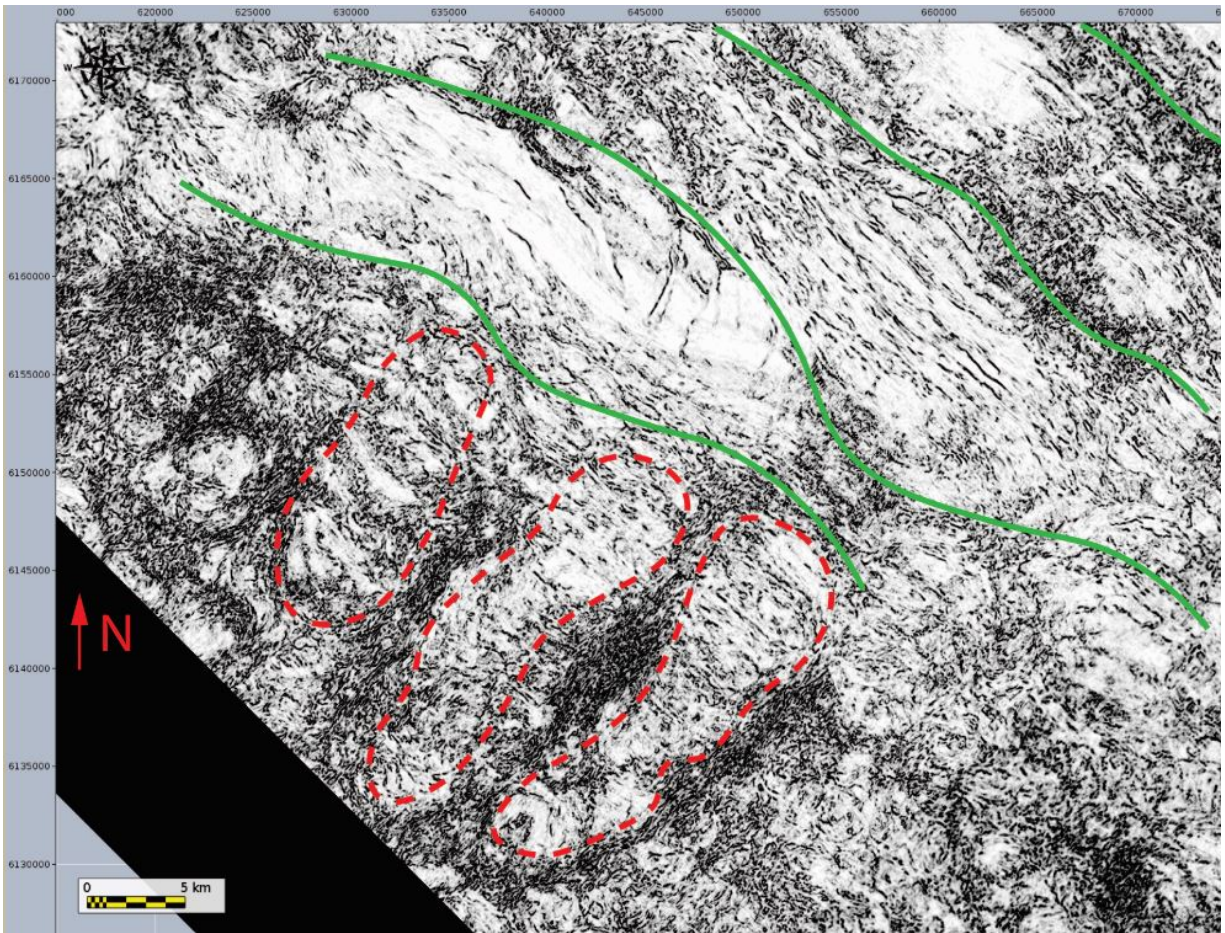


Figure 145: Interpreted close-up from 8 km depth seismic time-slice. Green Lines: Listric Faults, Dashed Red Closures: Elongated Depocenters/Minibasins.

VI. Synthesis of White Pointer Deltaic Interval on 3D Seismic Time-Slice View

White Pointer is a dynamic delta setting evolving from a gravitationally-gliding listric pattern into thrust complex above the shale-prone detachment level; the Blue Whale formation. Based on the structural analysis on time slice view, the deltaic wedge can be evaluated under two main domains based on its structural evolution;

1. Listric Fault Domain comprising of proximal and central portions of the delta interval in which;
 - a. Proximal part is dominated by large-scale listric faults rooting into the detachment surface of shale-driven Blue Whale formation displaying a pure gravitationally-gliding structural pattern.
 - b. Central part is dominated by smaller-scale listric faults, translation features (e.g. shale rollovers and rafts) and some pre-shortening elements (e.g. initial thrusting). This portion of the delta represents the transitional part in between the proximal and distal delta sections.
2. Minibasin Domain scattered through the distal part of the delta comprising of a complex thrust domain with mobilized shale features detached from their sole and carried upwards via thrust faults. This interval forms the point of interest for this shale mobilization research and stands out with these components observed on time-slice view;
 - a. Circular minibasin formations observed through the shallower deltaic parts of the distal delta-toe setting separated by patchy shale accumulations.
 - b. Elongated minibasin formations observed through the deeper deltaic parts of the distal delta-toe setting separated by ridge-like shale deposits.

Such a change in structure through time points out to an early difference of behavior in the shallower sections of the minibasin domain suggesting a mechanism driven by gravitational-gliding at depth (Lower White Pointer level) passing laterally to a mechanism governed by active shale mobilization (Mid-to-Upper White Pointer), later favoring a thrust complex/duplexation. Depocenters within this interval are observed to be separated by features resembling *salt tectonism* (e.g. welds and walls).

Moreover, a strikingly-similar features resembling *salt diapirism* are observed through the NW corner of the dataset. This portion is depicted with three noticeable signatures at surface (5 km time-slice):

- i. Polygonal cracks in the middle
- ii. Primary radial faults surrounding the polygonal cracks
- iii. Caldera-like depressions peripherally located around the primary radial faults followed by a secondary radial fault setting in a circular pattern

Caldera-like formations may represent the depression-related collapse caused by domal shale-rise underneath. Not all of these radial fault signatures at surface are followed by a caldera-like depression as their occurrence depend on the amount of shale they have originated from. However, a noticeable portion of 3D dataset NW corner is covered with radial cracks/faults emerging from a centric point of interest at 5 km depth surface just like salt diapir surface expressions noted in numerous places around the world. The following chapter will be detailing these observations/findings of Blue Whale shale-related mobilization features on seismic time slice and cross-section view.

Chapter 8: Mobilized Shale Deformation Geometries

This section will be reviewing the 3D seismic data observations from Ceduna Sub-Basin, White Pointer Delta interval under two relevant categories;

- Salt-Like Seismic Findings
- Shale-Specific Seismic Findings

Both of these sections and associated seismic interpretations aim to display the mobilization pattern of Blue Whale shales overridden by the White Pointer Delta Interval. *Salt-Like Seismic Findings* Section showcases the examples we observe in a typical salt-prone settings such as 'Wedges', 'Welds' and 'Minibasins' mobilized above a ductile substrate. In this section, we will be looking at shale mobilization analogies that has previously been identified with salt (and certain shale-prone geo-dynamic locations) and recorded within the surrounding sedimentary strata (e.g. halokinesis for salt, argilokinesis for shale).

Different than salt, the second section, *Shale-Specific Seismic Findings* will be displaying the seismic examples of 'thrusting', 'duplexation of thrusting' and 'shale-cored domal highs' accompanied by brittle tectonism elements as an internal mobilization mechanism distinctive to shale. In this section, we will be looking at the seismic representations of 3D cube inline/xline views from the distal part of White Pointer Delta, where we observed 'diapir-like signatures' on time slice structural analysis (Chapter 7, Part V, Structural Time-Slice Analysis of White Pointer Delta with 3D Seismic Cube).

I. Salt-Like Seismic Findings

A. Wedging and Unconformities

When there is a ductile medium (e.g. salt or shale) underlying a sedimentary cover associated with differential loading, certain sediment unconformity patterns such as onlap, top lap and downlap emerge from wedging of sediments deposited on this ductile medium during flow. As a result, the sediment sequence/strata adjacent to *wedges* records the stratigraphic changes associated to mobilization/plasticity. Such stratigraphic terminations expressed on strata within a depositional sequence depict vital evidences that can be used to understand the depositional setting conditions associated with the lower strata of a sedimentary environment and hence the mobility indications of salt/shale.

The distal part of Ceduna Sub-Basin, White Pointer Delta deposits display remarkable wedging and unconformity examples interacted with the mobilized shale features of Blue Whale Formation. Such features compile with salt geometry and its associated plastic deformation pattern observed in salt-prone environments. The onlaps observed on the dataset around the remnant shale packs/ridges point out to an initial down-building of minibasins. These localized wedging strata surrounding the remnant mother shale deposits are the first order shale mobilization features differentiated from the gravitationally gliding delta pattern (Figure 146).

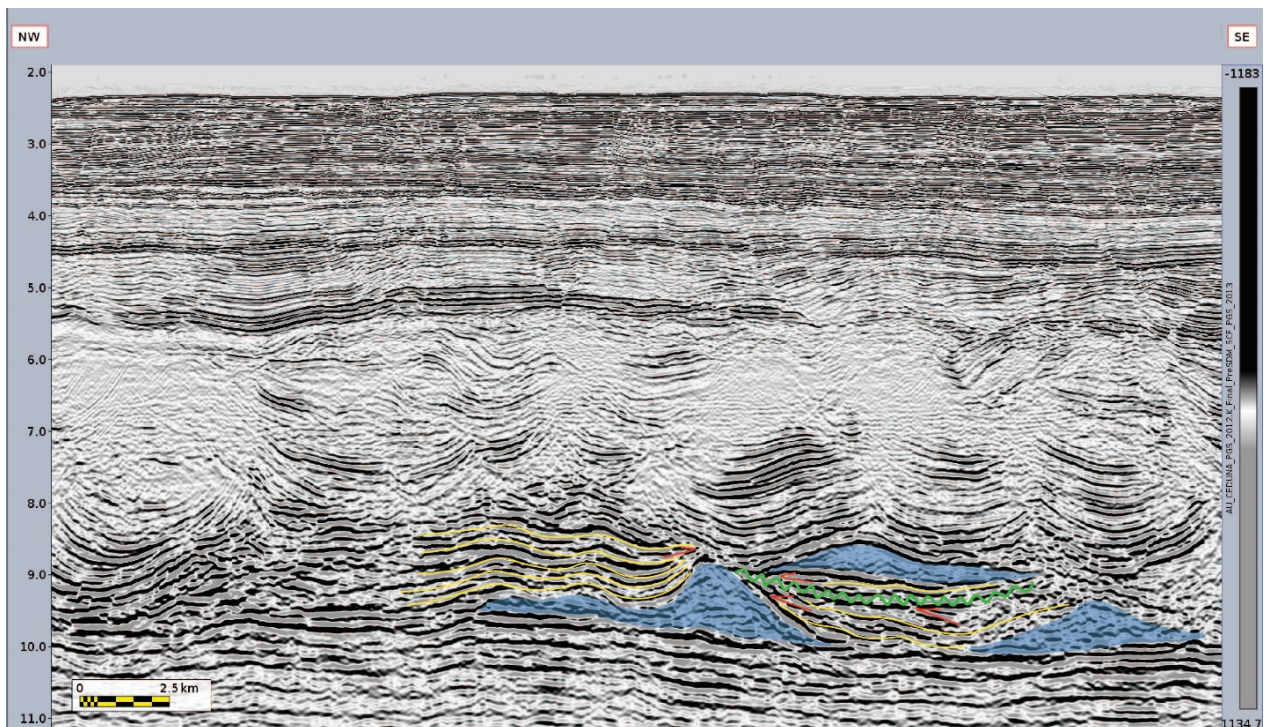


Figure 146: Wedging and unconformity demonstration from Ceduna Sub-Basin White Pointer Delta. Blue Packs: Blue Whale Formation, Yellow Markers: Delta Sediments, Red Arrows: Onlap/Toplap Truncations, Green Marker: Surface Unconformity (image courtesy of PGS).

These wedging features seen on Ceduna Sub-Basin White Pointer Delta interval indicate ridge-like shale deposits located at the base of the delta. Arrival of early White Pointer formation brings the first pulse of deltaic sediment input into the region and starts to build up around these Blue Whale shale remnants. The very first indication of ductility and hence the plastic behavior of shale comes from these stratified, conformably-wedged and layered sediment recordings. As previously discussed, shale and salt deformation are both triggered by differential loading and therefore, different pulses of sedimentary input channels variable stress above the ductile medium based on basin geometry and/or tectonism.

In White Pointer Delta case, thick layer of Blue Whale shales arrive into the system as a maximum flooding surface, and deposit rapidly setting the ground for the overlying delta system. Deltaic sediments start to infill the space and pelage over this thick shale layer. Thickening sediment input triggers the mobilization of Blue Whale formation and leads to wedging patterns (e.g. onlaps, toplaps, pinch-outs, unconformities) surrounding the mother shale patches resembling salt deformation. As more sediments are introduced into the system, the stratified and layered signature of sediment recordings get compacted (syn-sedimentarily) at depth displaying slow-distribution patterns of strain and rheology (Figure 147).

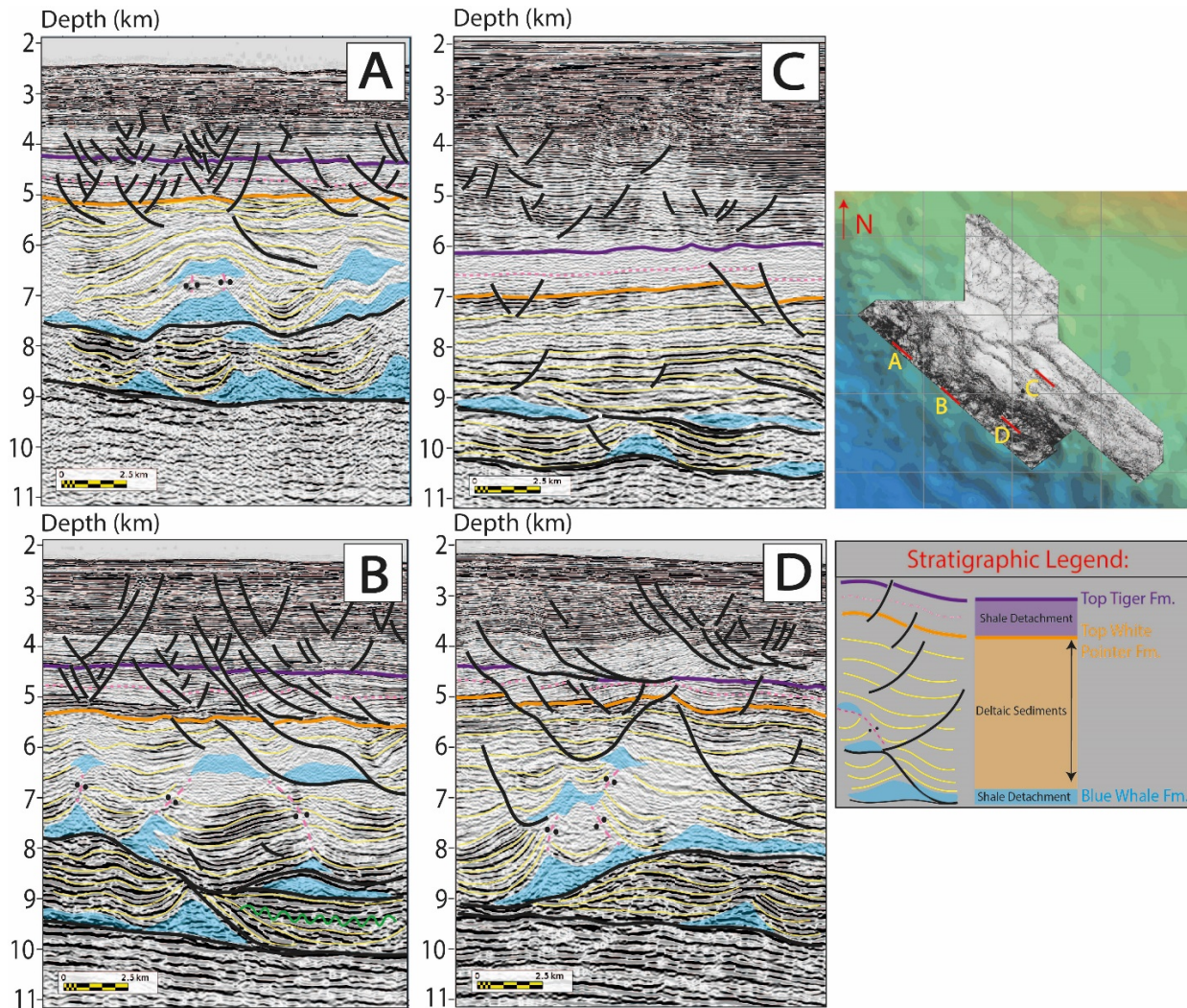


Figure 147: Ceduna Sub-Basin, White Pointer Delta wedging examples collected from various parts of the delta (image courtesy of PGS).

B. Welding

Welding defines the remnant migration path of salt and/or shale deposits that are detached from a ductile body and mobilized through a sedimentary package while leaving signature marks on sediment recordings (e.g. halokinesis for salt, argilokinesis for shale). Welding path, *an ancient migration route of a ductile medium*, gives us clues about the viscous deformation pattern associated with salt/shale movement. Shale tectonics structures observed in Ceduna Sub-Basin, White Pointer Delta, above the duplexed minibasin domain are strikingly similar to salt weld/minibasin formation phenomena seen in salt tectonics related regions. In this section we will be describing these features associated with mobilized shale at the distal toe.

The weld structures observed in White Pointer Delta, symmetrically (parallel-weld geometry) or asymmetrically (cross-weld geometry) separate the sediment growth strata on each side of the welded 'shale walls'. Those structures accommodate 2-4 km depth of minibasins deposited above the clay-ramp introduced into the system by duplexation. Numerous seismic examples from the region display the mobilized shale migration path marked by welding in the area, which suggest that the minibasin development on ductile shale is a really generalized pattern.

As it is briefly discussed and illustrated on the previous sections, the minibasin domain is distinctively different than the listric domain on White Pointer Delta interval. Deeper parts of White Pointer Delta are dominated by ridge-like shale deposits that are channelized and emplaced through the distal part purely by gravitational gliding initially, while the elongated depo-centers surrounding these shale ridges preserve their shape (visible on time-slice view) and characteristics as the delta interval continues to build-up. Early minibasin down-building and wedging correspond to that portion of the delta. Onset of thrusting and duplexation brings formerly developed minibasins onto this preserved down-building domain and continues to build-up fish-tail structures and translated minibasins above. Later in the deposition history, heavily thrust domain branches into more fish-tail thrusts making the system more compacted and rigid.

These fish-tail thrusts continue to get stacked/accommodate the migrating and gliding delta cell above the elevated clay ramp formed by duplexation. Duplexed minibasins, which are now placed above the elevated clay ramp, start to accommodate the late arrivals of White Pointer sequence within these translated minibasin-pods. Arrival of additional deltaic sediments throughout the late stages of White Pointer development introduces more stress to the distal part. Progression of the delta (migration of the gravitational cell) above this elevated surface plane leads to shale welding in between the pre-defined minibasins. Both inline and xline seismic views display these welding features associated with translated minibasins above the clay ramp (Figure 148).

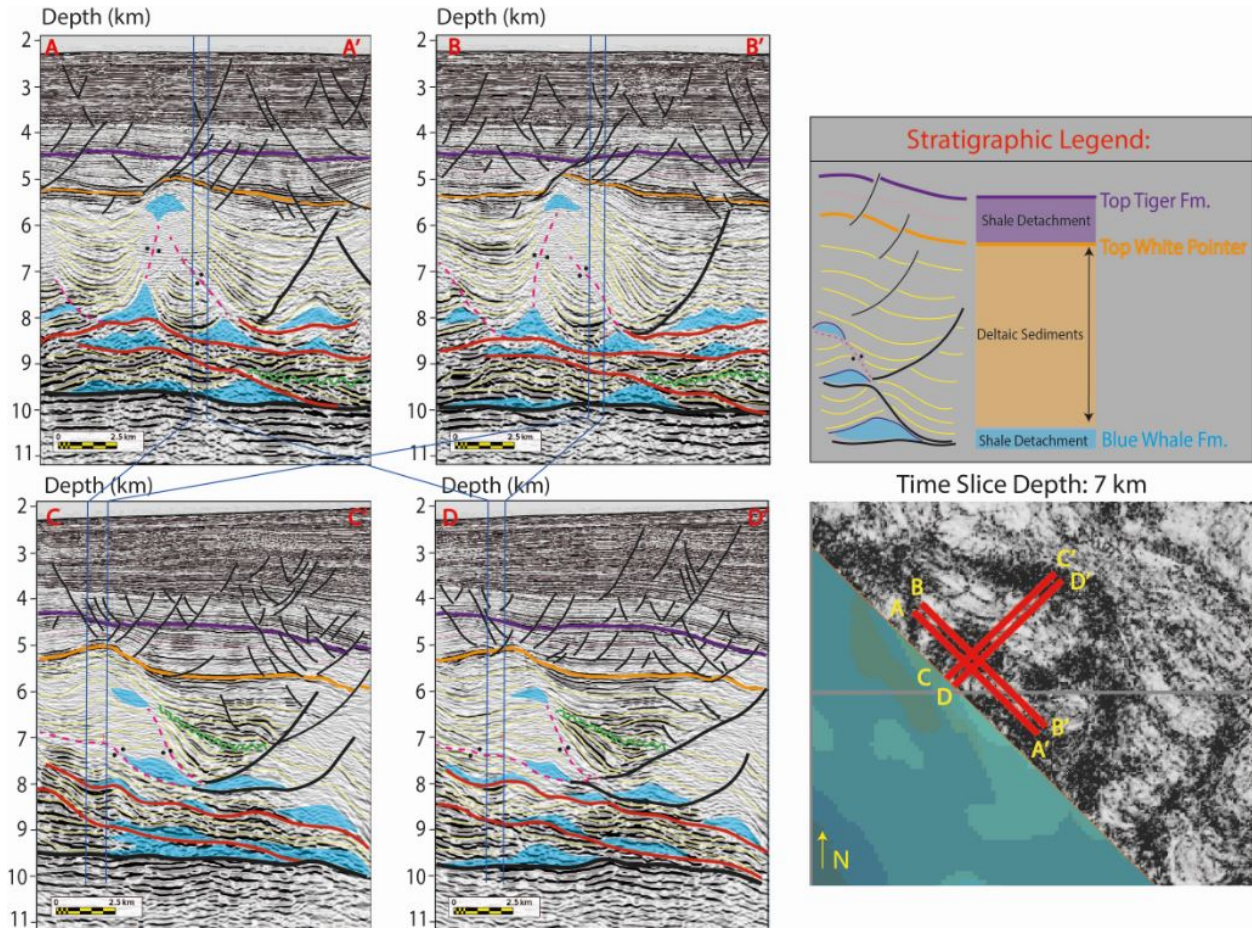


Figure 148: Welding Examples from Ceduna Sub-Basin, White Pointer Delta. Purple Markers: Top Tiger Fm. Orange Markers: Top White Pointer Fm. Yellow Markers: White Pointer Delta Sediments. Blue Patches: Blue Whale Fm. Dashed Pink Lines with Black Dots: Welds. Green Undulations: Unconformity Surfaces. Bold Black Lines: Large-Scale Listric Faults. Thin Black Lines: Small-Scale Normal Faults. Detachment Level is marked with bold black line underneath the Blue Whale Fm. Red Lines: Thrust Faults. Dark Blue lines depict the inline-xline crossings. All seismic lines are in PSDM (image courtesy of PGS)

Through time, translated minibasin strata separated by shale welds evolve into more rounded shape depo-centers compared to the elongated strata below. As the delta becomes more mature, White Pointer gravitational cell continues to migrate further. However, it adopts a slower pace as the clay ramp becomes more prominent and the overlying minibasin domain separated by shale welds accumulates additional deltaic sediments arriving to the distal part. As a result of this dynamic evolution, some of these aforementioned shale welds lead to shale-cored domal highs associated with shale mobilization. The following section will be describing the welded minibasins formed above the thrust strata fed by intermediate detachment levels (branching thrusts) and clay ramp (duplexation).

C. Minibasins

Minibasins are geologic formations initially attributed to salt withdrawal in the literature as they are defined as *sediment-filled regions of subsidence into a larger salt body* (Jackson and Talbot, 1991; for review, see Hudec et al., 2009). However, with advanced seismic imaging techniques and (newly) discovered/re-evaluated outcrops with satellite images (e.g. Makran, Iran; Northern Borneo; Rakhine State, Myanmar), we now know that shale can also act as a ductile medium similar to salt and derive minibasin formations.

The previous time slice structural analysis section described the sub-surface expressions seen on time-slice view. In this analysis, we differentiated two structurally-varying domains; (i) minibasin domain, and (ii) the listric fault domain. Identified minibasin domain displayed circular patterns around the top of the White Pointer Delta (5 km time-slice view), while the deeper sections evolved into elongated forms separated by shale ridges at the distal delta-toe part (8 km time-slice view). These minibasin formations are sedimentary pods that sink into the underlying clay interval (Blue Whale Formation) due to their own mass. Locus of minibasin depo-centers evolve/change with the distribution of differential loading. In other words, they conformably nestle within the ductile shale medium in a buoyant sense based on their size/sediment load and got separated from each other via mobilized shale walls and/or welded shale intrusions. Such mobilized shale structures initially originate from the thick Blue Whale Formation (mother shale) via branching thrust faults and duplexation of the thrust domain (Figure 149).

In geo-chronological order, shale mobilization of White Pointer Delta started initially with early minibasin down-building at the frontal part of the delta, where wedging around the remnant shale deposits are observed. As the delta progressed over time (Early-to-Mid White Pointer era), shortening becomes prominent at the distal toe and led to initiation of thrusting above the Blue Whale detachment level. Duplexation of primarily founded minibasins started to take place, where we see thrusting due to advanced shortening. As a result of this duplexation, an elevated clay ramp was formed above a thrust sheet riding on top of the first order minibasins. These preliminary minibasins were reserved underneath the advancing thrust plane rooting the clay ramp as the delta deposition continued.

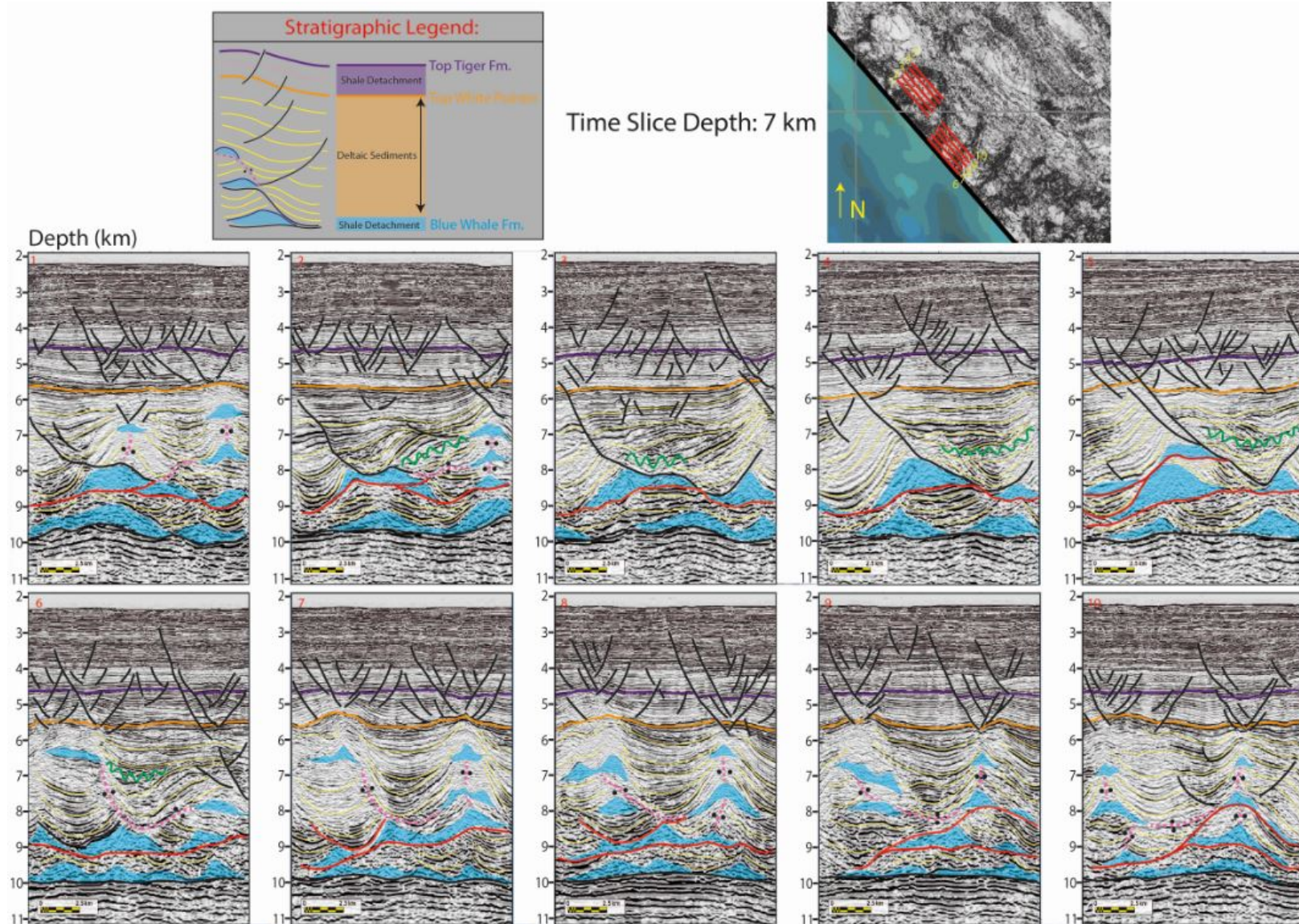


Figure 149: Ceduna Sub-Basin, White Pointer Delta Minibasin Examples. Purple Markers: Top Tiger Fm. Orange Markers: Top White Pointer Fm. Yellow Markers: White Pointer Delta Sediments. Blue Patches: Blue Whale Fm. Dashed Pink Lines with Black Dots: Welds. Green Undulations: Unconformity Surfaces. Bold Black Lines: Large-Scale Listric Faults. Thin Black Lines: Small-Scale Normal Faults. Detachment Level is marked with bold black line underneath the Blue Whale Fm. Red Lines: Thrust Faults. Dark Blue lines depict the inline-x-line crossings. All seismic lines are in PSDM (image courtesy of PGS).

II. Shale-Specific Seismic Findings

A. Thrusting and Duplexation

The Ceduna Sub-Basin, early setting of White Pointer Delta is dominated by down-building features at the distal-toe part as a result of deltaic sediments arriving down-slope into the region and deposited above the thick Blue Whale shale formation. Differential loading triggers the shale layer underneath to deform and accommodate the sediments above in a viscous manner and thereafter, wedging takes place around the shale deposits that have ridged their way to the distal part under gravitational constraints in a gravitationally-gliding context.

In White Pointer Delta interval, thrusting started with early shortening features towards the northern end of the central deltaic domain, where we observe translation features and elongated listric faulting above Blue Whale shales. Shortening is accommodated and translated into the distal part via branching thrust faults in order to compensate the compressional load resulting from the down slope gravitationally-gliding deltaic wedge. Accumulation of stress grows with incoming sediment input and leads to multiplied thrust mediums above the detachment level carrying the shortening structures further down in the distal domain. These intermediate detachment levels carry the mobilized shale patches along their fault planes onto topographically higher places within the delta interval. As a result, the down-building strata (early White Pointer strata) (i) leave wedging and unconformity prints (e.g. onlaps, downlaps, toplaps) on well-imaged 3D seismic view around Blue Whale shale deposits and (ii) get compacted with the arrival of new thrust sheets being introduced into the system (Figure 150).

The singularity of the White Pointer Delta distal domain comes from the *duplexation pattern* observed at the transition of central-to-distal domain, where the ramp-like thrust sheet carries the Early White Pointer depo-centric strata accumulated further down into the distal delta toe while riding above more distal primarily-deposited White Pointer strata. In other words, the duplex thrust serves as a large-scale scooping spoon translating the same-age minibasin-like depo centers composed of Lower White Pointer onto their more distal counterparts. This unique structure is observed all through the White Pointer Delta interval both in 3D and 2D (with less clarity) seismic images (Figure 121).

Duplexation indicates a big-scale mobilization structure within the delta. Listric faults translate the gravitationally-gliding delta deposit further down-slope while the thrust strata underlined by a thick shale interval detaches from main detachment surface, carries shale depo-centers downdip and creates a secondary shale-interacted domain within the distal delta section. This domain represents a complex geologic structure, where we observe a shale-driven detachment level overlaid by (i) early down-building delta sediments wedging around shale ridges, (ii) intermediate detachment levels/thrust sheets intercalated with the down-building series, and (iii) duplexation of the thrust strata serving as a clay ramp to carry the same-age deltaic deposits further down in the delta onto a higher stratigraphic level. As a consequence, Blue Whale shale deposits detaches from their root and mobilized/carried away upwards introducing a new stratigraphic order within White Pointer Delta interval (Figure 150).

Overall, the duplexed thrust domain differentiates from the gravitationally gliding listric fault system characterizing the proximal-to-central part of White Pointer Delta. At the distal part, thrust sheets appear at the toe of the delta, where we observe shortening and down-building leading to first-order minibasin formations at the base followed by thrusting (e.g. intermediate detachment levels) and duplexation of formerly built minibasins at the rear onto the first order minibasins further down in the delta. Migration of duplexed minibasins onto this frontier part of the delta introduces additional stress into the system. As clays are hardened and compacted due to dehydration during this process, they lose their ability to be mobilized in a ductile manner and become more rigid. Rigidity and immobility of this shale-prone system initiate the fish-tail thrust features in the area.

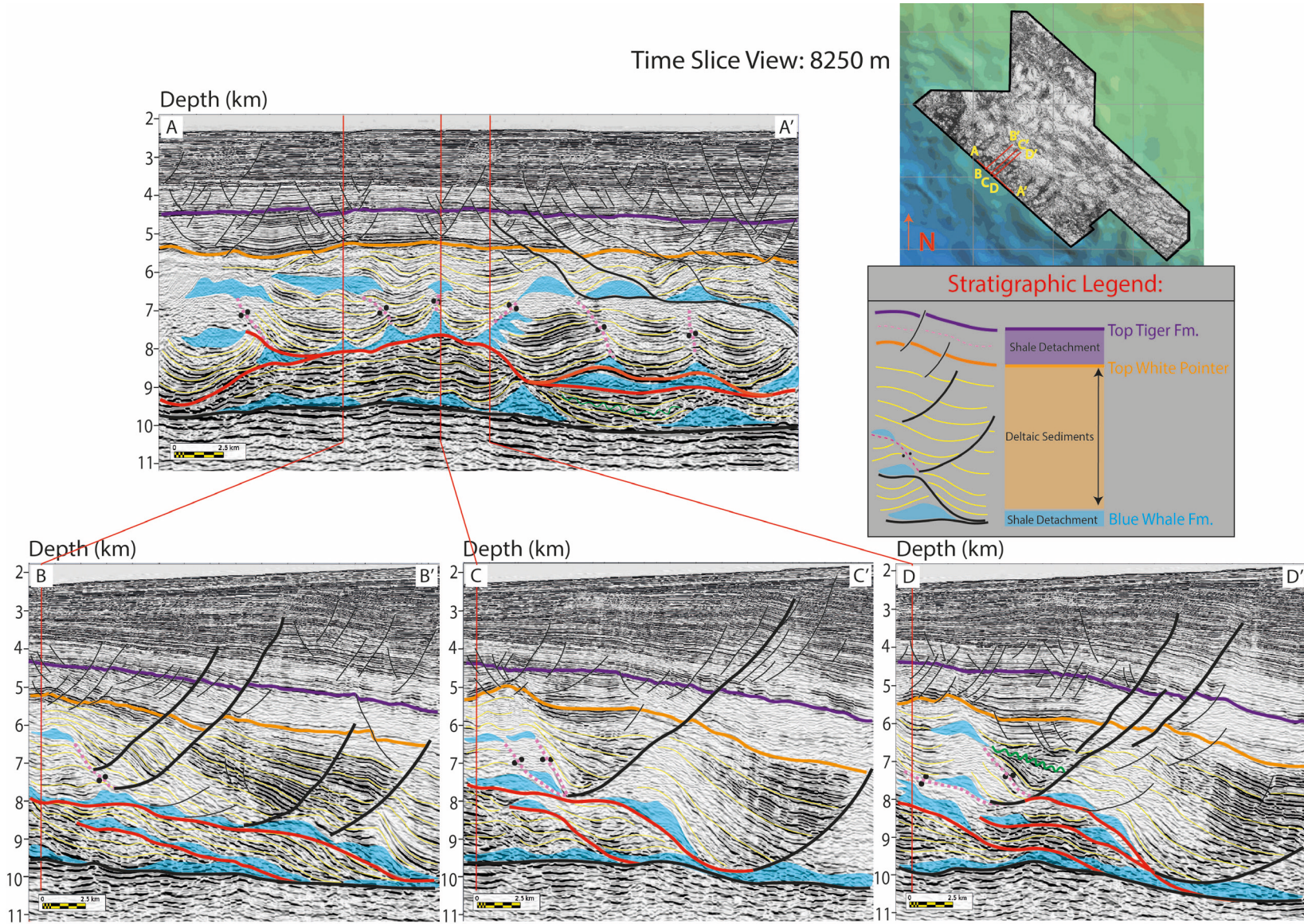


Figure 150: Thrusting and duplexation seen on 3D seismic inline and xline view. See the map on the top right corner of the figure for location. Line A-A' shows the inline seismic view, while the lines B-B', C-C', D-D' depict the xline views crossing through the A-A' inline. Purple Markers: Top Tiger Fm. Orange Markers: Top White Pointer Fm. Yellow Markers: White Pointer Delta Sediments. Blue Patches: Blue Whale Fm. Dashed Pink Lines with Black Dots: Welds. Bold Black Lines: Large-Scale Listric Faults. Thin Black Lines: Small-Scale Normal Faults. Detachment Level is marked with bold black line underneath the Blue Whale Fm. Red Lines: Thrust Faults. All seismic lines are in PSDM (image courtesy of PGS).

B. Fishtail Structures

Fish-tail structures consist of detachment folds cored by a static wall of internal stacked thrust faults arranged in a geometric pattern resembling a fish tail (Soleimany et al., 2013), forming a vertical zig-zag pattern. As it is stated by Drozdowski (1979) and Harrison and Bally (1988), a fish-tail structure corresponds to conjugate thrusts with opposing vergences generated during horizontal shortening. An interbedded decollement level is essential for fish-tail thrust formation. Absence of syn-kinematic sediment loading reduces the shortening rate and viscous resistance, which increases the rate of efficient decoupling (Couzens-Schultz et al., 2003; Darnault et al., 2016).

In the Ceduna Sub-Basin, the White Pointer Delta shows fish-tail structures that are formed at the distal toe, where we observe branching and duplexation of thrusts. They emerge from the cores of shale ridges as an alternative way to enable shale mobilization upwards and subsequent detachment folding in the system. The interbedded strata and decollement level observed at distal White Pointer Delta is a very favorable setting for such thrust geometries with incoming sedimentary input. Gliding delta pattern (White Pointer gravitational cell) is translated onto the upper level with duplexation and continues to glide above the clay ramp with a reduced speed due to elevation and loss of kinetic energy. Thrust faults with alternating vergences stack up in a geometrically arranged vertical zig-zag pattern in order to accommodate the motion of rigid/dehydrated shale packages underneath the gliding delta interval. These fish-tail thrusts advance/build-up as the gravitational cell migrates forward with a slowed pace.

Figure 151 depicts a cartoon representation of 3D seismic data cube with inline and xline view of a detected fish-tail structure in the dataset. This structure is located to the NW corner of the dataset, where we observed clustering of welded shale deposits at the deeper time-slice section (8 km). Such welded shale patches and associated fish-tail features indicate piling of shale deposits as a result of differential loading at the distal end and excessive sedimentary input entering into the deltaic system. On the inline view of Figure 151, we see two inflated Blue Whale shale piles consisting of stacked thrust sheets (forming the fish-tail structures). These basal highs are overlaid by bowl-shaped sediment covers (minibasin geometry), which are topped by shale-cored domal highs surrounded with radial faulting (e.g. similar to salt diapirs found in salt-prone deltas). The xline view shown in the same figure displays Blue Whale shale deposits arriving into the distal area via scooping listric faults carrying the delta deposits from the rear end (proximal-to-central delta) and dumping the load onto the stacked thrust pile displaying internal zig-zag patterns explained with fish-tail structures. The color differentiation seen on figure's stratigraphic legend for the White Pointer Delta sediment column represents the sequential strata associated to (i) minibasin evolution & welding (light grey color) and (ii) fold growth (dark grey color), which will be addressed in detail later in the text.

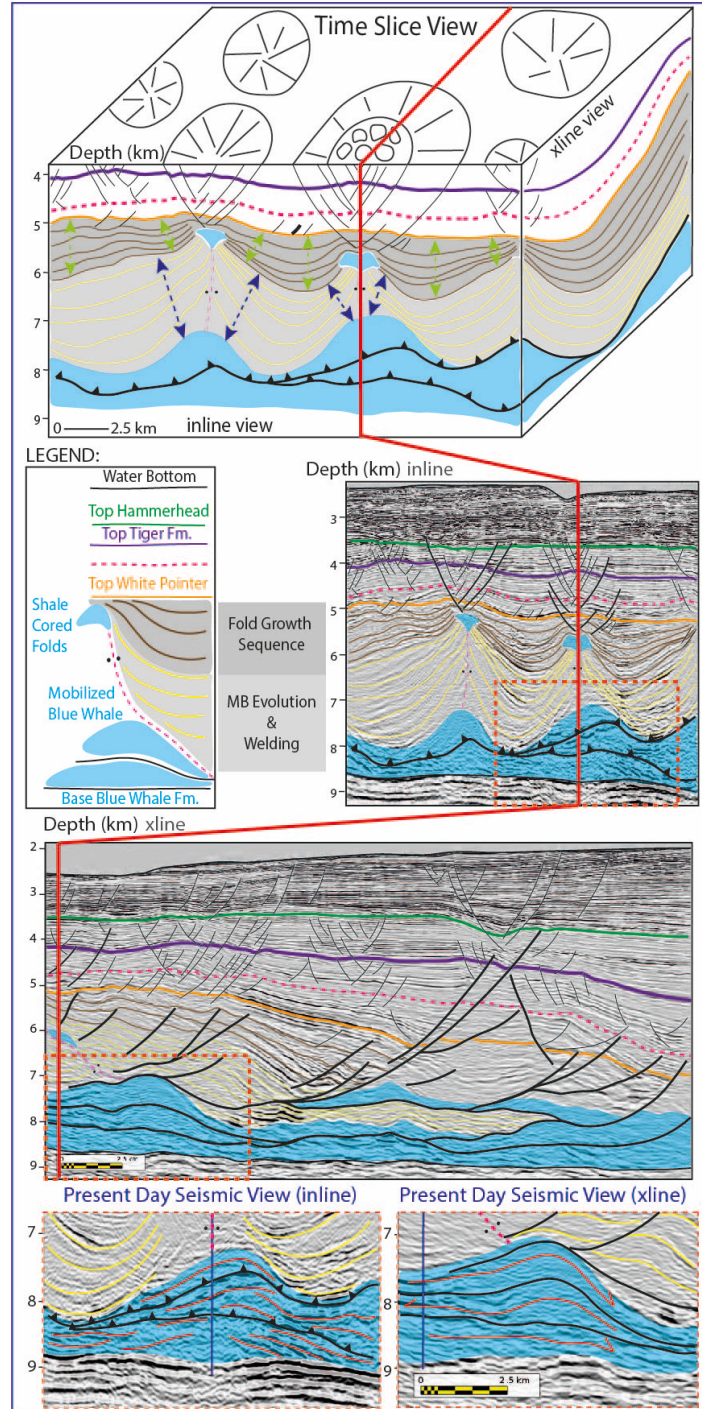


Figure 151: 3D Seismic data cube representation with inline and xline view of a fish-tail structure from Ceduna Sub-Basin. See the legend on the figure for stratigraphic information. Bold Black Lines with Triangles: Out-of-Plane Thrust Fault View. All seismic lines are in PSDM (image courtesy of PGS)

Figure 152 gives the possible evolution diagram of a fish-tail structure observed in the dataset. This diagram aims to explain the progressive building of a fish-tail structure and its late transformation. The first two columns of the diagram depicts two scenarios on inline view, where a fish-tail structure stacks up with arrival of deltaic sediments through various stages of delta evolution. During these stages, the minibasins forming on the sides of stacked thrust sheets (zig-zaggy fish-tail structures) might possibly have

two shale escape models driven by fluidization; (i) minibasins gliding away from shale accumulation, and (ii) minibasins gliding towards shale accumulation:

- Minibasins gliding away from shale accumulation: Depo-centric sediment pods separated from each other via downward escaping shale inflations.
- Minibasins gliding towards from shale accumulation: Depo-centric sediment pods separated from each other via upward escaping shale inflations.

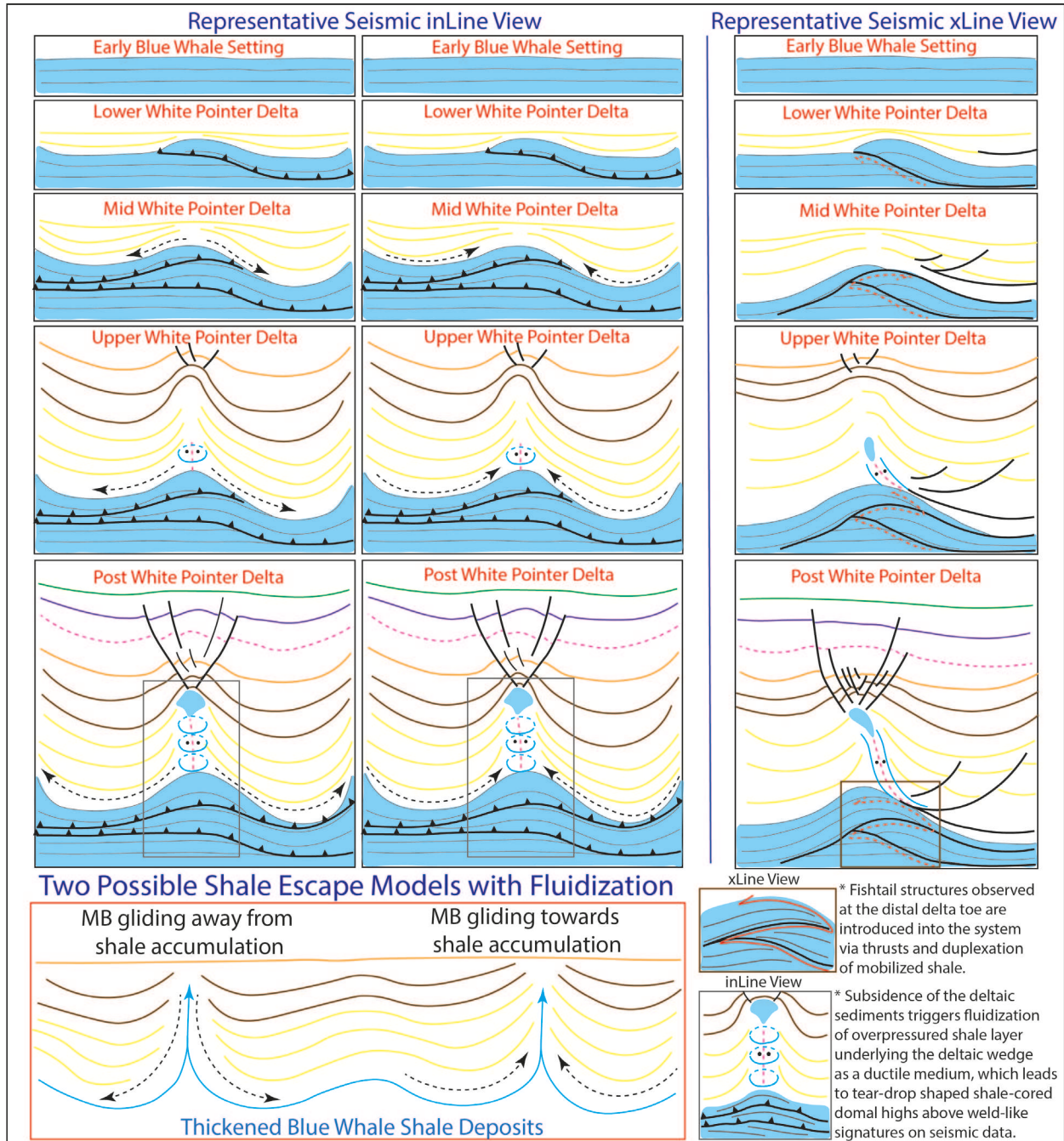


Figure 152: Schematic diagram of fish-tail structure evolution observed on inline and xline view of Ceduna Sub-Basin 3D seismic cube. Post fish-tail building will be detailed in the following sections. See the legend of Figure 151 for stratigraphic level information.

The ‘fishtail’ structures detected in our Ceduna Sub-Basin seismic dataset strikingly resemble the ‘triangle zones’ described by Wu et al., 2019 in their article called ‘Growth of triangle zone fold-thrusts within the NW Borneo deep-water fold belt, offshore Sabah, southern South China Sea (Figure 153). Therefore, our aim is not to stress and dictate on the name but to define the characterization of these structural formations in our research by giving our explanation of subject matter and comparing to the examples of NW Borneo as they also propose a well-imaged view.

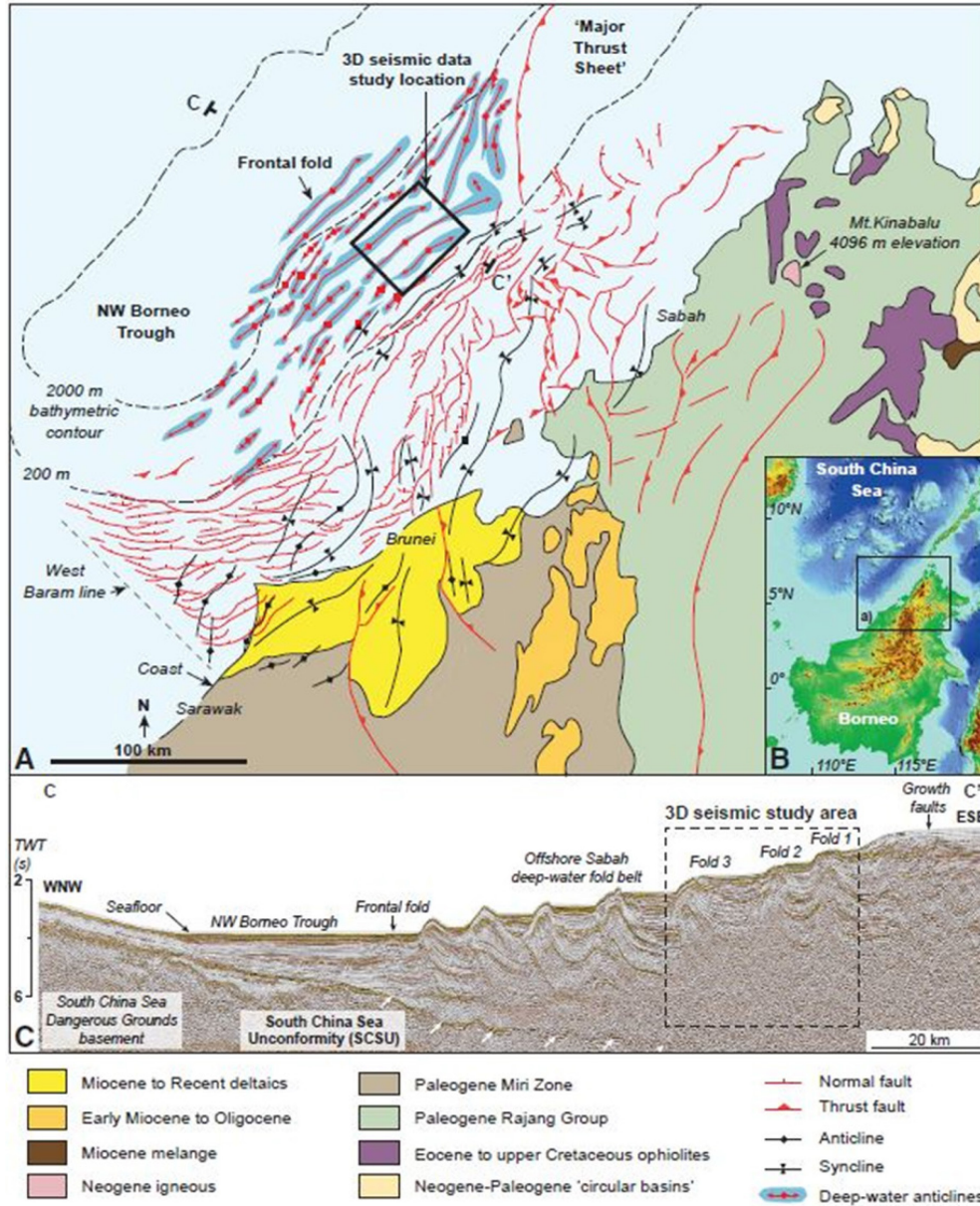


Figure 153: (A) Geological map of NW Borneo margin (compiled from Hinz et al., 1989; Hutchison, 1996; Sandal, 1996; Morley et al., 2003, 2008). Deep-water fold belt anticlines were interpreted from time structure maps in Grant (2004) and Gee et al. (2007). (B) Digital elevation model (DEM) location map. (C) Reprocessed BGR8620 two-dimensional seismic line C-C' showing the regional structural setting. The 3-D seismic area includes three folds within the inboard fold belt that we call fold 1 to fold 3. The deep-water fold belt basal detachment was projected into the 3-D study area near the lower limit of the 3-D seismic volume at a depth of ~7 s TWT (~13 km depth) from previous studies (Cullen, 2010; Cullen and de Vera, 2012). The South China Sea unconformity (SCSU) bright reflectors, shown by white arrows, mark the base of the South China Sea postrift sediments and are below the 7 s TWT limit of the 3-D seismic volume. TWT—two-way traveltime (image retrieved from Wu et al., 2019).

As it is stated by Wu et al. (2019); *triangle zones (a.k.a wedge thrust systems) are thrust-related folds that are formed by linked, oppositely dipping thrusts soling into one or more detachment levels and they accommodate shortening by coeval activity of a basal thrust and an associated backthrust of opposite vergence* (Figure 154).

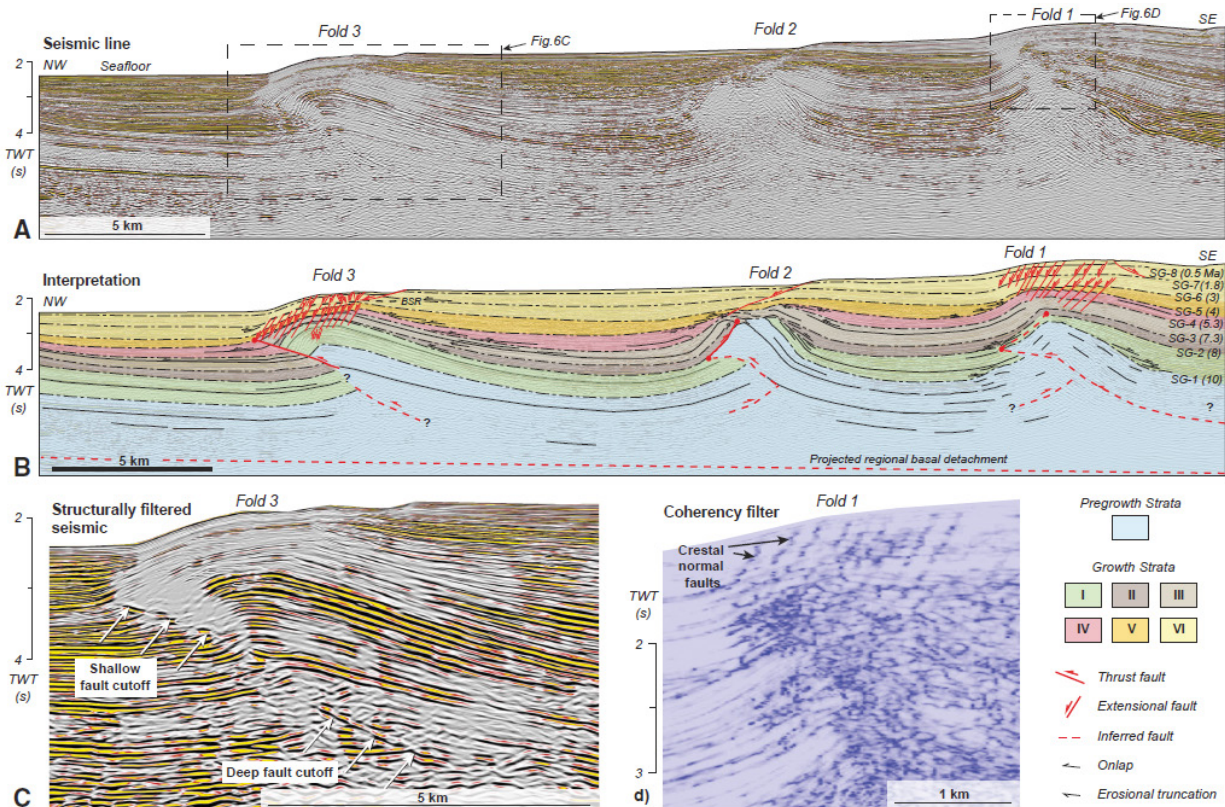


Figure 154: Regional seismic dip line T24600 across the central offshore Sabah study area, where growth strata have been scaled to show ~1:1 scale: (A) uninterpreted seismic line, (B) line drawing interpretation of A, (C) structural-filtered display of fold 3 in A, showing lack of vertical continuity between shallow and deep thrust fault cutoffs, and (D) coherency-filtered display of fold 1 in A, showing an array of shallow, seaward-dipping extensional faults. The structures in the study area are characterized by blind, forward-vergent thrusts, footwall synclines, shorter forelimbs, and long backlimbs. The footwall synclines cannot be fully explained by seismic velocity pull-up artifacts, which are approximately on the order of 100 ms two-way time (~100 m) under the thrust-related folds (see Fig. S1 [text footnote 1]). Faults are dashed where inferred. Ages of syngrowth units (SG) are labeled in Ma. BSR—bottom simulating reflector (image retrieved from Wu et al., 2019).

The research of Wu et al., 2019, differs the style of identified triangle zone thrusts from typical triangle zones, which usually occur as a single structure near the deformation front and are often buried by syntectonic sediments (e.g., Price, 1981), and explains the complexity of these triangle zones thrusts via their origination from multiple detachment levels rather than a single one. Given in their proposed kinematic model for these zones, they explain the mechanism they propose for the evolution of triangle zone thrusts (Figure 155).

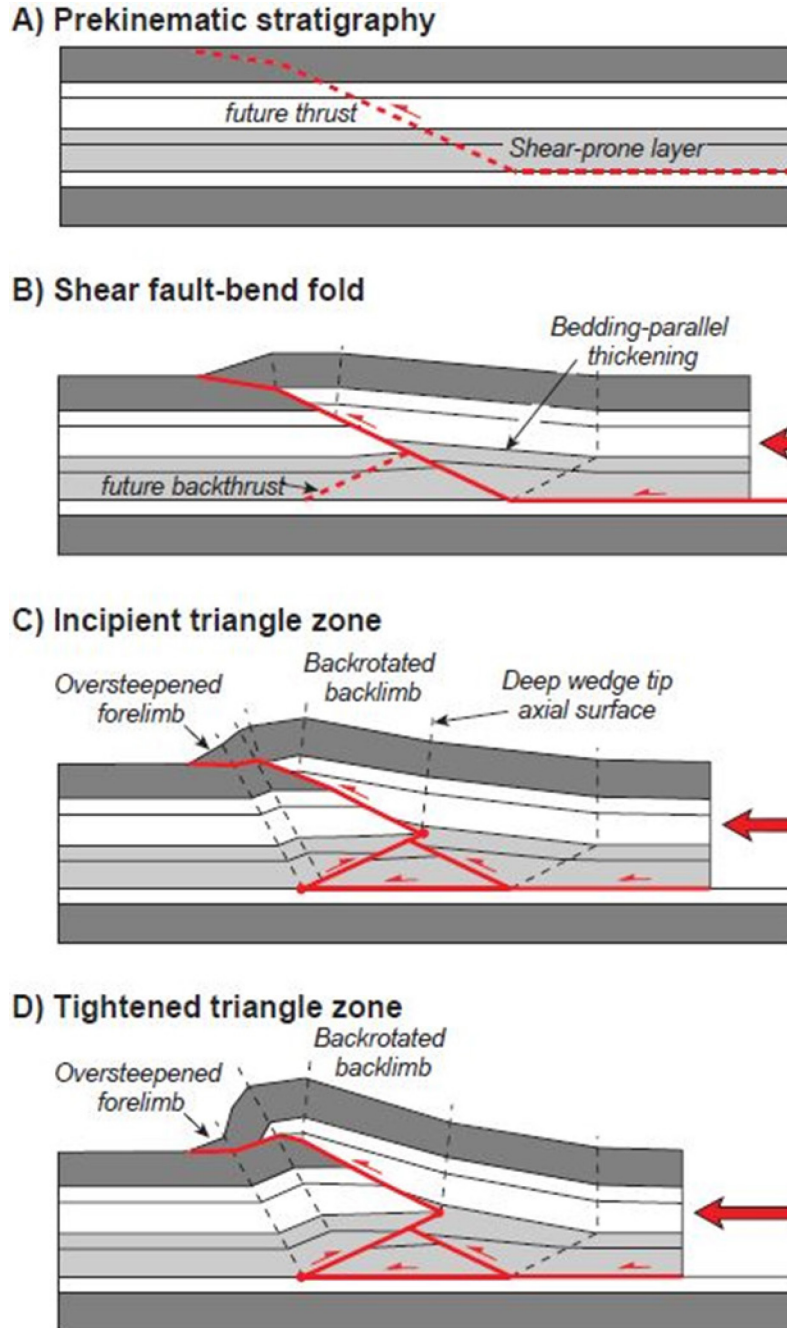


Figure 155: (A–D) Proposed kinematic model for the triangle zones in fold 3. A shear fault-bend fold (redrawn from Suppe et al., 2004) in A and B is deformed by a late-stage footwall backthrust in C. Tightening of the triangle zone fold-thrust in D oversteepens the forelimb and back-rotates the backlimb. The final fold geometry shows similarities to the offshore Sabah folds in this study (image retrieved from Wu et al., 2019).

In our Ceduna Sub-Basin 3D seismic dataset, we did not detect an additional detachment layer (other than the shale-prone Blue Whale maximum flooding surface) feeding the ‘fishtail structures’ we have identified, however, it is our belief that the excessive amount of ductile substrate coming from a single or multiple source can efficiently form such structures in deep water fold and thrust belt systems depending on the thickness and abundance of clay content.

C. Shale-Cored Domal Highs

The distal part of Ceduna Sub-Basin, White Pointer Delta differentiates from its proximal-to-central end due to the shortening and branching thrust faults being introduced into the system as a result of compression carried with incoming sedimentary input. The load of the deltaic wedge detaching above the Blue Whale shales migrates forward with the gravitational cell triggered by listric faulting through proximal-to-central part and duplexation of the thrust domain through end of central-to-distal part. Within the distal portion, where we observe duplexation of the thrust domain, translated minibasins above the duplexed clay ramp, we also observe shale-cored domal features around the edges of minibasin walls with certain characteristics (Figure 149).

At first glance, these structures strikingly resemble the diapir features [*upside down tear drop-like geologic intrusions that emerge from a ductile/plastically deformable setting and pierce through a sedimentary layer creating a deformation pattern recorded by the surrounding sediment strata*] found in salt provinces. They display a rounded (caldera-like) collapse surrounding a radial fault cluster emerged in a centric (point-based) manner. However, as it will be further described hereafter, these formations differ from salt-based diapirs in terms of internal structure and evolutionary pattern even if they give almost the exact surface signature on time slice view.

i. Geometry of Shale-Cored Domal Features

The domal features are introduced into the system during the last stage of deltaic evolution following the shale welding and minibasin growth. Based on our seismic investigation (see below), these domal features are most likely (i) initiated/triggered by fluidization of clays following the fishtailing within the stacked thrust domain, (ii) migrated upwards via *welding* channels in between the minibasin formations, and (iii) accumulated above the welded strata in domal forms. Following their settlement, these domal highs later on lead to surrounding caldera-like depressions and fault signatures resembling salt diapirism we see today on time-slice views (Figure 156). Figure 157 shows the best diapiric shale dome example we have in Ceduna 3D data cube; mainly due to its scale, size and surface footprint/signature we observed on time-slice view (5 km depth).

We present eight seismic line views with their interpretations for the case study shown in Figure 157. We have chosen three xline views, five inline views and an arbitrary line view passing through the radial faults connecting the primary and secondary caldera collapses surrounding the diapiric depression (please see the 5km time-slice map on top right hand corner of the figure for line locations). As it is seen on interpreted seismic scheme (inline, xline and arbitrary line representation), shale-cored domal highs evolve through thrusting and duplexation of the thrust domain bringing the rear minibasin domain further ahead on top of the initially deposited minibasins, which were originally located farther down dip in the section. Welding takes place above this duplexed thrust plane (the clay ramp), where we observe upward minibasin evolution. Shale domes emerge at last during the final stage of evolution; where fluidization of mobilized shales lead to shale escapes topping the minibasin strata. Later in the evolution, with newly deposited sedimentary cover (Tiger Formation followed by the Hammerhead deltaic succession of the of Ceduna Sub-Basin system) these shale-cored tops develop peripheral surface patterns in order to accommodate the later stress of the deltaic load.

When observed on time-slice view, this stress-related pattern evolves into three main structurally different sub-categories; which are namely, (i) polygonal cracking, (ii) primary radial faulting, and (iii) caldera-like collapses. In extremely well-developed cases, these categories can be repeated/multiplied around the shale-cored disharmonic fold formations depending on the *amplitude of shale mobility* followed by *fluidization of these mobilized shales* at the crest into secondary radial faulting and secondary caldera-like collapses surrounding these radial cracks (such as in Figure 156). However, it should be noted that all of these elements (polygonal cracking, radial faulting and collapsed calderas) only emerge with significant amount of shale accumulation combined with certain parameters (e.g. fluidization, amount of free gas, hydrocarbons and internal shale-fluid-compaction processes taking place in between) and not necessarily in every shale-cored dome case. Consequently, besides this well-preserved example given in Figure 157, most of these structures simply develop via (i) polygonal cracking and radial faulting and/or just (ii) radial faulting on the surface (as it is pointed out in Figure 142).

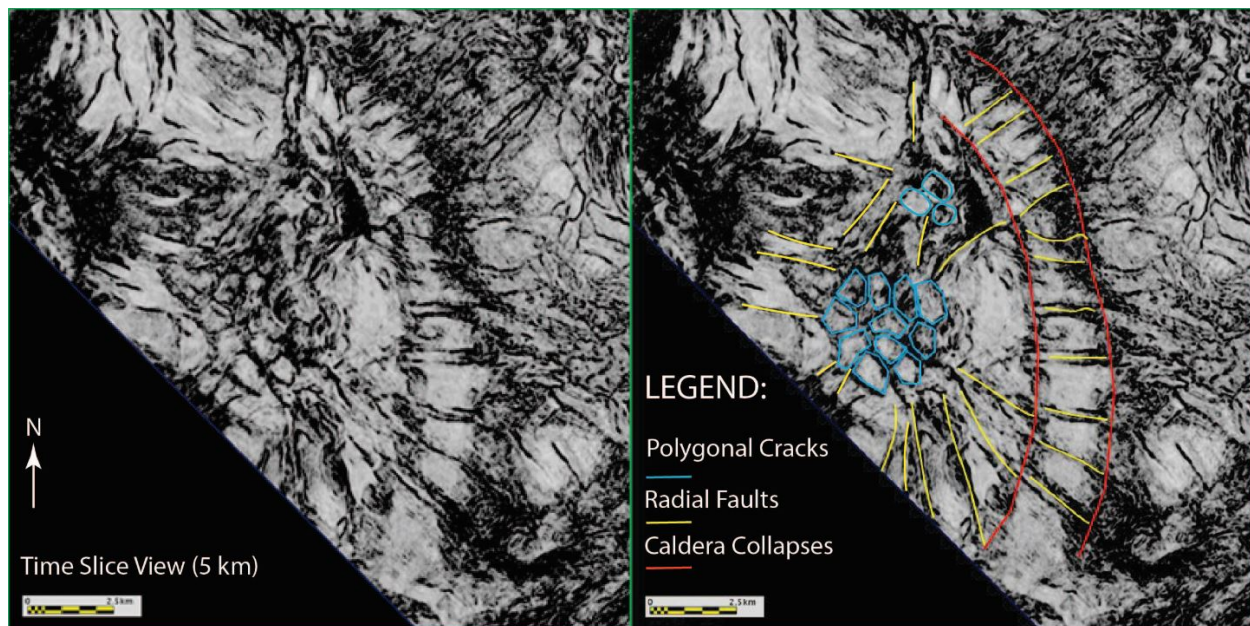


Figure 156: Shale-cored domal high surface expression at 5 km time-slice (image courtesy of PGS)

However, the geometry of shale-cored domal highs seen on Ceduna Sub-Basin, White Pointer Delta interval, frankly resemble the *injection folds* more than *salt diapirs* due to their difference of evolution (e.g. thrust strata for shale) and internal structure (e.g. fluidization). Therefore, calling these shale-cored features as '*shale diapirs*' might be misleading. In terms of salt tectonism, Jackson & Hudec (2017) summarizes these *injection fold* structures, [where the crest of a buckling anticline extends by normal faulting, forming a weak zone that eventually actively pierces by a diapir of pressurized salt], as *active diapirs formed in the crests of contractional anticlines* (Belousov 1959), as an anticline amplifies, its mobile core is tectonically pressurized by displacement loading imposed by the tightening fold limbs. Then, if the overburden is thin enough, the salt core breaks out actively to the surface and the diapirs formed by fold injection have an ancient pedigree. Such diapir typically forms way smaller than the injection fold from which it emerged. Even though this phenomena was depicted by Lohest (1921) and Torrey & Fralich (1926), and *injection folding* was regarded by Stille (1925) as the main way of forming a salt stock, the idea was later neglected for many decades but it is being re-recognized as an important type of diapir in fold belts studied today (Jackson and Hudec, 2017).

Similar to salt diapirs and injection folds, the arched roof of these shale-cored domal highs tends to be resulted from compaction. As explained by Billingsley (1982), *drape compaction arches strata where sediments of varying thickness compact by an equal percentage*, therefore, (1) thinner sediments in the diapir roof subside less than adjacent thicker sediments while (2) folding by drape compaction decreases upward and result in an apparent growth anticline even in post-kinematic strata above a deep static anticline (Jackson and Hudec, 2017). The thicker the shale-cored domal high roof gets, bigger the amount of arching (more bended) is established in the system.

In our case, we define these structures as shale escape features emerging from two-step building; (i) first step of thrusting (*resulting of compression accumulated at a shale-prone delta toe*) aided with fish-tailing & duplexation and followed by (ii) fluidization of mobilized clays (*resulting from thrusting, fish-tailing and duplexation*) above a clayey ramp. Therefore, since salt diapirs do not require a fluidization mechanism and/or a thrusting strata to evolve, these shale-cored domal highs are more likely to be disharmonic folds amplified by shale mobility and fluidization of shales at the crest, rather than simple '*shale diapirs with direct comparison to salt diapirs*' as they are referred in the literature. Moreover, the study of Choudri et al. (2010) supports the conceptual idea we propose with our findings and interpretation of shale-cored domal structures in the distal part of Ceduna Sub-Basin, White Pointer Delta; *when sediment loading and basin-margin uplifting are present, the geo-history of the basin, which can specifically be influenced by (i) sediment loading pattern, (ii) shifting of depo-centers, (iii) shelf width, and (iv) slope geometry, can determine the extent, locale and intensity of these shale-cored structures.*

It is worth noting that fluidization occurs late in the story of fold development. As proposed by Blouin et al. (2019a, b), free gas (mostly methane) production during sediment burial and maturation is a key triggering factor in mobilizing clays. In our case, this phenomenon seem to occur late, affecting through radial faulting and caldera like collapse the sedimentary pile after the deposition of the Tiger Formation beds since they appear isopachous, contrarily to the White Pointer succession, which is thinning toward the anticline crest. This timing is in line with the potential maturation of the deep White Pointer source rock as proposed by Totterdell et al. (2008).

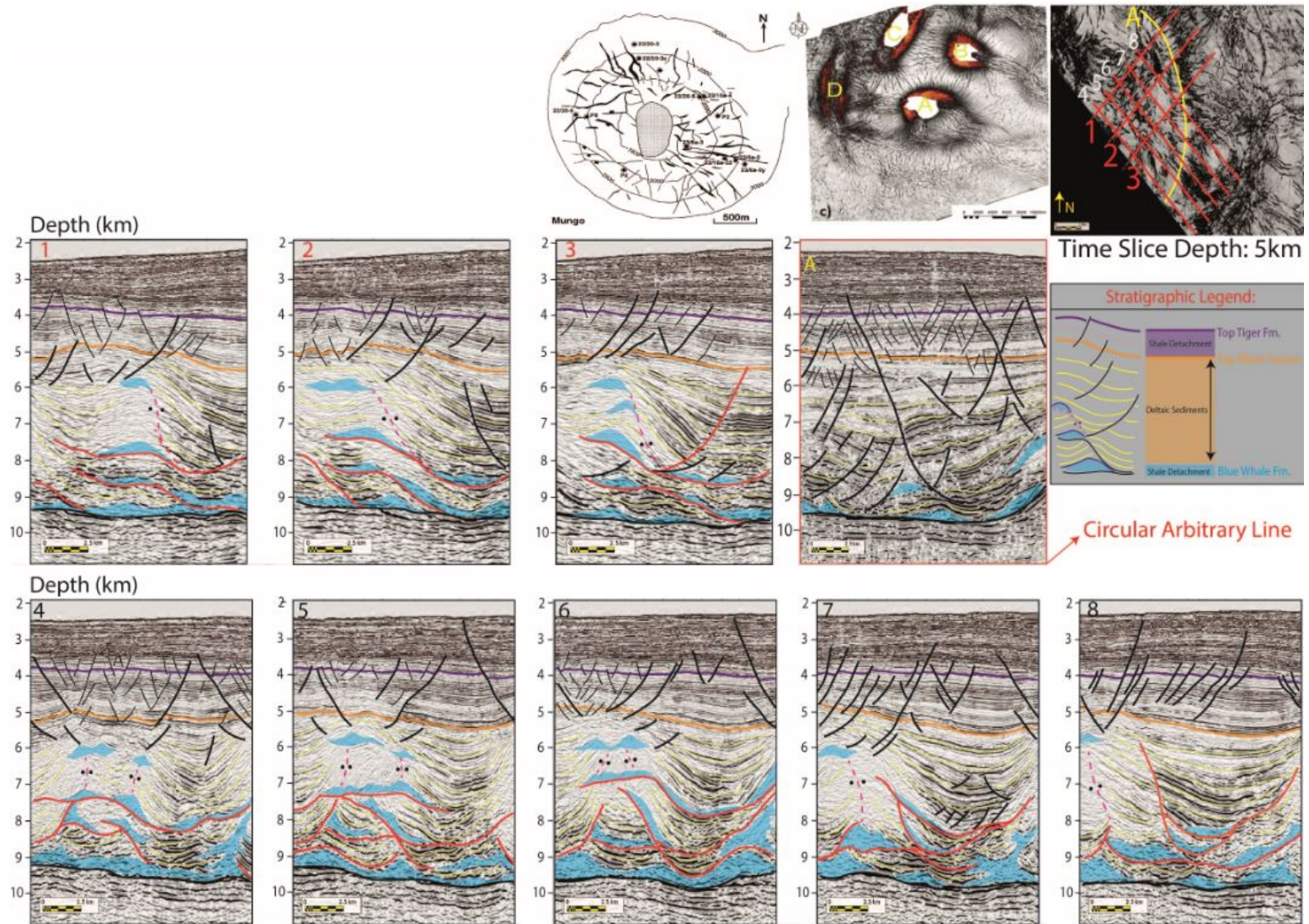


Figure 157: Ceduna Sub-Basin, White Pointer Delta Minibasin Examples. Purple Markers: Top Tiger Fm. Orange Markers: Top White Pointer Fm. Yellow Markers: White Pointer Delta Sediments. Blue Patches: Blue Whale Fm. Dashed Pink Lines with Black Dots: Welds. Green Undulations: Unconformity Surfaces. Bold Black Lines: Large-Scale Listric Faults. Thin Black Lines: Small-Scale Normal Faults. Detachment Level is marked with bold black line underneath the Blue Whale Fm. Red Lines: Thrust Faults. Dark Blue lines depict the inline-xline crossings. All seismic lines are in PSDM (image courtesy of PGS). Examples for salt diapir surface expressions in the upper panel; left image retrieved from Davison et al., 2000; right image retrieved from Harding & Huuse, 2015.

ii. Formation and Evolution of Shale-Cored Domal Highs

There are two domains we have identified within the White Pointer Delta minibasin interval, which can be summarized as; (1) Minibasin Evolution and Welding and (2) Fold Growth Sequence. These domains are specific to the distal part of the delta, where we observe 'shale-cored folding'. The Figure 158 describes the conceptual formation model in ten related frames we propose for 'shale-cored folding and its associated geometry' with an evolutionary scenario leading to radial faults, polygonal cracks and caldera-like collapses we pointed out in the previous section.

(1) Minibasin Evolution and Welding: Primary Domain

Primary domain defines the minibasin interval between the top of fish-tail thrusts and the shale-cored disharmonic folds. It is characterized by equally balanced -isopachous- package of White Pointer deltaic deposits surrounding the domal highs triggered by fluidized shales welded from the duplexed/translated clay ramp. This interval marks the shale fluidization era, where we observe active rising/mobilization of shale-cores.

(2) Fold Growth Sequence: Secondary Domain

Secondary domain is defined by the unequally balanced -non isopachous- package of White Pointer deltaic deposits occupying the interval from the top of shale-cored domal highs up to the Top White Pointer / Base Tiger Formation. This fold growth sequence marks the post-fluidization era, where the active shale-rising is ceased and faulting commenced above these domal features.

Pre-Delta Environment:

Frame 1: The maximum flooding surface (Blue Whale Formation) occupies the pre-deltaic setting and creates a thick layer of shale unit. In places, this settlement is preserved as early gravitational gliding patterns such as gravity-driven, shale rollers. We rather observe the development of elongated depocenters in the direction of gliding separated by shale ridges, showing thinning of beds against the shale ridges, which leads to gravitational lows in between these ridges with incoming sediment supply throughout the frontal part of sub-basin, what would later be called the distal White Pointer Delta.

Early-Delta Environment:

Frame 2: Following the gravitational ups and lows nestling in the distal part as a result of gravitational gliding and early downbuilding, minibasin development resumes around these shale ridges/deposits at the distal delta toe. The early deltaic sediments wedge against the shale piles and build upwards above the Blue Whale detachment level with incoming load.

Frame 3: The more sediments enter into the system, the greater compressional stress builds up at the delta toe leading to branching of the thrust domain above the shale-prone detachment level. Early thrusting takes place at the delta toe and hardens the clays underlying the downbuilding strata. This stage also initiates the fish-tailing.

Frame 4: Fish-tailing progresses with incoming sediments and consequently hardening clays. Shales from rear-back detach from its base Blue Whale mother shale level and are carried forward via advancing thrust sheets underneath the accumulating delta deposits. This stage also marks the initiation of duplexation.

Mid-Delta Environment:

Frame 5: Duplexation of the thrust plane translates the minibasin, which have been formed in response to downbuilding on top of the distal minibasin strata. Thickened thrust domain proposes a clay ramp within the system, which kinematically slows down the incoming delta sediments to climb and pass above the ramp. Fish-tailing continues to breach in between as minibasins are translated on top of the duplexed clay plug/deposits.

Frame 6: As translated minibasins are filled with more sediments arriving from rear delta, hardened clays become more compacted underneath, probably leading to overpressurization. Fluidization of these hardened clays initiates early fluid escape paths (initial welding). Disharmonic folding starts to take place in between these translated minibasins as minibasins of White Pointer Delta migrates onto the duplexed/fishtailed thrust interval dragging the clay ramp further away in the delta front.

Late-Delta Environment:

Frame 7: Commencement of clay mobilization above the thrust domain in between the minibasins signifies the course of welding (migration path) for overpressured clay deposits, leading to shale-cored domal highs/escapes in the region resembling diapiric salt tops (only in appearance, not in evolutionary pattern). Minibasin deposition pace down and transitions from evolution (primary domain) into fold growth era (secondary domain).

Frame 8: Fluidized shale escape features initiate small scale faulting and radial cracks around the domal highs emerged from these shale-cored depositions above the welded migration paths. White Pointer formation begins to deplete and deform locally by normal faulting, probably in response to both folding and fluid escape. The delta starts to stabilize as the White Pointer gravitational cell movement ceases upon arrival of Tiger Formation.

Post-Delta Environment:

Frame 9: Arrival of Tiger Formation (future detachment level for Hammerhead Delta) marks the end of White Pointer Delta interval and leads to a pause in the radial faulting on the crest of the shale-cored domal highs. A secondary gravitational cell movement triggered by basin geometry starts to form for the younger deltaic system (Hammerhead Delta) prograding above the White Pointer Delta setting. Mobilized Blue Whale shale features observed within the White Pointer Delta interval are stabilized at the distal delta toe.

Frame 10: Hammerhead Delta interval develops above the Tiger Formation defining its detachment surface, while the newly formed gravitational cell formation observed at Hammerhead Delta level leaves the previously formed White Pointer Delta and its distal delta mobilized shale features preserved in a fossilized manner within the deltaic interval resembling salt tectonics. Probable maturation of deep source rocks and methane production, associated with diagenetic modification of the clay assemblage help to further mobilize the clays in the core of the domes, resuming radial faulting above the aforementioned shale-cored domal highs and lead to caldera-like collapses in places depending on the shale supply underneath and its fluidization pattern/extent.

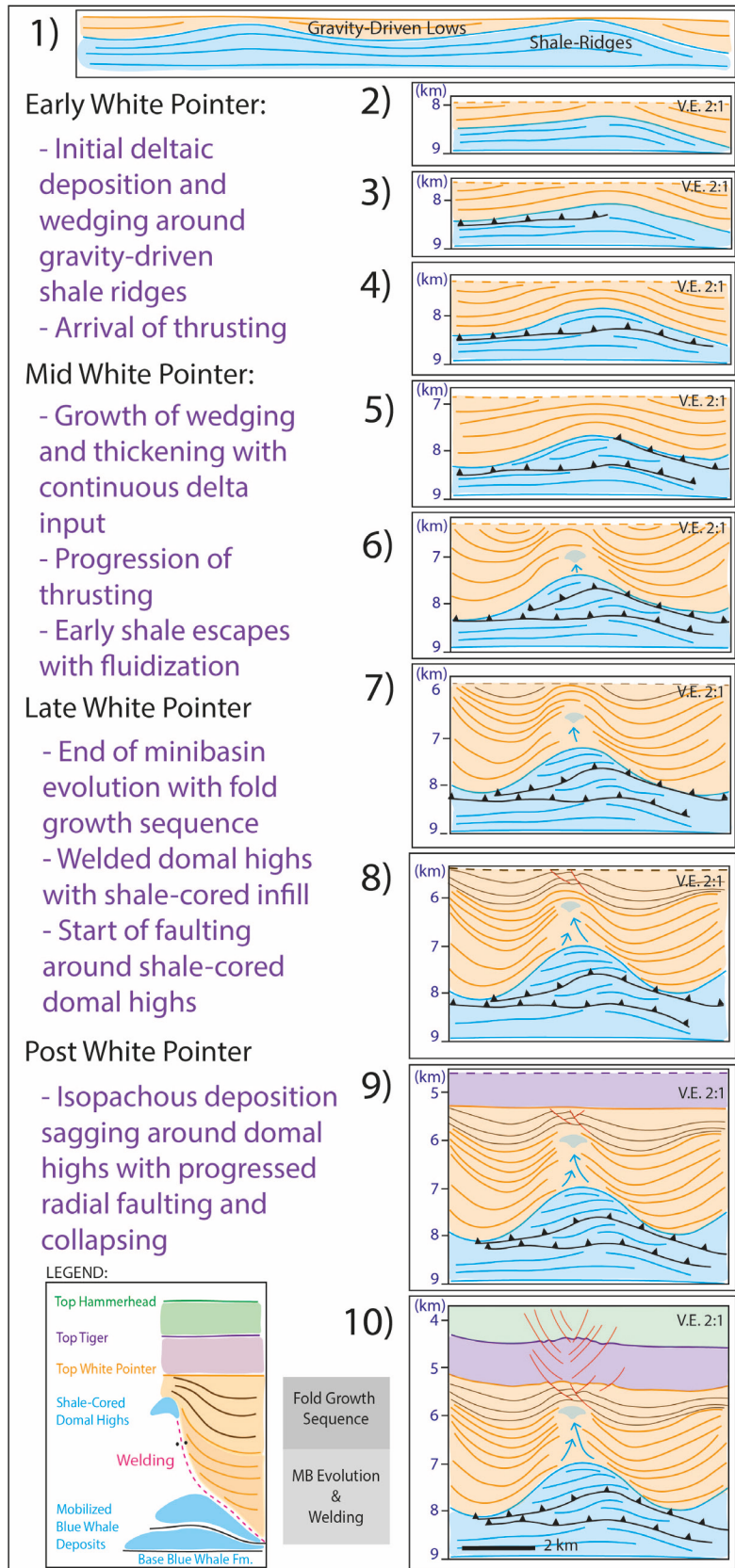


Figure 158: Geo-Chronological Evolution Diagram of White Pointer Delta Shale-Cored Domal Highs above Fishtail Structures.

III. The Kinematic Scenario Proposed for White Pointer Delta

Based on the seismic data findings we presented in the previous chapters, here we propose a kinematic scenario that explains the shale mobilization in the White Pointer Delta (Ceduna Sub-Basin). The kinematic scenario details the overall evolution of White Pointer Delta with an emphasis on shale mobilization stages observed at the distal part. In a chronological order, the sections below will aim to address the evolution of the delta represented by the White Pointer Gravitational Cell formation and its migration through time (Figure 159).

In Figure 159, the chronology of Argilokinesis is presented by ten stages: [a] *Early White Pointer Delta Setting*, [b] *Early-to-Mid White Pointer Delta Setting*, [c] *Early Mid White Pointer Delta Setting*, [d] *Mid White Pointer Delta Setting*, [e] *Late Mid White Pointer Delta Setting*, [f] *Late White Pointer Delta Setting*, [g] *End of White Pointer Delta Setting*, [h] *Early Tiger Setting*, [i] *Late Tiger – Early Hammerhead Delta Setting*, and [j] *Hammerhead Delta Setting*.

There are four domains detailing the development of delta and clay mobilization in the area, which are namely; (1) extension, (2) translation, (3) shortening and (4) down-building. To put it in a nutshell; (1) *extension domain* is where we observe extensional delta features triggered by the gravity-driven listric faults, (2) *translation domain* is where we see shale-related translation features such as shale rollers, (3) *shortening domain* represents the shortening/compression elements such as fish-tail features and thrusts, (4) *down-building domain* appears at the very distal part of the delta (delta toe), where we first observe the initiation of minibasins with down-building strata around the piling up gravity-driven shale deposits.

[a] Early White Pointer Delta

Early settlement of White Pointer Delta is designated by initial listric faults starting to form at the proximal part of the delta triggered purely by gravitational gliding. Growing listric faults sole into the Blue Whale detachment level comfortably with large offsets with incoming sedimentary input. Ductile shale layers of Blue Whale Formation start to pile up and create elongated patches/ridges at the distal part of the delta as a result of gravitational gliding and/or channelizing, where we observe the initial down-building features (e.g. wedging) associated to the interaction between incoming sediments and the ductile shale. White Pointer gravitational cell is formed during this period as an actively migrating delta interval above the ductile Blue Whale shale detachment (Figure 159a).

[b - c] Lower-to-Early Mid White Pointer Delta

This period marks the advancement of listric faulting with continuously sediment supply. These faults further advance down-slope from proximal-to-central part of the delta, while small-scale thrust features start to form at the delta toe as a compressional response against the extension proposed by these listric faults. Early shortening structures are introduced into the system during this time. The White Pointer gravitational cell becomes more prominent in its shape (Figure 159b). Down-building strata continues to stack with compaction as the sedimentary load and compressional response to this sedimentary load build up within the system (Figure 159c).

[d] Mid White Pointer Delta

By Mid White Pointer Delta period, the thrust duplex starts to take its proper form and commences to move forward as a scooping spoon-like ramp in the delta-toe section. Shortening features become more prominent with elongated translation of listric faults. Additional thrust faults appear in front of the duplexed thrust sheet in order to accommodate further stress. This era also initiates branching thrust faults (intermediate detachment levels) of the system as well as fish-tailing within these thrust faults (Figure 159d).

[e] Late Mid White Pointer Delta

Mid-Upper White Pointer setting showcases the progress on delta evolution and migration of White Pointer gravitational cell. Extension, translation, shortening and down-building domains migrates further down the delta slope above the ductile Blue whale shales. Listric faults become larger and shortening progresses at the distal portion. Blue Whale shale deposits get compacted/hardened as shortening advances with multiplied thrust levels. Minibasin down-building domain at the distal toe is duplexed by the 'scooping thrust plane' carrying the formerly built minibasin developed in the proximal domain on top of the forwardly settled down-building/minibasin strata in a more distal position. Duplexation of these minibasins leads to an elevated clay-ramp at the distal part. The down-building strata of initial minibasins underneath the duplexation plane gets more compacted as the clay ramp starts to ride on top and the *Post-Duplex* package starts to build behind the duplexing wedge (Figure 159e).

[f] Late White Pointer Delta

Late White Pointer delta period marks the transfer of the rear-back minibasin domain fully translated above the frontal down-building domain. At this stage, it becomes kinematically challenging for the late arriving deltaic sediments to climb above this duplexed clay ramp. Therefore, advanced compaction and fish-tailing takes place within the duplexed wedge, while newly formed thrust faults are introduced onto the thrust complex front. The sediment supply that has been carried forward above the primary down-building strata with *duplexation* starts to spill over the thrust front complex and the abyssal plain (Figure 159f).

[g] End of White Pointer Delta

During Upper White Pointer Delta deposition, duplexed minibasins riding above the clay-ramp start to accommodate newly arriving deltaic sediments that are introduced into the system as *Post-Duplex* package. This process triggers initial shale welds/escape paths forming in between these minibasins probably associated to early features of fluidization. The White Pointer gravitational cell shrinks as it migrates forward and upwards above the duplexed clay-ramp due to compaction and loss of kinetic energy against the elevated shale barrier. Disharmonic folding takes place as a result of gravitational cell shrinkage and migration. During this time of deposition, the down-building domain underneath the duplexed clay ramp is locked in space with no more mobility. This stage marks the end of White Pointer delta deposition as Tiger Formation starts to build up and sets the scene as the detachment level for the younger Hammerhead delta formation to arrive (Figure 159g).

[h] Early Tiger Deposition

Upon cessation of White Pointer Delta deposition, secondary maximum flooding surface (Tiger Formation) arrives and spills over the formerly sealed deltaic system. During this stage, fluidization of mobilized/duplexed Blue Whale shales continues and leads to progressed disharmonic folding above the duplexed strata via advanced welding. These disharmonic folds evolve into well-preserved shale-cored domal highs resembling salt diapirs on seismic view and time-slice sections (Figure 159h).

[i] Late Tiger – Early Hammerhead Deposition

Tiger Formation conformably covers the whole region, showing a thickening at large scale within the top part of the White Pointer Delta, due to capturing of the sediments between the slope and the bathymetric high formed by the duplexed domain. By this time, the Late Santonian – Maastrichtian Age Hammerhead Delta starts to build up above the Tiger Formation shale deposits. Further down within the thrust complex/front domain, a secondary extensional system with small-scale listric faulting evolves above the *duplexation* sediment package. As the White Pointer Delta interval is locked and compacted in between, the shale welds/walls separating duplexed minibasins speed up fluid escape via and clay fluidization probably in response to early gas maturation processes, which end up with further development of shale-cored domal highs in the region. Progressive fold growth triggers small-scale faulting around these domal highs, which in some places turn into radial fault zones surrounding these shale-cored highs. Continued deposition of Tiger Formation initiates small-scale radial faulting around these shale-cored domal highs, which distinctively differentiates from large-scale listric faulting we have observed previously in the deltaic system. These radial fault areas can eventually collapse and create caldera-like depressions around these welded shale-cored tops. This stage also marks the absolute end of White Pointer Delta gravitational cell activity as migration of its deltaic wedge gets ceased and locked in space within the Blue Whale and Tiger Formations (Figure 159i).

[j] Hammerhead Delta Formation

Deposition of Hammerhead Delta formation seals the White Pointer Delta interval shale mobilization activity in the region. During this period, sediment progradation takes place and Hammerhead Delta starts to fully develop above the White Pointer Delta initiating the secondary gravitational cell formation riding above the former one. The Hammerhead Delta gravitational cell formation migrates further down the basin as sediment progradation continues. The whole system adapts into a stable and balanced state as the deeper portion of Ceduna Sub-Basin, White Pointer Delta interval becomes immobile. The fossilized White Pointer Delta gravitational cell interval preserves all of the mobilized shale features represented by: primarily built down-building strata/minibasins, wedging, duplexed thrust plane/minibasin domain overriding these primary minibasins, fish-tail thrust features, minibasin evolution/fold growth, welding, shale-cored domal highs and radial faulting/collapsing associated to these fluidized shale tops at the distal toe (Figure 159j).

Argilokinesis Occurring in Natural Cases

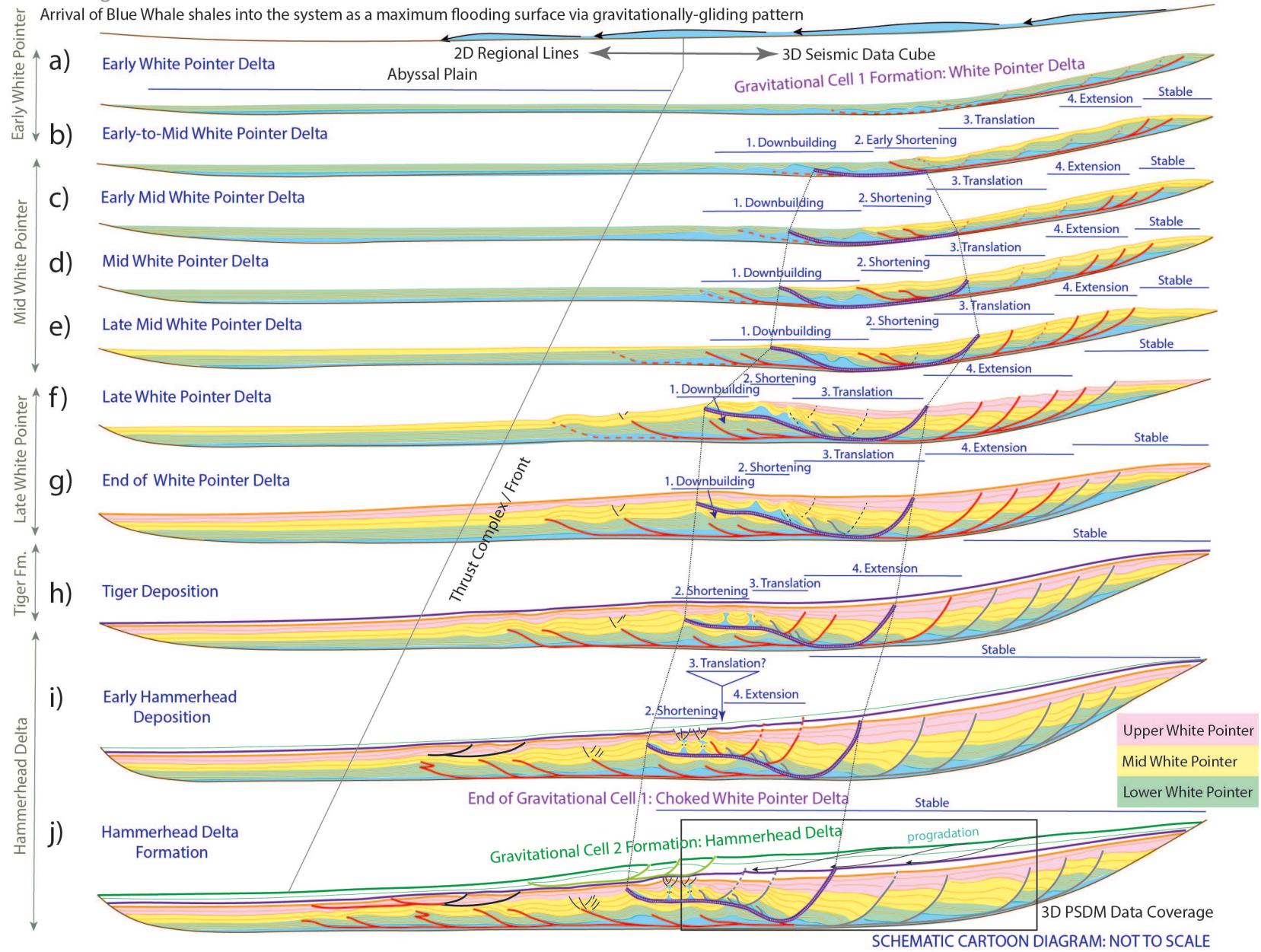


Figure 159: Ceduna Sub-Basin, White Pointer Delta Kinematic Scenario explained in evolutionary geologic stages (see the text for explanation).

PART IV: Discussion and Perspectives on Shale Mobility

This part of the thesis is devoted to the findings and perspectives on Shale Mobility based on the conducted fieldwork study of Rakhine State, Myanmar and seismic study of Ceduna Sub-Basin. The purpose of this part is to wrap up the thesis research and present a discussion about the findings and noted implications. It consists of two sub-chapters complimenting the subject: (i) Rakhine State, Myanmar Fieldwork Case-Study and (ii) Discussion and General Conclusions on Shale Mobility Based on Conducted Fieldwork and Seismic Study.

Chapter 9: Fieldwork Case-Study: Rakhine State, Myanmar

I. Fieldwork Information:

Purpose and Objectives:

The Myanmar preliminary field work mission defines the geologic outcrop leg of this PhD research study with an aim to supplement the seismic findings of Ceduna Sub-Basin dataset for mobilized shale deformation mechanisms leading to salt-like 'diapiric forms', minibasins, and canopy structures during the growth of a Late Cretaceous submarine clastic delta times within the Rakhine State region of Myanmar we see today. The previous part of this PhD research was solely based on subsurface data (2D and 3D seismic lines), this section will be making a synthesis of field work examples and compare the findings to seismic observations, in order to better help constrain the condition and mechanisms responsible for a ductile, long-term mobilization of shales.

Based on the literature review and Google Earth satellite image investigation we have made, the Ramree Island / Cheduba region along the West Coast of Myanmar is a very promising area for the subject. There are numerous outcrops with shale mélangé including blocks of older and contemporaneous rocks.

Logistics:

The geologic fieldwork mission of Rakhine State Myanmar took place in November, 2018, with three participants from French Universities; with the geologic field trip leader Prof. Dr. Jean-Paul Callot (LFCR, UPPA), PhD student Gulce Dinc (University of Pau - UPPA / Total E&P), and secondary geologic field trip advisor Prof. Dr. Francis Odonne (GET, University of Toulouse) in 8 days. The organization of the whole field mission was conducted by Dr. Saw Mu Tha Lay Paw (PhD, Geologist, consultant for university field trips and expert on missions for oil companies) and Win Htet, (BSc, Geologist, logistician for field trips). During this period, two PhD candidates of Sedimentology Major (Ayemyat Maw and Phyo Phyo) from Yangon University, Myanmar, have attended the mission and benefited the visited sites of this fieldwork for their own PhDs subjects. A medical doctor (Dr. Kong) was present at all times with the group in order

to avoid any medical complication that might arise. A domestic flight (from Yangon to Ngapali – Thandwe), and two 4x4 field cars were utilised during the course of the mission. Accommodations were arranged either in hotels or resorts located within the close vicinity of visited geo-locations.

The fieldwork mission accomplished successfully while complying with all security protocols and advised HSE requirements. The major drawbacks are noted to be; (i) the quality and quantity of exposable outcrops due to the vegetation cover, (ii) potential risks associated to driving on the road (mainly at dusk time), and the time spent accessing to the geologic spots/overnight accommodation places due to road conditions and traffic with an average speed of 30 km/h.

Overall, we have concluded that the field trips in this area are quite doable and safe to organise with welcoming people, easy logistics and potentially not-so-long driving times from accommodation places to the points of interest. Besides the monsoon period (during the dry season between mid-October to April) there are few accessibility problems related to excessive water and concerns about harmful insects (e.g. mosquitoes).

Remarks:

During this mission we focused on Myanmar, Rakhine State, Ramree – Cheduba Island region, where we observed sub-circular minibasin formations (supposedly of Oligocene Age) ‘floating’ within the Eocene turbidites described either as a tectonic clay-mélange or over-pressured clays reworking both the reworked elements of the mobilized flysch and the host rock. The following sections will be geologically describing the region, structurally defining the study area and detailing the fieldwork findings we have acquired.

II. Study Area: Rakhine State, Myanmar

Today, Myanmar is located on the northwestern part of the Southeast Asia, bounded to the west by India, Bangladesh, Andaman Sea, Bay of Bengal, and to the east by China, Laos, and Thailand. It consists of 7 administrative states. Rakhine State is located on the western coast, bordered by Chin State to the north, Magway Region, Bago Region and Ayeyarwady Region to the east, the Bay of Bengal to the west, and the Chittagong Division of Bangladesh to the northwest. The state is separated from central Burma by Arakan Mountains. It occupies an area of 36,762 sq km and its capital is Sittwe (Figure 160).

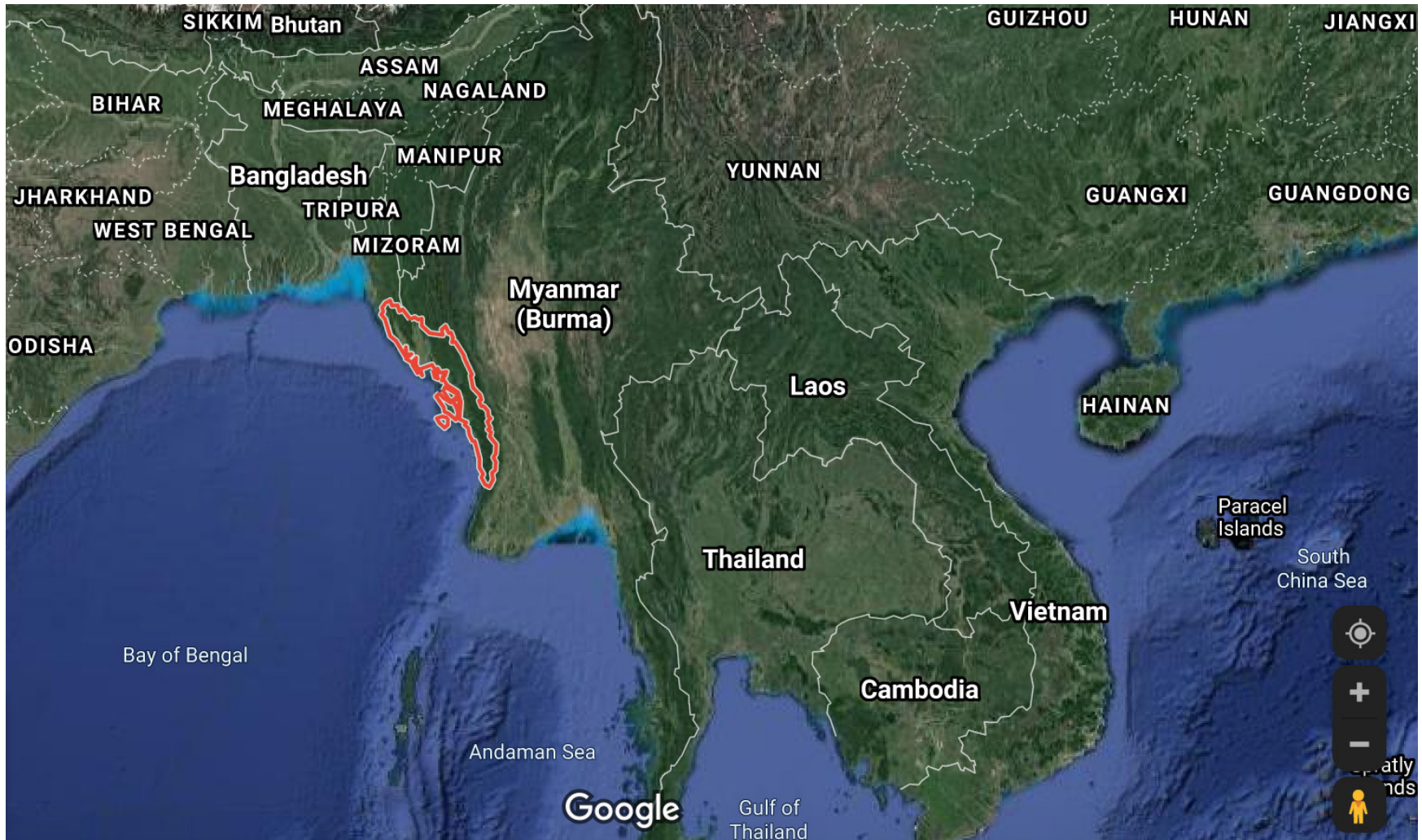


Figure 160: Google Map view of Rakhine State, Myanmar and the surrounding region. Study area is indicated with red geometrical closure (Image Courtesy of Google Earth, 2020).

III. Geological Setting and Geodynamic Context

Myanmar is located at the junction between two maritime and oceanic basins, the Andaman sea to the south and the Bay of Bengal to the west and northwest. The Andaman Sea Basin is located at the intersection of the India Plate, the Eurasian Plate and the Southeast Asian plates (Curry, 2005; Khan & Chakraborty, 2005; Raju et al. 2012; Rangin et al. 2013; Sautter et al. 2017). Deformation of the basin is probably controlled by (i) the oblique subduction of the Indian Plate to the NNE as well as (ii) the dextral strike-slip movement of Sagaing Fault (He & Zhou, 2018). This basin is known to undergone three tectonic deformation stages (Khan & Chakraborty, 2005; Morley, 2012; 2013; Xu et al. 2012), which are namely;

- Oblique extensional deformation stage during the Early Miocene – Late Miocene
- Rifting stage during the Miocene–Pliocene stage
- Post-Rift deposition stage

Present-day tectonic framework shows and describes the region under five composed domains: the accretionary wedge, the fore-arc depression, the volcanic island arc, the back-arc depression and the Shan Plateau (He et al. 2011; Zhu et al. 2012) (Figure 161).

Myanmar lies at the junction of Alpine-Himalayan Orogenic Belt and the Indonesian Island Arc System. The Indo-Myanmar Ranges (IMR) extend from the East Himalayan Syntaxis (EHS) southward along the eastern side of Bay of Bengal to the Andaman Sea comprising the Naga Hills Tract (North), the Chin Hills (middle) and the Rakhine Region (South). The Indo-Myanmar Ranges are developed along the western margin of the Myanmar microplate situated between the Eurasian and Indian Plate. It is considered to have formed as an accretionary wedge linked to the eastward subduction of thinned continental crust beneath the Bengal Basin under the West Myanmar Block. This region is shaped as a forearc sliver bounded to the west by a subduction zone/strike-slip margin, to the east by a strike-slip fault (the Sagaing Fault), south by a spreading center, and north by a compressional plate boundary. Most authors agree that the Myanmar region separated from Gondwana during Phanerozoic (541 Ma) (Khin et al., 2017; Zaw et al., 2017).

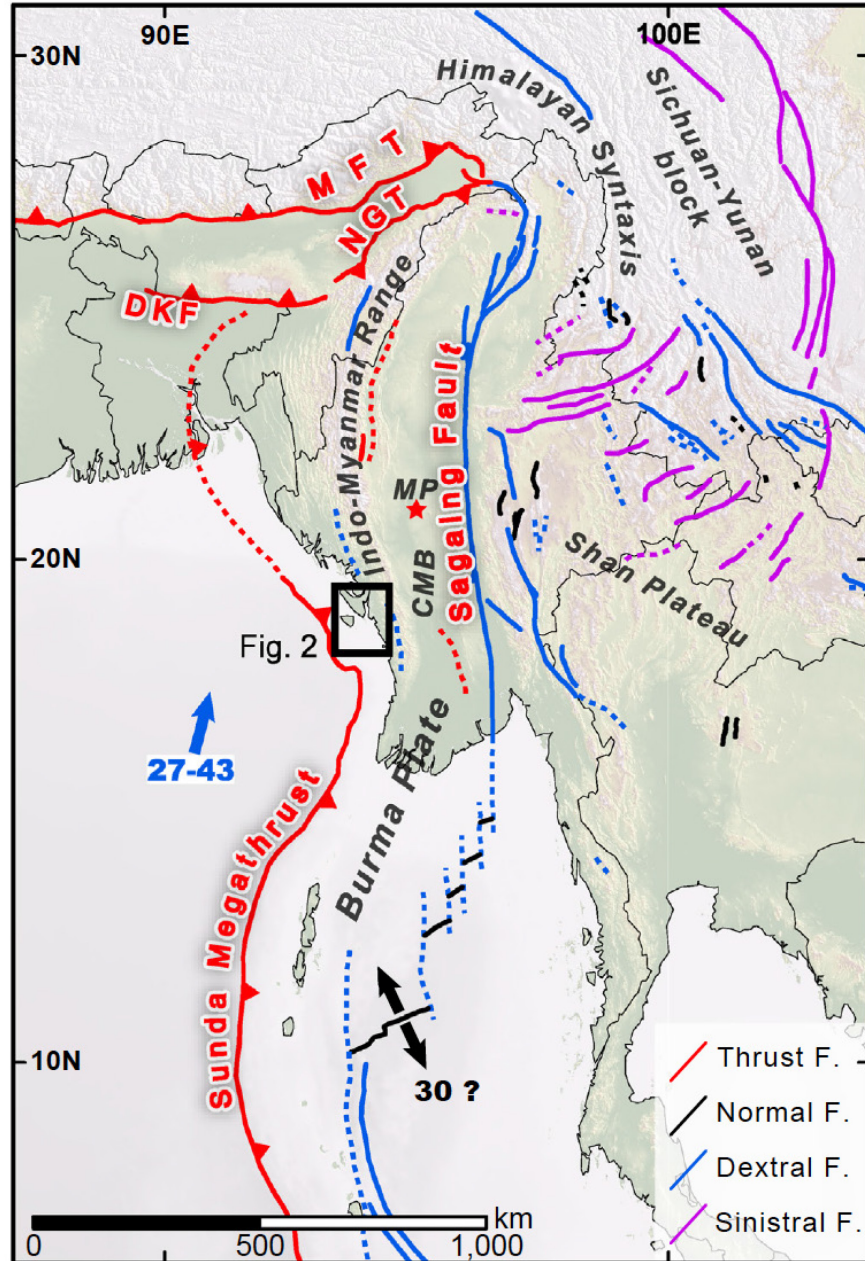


Figure 161: Regional tectonic map (modified from Wang et al., 2014) Blue arrow shows the direction of Indian plate motion relative to Sunda Plate (e.g. Socquet et al., 2006). The black arrows show the opening direction of the Central Andaman spreading center. Velocities are in mm/yr. Burma Plate (Curry et al., 1979) is bounded by the Sunda Mega Thrust; NGT = Naga Thrust; CMB: Central Myanmar Basin; MP: Mt. Pona (red star). Box shows location of the central coastal region (image retrieved from Moore et al., 2019).

Within this region, mud diapirs have been observed mainly in the belts of the accretionary wedge and the back-arc depression (e.g. Nielsen, Chamot-Rooke & Rangin, 2004; Zhu, Xie & Qiu, 2010). The accretionary wedge of the Andaman Sea Basin has a westward concaved boundary. Based on multibeam bathymetric data, different structural styles and shortening amounts have been noted in different segments of the accretionary wedge (He & Zhou, 2018), which may account for the development of several right-lateral strike-slip faults (Nielsen, Chamot-Rooke & Rangin, 2004). According to drilling results (Hu & Zhou, 2018);

1. The southern segment of the accretionary wedge composes of thin Miocene to Holocene strata, the lower part and the upper part of which consist of marine shale with intercalations of thin sand layers and littoral–neritic sand interbedded with shale, respectively.
2. The middle segment of the accretionary wedge consists of ≈ 7 km thick Eocene – upper Miocene sediments (Robinson et al. 2007; Zhu, Xie & Qiu, 2010; Cai et al. 2012).
3. The northern segment of the accretionary wedge consists of nearly 3,600 m thick Miocene sediments (Uddin & Lundberg, 2004). Generally, the accretionary wedge has relatively thin strata and low geothermal gradients.

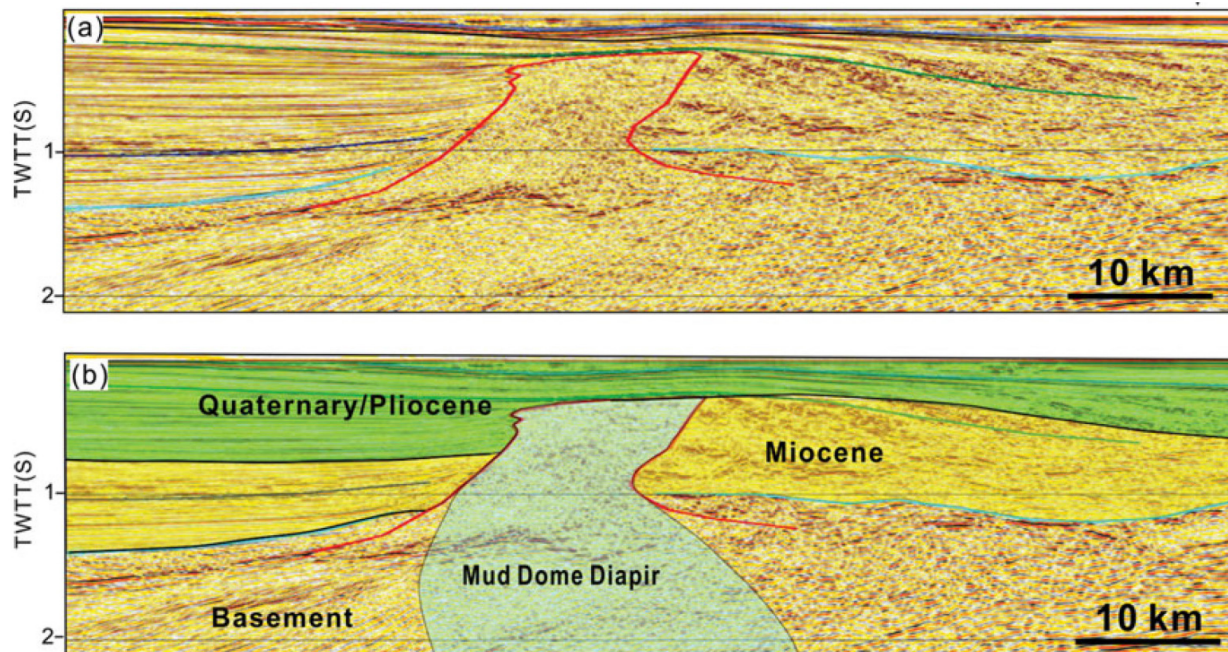


Figure 162: Mud dome diapir in the seismic profile across the northern segment of the accretionary wedge of the Andaman Sea Basin (see He & Zhu, 2018 for line location to the south of Ramree and Cheduba Islands) (image retrieved from He & Zhou, 2018).

As it is stated by Hu & Zhou (2018), the mud domes and mud volcanoes were found mainly in the northern segment of the accretionary wedge, which can be up to ≈ 8 km wide (Figure 162), wider than that of the turtleback mud diapirs in the southern segment. Based on the strata seen in Figure 162: on both sides of the mud dome diapirs are often distorted and show chaotic seismic reflections. Mud volcanoes were found mainly in the Ramree Lobe (Nielsen, Chamot-Rooke & Rangin, 2004). The structural sketch map of Western Myanmar (Figure 163) focuses on the western part of Myanmar with its structural elements and the two interpreted versions of the seismic lines seen on that sketch map are given in Figure 164 - Figure 165 with their shale tectonism related findings.

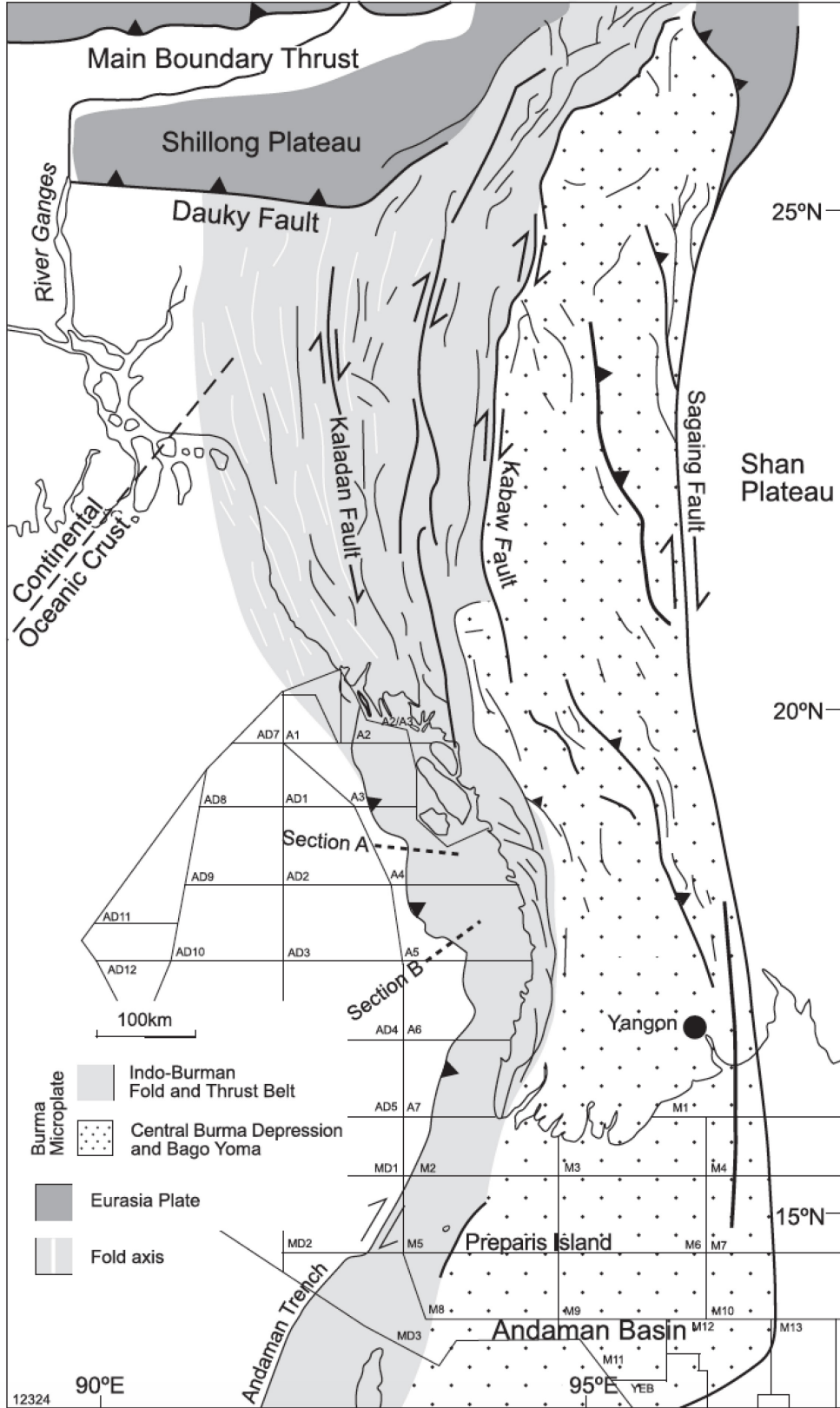


Figure 163: Structural sketch map of Western Myanmar showing the two seismic line locations (Section A and Section B) (modified from Morley et al., 2011) (image retrieved from Racey & Ridd, 2015).

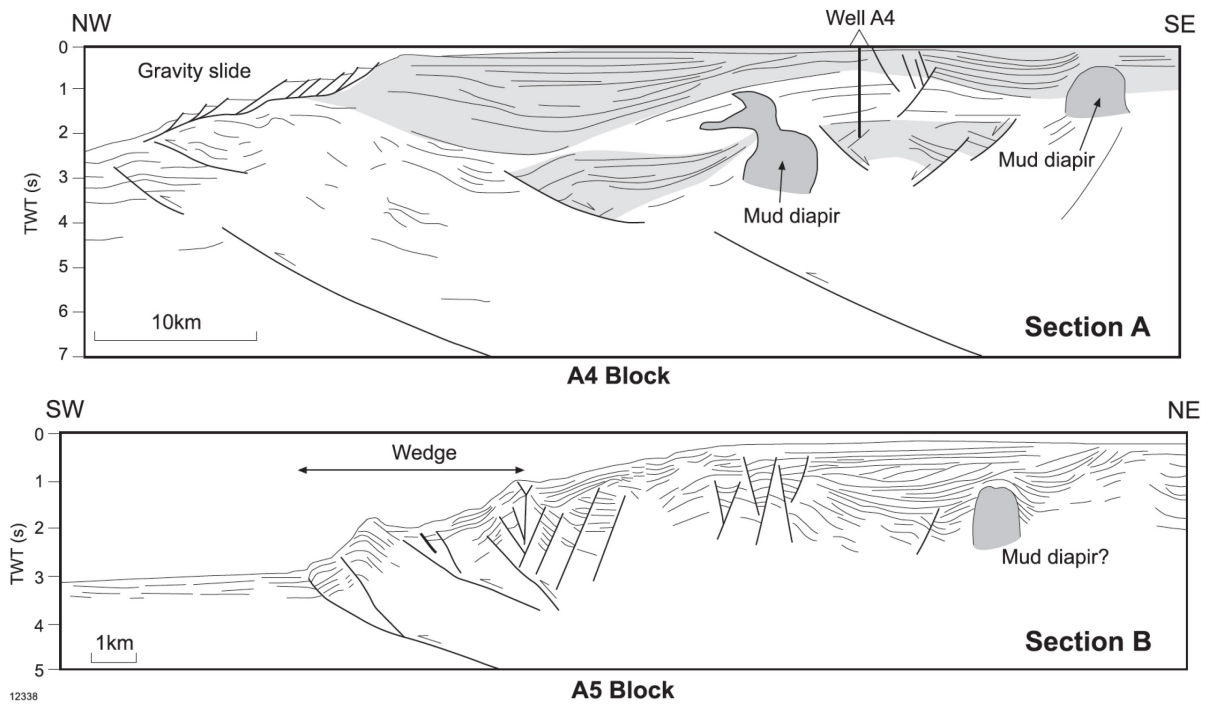


Figure 164: Representative cross-sections through offshore Rakhine blocks A4 (top) and A5 (bottom) (modified from Morley et al., 2011) (image retrieved from Racey & Ridd, 2015).

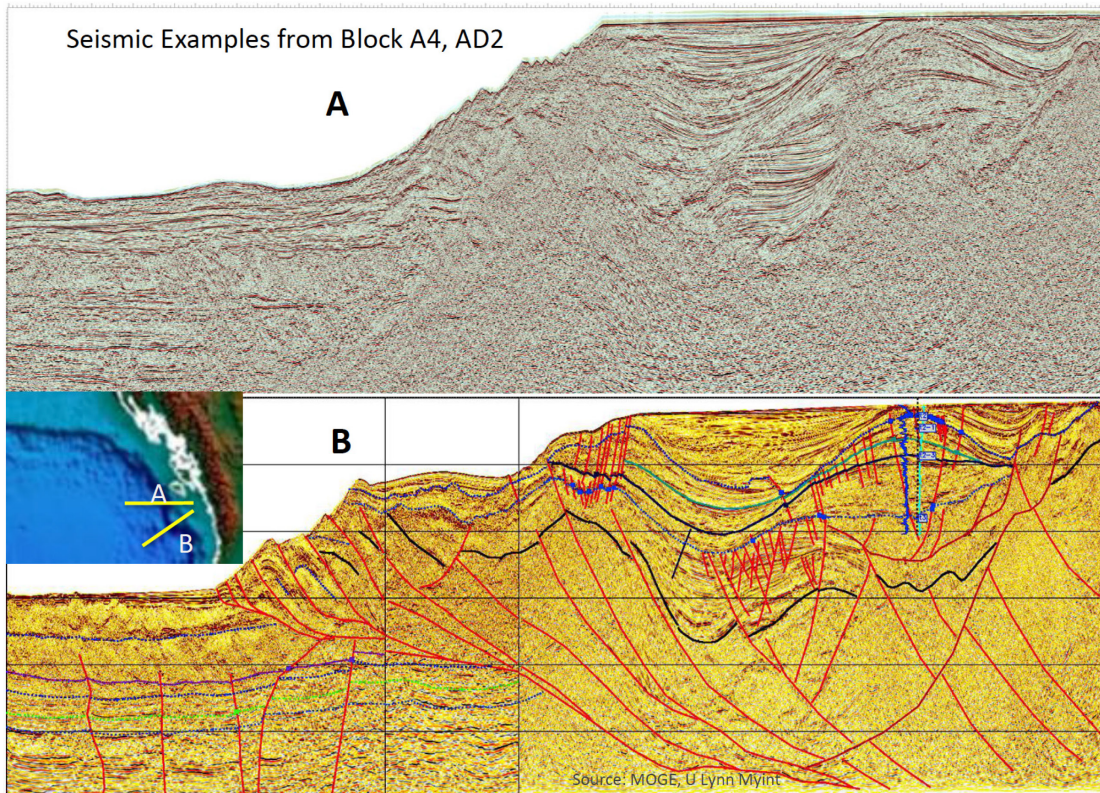


Figure 165: Rakhine Basin seismic examples (Courtesy of MOGI, U Lynn Myint) (image retrieved from Cliff & Carter, 2016) Note the very nice turtle-back-like depo center inverted and located on the right hand side of seismic line A, which is similarly imaged on seismic line B.

IV. Coastal Region of the Rakhine State, Western Myanmar: Ramree and Cheduba Islands

The study of Moore et al. (2019) describes the western margin of Myanmar, the Rakhine Coast as a region of offshore islands with *exposures of chaotic rock terranes along wave-cut terraces that allow characteristics of tectonic, sedimentary and diapiric mélanges to be recognized*. The tectonic collage composes of Cretaceous-Neogene turbidites with blocks of gabbro, pillow basalt, serpentinite, banded chert, limestone and schist (Brunnschweiler, 1966; Bender, 1983; Mitchell, 1993; Pivnik et al., 1998; Acharyya, 2007; Maurin and Rangin, 2009) and the mélange found within is said to include fragments of Cretaceous ophiolites that are in touch with Eocene turbidite units, while the turbidites accommodate sheared shale-rich beds of soft-sediment deformation interlayered between thick and undeformed sandy beds, all of which, are defined as *mass transport deposits (MTDs)*.

The same paper suggests that these MTDs are most likely to be *formed during deposition of the initial detritus of the Himalayan orogenic zone, probably trench slope basins on the accretionary prism*. Based on their study, the diapiric mélanges are formed by the fragments of units carried upwards via the active mud volcanoes intruding towards the exhumed ophiolitic and turbiditic thrust slices. Their distinction documents the structure of (1) tectonic mélanges as *'shear zones with incorporated fragments of Cretaceous ophiolitic lithologies'*, (2) sedimentary broken formations -ondolistostromes- as *'mass transport deposits (MTDs) within folded, but not sheared, Eocene/Oligocene turbidite sequences'*, and (3) diapiric mélanges as *'deposits of active mud volcanoes (MVs) that carry fragments of older rock units from depths of a few km'*.

In a chronological order, the oldest exposed rocks of Coastal Rakhine are ophiolitic fragments with tectonized serpentinite bodies, pillow lavas and Upper Cretaceous radiolarian chert (Bannert et al., 1978; Bannert et al., 2011), while the main exposure is found to be the Eocene-to-Oligocene turbiditic deposits of the 'Indoburman Flysch' as exposed along the wave-cut coastal terraces (e.g., Swe and Tun, 2008) (Moore et al., 2019). Miocene conglomerates and shallow-water sandstones of Ramree and Cheduba Islands (Bannert et al., 2011) overlain this deepwater siliciclastic unit represents a detritus derived mainly from the Myanmar arc to the east (e.g., Allen et al., 2008b). As the Indo-Myanmar wedge folding takes place from Middle-to-Late Miocene, Oligocene and older stratal units dip steeply (N70°; Bannert et al., 1978), with a deformation pattern carrying on into the recent sediments (Nielsen et al., 2004; Maurin and Rangin, 2009; Morley et al., 2011; Rangin, 2017 in Moore et al., 2019).

Moore et al. (2019) defines the terms used in their research and analysis as follows;

[Mélange (e.g., Silver and Beutner, 1980; Cowan, 1985; Wakabayashi and Dilek, 2011): chaotic rock bodies, mappable at 1:25,000 or smaller scale, of mixed blocks composed of exotic (with respect to the lithostratigraphic unit of the matrix and/or its depositional environment) and native rocks in a pervasively deformed matrix]

[Broken Formation (e.g., Hsu, 1968): chaotic rock units in which blocks are only of native nature with respect to the matrix (i.e., not exotic, but of the same original lithostratigraphic unit or depositional environment; see also "broken" and "dismembered units", described by Raymond, 1984)]

(1) Tectonic Mélanges (Shear Zones)

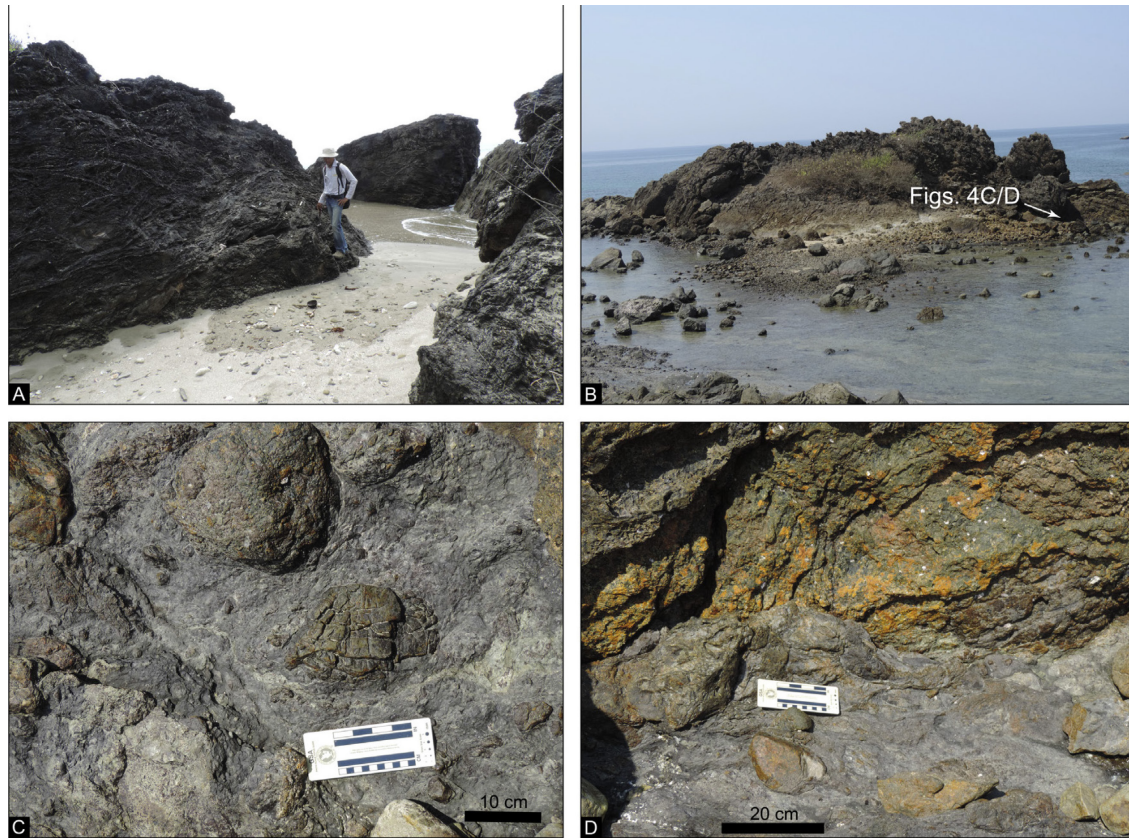


Figure 166: Outcrop photos of sheared serpentinite. (A) Large randomly-oriented blocks cut by veins, exposed on SW coast of Cheduba Island. (B) Large block with shear zone at base exposed at Mazin Point. (C and D) Closeup of the base of the large block pictured in (B) showing smaller serpentinite phacoids surrounded by sheared serpentinite matrix; the phacoids are similar in appearance to the adjacent parts of the large block (image retrieved from Moore et al., 2019).

As it is stated by Moore et al. (2019);

- Although contact relationships between the serpentinite bodies and adjacent rocks are generally difficult to discern, shear zones are characterized by phacoids of peridotite intersheared with clays that are similar to those of the adjacent outcrop of sedimentary rocks.
- The peridotite blocks are highly serpentinitized and sheared, but there is no indication of high pressure or temperature metamorphism. In most localities they are cut by quartz and magnesium carbonate veins.
- Petrographic inspection in hand specimen, thin section and electron microprobe showed in-situ replacement textures consistent with an advanced level of listwanite formation: a low-temperature reactive transformation of an ultramafic protolith into a quartz-carbonate assemblage (e.g., Robinson et al., 2005).
- In several of the collected samples, the only indicators of the ultramafic origin are abundant and chemically well-preserved chromian spinels. Within-sample chemical heterogeneity of the spinels, which are inert to the pervasive listwanite-forming reactions by low-temperature carbonate-rich fluids, indicate that mechanical mixing signature of a range of peridotite protoliths is preserved, possibly within a mélangé-forming shear zone (Hellebrand et al., in prep).

- In many localities, the shear zones are cut by carbonate veins. Analyses of carbon and oxygen isotopes on four samples of veins show $\delta^{13}\text{C}$ values (relative to PeeDee Belemnite (PDB)) that range from -9.8‰ to -7.2‰ , indicative of input of carbon from thermal maturation of organic matter. The range of $\delta^{18}\text{O}$ values from -12.2‰ to -5.9‰ (PDB) is large, and there is no correlation between C and O isotopes. These results suggest mixing between fluids with variable components of light and heavy C and O.

(2) Sedimentary Broken Formations (Mass Transport Deposits -MTDs-; Endolistostromes)

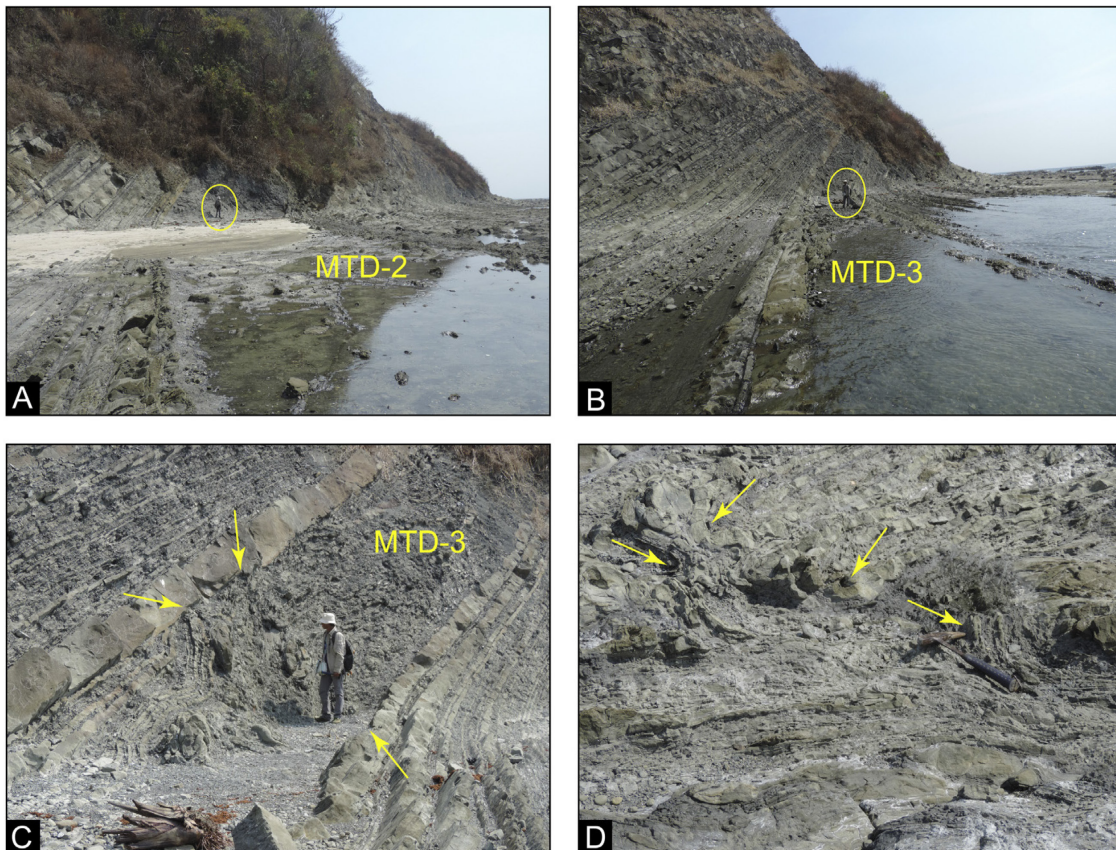


Figure 167: Outcrop photos of steeply- to vertically-dipping turbidite units with interbedded MTDs 2 and 3 (yellow circle = 1.7 m geologist for scale). (A) MTD-2 with thick undeformed sandstone beds above. (B) MTD-3 with undeformed sandy turbidite beds above and below. (C) Detail of MTD-3 showing internal deformation and relationships with overlying and underlying sandstone beds. Yellow arrows show local erosive contacts. (D) Chaotic internal structure of MTD-3; yellow arrows point to folded strata (image retrieved from Moore et al., 2019).

As it is stated by Moore et al. (2019);

- Morley (2014) described an outcrop within the coastal section of Eocene deep-water sediments at Ngapali Beach. The Eocene section at Ngapali is N300 m thick and is well exposed along an extensive wave cut platform (Morley, 2014; Fig. 7). Bedding strike ranges from NE to NNW with westerly dips of $60\text{--}85^\circ$.
- The deposits are interpreted as turbidite lobes deposited in a middle to outer fan setting, with channelized turbidites suggesting a more inner fan setting occurring only at the top of the section. Morley (2014), describes deformation of the section that he interprets as being initially triggered by loading during deposition, further suggesting that the sandstones involved in the deformation

lay within a few meters of the seafloor or were actually being deposited during deformation, hence were unlithified and water-rich at the time of deformation. Many of the turbidite beds on the extensive wave cut platform show classic sedimentary load structures, including sandstone injections into overlying beds.

- Numerous localized sedimentary (gravitational) chaotic rock units without exotic blocks (i.e., sedimentary broken formation or endolistostromes or sedimentary complexes, see Festa et al., 2019 for details), which represent ancient mass-transport deposits (MTDs) are present in the Eocene section.
- They range in size from thin slumped shales a few meters thick, to major complexes 100+ m thick. These MTDs are “sandwiched” between thick, undeformed sandstone beds. Within the MTDs, slump folds display truncation of their hinges and limbs.
- The shale beds are locally sheared, and the sandier inter-beds are folded, overturned, and boudinaged. Pinch-and-swell structures are common. Locally there are erosive contacts at the tops and bases of the slump beds, indicating that the MTDs were exposed at the seafloor.
- Clastic dikes occur within thick sandy beds attesting to the local overpressures. Minor thrusts and folds are highly irregular in orientation and do not cut up-section, indicating that they formed prior to the later compressional deformation that generated the near-vertical regional dips.
- The MTDs are only developed within specific horizons, while intervening beds between the MTDs remain undeformed, suggesting that the MTDs are the result of soft-sediment deformation (SSD; Alsop et al., 2017c).

(3) Diapiric Mélanges (Mud Volcanoes)

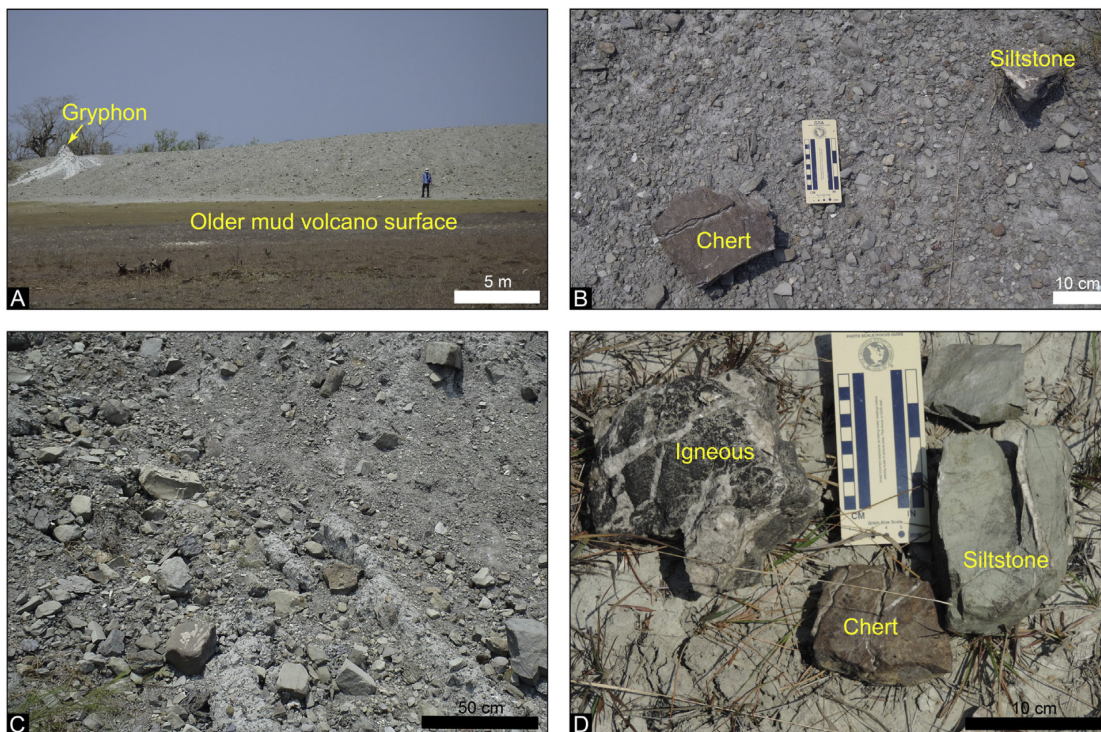


Figure 168: Outcrop photos of mud volcanoes. (A) Side view of young MV that formed on top of an older mud volcano surface. Gryphon is an active mud vent. (B) Photo of surface of active mud volcano showing variation in size of fragments exposed on the surface. Note angular chert fragment. (C) Exposure of deeper part of MV along stream cut. Note random orientation of clasts and lack of fabric. (D) Clasts on surface of the MV. Note that clasts are subrounded (image retrieved from Moore et al., 2019).

As it is stated by Moore et al. (2019);

- Most of the mud volcanoes (MV) are actively emitting mud through 10–20 m-wide “pancake” vents (Fig. 12) or 1–3 m high mud cones, also known as “gryphons” (Mazzini and Etiope, 2017).
- Some of them are essentially continually erupting (at least for the times of our visits in 2013,4,5), while others are dormant.
- Gas samples collected from the MVs on Ramree Island are 99.3–100% methane with a $\delta^{13}\text{C}$ of -45.6‰ to -48.1‰ , indicating a thermogenic origin (Racey and Ridd, 2015). These MVs are very similar to those described on the Amdaman Islands, south of Myanmar (Ray et al., 2013; Bandopadhyay and Carter, 2017).
- Preliminary geochemical analyses of the MV fluids using boron (B) and lithium (Li) isotope geochemistry provide some constraints on their depth of origin. The mud is enriched in B relative to seawater, indicating a contribution from release of B at depth, which was previously adsorbed to clayminerals (Kopf and Deyhle, 2002).
- Lithium is also enriched relative to sea water, and Li isotope ratios are less than seawater. Enriched Li isotope values between 16 and 30‰ suggest mobilization from a several kilometer-deep source and agree with results from other cold seeps and MVs in other subduction environments (Scholz et al., 2010; Saffer and Kopf, 2016).
- The clasts range from sand-sized grains to blocks up to 50 cm in length. The dominant lithologies are well indurated turbiditic sandstones and siltstones, but clasts of chert and basic igneous rocks are also present
- Bannert et al. (1978) report that mud samples from the MVs contain fossils from the underlying Eocene and Oligocene “flysch” sediments.
- Vitrinite reflectance measurements on nine samples of Eocene-Oligocene sandstone clasts collected from the MVs using the methods of Fukuchi et al. (2017). Five samples produced reliable mean values of 0.66–1.77 R₀.

Summarizing Remarks on Western Myanmar by Moore et al. (2019)

As a conclusion, Moore et al. (2019) defined the Western Myanmar coast with *tectonic shear zones* containing exotic (ophiolitic) blocks in a strong shear fabric (tectonic *mélanges* as they call them). Since they detected no associated exotic blocks adjacent to the shear zones with diminishing degree of shear fabric, they called these areas as (tectonic) broken formations. The MTDs that have resulted from soft-sediment deformation and formed between thick sandstone beds are called as sedimentary broken formations (endolistostromes) within the Paleogene sedimentary units, where no major shear deformation took place away from the ophiolitic shear zones. Young mud volcano deposits are found to carry small exotic clasts exhibiting no such consistent orientation or certain shear fabric pattern and therefore recognized as diapiric *mélanges*.

Following the literature review of the area given above, the next sections of this thesis chapter will be giving a compilation of the fieldwork observations taken under this PhD research project (November, 2018) with an aim to propose our preliminary outcrop investigation around the Ramree Island, located within the Rakhine State of Myanmar.

V. Visited Sights: Minibasin Formations and Mud Volcanoes

Despite poor outcrop conditions and the vegetation cover limiting access to these outcrop sites, during 64 samples have been collected. Figure 169 shows the spatial distribution of the spotted outcrops, plus three other spots located further south and visited on the way back to Yangon.

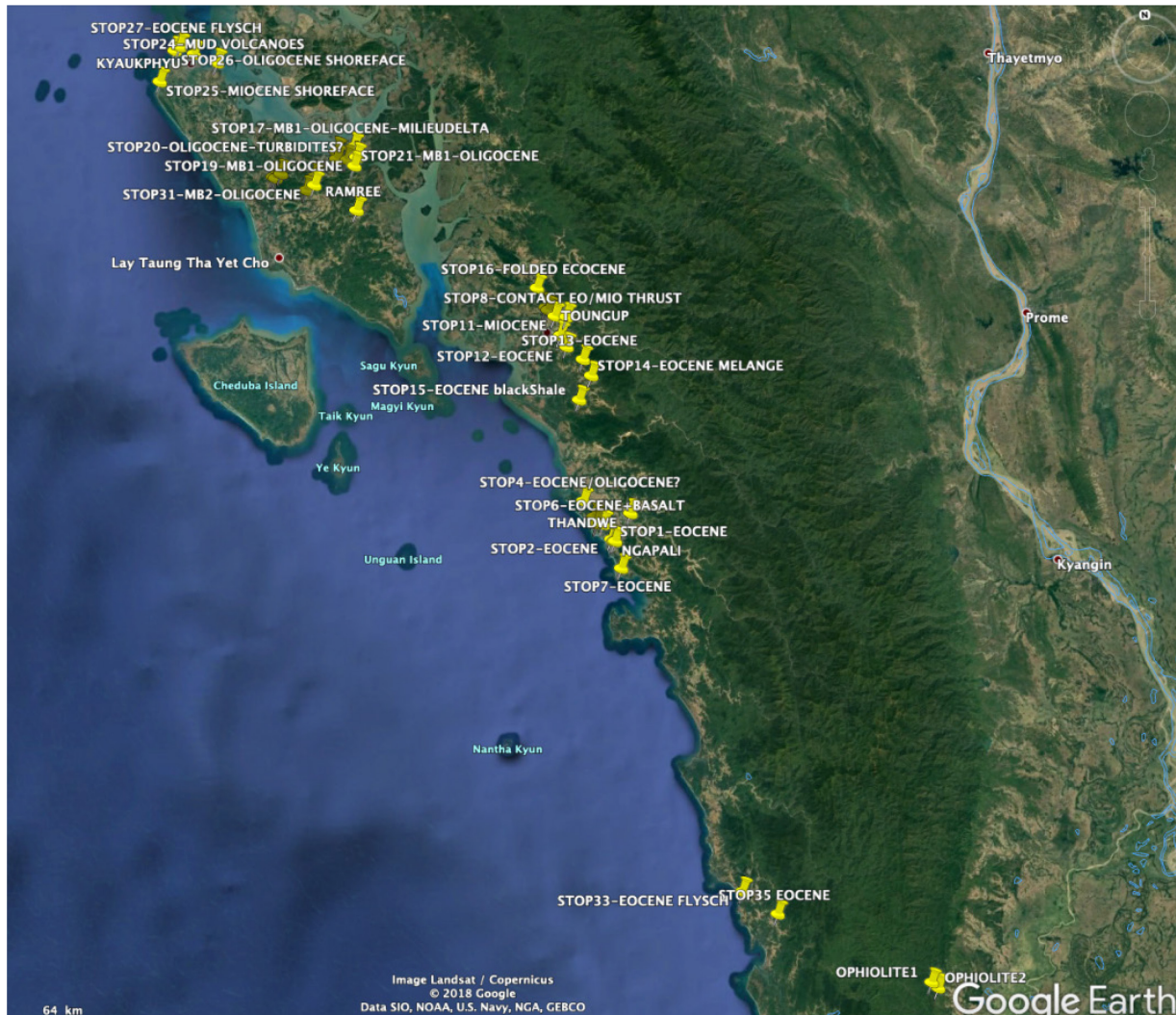


Figure 169: Location map of visited sites during the fieldwork (Image Courtesy of Google Earth).

These visited sites included;

1. Ngapali shoreline with Eocene successions and major debris flows (Figure 170) and the road from Ngapali to Toungup with Eocene Age black shales (Figure 171)
2. Central Ramree Island with Oligocene Age minibasin formations (Figure 172-Figure 173)
3. Kyaukphyu (Northern Ramree Island) with Mud Volcanoes (Figure 174) and Eocene-to-Miocene formations cropping out at low tide (Figure 175)



Figure 170: Visited sites of Ngapali along the shoreline (image courtesy of Google Earth).



Figure 171: Visited sites of Ngapali - Toungup Road (image courtesy of Google Earth).



Figure 172: Central Ramree minibasin formation with visit site/sampling locations (image courtesy of Google Earth).

The Central Ramree area stratigraphic column of Figure 173 (Maurin & Rangin, 2009) shows:

- A: Turbidites in perched circular synclines overlooking a peneplain more or less at sea level where a melange is cropping out. The turbidites in the synclines are dated Oligocene–early Miocene on foraminifera (sample MY06/97 (N9° 11.810' N; 93° 49.583' E) that contains Oligocene or early Miocene planktons).
- B: A large block (over 100 m) of nummulite-rich bioclastic limestone.
- C: Below and between them, in the melange, common veins with no preferential orientations and hydrofractured boulders.
- D: Turbidites that could be lateral equivalent of the black shaly matrix.
- E: Sandstone and shale possibly belonging to the Triassic Halobia sandstone to Chattian on foraminifera (sample MY06/112 (19° 05.25' N; 94° 11.247' E) that contains *Reticulofenestra bisecta* and *Cyclicargolithus floridanus*).
- F: Polymictic conglomerates with quartz and cherts.
- G: The formation cropping out in the peneplain, along the sea in Ramree, and to the south in Sandoway, is a melange made of a black shaly matrix in which most of the rocks forming the core of the Arakan Range are observed as olistoliths: pillow lava.

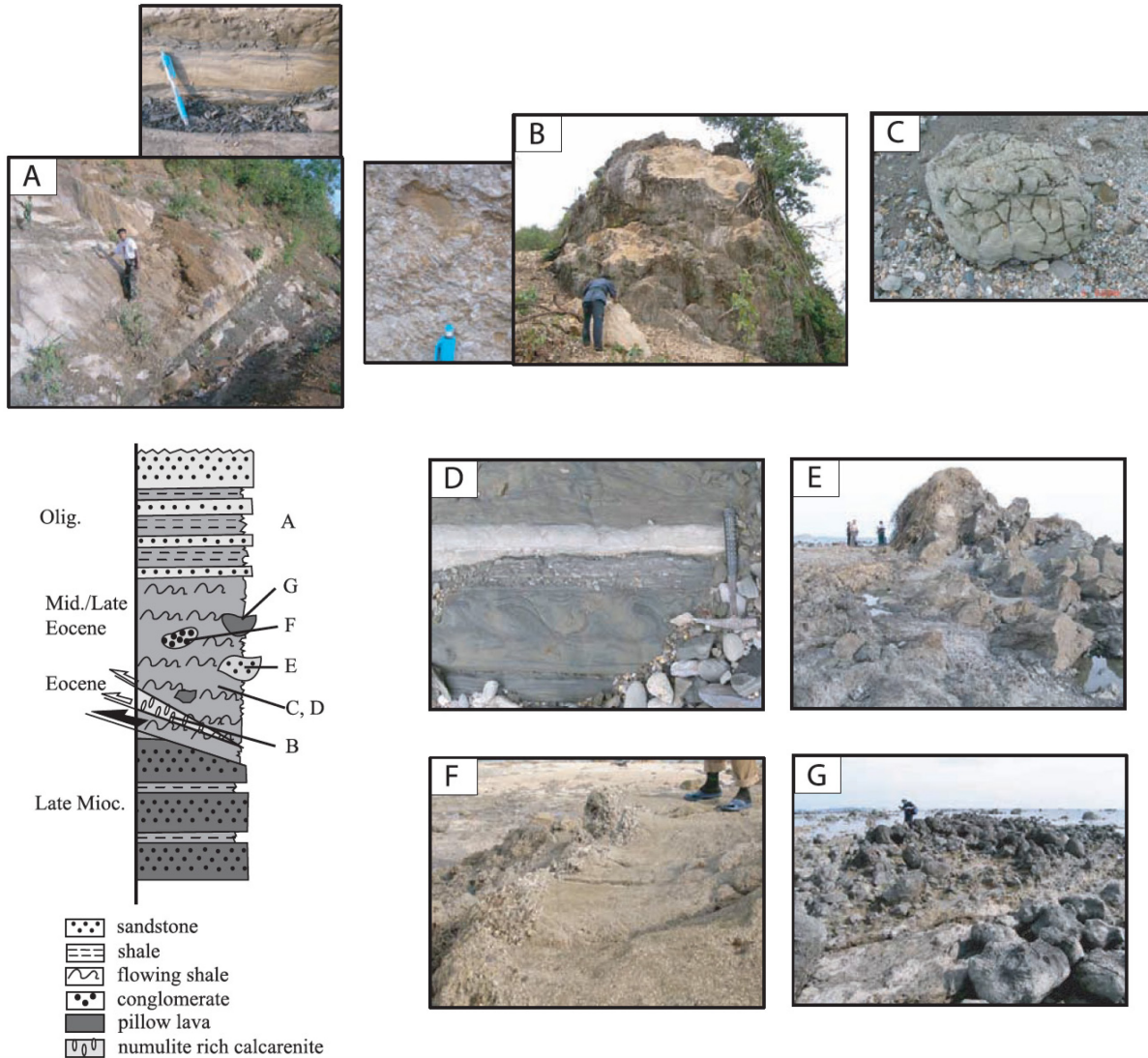


Figure 173: Approximate stratigraphic column of central Ramree area and pictures illustrating these various stratigraphic units (image retrieved from Maurin & Rangin, 2009).



Figure 174: Northern Ramree Island Mud Volcano Site, Rakhine State, Myanmar.



Figure 175: Northern Ramree island visit site/sampling locations (image courtesy of Google Earth).

VI. Lithologic Facies and Stratigraphic Information

The following sections will be detailing the observed lithological facies and stratigraphic intervals of visited fieldwork sites in Rakhine Basin, Myanmar.

A. Eocene

Eocene deposits of Ramree-Cheduba Island region are mainly formed of flysch sequences. They appear to be originated mostly of deep turbidite fan facies in the northern Ramree domain, and potentially more proximal in the Ngapali area, where larger beds and coarser sands (with wood fragments) are present. Sandstone facies consist of moderate-to-poorly consolidated sequences, hence they suggest a moderate burial. A generally bed-perpendicular with orthogonal sets and shortening parallel sets of fracturation is recognized within the sequence, suggesting both an inheritance from compaction, and superimposition of the deformation stages.

In the Ngapali area, three major debris flows are recognized (Figure 176). The thickest of which appear to be ~50 m thick at minimum. They generally contain mostly brecciated elements from the host rock itself (i.e. Eocene turbidites) but they also display quite a complete sampling section of the belt rocks such as limestones (mostly of Jurassic-Cretaceous Age), basalts, and ophiolite blocks indicating a large reworking of Arakan Belt core and suture zone.



Figure 176: Debris flow observed at Southern Ngapali shoreline (~ 15m thick) (Stop 1).

In the Central Ramree region, Eocene facies only outcrop as *black shale melange* containing the same spectra of exotic blocks. While not all outcrops reveal these shales significantly, some large exotic blocks display well-preserved outcrops (Figure 177).



Figure 177: Eocene Age black shale mélangé sighted at Central Ramree (Stop 14).

In several places the same Eocene flysch shows nice evidence of the shortening at the origin of the Arakan shale belt (Figure 178). At these locations, it is possible to locally and properly find the organisation of fold train, their spatial orientation and associated decollement level.

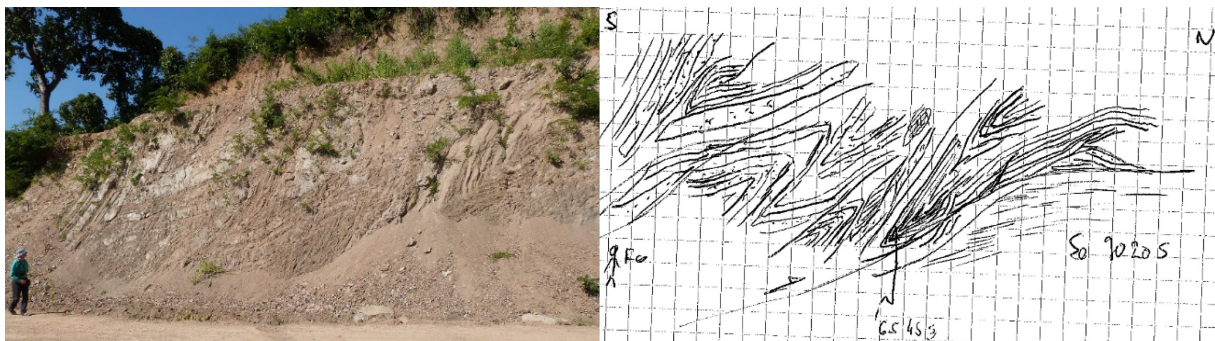


Figure 178: Strongly folded flysch formation in backthrust position (NE to the right of the right side of the picture (Stop 16).

There are evidences of mobile shale level deformation such as development of a diffuse foliation and S/C like bands, sigmoidal lenses, and crenulation folding as it is seen in Figure 179.

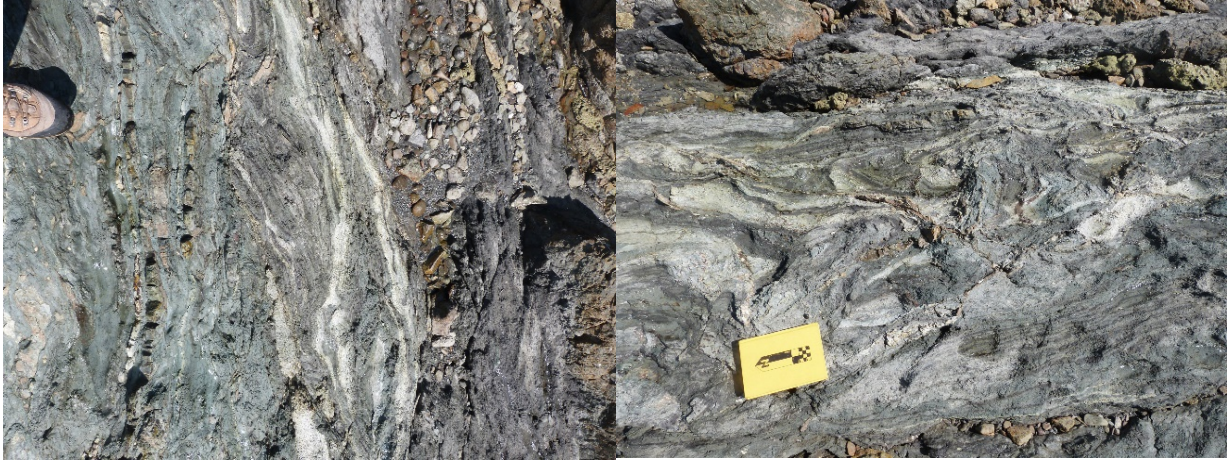


Figure 179: Left hand-side figure: Foliated shales with incipient S/C bands. Right hand-side figure: Recumbent folding of sandy levels (Stop 4).

In the northern section of Ramree island, the Eocene flysch belt display spectacular internal structure within the sand levels of the regularly alternating sand and clays (Figure 180), which can be related to a specific current pattern, some of which are typically related to reflection of current patterns in small closed basins (e.g. the Marmara Sea). The size and geometry of an Eocene flysch basin can be seen in Figure 181.



Figure 180: Left hand-side figure: Alternating sand and clay sequences within the Eocene Flysch Belt of Northern Ramree. Right hand-side figure: 35cm sand body displaying the internal structure of a sand sequence with a complex dynamic emplacement.

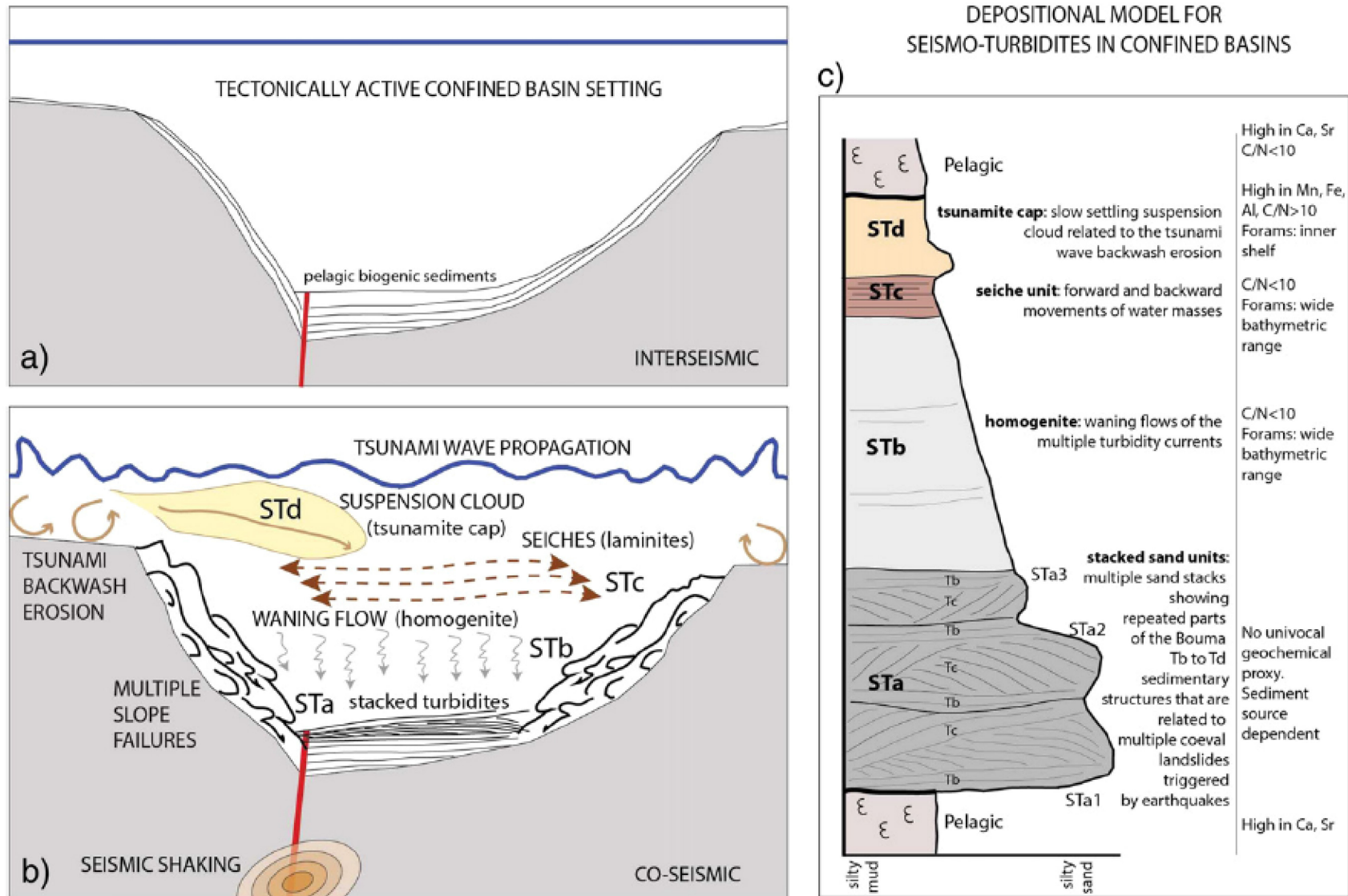


Figure 181: Example of an interpretative model and its representative log showing the seismo-turbidites from Calabrian Sea (image retrieved from Polonia et al., 2017).

B. Oligocene

Oligocene rocks are recognized in the Ramree Island. Along the shoreline, these formations crop out as elongated thick sand bars, with mega dunes, large trough cross bedding, stacked and formed in a long and narrow topographic ridge in present day (Figure 182). The sequences of this sandstone formation suggest a stacked system of sand bars in littoral, shoreface facies, probably dominated by waves and currents, while the sandstone examples of northern Ramree Island are clearly poorly consolidated with low burial signatures.



Figure 182: Left hand-side figure: Along-strike view of a littoral sand bar. Right hand-side figure: Large-scale channel-like structures.

However, the Oligocene deposits recognized within the minibasin formations [depo-centric forms of deposition accumulated above a thick shale layer], are quite different as they form organized sequence of alternating sandstone and clay facies, clearly coarsening and thickening upward with few flute casts and horizontal bio-turbations, while in some places organized in tractive features such as dunes, 2D ripples, and through cross-beddings. Altogether, these observations suggest a deltaic sequence (Figure 183). In the NE domain of the eastern minibasin, the top part of the first organized sequence shows rubified clays in between the sand levels of probable paleo-soils (Figure 183), which evidence a top delta domain. The organization of the minibasin topography, that is separated from its surroundings with a bowl-like depositional pattern, seems to be controlled by stacking deltaic sequence, with levels of alternating clay/sandstone sequences capped by thick sands forming a structural surface on one side (Figure 184) and thinner less decomposed sequences (potentially bottom sets and pro-delta clays) on the other side. The age of these deposits is Oligocene as they are confirmed by micro-fauna (see the PhD of T. Maurin, 2009).



Figure 183: Left hand-side figure: Delta-like alternanc of sand and clay with 3D ripples and through cross-beds (Stop 19). Right hand-side figure: Oligocene Age potential paleo-soil in the upper part of an alternating sand-clay level (Stop 18).



Figure 184: N directed view of the second main sequence of the minibasin showing the major sandy levels capping the deltaic sequence.

C. Miocene

Miocene Age sands are visited only along the NW coast of the Ramree island, where they present alternating sandstones and silt/clay levels, with large through cross-bedding, and channels in the sand bars, suggesting a shore-face system reworking through currents with the inputs, in a more distal setting than the Oligocene level.

IV. Field Observations: Mobile Shale Evidences

The following sections will be detailing the shale mobilization patterns/forms observed during the Rakhine State fieldwork in Myanmar.

i. Debris Flow and Mass Transport Complexes (MTCs)

The debris flow formations of the Ramree Island crop out quite well, which makes it possible to have a detailed analysis of the foliation within the shale strata (at low tide). The visited sites clearly show a bed-like organization; bed-parallel for Stops 1, 2, 5, where a flattening fabric seems to dominate, with large obliquity (Figure 185). At Stop 4, where the foliation dips at 50° with respect to bedding and becomes parallel to the cover beds at the top of the debris flow, suggests a quite early mobilization of the clays associated to the deposition of sandy level on top (Figure 186).

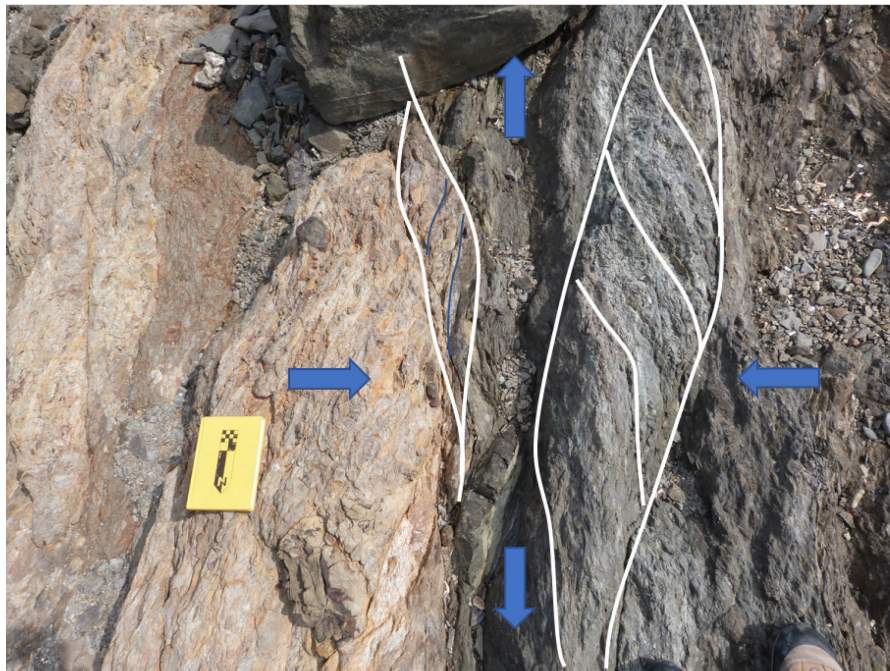


Figure 185: Flattening fabric within the clay debris flow. Two directions of shear are observed (Top South and Top North) with respect to the vertical bedding. This formation is observed on a 5m thick upper contact of flow with a clear alteration of clay mélangé (Stop 5).



Figure 186: Steep foliation within the major debris flow turning parallel to bedding below the upper limit of the debris flow (Stop 4).

ii. Exotic Blocks

The mobilized clay level shows a wide range of scale and origin of the mobile blocks from cm to decameters, including limestones, ophiolites, sandstones and basalts, which points out to existence of rock formations with great variance added into the mobile clay matrix (Figure 187).



Figure 187: Example of mobilized block in the *mélange*. Left hand-side figure: An ophiolite block in a flattening fabric. Right hand-side figure: Pebbles and cuttings floating within the clay matrix (cm scale).

iii. Cover Deformation

The top of the major debris flow crops out in some locations (Stop 1-2-4-5), which allows to evidence the style and timing of deformation of the earliest beds deposited within the *mélange*. It appears that the alternating sand/clay deposits show a likely soft-sediment related deformation pattern with (i) a change in thickness associated to faults, (ii) escape fluid features associated to faulting, (iii) dip changes with depth, and (iv) flattened layers on top of deformed basal ones. Thus, it suggests us that the clay mobility was active at shallow depth with small loads, precluding an over-pressurization mechanism, but also a quite slow movement and distribution in order to allow for a sedimentary record. Associated with this syn-sedimentary character, we also noted that in most of the cases, the deformation recorded an (early) radial or distributed extension, suggesting a spreading pattern under its own load/weight (Figure 188).



Figure 188: Syn-sedimentary gravitational spreading/gliding on top of the debris flow (Stop 4).

iv. Minibasins

Geometry

The two major minibasins (spectacularly visible at Satellite images) appear as sub-rounded bubble-like structures in the region and suggest a strong evidence for sinking into the clay *mélange* (Figure 189). They show asymmetric and sequentially organized pattern hinting at a deltaic origin of alternating sand-clay deposits. In particular, the thickness contrast from one side to the other, associated to the faciologic changes shows each of these basins consisting in a former clastic delta (Figure 189). Besides their distinct geometry with naturally variable dips with depth (from flat top-delta layers to basin-dipping fore-set and flat pro-delta shales), these minibasins show a 40° dip variation for 100 m at Stop 17 and 18. Decrease of this dip-angle is much greater than expected for a simple delta geometry. This observation points out to a delta setting, which was folded during the course of the sedimentation (differential loading) and therefore, the Eocene clay *mélange* or *flysch* were mobile close to surface during the deposition period of these Oligocene deltas.

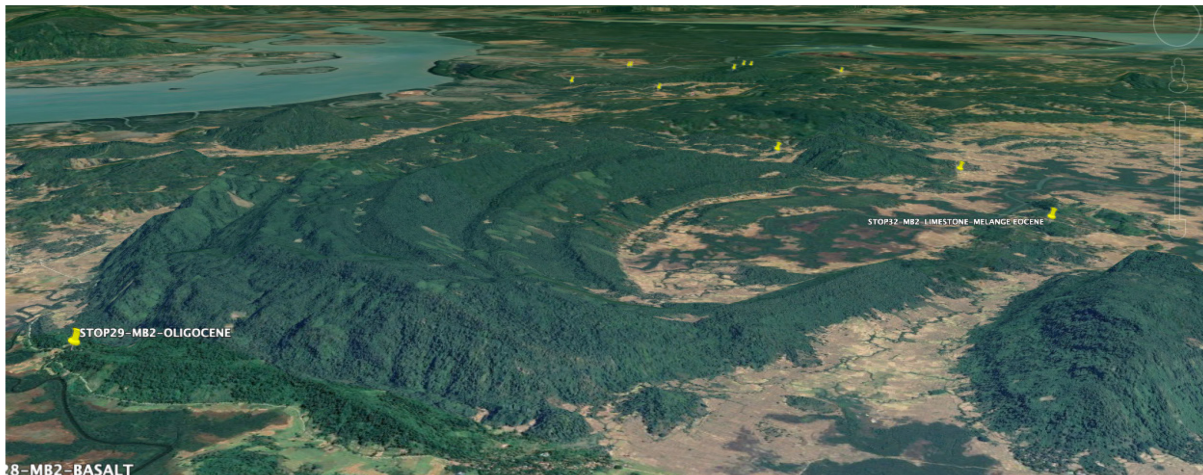


Figure 189: Satellite view of Minibasin 2 from East direction showing the sequential organization and geometry (Image Courtesy of Google Earth). Note the strong decrease of the basin thickness from left (NW) to right (SE) related to the deltaic geometry, which is much thinner from the delta foreset packages to the bottom set.

Potential Evolution and Origin of These Minibasins

In addition to these two major minibasin formations, several other ridges of the region also display comparable geometries possibly related to/originated from similar localized depo-centers. Their distribution are not randomly scattered in the area, they display a location-based orientation in the central Ramree region. Our idea is that, since the Burmese flysch fold belt is mostly fed by the Gange-Brahmaputre deltaic deposits, these minibasin formations were most likely originated/superimposed from a quasi-punctual local source, generating the differential loading plug [or at least from a much more concentrated space compared to the deep deltaic fan of Great Bight Basin, White Pointer Delta], during Eocene shale mobilization and minibasin forming era (Figure 190). A possible interpretation of such a local deltaic facies could come/originate from the paleo Irrawaddy River, joining to Sea of Bengal at the present-day locus of the Ramree-Cheduba domain, before being deflected to the South due to the growth of the Arakan Fold and Thrust Belt System.



Figure 190: Possible paleo-geographic path related to a northerly directed source of clastics super-imposed on Bengal / Bramahputre clastics forming minibasin-like depo-centers onto the mobile Eocene clays.

V. Mud Volcanoes

Description

There are two mud volcanoes spotted at the Ramree Island. The first one produces three edifices directed at NE, and a small apparatus one km further south (Figure 191). The second mud volcano is observed at the central Cheduba Island. The Ramree Island mud volcano, that we have investigated, consists of (i) an active griffon, (ii) a shield-like volcano with a ductile mud cake core and bubbling mud, and (iii) an older and drier shield volcano (Figure 192).



Figure 191: Ramree Island mud volcano satellite image, Rakhine State, Myanmar (Image Courtesy of Google Earth).



Figure 192: Ramree Island mud volcano, Rakhine State, Myanmar.

Suspected Origin

The Eocene flysch of interest appears to be isolated from deep burial and thus avoid the potential present-day burial we witness in the eastern part of the Ramree Island. Therefore, these mobilized clays can (i) either come from a greater depth (i.e. from beneath the Ramree thrust) mobilized during compression from overpressured shales (see Figure 193-Figure 194 and Maurin & Rangin, 2009), or else (ii) are mobilized at shallower depth due to a large presence of gas at depth since the presence of free methane can be a good candidate to initiate clay liquefaction even if the clays are poorly overpressured (as in the case of the Lusi mud volcano. Also see the thesis of A. Blouin for detailed explanation, Blouin 2019). Given this rationale, we suspect these volcanoes to originate from under-thrust at Eocene level, triggered by maturation of the organic matter (Figure 193-Figure 194).

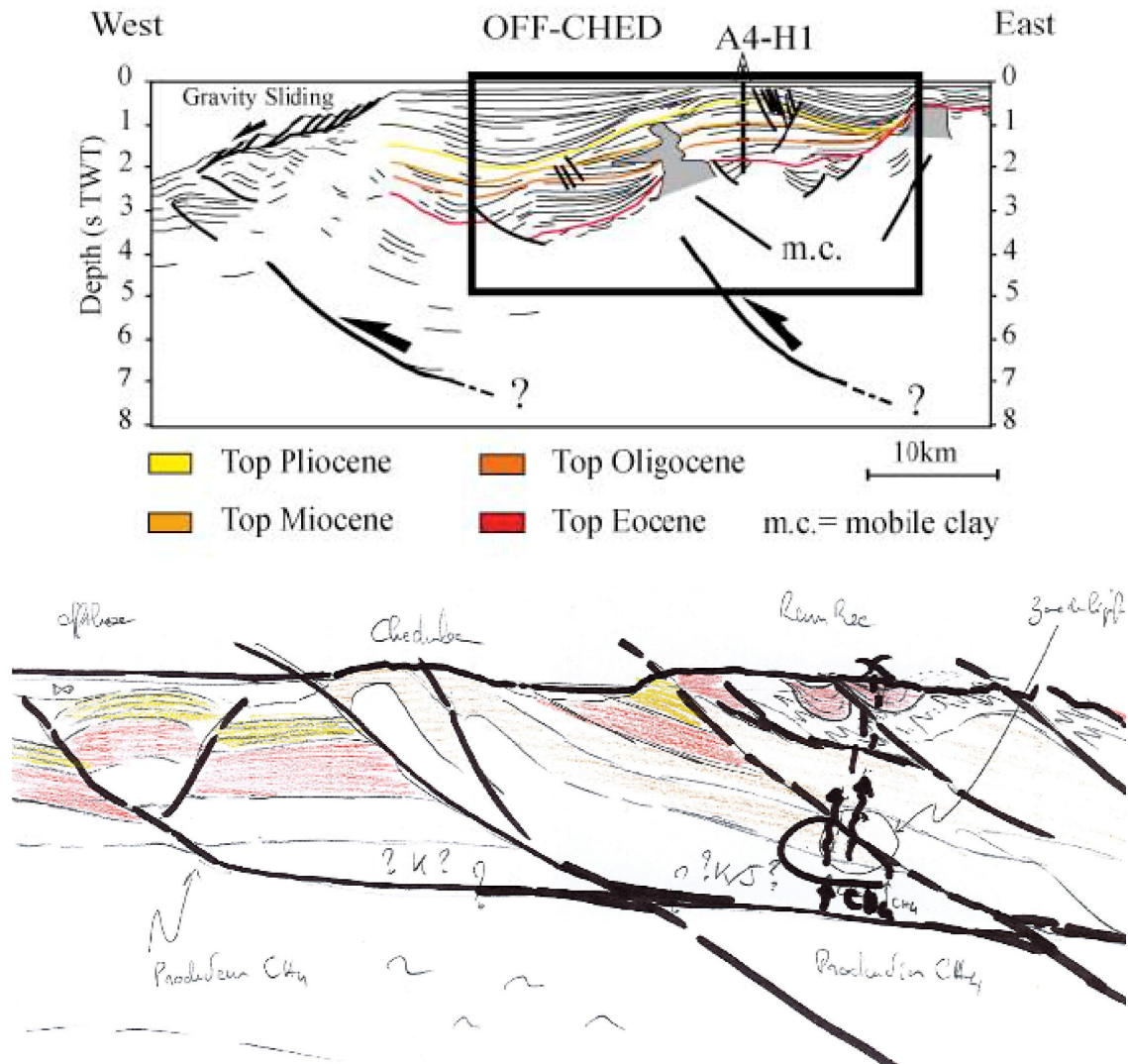


Figure 193: Upper sketch: A seismic line interpretation from offshore Cheduba Island showing the thrust slices and remobilized clays (Maurin and Rangin, 2009). Lower sketch: Synthetic EW oriented cross-section showing the possible location of hydrocarbon levels sourcing mud volcanoes from the lower tectonic slices below the Ramree Thrust (Yellow: Miocene, Red: Oligocene, Brown and marked folded lines: Eocene).

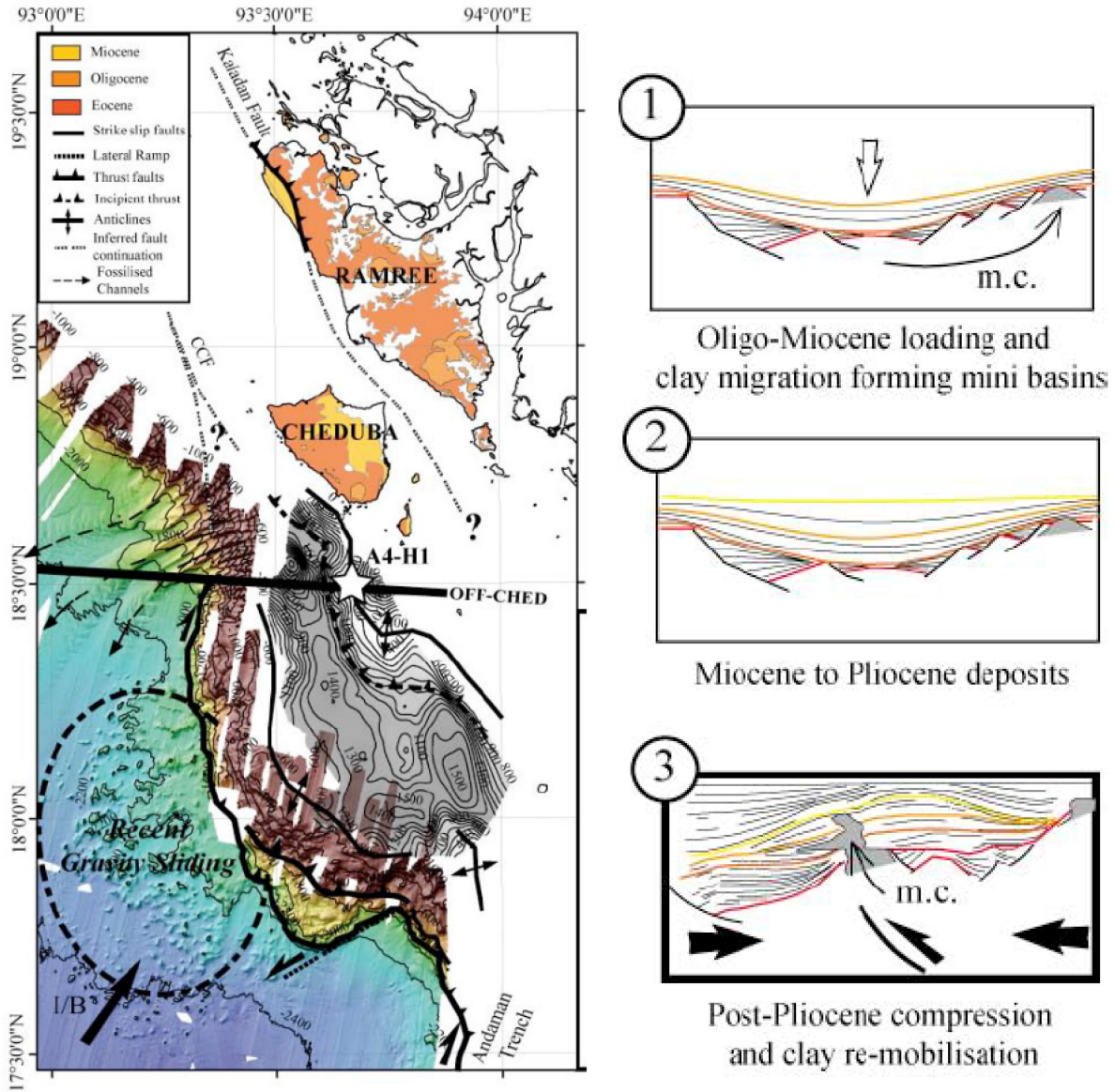


Figure 194: Left hand-side figure: Geological Map of Ramree and Cheduba Islands with the location of two main thrust faults and the seismic line. Right hand-side figure: A possible scenario for clay mobilization for minibasins and mud volcanoes (Maurin and Rangin, 2009) Both mechanisms are still to be tested and understood.

VII. Conclusion on Fieldwork Findings and Collected Samples

Despite poor outcropping conditions and vegetation cover, we have succeeded to visit 33 outcrop sites and collect 64 samples of with good-to-reasonable quality. Based on our field observations, it appears that the Eocene flysch of Ramree region is largely remobilized and may have been mobile at shallow depth as a debris flow or more regionally as a mass transport complex (MTC). Such pattern appears comparable to the mobilization of the flysch in the Makran Fold and Thrust Belt (see Ruh et al., 2018). Above this debris flow and MTC layers, early sediments appear to stimulate the clay mobility before a complete compaction occurs. The Oligocene deposits on top of the Eocene layer are not of turbiditic origin but rather shoreface-to-deltaic deposition origin in the Ramree-Cheduba area. Their geometries suggest a syn-sedimentary deposition forming rounded depo-centers sinking into the clay mélange. Distribution of these depo-centers suggests a punctual source of sedimentary income arriving from northeastward Ramree region (possibly of paleo Irrawady River origin), while the Oligocene and Miocene deposits correspond to shoreface facies.

A detailed petrographic and quantitative inspection is required to confirm these field observations but our initial conclusion lies towards a scenario, where the shale deformation of Eocene clays did not occur at a great depth with big pressure and overpressures, but rather took place at shallow depth in a distributed slow-motion manner similar to our findings from Ceduna Sub-Basin, White Pointer Delta and Salt Tectonics as it is referred to in the literature.

The rock samplings we have collected, are aimed to be used for petrographic analyses in the future in order to understand the temperature and pressure conditions of shale during the time of burial as well as the environmental effects such as fluid content or thermal gradient. For conclusive remarks, a comprehensive petrographic study, further research and lab work are required in order to:

- Better identify the observed facies and define clay assemblage via X-Ray diffraction methods, micro-probe analysis etc.
- Examine the burial and maturity for both clays and sandstones and estimate past temperature/burial conditions from syn-deformation calcite cements as / isotopic compositions
- Compare lab samples/findings of mud and mud volcanoes

Following the future petrology researches to be conducted, we expect to find better clues or answers about burial conditions controlling clay mobility.

Chapter 10: Discussion and General Conclusions on Shale Mobility Based on Conducted Fieldwork and Seismic Study

Rakhine State, Myanmar Field Work Study

A comprehensive petrographic study is necessary to reach conclusive results, however our observations suggest that a shale mobilization occurred at shallow depth, under small burial and pressure conditions. The Oligocene deposits of Ramree - Cheduba area are found to be of shore-face deltaic origin and not turbiditic, which suggests a syn-sedimentary deposition sinking into a clay-controlled rounded depo-center similar to salt-based examples. Distribution of these depo-centers point out to a punctual source of sedimentation coming from the NE. Findings suggest that mobile Eocene clays were deformed at shallow depth and rapidly accommodated the subsequent deposition in a distributed slow-motion manner like salt. Unlike the previously thought overpressured shale phenomena, we propose a slow-motion shale deformation pattern driven by shale strain for the region.

Ceduna Sub-Basin, White Pointer Delta Seismic Study

The 3D seismic dataset lines we utilized for this research enabled us to have a more detailed look at the distal part of the White Pointer Delta and led us to better identify the distal Blue Whale interval with imbricated thrust sheets, shale-interacted features associated with these thrusts (intermediate detachment levels), and duplexation of these formations evidencing the shale mobilization of the delta.

The seismic dataset collected from Ceduna Sub-Basin point out to a real physical analogue for salt tectonics, as well as several other studies referring to the possibility of shale becoming mobile/viscous at large scale under unknown controlling factors. The kinematic scenario given in Chapter 10 displays an overall view of White Pointer Delta based on the observations we have made on 2D and 3D seismic lines. The 3D portion displays a well-imaged system of shale-gliding deltaic pattern associated with mobilization structures and early shale-sediment interaction at observable seismic scale, while the 2D portion covers the regional view extending from basin margin slope down to the abyssal plain.

- The delta dynamics initiates with down-building features (e.g. primary minibasin formations) riding above the channelized shale ridges. These shale ridges are gravity-driven piles of shale that are mobilized/shaped by basin geometry and deltaic wedge setting.
- Early deposits of White Pointer Delta and salt-like deformation geometries builds upon these mother-shale remnants in terms of wedging and first-order minibasinal forms at the distal delta-toe. Incoming sedimentation triggers the settling sediment load to be transferred down-the-delta-slope above the ductile shale medium via extensional faulting (gravity-driven listric faults).
- The transition between proximal-to-central part of the delta is marked by elongated sediment patches divided by listric fault offsets and some translation structures such as shale roll-overs.
- The central-to-distal part is marked by a significant thrust fault domain, where the tip of listric faults soling into the Blue Whale detachment level transitions into a regional thrust front and rides

above the formerly built down-building domain resembling a hardened, kinematically elevated ramp.

- Upon duplexation, branched thrust sheets (intermediate detachment levels) lead to fish-tailing within this lithified strata.
- Fluidized shale-driven welds create disharmonic folding and carry shale-cored patches further up in the section in between the minibasins, which initiates radial faulting as a result of stress surrounding these shale-cored overpressured domal highs.
- In certain places, such disharmonic fold formations exceed the surficial stress pattern and lead to secondary radial fault halos separated from the first patch with peripheral caldera-like collapses depending on the mobilized/translated shale supply.
- Hammerhead Delta conformably progrades over Tiger shales and settles down with its listric fault system soling into shale-driven Tiger detachment level separated structurally and independently from the former White Pointer deltaic setting.
- All of the shale mobilization patterns identified within White Pointer Delta interval gets further compacted and fossilized underneath preserving its shape and structure we observe on well-imaged seismic datasets like in Ceduna Sub-Basin today.
- It is still not quite obvious why the nature favors one kind of mechanism (fluidization of shales) over the other (slow distributed deformation of shales with strain) in certain geologic locations and/or transitions from one into another. However, it is clear that shale behaves in a salt-like viscous manner and fluidizes when it is thick and over-pressurized in a geologic setting.
- Passing from one phase into another requires (i) confining pressure, (ii) high sedimentation rate and (iii) over-pressurization of pore fluid functioning with geothermal gradient and maturation. All of these aspects push the system towards a fluidization mechanism represented either by mud volcanoes or 'diapir-like' shale-cored domal highs, both of which emerge as a mobilization mechanism driven by shale tectonism.

Conclusions:

Shale tectonics is a broad research topic focusing on shale deformation mechanisms. As it is aimed to be addressed in this thesis, clays display a brittle deformation pattern on small scale and act very rapidly, in terms of mud volcanoes, when liquefied under stress. At large scale; they display plastic deformation pattern and behave like a fluid in a viscous manner mimicking salt deposits.

Similar to salt, clays deform under stress and differential loading. The deformation signature associated with shale mobilization can be recorded by the sediment strata surrounding shale remnants (e.g. argilokinesis). Moreover, clays resemble diapiric salt structures on not-so-clear seismic views and classic salt-like patterns can be identified evidencing clay behaving as salt.

Different than salt, they can be fluidized and emerge as mud volcanoes in various geo-locations on Earth. However, when investigated with well-imaged seismic datasets and supplementary outcrop studies, certain internal mechanisms differentiate from simple salt tectonism. In the investigated Ceduna Sub-Basin area, we proposed a duplexation mechanism for initiation of shale mobility above the early down-building structures.

Based on our conducted research and findings; it is our belief that the distal part of Ceduna Sub-Basin, White Pointer Delta, is under the heavy influence of argilokinesis and shale mobilization is the dominant source for the observed deformation structures. Observable deformation structures such as; wedges, welds, minibasins and diapiric tops, point out to a plastically deforming viscous material characterization similar to salt. Moreover, structural analysis conducted on time-slice view display striking resemblance to diapiric depressions associated with salt.

Our results suggest a strong relationship with plastic deformation pattern for shales. With this research, we are able to constrain a geometric analogy of salt with our current shale findings. It is of utmost importance to further investigate these analogies in order to conclude on the fact that at large scale; shale can mimic salt deformation and the concept of salt tectonics can be applied to shale tectonics with certain internal mobilization mechanisms such as duplexation of the thrust domain, sub-seismic scale fish-tailing, fluidization of shales and free gas content. First hand results of our research support this idea and encourage a promising path for the way forward.

References and Bibliography

(A)

- Abdullah, W.S., Al-Zou'bi, M.S., Alshibli, K.A., 1997. On the physicochemical aspects of compacted clay compressibility. *Can. Geotech. J.* 34, 551–559. <https://doi.org/10.1139/t97-027>
- Abrams, M.A., 1996, Geochemical artifacts of rapidly-subsiding basins—Example from western part of South Caspian Basin, Republic of Azerbaijan [abs.], in *Oil and gas petroleum systems in rapidly subsiding basins: AAPG/ASPG (American Association of Petroleum Geologists/Azerbaijan Society of Petroleum Geologists) Research Symposium, Baku, Azerbaijan, October 6–9, 1996*
- Acharyya, S.K., 2007. Collisional emplacement history of the Naga-Andaman ophiolites and the position of the eastern Indian suture. *J. Asian Earth Sci.* 29, 229–242.
- Ajakaiye, D.E., Bally, A.W., 2002. Manual and atlas of structural styles on reflection profiles from the Niger Delta. In: *AAPG Continuing Education Course Notes Series*, pp. 102
- Al-Areeq, N.M., Al-Badani, M.A., Salman, A.H., Albaroot, M.A., 2018. Petroleum source rocks characterization and hydrocarbon generation of the Upper Jurassic succession in Jabal Ayban field, Sabatayn Basin, Yemen. *Egyptian Journal of Petroleum* 27, 835–851. <https://doi.org/10.1016/j.ejpe.2017.12.005>
- Al-Ghamdi, A. M., & Watkins, J. S. (1996). Structural styles and depositional history of North and South Padre Island OCS areas, Offshore South Texas. In J. O. Jones & R. L. Freed, *Structural framework of the Northern Gulf of Mexico. Special Publication of the Gulf Coast Association of Geological Societies* (pp. 1–8). Gulf Coast Association of Geological Societies
- Allen, P.A. and Allen, J.R. (2013). *Basin analysis: Principles and application to petroleum play assessment*. John Wiley & Sons, Chichester, 632 p.
- Allen, P. A. & Allen, J. R. (2005) *Basin Analysis: Principles & Applications*, Oxford, Blackwell Publishing, 549pp.
- Allen, R., Najaman, Y., Carter, A., Barfod, D., Bickle, M.J., Chapman, H.J., Garzanti, E., Vezzoli, G., Ando, S., Parrish, R.R., 2008b. Provenance of the Tertiary sedimentary rocks of the Indo-Burman Ranges, Burma (Myanmar): Burman arc or Himalayanderived? *J. Geol. Soc.* 165, 1045–1057.
- Aloisi, G., C. Pierre, J-M. Rouchy, J-P. Foucher, J Woodside., and MEDINAUT Scientific Party. (2000). Methane-related authigenic carbonates of eastern Mediterranean Sea mud volcanoes and their possible relation to gas hydrate destabilisation. *Earth and Planetary Science Letters*, 184, 321-388
- Alonso, B., and A. Maldonado, 1992, Plio-quadernary margin growth patterns in a complex tectonic setting: Northeastern Alboran Sea: *Geo-Marine Letters*, v. 12, p. 137–143
- Alsop, G.I., Holdsworth, R.E., McCaffrey, K.J.W., 2007. Scale invariant sheath folds in salt, sediments and shear zones. *J. Struct. Geol.* 29, 1585–1604.
- Alsop, G.I., Marco, S., 2014. Fold and fabric relationships in temporally and spatially evolving slump systems: a multi-cell flow model. *J. Struct. Geol.* 63, 27–49.
- Alsop, G.I., Weinberger, R., Levi, T., Marco, S., 2016. Cycles of passive versus active diapirism recorded along an exposed salt wall. *Journal of Structural Geology* 84, 47–67. <https://doi.org/10.1016/j.jsg.2016.01.008>
- Alsop, G.I., Weinberger, R., Marco, S., Levi, T., 2017c. Identifying soft-sediment deformation in rocks. *Journal of Structural Geology*. <https://doi.org/10.1016/j.jsg.2017.09.001>

- Artyushkov, E.V., 2007. Formation of the superdeep South Caspian basin: subsidence driven by phase change in continental crust. *Russian Geology and Geophysics*. Volume 48, Issue 12, 10 December 2007, Pages 1002-1014. <https://doi.org/10.1016/j.rgg.2007.11.007>
- Athy LF (1930a) Density, porosity, and compaction of sedimentary rocks. *AAPG Bull* 14(1):1–24
- Audet, D.M.; McConnell, J.D.C. Forward modeling of porosity and pore pressure evolution in sedimentary basins. *Basin Res.* 1992, 4, 147–162.
- Audet, P. and Burgmann, R., 2011. Dominant role of tectonic inheritance in supercontinent cycles. *Nat. Geosci.*, 4, 184–187.
- Ave Lallemand, H. 1997. Transpression, displacement partitioning, and exhumation in the eastern Caribbean/South American plate boundary zone. *Tectonics*, 16, 2, pp 272-289.
- Ave Lallemand, H.G., and Oldow, J.S. 2000. Active displacement partitioning and arc-parallel extension of the Aleutian volcanic arc based on Global Positioning System geodesy and kinematic analysis. *Geology*, 28, pp 739-742.
- Atwater, G.I., Forman, M.J., 1959. Nature of growth of southern Louisiana salt domes and its effect on petroleum accumulation. *Am. Assoc. Pet. Geol., Bull.; (United States)* 2592–2622.

(B)

- Back, S., Morley, C.K., 2015. Growth faults above shale – Seismic-scale outcrop analogues from the Makran foreland, SW Pakistan. <https://doi.org/10.1016/j.marpetgeo.2015.11.008>
- Balaguru, A., Nichols, G., Hall, R., 2003. The origin of the “circular basins” of Sabah, Malaysia. *BGSM* 46, 335–351. <https://doi.org/10.7186/bgsm46200355>
- Bandyopadhyay, P.C., Carter, A., 2017. Chapter 6. Geological framework of the Andaman–Nicobar Islands. In: Bandyopadhyay, P.C., Carter, A. (Eds.), *The Andaman-Nicobar Accretionary Ridge: Geology, Tectonics and Hazards*. Geological Society, London, *Memoirs* vol. 47, pp. 75–93.
- Bannert, D., Helmcke, D., Ritzkowski, S., 1978. Final Report on the Geology of Ramree and Cheduba Islands (Arakan Coast). Hannover, p. 72.
- Bannert, D., Sang Lyen, A., Hty, T., 2011. The geology of the Indoburman Ranges in Myanmar. *Geol. Jahrb.* 101 (B), 5–101.
- Barber, A.J., Tjokrosapoetro, S., Charlton, T.R., 1986. Mud volcanoes, shale diapirs, wrench faults, and melanges in accretionary complexes, eastern Indonesia. *Am. Assoc. Pet. Geol., Bull.; (United States)* 70:11, 1729–1741.
- Barker, C. (1990). Calculated volume and pressure changes during the thermal cracking of oil to gas in reservoirs. *AAPG Bulletin*, 74, 1404–1413
- Barton, D.C., 1933. Mechanics of formation of salt domes with special references to Gulf Coast salt domes of Texas and Louisiana. *AAPG Bulletin*.
- Bastia, R., 2006. An overview of Indian sedimentary basins with special focus on emerging east coast deepwater frontiers. *The Leading Edge* 25, 818-829
- Battani, A., Prinzhofer, A., Deville, E., Ballentine, C.J., 2010. Trinidad mud volcanoes : The origin of gas, in: Wood, L.J. (Ed.), *Shale Tectonics*, AAPG Memoir 93. pp. 223–236.
- Bayer R, Chery J, Tatar M, Vernant P, Abbassi M, Masson F, Nilforoushan F, Doerflinger E, Regard V, Bellier O (2006) Active deformation in Zagros-Makran transition zone inferred from GPS measurements. *Geophys J Int* 165(1):373–381
- Bein, J. and Taylor, M.L., 1981. The Eyre Sub-basin: recent exploration results. *The APEA Journal*, 21, 91–98.

- Belousov, V.V., 1959. Types of Folding and Their Origin. *International Geology Review* 1, 1–21. <https://doi.org/10.1080/00206815909473393>
- Bender, F., 1983. *Geology of Burma*. Gebruder Borntraeger, Berlin, 293 p.
- Berberian, M. 1983. The southern Caspian: a compressional depression floored by a trapped, modified oceanic crust. *Canadian Journal of Earth Sciences*, 20, 163–183.
- Beslier, M.-O., Royer, J.Y., Girardeau, J., Hill, P.J., Boeuf, E., Buchanan, C., Chatin, F., Jacovetti, G., Moreau, A., Munsch, M., Partouche, C., Robert, U. and Thomas, S., 2004. Une large transition continent-ocean en pied de marge sud-ouest australienne: premiers resultats de la campagne MARGAU/MD110. *Bull. Soc. Ge'ol. Fr.*, 6, 629–641.
- Best, J.L., Wignall, P.B., Stirling, E.J., Obrock, E. and Bryk, A. (2016) The Tullig and Kilkee cyclothems in Southern County Clare. In: *A Field Guide to the Carboniferous Sediments of the Shannon Basin, Western Ireland* (Eds J.L. Best and P.B. Wignall), *Int. Assoc. Sedimentol. Field Guide*, 240–328
- Biju-Duval, B., Le Quellec, P., Mascle, A., Renard, V., Valery, P., 1982. Multi-beam bathymetric survey and high resolution seismic investigations on the Barbados ridge complex eastern Caribbean: a key to the knowledge and interpretation of an accretionary wedge. *Tectonophysics* 80, 275-304
- Biju Duval, B., Moore, J.C., Shipboard Scientific Party, 1984. Site 543: oceanic reference site east of the Barbados ridge complex. In: *Initial Reports of the Deep Sea Drilling Project*, vol. 78A. U.S. Government Printing Office, Washington, D.C, pp. 227e293. <http://dx.doi.org/10.2973/dsdp.proc.78a>
- Billingsley, L. E., 1982, Geometry and mechanisms of folding related to growth faulting in Nordheim Field area (Wilcox), De Witt County, Texas: *Gulf Coast Association of Geological Societies Transactions*, 32, 263–274.
- Bird, P., 1984, Hydration-phase diagrams and friction of mont-morillonite under laboratory and geologic conditions, with implications for shale compaction, slope stability, and strength of fault gouge: *Tectonophysics*, v. 107, p. 235–260.
- Bjorlykke, K., Hoeg, K., 1997. Effects of burial diagenesis on stresses, compaction and fluid flow in sedimentary basins. *Marine and Petroleum Geology* Volume 14, Issue 3, May 1997, Pages 267-276 [https://doi.org/10.1016/S0264-8172\(96\)00051-7](https://doi.org/10.1016/S0264-8172(96)00051-7)
- Bjorlykke, K., 1998. Clay mineral diagenesis in sedimentary basins – a key to the prediction of rock properties. In: *Examples from the North Sea Basin*. *Clay Miner.* 33. pp. 15–34.
- Blakely, R. J., B. L. Sherrod, C. S. Weaver, R. E. Wells, A. C. Rohay, E. A. Barnett, and N. E. Knepprath (2011), Connecting the Yakima fold and thrust belt to active faults in the Puget Lowland, Washington, *J. Geophys. Res.*, 116, B07105, doi:10.1029/2010JB008091
- Blanchard, S., Matheson, E.J., Fielding, C.R., Best, J.L., Bryk, A.B., Howell, K.J., Monson, C.C., Mahoney, G., Peakall, J., 2019. Early burial mud diapirism and its impact on stratigraphic architecture in the Carboniferous of the Shannon Basin, County Clare, Ireland. *Sedimentology* 66, 329–361. <https://doi.org/10.1111/sed.12492>
- Blatt, H. & Tracy, R. J. 1996. *Petrology. Igneous, Sedimentary, and Metamorphic*, 2nd ed. xix + 529 pp. New York, Basingstoke: W. H. Freeman & Co. ISBN 0 7167 2438 3. *Geological Magazine* 134(01):121 – 142. DOI: [10.1017/S0016756897506133](https://doi.org/10.1017/S0016756897506133)

- Blouin, A., 2019. Thesis of PhD. Génération de boue à partir de sédiments stratifiés dans un contexte de volcanisme de boue ; le rôle du gaz. Université de Pau et des Pays de l'Adour (UPPA) / IFREMER, France, 344 p.
- Blouin, A., Imbert, P., Sultan, N., Callot, J., 2019a. Evolution Model for the Absheron Mud Volcano: From In Situ Observations to Numerical Modeling. *J. Geophys. Res. Earth Surf.* 124, 766–794. <https://doi.org/10.1029/2018JF004872>
- Blouin, A., Sultan, N., Callot, J.-P., Imbert, P., 2019b. Sediment damage caused by gas exsolution: A key mechanism for mud volcano formation. *Engineering Geology* 263, 105313. <https://doi.org/10.1016/j.enggeo.2019.105313>
- Blouin A., Sultan N., Pierron A., Imbert P., Callot J.C., (2020). Evolution Model for the Absheron Mud Volcano: From Stratified Sediments to Fluid Mud Generation. *JCR Earth Surface* Volume125, Issue12. <https://doi.org/10.1029/2020JF005623>
- Bogg, S., 2012, *Principles of Sedimentology and Stratigraphy* (5th Edition). Pearson Prentice Hall, Upper Saddle River, N.J., 608 p.
- Bol, A.J., van Hoorn, B., 1980. Structural Styles in Western Sabah Offshore. *Geological Society of Malaysia Bulletin* 12, 1–16. <https://doi.org/10.7186/bgsm12198001>
- Bolton, A., & Maltman, A. (1998). Fluid-flow pathways in actively deforming sediments: the role of pore fluid pressures and volume change. *Marine and Petroleum Geology*, 15, 281–297
- Bonini, M., Maestrelli, D., 2020. Earthquake triggering of mud volcanoes and fluid seepage systems in fold-and-thrust belts and subduction zones (other). display. <https://doi.org/10.5194/egusphere-egu2020-3673>
- Bonini, M., Maestrelli, D., Sani, F., 2020. Tectonic structures vs genesis and activity of mud volcanoes: examples from Emilia and Marche (Northern Apennines, Italy) (other). oral. <https://doi.org/10.5194/egusphere-egu2020-3664>
- Boreham, C.J., Krassay, A.A. and Totterdell, J.M., 2001. Geochemical comparisons between asphaltites on the southern Australian margin and Cretaceous source rock analogues. In: Hill, K.C. and Bernecker, T. (Eds), *Eastern Australasian Basins Symposium: a refocused energy perspective for the future*. Petroleum Exploration Society of Australia, Special Publication, 531–541.
- Borgia, A., Grieco, G., Brondi, F., Badali, M., Merle, O., Pasquarè, G., Martelli, L., di Nardo, T., 2006. Shale diapirism in the Quaternary tectonic evolution of the Northern Apennine, Bologna, Italy. *J. Geophys. Res.* 111, B08406. <https://doi.org/10.1029/2004JB003375>
- Bosellini, A. (1992), The continental margins of Somalia: structural evolution and sequence stratigraphy, in *Geology and Geophysics of Continental Margins*, AAPG Mem., vol. 53, edited by J. S. Watkins et al., pp. 185–205
- Bossart, P., Meier, P.M., Moeri, A., Trick, T., Mayor, J.-C., 2002. Geological and hydraulic characterisation of the excavation disturbed zone in the Opalinus Clay of the Mont Terri Rock Laboratory. *Eng. Geol.* 66, 19–38
- Booth-Rea, G., C. R. Ranero, J. M. Martinez-Martinez, and I. Grevemeyer, 2007, Crustal types and tertiary tectonic evolution of the Alboran sea, western Mediterranean: *Geochemistry, Geophysics, Geosystems*, v. 8, doi:10.1029/2007GC001639
- Bourgois, J. A., A. Mauffret, N. A. Ammar, and N. A. Demnati, 1992, Multichannel seismic data imaging of inversion tectonics of the Alboran ridge (western Mediterranean Sea): *Geo-Marine Letters*, v. 12, p. 117–122

- Bourlange, S., Henry, P., 2007. Numerical model of fluid pressure solitary wave propagation along the décollement of an accretionary wedge: application to the Nankai wedge: Fluid pressure solitary wave propagation. *Geofluids* 7, 323–334. <https://doi.org/10.1111/j.1468-8123.2007.00181.x>
- Bourlange, S., Henry, P., Moore, J.C., Mikada, H., Klaus, A., 2003. Fracture porosity in the décollement zone of Nankai accretionary wedge using Logging While Drilling resistivity data. *Earth and Planetary Science Letters* 209, 103–112. [https://doi.org/10.1016/S0012-821X\(03\)00082-7](https://doi.org/10.1016/S0012-821X(03)00082-7)
- Bowers, G.L. Pore pressure estimation from velocity data: Accounting for overpressure mechanisms besides undercompaction. *SPE Drill. Complet.* 1995, 10, 89–95
- Bowers, G.L.; Katsube, T.J. The role of shale pore structure on the sensitivity of wire-line logs to overpressure. In *Pressure Regimes in Sedimentary Basins and Their Prediction*; Hu_man, A., Bowers, G., Eds.; AAPG Memoir 76: Tulsa, OK, USA, 2002; pp. 43–60
- Brace, W., Kohlstedt, D., 1980. Limits on lithospheric stress imposed by laboratory experiments. *J. Geophys. Res. Solid Earth* 85 (B11), 6248–6252.
- Bradshaw, B. E., & Watkins, J. S. (1996). Growth fault evolution in offshore Texas. In J. O. Jones & R. L. Freed, *Structural framework of the Northern Gulf of Mexico*. Special Publication of the Gulf Coast Association of Geological Societies (pp. 103–110). Gulf Coast Association of Geological Societies.
- Bradshaw, B.E., Rollet, N., Totterdell, J.M. and Borissova, I. (2003). A Revised Structural Framework for Frontier Basins on the Southern and Southwestern Australian Continental Margin. *Geoscience Australia Record 2003 / 03*, Canberra.
- Brami, T.R., Pirmez, C., Archie, C., Heeralal, S., Holman, K.L., 2000. Late Pleistocene deep-water stratigraphy and depositional processes. *Mem. GCSSEPM* 20, 104-115
- Braun J (2006) Recent advances and current problems in modelling surface processes and their interaction with crustal deformation. *Geological Society, London, Special Publications* 253: 307–325.
- Bredehoeft, J.D., Djevanshir, R.D., Belitz, K.R., 1988. Lateral fluid flow in a compacting sand-shale sequence: south Caspian basin. *AAPG Bull.*; (United States) 72:4.
- Breen, N.A., Tagudin, J.E., Reed, D.L., Silver, E.A., 1988. Mud-cored parallel folds and possible melange development in the north Panama thrust belt. *Geol* 16, 207. [https://doi.org/10.1130/0091-7613\(1988\)16\[207:MPFAPM\]2.0.CO;2](https://doi.org/10.1130/0091-7613(1988)16[207:MPFAPM]2.0.CO;2)
- Briggs, S.E., Davies, J.A., Cartwright, J.A., Morgan, R., 2006. Multiple detachment levels and their control on fold styles in the compressional domain of the deep-water west Niger Delta. *Basin Res.* 18, 435–450.
- Brown, K. M., and G. K. Westbrook, 1987, The tectonic fabric of the Barbados ridge accretionary complex: *Marine and Petroleum Geology*, v. 4, p. 71–81, doi:10.1016/0264-8172(87)90022-5
- Brown, K., Westbrook, G.K., 1988. Mud diapirism and subcretion in the Barbados Ridge Accretionary Complex: The role of fluids in accretionary processes. *Tectonics* 7, 613–640. <https://doi.org/10.1029/TC007i003p00613>
- Brown, K. M. (1990) 'The nature and hydrogeologic significance of mud diapirs and diatremes for accretionary systems', *Journal of Geophysical Research*, 95(B6), p. 8969. doi: 10.1029/JB095iB06p08969

- Bruce, C.H., 1973. Pressured Shale and Related Sediment Deformation—Mechanism for Development of Regional Contemporaneous Faults. AAPG Bulletin 57, 1842–1842. <https://doi.org/10.1306/819A4352-16C5-11D7-8645000102C1865D>
- Brun, J.-P., Fort, X., 2011. Salt tectonics at passive margins: Geology versus models. *Marine and Petroleum Geology* 28, 1123–1145. <https://doi.org/10.1016/j.marpetgeo.2011.03.004>
- Brun, J.-P., Mauduit, T.P.-O., 2008. Rollovers in salt tectonics: The inadequacy of the listric fault model. *Tectonophysics* 457, 1–11. <https://doi.org/10.1016/j.tecto.2007.11.038>
- Brun, J.-P., Merle, O., 1985. Strain patterns in models of spreading-gliding Nappes. *Tectonics* 4, 705–719. <https://doi.org/10.1029/TC004i007p00705>
- Brunet, M.-F., Korotaev, M., Ershov, A., Nikishin, A., 2003. The South Caspian basin : a review of its evolution from subsidence modelling. In : Brunet M.F. & Clothing S. (Eds), *Integrated PeriTethyan Basins Studies (Peri-Tethys Programme)*. *Sedimentary Geology* 156, 119–148. [https://doi.org/10.1016/S0037-0738\(02\)00285-3](https://doi.org/10.1016/S0037-0738(02)00285-3)
- Brunet, M.-F., Shahidi, A., Barrier, E., Muller, C. & Saïdi, A. 2007. Geodynamics of the South Caspian Basin southern margin now inverted in Alborz and Kopet Dagh (Northern Iran). In: *European Geosciences Union EGU, General Assembly, Vienna, Austria, 16–20 April*. *Geophysical Research Abstracts*, 9, 08080.
- Brunnschweiler, R.O., 1966. On the geology of the IndoBurman ranges. *J. Geol. Soc. Australia* 13, 137–194.
- Buffler, R. T., F. J. Shaub, J. S. Watkins, and J. L. Worzel (1978), *Anatomy of the Mexican Ridges, southwestern Gulf of Mexico*, in *Geological and Geophysical Investigations of Continental Margins*, edited by J. S. Watkins, L. Montadert, and P. W. Dickerson, AAPG Mem., 29, 319 – 327.
- Buller, A.T., Bjorkum, P.A., Nadeau, P.H., Walderhaug, O., 2005. Distribution of hydrocarbons in sedimentary basins. *Res. & Tech. Mem. 7 (Statoil ASA, Stavanger, 15 pp.)*.
- Burg, J.-P., 2018. Geology of the onshore Makran accretionary wedge: Synthesis and tectonic interpretation. *Earth-Science Reviews* 185, 1210–1231. <https://doi.org/10.1016/j.earscirev.2018.09.011>
- Burg, J.-P., Dolati, A., Bernoulli, D., Smit, J., 2013. structural style of the Makran Tertiary accretionary complex in SE-Iran, in: Al Hosani, K., Roure, F., Ellison, R., Lokier, S. (Eds.), *Lithosphere Dynamics and Sedimentary Basins: The Arabian Plate and Analogues*, *Frontiers in Earth Sciences*. Springer Berlin Heidelberg, Berlin, Heidelberg, pp. 239–259. https://doi.org/10.1007/978-3-642-30609-9_12
- Burollet, P., 1975. Tectonique en radeaux en Angola. *Bulletin de la Société Géologique de France* 17, 503–504.
- Burov EB (2007) Plate rheology and mechanics. In: Watts AB (ed.) *Treatise on Geophysics. Crust and Lithosphere Dynamics*, vol. 6, pp. 99–151. Amsterdam: Elsevier.
- Burov, E. B., and Diament, M. (1995). The effective elastic thickness (T_e) of continental lithosphere: What does it really mean? (Constraints from mechanics, topography and gravity): *Journal of Geophysical Research*, v. 100, p. 3905–3927.
- Busby, C.J., and Ingersoll, R.V. (1995). *Tectonics of sedimentary basins*: Oxford, Blackwell Science, 579 p.
- Busby, C. J. (2013), Birth of a plate boundary at ca. 12 Ma in the Ancestral Cascades arc, Walker Lane belt of California and Nevada, *Geosphere*, 9, 1147–1160

(C)

- Cai, W., Zhu, G., Jiang, Y., Yang, S. & Li, A. 2012. Petroleum geologic characteristics and exploration potential of accretionary wedge in Myanmar. *Natural Gas Geoscience* 23, 742–7.
- Callec, Y., Deville, E., Desaubliaux, G., Griboulard, R., Huyghe, P., Mascle, A., Mascle, G., Noble, M., Padron De Carillo, C., Schmitz, J., 2010. The Orinoco turbidite system: tectonic controls on seafloor morphology and sedimentation. *AAPG Bull.* 94 (6), 869-887
- Callot, J.-P., Ribes, C., Kergaravat, C., Bonnel, C., Temiz, H., Poisson, A., Vrielynck, B., Salel, J.F., Ringenbach, J.-C., 2014. Salt tectonics in the Sivas Basin, Turkey: Crossing salt walls and mini basins. *Bulletin de la Societe Geologique de France* 185, 34–42.
<https://doi.org/10.2113/gssgfbull.185.1.33>
- Callot, J.-P., Salel, J.-F., Letouzey, J., Daniel, J.-M., Ringenbach, J.-C., 2016. Three-dimensional evolution of salt-controlled minibasins: Interactions, folding, and megaflap development. *Aapg Bulletin* 100, 1419–1442. <https://doi.org/10.1306/03101614087>
- Campillo, A. C., A. Maldonado, and A. Mauffret, 1992, Stratigraphic and tectonic evolution of the western Alboran Sea: Late Miocene to Recent: *Geo-Marine Letters*, v. 12, 905 p. 165–172
- Cande, S. C., and J. C. Mutter (1982), A revised identification of the oldest sea-floor spreading anomalies between Australia and Antarctica, *Earth Planet. Sci. Lett.*, 58, 151 – 160, doi:10.1016/0012-821X(82)90190-X.
- Cannon, R. T., W. M. N. S. Siambi, and F. M. Karanja (1981), The proto-Indian Ocean as a probable Paleozoic/Mesozoic tri-radial rift system in East Africa, *Earth Planet. Sci. Lett.*, 52, 419–426, doi:10.1016/0012-821X(81)90194-1
- Carter, N.L., Horseman, S.T., Russell, J.E., Handin, J., 1993. Rheology of rocksalt. *Journal of Structural Geology* 15, 1257–1271. [https://doi.org/10.1016/0191-8141\(93\)90168-A](https://doi.org/10.1016/0191-8141(93)90168-A)
- Carter A, Najman Y, Bahroudi A, Bown P, Garzanti E, Lawrence RD (2010) Locating earliest records of orogenesis in western Himalaya: evidence from Paleogene sediments in the Iranian Makran region and Pakistan Katawaz basin. *Geology* 38(9):807–810
- Catuneanu, O., Wopfner, H., Eriksson, P.G., Cairncross, B., Rubidge, B.S., Smith, R.M.H. & Hancox, P.J. (2005) The Karoo Basins of South-Central Africa. *Journal of African Earth Sciences*, 43, 211-253
- Cedeño, A., Rojo, L.A., Cardozo, N., Centeno, L., Escalona, A., 2019. The Impact of Salt Tectonics on the Thermal Evolution and the Petroleum System of Confined Rift Basins: Insights from Basin Modeling of the Nordkapp Basin, Norwegian Barents Sea. *Geosciences* 9, 316.
<https://doi.org/10.3390/geosciences9070316>
- Chamot-Rooke, N., Rabaute, A., Kreemer, C., 2005. Western Mediterranean Ridge mud belt correlates with active shear strain at the prism-backstop geological contact. *Geol* 33, 861.
<https://doi.org/10.1130/G21469.1>
- Chapman, R.E., 1974. Clay Diapirism and Overthrust Faulting. *GSA Bulletin* 85, 1597–1602.
[https://doi.org/10.1130/0016-7606\(1974\)85<1597:CDAOF>2.0.CO;2](https://doi.org/10.1130/0016-7606(1974)85<1597:CDAOF>2.0.CO;2)
- Chattin, F., Robert, U., Montigny, R. and Whitechurch, H., 1998. La zone Diamantine (Ocean Indien oriental), témoin de la separation entre l’Australie et l’Antarctique: arguments petrologiques et geochemique. *CR Acad. Sci. Paris*, 326, 839–845.

- Choudhuri, Mainak, Debajyoti Guha, Arindam Dutta, Sudipta Sinha, and Neeraj Sinha, 2010, Spatiotemporal variations and kinematics of shale mobility in the Krishna-Godavari basin, India, in L. Wood, ed., *Shale tectonics: AAPG Memoir 93*, p. 91 – 109
- Clark, J., Sapura Energy, 2017. Neogene Tectonics of Northern Borneo.
- Clennell, M., Knipe, R., Fisher, Q., 1998. Fault zones as barriers to, or conduits for, fluid flow in argillaceous formations. A microstructural and petrophysical perspective. In: *Fluid Flow Through Faults and Fractures in Argillaceous Formations*. OECD Proceedingspp. 125–139.
- Cloetingh S, Cornu T, Ziegler PA, and Beekman F (2006) Neotectonics and intraplate continental topography of the northern Alpine Foreland. *Earth-Science Reviews* 74: 127–196.
- Cloetingh, S., and Burov, E. B. (1996). Thermomechanical structure of European continental lithosphere: Constraints from rheological profiles and EET estimates: *Geophysical Journal International* 124: 695-723.
- Cloetingh, S., Ziegler, P.A., Beekman, F., *Andriessen P. A. M., Hardebol N., Dezes P.,* (2005). Intraplate deformation and 3D rheological structure of the Rhine Rift System and adjacent areas of the northern Alpine foreland. *Int J Earth Sci (Geol Rundsch)* 94, 758–778. <https://doi.org/10.1007/s00531-005-0502-3>
- Cloetingh, S., Ziegler, P.A., 2007. Tectonic Models for the Evolution of Sedimentary Basins, in: Schubert, G. (Ed.), *Treatise on Geophysics*. Elsevier, Amsterdam, pp. 485–611. <https://doi.org/10.1016/B978-044452748-6.00109-7>
- Cloke, I.R., Moss, S.J., Craig, J., 1999. Structural controls on the evolution of the Kutai Basin, East Kalimantan. *Journal of Asian Earth Sciences* 17, 137–156. [https://doi.org/10.1016/S0743-9547\(98\)00036-1](https://doi.org/10.1016/S0743-9547(98)00036-1)
- Close, D.I., Stagg, H.M.J. and O'Brien, P.E., 2007. Seismic stratigraphy and sediment distribution on the Wilkes Land and Terre Adélie margins, East Antarctica. *Mar. Geol.*, 239, 33–37.
- Close, D.I., Watt, A.B. and Stagg, H.M.J., 2009. A marine geophysical study of the Wilkes Land rifted continental margin, Antarctica. *Geophys. J. Int.*, 177, 430–450.
- Cobbold, P.R., Mourgues, R., Boyd, K., 2004. Mechanism of thin-skinned detachment in the Amazon Fan: assessing the importance of fluid overpressure and hydrocarbon generation. *Mar. Pet. Geol.* 21, 1013–1025
- Cobbold, P.R., Clarke, B.J., Loseth, H., 2009. Structural consequences of fluid overpressure and seepage forces in the outer thrust belt of the Niger Delta. *Pet. Geosci.* 15, 3–15.
- Cobbold, P.R., Zanella, A., Rodrigues, N., Loseth, H., 2013. Bedding-parallel fibrous veins (beef and cone-in-cone): worldwide occurrence and possible significance in terms of fluid overpressure, hydrocarbon generation and mineralization. *Mar. Pet. Geol.* 43, 1–20.
- Coffin, M. F., and P. D. Rabinowitz (1982), A multichannel seismic transect of the Somalian continental margin, *Proceedings 1982 Offshore Technological Conference*, Vol. 2, pp. 421–430
- Coffin, M. F. & Rabinowitz. P. D. (1988), Evolution of the conjugate East African-Madagascan margins and the western Somali Basin, *Geol. Soc. Am. Spec. Pap.*, 226,1–79
- Coffin, M. F., and P. D. Rabinowitz (1992), The Mesozoic East African and Madagascan conjugate margins: Stratigraphy and tectonics, in *Geology and Geophysics of Continental Margins*, AAPG Mem., vol. 53, edited by J. S. Watkins et al., pp. 207–246
- Cohen, H. A., and K. McClay (1996), Sedimentation and shale tectonics of the northwestern Niger Delta front, *Mar. Pet. Geol.*, 13, 313 – 328, doi:10.1016/0264-8172(95)00067-4.

- Cohen, H.A., McClay, K., 1996. Sedimentation and shale tectonics of the northwestern Niger Delta front. *Marine and Petroleum Geology* 13, 313–328. [https://doi.org/10.1016/0264-8172\(95\)00067-4](https://doi.org/10.1016/0264-8172(95)00067-4)
- Coleman, J.M & Prior, D.B. 1980. Deltaic sand bodies. *American Association of Petroleum Geologists, Continuing Education Course Notes Series*, 15, 171p.
- Colgan, J. P., A. E. Egger, D. A. John, B. Cousens, R. J. Fleck, and C. D. Henry (2011), Oligocene and Miocene arc magmatism in northeastern California: Evidence for post-Eocene subduction segmentation of the subducting Farallon plate, *Geosphere*, 7, 733–755
- Collinson, J.D., Martinsen, O., Bakken, B. and Kloster, A. (1991) Early fill of the Western Irish Namurian Basin: a complex relationship between turbidites and deltas. *Basin Res.*, 3, 223–242
- Colman-Sadd, S.P., 1978. Fold development in Zagros simply folded belt, Southwest Iran. *AAPG Bull.* 62, 984–1003
- Colwell, J.B., Stagg, H.M.J., Direen, N.G., Bernardel, G. and Borissova, I., 2006. The structure of the continental margin off Wilkes Land and Terre Adélie coast, east Antarctica. In: *Antarctica: Contributions to Global Earth Sciences* (D.K. Futterer, D.K. Damaske, G. Kleinschmidt, H. Miller and F. Tessensohn, eds), pp. 327–340. Springer-Verlag, Berlin.
- Comas M. C., V. Garcia-Duenas, and M. J. Jurado, 1992, Neogene tectonic evolution of the Alboran Sea from MCS data: *Geo-Marine Letters*, v. 12, p. 157–164
- Comas, M. C., J. J. Danobeitia, J. Alvarez-Marroñ, and J. I. Soto, 1997, Crustal reflections and structure in the Alboran Basin: Preliminary of the ESCI-Alboran survey: *Revista de la Sociedad Geologica de Espana*, v. 8, p. 529–542
- Comas, M. C., J. P. Platt, J. I. Soto, and A. B. Watts, 1999, The origin and tectonic history of the Alboran Basin: Insights from leg 161 results, in R. Zahn, M. C. Comas, and A. Klaus, eds., *Proceedings of the Ocean Drilling Program, Scientific Results*, v. 161, p. 555–579
- Condie, K.C., *Earth as an Evolving Planetary System* (3rd Edition), 2016. ISBN: 978-0-12-803689-1, eBook ISBN: 9780128037096, <https://doi.org/10.1016/C2015-0-00179-4>
- Connors, C.D., Radovich, B., Danforth, A., Venkatraman, S., 2009. The structure of the offshore Niger Delta. In: *Trabajos de Geologia*. 29. Universidad de Oviedo, pp. 182–188
- Cooper, C. (2001). Mud volcanoes of the South Caspian Basin. Seismic data and implications for hydrocarbon systems (extended abstract). *American Association of Petroleum Geologists Convention Abstracts*, CD-ROM, 5p
- Corredor, F., Shaw, J.H., Bilotti, F., 2005. Structural styles in the deep-water fold and thrust belts of the Niger Delta. *Bulletin* 89, 753–780. <https://doi.org/10.1306/02170504074>
- Couzens-Schultz B., Vendeville B., Wiltshcko D., 2003. Duplex style and triangle zone formation: insights from physical modeling. *Journal of Structural Geology* 25, 1623-1644.
- Cowan, D.S., 1985. Structural styles in Mesozoic and Cenozoic melanges in the western Cordillera of North America. *Geol. Soc. Am. Bull.* 96, 451–462.
- Curray, J.R., 2005. Tectonics and history of the Andaman Sea region. *J. Asian Earth Sci.* 25: 187–232. <http://dx.doi.org/10.1016/j.jseae.2004.09.001>.
- Coward, M., Stewart, S., 1995. Salt-Influenced Structures in the Mesozoic-Tertiary Cover of the Southern North Sea, U.K. 229–250.
- Coward, M. And Ries, A. 2001. Petroleum systems in the compressional/transpressional margin of Eastern Venezuela and Trinidad *American Association of Petroleum Geologists. Annual Meeting Expanded Abstracts*, pp 43.

- Critescu, N.D., 1998. Evolution of damage in rocksalt, in: Mechanical Behavior of Salt, Clausthal-Zellerfeld, Trans Tech Publications, Series on Rock and Soil Mechanics. pp. 131–142.
- Critescu, N.D., Hunsche, U., 1988. Time effects in rock mechanics. John Wiley & Sons 342.
- Cruciani, F., Barchi, M.R., 2016. The Lamu Basin deepwater fold-and-thrust belt: An example of a margin-scale, gravity-driven thrust belt along the continental passive margin of East Africa. *Tectonics* 35, 491–510. <https://doi.org/10.1002/2015TC003856>
- Croizé, D., Bjørlykke, K., Jahren, J. and Renard, F., 2010, Experimental mechanical and chemical compaction of carbonate sand. *Journal of Geophysical Research: Solid Earth*, 115, B11204, doi:10.1029/2010JB007697
- Croker, P. F., 1995, The Clare Basin: a geological and geophysical outline, in P.F. Croker, and P.M. Shannon, eds., *The petroleum geology of Ireland's offshore basins: Geological Society of London Special Publication no. 93*, p. 327-339

(D)

- Dahlen, F.A., 1990. Critical taper model of fold-and-thrust belts and accretionary wedges. *Annu Rev Earth Planet Sci* 18, 55–99
- Damuth, J.E., 1994. Neogene gravity tectonics and depositional processes on the deep Niger Delta continental margin. *Marine and Petroleum Geology* 11, 320-346
- Darin, M.H., Umhoefer, P.J., n.d. Structure and kinematic evolution of the southern Sivas fold-thrust belt, Sivas Basin, Central Anatolia, Turkey 26.
- Darnault, R., Callot, J-P., Ballard, J-F., Fraise, G., Mengus, J-M., Ringenbach, J-C., 2016. Control of syntectonic erosion and sedimentation on kinematic evolution of a multidecollement thrust zone: Analogue modeling of folding in the southern subandean of Bolivia. *Journal of Structural Geology*, Elsevier, 2016, 89, pp.30-43. [10.1016/j.jsg.2016.05.009](https://doi.org/10.1016/j.jsg.2016.05.009)
- Dasgupta, S.; Chatterjee, R.; Mohanty, S.P. Magnitude, mechanisms and prediction of abnormal pore pressure using well data in the Krishna Godavari Basin, East coast of India. *AAPG Bull.* 2016, 100, 1833–1855
- Dasgupta, T., Mukherjee, S., 2020. Compaction of Sediments and Different Compaction Models, in: *Sediment Compaction and Applications in Petroleum Geoscience, Advances in Oil and Gas Exploration & Production*. Springer International Publishing, Cham, pp. 1–8. https://doi.org/10.1007/978-3-030-13442-6_1
- Davies, J.L. 1980. Geographical variations in coastal development. Longman, London, 212p. → Correct Davis in the text
- Davies, R.J., Stewart, S.A., 2005. Emplacement of giant mud volcanoes in the South Caspian Basin: 3D seismic reflection imaging of their root zones. *Journal of the Geological Society* 162, 1–4. <https://doi.org/10.1144/0016-764904-082>
- Davis, D., Suppe, J., Dahlen, F.A., 1983. Mechanics of fold-and-thrust belts and accretionary wedges. *J. Geophys. Res.* 88 (B2), 1153–1172
- Davis, D. M., and T. Engelder, 1985, The role of salt in fold-and-thrust belts: *Tectonophysics*, 119, 67–88.
- Davison, I., 2009. Faulting and fluid flow through salt. *Journal of the Geological Society* 166, 205–216. <https://doi.org/10.1144/0016-76492008-064>

- Davison, I., Alsop, G.I., Evans, N., Safaricz, M., 2000. Overburden deformation patterns and mechanisms of salt diapir penetration in the Central Graben North Sea. *Marine and Petroleum Geology* 17, 601–618.
- Day-Stirrat, R, J., 2011. Diagenetic and Seismic Concerns Associated with Interpretation of Deeply Buried ‘Mobile Shales,’ in: *Shale Tectonics*. American Association of Petroleum Geologists, pp. 5–27. <https://doi.org/10.1306/13231306M93730>
- De Mets, C., R. G. Gordo, A. F. Argus, and S. Stein, 1990, Current plate motions: *Journal of Geophysical International*, v. 101, p. 425–478
- Dehandschutter, B., Vanduycke, S., Sintubin, M., Vandenberghe, N., Wouters, L., 2005. C.K. Morley et al. *Earth-Science Reviews* 176 (2018) 19–50 Brittle fractures and ductile shear bands in argillaceous sediments: inferences from Oligocene Boom Clay (Belgium). *J. Struct. Geol.* 27 (6), 1095–1112.
- Delisle, G., Teschner, M., Faber, E., Panahi, B., Guliev, I., Aliev, C., 2010. First approach in quantifying fluctuating gas emissions of methane and radon from mud volcanoes in Azerbaijan. *AAPG Memoir* 93 209–222.
- Deng, Y.F., Cui, Y.J., Tang, A.M., Li, X.L., Sillen, X., 2012. An experimental study on the secondary deformation of Boom clay. *Applied Clay Science* 59–60, 19–25. <https://doi.org/10.1016/j.clay.2012.02.001>
- Desbois, G., Urai, J.L., Kukla, P.A., 2009. Morphology of the pore space in claystones – evidence from BIB/FIB ion beam sectioning and cryo-SEM observations. *eEarth Discuss.* 4, 1–19. <https://doi.org/10.5194/eed-4-1-2009>
- Desbois, G., Závada, P., Schléder, Z., Urai, J.L., 2010. Deformation and recrystallization mechanisms in actively extruding salt fountain: Microstructural evidence for a switch in deformation mechanisms with increased availability of meteoric water and decreased grain size (Qum Kuh, central Iran). *Journal of Structural Geology* 32, 580–594. <https://doi.org/10.1016/j.jsg.2010.03.005>
- Deville, E. et al. (2003) ‘The origin and processes of mud volcanism: new insights from Trinidad’, *Geological Society, London, Special Publications*, 216(1), pp. 475–490. doi: 10.1144/gsl.sp.2003.216.01.31
- Deville É., A Prinzhofer. (2003). Les volcans de boues: *Pour la Science*, Juin 2003, M 02687-308, 26-31
- Deville E., A. Mascle, S.-H. Guerlais, C. Decalf, B. Colletta (2003a). Lateral Changes of Frontal Accretion and Mud Volcanism Processes in the Barbados Accretionary Prism and some Implications. In: C. Bartonini, R.T. Buffler and J. Blickwede, Eds. *The circum-Gulf of Mexico and the Caribbean. Hydrocarbon habitats, basin formation, and plate tectonics. AAPG Memoir* 79, 656-674.
- Deville, E., A. Battani, R. Griboulard, S. Guerlais, J.P. Herbin, J.P. Houzay, C. Muller, A. Prinzhofer (2003b) Mud volcanism origin and processes: New insights from Trinidad and the Barbados Prism. in P. Van Rensbergen, R.R. Hillis, A.J. Maltman, C. Morley (eds.), *Spec. Pub. Geological Society* (London), *Subsurface Sediment Mobilization*, 216, 475-490
- Deville, E. et al. (2006) ‘Liquefied vs stratified sediment mobilization processes: Insight from the South of the Barbados accretionary prism’, *Tectonophysics*, 428(1–4), pp. 33–47. doi: 0.1016/j.tecto.2006.08.011.

- Deville, E. (2009) 'Mud Volcano Systems', in Lewis, N., and Moretti, A. (eds) *Volcanoes: Formation, Eruptions and Modelling*. Nova Science Publishers, pp. 95-125 (404).
- Deville, J.P., Fritz, B., Jarrett, M., Development of Water-Based Drilling Fluids Customized for Shale Reservoirs. 2011. SPE Drilling & Completion 26(4):484-491. DOI: [10.2118/140868-PA](https://doi.org/10.2118/140868-PA)
- Deville, E., Mascle, A., (2011). The Barbados Ridge: a mature accretionary wedge in front of the Lesser Antilles Active Margin (Chapter 21). In: Bally, A.W., Roberts, D.G. (Eds.), Special Volume: Principles of Geologic Analysis. Elsevier, pp. 581e607. <http://dx.doi.org/10.1016/B978-0-444-53042-4.00021-2>
- Deville, E., Mascle, A., Callec, Y., Huyghe, P., Lallemand, S., Lerat, O., Mathieu, X., Padron de Carillo, C., Patriat, M., Pichot, T., Loubrieux, B., Granjeon, D., 2015. Tectonics and sedimentation interactions in the east Caribbean subduction zone: An overview from the Orinoco delta and the Barbados accretionary prism. *Marine and Petroleum Geology* 64, 76–103. <https://doi.org/10.1016/j.marpetgeo.2014.12.015>
- Devlin, W.J., Cogswell, J.M., Gaskins, G.M., Isaksen, G.H., Pitcher, D.M., Puls, D.P., Stanley, K.O., 1999. South Caspian Basin: Young, Cool, and Full of Promise. *GSA TODAY* 9.
- Dewangan. P., Ramprasad, T., Ramana M.V., Mazumdar, A., Desa, M., Badesab, F.K., 2010. Seabed morphology and gas venting features in the continental slope region of Krishna-Godavari basin, Bay of Bengal: Implications in gas–hydrate exploration *Marine and Petroleum Geology* 27 (2010) 1628-1641
- Dewey, J.F. and Bird, J.M., 1970, Mountain belts and the new global tectonics: *J. Geophysical Research* (75) p. 2625-2647.
- Dewey, J. F., M. R. Hempton, W. S. F. Kidd, F. Saroglu, and A. M. C. Sengor, (1986). Shortening of continental lithosphere: The neotectonics of Eastern Anatolia—a young collision zone, in *Collision Tectonics*, Geological Society special publications no: 19, edited by M. P. Coward and A. C. Ries, 3 – 36.
- Dickinson, G. (1953) Geological Aspects of Reservoir Pressure in Gulf Coast Louisiana. *Am. Assoc. Pet. Geol. Bull.*, 37, 410-432
- Dickinson, W.R. (1974a) Sedimentation within and beside ancient and modern magmatic arcs. *Society of Economic Paleontologists and Mineralogists Special Publication*, 19, 230–239.
- Dickinson, W.R. (1974b) Plate tectonics and sedimentation. *Society of Economic Paleontologists and Mineralogists Special Publication*, 22, 1–27.
- Dickinson, W. R. (2008), Accretionary Mesozoic-Cenozoic expansion of the Cordilleran continental margin in California and adjacent Oregon, *Geosphere*, 4, 329–353
- Dietz, (1963). Collapsing Continental Rises: An Actualistic Concept of Geosynclines and Mountain Building. *Journal of Geology* 1963
- Dietz, (1963). Meteorite Impacts, Lunar Maria, Lopoliths and Ocean Basins (response to Gallant). *Nature* 1963
- Dietz, (1963). A Theory of Ocean Basin Origin. *Undersea Technology* 1963
- Dietz, (1963). Origin of the Continental Slopes. Presented at the American Association of Petroleum Geology convention 1963
- Dimitrov, L. I. (2002) 'Mud volcanoes—the most important pathway for degassing deeply buried sediments', *Earth-Science Reviews*, 59(1–4), pp. 49–76. doi: 10.1016/S0012-8252(02)00069-7

- DiPietro, J., 2018. *Geology and Landscape Evolution (2nd Edition) Paperback* ISBN: 9780128111918, eBook ISBN: 9780128111925
- Direen, N.G., Stagg, H.M.J., Symonds, P.A. and Colwell, J.B., 2011. Dominant symmetry of a conjugate southern Australian and East Antarctic magma-poor rifted margin segment. *Geochem. Geophys. Geosyst.*, 12, Q02006.
- Direen, N.G., Borissova, I., Stagg, H.M.J., Colwell, J.B. and Symonds, P.A., 2007. Nature of the continent–ocean transition zone along the southern Australian continental margin: a comparison of the Naturaliste Plateau, SW Australia, and the central Great Australian Bight sectors. In: *Imaging, Mapping and Modelling Continental Lithosphere Extension and Breakup* (G.D. Karner, G. Manatschal and L.M. Pinheiro, eds). *Geol. Soc. London Spec. Publ.*, 282, 235–261.
- Dolan, P., Burggraf, D., Soofi, K., Fitzsimmons, R., Aydemir, E., Al, S.O., Strickland, L., 2004. Challenges to exploration in frontier basins – the Barbados accretionary prism. In: *AAPG International Conference, October 24–27, 2004, Cancun, Mexico*, (6 pp.).
- Dolati, A., 2010, *Stratigraphy, structural geology and low-temperature thermochronology across the Makran accretionary wedge in Iran [Ph.D. thesis]: Zürich, Switzerland, Eidgenössische Technische Hochschule (ETH)*, 306 p
- Dorsey, R. J., and T. A. LaMaskin (2007), Stratigraphic record of Triassic-Jurassic collisional tectonics in the Blue Mountains province, northeastern Oregon, *Am. J. Sci.*, 307, 1167–1193
- Doust, H., Omatsola, E., 1989. Niger delta, Divergent/Passive Margin Basins. *AAPG Memoir*. pp. 201–238
- Drozdowski, G., 1979. Grundmuster der Falten – und Bruchstrukturen im Ruhrkarbon. *Zeitschrift deutsche. Geologische Gesellschaft*, 130, 51-67.
- Dubacq, B., Plunder, A., 2018. Controls on Trace Element Distribution in Oxides and Silicates. *J Petrology* 59, 233–256. <https://doi.org/10.1093/petrology/egy027>
- Duerto, L. ; McClay, K. 2002. 3D geometry and evolution of shale diapirs in the Eastern Venezuelan basin AAPG annual convention, Houston, Abstract. CD-ROM
- Duerto, L., 2007. *Shale tectonics, eastern Venezuelan basin (Ph.D.)*. Royal Holloway, University of London.
- Duerto, L., McClay, K., 2009. The role of syntectonic sedimentation in the evolution of doubly vergent thrust wedges and foreland folds. *Marine and Petroleum Geology* 26 (7), 1051–1069
- Duerto, L., McClay, K., 2011. Role of the shale tectonics on the evolution of the Eastern Venezuelan Cenozoic thrust and fold belt. *Marine and Petroleum Geology, Thematic Set on: Tectonics, basinal framework, and petroleum systems of eastern Venezuela, the Leeward Antilles, Trinidad and Tobago, and offshore areas* 28, 81–108. <https://doi.org/10.1016/j.marpetgeo.2009.11.005>
- Duval, B., Cramez, C. & Jackson, M.P.A. 1992. Raft tectonics in the Kwanza Basin, Angola. *Marine and Petroleum Geology*, 9, 389-404.

(E)

- Edwards, M.B. 1976. Growth faults in upper Triassic deltaic sediments, Svalbard. *American Association of Petroleum Geologists Bulletin*, 60, 341-355
- Egan S.S., Jon Mosar, M.F. Brunet, T. Kangarli, 2009. Subsidence and uplift mechanisms within the South Caspian Basin: insights from the onshore and offshore Azerbaijan region. *Geological Society, London, Special Publications* 312: 219-240

- Ekeocha, N.E., 2014. Geotechnical Implications of Using Shale as Subgrade Materials 04, 6.
- Ellouz-Zimmermann N, Deville E, Müller C, Lallemand S, Subhani AB, Tabreez AR (2007a) Impact of sedimentation on convergent margin tectonics: example of the Makran Accretionary Prism (Pakistan). In: Lacombe O , Lavé J, Roure F, Vergès J (eds) Thrust belts and foreland basins: from fold kinematics to hydrocarbon systems. Springer, Berlin, pp 325–348
- Elsley, G.R., Tieman, H., 2010. A Comparison of Prestack Depth and Prestack Time Imaging of the Paktoa Complex, Canadian Beaufort MacKenzie Basin 93, 79–90.
<https://doi.org/10.1306/13231309M933419>
- Emery, K.O., Uchupi, E., Phillips, J., Bowin, C.O., Mascle, J., 1975. Continental margin off western Africa; Angola to Sierra Leone. AAPG Bulletin 59, 2209-2265
- Epard, J.L., Groshong, R.H., 1995. Kinematic model of detachment folding including limb rotation, fixed hinges and layer-parallel strain. Tectonophysics 247, 85–103
- Ercilla, G., B. Alonso, and J. Baraza, 1992, Sedimentary evolution of the northwestern Alboran Sea during the Quaternary: Geo-Marine Letters, v. 12, p. 144–149
- Ershov, A. V., Brunet, M.-F., Korotaev, M. V., Ikishin, A. M. & Bolotov, S. N. 1999. Late Cenozoic burial history and dynamics of Northern Caucasus molasse basin: implications for foreland basin modelling. Tectonophysics, 313, 219–241
- Escosa, F.O., Rowan, M.G., Giles, K.A., Deatrick, K.T., Mast, A.M., Langford, R.P., Hearon, T.E., Roca, E., 2019. Lateral terminations of salt walls and megaflaps: An example from Gypsum Valley Diapir, Paradox Basin, Colorado, USA. Basin Res 31, 191–212.
<https://doi.org/10.1111/bre.12316>
- Espurt, N., Callot, J.-P., Roure, F., Totterdell, J.M., Struckmeyer, H.I.M., Vially, R., 2012. Transition from symmetry to asymmetry during continental rifting: an example from the Bight Basin–Terre Adélie (Australian and Antarctic conjugate margins). Terra Nova 24, 167–180.
<https://doi.org/10.1111/j.1365-3121.2011.01055.x>
- Espurt, N., Callot, J.-P., Totterdell, J., Struckmeyer, H., Vially, R., 2009. Interactions between continental breakup dynamics and large-scale delta system evolution: Insights from the Cretaceous Ceduna delta system, Bight Basin, Southern Australian margin: CONTINENTAL BREAKUP AND DELTA SYSTEM. Tectonics 28, n/a-n/a. <https://doi.org/10.1029/2009TC002447>
- Etiope, G., Feyzullayev, A., Baciu, C.L., and Milkov, A.V., 2004, Methane emission from mud volcanoes in eastern Azerbaijan: Geology, v. 32, no. 6, p. 465–468
- Etiope, G. et al. (2009) ‘Terrestrial methane seeps and mud volcanoes: A global perspective of gas origin’, Marine and Petroleum Geology, 26(3), pp. 333–344. doi: 10.1016/j.marpetgeo.2008.03.001
- Evamy, B.D., Haremboure, J., Kamerling, P., Knaap, W.A., Molloy, F.A., Rowlands, P.H., 1978. Hydrocarbon Habitat of Tertiary Niger Delta. AAPG Bulletin 62, 1–39.
<https://doi.org/10.1306/C1EA47ED-16C9-11D7-8645000102C1865D>
- Ewing, T.E., 1986. Structural Styles of the Wilcox and Frio Growth-Fault Trends in Texas: Constraints on Geopressured Reservoirs.

(F)

- Fan, C.Y.; Wang, Z.L.; Wang, A.G.; Fu, S.T.; Wang, L.Q.; Zhang, Y.S.; Kong, X.X.; Zhang, X. Identification and calculation of transfer overpressure in the northern Qaidam Basin, northwest China. AAPG Bull. 2016, 100, 23–39

- Faas, R.W., O'Brien, N.R., 1991. The Signatures of Clay Microstructure—Overview, *Microstructure of Fine-grained Sediments*. Springer, pp. 3–32.
- Faugeres, J.C., Gonthier, E., Griboulard, R., Masse, L., 1993. Quaternary sandy deposits and canyons on the Venezuelan margin and South Barbados accretionary prism. *Mar. Geol.* 110 (1-2), 115-142
- Faulds, J. E., and C. D. Henry (2008), Tectonic influences on the spatial and temporal evolution of the Walker Lane: An incipient transform fault along the evolving Pacific-North American plate boundary, in *Ores and Orogenesis: Circum-Pacific Tectonics, Geologic Evolution and Ore Deposits*, edited by J. E. Spencer, and S. R. Titley, Ariz. Geol. Soc. Dig., 22, 437–470
- Falvey, D.A., 1974 - The development of continental margins in plate tectonic theory. *The APEA Journal*, vol. 14, pp. 95-107.
- Fernandez-Ibanez, F., J. I. Soto, M. D. Zoback, and J. Morales, 2007, Present-day stress field in the Gibraltar arc: *Journal of Geophysical Research*, v. 112, doi:10.1029/2006JB004683
- Fernández-Ibáñez, F., Soto, J.I., 2017. Pore pressure and stress regime in a thick extensional basin with active shale diapirism (western Mediterranean). *Bulletin* 101, 233–264. <https://doi.org/10.1306/07131615228>
- Fertl, W.H. (1976) *Abnormal Formation Pressures*, *Developments in Petroleum Science*, 2, Elsevier, Amsterdam
- Festa, A., Pini, G.A., Ogata, K., Dilek, Y., 2019. Diagnostic features and field-criteria in recognition of tectonic, sedimentary and diapiric mélanges in orogenic belts and exhumed subduction-accretion complexes. *Gondwana Research* 7X, xxx-yyy.
- Fisher, A.T., Hounslow, M.W., 1990a. Transient fluid flow through the toe of the Barbados accretionary complex: constraints from the Ocean Drilling Program Leg 110 heat flow studies and simple models. *J. Geophys. Res.* 95, 8845–8858.
- Fisher, A., Hounslow, M., 1990b. Heat flow through the toe of the Barbados accretionary complex. In: *Proceedings Initial Reports (Part B) Ocean Drilling Project*, Sci. Results. 110. pp. 345–363.
- Ford, M., 2004, Depositional wedge tops: Interaction between low basal friction external orogenic wedges and flexural foreland basins: *Basin Research*, v. 16, p. 361–375, doi:10.1111/j.1365-2117.2004.00236.x
- Fraser, A.R. and Tilbury, L.A., 1979. Structure and stratigraphy of the Ceduna Terrace region, Great Australian Bight. *The APEA Journal*, 19, 53–65.
- Fukuchi, R., Yamaguchi, A., Yamamoto, Y., Ashi, J., 2017. Paleothermal structure of the Nankai inner accretionary wedge estimated from vitrinite reflectance of cuttings. *Geochemistry Geophysics Geosystems* 18, 3185–3196. <https://doi.org/10.1002/2017GC006928>.

(G)

- Garcia-Duenas, V., J. C. Balanya, and J. M. Martinez-Martinez, 1992, Miocene extensional detachments in the outcropping basement of the northern Alboran Basin (Betics) and their tectonic implications: *Geo-Marine Letters*, v. 12, p. 88–95.
- Ge, H.X., Jackson, M.P.A. & Vendeville, B.C. 1997. Kinematics and dynamics of salt tectonics driven by progradation. *American Association of Petroleum Geologists Bulletin*, 81, 398-423

- Gealy, B.L., n.d. Topography of the continental slope in northwest Gulf of Mexico. Geological Society of America Bulletin 203–228. Geomorphology and Morphotectonic Analysis of north Borneo, 2016. 140.
- Gieskes, J.M., Vrolijk, P., Blanc, G., 1990. Hydrogeochemistry of the northern Barbados accretionary complex transect: Ocean Drilling Project Leg 110. J. Geophys. Res. Solid Earth 95 (B6), 8809–8818
- Giles, M.R., 1997, Diagenesis: A quantitative perspective - Implications for basin modelling and rock property prediction. Kluwer Academic Publisher, Dordrecht, 526 p
- Giles, K. A., and T. F. Lawton, 2002, Halokinetic sequence stratigraphy adjacent to the El Papalote diapir, northeastern Mexico: American Association of Petroleum Geologists Bulletin, 86, 823–840.
- Giles, K.A., Rowan, M.G., 2012. Concepts in halokinetic-sequence deformation and stratigraphy. Geological Society, London, Special Publications 363, 7–31. <https://doi.org/10.1144/SP363.2>
- Gill, W.D. (1979) Syndepositional sliding and slumping in the West Clare Namurian Basin, Ireland. Geol. Surv. Ireland Spec. Pap., 4, 31
- Giraldo, C., Alvarez, E., Odehnal, M., Gonzalez, G., De Lisa, V., Hernandez, G., 2000. New Insight Into the Mud Diapirs Exploration in the Eastern Venezuela Basin. Annual Meeting Expanded Abstracts - American Association of Petroleum Geologists, 55.
- Golonka, Jan, 1999. Abstract: Geodynamic Evolution of the South Caspian Basin. Bulletin 83. <https://doi.org/10.1306/E4FD36E9-1732-11D7-8645000102C1865D>
- Golonka, J., 2007. Phanerozoic Paleoenvironment and Paleolithofacies Maps. Mesozoic. Mapy paleoœrodowiska i paleolitofacji fanerozoiku. Mezozoik. Geologia-2007-Tom 33-Zeszyt 2-211–264
- Gonthier, E., Faugeres, J.C., Bobier, C., Griboulard, R., Huyghe, P., Masse, L., Pujol, C., 1994. Le prisme d'accretion tectonique Sud-Barbade. Rev. Aquitaine Ocean 1, 105 pages
- Gonzalez-Mieres, R., Suppe, J., 2006. Relief and shortening in detachment folds. J. Struct. Geol. 28, 1785–1807.
- Goultly, N.R., Ramdhan, A.M., Jones, S.J., 2013. Chemical compaction of mudrocks in the presence of overpressure. Pet. Geosci. 18, 471–479
- Goultly, N.R., Sargent, C., Andras, P., Aplin, A.C., 2016. Compaction of diagenetically altered mudstones - Part 1: Mechanical and chemical contributions. Marine Petrol. Geol. 77, 703–713.
- Gradstein, F.M., Ogg, J.G. and Smith, A.G., 2004. A geologic time scale 2004. Cambridge University Press, 589p.
- Graham, R., Jackson, M., Pilcher, R., Kilsdonk, B., 2012. Allochthonous salt in the sub-Alpine fold–thrust belt of Haute Provence, France. Geological Society, London, Special Publications 363, 595–615. <https://doi.org/10.1144/SP363.30>
- Grando, G., McClay, K., 2007. Morphotectonics domains and structural styles in the Makran accretionary prism, offshore Iran. Sedimentary Geology - SEDIMENT GEOL 196, 157–179. <https://doi.org/10.1016/j.sedgeo.2006.05.030>
- Gräsle, W., Plischke, I., 2011. LT-A Experiment: Mechanical Behavior of Opalinus Clay, Data report from Phase 15. Mont Terri Technical Note TN 2010-86.
- Graue, K., 2000. Mud volcanoes in deepwater Nigeria. Marine and Petroleum Geology 17, 959–974. [https://doi.org/10.1016/S0264-8172\(00\)00016-7](https://doi.org/10.1016/S0264-8172(00)00016-7)

- Grauls, D. and Cassignol, C. (1992) Fluid Pressure Induced Open Fracture Anomaly. Characterization from Well Data and Seismic Velocities. Mechanisms and Implications. Bulletin Elf Aquitaine, 16, 276-284, December 1992
- Grauls, D.J.; Baleix, J.M. Role of overpressures and in situ, stresses in fault-controlled hydrocarbon migration: A case study. Mar. Pet. Geol. 1994, 11, 734–742
- Grauls, D., 1999. Overpressures: Causal Mechanisms, Conventional and Hydromechanical Approaches. Oil & Gas Science and Technology - Rev. IFP 54, 667–678.
<https://doi.org/10.2516/ogst:1999056>
- Gregory, A.S., Whalley, W.R., Watts, C.W., Bird, N.R.A., Hallett, P.D., Whitmore, A.P., 2006. Calculation of the compression index and precompression stress from soil compression test data. Soil & Tillage Research 89, 45–57. <https://doi.org/10.1016/j.still.2005.06.012>
- Griboulard, R., Bobier, C., Faugeres, J.C., Vernet, G., 1991. Clay diapiric structures within the strike-slip margin of the southern Barbados prism. Tectonophysics 192, 383–400.
- Griboulard, R., Gonthier, E., Le Drezen, E., Faugeres, J.C., Bobier, C., 1996. Le Prisme d'accrétion tectonique Sud-Barbade. Atlas d'images acoustiques. Revue Aquitaine-Océans (2) (78 pp.)
- Guillon, S. and Keskes, N. (2004) 'Sismage and the 3D Visualization at Total', in AAPG International Conference, pp. 1–3.
- Gutscher, M.-A., Dominguez, S., Westbrook, G.K., Le Roy, P., 2009a. Deep structure, re-cent deformation and analog modeling of the Gulf of Cadiz accretionary wedge: implications for the 1755 Lisbon earthquake. Tectonophysics 475, 85–97. <http://dx.doi.org/10.1016/j.tecto.2008.11.031>.

(H)

- Haack, R.C., Sundararaman, P., Diedjomahor, J.O., Xiao, H., Gant, N.J., May, E.D., Kelsch, K., 2000. Niger Delta petroleum systems, Nigeria. In: Mello, M.R., Katz, B.J. (Eds.), Petroleum systems of South Atlantic margins. vol. 73. AAPG Memoir, pp. 213–231
- Hall, R., and C. K. Morley, 2004, Sundaland basins, in P. Clift, P. Wang, W. Kuhnt, and D. E. Hayes, eds., Continent ocean interactions within the east Asian marginal seas: American Geophysical Union Geophysical Monograph 149, p. 55–85. DOI: 10.1029/149GM04
- Haq, B.U., Hardenbol, J. and Vail, P.R., 1988. Mesozoic and Cenozoic chronostratigraphy and eustatic cycles. In: Wilgus, C.K., Hastings, B.S., Kendall, C.G.St.C., Posamentier, H.W., Ross, C.A. and Van Wagoner, J.C. (Eds), Sea-level changes: an integrated approach. Society of Economic Paleontologists and Mineralogists, Special Publication 42, 71–108.
- Harding, R., Huuse, M., 2015. Salt on the move: Multi stage evolution of salt diapirs in the Netherlands North Sea. Marine and Petroleum Geology 61, 39–55.
<https://doi.org/10.1016/j.marpetgeo.2014.12.003>
- Harms, J.C., Cappel, H.N., Francis, D.C., 1984b. The Makran coast of Pakistan: its stratigraphy and hydrocarbon potential. In: Haq, B.U., Milliman, J.D. (Eds.), Marine Geology and Oceanography of Arabian Sea and Coastal Pakistan. Van Nostrand Reinhold, New York, pp. 3–26
- Harris, P.T., Heap, A.D., Post, A., Whiteway, T., Potter, A. and Bradshaw, M. 2007. Marine zone management and the EPBC Act: How environmental marine geological information reduces risk in petroleum exploration. The APPEA Journal, 329-344

- Harrison, J.C., Bally, A.W., 1988. Cross sections of the Parry Islands fold belt on Melville Island. *Canadian Petroleum Geology Bulletin*, 36, 311-332.
- He, W., Mei, L., Zhu, G., Yang, S., Hu, Z., Xiao, S. & Zou, Y. 2011. Study on tectonic and evolution characteristics of basins in Andaman Sea. *Fault-Block & Gas Field* 18, 178–82.
- He, W., and Zhou, J. (2018). Structural features and formation conditions of mud diapirs in the Andaman Sea Basin. *Geological Magazine*, 156(4), 659-668. doi:10.1017/S0016756818000018
Check the date of Zhou on the text
- He, W., Zhou, J., 2019. Structural features and formation conditions of mud diapirs in the Andaman Sea Basin. *Geological Magazine* 156, 659–668.
<https://doi.org/10.1017/S0016756818000018>
- Hedberg, H. D. (1974) 'Relation of Methane Generation to Undercompacted Shales, Shale Diapirs, and Mud Volcanoes', *AAPG Bulletin*, 58(4), pp. 661–673. doi: 10.1306/83D91466-16C7-11D7-8645000102C1865D
- Heidari, M., Nikolinakou, M.A., Hudec, M.R., Flemings, P.B., 2016. Geomechanical analysis of a welding salt layer and its effects on adjacent sediments. *Tectonophysics* 683, 172–181.
<https://doi.org/10.1016/j.tecto.2016.06.027>
- Henry P., Siegfried Lallemand, Ko-ichi Nakamura, Urumu Tsunogai, Stephane Mazzotti, Kazuo Kobayashi, 2002. Surface expression of fluid venting at the toe of the Nankai wedge and implications for flow paths. *Marine Geology* 187 (2002) 119-143
- Hermanrud, C.; Wensaas, L.; Teige, G.M.G.; Nordgård, H.M.; Hansen, S.; Vik, E. Shale porosities from well logs on Haltenbanken (O_shore Mid-Norway) show no influence of overpressuring. In *Abnormal pressures in Hydrocarbon Environments*; Law, B.E., Ulmishek, G.F., Slavin, V.I., Eds.; AAPG Memoir 70: Tulsa, OK, USA, 1998; pp. 65–85
- Hesse, S., Back, S., Franke, D., 2010. The structural evolution of folds in a deepwater fold and thrust belt – a case study from the Sabah continental margin offshore NW Borneo, SE Asia. *Marine and Petroleum Geology* 27, 442–454. <https://doi.org/10.1016/j.marpetgeo.2009.09.004>
- Higgins, G.E., J.B. Saunders (1974). Mud Volcanoes: Their nature and origin. *Verhandlungen Naturforschenden Gesellschaft in Basel*, 84, 101-152
- Higgins, S., Clarke, B., Davies, R.J., Cartwright, J., 2009. Internal geometry and growth history of a thrust-related anticline in a deep water fold belt. *J. Struct. Geol.* 31 (12), 1597–1611
- Hill, A.J., 1995. Bight Basin. In Drexel, J.F. and Preiss, W.V., eds., *The geology of South Australia. Vol. 2, The Phanerozoic.* South Australia Geological Survey Bulletin, 54, 133–149
- Hinz, K., Fritsch, J., Kempter, E.H.K., Manav Mohammad, A., Meyer, J., Mohammad. D., Vosberg, U., Weber, J. Benavidez, J. 1989. Thrust tectonics along the northwestern continental margin of Sabah/Borneo. *Geologische Rundschau*, 78, 705-730
- Hoa, T.T.K., n.d. Structural evolution of shale diapirs from reactive rise to mud volcanism: 3D seismic data the Baram delta, offshore Brunei Darussalam 19.
- Homza, T.X., Wallace, W.K., 1997. Detachment folds with fixed hinges and variable detachment depth, northeastern Brooks Range, Alaska. *J. Struct. Geol.* 19, 337–354
- Hongxing Ge, Martin P. A. Jackson, 1997. Kinematics and Dynamics of Salt Tectonics; Driven by Progradation. *Bulletin* 81 (1997). <https://doi.org/10.1306/522B4361-1727-11D7-8645000102C1865D>

- Hooper, R.J., Fitzsimmons, R.J., Grant, N., Vendeville, B.C., 2002. The role of deformation in controlling depositional patterns in the south-central Niger Delta, West Africa. *Journal of Structural Geology* 24, 847–859. [https://doi.org/10.1016/S0191-8141\(01\)00122-5](https://doi.org/10.1016/S0191-8141(01)00122-5)
- Hower, J., Eslinger, E.V., Hower, M.E., Perry, E.A., 1976. Mechanism of burial metamorphism of argillaceous sediments, 1. Mineralogical and chemical evidence. *Geol. Soc. Am. Bull.* 87, 725–737
- Hubbert, M.K., 1937. Theory of scale models as applied to the study of geologic structures. *GSA Bulletin* 48, 1459–1520. <https://doi.org/10.1130/GSAB-48-1459>
- Hubbert, M.K., Rubey, W.W., 1959. Mechanics of fluid-filled porous solids and its application to overthrust faulting I. *Geol. Soc. Am. Bull.* 70, 115–166
- Hudec, M. R., M. P. A. Jackson, and D. D. Schultz-Ela, 2009. The paradox of minibasin subsidence into salt: Clues to the evolution of crustal basins: *Geological Society of America Bulletin*, 121, 201–221, doi:10.1130/B26275.1.
- Hudec, M.R., Jackson, M.P.A., 2007. Terra infirma: Understanding salt tectonics. *Earth-Science Reviews* 82, 1–28. <https://doi.org/10.1016/j.earscirev.2007.01.001>
- Hudec, M.R., Jackson, M.P.A., 2006. Advance of allochthonous salt sheets in passive margins and orogens. *AAPG Bulletin* 90, 1535–1564. <https://doi.org/10.1306/05080605143>
- Hudec, M.R., Jackson, M.P.A., and Schttltz-Ela, D.D., 2009, The paradox of minibasin subsidence into salt: Clues to the evolution of crustal basins: *Geological Society of America Bulletin*, v. 121, p. 201–221, <https://doi.org/10.1130/B26275.1>
- Hudec, M.R., Jackson, M.P.A., Cottington, N., Vendeville, B.C., Schultz-Ela, D.D., Dooley, T.P., University of Texas at Austin, Bureau of Economic Geology, American Association of Petroleum Geologists, Applied Geodynamics Laboratory, 2011. *The salt mine: a digital atlas of salt tectonics*. Bureau of Economic Geology, Jackson School of Geosciences, University of Texas at Austin ; American Association of Petroleum Geologists, Austin, Tex.; Tulsa, Okla.
- Hsu, K.J., 1968. The principles of mélanges and their bearing on the Franciscan-Knoxville paradox. *Geol. Soc. Amer. Bull.* 79, 1063–1074.
- Hughes, M. G., Nichol, S., Przeslawski, R., Totterdell, J., Heap, A., Fellows M., and Daniell, J., 2009. Ceduna Sub-basin: Environmental Summary. *Geoscience Australia, Record 2009/09*
- Humphreys, E. D. (2008), Cenozoic slab windows beneath the western United States, in *Ores and Orogenesis: Circum-Pacific Tectonics, Geologic Evolution and Ore Deposits*, edited by J. E. Spencer and S. R. Titley, *Ariz. Geol. Soc. Dig.*, 22, 389–396
- Huyghe, P., Griboulard, R., Faugeres, J.C., Gonthier, E., Bobier, C., 1996. Geometrie des bassins transportes a l'aplomb de la terminaison meridionale du prisme de la Barbade. *Bull. Soc. Geol. Fr.* 167 (3), 348-359
- Huyghe, P., Mugnier, J.L., Griboulard, R., Deniaud, Y., Gonthier, E., Faug_eres, J.C., 1999. Review of the tectonic control and sedimentary patterns in Late Neogene piggyback basins on the Barbados ridge complex, *Caribbean Basins: Sedimentary Basins of the World*, 4 edited by P. Mann (Series Editor: K.J. Hsü), pp. 369-388
- Huyghe, P., Foata, M., Deville, E., Mascle, G., CarambaWorking Group, 2004. Channel profiles through the active thrust front of the southern Barbados prism. *Geology* 32 (5), 429-432

(I)

- Ikari, M.J., Saffer, D.M., Marone, C., 2009a. Frictional and hydrologic properties of clayrich fault gouge. *J. Geophys. Res.* 114. <http://dx.doi.org/10.1029/2008JB006089>
- Ikari, M.J., Saffer, D.M., Marone, C., 2009b. Frictional and hydrologic properties of clayrich fault gouge. *J. Geophys. Res. Solid Earth* 114 (B5).
- Ivanov, M.K., Limonov, A.F., van Weering, Tj.C.E., 1996. Comparative characteristics of the Black Sea and Mediterranean Ridge mud volcanoes. *Marine Geology, The Mediterranean Ridge Diapiric Belt* 132, 253–271. [https://doi.org/10.1016/0025-3227\(96\)00165-X](https://doi.org/10.1016/0025-3227(96)00165-X)

(J)

- Jabatan Sains Bumi, UKM Sabah, Beg Berkunci No. 62, 88996, Kota Kinabalu, Tongkul, F., 1990. Structural style and tectonics of Western and Northern Sabah. *BGSM* 27, 227–239. <https://doi.org/10.7186/bgsm27199011>
- Jackson, C.A.-L., Lewis, M.M., 2012. Origin of an anhydrite sheath encircling a salt diapir and implications for the seismic imaging of steep-sided salt structures, Egersund Basin, Northern North Sea. *Journal of the Geological Society* 169, 593–599. <https://doi.org/10.1144/0016-76492011-126>
- Jackson, C.A.-L., Jackson, M.P.A., Hudec, M.R., 2015. Understanding the kinematics of salt-bearing passive margins: A critical test of competing hypotheses for the origin of the Albian Gap, Santos Basin, offshore Brazil. *Geological Society of America Bulletin* 127, 1730–1751. <https://doi.org/10.1130/B31290.1>
- Jackson, M.EA. & Talbot, C.J. 1986. External shapes, strain rates and dynamics of salt structures. *Geological Society of America Bulletin*, 97, 305-323
- Jackson, M.P.A., Hudec, M.R., 2017. *Salt Tectonics: Principles and Practice*. Cambridge University Press, Cambridge. <https://doi.org/10.1017/9781139003988>
- Jackson, M.P.A., Vendeville, B.C., 1994. Regional extension as a geologic trigger for diapirism. *GSA Bulletin* 106, 57–73. [https://doi.org/10.1130/0016-7606\(1994\)106<0057:REAAGT>2.3.CO;2](https://doi.org/10.1130/0016-7606(1994)106<0057:REAAGT>2.3.CO;2)
- Jackson, M.P.A., Vendeville, B.C., Schultz-Ela, D.D., 1994. Structural Dynamics of Salt Systems. *Annual Review of Earth and Planetary Sciences* 22, 93–117. <https://doi.org/10.1146/annurev.ea.22.050194.000521>
- Jackson, M. P. A., and C. J. Talbot, 1991, A glossary of salt tectonics: Austin, TX, The University of Texas at Austin, Bureau of Economic Geology, Geologic Circular 91-4, 44 p.
- Jahani, S., Hassanpour, J., Mohammadi-Firouz, S., Letouzey, J., Frizon de Lamotte, D., Alavi, S.A., Soleimany, B., 2017. Salt tectonics and tear faulting in the central part of the Zagros Fold-Thrust Belt, Iran. *Marine and Petroleum Geology* 86, 426–446. <https://doi.org/10.1016/j.marpetgeo.2017.06.003>
- Jahren, J., Thyberg, B., Marcussen, Ø., Winje, T., Bjørlykke, K., Faleide, J.I., n.d. From Mud to Shale: the Role of Microquartz Cementation; #50206 (2009) 29.
- James, D.M.D., Muzium Brunei, Brunei Shell Petroleum Company, 1984. The Geology and hydrocarbon resources of Negara Brunei Darussalam. Muzium Brunei, Bandar Seri Begawan.
- Jong, K.A.D., Scholten, R., 1973. *Gravity and Tectonics*. John Wiley & Sons Inc, New York.
- Jong, J., Kessler, F.L., Goldbach Geoconsultants O&G and Lithium Exploration, Germany, 2019. The Setap Shale Formation on either side of the Baram Line Divide: Facies aspects and tectonic implications. *BGSM* 67, 53–65. <https://doi.org/10.7186/bgsm67201907>

- Judd, A. G. and Hovland, M. (2007) 'Seabed fluid flow: the impact of geology, biology and the marine environment', *Cambridge University Press*, (February), pp. 1–442. doi: 10.1007/s00254-004-1086-0

(K)

- Kameda, J., Yamaguchi, A., Saito, S., Sakuma, H., Kawamura, K., Kimura, G., 2011. A new source of water in seismogenic subduction zones: A SOURCE OF WATER IN SEISMOGENIC ZONE. *Geophys. Res. Lett.* 38, n/a-n/a. <https://doi.org/10.1029/2011GL048883>
- Karam, P., Mitra, S., 2016. Experimental studies of the controls of the geometry and evolution of salt diapirs. *Marine and Petroleum Geology* 77, 1309–1322. <https://doi.org/10.1016/j.marpetgeo.2016.05.010>
- Keen, C.E., G.S. Stockmal, H. Wellsink, G. Quinlan, and B. Mudford, Deep crustal structure of the rifted margin northeast of Newfoundland results from LITHOPROBE East, *Can. J. Earth Sci.*, 24, 1537-1549, 1987.
- Kehle, R.O., 1970. Analysis of Gravity Sliding and Orogenic Translation. *GSA Bulletin* 81, 1641–1664. [https://doi.org/10.1130/0016-7606\(1970\)81\[1641:AOGSAO\]2.0.CO;2](https://doi.org/10.1130/0016-7606(1970)81[1641:AOGSAO]2.0.CO;2)
- Kehle, R.O. 1989. The origin of salt structures. In: Schremer, C.B. (ed.) *Evaporites and hydrocarbons*. Columbia University Press, New York, 345-404.
- Keller, L.M., Schuetz, P., Erni, R., Rossell, M.D., Lucas, F., Gasser, P., Holzer, L., 2013. Characterization of multi-scale microstructural features in Opalinus Clay. *Microporous Mesoporous Mater.* 170, 83–94
- Kent, D. V., and F. M. Gradstein (1985), A Cretaceous and Jurassic geochronology, *Geol. Soc. Am. Bull.*, 96, 1419–1427, doi:10.1130/0016-7606 (1985)96<1419:ACAJG>2.0.CO;2
- Kergaravat, C., Ribes, C., Callot, J.-P., and Ringenbach, J.-C., 2017, Tectono-stratigraphic evolution of salt-controlled minibasins in a fold and thrust belt, the Oligo-Miocene central Sivas Basin: *Journal of Structural Geology*, v. 102, p. 75–97, <https://doi.org/10.1016/j.jsg.2017.07.007>
- Khalilov, N.V., Kerimov, A.A., 1983. Origin of mud volcanism and diapirism. *International Geology Review* 25, 877–881. <https://doi.org/10.1080/00206818309466779>
- Khan, P. & Chakraborty, P. 2005. Two-phase opening of Andaman Sea: a new seismotectonic insight. *Earth & Planetary Science Letters* 229, 259–71.
- Kim, Y., Lee, E.Y., 2018. Numerical analysis of sedimentary compaction: Implications for porosity and layer thickness variation. *Journal of the Geological Society of Korea* 54, 631–640. <https://doi.org/10.14770/jgsk.2018.54.6.631>
- King, R.C., Tingay, M.R.P., Hillis, R.R., Morley, C.K., Clark, J., 2010. Present-day stress orientations and tectonic provinces of the NW Borneo collisional margin. *J. Geophys. Res.* 115, B10415. <https://doi.org/10.1029/2009JB006997>
- King, R., Morley, C.K., 2017. Wedge Geometry and Detachment Strength in Deepwater Fold-thrust Belts: *Earth Science Reviews*. 165. pp. 268–279
- King, R.C. and Backe, G., 2010. A balanced 2D structural model of the Hammerhead Delta-Deepwater Fold-Thrust Belt, Bight Basin, Australia. *Aust. J. Earth Sci.*, 57, 1005–1012.
- King, S.J. and Mee, B.C., 2004. The seismic stratigraphy and petroleum potential of the Late Cretaceous Ceduna Delta, Ceduna Sub-basin, Great Australian Bight. In: Boulton, P.J., Johns, D.R. and Lang, S.C. (Eds), *Eastern Australasian Basins Symposium II*. Petroleum Exploration Society of Australia, Special Publication, 63–73.

- Kinsman, D.J.J. (1975) Rift valley basins and sedimentary history of trailing continental margins, in Fischer, A.G. and Judson, S., eds., *Petroleum and global tectonics*. Princeton, NJ, Princeton University Press, 83–126
- Kirkham, C. B. (2015) 'A 3D seismic interpretation of mud volcanoes within the western slope of the Nile Cone'. Cardiff University
- Klemperer, S.L. (1989) Short Paper: seismic reflection evidence for the location of the Iapetus suture west of Ireland. *J. Geol. Soc. London*, 146, 409–412
- Knapp, C. C., Knapp, J. H. & Connor, J. A. 2004. Crustal-scale structure of the South Caspian Basin revealed by deep seismic reflection profiling. *Marine and Petroleum Geology*, 21, 1073–1081
- Knox, G.J. & Omatsola, E.M. 1989. Development of the Cenozoic Niger Delta in terms of the 'Escalator Regression' model and impact on hydrocarbon distribution. In: Van der Linden, W.J.M., Cloetingh, S.A.P.L., Kaasschieter, J.P.K., & Van der Gun, J.A.M. (eds) *Proceedings KNGMG symposiums coastal lowlands, geology and geotechnology*. Kluwer Academic Publishers, Amsterdam, 181-202.
- Kopf, A., and J. H. Behrmann, 2000, Extrusion dynamics of mud volcanoes on the Mediterranean Ridge accretionary complex, in B. Vendeville, Y. Mart, and J.-L. Vigneresse, eds., *From the Arctic to the Mediterranean: Salt, shale, and igneous diapirs in and around Europe*: Geological Society Special Publication 174, p. 169–204
- Kopf, A.J., 2002. Significance of Mud Volcanism. *Reviews of Geophysics* 40, 2-1-2–52. <https://doi.org/10.1029/2000RG000093>
- Kopf, A., Deyhle, D., 2002. Back to the roots: boron geochemistry of mud volcanoes and its implications for mobilization depth and global B cycling. *Chem. Geol.* 192, 195–210.
- Kopf, A., M. Ben Clennell, and K. M. Brown, 2005, Physical properties of muds extruded from mud volcanoes: Implications for episodicity of eruptions and relationship to 1066 seismicity, in *Mud volcanoes, geodynamics and seismicity: NATO Science Series 51*, p. 263–283
- Kopp, C., Fruehn, J., Flueh, E.R., Reichert, C., Kukowski, N., Bialas, J., Klaeschen, D., 2000. Structure of the Makran subduction zone from wide-angle and reflection seismic data. *Tectonophysics* 329 (1–4), 171–191
- Kovacevic, M.A., n.d. Seismic characterisation and tectonic significance of listric fault systems in the Ceduna sub-basin 27.
- Kruger, S.W., Grant, N.T., 2012. The growth history of toe thrusts of the Niger Delta and the role of pore pressure. In: McClay, K., Shaw, J., Suppe, J. (Eds.), *Thrust-Related Folding*. AAPG Mem. Vol. 94. pp. 357–390
- Kyi Khin, Khin Zaw, Lin Thu Aung, 2017. Chapter 4 Geological and tectonic evolution of the Indo-Myanmar Ranges (IMR) in the Myanmar region. Geological Society, London, *Memoirs* 48, 65–79. <https://doi.org/10.1144/M48.4>

(L)

- Labaume, P., Maltman, A.J., Bolton, A., Tessier, D., Ogawa, Y., Takizawa, S., 1997. Scaly fabrics in sheared clays from the decollement zone of the Barbados accretionary prism. *Proceedings of the Ocean Drilling Program, Scientific Results, Proceedings of the Ocean Drilling Program, scientific results, Northern Barbados Ridge; covering Leg 156 of the cruises of the drilling vessel JOIDES Resolution, Bridgetown, Barbados, to Bridgetown, Barbados, sites 947-949, 24 May-24 July 1994* 156, 59.

- Lahann, R.W., Swarbrick, R.E., 2011. Overpressure generation by load transfer following framework weakening due to smectite diagenesis. *Geofluids* 11, 362–375. *Earth-Science Reviews* 176 (2018) 19–50
- Lahann, R.W. Gulf of Mexico overpressure and clay diagenesis without unloading: An anomaly? *AAPG Bull.* 2017, 101, 1859–1877
- Lambiase J., Ridha S. Riadi, Nadia Nirsal & Salahuddin Husein, 2017. Transgressive successions of the Mahakam Delta Province, Indonesia. From: Hampson, G. J., Reynolds, A. D., Kostic, B. & Wells, M. R. (eds) 2017. *Sedimentology of Paralic Reservoirs: Recent Advances*. Geological Society, London, Special Publications, 444, 335–348. <https://doi.org/10.1144/SP444.2>
- Lanadito, A.P., Trisnasih, A., Putra, C.M.E., Harun, M.R., Hasani, N., Suseno, P., Wiguna, R.R.S., Handayani, T., n.d. Mahakam Delta system: the integration of outcrops, modern depositional processes and subsurface data 76.
- Larrasoaña, J.C., Roberts, A.P., Musgrave, R.J., Gràcia, E., Piñero, E., Vega, M., Martínez-Ruiz, F., 2007. Diagenetic formation of greigite and pyrrhotite in gas hydrate marine sedimentary systems. *Earth and Planetary Science Letters* 261, 350–366. <https://doi.org/10.1016/j.epsl.2007.06.032>
- Laubscher, H.P., 1977. Fold development in the Jura. *Tectonophysics* 37, 337–362
- Laurich, B., 2015. *Evolution of Microstructure and Porosity in Faulted Opalinus Clay*. RWTH Aachen University, Aachen, Germany (PhD thesis, 209 pp.)
- Laurich, B., Urai, J.L., Nussbaum, C., 2017. Microstructures and deformation mechanisms in Opalinus Clay: insights from scaly clay from the Main Fault in the Mont Terri Rock Laboratory (CH). *Solid Earth* 8, 27–44.
- Law, B.E.; Spencer, C.W. Abnormal pressures in hydrocarbon environments. In *Abnormal Pressures in Hydrocarbon Environments*; Law, B.E., Ulmishek, G.F., Slavin, V.I., Eds.; AAPG Memoir 70: Tulsa, OK, USA, 1998; pp. 1–11
- Lee, E.Y., Novotny, J. and Wagreich, M., 2019, *Subsidence Analysis and Visualization - For Sedimentary Basin Analysis and Modelling*. Springer, Cham, 56 p
- Legeay, E., Pichat, A., Kergaravat, C., Ribes, C., Callot, J.-P., Ringenbach, J.-C., Bonnel, C., Hoareau, G., Poisson, A., Mohn, G., Crumeyrolle, P., Kavak, K.S., Temiz, H., 2019a. Geology of the Central Sivas Basin (Turkey). *Journal of Maps* 15, 406–417. <https://doi.org/10.1080/17445647.2018.1514539>
- Legeay, E., Ringenbach, J.-C., Kergaravat, C., Pichat, A., Mohn, G., Kavak, K., Callot, J.-P., 2019b. Structure and kinematics of the Central Sivas Basin (Turkey): A mixed fold- and salt-and-thrust belt. *AAPG ACE* 2019.
- Legeay, E., Ringenbach, J.-C., Kergaravat, C., Pichat, A., Mohn, G., Vergés, J., Kavak, K.S., Callot, J.-P., 2019c. Structure and kinematics of the Central Sivas Basin (Turkey): salt deposition and tectonics in an evolving fold-and-thrust belt. *Geological Society, London, Special Publications* SP490-2019–92. <https://doi.org/10.1144/SP490-2019-92>
- Lemaître, J., Desmorat, R., 2005. *Engineering Damage Mechanics: Ductile, Creep, Fatigue and Brittle Failures*. Springer, Berlin, New York
- Lewis, N., Moretti, A. (Eds.), 2009. *Volcanoes: formation, eruptions and modelling*. Nova Science Publishers, New York.

- Li, C., Luo, X., Zhang, L., Wang, B., Guan, X., Luo, H., Lei, Y., 2019. Overpressure Generation Mechanisms and Its Distribution in the Paleocene Shahejie Formation in the Linnan Sag, Huimin Depression, Eastern China. *Energies* 12, 3183. <https://doi.org/10.3390/en12163183>
- Littke, R., Bayer, U., Gajewski, D. & Nelskamp, S. 2008. Dynamics of Complex Intracontinental Basins: The Central European Basin System. Springer, Berlin.
- Lohest, M., 1921, A propos des plis diapirs. Rappel de quelques principes de tectonique: Société Géologique de Belgique *Annales*, 44, B94–B107.
- Lord, S.A., 2015. Diapirs and Salt Domes, The Mechanism of Formation. SAND2015-2108C.
- Luo, X.R.; Vasseur, G. Modeling of pore pressure evolution associated with sedimentation and uplift in sedimentary basins. *Basin Res.* 1995, 7, 35–52
- Luo, X.R.; Dong, W.L.; Yang, J.H.; Yang, W. Overpressuring mechanisms in the Yinggehai Basin, South China Sea. *AAPG Bull.* 2003, 87, 629–645
- Luo, X.R. Allogenic overpressuring associated with faulting and geological consequences. *Acta Geol. Sin.* 2004, 78, 641–648
- Luo, X.R.; Vasseur, G. Contributions of compaction and aquathermal pressuring to geopressure and the influence of environmental conditions. *AAPG Bull.* 1992, 76, 1550–1559

(M)

- MacDonald, J., Backé, G., Holford, S., Hillis, R., 2012. Geomechanical modelling of fault reactivation in the Ceduna Sub-basin, Bight Basin, Australia. *Geological Society of London Special Publications* 367, 71–89. <https://doi.org/10.1144/SP367.6>
- MacDonald, J., Holford, S., King, R., 2012. Structure and Prospectivity of the Ceduna Delta-Deep-Water Fold-Thrust Belt Systems, Bight Basin, Australia. *GCSSEPM*. <https://doi.org/10.5724/gcs.12.32.0779>
- MacDonald, J.D., 2013. Origin and structure of the Ceduna delta system, offshore South Australia. The University of Adelaide, Faculty of Science, The Australian School of Petroleum.
- MacDonald, J.D., Holford, S.P., Green, P.F., Duddy, I.R., King, R.C., Backé, G., 2013. Detrital zircon data reveal the origin of Australia's largest delta system. *Journal of the Geological Society* 170, 3–6. <https://doi.org/10.1144/jgs2012-093>
- Magara, K. *Compaction and Fluid Migration: Practical Petroleum Geology*; Elsevier Science: Amsterdam, The Nederland, 1978; pp. 1–215.
- Magara K (1980) Comparison of porosity depth relationships of shale and sandstone. *J Pet Geol* 3:175–185
- Maloney, D., Davies, R., Imber, J., Higgins, S., King, S., 2010. New insights into deformation mechanisms in the gravitationally driven Niger Delta deep-water fold and thrust belt. *AAPG Bull.* 94, 1401–1424
- Maloney, D.P., 2011. Seismic Analysis of the Niger Delta Gravitational Detachment System. Durham theses. Durham University 274 pp. <http://etheses.dur.ac.uk/3212/>
- Maltman, A., Labaume, P., Housen, B., 1997. In: Shipley, T.H., Ogawa, Y., Blum, P., Bahr, J.M. (Eds.), 22. Structural Geology of the Décollement at the Toe of the Barbados Accretionary Prism. 156. pp. 279–292 *Proc. Ocean Drill. Prog., Sci. Res*
- Maltman, A.J., Bolton, A., 2003. How sediments become mobilized. *Geological Society, London, Special Publications* 216, 9–20. <https://doi.org/10.1144/GSL.SP.2003.216.01.02>

- Mann, D.M. and Mackenzie, A.S. (1990) Prediction of Pore Fluid Pressures in Sedimentary Basins. *Marine and Petroleum Geology*, 7, 55-65
- Martinelli, G., Judd, A., 2004. Mud volcanoes of Italy. *Geological Journal* 39, 49–61. <https://doi.org/10.1002/gj.943>
- Martinsen, O.J. (1989) Styles of soft-sediment deformation on a Namurian (Carboniferous) delta slope, Western Irish Namurian Basin, Ireland. In: *Deltas: Sites and Traps for Fossil Fuels* (Eds M.K.G. Whateley and K.T. Pickering), *Geol. Soc. Lond. Spec. Publ.*, 41, 167–177
- Martinsen, O.J., Lien, T., Walker, R.G. and Collinson, J.D. (2003) Facies and sequential organization of a mudstonedominated slope and basin floor succession: the Gull Island Formation, Shannon Basin, Western Ireland. *Mar. Petrol. Geol.*, 20, 789–807
- Martinsen, O.J., Pulham, A.J., Elliott, T., Haughton, P., Pierce, C., Lacchia, A.R., Barker, S., Latre, A.O., Kane, I., Shannon, P., Sevastopulo, G.D., 2017. Deep-water clastic systems in the Upper Carboniferous (Upper Mississippian–Lower Pennsylvanian) Shannon Basin, western Ireland. *Bulletin* 101, 433–439. <https://doi.org/10.1306/021417DIG17099>
- Mascle, A., Moore, J.C., Shipboard Scientific Party, 1988. Site 672. In: *Proceedings of the Ocean Drilling Program, Part A, Initial Report*, vol. 110. Ocean Drilling Program, College Station, Texas, pp. 205-310
- Mascle, A., Endignoux, L., Chennouf, T., 1990. Frontal accretion and piggyback basin development at the southern edge of the Barbados ridge accretionary complex. In: Moore, J.C., Mascle, A., et al. (Eds.), *Proc. of the ODP, Sci. Results, Ocean Drilling Project, 110*. Ocean Drilling Program, College Station, TS, pp. 17-28
- Masson F, Anvari M, Djamour Y, Walpersdorf A, Tavakoli F, Daignières M, Nankali H, Van Gorp S (2007) Large-scale velocity field and strain tensor in Iran inferred from GPS measurements: new insight for the present-day deformation pattern within NE Iran. *Geophys J Int* 170: 436–440
- Matthews, K.J., Hale, A.J., Gurnis, M., Muller, R.D. and DiCaprio, L., 2011. Dynamic subsidence of eastern Australia during the Cretaceous. *Gondwana Res.*, 19, 372–383.
- Mauffret, A., A. Ammar, C. Gorini, and H. Jabour, 2007, The Alboran Sea (westernMediterranean) revisited with a view from the Moroccan margin: *Terra Nova*, v. 19, p. 195–203. McClay, K., T. Dooley, A. Ferguson, and J. Poblet, 2000, Tectonic evolution of the Sanga Sanga block, Mahakam delta, Kalimantan, Indonesia: *AAPG Bulletin*, v. 84, p. 765–786
- Maurin, T., Rangin, C., 2009. Structure and kinematics of the Indo-Burmese Wedge: Recent and fast growth of the outer wedge. *Tectonics* 28. <https://doi.org/10.1029/2008TC002276>
- Mazzini, A. and Etiope, G. (2017) ‘Mud volcanism: An updated review’, *Earth-Science Reviews*. Elsevier B.V., 168, pp. 81–112. doi: 10.1016/j.earscirev.2017.03.001
- McClay, K., Dooley, T. & Zamora, G. 2003. Analogue models of delta systems above ductile substrates. In: Van Rensbergen, E, I-Lrllis, R.R., Maltman, A.J. & Morley, C.K. (eds) *Subsurface Sediment Mobilization*. Geological Society, London, Special Publications, 216, 411-428
- McClay, K., Dooley, T., Fer, A., 2000. Tectonic Evolution of the Sanga Sanga Block, Mahakam Delta, Kalimantan, Indonesia. *Bulletin* 84. <https://doi.org/10.1306/A96733EC-1738-11D7-8645000102C1865D>
- McClay, K. R., T. Dooley, and G. Lewis (1998), Analog modeling of progradational delta systems, *Geology*, 26, 771 – 774, doi:10.1130/0091-7613(1998)026<0771:AMOPDS>2.3.CO;2.
- McKerrow, W. S., and N. J. Soper, 1989, The Iapetus suture in the British Isles: *Geological Magazine*, v. 126, p. 1-8

- McNeill, L., Goldfinger, C., Kulm, L., Yeats, R., 2000. Tectonics of the Neogene Cascadia forearc basin: Investigations of a deformed Late Miocene unconformity. *Geological Society of America Bulletin - GEOL SOC AMER BULL* 112, 1209–1224. [https://doi.org/10.1130/0016-7606\(2000\)112<1209:TOTNCF>2.3.CO;2](https://doi.org/10.1130/0016-7606(2000)112<1209:TOTNCF>2.3.CO;2)
- McQuarrie N, Stock JM, Verdel C, Wernicke BP (2003) Cenozoic evolution of Neotethys and implications for the causes of plate motions. *Geophys Res Lett* 30:2036. doi:10.1029/2003GL017992 (in Burg et al., 2013)
- McQuarrie, N., 2004. Crustal scale geometry of the Zagros fold-thrust belt, Iran. *J. Struct. Geol.* 26, 519–535
- Meissner, F.F., 1981. Abnormal pressures produced by hydrocarbon generation and maturation and their relation to processes of migration and accumulation. *AAPG Bull.* 65, 24–67
- Mesri, G., Vardhanabhuti, B., 2009. Compression of granular materials. *CAN GEOTECH J* 46, 369–392. <https://doi.org/10.1139/T08-123>
- Meschede M. (2015) Accretionary Wedge. In: Harff J., Meschede M., Petersen S., Thiede J. (eds) *Encyclopedia of Marine Geosciences*. Springer, Dordrecht. https://doi.org/10.1007/978-94-007-6644-0_101-1
- Messent, B.E.J., 1998. Great Australian Bight: well audit. Australian Geological Survey Organisation Record 1998/37.
- Mikada, H., Moore, G.F., Taira, A., Becker, K., Moore, J.C., Klaus, A. (Eds.), 2005. Proceedings of the Ocean Drilling Program, 190/196 Scientific Results, Proceedings of the Ocean Drilling Program. Ocean Drilling Program. <https://doi.org/10.2973/odp.proc.sr.190196.2005>
- Milkov, A., 2000. Worldwide Distribution of submarine Mud Volcanoes and Associated Gas Hydrates. *Marine Geology* 167, 29–42. [https://doi.org/10.1016/S0025-3227\(00\)00022-0](https://doi.org/10.1016/S0025-3227(00)00022-0)
- Miller, J.McL., Norvick, M.S., Wilson, C.J.L., 2002. Basement controls on rifting and the associated formation of ocean transform faults—Cretaceous continental extension of the southern margin of Australia. *Tectonophysics* 359, 131–155. [https://doi.org/10.1016/S0040-1951\(02\)00508-5](https://doi.org/10.1016/S0040-1951(02)00508-5)
- Mills, P.C., 1983. Genesis and diagnostic value of soft-sediment deformation structures – a review. *Sed. Geol.*, 35, 83–104
- Mitchell, A.H.G., 1993. Cretaceous–Cenozoic tectonic events in the western Myanmar (Burma)–Assam region. *J. Geol. Soc.* 150, 1089–1102.
- Mitchell, C., Boreham, C.J., Totterdell, J., Geoscience Australia, 2009. Bight Basin geological sampling and seepage survey: RV Southern Surveyor survey SS01/2007. Geoscience Australia, Canberra.
- Mitra, S., 2002. Structural models of faulted detachment folds. *AAPG Bull.* 86, 1673–1894
- Mohr, M., Kukla, P.A., Urai, J.L., Bresser, G., 2005. Multiphase salt tectonic evolution in NW Germany: seismic interpretation and retro-deformation. *Int J Earth Sci (Geol Rundsch)* 94, 917–940. <https://doi.org/10.1007/s00531-005-0039-5>
- Mondol, N. H., K. Bjørlykke, J. Jahren, and K. Høeg, 2007, Experimental mechanical compaction of clay mineral aggregates— Changes in physical properties of mudstones during burial: *Marine and Petroleum Geology*, v. 24, p. 289–311
- Mondol, N. H., J. Jahren, K. Bjørlykke, and I. Brevik, 2008, Elastic properties of clay minerals: The Leading Edge, v. 27, p. 758–770

- Moore, J., Mascle, A., Taylor, E., Andreieff, P., Alvarez, F., Barnes, R., Beck, C., Behrmann, J., Blanc, G., Brown, K., 1987. Expulsion of fluids from depth along a subduction-zone décollement horizon. *Nature* 326 (6115), 785–788
- Moore, J.C., Moore, G.F., Cochrane, G.R., Tobin, H.J., 1995. Negative-polarity seismic reflections along faults of the Oregon accretionary prism: indicators of overpressuring. *J. Geophys. Res. Solid Earth* 100 (B7), 12895–12906.
- Moore, T.E., Wallace, W.K., Bird, K.J., Karl, S.M., Mull, C.G., and Dillon, J.T. (1994). Geology of northern Alaska, in Plafker, G., and Berg, H.C., eds., *The Geology of Alaska: Boulder, Colorado, Geological Society of America, The Geology of North America, v. G-1. p. 49-138*
- Moore, G.F., Lin Thu Aung, Fukuchi, R., Sample, J.C., Hellebrand, E., Kopf, A., Win Naing, Win Min Than, Tin Naing Tun, (2019). Tectonic, diapiric and sedimentary chaotic rocks of the Rakhine coast, western Myanmar, *Gondwana Research, Volume 74, 2019, Pages 126-143, ISSN 1342-937X, <https://doi.org/10.1016/j.gr.2019.04.006>.*
- Morgan, J.P., Coleman, J.M., Gagliano, S.M., 1968. Mudlumps: Diapiric Structures in Mississippi Delta Sediments¹, in: Braunstein, J., O’Brien, G.D. (Eds.), *Diapirism and Diapirs: A Symposium. American Association of Petroleum Geologists, pp. 145–161. <https://doi.org/10.1306/M8361C10>*
- Morgenstern N.R. & Tchalenko J.S. (1967a) Shear strength properties of natural soils and rocks, Vol. 1, 147, Norwegian Geotechnical Institute, Oslo.
- Morgenstern N.R. & Tchalenko .LS. (1967b) *Proc. R. Soc., on. A*, 300, 218.
- Morgenstern N.R. & Tchalenko J.S. (1967c) *Proc. R. Soc. Lon. A*, 300, 235.
- Morley, C. 2012. Late Cretaceous – Early Paleogene tectonic development of SE Asia. *Earth Science Reviews* 115, 37–75.
- Morley, C. 2013. Discussion of tectonic models for Cenozoic strike-slip fault-affected continental margins of mainland SE Asia. *Journal of Asian Earth Sciences* 76, 137–51.
- Morley, C. K., King, R., Hillis, R., Tingay, M. and Backe, G., 2011. Deepwater fold and thrust classification, tectonics, structure and hydrocarbon prospectivity: A Review. *Earth Science Reviews*, 104, 41-91.
- Morley, C.K., Guerin, G., 1996. Comparison of gravity-driven deformation styles and behavior associated with mobile shales and salt. *Tectonics* 15, 1154–1170. <https://doi.org/10.1029/96TC01416>
- Morley, C.K., Crevello, P., Ahmad, Z.H., 1998. Shale tectonics and deformation associated with active diapirism: the Jerudong Anticline, Brunei Darussalam. *Journal of the Geological Society* 155, 475–490. <https://doi.org/10.1144/gsjgs.155.3.0475>
- Morley, C., 2003. Mobile shale related deformation in large deltas developed on passive and active margins. *Geological Society, London, Special Publications* 216, 335–357. <https://doi.org/10.1144/GSL.SP.2003.216.01.22>
- Morley, C.K., 2007. Interaction between critical wedge geometry and sediment supply in a deep water fold belt. *Geology* 35 (2), 139–142
- Morley, C.K., Tingay, M., Hillis, R., King, R., 2008. Relationship between structural style, overpressures, and modern stress, Baram Delta Province, northwest Borneo. *J. Geophys. Res.* 113, B09410. <https://doi.org/10.1029/2007JB005324>

- Morley, C.K., King, R., Hillis, R., Tingay, M., Backe, G., 2011. Deepwater fold and thrust belt classification, tectonics, structure and hydrocarbon prospectivity: a review. *Earth Sci. Rev.* 104 (1–3), 41–91
- Morley, C.K., 2014. Outcrop examples of soft-sediment deformation associated with normal fault terminations in deepwater, Eocene turbidites: a previously undescribed conjugate fault termination style? *J. Struct. Geol.* 69, 189–208.
- Morley, C.K., von Hagke, C., Hansberry, R., Collins, A., Kanitpanyacharoen, W., King, R., 2017. Review of major shale-dominated detachment and thrust characteristics in the diagenetic zone: part I, meso- and macro- scopic scale. *Earth Sci. Rev.* (in press)
- Morley, C.K., von Hagke, C., Hansberry, R., Collins, A., Kanitpanyacharoen, W., King, R., 2018. Review of major shale-dominated detachment and thrust characteristics in the diagenetic zone: Part II, rock mechanics and microscopic scale. *Earth-Science Reviews* 176, 19–50.
<https://doi.org/10.1016/j.earsci.2017.09.015>
- Moscardelli, L., Wood, L., Mann, P., 2006. Mass-transport complexes and associated processes in the offshore area of Trinidad and Venezuela. *AAPG Bull.* 90 (7), 1059-1088
- Moss, S.J., Chambers, J.L.C., 1999. Tertiary facies architecture in the Kutai Basin, Kalimantan, Indonesia. *Journal of Asian Earth Sciences* 17, 157-181
- Mountfield, R. A., Y. M. Chevalier, G. A. Haddad, L. C. Kuo, and A. C. Weinzapfel, 2002, Petroleum systems and exploration potential of the western Alboran Basin: Marrakech International Oil and Gas Conference, Abstract Book.
- Mourgues, R., Lecomte, E., Vendeville, B., Raillard, S., 2009. An experimental investigation of gravity-driven shale tectonics in progradational delta. *Tectonophysics* 474, 643–656.
<https://doi.org/10.1016/j.tecto.2009.05.003>
- Mrazec, L., 1907. Despre cute cu simbare de străpungere [On folds with piercing cores]. *Buletinul Societății de Științe din București* 6–8.
- Muggeridge, A.; Abacioglu, Y.; England, W.; Smalley, C. The rate of pressure dissipation from abnormally pressured compartments. *AAPG Bull.* 2005, 89, 61–80
- Muntingh, A., and L. F. Brown (1993), Sequence stratigraphy of petroleum plays, post-rift Cretaceous rocks (lower Aptian to upper Maastrichtian), Orange Basin, western offshore, South Africa, in *Siliciclastic Sequence Stratigraphy—Recent Developments and Applications*, edited by P. Weimer and H. W. Posamentier, *AAPG Mem.*, 58, 71–97.
- Musgrave, A.W., Hicks, W.G., 1968. Outlining Shale Masses by Geophysical Methods¹, in: Braunstein, J., O’Brien, G.D. (Eds.), *Diapirism and Diapirs: A Symposium*. American Association of Petroleum Geologists, p. 0. <https://doi.org/10.1306/M8361C8>
- Musgrave, A.W., Hicks, W.G., 1966. Outlining Shale Masses By Geophysical Methods. Presented at the 50th Annual Meeting of the Association in New Orleans, April 26-29, 1965. Modified from Geophysics by permission of Society of Exploration Geophysicists.

(N)

- Nadeau, P.H., Peacor, D.R., Yan, J., Hiller, S., 2002. I/S precipitation in pore space as the cause of geopressuring in Mesozoic mudstones, Egersund Basin, Norwegian Continental Shelf. *Am. Mineral.* 87, 1580–1589
- Nadeau, P.H., 2011. Earths energy “Golden Zone”: a synthesis from mineralogical research. *Clay Miner.* 46, 1–24

- Naylor, M., Sinclair, H.D., 2008. Pro- vs. retro-foreland basins. Basin Research Volume20, Issue3, pp 285-303. <https://doi.org/10.1111/j.1365-2117.2008.00366.x>
- Nelson, C.H., Gutiérrez Pastor, J., Goldfinger, C., Escutia, C., 2012. Great earthquakes along the Western United States continental margin: implications for hazards, stratigraphy and turbidite lithology. Nat. Hazards Earth Syst. Sci. 12, 3191–3208. <https://doi.org/10.5194/nhess-12-3191-2012>
- Nelson, T.H., 1991. Salt tectonics and listric-normal faulting, in: Salvador, A. (Ed.), The Gulf of Mexico Basin. Geological Society of America, U.S.A, pp. 73–89. <https://doi.org/10.1130/DNAG-GNA-J.73>
- Nielsen, C., Chamot-Rooke, N. & Rangin, C. 2004. From partial to full strain partitioning along the Indo-Burmese hyper-oblique subduction. Marine Geology 209, 303–327.
- Norvick, M.S. and Smith, M.A., 2001. Mapping the plate tectonic reconstruction of southern and southeastern Australia and implications for petroleum systems. The APPEA Journal, 41, 15–35
- Nyaberi, M. D., and B. K. Rop (2014), Petroleum Prospects of Lamu Basin, South-Eastern Kenya, J. Geol. Soc. India, 83, 414–422
- Nyagah, K. (1995), Stratigraphy, depositional history and environments of deposition of Cretaceous through Tertiary strata in the Lamu Basin, southeast Kenya and implications for reservoirs for hydrocarbon exploration, Sediment. Geol., 96(1–2), 43–71

(O)

- Obiadi, I.I., Cm, O., 2016. Structural Deformation and Depositional Processes: Insights from the Greater Ughelli Depobelt, Niger Delta, Nigeria. Oil & Gas Research 2, 1–8. <https://doi.org/10.4172/2472-0518.1000118>
- Oliveira, M. J. R., P. Santarem, A. Moraes, P. V. Zalan, J. L. Caldeira, A. Tanaka, and I. J. Trosdorf, 2012, Linked extensional-compressional tectonics in gravitational systems in the Equatorial Margin of Brazil, in D. Gao, ed., Tectonics and sedimentation: Implications for petroleum systems: AAPG Memoir 100, p. 159–178, doi:10.1306/13351552M1003532.
- Onajite, E., 2014. Seismic Data Analysis Techniques in Hydrocarbon Exploration. Elsevier. <https://doi.org/10.1016/C2013-0-09969-0>
- Osborne, M. J. and Swarbrick, R. E. (1997) 'Mechanisms for Generating Overpressure in Sedimentary Basins : A Reevaluation 1', AAPG Bulletin, 6(6), pp. 1023–1041
- Ostos, M. 1990. Tectonic evolution of the south-central margin of the Caribbean based on geochemical data: Thesis of PhD, Rice University, Houston, Texas, 411 p.
- Ott, H.L., 1987. The Kutei BasinDa unique structural history. Indonesian Petroleum Association, Proceedings 16th Annual Convention, Jakarta 1, 307±317
- Ougier-Simonin, A., Renard, F., Boehm, C., Vidal-Gilbert, S., 2016. Microfracturing and microporosity in shales. Earth Sci. Rev. 162, 198–226

(P)

- Parisio, F., Samat, S., Laloui, L., 2015. Constitutive analysis of shale: a coupled damage plasticity approach. International Journal of Solids and Structures 75–76, 88–98. <https://doi.org/10.1016/j.ijsolstr.2015.08.003>
- Passchier, C.W., Trouw, R.A.J., 1998. Microtectonics. Springer-Verlag, Berlin Heidelberg. <https://doi.org/10.1007/978-3-662-08734-3>
- Paterson, D.W. 1997. Petroleum Systems of the Kutei Basin, Kalimantan, Indonesia. IPA Petroleum Systems Symposium, 709-726

- Paterson, M. S. & Wong T.F. 2005. *Experimental Rock Deformation – The Brittle Field*, 2nd ed. 348 pp. Berlin, Heidelberg, New York: Springer-Verlag. ISBN 3 540 24023 3
- Patrício, M., Mattheij, R., 2010. Crack paths in composite materials. *Eng. Fract. Mech.* 77 (12), 2251–2262.
- Peach, C.J., Spiers, C.J., 1996. Influence of crystal plastic deformation on dilatancy and permeability development in synthetic salt rock. *Tectonophysics* 256, 101–128.
[https://doi.org/10.1016/0040-1951\(95\)00170-0](https://doi.org/10.1016/0040-1951(95)00170-0)
- Peach, C.J., Spiers, C.J., Trimby, P.W., 2001. Effect of confining pressure on dilatation, recrystallization, and flow of rock salt at 150°C. *Journal of Geophysical Research: Solid Earth* 106, 13315–13328. <https://doi.org/10.1029/2000JB900300>
- Peel, F.J., 2014a. How do salt withdrawal minibasins form? Insights from forward modelling, and implications for hydrocarbon migration. *Tectonophysics* 630, 222–235.
<https://doi.org/10.1016/j.tecto.2014.05.027>
- Peel, F.J., 2014b. The engines of gravity-driven movement on passive margins: Quantifying the relative contribution of spreading vs. gravity sliding mechanisms. *Tectonophysics* 633, 126–142.
<https://doi.org/10.1016/j.tecto.2014.06.023>
- Peltonen, C., Marcussen, Ø., Bjørlykke, K., Jahren, J., 2009. Clay mineral diagenesis and quartz cementation in mudstones: The effects of smectite to illite reaction on rock properties. *Marine and Petroleum Geology* 26, 887–898. <https://doi.org/10.1016/j.marpetgeo.2008.01.021>
- Perrier R, Quiblier J (1974) Thickness changes in sedimentary layers during compaction history; methods for quantitative evaluation. *AAPG Bull* 58:507–520
- Phillips, W. E. A., C. J. Stillman, and T. Murphy, 1976, A Caledonian plate tectonic model: *Journal of the Geological Society of London*, v. 132, p. 579-609
- Pilcher, R.S., Kilsdonk, B., Trude, J., 2011. Primary basins and their boundaries in the deep-water northern Gulf of Mexico: Origin, trap types, and petroleum system implications. *Bulletin* 95, 219–240. <https://doi.org/10.1306/06301010004>
- Pindell, J. 1993. Mesozoic-Cenozoic paleogeographic evolution of northern South America. *AAPG Bulletin Abstracts* 77, 2, pp 340
- Pindell J., Higgs R. Y Dewey J. (1998). Cenozoic palinspastic reconstruction, paleogeographic evolution and hydrocarbon setting of the northern margin of South America. *SEPM Special Publication*, 58, pp 45-85.
- Pinna, G., Carcione, J. M, Poletto F. 2011. Kerogen to oil conversion in source rocks. Pore-pressure build-up and effects on seismic velocities. *Journal of Applied Geophysics* 74(4):229-235 DOI: 10.1016/j.jappgeo.2011.05.006
- Pivnik, D.A., Nyein, K., Nyunt, M., Maung, P.H., Nahm, J., Tucker, R.S., Smith, G.O., 1998. Polyphase deformation in a fore-arc/back-arc basin, Salin subbasin, Myanmar (Burma). *Am. Assoc. Pet. Geol. Bull.* 82, 1837–1856.
- Planke, S., Svensen, H., Hovland, M., Banks, D.A., Jamtveit, B., 2003. Mud and fluid migration in active mud volcanoes in Azerbaijan. *Geo-Mar Lett* 23, 258–268.
<https://doi.org/10.1007/s00367-003-0152-z>
- Platt, J. P., S. Allerton, A. Kirker, C. Mandeville, A. Mayfield, 1157 E. S. Platzman, and A. Rimi, 2003, The ultimate arc: Differential displacement, oroclinal bending, and vertical axis rotation in the external Betic-Rif arc: *Tectonics*, v. 22, 1160 p. 1017–1046. 1161

- Platt, J. P., R. Anczkiewicz, J. I. Soto, S. P. Kelley, and M. Thirlwall, 2006, Early Miocene continental subduction and rapid exhumation in the western Mediterranean: *Geology*, v. 34, p. 981–984.
- Poblet, J., Lisle, R.J., 2011. Kinematic evolution and structural styles of fold-and-thrust belts. Geological Society, London, Special Publications 349, 1–24. <https://doi.org/10.1144/SP349.1>
- Polonia, A., Nelson, C.H., Romano, S., Vaiani, S.C., Colizza, E., Gasparotto, G., Gasperini, L., 2017. A depositional model for seismo-turbidites in confined basins based on Ionian Sea deposits. *Marine Geology* 384, 177–198. <https://doi.org/10.1016/j.margeo.2016.05.010>
- Post, P., Olson, D., Lyons, K., Palmes, S., Harrison, P., Rosen, N. (Eds.), 2004. Salt Sediment Interactions and Hydrocarbon Prospectivity: Concepts, Applications, and Case Studies for the 21st Century: 24th Annual. SOCIETY OF ECONOMIC PALEONTOLOGISTS AND MINERALOGISTS. <https://doi.org/10.5724/gcs.04.24>
- Price, R.A., 1981, The Cordilleran foreland thrust and fold belt in the southern Canadian Rocky Mountains, in McClay, K.R., and Price, N.J., eds., *Thrust and Nappe Tectonics*: Geological Society [London] Special Publication 9, p. 427–448, <https://doi.org/10.1144/GSL.SP.1981.009.01.39>.
- Pulham, A.J. (1989) Controls on internal structure and architecture of sandstone bodies within Upper Carboniferous fluvial-dominated deltas, County Clare, western Ireland. In: *Deltas: Sites and Traps for Fossil Fuels* (Eds M.K.G. Whateley and K.T. Pickering), *Geol. Soc. Lond. Spec. Publ.*, 41, 179–203

(R)

- Rabinowitz, P. D., M. F. Coffin, and D. Falvey (1983), The separation of Madagascar and Africa, - *Science*, 220, 67–69, doi:10.1126/science.220.4592.67
- Racey, A., Ridd, M.F., 2015. *Petroleum geology of Myanmar*. The Geological Society, London Memoirs 45.
- Raimbourg, H., Thiéry, R., Vacelet, M., Famin, V., Ramboz, C., Boussafir, M., Disnar, J.-R., Yamaguchi, A., 2017. Organic matter cracking: A source of fluid overpressure in subducting sediments. *Tectonophysics* 721, 254–274. <https://doi.org/10.1016/j.tecto.2017.08.005>
- Raju, D. S. N., A. Bhandari, and P. Ramesh, 2005a, Table 27: Relative sea level fluctuations and hydrocarbon occurrences in the Cretaceous and Cenozoic in India (first version), in D. S. N. Raju, J. Peters, R. Shankar, and G. Kumar, eds., *An overview of litho-bio-chrono-sequence stratigraphy and sea level changes of Indian sedimentary basins: Association of Petroleum Geologists, India Special Publication 1*, 213 p
- Raju, K., Ray, D., Mudholkar, A., Murty, G., Gahalaut, V., Samudrala, K., Paropkari, A., Ramachandran, R. & Surya Prakash, L. 2012. Tectonic and volcanic implications of a cratered seamount off Nicobar Island, Andaman Sea. *Journal of Asian Earth Sciences* 56, 42–53.
- Ramberg, H., 1981. *Gravity, Deformation, and the Earth's Crust*. Academic Press Inc, London ; New York.
- Rangin, C., Maurin, T., Masson, F., 2013. Combined effects of Eurasia/Sunda oblique convergence and East-Tibetan crustal flow on the active tectonics of Burma. *J. SE Asia Earth Sci.*, 76 (2013), pp. 185-194
- Rangin, C., 2017. Active and recent tectonics of the Burma Platelet in Myanmar. In: Barber, A.J., Khin Zaw and Crow, M.J. (eds), *Myanmar – Geology, Resources and Tectonics*. Geological Society, London Geological Society, London, Memoirs 48, 53–64.

- Rao, G. N., 2001, Sedimentation, stratigraphy, and petroleum potential of Krishna-Godavari Basin, east coast of India AAPG Bulletin, v. 85, no. 9, p. 1623–1643
- Raymond, G.P., 1966. Laboratory Consolidation of Some Normally Consolidated Soils. *Can. Geotech. J.* 3, 217–234. <https://doi.org/10.1139/t66-026>
- Raymond, L.A., 1984. Melanges: their nature, origin, and significance. *Geological Society of America Special Paper* 198, 170.
- Ray, J.S., Kumar, A., Sudheer, A.K., Deshpande, R.D., Rao, D.K., Patil, D.J., Awasthi, N., Bhutani, R., Bhushan, R., Dayal, A.M., 2013. Origin of gases and water in mud volcanoes of Andaman accretionary prism: implications for fluid migration in forearcs. *Chem. Geol.* 347, 102–113.
- Raza, A., Hill, K.C. and Korsch, R.J., 1995. Mid-Cretaceous regional uplift and denudation of the Bowen–Surat basins, Queensland and its relation to Tasman Sea rifting. In: Follington, I.L., Beeston, J.W. and Hamilton, L.H. (Eds), *Bowen Basin Symposium 1995—150 years on*. Geological Society of Australia, supplement.
- Reeves, C. V., F. M. Karanja, and I. N. Macleod (1987), Geophysical evidence for a Jurassic triple-junction in Kenya, *Earth Planet. Sci. Lett.*, 81, 299–311, doi:10.1016/0012-821X(87)90166-X
- Reeves, C. V. (2014), The position of Madagascar within Gondwana and its movements during Gondwana dispersal, *J. Afr. Earth Sci.*, 94, 45–57, doi:10.1016/j.jafrearsci.2013.07.011
- Renard, F., Dysthe, D., Feder, J., Jamtveit, B., n.d. Healing of fluid-filled microcracks 7. *Retrospective Salt Tectonics, 1995.* , in: *Salt Tectonics*. American Association of Petroleum Geologists, pp. 1–28. <https://doi.org/10.1306/M65604C1>
- Renard F., Dysthe, D., Feder, J., and Jamtveit, B. (2002). Healing of fluid-filled microcracks, In: "Poromechanics II", Ed. by J.-L. Auriault et al., *Proceedings of the second Biot Conference on poromechanics*, A. A. Balkema Publishers, pp. 925-931
- Renard, F., Dysthe, D., 2003. Pressure solution. In: Middleton, G.V. (Ed.), *Encyclopedia of Sediments and Sedimentary Rocks*. Kluwer, pp. 542–543.
- Rhein, M., Stramma, L., Krahnmann, G., 1998. The spreading of Antarctic bottom water in the tropical Atlantic. *Deep-Sea Res. I* 45, 507e527
- Ribes, C., Kergaravat, C., Crumeyrolle, P., Lopez, M., Bonnel, C., Poisson, A., Kavak, K.S., Callot, J.-P., Ringenbach, J.-C., 2016. Factors controlling stratal pattern and facies distribution of fluvio-lacustrine sedimentation in the Sivas mini-basins, Oligocene (Turkey) 596–621. - <https://doi.org/10.1111/bre.12171>
- Rider, M.H. (1974) The Namurian of west County Clare. *Proc. Roy. Irish Acad.*, 74B, 125–142
- Rieke HH, Chilingarian GV (1974) *Compaction of Argillaceous Sediments*. Elsevier, New York, p 424
- Ringenbach, J.C., Callot, J.P., Group, S., 2017. Salt Tectonics in the Sivas Basin (Turkey) - Outstanding Seismic Analogues. Presented at the First EAGE/ASGA Petroleum Exploration Workshop, Luanda, Angola. <https://doi.org/10.3997/2214-4609.201702341>
- Robert, R., Souloumiac, P., Robion, P., David, C., 2019. Numerical Simulation of Deformation Band Occurrence and the Associated Stress Field during the Growth of a Fault-Propagation Fold. *Geosciences* 9, 257. <https://doi.org/10.3390/geosciences9060257>
- Roberts D.G., 2012. *Regional Geology and Tectonics: Principles of Geologic Analysis* 1st Edition. Hardcover ISBN: 9780444530424, eBook ISBN: 9780080951867
- Robertson, R. P., and K. Burke, 1989, Evolution of the southern Caribbean plate boundary vicinity of Trinidad and Tobago: AAPG Bulletin, v. 73, no. 1, p. 490–509

- Robertson, A.H.F., Kopf, A., 1998. Tectonic setting and processes of mud volcanism on the Mediterranean Ridge accretionary complex: Evidence from leg, in: Proceedings of the Ocean Drilling Program, 160 Scientific Results, Proceedings of the Ocean Drilling Program. Ocean Drilling Program, pp. 665–680. <https://doi.org/10.2973/odp.proc.sr.160.1998>
- Robinson, P.T., Malpas, J., Zhou, M.-F., Ash, C., Yang, J.-S., Bai, W.-J., 2005. Geochemistry and origin of listwanites in the Sartohay and Luobusa ophiolites, China. *Int. Geol. Rev.* 47, 177–202.
- Robinson, R., Bird, M., Oo, N., Hoey, T., Aye, M., Higgitt, D., Lu, X., Swe, A., Tun, T. & Win, S. 2007. The Irrawaddy river sediment flux to the Indian Ocean: the original nineteenth-century data revisited. *Journal of Geology* 115, 629–40.
- Rodriguez, L. 1999. Tectonic analysis, stratigraphy and depositional history of the Miocene sedimentary section, central Eastern Venezuela Basin. Unpublished PHD Thesis, University of Texas at Austin, Austin, TX, 212 p
- Rose, R., Hartono, P., 1978. Geological evolution of the Tertiary Kutai- Melawi Basin, Kalimantan, Indonesia. Indonesian Petroleum Association, Proceedings 7th Annual Convention, Jakarta 1, 225-252
- Rowan, M., Lawton, T., Giles, K., 2012. Anatomy of an exposed vertical salt weld and flanking strata, La Popa Basin, Mexico. *Geological Society of London Special Publications* 363, 33–57. <https://doi.org/10.1144/SP363.3>
- Rowan, M. G., F. J. Peel, and B. C. Vendeville, 2004, Gravity-driven fold belts on passive margins, in K. R. McClay, ed., *Thrust tectonics and hydrocarbon systems: AAPG Memoir* 82, p. 157– 182. <https://doi.org/10.1306/61EECE28-173E-11D7-8645000102C1865D>
- Rowan, M.G., 1995. Structural Styles and Evolution of Allochthonous Salt, Central Louisiana Outer Shelf and Upper Slope 199–228.
- Rowan, M.G., Giles, K.A., Hearon IV, T.E., Fiduk, J.C., 2016. Megaflaps adjacent to salt diapirs. *Bulletin* 100, 1723–1747. <https://doi.org/10.1306/05241616009>
- Rowan, M.G., Lawton, T.F., Giles, K.A., Ratliff, R.A., 2003. Near-salt deformation in La Popa basin, Mexico, and the northern Gulf of Mexico: A general model for passive diapirism. *AAPG Bulletin* 87, 733–756. <https://doi.org/10.1306/01150302012>
- Rowan, M.G., Peel, F.J., Vendeville, B.C., 2004. Gravity-driven fold belts on passive margins, in: *Thrust Tectonics and Hydrocarbon Systems*. pp. 157–182.
- Ruh, J.B., Vergés, J., Burg, J.-P., 2018. Shale-related minibasins atop a massive olistostrome in an active accretionary wedge setting: Two-dimensional numerical modeling applied to the Iranian Makran. *Geology* 46, 791–794. <https://doi.org/10.1130/G40316.1>
- Ruth, P.V.; Hillis, R.; Tingate, P. The origin of overpressure in the Carnarvon Basin, western Australia: Implications for pore-pressure prediction. *Pet. Geosci.* 2004, 10, 247–257
- Rutledge, A.K., Leonard, D.S., 2001. Role of multibeam sonar in oil and gas exploration and development. In: *Offshore Technology Conference* 12956, 12 pages

(S)

- Saffer, D.M., Tobin, H.J., 2011. Hydrogeology and Mechanics of Subduction Zone Forearcs: Fluid Flow and Pore Pressure. *Annu. Rev. Earth Planet. Sci.* 39, 157–186. <https://doi.org/10.1146/annurev-earth-040610-133408>
- Saffer, D.M., Kopf, A.J., 2016. Boron desorption and fractionation in Subduction Zone Fore Arcs: implications for the sources and transport of deep fluids. *Geochem. Geophys. Geosyst.* 17, 4992–5008.

- Sahu, J. N., 2005, Deepwater Krishna-Godavari Basin and its potential: *Petromin*, April issue, v. 31, p. 26–34
- Salager, S., François, B., Nuth, M., Laloui, L., 2013. Constitutive analysis of the mechanical anisotropy of Opalinus Clay. *Acta Geotech.*, 1–18
- Sandal, S.T. 1996. The Geology and Hydrocarbon Resources of Negara Brunei Darussalam, (1996 revision). Brunei Shell Petroleum Company/Brunei Museum, Syabas Bandar Seri Begawan, Brunei Darussalam, 243 pp
- Satyavani, N., Alekhya, G., Sain, K., 2015. Free gas/gas hydrate inference in Krishna–Godavari basin using seismic and well log data. *Journal of Natural Gas Science and Engineering* 25, 317–324. <https://doi.org/10.1016/j.jngse.2015.05.010>
- Sautter, B., Pubellier, M., Josselin, P., Dattilo, P., Kerdraon, Y., Choong, C.H., Menier D., 2017. Late Paleogene rifting along the Malay Peninsula thickened crust. *Tectonophysics* 710–711 (2017) 205–224. DOI: 10.1016/j.tecto.2016.11.035
- Sayers, J., Symonds, P., Direen, N.G. and Bernardel, G., 2001. Nature of the continent-ocean transition on the nonvolcanic rifted margin of the central Great Australian Bight. In: *Non-Volcanic Rifting of Continental Margins: A Comparison of Evidence from Land and Sea* (R.C.L. Wilson, R.B. Whitmarsh, B. Taylor and N. Froitzheim, eds). *Geol. Soc. London Spec. Publ.*, 187, 51–77.
- Sayers, J., Symonds, P., Direen, N.G. and Bernardel, G., 2001. Nature of the continent–ocean transition on the non-volcanic rifted margin of the central Great Australian Bight. In Wilson, R.C.L., Whitmarsh, R.B., Taylor, B. and Froitzheim, N., eds., *Non-volcanic rifting of continental margins: a comparison of evidence from land and sea*. Geological Society of London, Special Publications, 187, 51–77
- Sayers, C.M.; Johnson, G.M.; Denyer, G. Pre-drill pore-pressure prediction using seismic data. *Geophysics* 2002, 67, 1286–1292
- Schardt, H., 1893. *Sur l’origine des préalpes romandes: Eclogae Geologicae Helvetiae*.
- Schléder, Z., Urai, J.L., 2007. Deformation and recrystallization mechanisms in mylonitic shear zones in naturally deformed extrusive Eocene–Oligocene rocksalt from Eyvanekey plateau and Garmsar hills (central Iran). *Journal of Structural Geology* 29, 241–255. <https://doi.org/10.1016/j.jsg.2006.08.014>
- Schléder, Z., Urai, J.L., 2005. Microstructural evolution of deformation-modified primary halite from the Middle Triassic Röt Formation at Hengelo, The Netherlands. *Int J Earth Sci (Geol Rundsch)* 94, 941–955. <https://doi.org/10.1007/s00531-005-0503-2>
- Scholz, F., Hensen, C., De Lange, G.J., Haeckel, M., Liebetau, V., Meixner, A., Reitz, A., Romer, R.L., 2010. Lithium isotope geochemistry of marine pore waters – insights from cold seep fluids. *Geochim. Cosmochim. Acta* 74, 3459–3475.
- Schultz-Ela, D.D., 2003. Origin of drag folds bordering salt diapirs. *Bulletin* 87, 757–780. <https://doi.org/10.1306/12200201093>
- Schultz-Ela, D.D., Jackson, M.P.A., Vendeville, B.C., 1993. Mechanics of active salt diapirism. *Tectonophysics* 228, 275–312. [https://doi.org/10.1016/0040-1951\(93\)90345-K](https://doi.org/10.1016/0040-1951(93)90345-K)
- Schlüter, H.U., Prexl, A., Gaedicke, Ch., Roeser, H., Reichert, Ch., Meyer, H., von Daniels, C., 2002. The Makran accretionary wedge: sediment thicknesses and ages and the origin of mud volcanoes. *Marine Geology* 185, 219–232. [https://doi.org/10.1016/S0025-3227\(02\)00192-5](https://doi.org/10.1016/S0025-3227(02)00192-5)

- Screaton, E., Saffer, D., Henry, P., Hunze, S., Gemeinschaftsaufgaben-GGA, G., 2002. Porosity loss within the underthrust sediments of the Nankai accretionary complex: Implications for overpressures 4.
- Senseny, P.E., Hansen, F.D., Russell, J.E., Carter, N.L., Handin, J.W., 1992. Mechanical behaviour of rock salt: Phenomenology and micromechanisms. *International Journal of Rock Mechanics and Mining Sciences & Geomechanics Abstracts* 29, 363–378. [https://doi.org/10.1016/0148-9062\(92\)90513-Y](https://doi.org/10.1016/0148-9062(92)90513-Y)
- Sevastopulo, G., 2001. The Lower Carboniferous (Tournaisian) crinoids from Hook Head, County Wexford, Ireland
- Sharples, A.G.W.D., 2014. Tectono-stratigraphic evolution of the Cenozoic Great Australian Bight. University of Manchester. PhD Thesis. 376p.
- Shaw, H.F., Primmer, T.J., 1989. Diagenesis in shales from a partly overpressured sequence in the Gulf Coast, Texas, USA. *Marine and Petroleum Geology* 6, 121–128. [https://doi.org/10.1016/0264-8172\(89\)90015-9](https://doi.org/10.1016/0264-8172(89)90015-9)
- Shikalibeily, E. S. & Grigoriants, B. V. 1980. Principal features of the crustal structure of the South- Caspian Basin and the conditions of its formation. *Tectonophysics*, 69, 113–121
- Shipley, T.H., Ogawa, Y., Blum, P., Bahr, J.M. (Eds.), 1997. Proceedings of the Ocean Drilling Program, 156 Scientific Results, Proceedings of the Ocean Drilling Program. Ocean Drilling Program. <https://doi.org/10.2973/odp.proc.sr.156.1997>
- Silver, E.A., Beutner, E.C., 1980. Melanges. *Geology* 8, 32–34.
- Sims, D.W., Morris, A.P., Wyrick, D.Y., Ferrill, D.A., Waiting, D.J., Franklin, N.M., Colton, S.L., Umezawa, Y.T., Takanashi, M., Beverly, E.J., 2013. Analog modeling of normal faulting above Middle East domes during regional extension. *AAPG Bulletin* 97, 877–898. <https://doi.org/10.1306/02101209136>
- Sleeman, A.G., Pracht, M., Geological Survey of Ireland, 1999. Geology of the Shannon estuary: a geological description of the Shannon estuary region including parts of Clare, Limerick and Kerry : to accompany the bedrock geology 1:100,000 scale map series, sheet 17, Shannon estuary.
- Smith, G., McNeill, L., Henstock, T.J., Bull, J., 2012. The structure and fault activity of the Makran accretionary prism: THE MAKRAN ACCRETIONARY PRISM STRUCTURE. *J. Geophys. Res.* 117, n/a-n/a. <https://doi.org/10.1029/2012JB009312>
- Smith-Rouch, L.S., n.d. Oligocene–Miocene Maykop/Diatom Total Petroleum System of the South Caspian Basin Province, Azerbaijan, Iran, and Turkmenistan 33.
- Soleimany, B., Nalpas T., Sabat, F., 2013. Multidetachment analogue models of fold reactivation in transpression: The NW Persian Gulf. *Geologica Acta*, Vol. 11, No 3, 265-276. Doi:10.1344/105.000001870
- Soto, J. I., M. C. Comas, and J. de la Linde, 1996, Espesor de sedimentos en la Cuenca de Alboran mediante una con-version sismica corregida: *Geogaceta*, v. 20, p. 382–385.
- Soto, J. I., Fernandez-Ibanez, F., Talukder, A., Martínez-García, P., 2010. Miocene shale tectonics in the northern Alboran Sea (Western Mediterranean), in: *Shale Tectonics : AAPG Memoir*. pp. 119–144. <https://doi.org/10.1306/13231312M933422>
- Speed, R. C., 1985, Cenozoic collision of the Lesser Antilles arc and continental South America and the origin of the El Pillar fault: *Tectonics*, v. 4, no. 1, p. 41–69, <https://doi:10.1029/TC004i001p00041>

- Spiers, C.J., Niemeijer, A., Zhang, X., De Meer, S., 2004. Kinetics of rock deformation by pressure solution and the role of thin aqueous films, in: Proceedings of the International Symposium on Physiochemistry of Water and Dynamics of Materials and the Earth – Structures and Behaviours of the Thin Film Water. 2003, Universal Academy Press, Frontier Science Series.
- Spiers, C.J., Schutjens, P.M.T.M., 1999. Intergranular Pressure Solution in NaCl: Grain-To-Grain Contact Experiments under the Optical Microscope. *Oil & Gas Science and Technology - Rev. IFP* 54, 729–750. <https://doi.org/10.2516/ogst:1999062>
- Stagg, H.M.V., Cockshell, C.D., Willcox, J.B., Hill, A.J., Needham, D.V.L., Thomas, B., O'Brien, G.W. and Hough, L.P., 1990. Basins of the Great Australian Bight region, geology and petroleum potential. Bureau of Mineral Resources, Australia, Continental Margins Program Folio, 5.
- Stagg, H. M. J., C. D. Cockshell, J. B. Willcox, A. J. Hill, D. V. C. Needham, B. Thomas, G. W. O'Brien, and L. P. Hough (1990), Basins of the Great Australian Bight region—Geology and petroleum potential, Folio 5, Cont. Margins Program, Bur. of Miner. Resour., Geol. and Geophys., Canberra, Australia.
- Stamps, D.S., Flesch, L.M., Calais, E., Ghosh, A., 2014. Current kinematics and dynamics of Africa and the East African Rift System. *J. Geophys. Res. Solid Earth* 119, 5161–5186. <https://doi.org/10.1002/2013JB010717>
- Stanca, R., Kearns, H., Paton, D., Hodgson, N., Rodriguez, K., Hussein, A., 2016. Offshore Somalia: crustal structure and implications for thermal maturity. *First Break* 34, 61–67.
- Stein, S., C. De Mets, R. G. Gordon, J. Brodholt, D. F. Argus, J. Engel, P. Lindgreen, C. Stein, D. Werns, and D. Woods, 1988, A test of alternative Caribbean plate relative motion models: *Journal of Geophysical Research*, v. 93, p. 3041– 3050, doi:10.1029/JB093iB04p03041.
- Stewart, S., Coward, M.P., 1995. Synthesis of salt tectonics in the southern North Sea. *Marine and Petroleum Geology* 12, 457–475. [https://doi.org/10.1016/0264-8172\(95\)91502-G](https://doi.org/10.1016/0264-8172(95)91502-G)
- Stewart, S., Davies, R., 2006. Structure and emplacement of mud volcano systems in the South Caspian Basin. *Aapg Bulletin - AAPG BULL* 90, 771–786. <https://doi.org/10.1306/11220505045>
- Stewart, S.A., 2007. Salt tectonics in the North Sea Basin: a structural style template for seismic interpreters. Geological Society, London, Special Publications 272, 361–396. <https://doi.org/10.1144/GSL.SP.2007.272.01.19>
- Stille, H., 1925, The upthrust of the salt masses of Germany: *American Association of Petroleum Geologists Bulletin*, 9, 417–441.
- Struckmeyer, H.I.M., Totterdell, J.M., Blevin, J.E., Logan, G.A., Boreham, C.J., Deighton, I., Krassay, A.A. and Bradshaw, M.T., 2001. Character, maturity and distribution of potential Cretaceous oil source rocks in the Ceduna Sub-basin, Bight Basin, Great Australian Bight. In: Hill, K.C. and Bernecker, T. (Eds), *Eastern Australian Basin Symposium: a refocused energy perspective for the future*. Petroleum Exploration Society of Australia, Special Publication, 543–552.
- Sultan, N. et al. (2012) 'Mechanical behaviour of gas-charged marine plastic sediments', *Geotechnique* 2(9), pp. 751–766. doi: 10.1680/geot.12.OG.002
- Suppe, J., 1985. Principles of structural geology. Prentice-Hall, Englewood Cliffs, N.J.
- Suppe, J., 2014. Fluid overpressures and strength of the sedimentary upper crust. *J. Struct. Geol.* 69, 481–492

- Svensen, H., F. Corfu, S. Polteau, Ø. Hammer, and S. Planke (2012), Rapid magma emplacement in the Karoo large igneous province, *Earth Planet. Sci.*, 325–326, 1–9, doi:10.1016/j.epsl.2012.01.015
- Swarbrick, R.E. Challenges of Porosity-Based Pore Pressure Prediction. In Proceedings of the 63rd EAGE Conference & Exhibition, Amsterdam, The Netherlands, 11–15 June 2001
- Swarbrick, R.E., Osborne, M.J., Yardley, G.S., 2002. Comparison of overpressure magnitude resulting from the main generating mechanisms. In: Huffman, A.R., Bowers, G.L. (Eds.), *Pressure Regimes in Sedimentary Basins and their Prediction*. AAPG Mem. 76. pp. 1–12
- Swarbrick, R.E. Review of pore-pressure prediction challenges in high-temperature areas. *Lead. Edge*. 2012, 31, 1288–1294

(T)

- Tagiyev, M.F., Nadirov, R.S., Bagirov, E.B., and Lerch, I., 1997, Geohistory, thermal history and hydrocarbon generation history of the north-west South Caspian Basin: *Marine and Petroleum Geology*, v. 14, no. 4, p. 363–382
- Talbot, C., Jackson, M., 1987. Internal Kinematics of Salt Diapirs. *AAPG Bulletin* 71, 1068–1093. <https://doi.org/10.1306/703C7DF9-1707-11D7-8645000102C1865D>
- Talbot, C.J., 1981. Sliding and other deformation mechanisms in a glacier of salt, S Iran. *Geological Society, London, Special Publications* 9, 173–183. <https://doi.org/10.1144/GSL.SP.1981.009.01.16>
- Talbot, C.J., Farhadi, R., Aftabi, P., 2009. Potash in salt extruded at Sar Pohl diapir, Southern Iran. *Ore Geology Reviews* 3–4, 352–366. <https://doi.org/10.1016/j.oregeorev.2008.11.002>
- Talbot, C.J., Jackson, M.P.A., 1987. Salt Tectonics. *Scientific American* 257, 70–79.
- Talbot, C. J., 1995, Molding of salt diapirs by stiff overburden, in M. P. A. Jackson, D. G. Roberts, and S. Snelson, eds., *Salt tectonics: A global perspective*: Tulsa, OK, American Association of Petroleum Geologists, *Memoir* 65, 61–75
- Talukder, M. A. R., 2003, La provincia diapirica de lodo en la Cuenca Oeste del Mar de Alboran: Estructuras, genesis y evolucion: Ph.D. thesis, Granada University, Granada, 251p.
- Tan, D.N.K., Lamy, J. M., 1990. Tectonic evolution of the NW Sabah continental margin since the Late Eocene. *Sabah Shell Petroleum Company Ltd.*, BGSM 27, 241–260. <https://doi.org/10.7186/bgsm27199012>
- Tanahashi, M., Ishihara, T., Yuasa, M., Murakami, F. and Nishimura, A., 1997. Preliminary report of the th95 geological and geophysical survey results in the Ross sea and Dumont d'Urville sea. *Proc. NIPR Symp. Antarct. Geosci.*, 10, 36–58.
- Tapley, D., Mee, B.C., King, S.J., Davis, R.C. and Leischner, K.R., 2005. Petroleum potential of the Ceduna Sub-basin: impact of Gnarlyknots-1A. *The APPEA Journal*, 45(1), 365–380.
- Teasdale, J.P., Pryer, L.L., Stuart-Smith, P.G., Romine, K.K., Etheridge, M.A., Loutit, T.S. and Kyan, D.M., 2003. Structural framework and basin evolution of Australia's southern margin. *The APPEA Journal*, 43, 13-37.
- Terzaghi, K., 1943. *Theoretical Soil Mechanics*. John Wiley, New York
- Terzaghi, K. and Peck (1968) *Soil Mechanics in Engineering Practice*. John Wiley and Sons, New York, N.Y

- Tesei, T., Lacroix, B., Collettini, C., 2015. Fault strength in thin-skinned tectonic wedges across the smectite-illite transition: constraints from frictional experiments and critical tapers. *Geology* 43, 923–926.
- Thyberg, B., Jahren, J., Winje, T., Bjorlykke, K., Faleide, J.I., Marcussen, O., 2010. Quartz cementation in Late Cretaceous mudstones, northern North Sea: changes in rock properties due to dissolution of smectite and precipitation of microquartz crystals. *Mar. Pet. Geol.* 27, 1201–1212
- Thyberg, B., Jahren, J., 2011. Quartz cementation in mudstones: sheet-like quartz cement from clay mineral reactions during burial. *Pet. Geosci.* 17, 53–63
- Tikku, A.A. and Cande, S.C., 1999. The oldest magnetic anomalies in the Australian–Antarctic Basin: are they isochrons? *Journal of Geophysical Research*, B1, 104, 661–677.
- Tingay, M.R.P.; Hillis, R.R.; Swarbrick, R.E.; Morley, C.K.; Damit, A.R. Vertically transferred overpressures in Brunei: Evidence for a new mechanism for the formation of high-magnitude overpressure. *Geology* 2007, 35, 1023–1026
- Tingay, M.R.P.; Hillis, R.R.; Swarbrick, R.E.; Morley, C.K.; Damit, A.R. Origin of overpressure and pore-pressure prediction in the Baram province, Brunei. *AAPG Bull.* 2009, 93, 51–74
- Tingay, M.R.P.; Morley, C.K.; Laird, A.; Limpornpipat, O.; Krisadasima, K.; Pabchanda, S.; Macintyre, H.R. Evidence for overpressure generation by kerogen –to-gas maturation in the northern Malay Basin. *AAPG Bull.* 2013, 97, 639–672
- Tingay, M. R. P. et al. (2015) ‘Initiation of the Lusi mudflow disaster’, *Nature Geoscience*, 8(7), pp. 493–494. doi: 10.1038/ngeo2472
- Torrey, P. D., and C. E. Fralich, 1926, An experimental study of the origin of salt domes: *Journal of Geology*, 34, 224–234.
- Totterdell, J.M., Blevin, J.E., Struckmeyer, H.I.M., Bradshaw, B.E., Colwell, J.B., Kennard, J.M., 2000. A new sequence framework for the great Australian bight: starting with a clean slate. *The APPEA Journal* 40, 95–118. <https://doi.org/10.1071/aj99007>
- Totterdell, J., Krassay, A., 2003. The role of shale deformation and growth faulting in the Late Cretaceous evolution of the Bight Basin, offshore southern Australia. *Geological Society, London, Special Publications* 216, 429–442. <https://doi.org/10.1144/GSL.SP.2003.216.01.28>
- Totterdell, J.M. and Bradshaw, B.E., 2004. The structural framework and tectonic evolution of the Bight Basin. In Boulton, P.J., Johns, D.R. & Lang, S.C., eds., *Eastern Australasian Basins Symposium II. Petroleum Exploration Society of Australia, Special Publication*, 41–61.
- Totterdell, J., Struckmeyer, H., Boreham, C., Mitchell, C., Monteil, E., Bradshaw, B., 2008. Mid–Late Cretaceous organic-rich rocks from the eastern Bight Basin: implications for prospectivity. *Symposium EABS III PESA*, 137–158.
- Totterdell, J., Mitchell, C., 2007. Bight Basin Geological Sampling and Seepage Survey. RV Southern Surveyor Survey SS01/2007. *Geoscience Australia, Record* 2009/24
- Totterdell, J.M., et al., in prep. Bight Basin geological sampling and seepage survey, R/V Southern Surveyor Survey SS01/2007: post-survey report. *Geoscience Australia Record*, 2008.
- Totterdell, J.M., Struckmeyer, H.I.M., Boreham, C.J., Mitchell, C.H., Monteil E., Bradshaw, B.E., 2008. Mid–Late Cretaceous organic-rich rocks from the eastern Bight Basin: implications for prospectivity. *PESA Eastern Australasian Basins Symposium III. Sydney*, 14–17 September, 2008
- Traugott, M. (1996) The Pore Pressure Centroid Concept: Reducing Drilling Risks. Abstract, *Compaction and Overpressure Current Research*, 9-10 December, IFP, Paris

- Tredrea, B., Horton, P., 2019. Seismic evidence for seal and reservoir in the Late Cretaceous Ceduna Delta, Great Australian Bight. ASEG Extended Abstracts 2019, 1–13.
<https://doi.org/10.1080/22020586.2019.12073233>
- Tremosa, J., Gailhanou, H., Chiaberge, C., Castilla, R., Gaucher, E.C., Lassin, A., Gout, C., Fialips, C., Claret, F., 2020. Effects of smectite dehydration and illitisation on overpressures in sedimentary basins: A coupled chemical and thermo-hydro-mechanical modelling approach. *Marine and Petroleum Geology* 111, 166-178. <https://doi.org/10.1016/j.marpetgeo.2019.08.021>
- Tuck-Martin, A., Adam, J., Eagles, G., 2018. New Plate Kinematic Model and Tectono-stratigraphic History of the East African and West Madagascan Margins. doi: 10.1111/bre.12294
- Turner, J.P. 1995. Gravity-driven structures and rift basin evolution: Rio Muni Basin, offshore Equatorial West Africa. *American Association of Petroleum Geologists Bulletin*, 79, 1138-1158.

(U)

- Uddin, A. & Lundberg, N. 2004. Miocene sedimentation and subsidence during continent–continent collision, Bengal Basin, Bangladesh. *Sedimentary Geology* 164, 131–46.
- C
- Urai, J.L., Schlöder, Z., Spiers, C.J., Kukla, P.A., 2008. Flow and Transport Properties of Salt Rocks in R. Littke, U. Bayer, D. Gajewski, and S. Nelskamp, eds., *Dynamics of complex intracontinental basins: The central European basin system*: Berlin, Springer, 277–290. http://www.ged.rwth-aachen.de/files/publications/publication_660.pdf

(V)

- Van Rensbergen, P., Morley, C., Ang, D., Hoan, T., Lam, N., 1999. Structural evolution of shale diapirs from reactive rise to mud volcanism: 3D seismic data from the Baram delta, offshore Brunei Darussalam. *Journal of the geological society* 156, 633–650.
- Van Rensbergen, P., Morley, C.K., 2000. 3D Seismic study of a shale expulsion syncline at the base of the Champion delta, offshore Brunei and its implications for the early structural evolution of large delta systems. *Marine and Petroleum Geology* 17, 861–872.
[https://doi.org/10.1016/S0264-8172\(00\)00026-X](https://doi.org/10.1016/S0264-8172(00)00026-X)
- Van Rensbergen, P., R.R. Hillis, A.J. Maltman, C.K. Morley (2003). Subsurface sediment mobilization: introduction. in P. Van Rensbergen, R.R. Hillis, A.J. Maltman, & C. Morley, eds., *Special publication of the Geological Society (London) on Surface Sediment Mobilization*, 216, 1-8
- Van Rensbergen, P., Morley, C.K., 2003. Re-evaluation of mobile shale occurrences on seismic sections of the Champion and Baram deltas, offshore Brueni. In: van Rensbergen, P., Hillis, R.R., Maltman, A.J., Morley, C.K. (Eds.), *Subsurface Sediment Mobilization*. *Geol. Soc. Lond. Spec. Publ. Vol. 216*. pp. 395–409
- Van Wees, J.D. and Beekman, F., 2000. Lithosphere rheology during intraplate basin extension and inversion: inferences from automated modelling of four basins in western Europe. *Tectonophysics*, 320, 219–242.
- Veevers, J. J., C. Mc, A. Powell, and S. R. Roots (1991), Review of sea-floor spreading around Australia: I. Synthesis of the patterns of spreading, *Aust. J. Earth Sci.*, 38, 373 – 389, doi:10.1080/08120099108727979.
- Veevers, J.J. 1981. Morphotectonics of rifted continental margins in embryo (East Africa), youth (Africa–Arabia), and maturity (Australia). *Journal of Geology*, 89, 57– 82.

- Vendeville, B.C., Jackson, M.P.A. 1993. Rates of Extension and deposition determine whether growth faults or salt diapirs form. *Proc. Gulf Coast Sec. Soc. Econ. Paleontol. Mineral. Found. Res. Conf., 14th, Houston, Texas*. In press.
- Vendeville, B.C., Jackson, M.P.A., 1992a. The rise of diapirs during thin-skinned extension. *Marine and Petroleum Geology* 9, 331–353
- Vendeville, B.C., Jackson, M.P.A., 1992b. The fall of diapirs during thin-skinned extension. *Marine and Petroleum Geology* 9, 354–371.
- Vendeville, B. C., 2005, Salt tectonics driven by sediment progradation: Part I—Mechanics and kinematics: AAPG Bulletin, v. 89, p. 1071– 1079, this volume.
- Vigny C, Huchon P, Ruegg J, Khanbari K, Asfaw LM (2006) Confirmation of Arabia plate slow motion by new GPS data in Yemen. *J Geophys Res* 111: B02402, doi:10.1029/2004JB003229
- Virgo, S., Abe, S., Urai, J.L., 2014. The evolution of crack-seal vein and fracture networks in an evolving stress field: insights from Discrete Element Models of fracture sealing. *J. Geophys. Res.* 119 (12), 8708–8727.
- Von Hagke, C., Oncken, O., Evseev, S., 2014. Critical taper analysis reveals lithological control of variations in detachment strength: an analysis of the Alpine basal detachment (Swiss Alps). *Geochem. Geophys. Geosyst.* 15 (1), 176–191
- Von Raumer J. F., Stampfli G. M., Bussy F., 2003. Gondwana-derived microcontinents — the constituents of the Variscan and Alpine collisional orogens. *Tectonophysics*, Volume 365, Issues 1–4, Pages 7-22. [https://doi.org/10.1016/S0040-1951\(03\)00015-5](https://doi.org/10.1016/S0040-1951(03)00015-5)

(W)

- Wagner, B.H., Jackson, M.P.A., n.d. Viscous flow during salt welding. *Tectonophysics* 510, 309–326.
- Walker, L.K., Raymond, G.P., 1968. The Prediction of Consolidation Rates in a Cemented Clay. *Can. Geotech. J.* 5, 192–216. <https://doi.org/10.1139/t68-022>
- Walker, T.R., 2007. Deepwater and frontier exploration in Australia—historical perspectives, present environment and likely future trends. *The APPEA Journal*, 47 (1), 15–38.
- Waltham, D., 1997. Why does salt start to move? *Tectonophysics, Structural Controls on Sedimentary Basin Formation* 282, 117–128. [https://doi.org/10.1016/S0040-1951\(97\)00215-1](https://doi.org/10.1016/S0040-1951(97)00215-1)
- Wannamaker, P. E., R. L. Evans, P. A. Bedrosian, M. J. Unsworth, V. Maris, and R. S. McGary (2014), Segmentation of plate coupling, fate of subduction fluids, and modes of arc magmatism in Cascadia, inferred from magnetotelluric resistivity, *Geochem. Geophys. Geosyst.*, 15, 4230–4253, doi:10.1002/2014GC005509.
- Warren, J. K., 2006, *Evaporites: Sediments, resources and hydrocarbons*: Berlin, Springer, 1036 p.
- Warren, J.K., Cheung, A., Cartwright, I., 2010. Organic geochemical, isotopic, and seismic indicators of fluid flow in pressurized growth anticlines and mud volcanoes in modern deep-water slope and rise sediments of offshore Brunei Darussalam: Implications for hydrocarbon exploration in other mud- and salt-diapir provinces, in: Wood, L.J. (Ed.), *Shale Tectonics*, AAPG Memoir 93. pp. 161–194.
- Warren, J., 2016. *Evaporites, A Geological Compendium*. Springer, New York (1657pp.) Richards, L., King, R.C., Collins, A.S., Morley, C.K., Warren, J., 2015. Macrostructures vs microstructures in evaporite detachments: an example from the Salt Range, Pakistan. *J. Asian Earth Sci.* 113, 922–934

- Waschbusch, P., Beaumont, C. and Korsch, R.J., 1999. Geodynamic modelling of aspects of the New England Orogen and adjacent Bowen, Gunnedah and Surat Basins. In: Flood, P.G. (Ed.), *New England Orogen: regional geology, tectonics and metallogenesis*. Earth Sciences, University of New England, Armidale, 203–210.
- Wakabayashi, J., Dilek, Y., 2011. Introduction: characteristics and tectonic settings of melanges, and their significance for societal and engineering problems, In: Wakabayashi, J., Dilek, Y. (Eds.), *Melanges: Processes of Formation and Societal Significance*. Geol. Soc. Amer. Special Paper 480, Boulder, v-x.
- Weinzapfel, A. C., R. A. Mountfield, Y. M. Chevalier, L. C. Kuo, K. A. Soofi, G. A. Haddad, and M. O. Strickland, 2003, New insights into the hydrocarbon prospectivity of an undrilled mud diapir province, west Alboran Basin, Morocco-Spain: AAPG Annual Meeting, Abstract Book
- Weller EA (1959) Compaction of sediments. AAPG Bull 43:273–310
- Wells, R. E., D. Bukry, R. Friedman, D. Pyle, R. Duncan, P. Haeussler, and J. Wooden (2014), Geologic history of Siletzia, a large igneous province in the Oregon and Washington Coast Range: correlation to the geomagnetic polarity time scale and implications for a long-lived Yellowstone hotspot, *Geosphere*, 10(4), 679–719, doi:10.1130/GES01018.1
- Westbrook, G.K., 1975. The structure of the crust and upper mantle in the region of Barbados and the Lesser Antilles. *J. R. Astron. Soc.* 43, 201-242
- Westbrook, G.K., 1982. The Barbados Ridge Complex, tectonics of a mature forearc system. In: Leggett, J.K. (Ed.), *Sedimentation and Tectonics in Ancient and Modern Active Plate Margins*, Special Publication Geological Society of London 10, pp. 275-290
- Westbrook, G.K., Smith, M.J., Peacock, J.H., Poulter, M.J., 1982. Extensive underthrusting of undeformed sediment beneath the accretionary complex of the Lesser Antilles subduction zone. *Nature* 300, 625-628
- Westbrook, G.K., Smith, M.J., 1983. Long décollements and mud volcanoes: Evidence from the Barbados Ridge Complex for the role of high pore-fluid pressure in the development of an accretionary complex. *Geology* 11, 279–283. [https://doi.org/10.1130/0091-7613\(1983\)11<279:LDAMVE>2.0.CO;2](https://doi.org/10.1130/0091-7613(1983)11<279:LDAMVE>2.0.CO;2)
- Westbrook, G.K., 1984. Magnetic lineations and fracture zones. In: Speed, R.C., et al. (Eds.), *Lesser Antilles Arc and Adjacent Terranes: Ocean Margin Drilling Program Regional Atlas Series*, vol. 10. Marine Science International, Woods Hole, Massachusetts sheet 5.
- Westbrook, G.K., Mascle, A., Biju-Duval, B., 1984. Geophysics and the structure of the Lesser Antilles Forearc. In: Biju-Duval, B., Moore, et al. (Eds.), *Initial Reports of the Deep Sea Drilling Project* U.S. Govt. Printing Office, Washington, 78 A, pp. 23-38.
- Wibowo, H.T., Prastisho, B., Prasetyadi, C., Yudiantoro, D.F., 2018. The evolution of Sidoarjo hot mudflow (Lusi), Indonesia. *IOP Conf. Ser.: Earth Environ. Sci.* 212, 012050. <https://doi.org/10.1088/1755-1315/212/1/012050>
- Wiener, R.W., Mann, M.G., Angelich, M.T., Molyneux, J.B., 2010. Mobile Shale in the Niger Delta: Characteristics, Structure, and Evolution, in: Wood, L.J. (Ed.), *Shale Tectonics*. American Association of Petroleum Geologists, p. 0. <https://doi.org/10.1306/13231313M933423>
- Wignall, P.B. and Best, J.L. (2000), The Western Irish Namurian Basin reassessed. *Basin Research* 12, 59-78

- Wignall, P.B. and Best, J.L. (2016) Basin models. In: A Field Guide to the Carboniferous Sediments of the Shannon Basin, Western Ireland (Eds J.L. Best and P.B. Wignall), Int. Assoc. Sedimentol. Field Guide, 35–47
- Willcox, J.B. and Stagg, H.M.J., 1990. Australia's southern margin: a product of oblique extension. *Tectonophysics*, 173, 269–281.
- Williams, M.C., Trehu, A.M., Braunmiller, J., 2002. Seismicity at the Cascadia Plate Boundary beneath the Oregon Continental Shelf. *Bulletin of the Seismological Society of America* 101(3):940-950. DOI: [10.1785/0120100198](https://doi.org/10.1785/0120100198)
- Williams, H.F.L., Hutchinson, I., Nelson, A.R., 2005. Multiple sources for late-Holocene tsunamis at Discovery Bay, Washington State, USA. *The Holocene* 15, 60–73. <https://doi.org/10.1191/0956683605hl784rp>
- Williams, S., Whittaker, J.M. and Muller, R.D., 2011. Full-fit, palinspastic reconstruction of the conjugate Australian-Antarctic margins. *Tectonics*, 30, TC6012
- Wilson, D. S., P. A. McCrory, and R. G. Stanley (2005), Implications of volcanism in coastal California for the deformation history of western North America, *Tectonics*, 24, TC3008, doi:10.1029/2003TC001621
- Wiltschko, D.V., Chapple, W.M., 1977. Flow of weak rocks in Appalachian plateau folds. *AAPG Bull.* 61, 6535–6570
- Withjack, M.O., Scheiner, C., 1982. Fault patterns associated with domes: an experimental and analytical study. *Am. Assoc. Pet. Geol., Bull.; (United States)* 66:3.
- Winker, C. D., and M. B. Edwards (1983), Unstable progradational clastic shelf margins, in *The Shelfbreak: Critical Interface on Continental Margins*, edited by D. J. Stanley and G. T. Moore, *Spec. Publ. Soc. Econ. Paleontol. Mineral.*, 33, 139 – 157.
- Wood, 2000. Chronostratigraphy and tectonostratigraphy of the Columbus Basin, eastern offshore Trinidad. *Bulletin* 84. <https://doi.org/10.1306/8626C721-173B-11D7-8645000102C1865D>
- Wood, L.J., 2010. *Shale Tectonics: AAPG Memoir 93*. AAPG.
- Wood L.J., in *Regional Geology and Tectonics: Phanerozoic Passive Margins, Cratonic Basins and Global Tectonic Maps*, published by David G. Roberts, A. W. Bally, 2012. DOI: 10.1016/B978-0-444-56357-6.00002-0
- Worrall, D.M., Snelson, S., 1989. Evolution of the northern Gulf of Mexico, with emphasis on Cenozoic growth faulting and the role of salt, in: Bally, A.W., Palmer, A.R. (Eds.), *The Geology of North America—An Overview*. Geological Society of America, pp. 97–138. <https://doi.org/10.1130/DNAG-GNA-A.97>
- Wright, J. E., and S. J. Wyld (2006), Gondwanan, Iapetan, Cordilleran interactions: A geodynamic model for the Paleozoic tectonic evolution of the North American Cordillera, in *Paleogeography of the North American Cordillera: Evidence for and Against Large-Scale Displacements*, edited by J. W. Haggart, R. J. Enkin, and J. W. H. Monger, *Geol. Assoc. Can. Spec. Pap.*, 46, 377–408
- Wu, S., Bally, A.W., 2000. Slope tectonics – Comparisons and contrasts of structural styles of salt and shale tectonics of the Northern Gulf of Mexico with shale tectonics of offshore Nigeria in Gulf of Guinea. In: Mohriak, W., Talwani, M. (Eds.), *Atlantic Rifts and Continental Margins*. *Geophys. Mono. Vol. 115*. AGU, Washington, pp. 151–172.
- Wu, J.E., McClay, K.R., 2011. Two-dimensional analog modelling of fold and thrust belts: dynamic interactions with syncontractional sedimentation and erosion. *AAPG Bull.* 94, 301–333.

- Wu, J., McClay, K., and de Vera, J., 2019, Growth of triangle zone fold-thrusts within the NW Borneo deep-water fold belt, offshore Sabah, southern South China Sea: *Geosphere*, v. 16, no. X, p. 1–28, <https://doi.org/10.1130/GES02106.1>.

(X)

- Xiaodong Yang, Frank J. Peel, Lisa C. McNeill, David J. Sanderson, 2020. Comparison of fold-thrust belts driven by plate convergence and gravitational failure. *Earth-Science Reviews* 203 (2020) 103136. <https://doi.org/10.1016/j.earscirev.2020.103136>
- Xu, S., Zheng, D., Zhu, G., Yang, S., Li, C. & Yang, C. 2012. Main controlling factors and models of gas accumulation in back arc depression of Andaman Sea, Burma. *Journal of Earth Science & Environment* 34, 29–34.

(Y)

- Yang, X., Peel, F.J., McNeill, L.C., Sanderson, D.J., 2020. Comparison of fold-thrust belts driven by plate convergence and gravitational failure. *Earth-Science Reviews* 203, 103136. <https://doi.org/10.1016/j.earscirev.2020.103136>
- Yardley, G. (1999) Lateral Transfer: a Source of Extreme Overpressure? Intended for publication in *Marine and Petroleum Geology*.
- Yardley, G.S.; Swarbrick, R.E. Lateral transfer: A source of additional overpressure? *Mar. Pet. Geol.* 2000, 17, 523–537.
- Yin, H., Jr, R.H.G., 2007. A three-dimensional kinematic model for the deformation above an active diapir. *AAPG Bulletin* 91, 343–363. <https://doi.org/10.1306/10240606034>
- Yuan, B., W. Xie, G. Liu, and C. Zhang (2012), Gravity field and tectonic features of Block L2 in the Lamu basin, Kenya, *Geophys. Prospect.*, 60, 161–178, doi:10.1111/j.1365-2478.2011.00961.x
- Yuasa, M., Niida, K., Ishihara, T., Kisimoto, K. and Murakami, F., 1997. Peridotite dredged from a seamount off Wilkes Land, The Antarctic: emplacement of a fertile mantle fragment at early rifting stage between Australia and Antarctica during the final breakup of Gondwanaland. In: *The Antarctic Region: Geological Evolution and Processes* (C.A. Ricci, ed.), pp. 725–730. Terra Antarctica, Siena.

(Z)

- Zanella, A., Cobbold, P.R., Rojas, L., 2014. Beef veins and thrust detachments in Early Cretaceous source rocks, foothills of Magallanes-Austral Basin, southern Chile and Argentina: structural evidence for fluid overpressure during hydrocarbon maturation. *Mar. Pet. Geol.* 55, 250–261
- Zhang, J.C. Effective stress, porosity, velocity and abnormal pore pressure prediction accounting for compaction disequilibrium and unloading. *Mar. Pet. Geol.* 2013, 45, 2–11
- Zhu, G., Xie, X. & Qiu, C. 2010. Petroleum geology and exploration potential in back-arc strike slip and extension basins: a case of Martaban Bay Basin in Andaman Sea, Myanmar. *China Offshore Oil & Gas* 22, 225–31.
- Zielinski, G.W., Bjorøy, M., Zielinski, R.L.B., Ferriday, I.L., 2007. Heat flow and surface hydrocarbons on the Brunei continental margin. *AAPG Bull.* 91, 1053–1080
- Zonenshain, L. P. & Le Pichon, X. 1986. Deep basins of the Black Sea and Caspian Sea as remnants of Mesozoic back-arc basins. *Tectonophysics*, 123, 181–211

Abstract:

Shale deforms under three major principles; (i) seismic scale plasticity (folding and faulting), (ii) fluidization (mud volcanism), and (iii) ductile strain/plasticity (distributed slow motion) and can mimic salt deformation under stress and strain. Ductility of these two rocks are governed by processes taking place beyond the 'scale of observation' (e.g. principle of crystalline plasticity for salt; shear bands, folding and faulting for shale) and 'distributed deformation'. Certain controlling factors such as confinement pressure, temperature, water content, rate of loading, and amount of sedimentation, define the ductile behavior of these rocks. When these controlling factors are met, ductile rocks (e.g. salt and shale) display behavioral similarity to viscous materials (e.g. fluids) in nature and their specific deformation-related signature (e.g. halokinesis and argilokinesis) can be recorded within the sedimentary package surrounding these rock formations.

However, the mobilization pattern of shales and hence the topic of *Shale Tectonism* is not yet as-well-identified-as salt due to the usual bad quality of acquired subsurface data (seismic) and the lack of well-preserved outcrop examples we are able to access around the world. Even though certain structures depicted as 'diapirs', 'canopy features', 'minibasins' and 'welds' have been recorded by the surrounding sedimentary cover in some natural cases and reported by researchers; unlike salt, no such conclusive remarks are made on the topic of shale mobility.

In this PhD study, we worked on a well-imaged high-quality 3D seismic dataset and aimed to make a geometrical analysis of deformation in a shale-prone system (Ceduna Sub-Basin located in Great Bight Basin, Offshore Australia) in order to compare it with Salt Tectonics. The main purpose was to display the importance of mobilized shales on the structural development as well as proposing a kinematic scenario for the whole deltaic system (White Pointer Delta) driven above a thick shale detachment level (Blue Whale Formation). We later combined our seismic findings with the fieldwork observations conducted in Rakhine State, Myanmar to strengthen its credibility. Following our research, we have come to realization that;

- At large scale; shales display plastic deformation pattern and behave like a fluid in a viscous manner mimicking salt deposits, while the deformation signature associated with shale mobilization can be recorded by the sediment strata surrounding these shale remnants (e.g. argilokinesis).
- From technical point of view, observed features such as wedges, welds, minibasins, and evolution towards a thrust duplex points out to a change in shale rheology expressed with a plastic deformation pattern and viscous-like flow of shales.
- Different than salt, shales can be fluidized and emerge as mud volcanoes in various geolocations on Earth. However, when investigated with well-imaged seismic datasets and supplementary outcrop studies, certain internal mechanisms differentiate from simple Salt Tectonism. In the studied Ceduna Sub-Basin area, we proposed a duplexation mechanism for initiation of shale mobility above the early down-building structures.

It is of utmost importance to further investigate these analogies in order to conclude on the fact that at large scale; shale can mimic salt deformation and the concept of Salt Tectonics can be applied to Shale Tectonics with certain internal mobilization mechanisms such as; duplexation of the thrust domain, sub-seismic scale fish-tailing, while the fluidization of shales and free gas content lead to mud volcanism different than salt. First hand results of our research support this idea and encourage a promising path for the way forward.

Key Words: Shale Tectonics, Ceduna Sub-Basin, White Pointer Delta, Shale Mobilization, Argilokinesis